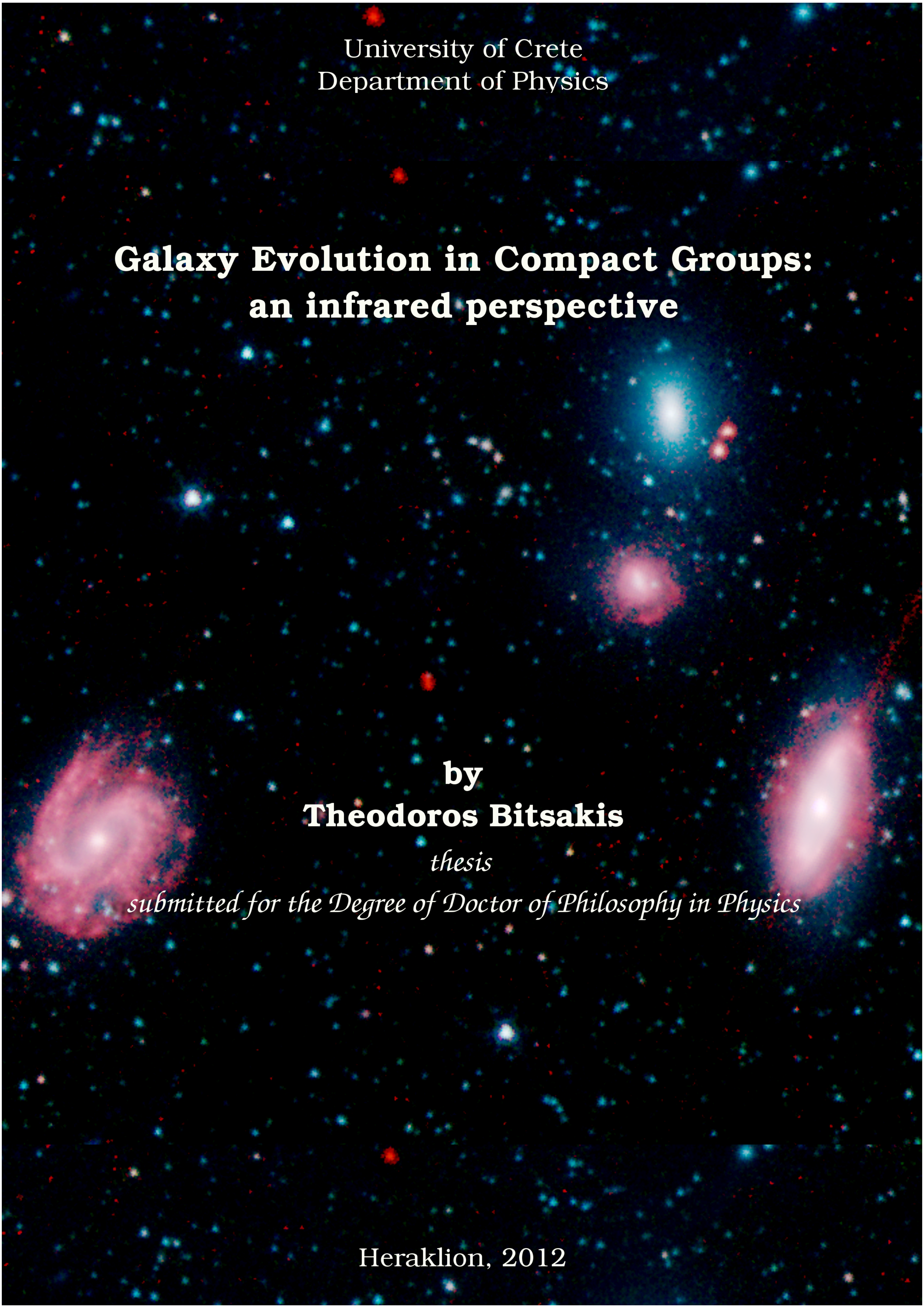

University of Crete
Department of Physics

Galaxy Evolution in Compact Groups: an infrared perspective

by
Theodoros Bitsakis

thesis
submitted for the Degree of Doctor of Philosophy in Physics

Heraklion, 2012

UNIVERSITY OF CRETE
DEPARTMENT OF PHYSICS

PhD THESIS

submitted for the degree of

DOCTOR OF PHILOSOPHY
IN
- PHYSICS -

by
Theodoros BITSAKIS

Galaxy Evolution in Compact Groups: an infrared perspective

COMMITTEE

Prof. Vassilis Charmandaris - UNIVERSITY OF CRETE (ADVISOR)
Dr. Emeric Le Floc'h - CEA/SACLAY (CO-ADVISOR)
Prof. Andreas Zezas - UNIVERSITY OF CRETE
Prof. Iosif Papadakis - UNIVERSITY OF CRETE
Prof. Nikos Kylafis - UNIVERSITY OF CRETE
Prof. Christos Chaldoupis - UNIVERSITY OF CRETE
Prof. Nikos Papanikolaou - UNIVERSITY OF CRETE

Date of the defense: December 07, 2012

Περὶληψη

Παρουσιάζουμε τα αποτελέσματα μας σχετικά με τις επιπτώσεις του περιβάλλοντος των συμπαγών ομάδων γαλαξιών στην εξέλιξη των μελών τους. Πραγματοποιήσαμε ανάλυση, από το υπεριώδες έως το μακρινό υπέρυθρο, για 32 συμπαγείς ομάδες γαλαξιών του Hickson, για τις οποίες αποκτήσαμε δεδομένα στο μέσο υπέρυθρο, από το διαστημικό τηλεσκόπειο Spitzer. Για να επεκτείνουμε την ανάλυση μας χρησιμοποιήσαμε και έναν αρκετά μεγαλύτερο και πιο πλήρη κατάλογο, αποτελούμενο από 1770 συμπαγείς ομάδες γαλαξιών, οι οποίες προσδιορίστηκαν εφαρμόζοντας τα κριτήρια του Hickson σε ολόκληρη την βάση δεδομένων του Sloan Digital Sky Survey. Στη συνέχεια προσαρμόσαμε τις Φασματικές Κατανομές Ενέργειας (SEDs) για όλους τους γαλαξίες του πρώτου δείγματος, χρησιμοποιώντας το θεωρητικό μοντέλο της da Cunha et al. (2008), υπολογίσαμε με ακρίβεια τις αστρικές μάζες, τον ρυθμό σχηματίσμου αστέρων (SFR), την απορρόφηση απο την σκόνη, καθώς και τις υπέρυθρες φωτεινότητες τους. Επίσης πραγματοποιήσαμε φωτομετρία στο υπεριώδες και υπολογίσαμε τις λαμπρότητες στο κοντινό και μέσο υπέρυθρο όλων των γαλαξιών στο κατάλογο που επιλέχθηκε απο το SDSS, με σκοπό να εξερευνήσουμε πως οι επιφανειακές λαμπρότητες, ο ρυθμός σχηματισμού άστρων, καθώς και η δραστηριότητα στον πυρήνα ποικίλλουν ως συνάρτηση του περιβάλλοντός τους. Ως δείγματα σύγκρισης χρησιμοποιήσαμε γαλαξίες που βρίσκονται στο πεδίο, σε αλληλεπιδρώντα ζεύγη, καθώς και σε γαλαξιακά σμήνη. Βρήκαμε ότι η κατηγοριοποιήση της εξελικτικής κατάστασης των συμπαγών ομάδων ως δυναμικά νέες και δυναμικά παλαιές, ανάλογα με το αν περιέχουν (ή όχι) λιγότερο από 25% ελλειπτικούς γαλαξίες, έχει φυσικό νόημα και είναι συνεπής με προήγουμενες κατηγοριοποιήσεις. Οι σπειροειδείς γαλαξίες στις δυναμικά νέες ομάδες έχουν ειδικό ρυθμό σχηματισμού άστρων, καθώς και χρώματα, στο οπτικό και υπέρυθρο, τα οποία είναι παρόμοια με αυτά γαλαξιών στο πεδίο ή σε αλληλεπιδρώντα ζεύγη. Αντιθέτως, οι σπειροειδείς γαλαξίες σε δυναμικά παλαιές ομάδες έχουν πιό κόκκινα χρώματα, καθώς αύξησαν τις άστρικές τους μάζες στο παρελθόν, κατα τη διάρκεια βαρυτικών αλληλεπιδράσεων. Εν τούτοις, οι κατανομές μάζας των σπειροειδών γαλαξιών με ενεργό πυρήνα είναι ανεξάρτητες από τη δυναμική κατάσταση της ομάδας τους. Όλα τα παραπάνω συμπεράσματα συστήνουν μιά εξελικτική διαδικασία κατά την οποία απαιτείται χρόνος ώστε το περιβάλλον να επηρεάσει σημαντικά τις διάφορες ιδιότητες των γαλαξιών. Τα αποτελέσματα των βαρυτικών αλληλεπιδράσεων και της συγχώνευσης μεταξύ γαλαξιών, διαμορφώνουν τη μορφολογία και την ιστορία σχηματισμού άστρων των συμπαγών ομάδων, οδηγώντας στην αύξηση του αριθμού των ελλειπτικών γαλαξιών που περιέχουν, καθώς και στην αύξηση της αστρικής μάζας των εναπομεινόντων σπειροειδών.

Abstract

We present our results on the impact of the environment of compact galaxy groups to the evolution of their members. We performed multiwavelength analysis, from the ultraviolet (UV) to the far-infrared (far-IR), for the 32 Hickson Compact Groups (HCGs) for which high quality Spitzer mid-IR maps were available. To expand our analysis we have used a larger more complete sample of 1770 compact groups defined by applying the Hickson's criteria to the whole Sloan Digital Sky Survey (SDSS) database. We have fitted the Spectral Energy Distributions (SEDs) of all galaxies of the first sample, using the state-of-the-art model of da Cunha et al. (2008) and accurately estimated their stellar masses, star formation rates (SFRs), and extinction, as well as their infrared luminosity and dust content. We have also performed photometry in the UV, using the Galaxy Evolution Explorer (GALEX) space telescope for all the galaxies in the SDSS groups. Additionally, we collected their near-IR and mid-IR fluxes, using the Two Micron All Sky Survey (2MASS) and the Wide-field Infrared Survey Explorer (WISE) respectively, in order to examine how their surface brightnesses (SBs), SFRs and nuclear activity vary as a function of their environment. As comparison/control samples we have used galaxies in the field, early-stage interacting pairs, and clusters. We find that classifying the evolutionary state of compact groups as dynamically "young" (or "old") depending on whether (or not) they contain less than 25% of early-type galaxies is physical and consistent with past classifications. Late-type galaxies in "young" groups have specific SFR, as well as NUV-r and mid-IR colors, which are similar to those of field and interacting pairs. However, late-type galaxies in "old" groups display redder colors, as they had built-up their stellar masses due to numerous tidal encounters in the past. Nevertheless, the mass distributions of late-type galaxies hosting an AGN are independent of the dynamical state of their group. Finally, we find that the SB profiles of the late-type galaxies evolve into earlier type systems before their SFR is reduced substantially. We suggest an evolutionary scenario in which it takes time for the group environment to visibly affect the properties of its members. The effects of tidal torques and minor merging shape the morphology and star formation history of the group galaxies, leading to an increase of the fraction of early-type members and a rapid built-up of the stellar mass in the remaining late-type systems.

To my grandfathers,
Thodoris Bitsakis† and Michalis Giannikakis

Acknowledgements

I would like to thank my supervisor V. Charmandaris for his patient guidance and support all these years. I am very grateful to E. Le Floc'h and T. Díaz-Santos for their suggestions and excellent comments.

I also acknowledge the members of the PhD committee, N. Kylafis, A. Zezas, I. Papadakis, C. Chaldoupis, and N. Papanikolaou, for their useful suggestions/discussions.

In addition, I would like to thank the people of Skinakas Observatory, G. Paterakis, T. Kougentakis, A. Steiakaki, and M. Paleologou, as well as my colleagues, P. Bonfini and G. Maravelias for their help in technical/scientific issues. I am also indebted to E. Vardoulaki and T. Karachalios for helping me correct this thesis.

Last but not least, I thank my family and friends for their love and support in good and difficult times.

The research for this thesis was partially supported by the European Union ToK grant 39965 and FP7-REGPOT 206469.

Contents

List of Figures **vii**

List of Tables **ix**

Glossary **xi**

1 Introduction **1**

1.1 Historical background 1

1.2 Galaxy formation 4

1.2.1 Dark matter in the early Universe 5

1.2.2 Structure and energy production in a galaxy 5

1.2.3 Galaxy interactions 10

1.2.3.1 Early observations 11

1.2.3.2 Tidal interactions and merging 11

1.2.4 Early-type galaxies: the final product of galaxy interactions . . . 14

1.3 Spatial distribution of galaxies 16

1.3.1 Clusters of galaxies 17

1.3.2 Groups of galaxies 18

1.3.2.1 Loose groups 19

1.3.2.2 Compact groups 20

1.4 Goals and description of this thesis 22

2 Samples and observations **25**

2.1 The samples 25

2.1.1 The Hickson Compact Group samples 25

2.1.2 The SDSS compact group sample 26

2.1.2.1 Sample selection 28

2.1.2.2 Galaxy classification 28

2.1.3 The control samples 32
2.1.3.1 Field galaxies 32
2.1.3.2 Interacting pairs 33
2.1.3.3 Cluster galaxies 33
2.2 The observations 33
2.2.1 Ultraviolet: Observing the stellar nurseries 35
2.2.2 Visible: Observing from the Earth 37
2.2.3 Near infrared: Looking at the old stars 39
2.2.4 Mid infrared: The signature of PAHs and dust 44
2.2.5 Far infrared: Unveiling the dust 48

3 Estimating the physical parameters 51
3.1 Empirical estimation of the physical parameteres 51
3.1.1 Stellar masses 51
3.1.2 Extinction correction and star formation rates 52
3.1.3 Specific star formation rates 54
3.2 Model derived physical parameters 55
3.2.1 LePHARE 55
3.2.2 MAGPHYS 57
3.2.2.1 Description of the model 58
3.2.2.2 Model library 59
3.2.2.3 Spectral energy distribution fits 60
3.2.3 Modeling the emission lines of the SDSS CG sample 60
3.3 Comparison of the empirical and theoretical modeling results 64
3.3.1 Evaluating the LePhare estimates 64
3.3.2 Evaluating the MAGPHYS estimates 65
3.3.3 Evaluating the emission line modeling results 68

4 Physical properties of the HCG galaxies 73
4.1 Evolutionary state of compact galaxy groups 73
4.2 Model derived physical properties 76
4.2.1 Stellar masses 76
4.2.2 Star formation rates 77
4.2.3 Specific SFRs 77
4.2.4 Infrared luminosities 78
4.2.5 Dust extinction 78
4.3 Late-type galaxies in groups 81

4.3.1 Enhanced stellar mass in dynamically "old" late-type systems . . 82
4.3.2 The Schmidt-Kennicutt law in HCG late-type galaxies 83
4.4 Early-type galaxies in groups 86
4.5 The colors of HCG galaxies 88
4.5.1 The UV-optical color bimodality 89
4.5.1.1 Color bimodality in field and cluster galaxies 89
4.5.1.2 The UV-optical colors of HCG galaxies 89
4.5.1.3 Extinction and the effects of dust 94
4.5.2 IRAC colors and AGN diagnostics 96
4.6 Dynamical properties of HCGs 99
4.6.1 Virial radius and neighbors distance 99
4.6.2 The mass content of compact groups 102
4.7 The impact of the compact group environment to the gas content 105
4.8 Cold dust in the intra-group medium 108

5 The SDSS CG sample 111
5.1 Evaluating the SDSS-HCG galaxy properties 112
5.1.1 Stellar masses 112
5.1.2 Star formations rates 115
5.1.3 Specific SFRs 115
5.1.4 UV-optical colors 118
5.1.5 The fractions and properties of the AGN-hosting galaxies in compact groups 120
5.2 Examining the radial profiles of the galaxies 122

6 Conclusions and future perspectives 127
6.1 Summary of the conclusions 127
6.2 The effects of tidal interactions in galaxies 129
6.3 Future perspectives 130
6.3.1 Ascertain group membership in the SDSS CG sample 130
6.3.2 Identify the presence of diffuse cold dust in the intragroup medium and complete the far-IR SEDs of HCG galaxies 131
6.3.3 Evolution of metallicity in the SDSS CG sample 133

A Publications 135

B HCG infrared morphology 223

References **263**

List of Figures

1.1 Herschel's view of our Galaxy . . . 2
1.2 The nebula of Andromeda . . . 3
1.3 Hubble's tuning fork diagram . . . 4
1.4 Millenium simulation . . . 6
1.5 Examples of late-type galaxies in the optical . . . 7
1.6 Integrated late-type galaxy spectra . . . 8
1.7 The mid-IR PAH emission features . . . 9
1.8 The classic BPT diagram . . . 10
1.9 The Antennae galaxies . . . 12
1.10 Rate of past merger remnants (Toomre's plot) . . . 13
1.11 Shells and ripples in galaxies . . . 14
1.12 Examples of early-type galaxies . . . 15
1.13 Integrated early-type galaxy spectra . . . 17
1.14 The Leo triplet . . . 19
1.15 Stephan's Quintet . . . 21

2.1 Multi-color Seyfert's Sextet . . . 27
2.2 Compact groups viewed by SDSS and WISE . . . 29
2.3 Redshift distributions of SDSS CGs . . . 29
2.4 Nuclear classification of the SDSS CG galaxies . . . 30
2.5 Galaxy classification of the SDSS CG sample . . . 31
2.6 Examples of the comparison samples . . . 32
2.7 The photometric band ranges . . . 34
2.8 Earth's atmospheric transmission . . . 35
2.9 GALEX - Stephan's Quintet . . . 36
2.10 Automated and manual UV photometry . . . 37
2.11 The Apache Point and CFHT observatories . . . 38

2.12 Dithering and On-Off methods in the near-IR 40
2.13 Skinakas Observatory 42
2.14 Skinakas NIR imaging of HCG 82 43
2.15 Spitzer Space Telescope images 45
2.16 Infrared Space Observatory 46
2.17 Far-Infrared Space Observatories (IRAS and AKARI) 49

3.1 Examples of LePhare SEDs 56
3.2 Example of model infrared SED 59
3.3 Examples of fitted observed SEDs 61
3.4 The observed relation between D4000 and the sSFR 63
3.5 Comparison of the stellar masses of the galaxies in *sample II* 66
3.6 Comparison of the SFRs 67
3.7 Comparison of the stellar mass ratios of the galaxies in *sample III* . . . 69
3.8 Comparison of the SFRs estimators applied on the galaxies of *sample III* 71

4.1 Examples of dynamically “young” and “old” groups 76
4.2 Distributions of the model derived physical parameters for the galaxies of *sample II* 79
4.3 The model derived extinction 80
4.4 Histograms of the sSFR of the late-type galaxies 83
4.5 The SFR distributions of the late-type galaxies and the Schmidt-Kennicutt law 85
4.6 Mid-IR colors of early-type galaxies 87
4.7 The total distributions of the UV-optical colors 91
4.8 Early and late-type galaxy UV-optical colors 92
4.9 Attenuated UV-optical in young and old groups 93
4.10 Unattenuated UV-optical colors in young and old groups 95
4.11 Stern mid-IR color diagnostic 97
4.12 HCG mid-IR color plot 98
4.13 The “strength” of dynamical interaction. 101
4.14 Distributions of the mass content of HCGs 103
4.15 HCG spectral characteristics 107
4.16 HCG spectral features versus sSFR 108
4.17 Cold dust in the intragroup medium 110

5.1 Stellar mass distribution of the galaxies in *sample III* 113

5.2 The stellar mass distributions in different dynamical states of the galaxies in *sample III* 114
5.3 The SFRs of the galaxies in *sample III* 116
5.4 The specific star formation rates of the galaxies in *sample III* 117
5.5 The UV-optical color bimodality in SDSS CG galaxies 119
5.6 The AGN fractions of the SDSS CG galaxies 121
5.7 The sSFR versus the n_{Sersic} in *sample III* 123
5.8 Distributions of the Sersic indices of the "green valley" late-type galaxies of *sample III* 125

6.1 Constraining galaxy SED fitting parameters using Herschel bands 132

A.1 SDSS spectra of the misclassified spirals 188

B.1 HCG 2 224
B.2 HCG 4 225
B.3 HCG 6 226
B.4 HCG 7 227
B.5 HCG 8 228
B.6 HCG 15 229
B.7 HCG 16 230
B.8 HCG 19 231
B.9 HCG 22 232
B.10 HCG 25 233
B.11 HCG 33 234
B.12 HCG 37 235
B.13 HCG 38 236
B.14 HCG 40 237
B.15 HCG 42 238
B.16 HCG 44 239
B.17 HCG 47 240
B.18 HCG 48 241
B.19 HCG 51 242
B.20 HCG 54 243
B.21 HCG 55 244
B.22 HCG 56 245
B.23 HCG 57 246

B.24 HCG 59 247
B.25 HCG 61 248
B.26 HCG 62 249
B.27 HCG 67 250
B.28 HCG 71 251
B.29 HCG 75 252
B.30 HCG 79 253
B.31 HCG 82 254
B.32 HCG 90 255
B.33 HCG 91 256
B.34 HCG 92 257
B.35 HCG 95 258
B.36 HCG 96 259
B.37 HCG 97 260
B.38 HCG 100 261

List of Tables

2.1 Summary of the samples 30
2.2 Summary of the observations held with the Skinakas NIR camera. 43
2.3 Observational Parameters of Spitzer Archival Data 47

4.1 Evolutionary classifications of the groups of samples I and II. 75
4.2 Efficiencies of compact group galaxies in Fig. 4.5b. 86

5.1 Fractions of SDSS CG galaxies in the NUV-r colorspace. 119

Glossary

AGB	Asymptotic Giant Branch; region of the Hertzsprung-Russell diagram populated by evolving low to medium-mass stars, which appear as red-giants
AGN	Active Galactic Nucleus; is a compact region at the centre of a galaxy that has very high luminosity. It is believed to be a result of accretion of mass by the supermassive black hole
CCD	Charged Couple Device; is a device which uses the movement of electrical charge for the purposes of digital imaging
HCG	Hickson Compact Groups; compact groups of galaxies which were defined using the criteria of Hickson (1982)
IMF	Initial Mass Function; is an empirical function that describes the mass distribution (the histogram of stellar masses) of a population of stars in terms of their theoretical initial mass
IR	Infrared; light between wavelength range of 8-1000μm. It is separated into near-IR, mid-IR, and far-IR
ISM	Interstellar Matter; is the gas and dust which is found in the interstellar space of a galaxy
KS-test	Kolmogorov-Smirnov test; is a statistical test that can be used to compare two samples. It quantifies a distance between the empirical distribution functions of two samples. When the probability is less than 1% the two samples are significantly different
OB stars	young newly born stars with very high masses and surface temperatures ($\sim$10000K) which radiation peaks at the UV wavelengths
PAH	Polycyclic Aromatic Hydrocarbons; large molecules which absorb the UV light and re-emit it in the mid-IR
PSF	Point Spread Function; describes the 2D distribution of light in the detectors focal plane for astronomical point sources
pc	parsec; unit of length. The distance corresponding to a parallax of one second ($3.0857 \cdot 10^{16}$ m)
SED	Spectral Energy Distribution; is the distribution of energy of a galaxy in all the wavelengths
SFR	Star Formation Rate; the rate with which a galaxy forms stars, in solar masses per year
SMBH	Super-Massive Black Hole; Such black holes are found in the centers of galaxies. They have large masses of more than $\sim 10^6$ M$_\odot$

GLOSSARY

sSFR	Specific Star Formation Rate; the SFR per unit mass, in Gyr^{-1}
ULIRG	Ultraluminous Infrared Galaxy; a galaxy in which a powerful starburst is taking place into its nucleus ($\mathrm{L} \sim 10^{12} \mathrm{L}_{\odot}$)
UV	Ultraviolet; light between wavelength range of 1500-2800Å

1

Introduction

1.1 Historical background

> “Δημὸκριτος πολλῶν καὶ μικρῶν καὶ
> συνεχῶν ἀστὲρων συμφωτιζομὲνων
> ἀλλὴλοις συναυγασμὸν διὰ τὴν
> πὺκνωσην” - Πλοὺταρχος [1]

With these words, Plutarch (46 – 120AD) in his work “Περὶ τῶν ἀρεσκὸντων τοῖς φιλοσὸφοις φυσικῶν δογμὰτων” (The Doctrines of the Philosophers), epitomized the cosmology of Democritus (460 – 370BC); the first person in history who supported the idea that the bright band on the night sky, which the Greeks named “Γαλαξὶας” (The Milky Way), consists of distant stars. Later, Aristotle (384 – 322BC) stated that the Galaxy is “the ignition of the fiery exhalation of some stars which were large, numerous and close together” and that the “ignition takes place in the upper part of the atmosphere, in the region of the world which is continuous with the heavenly motions”. However, for more than two thousand years the pioneering idea of Democritus remained non-demonstrable until 1610. The same year Galileo turned his telescope towards the sky and noticed that the Milky Way was a vast collection of individual stars. Later he wrote that “the Galaxy is nothing else than a congeries of innumerable stars distributed in clusters”.

In 1750, british astronomer T. Wright published his book with the title “An original theory or new hypothesis of the Universe”; there he explained the appearance of the Milky Way as “an optical effect due to our immersion in what locally approximates to

---

[1] “Democritus believes that [galaxy] consists of many small stars, which illuminate each other and they are combined because of their density” - Plutarch.

a flat layer of stars". He speculated that the galaxy might be a rotating body of a large number of stars held together by gravitational forces, similar to the solar system but on a much larger scale. Thus the resulting disk of stars can be seen as a band on the sky from our perspective being inside the disk. This idea was taken up and elaborated by Immanuel Kant (1724-1804) in his "Allgemeine Naturgeschichte und Theorie des Himmels" (Universal Natural History and Theory of Heaven). Kant proposed that the Milky Way was a large disk of stars, which formed from a large spinning cloud of gas. He also suggested the possibility that other nebulae might also be similarly large and distant disks of stars (called "island universes"), introducing for first time in history an astronomy extending beyond the solar system, to galactic and extragalactic realms. Nevertheless, the first attempt to describe the shape of the Milky Way and the position of the Sun within it was done by W. Herschel in 1785. He produced the "image" of the Galaxy (Fig. 1.1) by counting the stars and their positions and he placed the solar system close to the center.

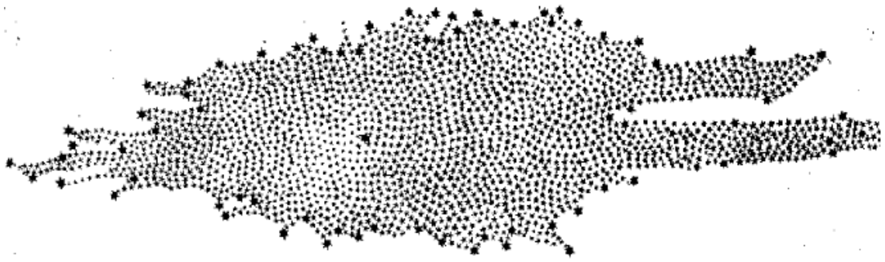

Figure 1.1: The shape of our Galaxy as deduced from W. Herschel (1785) by counting the stars and their positions.

When Kant introduced the hypothesis of the "island universes" there were no data supporting it. However, towards the end of the 18th century, C. Messier compiled a catalog containing 109 brightest objects with nebulous appearance. This catalog was later followed by a larger catalog of 5,000 nebulae assembled by W. Herschel. Few years later, W. Rosse built the "Leviathan of Parsonstown"; a 72-inch telescope, the largest in the world at those days, and using its unique resolution he managed to distinguish between elliptical and spiral nebulae. Using his telescope he was also distinguished individual point sources in some of these nebulae, supporting Kant's earlier speculation. In 1912, V. Slipher performed spectroscopic studies for some of the brightest nebulae and discovered that they display high redshifts, indicating that they are moving away from our Galaxy.

However, at the beginning of the 20th century, the nature and the size of the spiral nebulae and the Universe was still an open question. In 1920, representatives of the two sovereign ideas were H. Shapley, who believed that these nebulae are within our Galaxy, and H. Curtis, who claimed that the nebula of Andromeda is another galaxy. The matter was finally settled in 1923 by a young american astronomer, E. Hubble. Using the 100-inch Mt. Wilson telescope, he identified some Cepheid variable stars which allowed him to estimate the distance of these spiral nebulae and place them beyond the limits of Milky Way (see Fig. 1.2).

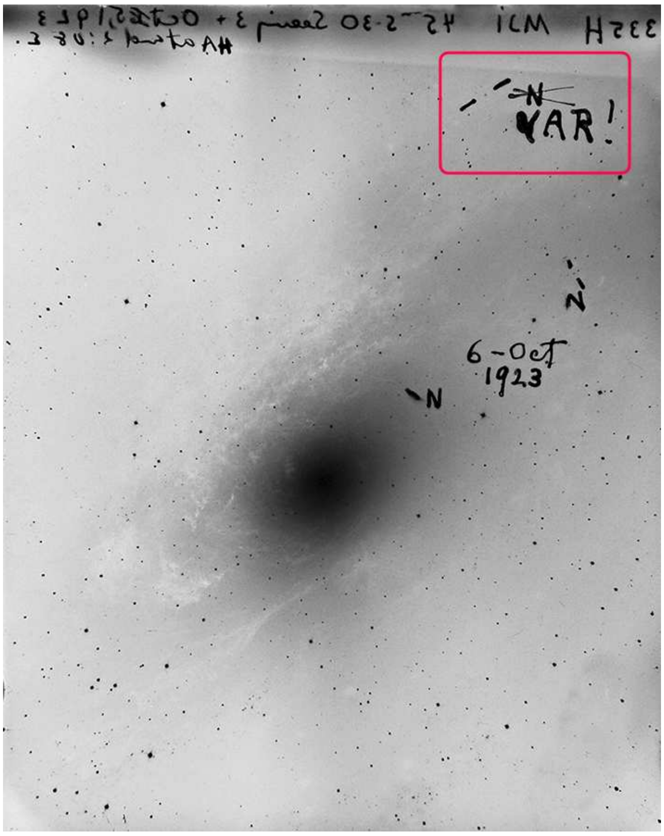

Figure 1.2: The original plate of M31 galaxy (Andromeda) taken by E. Hubble in October 6, 1923. The marked object on the right of the image is the first Cepheid variable.

Few years later, Hubble produced a classification of the nebulae depending on their morphology. This is the famous "Hubble's tuning fork diagram" (Fig. 1.3). According to this classification, galaxies are separated into three main categories based on their visual appearance. The spiral galaxies (S's or SB's) which consist of a flattened disk, spiral structure, and a central bulge, the elliptical galaxies (E's) which are smooth and featureless, and the lenticular galaxies (S0's or SB0's) which are something between the previous two, having a central bulge and a flattened disk but with no evidence of spiral structure. Finally, there is also another category which cannot be included in the previous ones, the irregular galaxies (Irr's), which do not have any obvious regular structure. The reason Hubble placed the galaxies in this order has to do with their several properties and colors, which will explained later. We must note that the former galaxies (E's and S0's) are grouped in one category, displaying very similar properties and they are named early-type galaxies, while the later, S's and Irr's, are grouped in another category are called the late-type galaxies. In the next sections we will show that these galaxies are the ones responsible for actively forming stars.

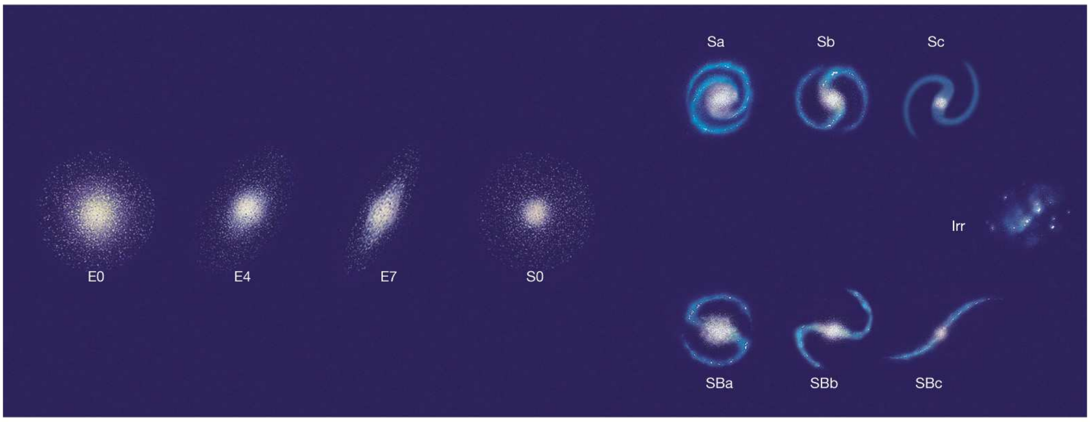

Figure 1.3: The galaxy morphological classification as proposed by E. Hubble in 1932. We can see starting from the left the elliptical, the lenticular, the spiral (with or without bar), and the irregular galaxies. [Image credit: Chasson E. & McMillan S.]

1.2 Galaxy formation

Since the 1930s, when astronomers realized the real nature of the galaxies, several questions emerged concerning the physics and the origin of these systems. How did they form and why do they appear to have such a variety of shapes and colors? In the following years, several of these questions would be answered and others would be born. In the next sections we will briefly describe what we know today about galaxy formation and evolution, as well as, some of the new questions which emerge from the new discoveries.

1.2.1 Dark matter in the early Universe

Just after the Big Bang, inflation expanded the small density perturbations into cosmological scales. Dark matter (matter of non baryonic origin) density non-linearities had as a result the formation of structures such as the filaments and the dark matter halos (see Fig. 1.4). The mass distribution of these dark matter halos can be described by the Press & Schechter (1974) relations. The baryons the normal matter, were initially distributed uniformly but then they fell into the gravitational well of the dark matter subhalos[1]. Depending on the mass of the dark matter subhalo, the baryonic matter has to pass from different processes to end-up into its gravitational center. For instance, in low mass subhalos, cold gas collapsed straight to their center. On the other hand in massive subhalos shock heating had as a result the increase in the temperature of gas. This hot gas would eventually end-up also in the center of the subhalo, but in order to do so, it had to radiate to loose energy in several stages. Peebles (1968) showed that in the early Universe, high energy cosmic background photons had cooled dark matter halos through Compton scattering. Eventually, the cooling process mentioned above will be replaced by the metal enrichment of the gas, which cools down through atomic processes, and molecules are formed. As we will discuss later, the molecular cooling is crucial to form stars and galaxies.

1.2.2 Structure and energy production in a galaxy

Once the gas collapses into the cores of theses dark matter structures, it ignites the formation of galaxies. Each dark matter subhalo is capable to produce a galaxy. At this stage the angular momentum of the collapsed material plays a very important role, as it is responsible for the formation of galaxy disks. According to numerical simulations, the conservation of angular momentum has as a result the creation of galactic disks of similar sizes with rotational velocities comparable to the observed ones (Benson, 2010). The disks of spiral galaxies retain some gas, and thus they are sites of ongoing star formation.

The spiral arms of a galaxy are also found on the disk. They are brighter than the rest of the disk since young massive OB stars are created there. Some other features which one can occasionally detect on a spiral galaxy are the galactic bar and the central bulge. Instabilities caused from the interaction (explained in the next section in more detail) of two galaxies may have as a result to the formation of a bar. This makes gas from the outskirts of the galactic disk to loose angular momentum and move towards

---

[1] Subhalos are small dark matter concentrations found within a massive halo

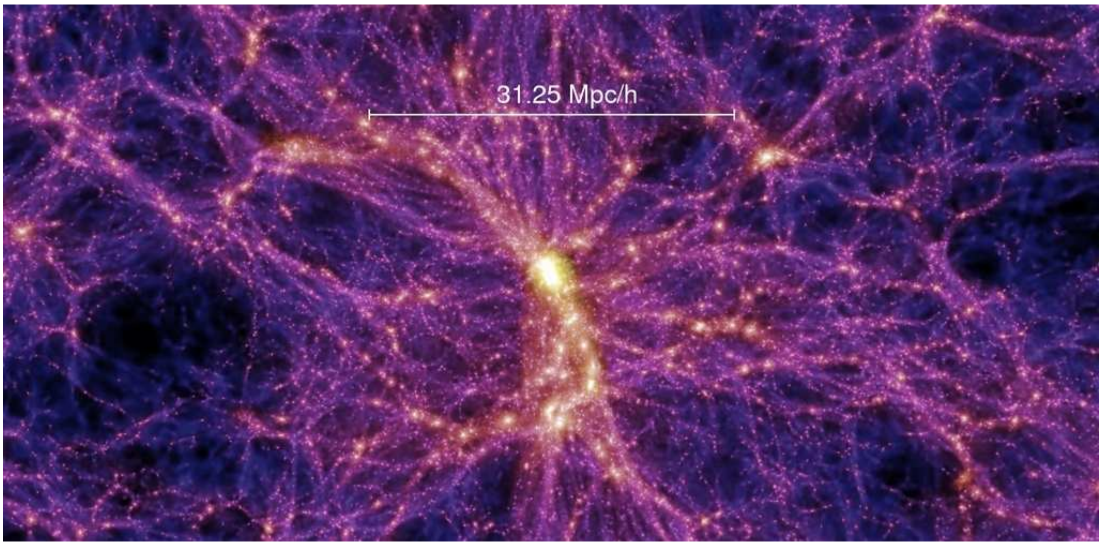

Figure 1.4: Part a numerical simulation which reproduces an image of the early Universe with the creation of dark matter structures. In the middle of the image one can see a large dark matter halo which will eventually form a cluster of galaxies [Image credit: The Millennium Simulation Project]

the center. Then, when it reaches the center the gas decelerates and shocks are created. The shocks lead to the loss of the orbital energy of the gas, which contracts and stars are formed. The result is the creation of the pseudo-bulge in the center of the galaxy.

On the other hand, irregular galaxies do not display any kind of of well defined structure; they do not have any central bulge or spiral arms and they are possibly results of collisions between galaxies. Disk galaxies, as well as irregulars belong to a category of galaxies, with on-going star formation activity, called the late-type galaxies, since they are placed in the late-types of the Hubble's tuning fork diagram. Two typical examples of late-type galaxies are presented in Fig. 1.5.

The azimuthally averaged light profiles of galaxies can be described by the Sersic relation, $I(R) \sim e^{-kR^{1/n}}$, where R is the distance from the center and n is the Sersic index. The disk of a spiral galaxy is described by an exponential brightness profile, $n = 1$, while the central bulge follows a de Vaucouleurs profile, $n = 4$. This result is of great importance in order to ascertain whether a galaxy, with not so obvious spiral structure, is a disk galaxy.

The color of spiral galaxies depends on their Hubble type, with the later types being the bluer. This means that the fraction of massive young blue stars increases along the Hubble sequence. In some cases of spiral galaxies we observe bright knots onto

Figure 1.5: On the left the optical image of a typical barred spiral galaxy (UGC 12158). On the right we can see the Magellanic clouds (LMC and SMC), two irregular galaxies which are visible from the southern hemisphere. [Image credit: Hubble Space Telescope, ESO]

their spiral arms; these are the most active star-forming regions of these galaxies. The formation of stars requires gas, and the gas fraction is greater in later types, as well as in the irregular galaxies. Star forming galaxies have optical spectra similar to those of young hot stars with strong emission lines (an example is presented at Fig. 1.6).

Despite the fact that the dust mass is less than 1% of the gas mass, dust is very important for the evolution of galaxies. It acts as a catalyst for the formation of molecules, as individual atoms of hydrogen and other elements , first “stick” on dust grains and then bond with to each other to form simple and more complex molecules (H_2, CO, HCN, etc.). The resulting cold molecular gas is the fuel for the formation of the next generation of stars. Dust is also the main source of infrared emission from galaxies, in addition to the cool old stars. It absorbs the stellar UV light from the young OB stars and re-emits it in the infrared.

Star formation is one of the most distinct features of late-type galaxies (Kennicutt, 1998). During this process one or more stars are forming as the denser parts of the molecular clouds collapse under their own gravity. As we mentioned above, young stars radiate in the ultraviolet wavelengths, heat up the interstellar dust, and excite the planar aromatic (so called “benzene”) rings of polycyclic aromatic hydrocarbons (PAHs), which in turn stretch and bend in some specific frequencies. Due to different

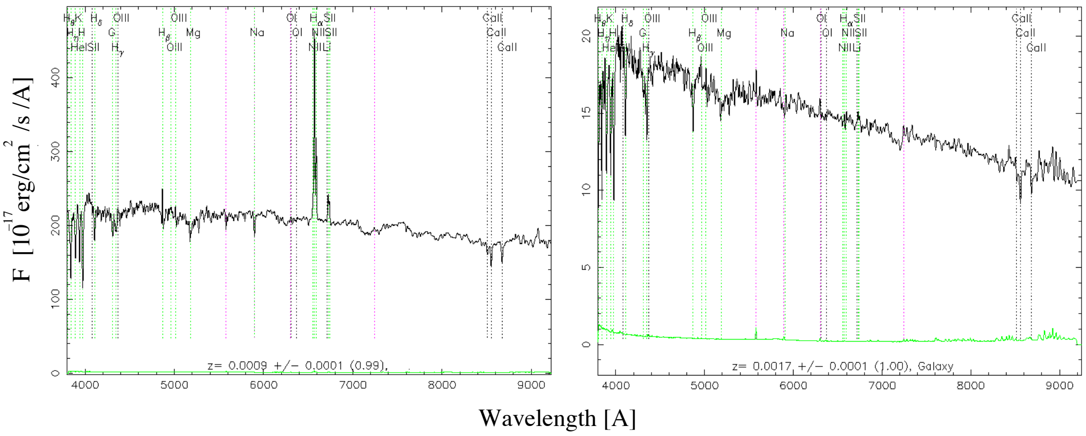

Figure 1.6: On the left, the integrated spectrum of a spiral galaxy (NGC 5457) displaying strong emission lines, sign of starburst activity, as well as, stellar continuum. On the right, the spectrum of an irregular galaxy (NGC 2552) completely dominated by young stars and H_{II} regions. [Image credit: SDSS]

number of carbon atoms in the PAH rings, the emission frequencies vary and they form emission bands around central wavelengths (3.3, 6.2, 7.7, 8.3, 11.3, and 12.7μm; see Fig. 1.7). Since dust and PAHs re-process radiation produced by stars, one may use their infrared emission to estimate the star formation rate (SFR) of a galaxy. These methods, in addition to other more “direct” approaches, such as the photospheric emission by young stars in the UV or the use of hydrogen recombination lines, will be discussed in more detail in Section 3.1.2).

In the central bulge, the gas clouds may collide with each other and as a result they can loose energy and, eventually, sink to form a fast-rotating inner disk. Moreover, as mentioned before, a bar can also transfer disk gas towards the center. There, the gas clouds will collapse to form stars. In all late-type galaxies, there is abundant gas in the central 100pc, and thus, a central starburst is often taking place. This process depends on the amount of available gas and may usually last few hundred million years. Such a powerful starburst, also surrounded by dust, can be seen as a ultraluminous infrared galaxy (ULIRG). These galaxies emit more than 90% of their bolometric luminosities, reaching in excess of $10^{12}L_{\odot}$, in the far-IR (Sparke & Gallagher, 2000).

However, the power source, behind the infrared emission of an ULIRG, can be also a dust enshrouded supermassive black hole (SMBH), which accretes matter in a high rate (Lonsdale *et al.*, 2006). Close to these SMBHs, the matter forms an accretion disk which is heated up. Such supermassive black holes are the energy sources of the so-called

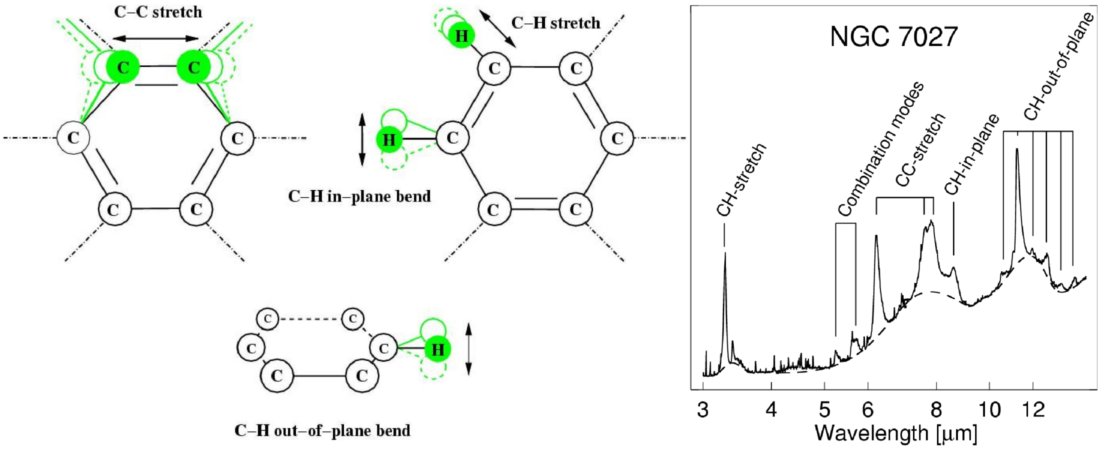

Figure 1.7: The mid-IR PAH emission features. On the left are presented the PAH stretching and bending modes between the C-C and C-H atoms. On the right, it is presented the mid-IR spectra of NGC 7027. We can see which modes are responsible for the several PAH features. [Image from Peeters *et al.* 2004]

Active Galactic Nuclei (AGN). AGN emit strongly over the whole electromagnetic spectrum, from the γ-rays to the radio. In some of these wavelengths (such us γ- and X-rays or radio) most normal galaxies, not hosting an AGN, hardly radiate at all. Many AGN are very luminous at the UV and optical wavelengths; this is sign of contribution from thermal sources (accretion disk), and it appears as the big blue bump in the spectral energy distribution (SED) of these galaxies. Also evident is the thermal infrared bump, due to emission from warm dust grains ($T \leq 1200K$) surrounding the central accretion disk (Carroll & Ostlie, 2006). According to the AGN unification model, the various types of AGN (Seyfert I and II, LINERs, Blazars, and radio galaxies) are all different classes of the same phenomenon, and they depend each time on the orientation of the object.

One can identify an AGN using a set of emission lines of the gas, which probe excitation by photons of different energy. As a result we can trace the strength and hardness of the ionization field and understand whether this can be produced only by stars. We can distinguish those lines into two main categories: (*i*) the broad-permitted lines (e.g. Hα, Hβ) coming from the accretion disk in the inner side of the torus, and (*ii*) the narrow-forbidden lines (e.g. [OIII], [NII]) originating from the gas clouds outside the torrus (Combes *et al.*, 2002). Balwin, Phillips, and Terelevich in 1981, demonstrated a diagnostic method to distinguish the nuclear activity in galaxies according to the relative strength of specific emission lines. The BPT diagram, as it was named, uses the ratios of [OIII]/Hβ against [NII]/Hα (or [OI]/Hα, or [SII]/Hα), to classify starburst and AGN hosted galaxies (see Fig. 1.8).

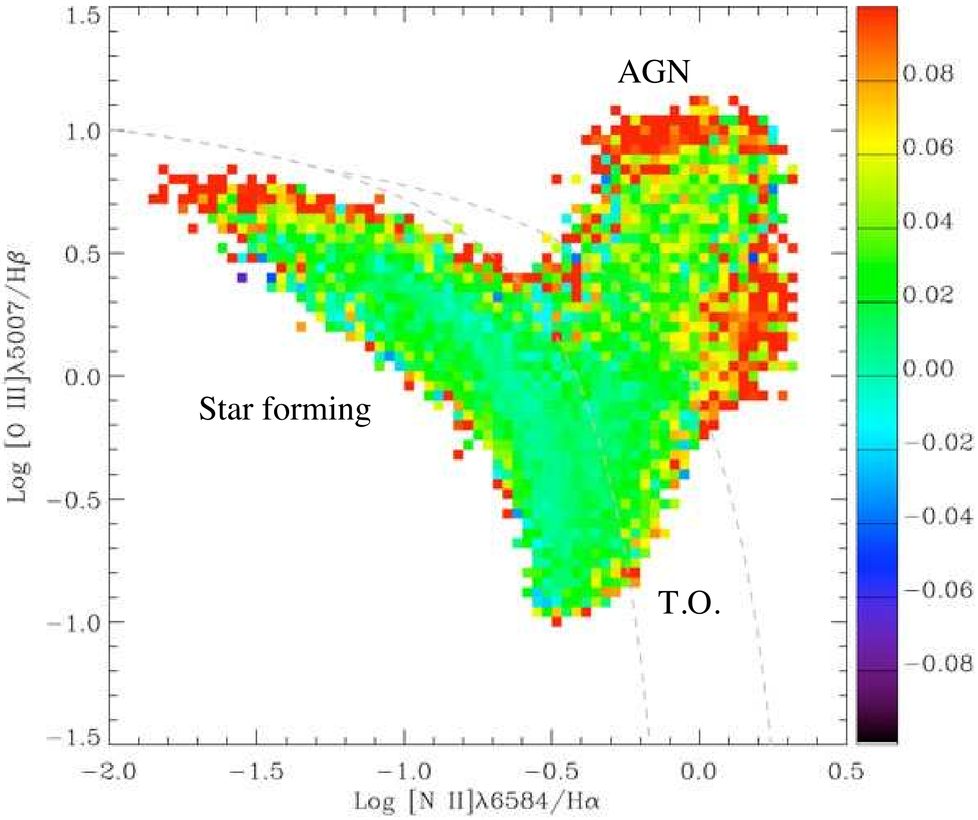

Figure 1.8: The classic BPT diagram of [N II] / Hα versus [O III] / Hβ, showing the distribution of SDSS emission line galaxies. The colors indicate the median logχ^2 of the fit of the Charlot and Bruzual 2008 (CB08) model library to the SDSS fibre spectra with those emission line ratios. The upper and lower dashed lines indicate the Kewley *et al.* (2006) and Kauffmann *et al.* (2003b) AGN dividing lines, respectively. Objects within those lines are classified as Transition Objects (TOs). [Image from Brinchmann *et al.* 2004]

1.2.3 Galaxy interactions

As mentioned before, galaxies evolve within large dark matter halos, usually containing a large number of galaxies. Therefore, gravitational interactions between galaxies occur very often. It has now been established that these interactions are strongly affecting the evolution of the galaxies, and as a consequence (Struck, 1999).

1.2.3.1 Early observations

Galaxy interactions were first studied in the 1940s by a Swedish astronomer, E. Holmberg. Using an analogue computer simulation, he predicted giant tides occurring between the galaxies, as well as a final merger. A decade later L. S. Spitzer and W. Baade introduced the idea of gas "stripping" in high velocity collisions, and they suspected that it should be common in dense galaxy clusters. In the 1960s, using the Palomar all-sky survey, H. Arp, took over a search of peculiar galaxies and published his famous *Atlas of Peculiar Galaxies*. A similar catalog was published by Velyaminov-Vorontsov in 1959 (the VV catalog). However, it was not still certain whether these disturbed systems were the results of tidal interaction between galaxies.

In 1972, Alar and Juri Toomre noted that the observed tails and plumes could be successfully reproduced with models involving collisional encounters. They also showed that such events are unlikely to be the result of galaxies approaching on random hyperbolic orbits (Toomre & Toomre, 1972). Few years later, R. Larson and B. Tinsley found that strongly interacting galaxies tend to be more blue than those of the same type being isolated (Larson & Tinsley, 1978). They suggested that the excess of blue light is emerging from newly born hot stars and that tidal interactions have enhanced the star formation activity in these galaxies. Moreover, a fraction of the light emitted by these bursts at ultraviolet and visible is absorbed by dust and re-emitted in the infrared. Therefore, in 1983 with the launch of the first infrared astronomical satellite (*IRAS*), it was showed that some of these starburst galaxies are indeed extremely bright in the infrared, emitting up to 98% of their luminosity at these wavelengths. In addition Toomre & Toomre (1972) noted another important issue, the connection between galaxy collisions and nuclear activity in galaxies. In the following years numerous observations and numerical simulations greatly improved our understanding on the importance of galaxy interactions.

1.2.3.2 Tidal interactions and merging

We now know that gravitational interactions between dark matter subhalos occur often in the Universe. Each galaxy with its halo will experience tidal forces which may strip outskirts or disrupt the whole galaxy producing a stellar and a gaseous filament. Especially, If these galaxies are spirals, then the stars of each galaxy will "feel" the gravitational potential of their companion which will throw them out of the equilibrium position. As a result, two internal spiral arms may join up to form a bridge which connects the two companions and disappears relatively quickly. On the other hand, the two external spiral arms will create two "antennae" which may remain for more than 2Gyr, as relics of the past interaction (see Fig. 1.9). Eventually, the two dark matter subhalos, which are gravitationally bound to their host halo, and have comparable masses, they will merge. To cause such a gravitational interaction, subhalos require a dissipative process which will reduce the orbital energies of the two galaxies. Dynamic friction, which is defined as the braking of a galaxy by the stars of another galaxy during their interaction, is playing this role by dragging subhalos towards the gravitational center. Such interactions have as a result to increase the velocity dispersions of the stars in the galaxies involved. Then, by destroying the disk structures in spiral galaxies, they make them to relax into an early-type de Vaucouleurs profiles (Carroll & Ostlie, 2006). There cannot be a direct morphological classification for peculiar galaxies, since there is a huge variety of forms. Assuming that the Hubble type of the galaxy can be defined, optical features as well as gas content and kinematical data can be used to identify a given galaxy.

Figure 1.9: The Antennae, two interacting galaxies (NGC 4038 & NGC 4039), both characterized as starburst. [Image credit: Hubble Space Telescope]

In 1977, the Estonian astronomer A. Toomre, observed some interacting galaxy pairs from Arp's catalog of interacting galaxies. Using his results, he tried to estimate the number of remnants from such past interactions. He realized that the number of such past remnants was similar to the number of elliptical galaxies in the present. Thus, he suggested that the elliptical galaxies are the results of the merging process of two or more galaxies of similar masses (Toomre, 1977). Based on the local galaxy merger rate over the Hubble time, he showed that the present number of elliptical galaxies can be explained if the Universe begins only with spiral galaxies (see Fig. 1.10).

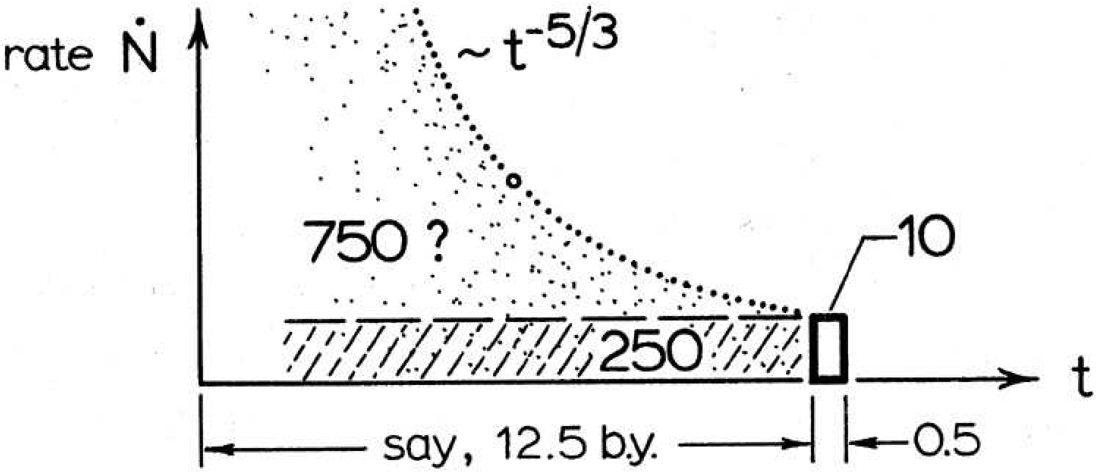

Figure 1.10: In this plot A. Toomre presents the 10 interacting galaxy pairs, which he estimated they would eventually merge within next 0.5 Gyr. Given the age of the Universe accepted at that time to be 12.5 Gyr, one would expect about 250 such remnants in the NGC catalog. If we assume a declining local merger rate (rate $\dot{N}$) over the Hubble time, at Euclidean flat Universe, the total number of such remnants in the present day should be around 750, which coincides with the number of elliptical galaxies in the second reference catalog (2RC). [Image from Toomre 1977]

Furthermore, about 25% of the ellipticals have very different velocity fields in their cores than those of their outer regions. Also, more than half of the ellipticals, as well as, 1/3 of the lenticulars, display faint shells (see Fig. 1.11a). Shells and ripples where discovered by H. Arp in 1961, though they first studied by Malin & Carter (1980), and Schweizer & Seitzer (1988) in 1980s. The shells are very thin and faint filaments, in the form of circular arcs, which actually are the projections of portions of spheres containing stars, centered in the center of the galaxy. Their luminosity is very weak in comparison with the luminosity of the hosting galaxy. However, using new image processing technics we are able to identify them. The shells are forming after the interaction and merging of a massive elliptical and small spiral galaxy. The first will hardly be disturbed in such a collision, whereas the second will lose its stars which, scattered on the gravitational field of the elliptical galaxy, will form the shells (Combes *et al.*, 2002).

Another important issue when two galaxies merge, whether they are spirals or ellipticals, is the formation of a binary system which contains the pre-existing supermassive

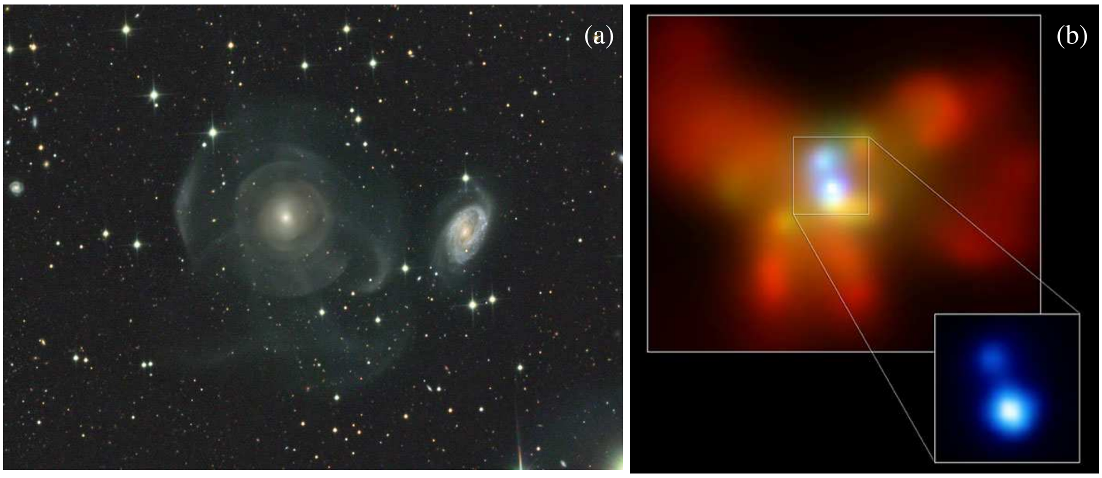

Figure 1.11: (a) Optical shells around NGC 474, related to stellar debris left over from absorbing small galaxies in the past billion years. (b) The X-ray image of NGC 6240, a luminous infrared galaxy produced by the collision of two smaller ones. The central region contains the binary system of the SMBHs. [Image credit: M. Schirmer & Chandra X-ray Observatory]

black holes from the centers of these galaxies. These supermassive black holes will end to the center of the new system, which will be created as result of the dynamical friction of the initial systems. The two black holes will probably form a well-separated binary system, with radius of just few pc (such is the case of NGC 6240; see Fig. 1.11b). These systems can be observed in the X-rays, because of the emission of the matter falling into them. In the end, this binary system will merge into a single system, due to energy loss from gravitational radiation, and angular momentum loss as stars are ejected from the central region.

Finally, as mentioned in the previous section, interactions produce stellar bars. More than 80% of the galaxies, which have a central bar, are found in galaxy binary systems. It has been shown that in the circumnuclear regions of barred galaxies, the gas inflow can result substantial star formation activity, as well as formation and fueling of a central SMBH (Shlosman *et al.*, 1989). However, it has also been suggested that the nuclear star clusters and the SMBH, can create instabilities, which eventually will destroy the bar (Heller, 1995).

1.2.4 Early-type galaxies: the final product of galaxy interactions

With the general term “early-type galaxies” we identify galaxies which are placed on the left of the Hubble sequence. These are the lenticular and the elliptical galaxies

(Fig. 1.12). The main characteristic of these galaxies is that they contain very little amount of gas, and as a consequence they display very low or no star formation activity. As we discussed in the previous sections they are the results of galaxy interactions and merging.

The term "elliptical galaxies" covers a very large class of galaxies, which differ, in masses and luminosities, by more than six orders of magnitude. We can distinguish them into: (*i*) normal ellipticals, (*ii*) dwarf ellipticals, (*iii*) cD galaxies, and (*iv*) dwarf spheroidals (dSph's). Some of them rotate rapidly while others hardly at all; some appear to be fairly spherical while others have a triaxial shape (Schneider, 2006). In this section we will present a summary of their main characteristics.

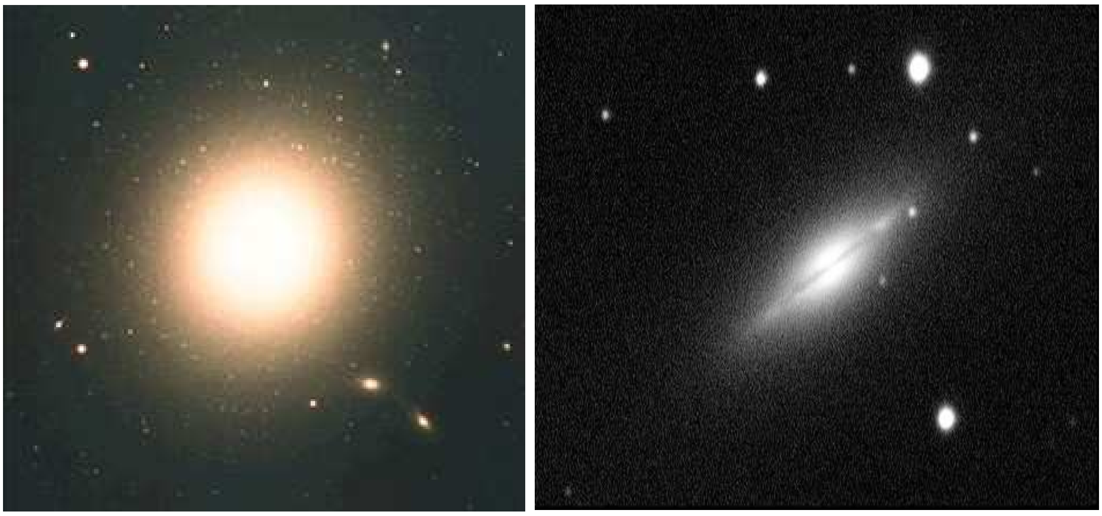

Figure 1.12: Two typical examples of early-type galaxies. On the left the giant elliptical galaxy M 87. On the right the NGC 5866, a lenticular galaxy seen edge-on. [Image credit: Anglo-Australian Observatory, Hubble Space Telescope]

In contrast to the spiral galaxies, the brightness profiles of elliptical galaxies are well described using a de Vaucouleurs profile (n$\sim$4). Their light is concentrated towards the center. The most massive of them, the cD galaxies (with stellar masses of about 10^{12}-10^{13}M$_{\odot}$), are significantly brighter than other ellipticals and they are usually found in the centers of rich clusters. Moreover, we observe that the more luminous the galaxy, the lower its central surface brightness and the larger its core. In 1961, H. Arp discovered some very fine structures encircling several elliptical galaxies. Later they were identified as "shells", remnants of small galaxies which has been merged by the larger galaxy. They can be observed by fitting a theoretical de Vaucouleurs profile to the galaxy and subtracting it from its observed image (see Section 1.2.3).

In some elliptical galaxies the isophotes appear to be “disky”, with more light along the major axis, since the galaxy contains an equatorial disk within it; in other cases we observe “boxiness”, with the most of the light to be concentrated into the “corners” of the ellipse (Combes *et al.*, 2002). Lenticular galaxies can be found between the “disky” ellipticals and the spiral galaxies. They are disk galaxies, with no obvious spiral structure, who lost or consumed most of their gas. They are dominated by a large central bulge, they may also have a central bar, and they are considered to be the transition state between spiral and elliptical galaxies. Their brightness profiles are described, as in spiral galaxies, using both an exponential profile for the disk, and a de Vaucouleurs profile for the bulge.

As we mentioned earlier, elliptical and lenticular galaxies were thought to be free of gas and dust. However, a closer inspection shows that they do have some dust mixed with cold gas in their nuclear regions. On the other hand, most elliptical galaxies contain large quantities of hot ionized gas, visible in the X-rays, which has been produced from the mass-loss of stars as they are aged.

Both elliptical and lenticular galaxies do not have any luminous blue stars. The brightest stars are the AGB stars and the red giants. Early-type galaxies appear red, when observed in the optical, which implies an old stellar population. The metallicity, of both elliptical and lenticular galaxies, increases towards their nuclear regions. Their integrated spectra show deep absorption lines of heavy elements, similar to K-star spectra (see Fig. 1.13). There is very little UV light since they are missing of young OB stars. Moreover, the metal absorption lines are strongest in the most luminous ellipticals (with luminosities $>10^{11}\mathrm{L}_{\odot}$), which means that big ellipticals are richer in heavy elements. In contrast, elliptical galaxies of intermediate luminosity have similar metallicities to those in the Sun. Finally, most elliptical galaxies, brighter than $M_B \sim$ 20, are strong radio sources. This emission comes from a very small region in the center of the galaxies, and as it is also the case for the late-type galaxies, they may host an AGN.

1.3 Spatial distribution of galaxies

As we mentioned in Section 1.2.1, two or more galaxies can interact and eventually become parts of the same DM halo. There, they are found under the same gravitational potential well, therefore, they will eventually interact and merge. Depending on the size of the dark matter hosting halo, there can be created a group or a cluster of galaxies. The transition between groups and clusters is smooth; the former are systems

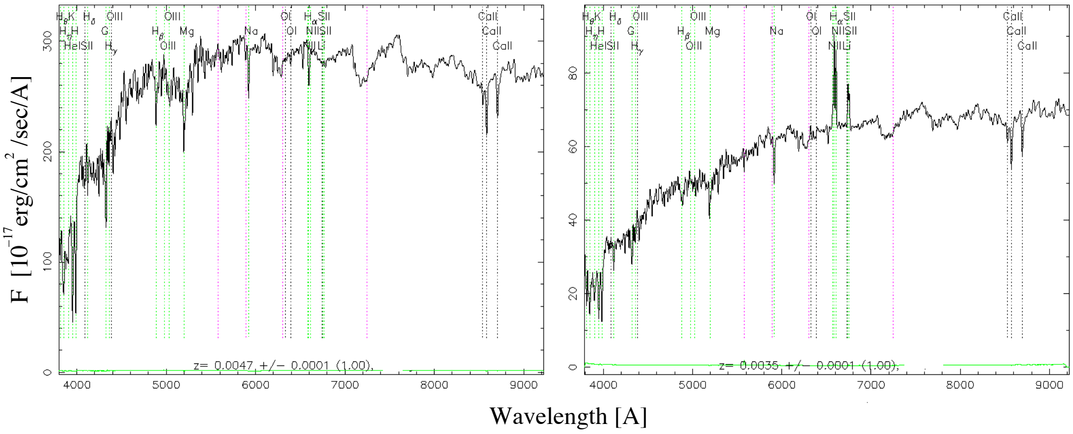

Figure 1.13: Left: The integrated spectrum of a typical elliptical galaxy (NGC 4121) with low UV emission and absorption lines. Right: The spectrum of a lenticular galaxy (NGC 4309) which is almost indistinguishable from that of the elliptical. [Image credit SDSS]

of typically less than 50 galaxies, while the later are systems containing from 50 to thousands of galaxies. The evolution of the galaxies, depending on the environment, can be differentiated, and it is one of the questions which will puzzle us in this work.

1.3.1 Clusters of galaxies

To identify a group or a cluster, one would expect that three dimensional criteria, such as the angular separation and the distance of the galaxies, should be applied. However, to measure the distance of each possible member galaxy, a spectroscopic redshift is needed, and especially in the case of clusters, which can host up to thousands of members, this may demand extensive observing time. For this reason, two dimensional criteria are usually used. The best such criteria for the identification of clusters refer to an over-density of galaxies within a specified solid angle, and were reported by G. O. Abell. According to these, a cluster must contain more than 50 galaxies in a magnitude interval $\mathrm{m}_3 \leq \mathrm{m} \leq \mathrm{m}_3 + 2$, where m_3 is the mass of the third brightest galaxy in the cluster. These galaxies must be located in a circle of radius $\theta_A = \frac{1'.7}{z}$, where z is the estimated redshift. His criteria were so reliable that only 10% of the clusters (at z<0.1) are not real but projections of sparser groupings (Katgert *et al.*, 1996). Clusters display diameters of about $\sim 1.5h^{-1}$Mpc (Schneider, 2006), and they are the most massive gravitationally bound structures in the Universe with dynamical masses between $10^{12} M_{\odot}$ and $10^{15} M_{\odot}$.

The largest rich clusters may contain thousands of galaxies. The nearest of these are about 20 Mpc away, in the constellations of Virgo and Fornax. Even richer than these are the Coma, Abell 1656, and the Perseus clusters. Coma is about $70h^{-1}$ Mpc away from us, it extends to linear scales of about 7 Mpc, and consists of a few thousand galaxies. All the galaxies near its core are ellipticals; the spirals are in its outskirts. Since galaxies are packed very tightly in clusters they display very high velocity dispersions of about 800-1000 km $\sec^{-1}$. Most of the luminous baryonic matter in galaxy clusters is not stars, or gas within galaxies, it is the hot gas, radiating in the X-rays, found in the inter-galactic space. Virgo has about 5×10^{13} $M_{\odot}$ of X-ray emitting gas within the core of the cluster. The cluster gas is hotter than the gas found around individual elliptical galaxies (typically $\sim10^{8}$K). In the cluster core, the gas is often dense enough to cool and thus it sinks towards the center as a cooling flow. We can estimate the dynamical masses of galaxy clusters using the motions of galaxies within them. Another method is to use weak gravitational lensing. The gravity of the entire cluster bends the light of galaxies, which are located behind it, slightly discording their shape. Using this bending, astronomers are able to infer the mass distribution of the cluster.

1.3.2 Groups of galaxies

Galaxy groups are systems which contain less than 50 galaxies. Conversely to the rich clusters, groups mainly host disk galaxies (such as the Local and the Ursa Major groups). The typical velocity dispersions of groups range between 100-500 km $\sec^{-1}$, which is less than the half of what is observed in galaxy clusters. As a result of their low relative speeds, galaxies “feel” each other more; therefore, the impulse is larger, and since this equals to the change of momentum, the change in the velocities of galaxies and their stars is larger. Moreover, since the HI gas extends more than the stellar disk in spiral galaxies, it is affected more easily by the interactions between the members of the groups. Thus, the atomic gas disks of the inner galaxies are smaller than those found in the periphery of the groups; it is diffused and ionized, and thus it becomes visible in the X-rays, reaching temperatures that exceed 10^{7} K; the higher the velocity dispersion of a group the hotter its X-ray gas. This hot gas is probably a mixture of material that was never captured into galaxies, and metal enriched gas that escaped from them.

Groups are separated into two main categories: (*i*) the loose groups, in which the relative separations between the galaxies are much larger than the sizes of the galaxies itself, and they display very low velocity dispersions of about 150 km $\sec^{-1}$, and (*ii*) the compact groups which display not much higher velocity dispersions (about 200 km sec^{-1}), but the relative separations between the galaxies are comparable to the sizes of the galaxies (just few kpc).

The final products of the groups are still puzzling us. We now believe most, in not all, galaxies in groups will eventually merge into one giant elliptical. The merged object might end-up as a giant elliptical galaxy (Sparke & Gallagher, 2000). Another possibility is that they may end-up into a fossil group. The latter is a system with an extended X-ray luminous halo, which is dominated by a very massive and bright elliptical galaxy. However, according to Mendes de Oliveira & Carrasco (2007) fossil groups are unlike to be the final products of compact groups, since they seem to be results of much higher density environments (such as clusters).

Figure 1.14: The Leo triplet, a small group of galaxies in the constellation Leo. It consists of the spiral galaxies M65, M66, and NGC 3628. [Image credit: R. Zmaritsch]

1.3.2.1 Loose groups

Loose groups are groups of 3-to-50 galaxies, separated by distances many times larger than the sizes of the individual galaxies. Their velocity dispersions are very low, and therefore, their galaxies experienced several tidal interactions with their neighbors. A very typical such group is the Leo triplet (see Fig. 1.14). It is believed that most loose groups will eventually evolve into compact groups. Moreover, Rood & Struble (1994) observed that 70% of the compact groups are located within loose groups.

1.3.2.2 Compact groups

Compact groups of galaxies were identified as gravitationally bound systems containing just a few galaxies (Hickson, 1997). Since the discovery in 1877 of Stephan's Quintet (see Fig. 1.15), the prototypical such group, a large number of others have been found by both visual and automated searches of the Palomar Observatory Sky Survey (POSS) plates. Although the criteria for assigning group membership based only on imaging data are often debated, it is now generally accepted that the most complete and better studied such sample is the one compiled by Hickson (1982). His catalog of the so–called Hickson Compact Groups (hereafter HCGs) consists of 451 galaxies contained in 100 groups of four or more galaxies, occupying compact configurations within relatively isolated regions where no excess of other surrounding galaxies can be seen. He defined a compact group as a group of galaxies with the following properties:

- $N(\Delta m{=}3)\geq 4$; the number of galaxies, within 3 mag of the brightest galaxy, must be greater or equal to 4,
- $\theta_N \geq 3\ \theta_G$; the angular diameter of the largest concentric circle, which contains no additional galaxies in this magnitude range or brighter, must be at least 3 times larger than the size of the group itself,
- $\mu_e \leq 26.0$ mag arcsec^{-2}; the total magnitude of the galaxies in arc sec^{-2}, averaged over θ_G

all magnitudes are measured in the r-band. The fact that the original selection of the HCG members did not include redshift information, led to the inclusion of interlopers among them, the most famous being NGC 7320 in Stephan's Quintet (HCG 92). This led to a debate as to whether compact groups are line-of-sight alignments of galaxy pairs within loose groups, or filaments seen end-on (Hernquist *et al.*, 1995; Mamon, 1986). However, the detection of hot X-ray gas in ∼75% of the HCGs by Ponman *et al.* (1996) implies that they do reside in a massive dark matter halo and thus are indeed physically dense structures. Numerical simulations indicate that in the absence of velocity information, raising the minimum surface brightness criterion for the group used by Hickson would help eliminate interlopers (McConnachie *et al.*, 2008).

Because of the nature of these groups, the high density enhancements in addition to the low velocity dispersions (∼250 km s^{-1}), make them ideal to study the effects of

Figure 1.15: Stephan's Quintet is a compact group, which contains 5 galaxies, in the constellation Pegasus (the big spiral galaxy in the bottom is projected in front of the group). It is also known as HCG 92. [Image credit: Kitt Peak National Observatory]

galaxy interactions. Hickson (1982) found that the majority of HCGs display an excess of elliptical galaxies, ∼31% of all members compared to the field, while the fraction of spiral galaxies and irregular is only 43%, nearly a factor of two less of what is observed in the field. Optical imaging by Mendes de Oliveira & Hickson (1993) showed that 43% of all HCG galaxies display morphological features of interactions and mergers, such as bridges, tails and other distortions. Similar indications of interactions are seen in maps of the atomic hydrogen distribution in selected groups by Verdes-Montenegro *et al.* (2001). Moreover, Hickson *et al.* (1989) found that the fractional distribution of the ratio of far-infrared (far-IR) to optical luminosity in HCG spiral galaxies is significantly larger than that of isolated galaxies, suggesting that for a given optical luminosity, spiral galaxies in groups have higher infrared luminosities. Comparison of HCG spirals with those in clusters of galaxies from Bicay & Giovanelli (1987) reveals that the distributions of the IR to optical luminosity, as well as the 60 to 100μm far-IR color are similar. Finally, nuclear optical spectroscopy studies indicate that almost 40% of the galaxies within these groups display evidence of an AGN (Martínez *et al.*, 2010; Shimada *et al.*, 2000). All these clues are consistent with an evolutionary pattern where tidal encounters and the accretion of small companions by the group members, redistribute the gas content of the groups and affect the morphology of their members.

Verdes-Montenegro *et al.* (2001) and Borthakur *et al.* (2010) have proposed an evolutionary sequence for the HCGs based on the amount and spatial distribution of their neutral atomic gas. Using HI maps they classified the groups into three phases based on the ratio of the gas content within the galaxies over the total observed in the group. According to their scenario, a loose galaxy group starts to contract under the gravity to form a more compact one. During this first phase the HI gas is still mostly found in the individual galaxies. Then as the group evolves, it enters the second phase and a fraction of the atomic hydrogen is extracted from the galaxy disks into the intragroup medium, probably due to tidal forces, and part of it becomes fully ionized. Finally, in the third phase, the dynamical friction leads to a decrease in the separation between the group members and the group becomes more compact. More than 80% of the HI originally in the disks of the galaxies has been displaced. Some of it is seen redistributed in a common envelope surrounding all groups members, and a fraction has likely been converted into molecular gas fueling star formation and/or accretion onto an AGN. A similar classification was proposed by Johnson *et al.* (2007) and Tzanavaris *et al.* (2010). These authors separated the groups using the ratio of the M_{HI} over the dynamical mass of the group, the so-called "HI richness", and found that it is correlated to the specific star formation (sSFR) of their galaxies. They also found that galaxies in gas-poor groups display colors representative of a normal stellar population and observed a bimodality in the mid-infrared colors, as well as in the sSFRs of their members. They suggested that this is caused by enhanced the star formation activity which lead the galaxies in groups to evolve faster. Finally, Walker *et al.* (2010) had concluded that a similar bimodality in the mid-IR is also observed in the colors of galaxies in the Coma Infall region.

1.4 Goals and description of this thesis

As we already presented in the previous paragraphs, there is strong observational evidence that environment is directly linked to the evolution of galaxies, both in terms of stellar populations and their morphological appearance. For instance, the morphology-density relation (Dressler, 1980), where the early-type galaxies are mostly found in dense environments (such as groups and clusters), while the late-type are mainly found in the field. There is also the color-density relation (Balogh *et al.*, 2004), where the redder galaxies are mostly found within denser environments. The fact that these galaxies are found to be redder than the corresponding systems in the field, could be attributed to the fact that they enhanced their old stellar populations, and/or reduced their star formation activity. The latter could be caused by gas loss (tidal or ram pressure stripping) from the interaction of the galaxies with the group or cluster hot dark matter halo, the intra-group (-cluster) medium, or due to tidal interactions between members, which can strip gas out of the disks. On the other hand, it is believed that tidal interactions, between galaxies, can induce star formation (Daddi *et al.*, 2010; Struck, 1999). Indeed, interactions cause turbulence and shocks in the disks of spiral galaxies with result to initiate the collapse of large molecular clouds, which in turn form stars. Moreover, Appleton *et al.* (2006) revealed an unexpected aspect of the complexity of galaxy evolution. They found that in Stephan's Quintet (HCG 92), large scale shocks lead to star formation and mechanical heating of the H_2 gas, outside the galaxy disks.

Therefore, several important questions emerge, concerning the nature and the evolution of galaxies within dense environments. Are tidal interactions enhancing the star formation rates of the galaxies in dense environments, due to turbulence and shocks, or do they reduce them, indirectly, due to gas loss? How do the colors and the internal properties of the galaxies, within dense environments, compare to those in the field? Since there is strong evidence of interaction between group members, which strip gas out of their disks, would it be possible that there is a weak star formation, due to shocked or compressed gas in the intragroup space? As we already mentioned, compact groups of galaxies are the most suitable systems to study such effects, due to their high galaxy densities and low velocity dispersions, galaxies have the time to strongly interact to each other and differentiate their properties and colors.

A necessary step in the determination of the evolutionary state of compact groups is the complete census and analysis of the stellar populations of member galaxies, their gas content and star formation properties. A multiwavelength analysis is crucial to estimate these galaxy properties, since looking at different bands we can measure the various galaxy properties, as well as examine the complete energy balance from the ultraviolet to the far-infrared. Yet, despite the availability of data in other wavelengths, there was lack of deep high-resolution wide-field infrared imaging, sensitive to probe the warm and cold dust content, thus the star formation properties and the extinction, in compact groups of galaxies. In this work we present the first extensive analysis of the evolution of galaxies in compact groups, from an infrared perspective, also including for the first time data from an all sky ultraviolet survey.

To do this initially we proposed and obtained high-resolution Spitzer observations for 14 Hickson compact groups of galaxies. Subsequently, searching the complete Spitzer Heritage Archive we identified 32 of the Hickson Compact Groups for which mid-infrared imaging was available and studied their properties using theoretical modeling of their spectral energy distribution from the ultraviolet to the far-infrared. Finally, we expanded our analysis using the compact group catalogue of McConnachie *et al.* (2009) which was created by applying the Hickson criteria to the one million galaxies of the optical Sloan Digital Sky Survey (SDSS). We cross-matched this catalogue with mid-infrared data from the Wide-field Infrared Survey Explorer (WISE), and performed additional ultraviolet photometry to all galaxies using the all sky UV survey of the Galaxy Evolution Explorer (GALEX). The resulting sample of 7417 galaxies in 1770 groups is the largest sample of compact groups with complete multiwavelength coverage to-date. It increases by a factor of 50 the number of groups available for study, while sampling a volume in the local universe nearly 64 times larger than the original one of Hickson.

In Chapter 2 of this thesis we present in detail the above mentioned samples, as well as the observations and data reduction techniques we used to calculate the flux densities across the electromagnetic spectrum. In Chapter 3 we discuss our methods of estimating the various physical parameters of the galaxies, such as the star formation rate (SFR), stellar mass, dust extinction, etc. A thorough presentation of the properties of all compact groups, as well as comparisons with control samples of field and cluster galaxies is the subject of Chapters 4 and 5. The conclusions and future perspectives of this work are summarized in Chapter 6. As an appendix we include finder charts of the 35 Hickson Compact Groups, a list of tables with the measured and derived properties, as well as the three refereed papers in which some of the above results have already been presented.

Chapter 2

Samples and observations

In this chapter we present the three samples of compact groups of galaxies studied in this thesis. The first (from now on *sample I*; Bitsakis *et al.* 2010) consists of 14 HCGs, for which we obtained near- and mid-IR data. Later, we expand this sample, using data which became publicly available in the Spitzer archive. Our second sample contains multiwavelength observations for 32 HCGs (*sample II*; Bitsakis *et al.* 2011). In the second part of this chapter, we present the much larger Sloan Digital Sky Survey compact group (SDSS CG) multiwavelength sample, or *sample III*. We also present the comparison samples, of field, early-stage interacting pair, and cluster galaxies, we used in this work. Finally, we show how we obtained their fluxes, by performing aperture photometry, or cross-correlating catalogs, as well as some information on the physical mechanisms probed at each wavelength.

2.1 The samples

2.1.1 The Hickson Compact Group samples

As we mentioned in Sect. 1.4, our main motivation was to study for first time the star formation properties and colors of the galaxies in compact groups. To do so, we had proposed for high-resolutions Spitzer mid-IR observations of 14 HCGs containing 69 galaxies, 31 of which are early-type and 38 are late-type (see Table 1 of Bitsakis *et al.* 2010). This sample was selected in a random fashion from the original catalog of Hickson (see Table 1 of Hickson 1982), and the number of groups was not large in order to request only a moderate amount of telescope time. Since, near-IR data were needed to probe the old stellar populations of these galaxies, the only constraint applied was that the group members had to be contained within $\sim 5' \times 5'$ in order to be efficiently imaged by the near infrared camera of Palomar 5m Hale telescope. This effectively constrained our sample to nearby groups with typically 4 or 5 members. Despite the small numbers of galaxies, the sample can be considered representative of Hickson's catalog having an early-type galaxy fraction of $\sim 40\%$ and a spiral and irregular galaxy fraction of $\sim 60\%$ of the total (55% and 45% for Hickson's catalog, respectively). Furthermore, as we will discuss in Section 4.2.1, Kolmogorov-Smirnov (KS) analysis indicates that the mass distribution of our sub-sample, estimated by their Ks-band luminosities, is representative of the whole HCG sample. Finally, nine galaxies of this sample were classified as AGN based on optical spectroscopy, even though this number is likely a lower limit given the sparse spectroscopic coverage.

Later, we expanded our original sample using as criterion the availability of high spatial resolution 3.6-to-24μm mid-infrared imaging from the Spitzer Space Telescope archive, as well as UV imaging from GALEX (thus, we excluded 3 groups of *sample I* since UV data were not available). The infrared data are essential to probe the properties of the energy production in nuclei of galaxies, some of which may be enshrouded in dust, while the UV is necessary to properly estimate the effects of extinction and accurately account for the global energy balance when we model their SED. These constrains resulted in a sample of 32 compact groups containing 135 galaxies (*sample II*), 62 (46%) of which are early-type (E's & S0's) and 73 (54%) are late-type (S/SB's & Irr's). This nearly triples the size of *sample I*. We verified that all galaxies of the groups are sufficiently separated in order to be able to obtain accurate photometry from the UV to the mid infrared, and that the average group properties such as type of galaxy, stellar mass, and star formation rates are representative of the whole Hickson sample. We should note that 7 groups contain interlopers along the line of sight. For these groups the number of physical members is three, below the lower limit of four members introduced by Hickson (1982). The complete photometry is presented in Table 2 of Bitsakis *et al.* (2011), a summary of the two HCG samples is shown in Table 2.1, and an example of the multiwavelength imaging is presented in Fig. 2.1.

2.1.2 The SDSS compact group sample

More recently, McConnachie *et al.* (2009) published the largest, up to the moment, catalog of compact groups of galaxies and motivated us to use it in order to improve our statistics, as well as to analyze the properties of compact group galaxies, which are found at 64 times larger volume. Their sample was selected by applying the criteria introduced by Hickson (1982), described in detail in Section 1.3.2.2, to the whole Sloan Digital Sky Survey Data Release 6 (SDSS DR6 Adelman-McCarthy, 2008)). As

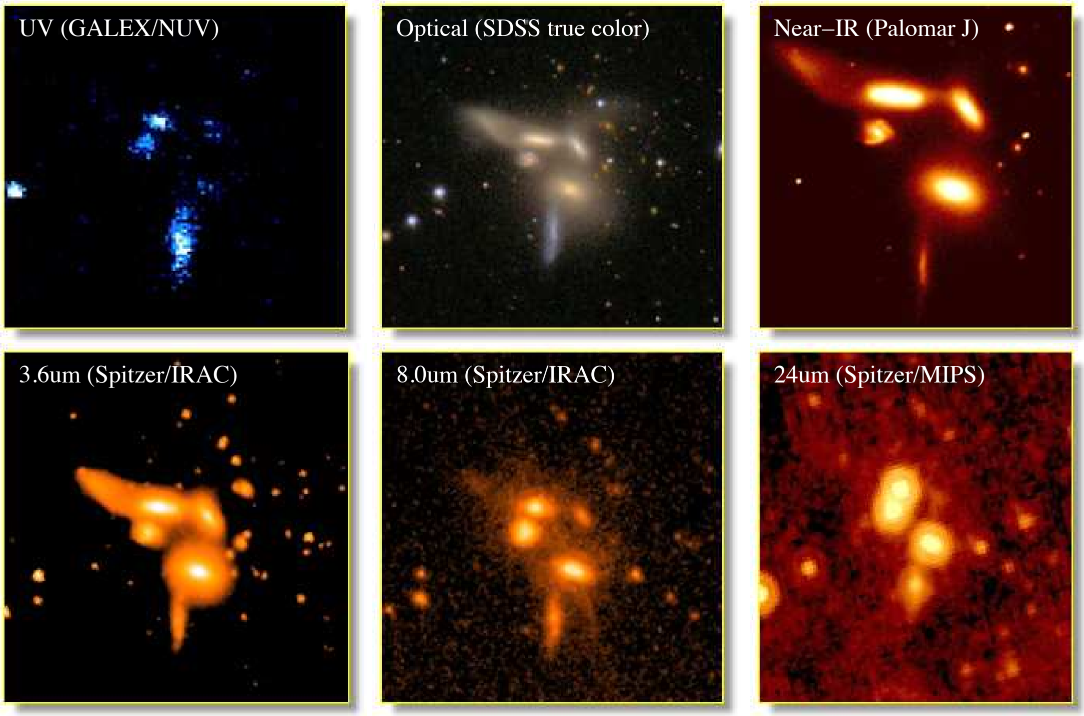

Figure 2.1: An example of the multi-wavelength data available for *sample II*. From the upper left to the lower right: the GALEX/UV, SDSS/optical, Palomar/J-band, and the Spitzer/3.6, 8.0 and 24μm images of Seyfert's Sextet (HCG79).

McConnachie *et al.* (2008) showed, by increasing the required minimum surface brightness, from 26 to 22 mags arcsec^{-2}, the proportion of genuine compact groups with no interlopers is increased from 29 to 75%. Moreover, they have imposed a faint end limit at Petrosian r-band magnitude of 18 mags, to ensure that the observational and the theoretical catalogs are robustly compared, and a bright end limit of 14.5 mags, to ensure that automatic de-blending of galaxies is reliable. Therefore, their final catalog contains 1 107 622 galaxies, and from these they identify 2297 compact groups, containing 9713 galaxies (see Catalog A of McConnachie *et al.* 2009).

2.1.2.1 Sample selection

The sample we describe here (*sample III*) was constructed from the McConnachie *et al.* (2009) Catalog A, using as a criterion the availability of UV, optical, near and mid-infrared photometry. Since the original sample of McConnachie *et al.* (2009) was selected using the SDSS DR7, there is available optical photometry for all the 9713 galaxies.

To obtain the UV fluxes of these galaxies, we downloaded the corresponding GALEX images and performed aperture photometry. The reason we did not use the fluxes published in the GALEX archive was because they are overestimated by 1-2 magnitudes (see Sect. 2.2.1). Since GALEX did not fully cover the whole sky, we obtained data only for 7890 galaxies (1880 compact groups) of the original sample. Finally, we cross-correlated our sample with the Two-Micron All Sky Survey (2MASS) and the WISE surveys and the final number of groups was further reduced.

Eventually, our *sample III* consists of 1770 groups (7417 galaxies) with UV, optical, near-IR, and mid-IR photometry (see Fig. 2.2). There is available optical SDSS spectroscopy for 3374 galaxies (released by MPA-JHU DR7); typically sampling 2 galaxies for each group. Using the spectra, we can estimate the redshift of each group. We see that most of the groups in this sample are at redshift of 0.091 (or 416 Mpc; see Fig. 2.3), which places them four times further than Hickson Compact Groups (HCGs; z∼0.022 or 95 Mpc), however, there are groups reaching up to z∼0.3 (∼1500Mpc).

2.1.2.2 Galaxy classification

A very important element in exploring the nature of compact groups, is the knowledge of the morphological classification of their galaxies. However, contrary to the previous two samples (*I* and *II*), there is no available classification for the galaxies of *sample III*.

We can classify a galaxy using its spectrum. Haines *et al.* (2007) showed that galaxies with EW(Hα)> 2Å are star forming, and we can classify them as late-type

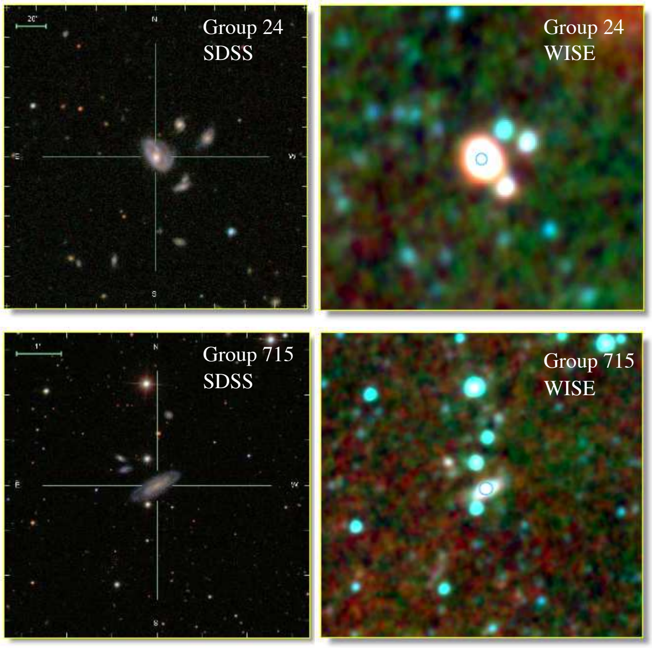

Figure 2.2: Optical (SDSS true color; left panels) and mid-IR (WISE "true color"; right panel) images of the 24th (top; at z∼0.018) and 715th (bottom; at z∼0.049) groups from Catalog A McConnachie *et al.* (2009)

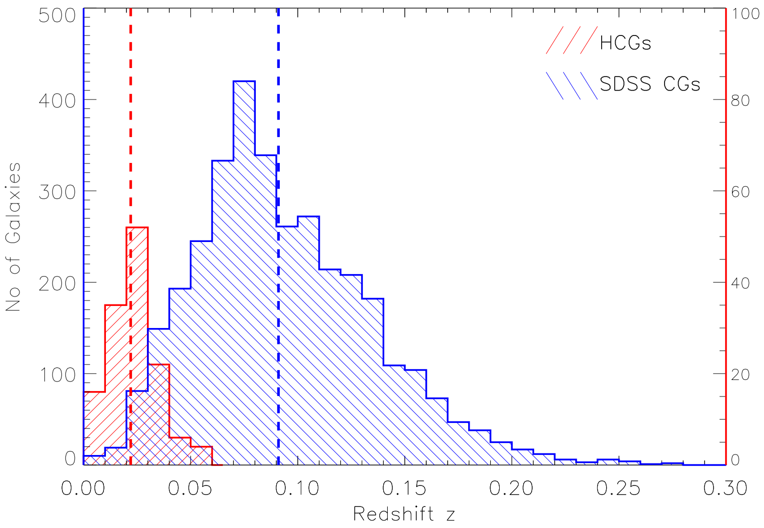

Figure 2.3: Redshift distribution of the 3374 in this sample with available spectra (in blue; left axis), as well as the 135 galaxies (32 groups) of our HCG *sample II* (in red; right axis). The dashed lines indicate the median values of the two samples.

(S's or SB's), while galaxies with EW(Hα)$<$ 2Å are passively evolving, and we can classify them as early-type (S0's or E's). Using this criterion we can classify the 3374 galaxies with spectra in *sample III*. We find that 1972 galaxies are late-type (58% of the total) and 1402 galaxies are early-type (42% of the total). These numbers are close to what is morphologically known for HCGs (51% and 49% respectively). Moreover, using their optical spectra we can classify their nuclei. Plotting the Kauffmann *et al.* (2003a) and Kewley *et al.* (2006) relations on the BPT diagram (see Fig. 2.4), we find that 42% of these galaxies host an AGN into their nucleus or they are transition objects (43% for HCGs).

Table 2.1: Summary of the samples

Sample ID	Number of groups	Number of galaxies	Number of Es/Ss	Available photometry	Number of gal. with spectra
sample I	14	69	31/38	optical, NIR, MIR, FIR	15
sample II	32	135	62/73	UV, optical, NIR, MIR, FIR	94
sample III	1770	7417	3985/3422	UV, optical, NIR, MIR	3374

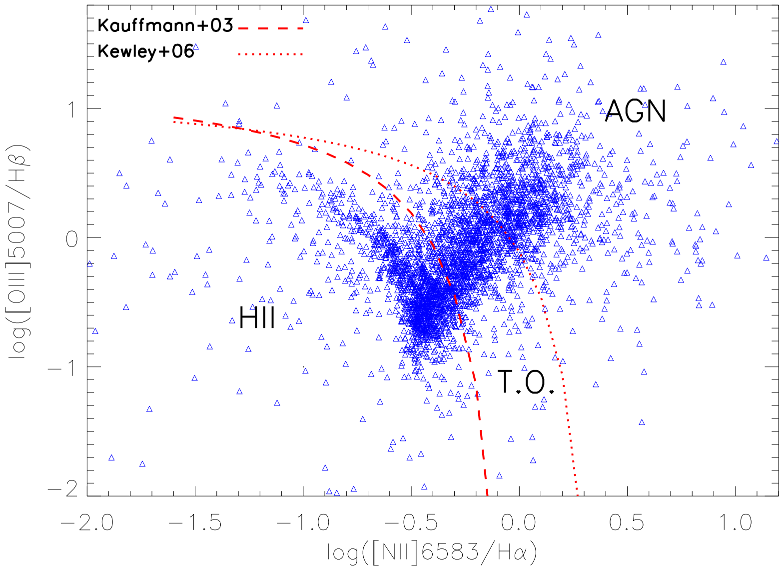

Figure 2.4: The BPT diagram of the 3374 galaxies with available spectra in our sample. The dashed line indicates the Kauffmann *et al.* (2003a), and the dotted line the Kewley *et al.* (2006) criteria.

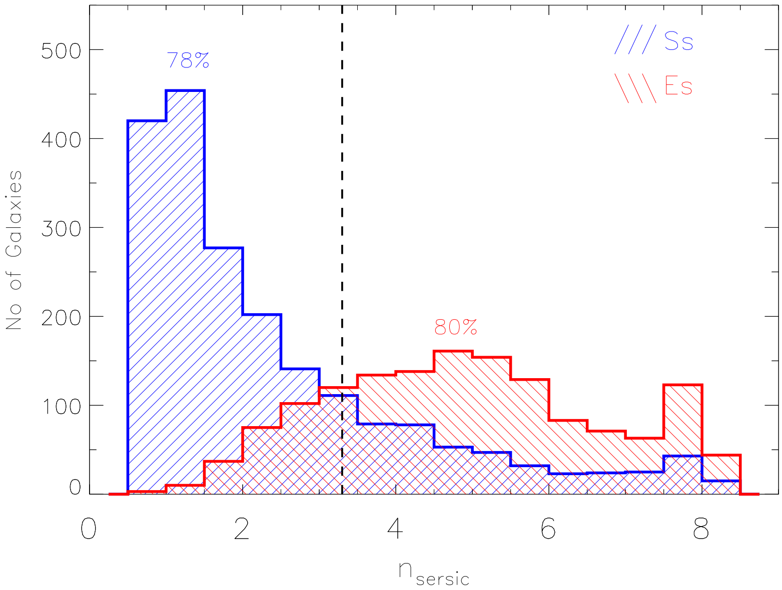

Figure 2.5: Distributions of the n_{Sersic} of 3374 late (blue) and early-type (red) galaxies (spectroscopically classified according to their EW(Hα). The dashed vertical line indicates the n_{Sersic}=3.3 separator.

To classify the remaining galaxies of this sample, for which no spectra were available, we relied on their SDSS r-band images in order to estimate their radial profiles (Sersic index; n_{Sersic}). We know that the surface brightness of the early-type galaxies can be fitted using a de Vaucouleurs radial profile ($n_{Sersic}\sim4$), while spiral galaxies are fitted with an exponential profile ($n_{Sersic}\sim1$). Using the Simard *et al.* (2011) published radial profiles for 1.12 million SDSS galaxies, we obtained the n_{Sersic} for 7407 galaxies of our sample. However, there was still an issue; at which n_{Sersic} we will separate the galaxies into late and early-type? To address this question, we plot in Fig. 2.5 the distributions of n_{Sersic} of the 3374 late and early-type galaxies with spectra. We find that if we place the separator at n_{Sersic}=3.3, 78% of the galaxies to the left are spectroscopically classified as late-type and 80% of the galaxies to the right are early-type. So if we classify the galaxies without spectra using the Sersic index criterion we finally find that out of the 7417 galaxies in our sample, 3422 (or 46%) are classified as late-type, 3985 (54%) are classified as early-type and 10 are not classified since no spectra or n_{Sersic} were available.

2.1.3 The control samples

In order to put the properties and evolution of the group galaxies into context, we must compare their observables and derived physical parameters with other control samples. Since dynamical interactions are the main drivers of galaxy evolution, we examined isolated field galaxies, as well as systems which are dynamically interacting, such galaxy pairs and galaxies found in clusters for which we could obtain data of similar wavelength coverage. The samples we used in our analysis are the following:

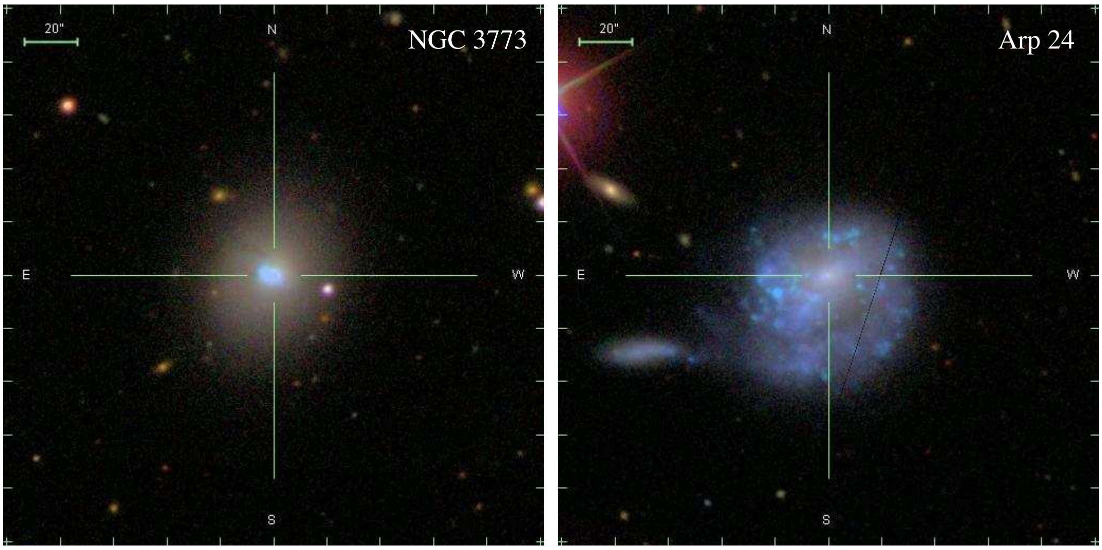

Figure 2.6: SDSS true color images of the: field elliptical galaxy NGC 3773 (left panel), and the early stage interacting pair Arp 24 (right panel). [Image credit: SDSS]

2.1.3.1 Field galaxies

A well studied sample with superb data coverage is the 75 "normal", mostly isolated field galaxies from the Spitzer Infrared Nearby Galaxies Survey (SINGS Dale *et al.*, 2005; Kennicutt *et al.*, 2003). We should note that the SINGS sample was selected explicitly to cover a wide range in Hubble type and luminosity and as a result it is not characteristic of a volume or flux limited population. Most objects are late-type systems that have angular sizes between $5'$ and $15'$. It also contains four early-type galaxies (NGC 855, NGC 1377, NGC 3773, and NGC 4125; see Fig. 2.6) with the last one being a LINER. Since the SINGS sample does not have many early type galaxies, we used the 9 isolated early-type galaxies with available mid-IR imaging described in Temi *et al.* (2004) and expanded it with another 4 isolated galaxies (NGC1404, NGC1199, NGC5363 & NGC5866) for which Spitzer mid-IR imaging was also available.

2.1.3.2 Interacting pairs

This sample is drawn from the 35 nearby (v<11.000 $\mathrm{km\,s^{-1}}$) early stage interacting galaxy pairs of Smith *et al.* (AJ) (see Fig. 2.6). The galaxies are tidally disturbed and fairly extended, having linear sizes $> 3'$. For the purposes of this work only 26 pairs from the initial sample were used, in which UV-to-far-IR data were available. As discussed in Bitsakis *et al.* (2010), the stellar mass distributions are similar between this sample as well ours and the SINGS.

2.1.3.3 Cluster galaxies

To compare in more detail the UV-optical colors of the galaxies in HCGs with the colors of galaxies found in the field, as well as in other groups and clusters, we used the volume limited sample of Haines *et al.* (2008). This sample contains 1994 galaxies in redshift range 0.005≤z≤0.037, selected by cross-correlating the SDSS-DR4 sample with the GALEX GR3 photometric catalogues. Using the Hα equivalent widths of M_r<-18 galaxies the authors were able to separate the galaxies into passively evolving and star-forming, having EW(Hα)<2Å and EW(Hα)>2Å respectively. To quantify the effects of local mass density and environment the authors calculated the local galaxy number density, ρ, in units of projected area, in Mpc^2, around a central galaxy and within a radial velocity bin of 500$\mathrm{km\,s^{-1}}$. They found that for $\rho < 0.5\mathrm{Mpc}^{-2}(500\,\mathrm{km\,s^{-1}})^{-1}$ they can produce a pure field sample. If a galaxy has $\rho > 4.0\mathrm{Mpc}^{-2}(500\,\mathrm{km\,s^{-1}})^{-1}$ there is a 90% probability that it lies within the virial radius of a group or a cluster.

2.2 The observations

As we explain earlier, for the purposes of our work, we used three samples of compact groups of galaxies, for which we had obtained their photometries and spectra. In order to derive the various physical parameters and colors of the galaxies in our samples, data from different bands are essential. Some of these data came from ground-based observations (such as the optical and the near infrared), and other were observed from space (like the UV, the mid- and the far-IR; see Fig. 2.7). This happens because the Earth's atmosphere absorbs most of the radiation at these wavelengths (i.e. UV, mid- and far-IR; see Fig. 2.8). In the next sections, we will describe what physical properties are probed at different wavelengths, and how we obtained the datasets for each one of our sample, at these bands.

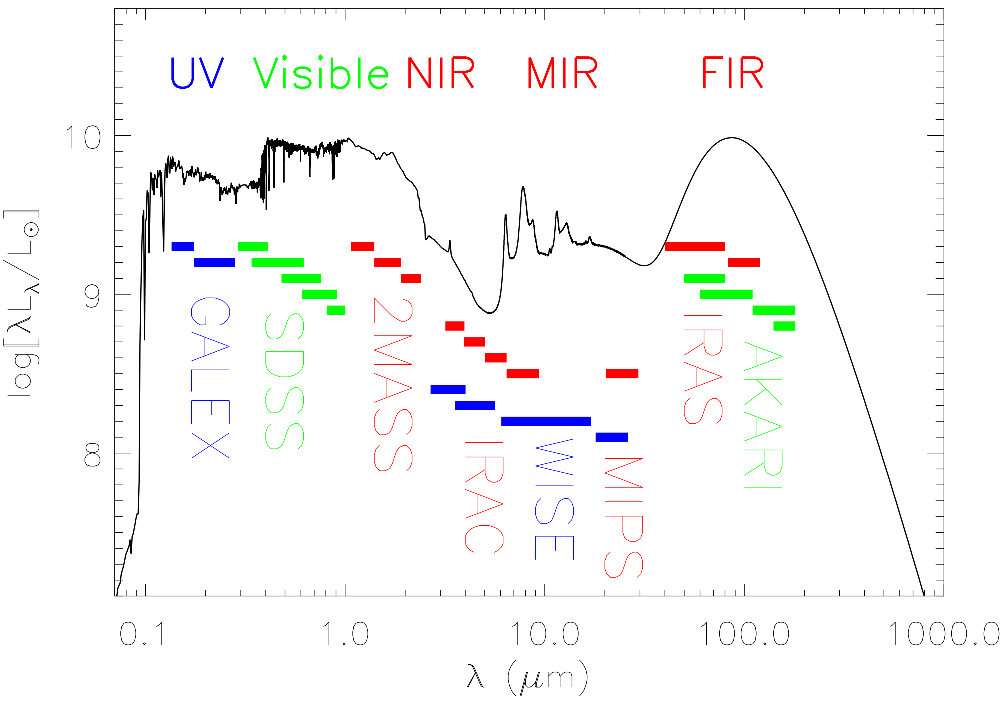

Figure 2.7: Here we present the theoretical SED of a spiral galaxy, on which we overlay the photometric bands of the instruments we used. From left: GALEX (FUV, NUV), SDSS (u, g, r, i, z), 2MASS (J, H, Ks), Spitzer/IRAC (3.6, 4.5, 5.7, and 8.0μm), WISE (3.4, 4.6, 12.0, and 22μm), Spitzer/MIPS 24μm, AKARI (60, 90, 140, and 160μm), and IRAS (60 and 100μm).

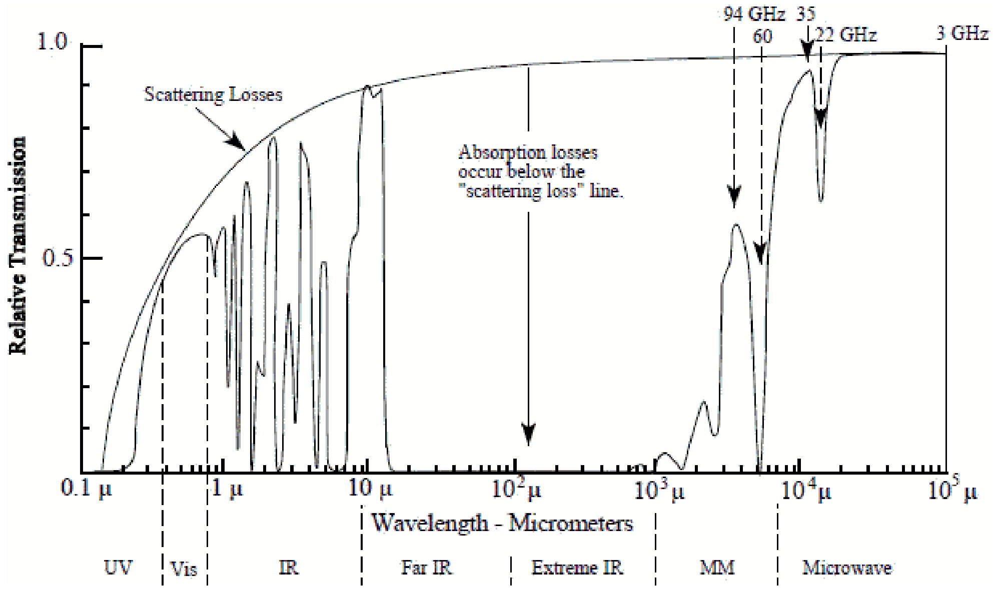

Figure 2.8: Graphical illustration of atmospheric transmission of Earth at the different wavelengths. As we can see, atmosphere is transparent mainly in the optical, near-IR, and radio wavelengths. [Image credit: Electronics Warfare and Radar Engineering Handbook]

2.2.1 Ultraviolet: Observing the stellar nurseries

The ultraviolet sky looks quite different from the familiar stars and galaxies seen in the visible light. Ultraviolet radiation (with wavelengths between approximately 912-3200Å) is produced by hot young stars with T>10000K. At these energies the spectrum of the galaxy is mostly dominated by young stars and bursts of less than 100Myr in age (Kennicutt, 1998); thus such observations can provide essential information for the evolution of star formation in galaxies. However, the ozone layer of the atmosphere of the Earth, absorbs most radiation below 3200Å, whereas neutral hydrogen absorbs all below 912Å. Thus, space observatories should be employed. The Galaxy Evolution Explorer (GALEX), is one such mission. It was launched in April 2003, and it orbits the Earth at an altitude of 697km, in an inclination of 29 degrees to the Earth's equator (see Fig. 2.9A). GALEX houses a 50cm diameter UV telescope that images the sky simultaneously in both FUV and NUV, centered at 1540Å and 2300Å, respectively. Its field of view (FOV) is approximately circular with a diameter of 1.2^o and a resolution of about 5.5" (FWHM) in the NUV (more technical details about the GALEX instruments can be found in Morrissey & Team 2005).

The UV data, presented in *sample II*, were obtained from the GALEX All Sky Survey (AIS; with 100sec on-source exposures), the Medium Imaging Survey (MIS;

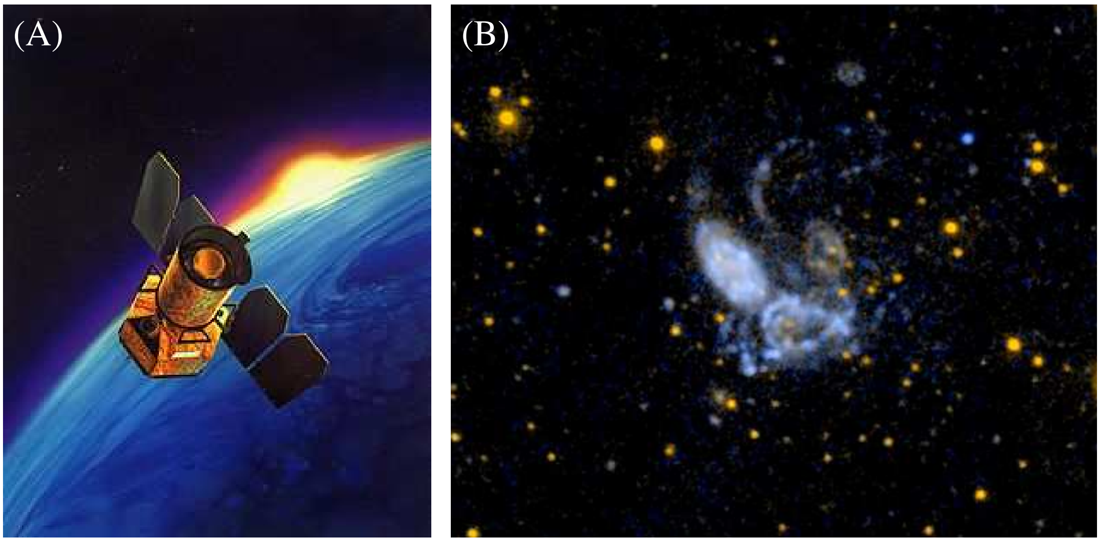

Figure 2.9: (A) An artists impression of GALEX. (b) Stephan's quintet (HCG 92), in the NUV and FUV bands as viewed by GALEX. [Image credit: NASA]

with 1500sec on-source exposures), as well as from Guest Investigator Data data (GI1-4; where the exposure time varies, but is typically ∼1500sec), publicly available in the GALEX archive; the data sets used in this paper are taken from the GALEX sixth data release (GR6). An example of a UV image is given in Fig. 2.9B. We performed aperture photometry and carefully calculated the isophotal contours around each one of our 135 sources to account for variations in the shape of the emitting region, since most of the sources have disturbed morphologies. By examining the local overall background for each galaxy, we defined a limiting isophote 3σ above it and we measured the flux within the region, after subtracting the corresponding sky. Finally, the conversion from counts to UV fluxes was done using the conversion coefficients given in the headers of each file.

The data of *sample III*, were obtained from GALEX AIS, MIS and GI1-4, as well as from Nearby Galaxy Survey (NGS; where the exposure time varies, but is typically 4000sec) and Deep Imaging Survey (DIS; where the exposure times where typically 4000sec). As in *sample II*, we also performed aperture photometry for the 7417 sources of this sample. Photometry for these galaxies was also available in the GALEX archive. This photometry was created automatically using SExtractor (Bertin & Arnouts, 1996) on the UV maps. In Fig. 2.10 we present the differences between the magnitudes, as derived from our photometry (marked with *phot*) and the ones from GALEX archive (marked with $GALEX$). We also present the running average of the standard deviations of the differences, where we can see that in many cases the differences are larger than 1 or even 2 magnitudes. This can be understood if one considers the morphology of these groups. In compact groups the galaxies are in close proximity to one another. As a result an automated method is not able to distinguish nearby members and mixes their PSFs; in those cases the given magnitudes are larger. In other cases, galaxies appear to have peculiar morphology and features, due to interactions, which usually makes an automated method to underestimate their flux.

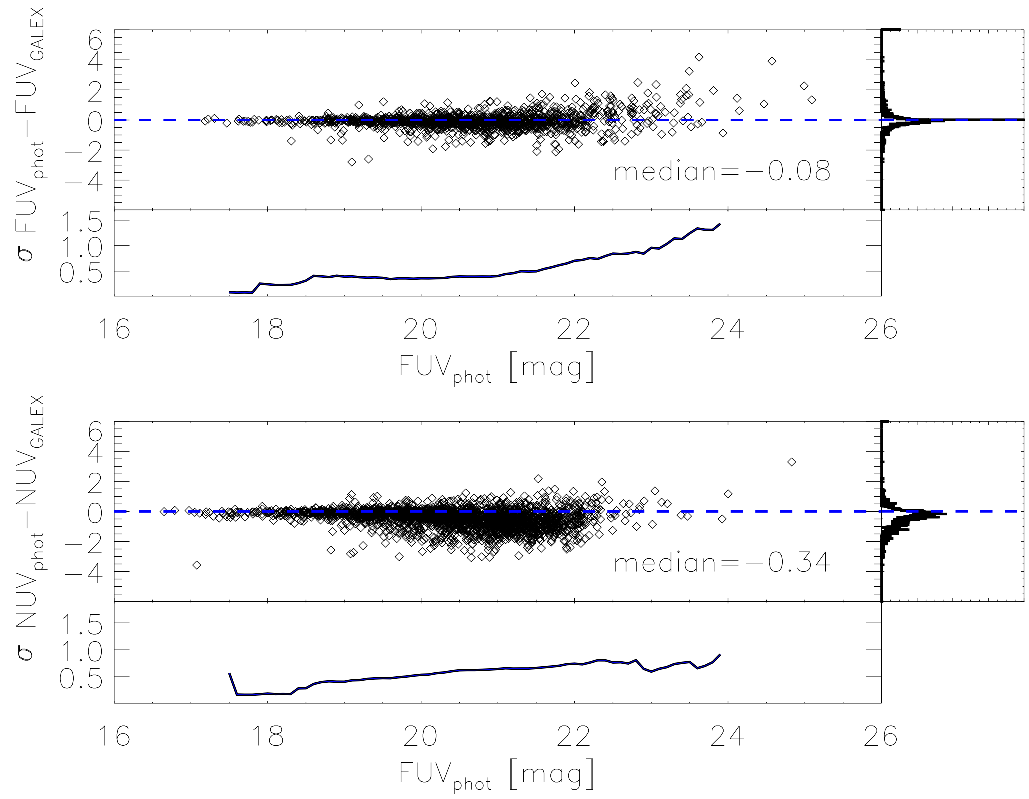

Figure 2.10: Differences between the magnitudes derived from our photometry (*phot*) and the ones from GALEX archive (*GALEX*) in FUV (top panel) and NUV (bottom panel) bands. In the bottom boxes are the standard deviations (σ) of the values created as running averages with a bin of 0.1 mags.

2.2.2 Visible: Observing from the Earth

We know that the atmosphere is largely transparent in the visible part of the spectrum (between 3200-7500Å; see Fig. 2.8). Thus, we can easily image the sky from the ground at these wavelengths. Since Galileo turned his telescope into the skies, in 1610, optical astronomy has evolved substantially, especially over the last few years with the discovery of the CCD and other technical achievements. However, it is not so easy to obtain a high quality astronomical image. In addition to a good telescope and astronomical instruments, a good site with dark sky and low atmospheric turbulence is also essential. The electronic devices which are attached on the telescope must be at very low temperature (under -100C) in order to avoid the thermal noise produced by them. Using a set of filters, we can look each time at different wavelength bands. Moreover, using a spectrograph, we are able to study the signatures from the several elements in the chromospheres of stars, as well as in the interstellar gas.

Figure 2.11: On the left the 2.5m Apache Point observatory in New Mexico which is used from the SDSS. In the middle, the Canada France Hawaii Telescope in Mauna Kea, Hawaii. On the right, true color image of Seyferts Sextet (HCG 79) as taken from SDSS. [Image credit: SDSS, and CHFT observatory]

Hickson *et al.* (1989), observed the groups in his catalog for 200sec in both B (blue) and R (red) bands using FOCAS1 on the Canada France Hawaii telescope, resulting images of 0.42" pixel^{-1} with a typical resolution of 1.2" (FWHM). Using these data we had obtained the optical fluxes of the galaxies of our samples I and II. In addition, imaging data for 74 galaxies, of *sample* II, as well as for 7417 galaxies of *sample* III, were recovered from the Sloan Digital Sky Survey (SDSS); in the u, g, r, i, z bands, centered at 3557, 4825, 6261, 7672 and 9097Å respectively. SDSS is a major multi-filter imaging and spectroscopic redshift survey, which is using a dedicated 2.5m optical telescope. Since 2000, when it started, it mapped 35% of the sky, taking 53.9sec exposures with a resolution of 0.396 arcsec/pixel. We used the latest SDSS Data Release 7 "model magnitudes", which reflect the integrated light from the whole galaxy and are best suited for comparisons with total photometry from ultraviolet to infrared wavelengths.

Optical spectra were also available for 94 galaxies, 70% of our *sample II* (15 of our *sample I*). Using the BPT diagram (see Sect. 1.2.2), Martínez *et al.* (2010) classified the nuclei of 67 of these galaxies, while the remaining classifications were obtained from Shimada *et al.* (2000), Hao (2005) and Véron-Cetty & Véron (2006). Galaxies without emission are referred as unclassified, as they display only stellar absorption features, "HII" are the galaxies with a starburst nucleus, and "AGN" (or LINER & Sy2) are the ones with an active nucleus. A number of galaxies are classified as transition objects (TO) since their emission line ratios are intermediate between Kauffmann *et al.* (2003a) and Kewley *et al.* (2006) criteria. Based on these results for the galaxies in our samples, with nuclear classification, 37% host an AGN, which is close to the 40% that Martínez *et al.* (2010) and Shimada *et al.* (2000) found for their samples. Finally, as mentioned in Sect. 2.1.2, we obtained the SDSS spectra of 3374 galaxies, of our *sample III*; almost two galaxies per group. The reason the spectroscopic coverage is not complete is because the SDSS spectroscopic survey had two restrictions: (*i*) all the galaxies must be brighter than 17.77 mags in the r-band, and (*ii*) the fibers could not point to two or more galaxies if they were closer than 55 arcsec, due to fiber collision constraints. Even though few galaxies were excluded because of the first criterion, since by definition the original sample of McConnachie *et al.* (2009) has galaxies brighter than 18 mags, most of the galaxies were not observed due to the second criterion. To examine this we had estimated the angular separation between the group members, using the great circle distance relation, where we noticed that half of the galaxies in groups are, indeed, closer than 55 arcsec. Finally, the size of the spectroscopic fiber of SDSS is 3arcsec in diameter, thus corrections must be applied in order to obtain the total light from extended objects (as described in Sect. 3.2.3). Using these spectra, we produced the BPT diagram, and by applying the same criteria as above, we derived their nuclear classifications (see Fig. 2.4).

2.2.3 Near infrared: Looking at the old stars

In 1800 W. Herschel discovered the near-infrared light (0.75-5μm). As Herschel was testing filters to observe sunspots, he passed the sunlight through a prism and held a thermometer just beyond the red end of the visible spectrum, to measure the ambient air temperature in the room. The thermometer, however, showed a higher temperature than the visible spectrum. He concluded that some kind of invisible light was heating up the thermometer with wavelengths beyond the visible.

In the near-infrared region, the hot blue stars, seen clearly in visible light, fade out and cooler stars come into view. Large red giant stars and low mass red dwarfs dominate the integrated near-IR emission of galaxies (typical temperatures 740-3000K). Furthermore, the longer near-IR wavelengths can penetrate more easily the dust and enable us to probe deeper into the enshrouded star forming regions of galaxies.

As we mentioned in the introduction of this section, the Earth's atmosphere is nearly transparent at these wavelengths, however, such observations are not so trivial due to Earth's atmospheric effects. The primary contributors to these effects are hydroxyl (OH), molecular oxygen (O_2), and water vapor molecules, which display several emission, as well as absorption lines at the near-IR wavelengths. During the night the OH lines vary in brightness on a timescale of 5-15 minutes with an amplitude of 5-10% as atmospheric wave phenomena change the local density of the species. As a consequence, it is impossible to take long exposures; one must take short exposures (of about 10-30 seconds) and subtract the sky from them. This can be achieved with two methods. One is to take one image on-source and one of the sky (on-off method; see Fig. 2.12A), and then subtract the sky background from our object; the sky pointings should have the same exposure time as the on-source observations. This method can be applied in large targets with size comparable or greater than the size of the CCD. The other, is to change the position of our object on the CCD every few seconds (dithering method; see Fig. 2.12B). This also helps in case there are bad pixels on our source and it can be applied also in small targets. In both cases the observer must be very careful if the object is an extended source so that only sky background and no stars are subtracted from the science target.

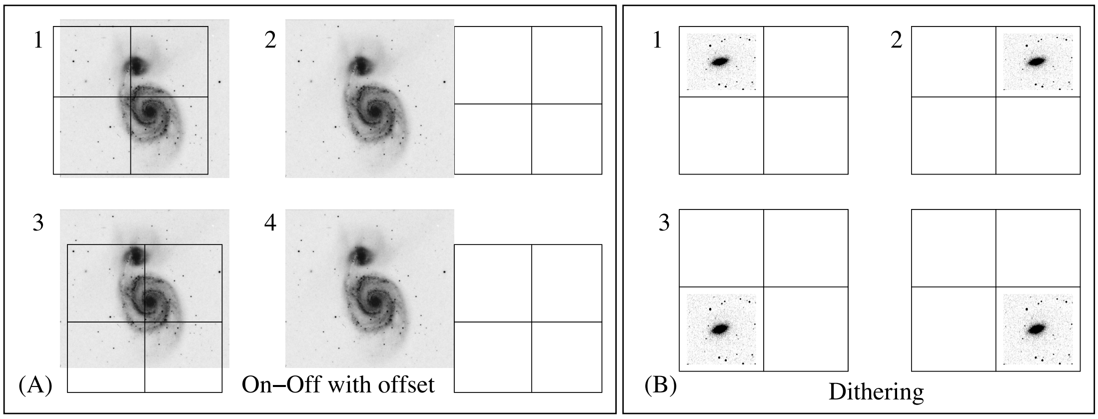

Figure 2.12: The two ways to observe in near infrared wavelengths. On the left the on-off method, appropriate for large targets, and on the right the dithering method, appropriate for small targets.

In order to have good observations in the near-infrared region, a very sensitive high resolution near-infrared camera is also essential. Using the Wien's displacement law the peak wavelength of a blackbody of temperature 300K is found to be at around 10μm. Thus, the camera and its electronics emit radiation in the region the observer is interested in and must be always cooled at very low temperatures (about 80K).

Therefore, to perform near-IR observations we have to follow a well established process. Since the night sky is always bright in the near-IR, we obtain the sky flats by taking several exposures, with the telescope resting and the sky passing in front of our camera, due to the motion of Earth. Moreover, our camera produces thermal noise even when it is cooled with liquid nitrogen. To remove this thermal noise we obtain several exposures using a blank filter (Darks), with duration similar to the on-source exposures. To convert the counts of each image into magnitudes, we acquire the images of near-IR standard stars that are stars with known near-IR magnitudes.

Using these technics, Slater (2004), performed deep near infrared observations for 18 of the groups in our *samples I* and *II*. They used the Wide Field Infrared Camera (WIRC) of the 5m Hale telescope at Palomar, during several observing runs in 2002 and 2003 observing periods. All groups were imaged in the J, H, and Ks bands for an on-source time of 20 minutes per filter. Once a World Coordinate System (WCS) was established for each image, they were pixel-resampled and co-added using the *Swarp* package. Source extraction was performed with SExtractor (Bertin & Arnouts, 1996). Their 1σ sensitivity limit was $\sim$ 21.5 mag arcsec^{-2} in J and H bands and $\sim$20.5 mag arcsec^{-2}.

In addition to the observations mentioned above, we performed deep near-IR imaging of another 5 groups (see Table 2.2), using the near-infrared camera at Skinakas observatory. It is located at the top of Ida mountain in the island of Crete (Greece) at an altitude of 1750m above sea-level (see Fig. 2.13). It is the result of the collaboration of three institutes, the university of Crete, the Foundation of Research and Technology-Hellas (FORTH), and the Max-Planck institute for extraterrestrial physics, in Garching. The site of the observatory was selected in 1984 based on the very good weather conditions and the very low atmospheric seeing (0.69 arcseconds) which makes it one of the best sites in the Mediterranean area. In 2007 Skinakas observatory obtained a wide field near-infrared camera which was mounted in the 1.3m telescope. The camera consists of a 1024×1024pixel HgCdTe Focal Plane Array, with 18.5×18.5μm pixels. The pixel scale of the camera is 0.378 arcseconds per pixel and the field of view is 6.5×6.5 arcminutes. The system is sensitive in the spectral range between 1-2.4μm and has two filter wheels. For our research, we used the three broad-band filters (J at 1.250, H at 1.635, and Ks at 2.150μm) to observe our 5 HCGs. The exposures duration were approximately 30min, on-source, the FWHM of stars were about 1.21-1.62arcsec, and the background sensitivity was estimated to be ∼18.5 mag arcsec^{-2} at J and ∼17.5mag arcsec^{-2} at K. In Table 2.2, we summarize our observations, concerning galaxies of *sample II*.

Figure 2.13: On the left, is the Skinakas observatory site, on Ida mountain at an altitude of 1750m. We can see the domes of the three telescopes (0.3m, 0.6m, and 1.3m) as well as the guesthouse and other facilities. On the right the near-infrared camera mounted on the 1.3m telescope is presented.

To perform the near-IR data reduction and photometry we developed a pipeline in *IDL*, which has also been available for future users of the near-infrared camera. Due to sizable telescope nodding, as well as dithering, it was necessary to perform astrometry on each of the shorter exposure images separately. This was done with the software package *WCSTools*, matching foreground stars to the USNO A2.0 and 2MASS point source catalogs. In Fig. 2.14 we display as an example HCG 82 in all three near-IR bands.

Finally, for remaining 9 groups of *sample II*, as well as for the 1770 groups of *sample III*, the near infrared fluxes were obtained from the Two Micron All Sky Survey (2MASS Skrutskie, 2006). The galaxies were imaged in J, H, and K bands, with 3-σ sensitivity limits of 15.8, 15.1, and 14.3 mag, respectively. In some cases, in *sample II*, where the proximity of galaxy pairs was affecting the reliability of the 2MASS photometry, we used the reduced 2MASS images and performed aperture photometry ourselves, defining the same aperture we used in other wavelengths. Moreover, because of the sensitivity limitations of 2MASS, we obtained photometry for only 6974 galaxies, out of 7417 galaxies of our *sample III*. However, we estimated the upper limits for the remaining 443 galaxies of this sample, which were under the detection

Table 2.2: Summary of the observations held with the Skinakas NIR camera.

Object	R.A.	Dec.	Filter	Exp. Time [sec]	Date of Observation
HCG2	7.875	8.431	J	1800	2011-09-15
HCG2	7.875	8.431	H	1800	2011-09-16
HCG2	7.875	8.431	Ks	1800	2011-09-17
HCG6	9.792	-8.395	J	1800	2010-09-21
HCG6	9.792	-8.395	H	1720	2010-09-23
HCG6	9.792	-8.395	Ks	1800	2010-09-23
HCG51	170.587	24.293	J	1800	2011-06-10
HCG51	170.587	24.293	H	1800	2011-06-11
HCG82	247.092	32.823	J	1800	2011-06-10
HCG82	247.092	32.823	H	1800	2011-06-10
HCG82	247.092	32.823	Ks	1840	2011-09-18
HCG97	356.845	-2.325	J	1400	2011-09-17
HCG97	356.845	-2.325	H	1400	2011-09-18
HCG97	356.845	-2.325	Ks	1400	2011-09-18

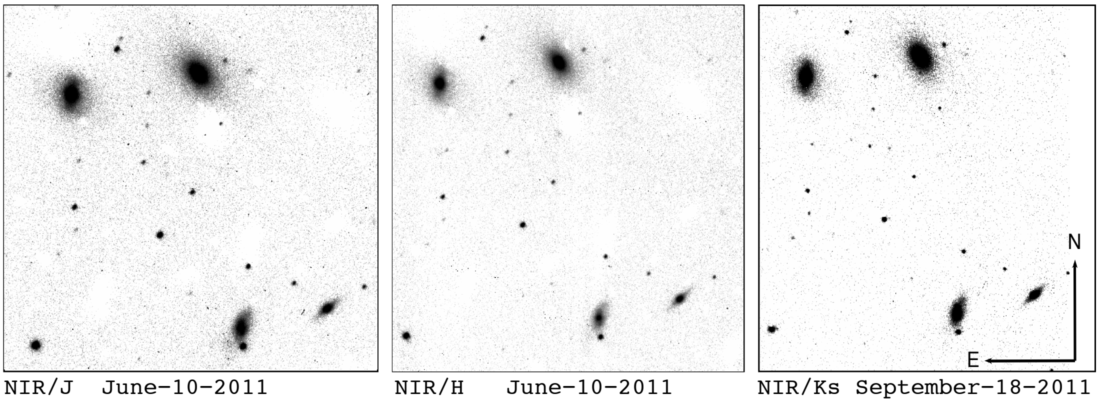

Figure 2.14: Imaging of HCG 82 in J, H, and Ks bands taken from Skinakas NIR camera on July and September of 2011.

limit. To do so, we have used the SDSS i and z bands to estimate their theoretical (R-I) and from there the theoretical (I-K), (H-K), and (J-H) colors.

2.2.4 Mid infrared: The signature of PAHs and dust

The mid-infrared is the area of the spectrum with wavelength range 5-40μm. There cool old stars, which were luminous in the near-IR wavelengths, begin to fade out. On the other hand, dust warmed by stellar light, such as the zodiacal dust lying on the plane of our solar system, starts to become very luminous. This dust is made of silicates, which range in size and emit most of their light at about 10μm. As we mentioned before, young stars radiate in the ultraviolet wavelengths, they heat up the interstellar dust and also excite the polycyclic aromatic hydrocarbons (PAHs), which in turn vibrate in some specific frequencies. Their vibrational modes absorb the UV photons from young stars and re-radiate them at 3.3, 6.2, 7.7, 8.6, 11.3, and 12.7μm. It is believed that in starburst galaxies about 20% of their infrared luminosity is coming from these bands (Dale *et al.*, 2005).

However, the atmosphere of Earth is opaque at these wavelengths (see Fig. 2.8; with only exceptions the N and Q bands at 7-14.5μm and 17-25μm, respectively) and thus we can only observe them from space. For that reason Spitzer Space Telescope (SST) was launched in August of 2003. Spitzer is an infrared telescope, with a primary mirror of 0.85m, and three instruments: the Infrared Array Camera (IRAC Fazio *et al.*, 2004) which has four (3.6, 4.5, 5.8 and 8.0μm) broadband filters, the Multi-band Imaging Photometer for Spitzer (MIPS Rieke *et al.*, 2004) with three bands at 24, 70, and 160μm, and an Infrared Spectrograph (IRS Houck *et al.*, 2004), which can obtain low-resolution (R$\sim$60-120) spectra in the 5-40μm range, as well as high resolution (R$\sim$600) in the 10-37μm range.

Observations of the 11 groups, of *sample I*, were obtained between 2008 January and 2009 March in all IRAC and the MIPS 24μm bands (PID: 40459). Moreover, we recovered the IRAC and MIPS 24μm data for 13 more groups (part of *sample II*), from the Spitzer archive. The IRAC observations were obtained with a 270sec exposure per filter for each set of cameras (see Fig. 2). All groups had a small enough angular size to fit within the $5' \times 5'$ field of view of IRAC. The on source time for the 24μm MIPS observations was 375.4sec.

The IRAC post-pipeline Basic Calibrated Data were downloaded and mosaiced onto the same grid with a pixel scale of $1.2'' \times 1.2''$. The 1σ sensitivity limits were varying slightly for each group due to changes in the background. Typical 3σ limits were measured to be $\sim$ 0.04 MJy sr^{-1}, $\sim$ 0.05 MJy sr^{-1}, $\sim$ 0.2 MJy sr^{-1} and $\sim$ 0.2 MJy sr^{-1}, for the 3.6, 4.5, 5.8 and 8.0μm filters, respectively. Since most of the galaxies have disturbed morphologies, often simple fixed aperture photometry was not the most appropriate method to measure the object flux. Thus, we carefully calculated the isophotal contours around each source in order to properly account variations in the shape of the emitting region. Examining the local background for each galaxy we defined a limiting isophote 3σ above the overall background and we measured the flux within this region, after subtracting the corresponding sky. In some cases even this method was challenging, so we defined the physical extent of each galaxy by hand using a polygon, and performed the photometry accordingly. The fluxes we report are for the same regions for all IRAC, as well as MIPS, images. Finally, we applied an extended source correction to our photometry by multiplying our measured fluxes with a correction factor of 0.91, 0.94, 0.71, and 0.74 for the corresponding 1 to 4 IRAC bands as indicated in the IRAC data handbook. The MIPS post-pipeline images have a pixel scale of $2.45'' \times 2.45''$ and their depth was measured to be $\sim$ 0.3 MJy sr^{-1} or $\sim$ 250μJy for a point source. In several cases the nuclei of galaxies were saturated and the frames were corrected using the IDP3 of IDL[1]. We estimate that our final uncertainties in the IRAC and MIPS photometry are $\sim$ 5%. In Fig. 2.15, it is presented the SST before its launch, as well they are illustrated two images of HCG 71 taken taken from IRAC and MIPS cameras respectively.

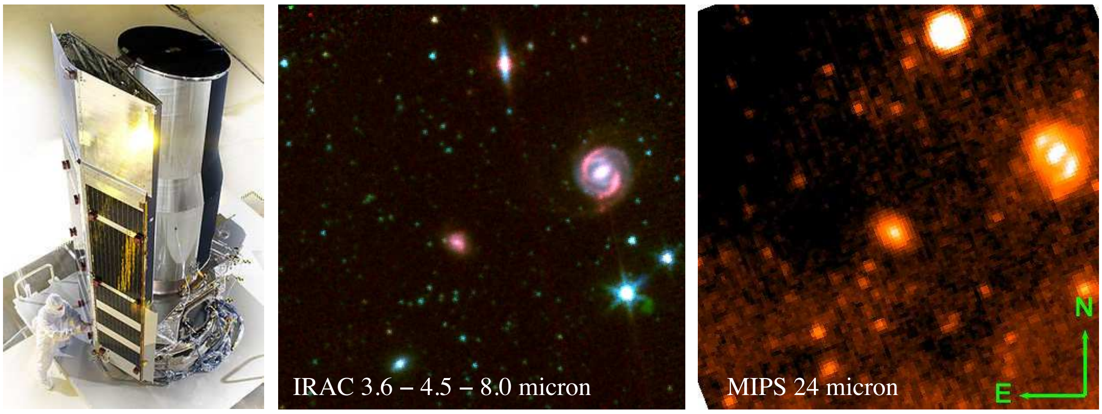

Figure 2.15: On the left the SST just before its launch in August of 2003. In the middle the IRAC "true" color image (the blue, green and red colors refer to IRAC 3.6, 4.5, and 8.0μ bands, respectively), and on the right the MIPS 24μm image of HCG71. [Image credit: Spitzer Science Center and T. Bitsakis]

In order to ascertain variations between the nuclear and total mid-IR SED of each

---

[1] IDP3 is the Image Display Paradigm 3 package available for the Interactive Data Language (IDL)

galaxy, we also performed nuclear photometry for our sources using the smallest aperture possible. The motivation behind this work was to examine whether the observed SEDs of some sources are dominated by the contribution of a strong nuclear emission, possibly due to the presence of an AGN. The apertures used were 3 pixel (3.6") in diameter for the IRAC images and 5 pixels (12.2") for the MIPS, based on the size of the corresponding point spread function (PSF).

Finally, we obtained the Spitzer mid-IR fluxes for 8 more groups from Johnson *et al.* (2007) and we included them into *sample II*. In brief, those IRAC observations were taken in high dynamic range with 270 or 540 sec exposures depending on the group. MIPS 24μm images were also obtained by the same authors with exposures of 180 or 260sec duration for the same reason. In Table 2.3, we present the observational parameters of the 35 groups of samples *I* and *II*.

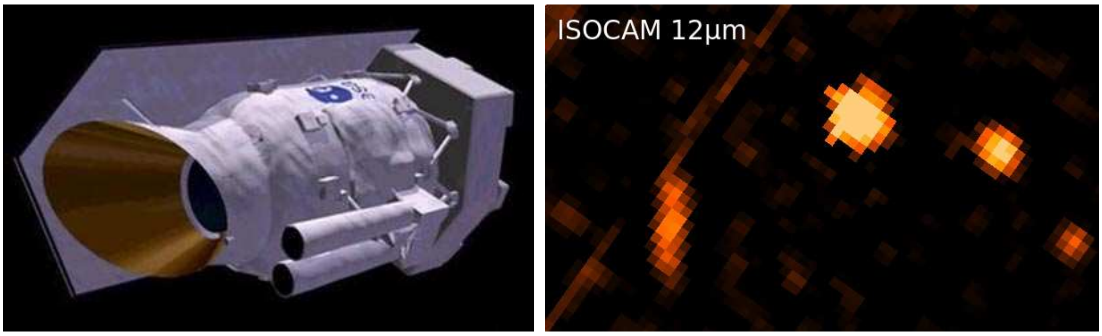

Figure 2.16: On the left an artists' impression of ISO. On the right, the ISOCAM 12μm image of HCG56. [Image credit: ESA]

Additional archival observations for 11 groups of *sample I*, were retrieved from the Infrared Space Observatory (ISO) data archive. ISO was launched by European Space Agency (ESA), in 1995. The observations were performed with the ISO/CAM instrument (Cesarsky & et al., 1996), using the LW10 filter (Program HCGROU-A). The LW10 filter is centered at $\lambda = 11.7\mu$m, and covers the $8.5 - 15.5\mu$m range so that it matches well the IRAS 12μm bandpass. The pixel size was $6'' \times 6''$ and is larger than the PSF of the telescope at this wavelength. The total on-source exposure time for the galaxies varied between 200 and 300 sec. The ISO/CAM data were analyzed with the CIR data processing software, an implementation of the algorithms of Starck *et al.* (1999) developed by P. Chanial. The standard ISO/CAM data reduction procedure was followed. First the data were read into the CIR environment. Then the "correct-dark-vilspa" routine was applied to correct for the dark current. This was followed by applying the multiresolution algorithm "correct-glitch-mr". Next, the "correct-

Table 2.3: Observational Parameters of Spitzer Archival Data

HCG ID	R.A. (J2000)	Dec. (J2000)	z	IRAC sec	MIPS_{24} sec	Observer PID
HCG02	00h31m30.0s	+08d25m52s	0.0144	180.0	260.0	3596
HCG04	00h34m15.9s	-21d26m48s	0.0269	10.0	18.3	40385
HCG06	00h39m10.1s	-08d23m43s	0.0379	150.0	375.4	50764
HCG07	00h39m23.9s	+00d52m41s	0.0141	180.0	260.0	3596
HCG15	02h07m39.0s	+02d08m18s	0.0228	300.0	375.4	50764
HCG16	02h09m31.3s	-10d09m31s	0.0132	180.0	260.0	3596
HCG19	02h42m45.1s	-12d24m43s	0.0140	180.0	260.0	3596
HCG22	03h03m31.3s	-15d40m32s	0.0090	180.0	260.0	3596
HCG25	03h20m43.7s	-01d03m07s	0.0212	300.0	375.4	50764
HCG26	03h21m54.2s	-13d38m45s	0.0316	270.0	375.4	40459
HCG33	05h10m47.9s	+18d02m05s	0.0260	270.0	375.4	40459
HCG37	09h13m35.6s	+30d00m51s	0.0223	270.0	375.4	40459
HCG38	09h27m38.8s	+12d16m51s	0.0292	270.0	375.4	40459
HCG40	09h38m54.5s	-04d51m07s	0.0223	270.0	375.4	40459
HCG42	10h00m21.8s	-19d38m57s	0.0133	180.0	260.0	3596
HCG44	10h18m00.5s	+21d48m44s	0.0046	360.0	917.5	159
HCG47	10h25m48.4s	+13d43m54s	0.0317	270.0	375.4	40459
HCG54	11h29m15.5s	+20d35m06s	0.0049	270.0	375.4	40459
HCG55	11h32m07.4s	+70d48m43s	0.0526	270.0	375.4	40459
HCG56	11h32m39.6s	+52d56m25s	0.0270	270.0	375.4	40459
HCG57	11h37m50.5s	+21d59m06s	0.0304	270.0	375.4	40459
HCG59	11h48m26.6s	+12d42m40s	0.0135	180.0	260.0	3596
HCG61	12h12m24.9s	+29d11m21s	0.0130	180.0	260.0	3596
HCG62	12h53m08.1s	-09d13m27s	0.0137	180.0	260.0	3596
HCG67	13h49m03.5s	-07d12m20s	0.0245	300.0	375.4	50764
HCG68	13h53m40.9s	+40d19m07s	0.0080	75.0	375.4	50764
HCG71	14h11m04.6s	+25d29m06s	0.0301	270.0	375.4	40459
HCG75	15h21m33.8s	+21d11m00s	0.0416	150.0	375.4	50764
HCG79	15h59m11.9s	+20d45m31s	0.0145	270.0	375.4	40459
HCG82	16h28m22.1s	+32d49m25s	0.0362	150.0	375.4	50764
HCG91	22h09m10.4s	-27d47m45s	0.0238	300.0	375.4	50764
HCG92	22h35m57.5s	+33d57m36s	0.0215	432.0	627.5	198
HCG95	23h19m31.8s	+09d29m31s	0.0396	270.0	375.4	40459
HCG97	23h47m22.9s	-02d19m34s	0.0218	300.0	375.4	50764
HCG100	00h01m20.8s	+13d07m57s	0.0178	300.0	375.4	50764

transient-fs" routine, based on the Fouks-Schubert transient correction method (Coulais & Abergel, 2000), was applied to the data to remove transient effects. The frames were flat-fielded using CIR's library flat field, and subsequently combined to produce a final image. Some masking on the edges of the images was performed to correct for bad pixels. Photometry was performed by selecting the regions of galaxies with emission greater than 3σ above the sky background noise. We estimate that the absolute uncertainty of our photometric measurements is $\sim 10\%$ and it is mainly due to errors on the correction of the detector transient effect.

Recently, the mid-IR all sky survey of the Wide-field Infrared Survey Explorer (WISE Wright *et al.*, 2010) was released. The WISE is a 40cm telescope, which performed an all sky astronomical survey, covering the 3.4, 4.6, 6.5 and 12.0μm bands (named w1-to-w4), with 5-σ sensitivity limits 19.70-to-14.40 mags, respectively. The WISE photometry (WPHOT) was automatically performed using profile fitting. However, if the PSFs of two or more galaxies are closer than the resolution of the telescope (6-to-12 arcsec), WPHOT reports a total photometry and a blending parameter which is the number of PSFs included in the aperture. Therefore, using the latest all sky release, we obtained the photometry, or the upper limits, for the 7417 galaxies of *sample III*.

2.2.5 Far infrared: Unveiling the dust

Moving away from the mid- to the far-infrared wavelengths, the stars have all vanished. Now we are able to see only very cold matter. This cold matter consists of gas and dust at very low temperatures (typically 20-40K). Sources of heating in molecular clouds include the ionization of carbon atoms from UV starlight, the photoelectric ejection of electrons from dust grains by UV starlight, the absorption of light energy into the lattice of dust grains, and the ionization of hydrogen by stellar X-rays. As we explained in the introduction, interactions cause dynamical instabilities in galactic disks which redistribute the gas and dust both towards their centers forming new stars, often as part of massive dust enshrouded nuclear starbursts, as well as in the extragalactic space in the form of plumes and tails. Since truly isolated galaxies are the exception rather than the rule, observations of the dust and gas at these wavelengths can provide us with crucial information about the evolution of galaxies. Nevertheless, as we mentioned before, the Earth's atmosphere is completely opaque in the far-infrared. Thus a space telescope is needed to obtain far-infrared observations. In 1983, NASA launched the first such telescope, the Infrared Astronomical Satellite (IRAS; see Fig. 2.17), which surveyed over 96% of the sky at 12, 25, 60, and 100μm. It observed more than 20,000 extended sources (Beichman *et al.*, 1988), with lower limit the 0.5Jy in the first three bands, and 1.5Jy in the 100μm band. The most important discovery of IRAS was the identification of galaxies which emit the major part of their energy in the far-infrared (Sanders & Morabel, 1996). Later, ISO and Spitzer space observatories could also observe at the far-IR wavelengths, however they did not perform all sky surveys. The next all sky survey was carried out by the AKARI satellite. AKARI –which means "light" in Japanese– was launched in 2006 by the Japanese Aerospace Exploration Agency (JAXA). Its all sky survey was accomplished by November of the same year, and mapped the far-infrared sky in the 65-160μm.

Figure 2.17: On the left the Infrared Astronomical Satellite (IRAS). On the right, the AKARI Astro-F space observatory. (Images by NASA and JAXA)

Using the IRAS all sky release, Allam *et al.* (1996) obtained integrated far-IR photometry at 60 and 100μm data for each group as a whole. However, because of the compact environment and small angular separation of the galaxies in the HCGs, the coarse angular resolution of IRAS at the 60 and 100μm ($\sim$100"), enabled us to resolve only 31 individual galaxies of our sample, which were sufficiently isolated and bright.

However, using the recently AKARI released data, we retrieved far-IR observations for 26 galaxies of *sample II* (22 of them were already resolved by IRAS). These observations were obtained with the Far-IR Surveyor (FIS) and processed with the AKARI official pipeline software version 20080530 (Okada *et al.*, 2008). The photometry using N60, WIDE-S, WIDE-L, and N160 filters, centered at 65, 90, and 140 160 μm was downloaded from the AKARI on-line archive and is reported along with the IRAS data in Table 2 of Bitsakis *et al.* (2011). We should note that the FWHMs of the AKARI PSF is $\sim$45" at 65 and 90μm and $\sim$60" at 140 and 160μm. Even though this is better than IRAS, as we will discuss in more detail later, it places restrictions in interpreting the far-IR properties of the groups and the spatial distribution of their cold dust content.

Chapter 3

Estimating the physical parameters

In Chapter 2, we presented our three samples of compact groups of galaxies. The first two are parts of the Hickson's catalog of compact groups, and the third is the much larger SDSS CG sample. As we also explained in the introduction, our main motivation is to study the evolution and properties of galaxies –within groups– from an infrared perspective. Thus, as we discussed near-IR imaging was obtained for all our samples, using ground based observations from 2MASS, Palomar, and Skinakas observatories, as well as mid-IR imaging from Spitzer and WISE space telescopes. Moreover, since young stellar populations mostly radiate in the UV and optical wavelengths. GALEX/UV and SDSS/optical data were also obtained for our two largest samples (II and III). Finally, in order to constrain the amount of energy which is absorbed in the UV and optical wavelengths and re-emitted at the infrared, far-IR data are essential. Thus, using the IRAS and AKARI surveys, we obtained the far-IR fluxes for several of our galaxies of *sample II*. In this chapter, we will use the fluxes of galaxies in all these bands, to estimate a number of physical parameters, using both empirical methods, as well as theoretical models based on fitting their UV–to–far-IR spectral energy distribution (SED).

3.1 Empirical estimation of the physical parameteres

3.1.1 Stellar masses

As already stated in Chapter 2, the integrated UV and blue optical emission in galaxies is dominated by short-lived young massive stars. As a result, it may fluctuate depending on the recent star formation history of each galaxy. On the other hand, their near-IR emission is dominated by old stellar populations, which live longer and it is not as affected by dust extinction as the UV-optical light. In addition, Bell & de Jong (2001) have shown that the near-IR mass-to-light (M/L) ratios, vary only by a factor less than 2. For all these reasons, it is believed that near-IR is the best estimator of galaxy stellar mass. The stellar masses of our galaxies were estimated using the Bell *et al.* (2003) prescription which was calibrated using a large sample of galaxies in the local universe. Their formula, based on the K-band luminosity, is:

$$\mathrm{M(M_{\odot}) = 10^{a+b(B-R)} \times L_{Ks}(L_{Ks,\odot})} \tag{3.1}$$

where B and R are the B- and R-band magnitudes of the galaxy, $\mathrm{L_{Ks}}$ its Ks-band luminosity in units of solar luminosities ($\mathrm{L_{Ks,\odot}} = 4.97 \times 10^{25}$W), a=-0.264, and b= 0.138, with systematic errors of ∼30% due to uncertainties in the star formation history and dust. Because these authors used a "diet" Salpeter Initial Mass Function (IMF), we corrected it to a Chabrier IMF, which our SED fitting model uses, multiplying their M/L by 0.81 as described in Zibetti *et al.* (2009). Finally, since the Bell *et al.* (2003) relation uses the models of Bruzual & Charlot (2003) (BC03), which do not take into account the contribution of thermally pulsing AGB stars, we applied the color correction as described in Zibetti *et al.* (2009) for the Charlot & Bruzual 2007 libraries (CB07), where a is -1.513 and b is 0.750 for the same colors. More recently, though, it has been shown that the contribution of these stars to the near-IR was overestimated and thus the older BC03 models describe better the real stellar masses (Zibetti *et al.*, 2012). Therefore, we will not use the corrections of Zibetti *et al.* (2009) on the galaxies of *sample III*.

3.1.2 Extinction correction and star formation rates

The rate by which a galaxy forms stars, is one of its most important properties, especially in interacting systems which evolve very rapidly as they consume the available gas. It can be used to probe the evolutionary histories of these galaxies. In the absence of narrow band imaging of the hydrogen recombination lines (i.e. Hα), two of the most common ways to estimate the SFR rely on prescriptions using their UV broad band emission from GALEX, or the mid-IR thermal dust emission from Spitzer/MIPS 24μm or WISE 22μm band.

Since a significant fraction of the bolometric luminosity of a galaxy is absorbed by interstellar dust and re-emitted in the thermal IR, mid-IR observations can probe the dusty interstellar medium and dust-enshrouded SFRs. The efficiency of the IR luminosity as a SFR tracer depends on the contribution of young stars to the heating of the dust and the optical depth of the dust in the star forming regions. Calzetti *et al.* (2007) using a wealth of multi-wavelength observations for 33 SINGS galaxies provided the following recipe:

$$\mathrm{SFR}_{24}(\mathrm{M}_{\odot}\mathrm{yr}^{-1}) = 1.27 \times 10^{-38}(\mathrm{L}_{24}(\mathrm{erg\,s}^{-1}))^{0.885} \tag{3.2}$$

to calculate the SFR from the 24μm luminosities obtained with Spitzer.

Similarly, to estimate the SFRs from the WISE 22μm band we used the formula described in Rieke *et al.* (2009) which is given by:

$$log(SFR) = A(z) + B(z)(log(4\pi D_L^2 f_{obs}) - 53), \tag{3.3}$$

where SFR is in $\mathrm{M}_{\odot}$ yr^{-1}, D_L is the luminosity distance in Mpc, and f_{obs} is the observed 22μm flux in Jy. The coefficients A(z) and B(z) depend on the redshift, and for the redshift range of our *sample III* (z$\sim$0.0-0.1) they were estimated to be A=0.417 and B=1.032 (see Table 1 of Rieke *et al.* 2009). Even though these were derived for the MIPS 24μm band, however it has been shown that the correlation between the L_{IR} and the inferred MIPS 24μm and WISE 22μm luminosities are nearly identical (Goto *et al.*, 2012), thus these coefficients can be used also for the WISE band. The total error attributed to this formula is about 0.2 dex, caused by the scatter in the $\mathrm{L}_{24}$$-$$\mathrm{L}_{IR}$ relation. To derive this relation Rieke *et al.* (2009) used an IMF8 (Rieke *et al.*, 1993), which is similar to the Chabrier (2003) one.

In the UV the integrated spectrum is dominated by young stars ($\sim$10Myr), and so the SFR scales linearly with luminosity. However in order to use the UV to trace SFR, we have to correct the attenuated UV fluxes for dust extinction. One method to do this is to use the β-slope correction,

$$\beta(GALEX) = \frac{log(f_{FUV}) - log(f_{NUV})}{log(\lambda_{FUV}) - log(\lambda_{NUV}))} \tag{3.4}$$

where f_{FUV} and f_{NUV} are the flux densities per unit wavelength in the FUV and NUV bands respectively, $\lambda_{FUV} = 1520$Å, and $\lambda_{FUV} = 2310$Å. Then we can apply the relation of Meurer *et al.* (1999) for starburst galaxies,

$$\mathrm{L}_{\mathrm{FUV,cor}} = 10^{0.4(4.43+1.99\beta)}\mathrm{L}_{\mathrm{FUV,obs}} \tag{3.5}$$

where $\mathrm{L}_{\mathrm{obs}}$ and $\mathrm{L}_{\mathrm{cor}}$ are the observed and extinction corrected FUV luminosities and finally we can derive the SFRs using the relation of Salim *et al.* (2007):

$$\mathrm{SFR}_{\mathrm{FUV}}(\mathrm{M}_{\odot}\mathrm{yr}^{-1}) = 6.84 \times 10^{-29}\,\mathrm{L}_{\mathrm{FUV,cor}} \tag{3.6}$$

for Chabrier (2003) IMF. The SFRs of the early-type galaxies cannot be estimated using this method, as their β-slope is mainly determined by the old stellar population rather than the dust extinction causing an overestimation of their extinction corrected UV luminosities. In addition, Kong *et al.* (2004) found that this method was also overestimating the UV luminosities of the normal star forming galaxies. They attributed this to the fact that Meurer *et al.* (1999) calibrated his method using a sample of starburst galaxies.

A similar relation, though, was proposed by Buat *et al.* (2005). These authors used the infrared to UV luminosity ratio to quantify the dust attenuation in the FUV band of GALEX for a wider sample which contains more quiescent galaxies. The formula they derived to correct for dust extinction is described by the following relation:

$$A_{\mathrm{FUV}} = 0.0333y^3 + 0.3522y^2 + 1.1960y + 0.4967 \tag{3.7}$$

where y=log($\mathrm{F}_{dust}/\mathrm{F}_{\mathrm{FUV}}$) is the ratio of the infrared to FUV flux densities. To derive these ratios for our galaxies we used the infrared luminosities estimated by our SED modelling, as well as the observed UV luminosities and estimated the SFR using the formula (4) of Iglesias-Páramo *et al.* (2006) :

$$\log[\mathrm{SFR}_{\mathrm{FUV}}(\mathrm{M}_{\odot}\mathrm{yr}^{-1})] = 0.63 \times (\log[\mathrm{L}_{\mathrm{FUV,corr}}(\mathrm{L}_{\odot})] - 9.51) \tag{3.8}$$

where the $\mathrm{L}_{FUV,corr}$ is the extinction corrected FUV luminosity (in $\mathrm{L}_{\odot}$) and the factor of 0.63 has been introduced to correct for the Chabrier IMF (Chabrier, 2003; da Cunha *et al.*, 2008).

3.1.3 Specific star formation rates

It has been shown by several studies that the normal star forming galaxies' stellar masses and SFRs are strongly correlated (Brinchmann *et al.*, 2004). Galaxies lying on this tight correlation are called "main sequence" galaxies. It seems that in main sequence star forming galaxies, stellar mass is a very important parameter which regulates their SFRs. Since normal star forming galaxies obey to this mass-SFR correlation, deviations may indicate changes in their normal star formation activity, due to induced star formation and/or gas loss.

The specific star formation rate (sSFR), the star formation rate per unit mass of a galaxy, is given by the following relation:

$$sSFR(yr^{-1}) = \frac{SFR(M_{\odot}yr^{-1})}{M(M_{\odot})} \tag{3.9}$$

and it provides an estimate on the amount of time required for a galaxy to double its stellar mass if it were to continue forming stars as the present rate.

3.2 Model derived physical parameters

To estimate the physical properties of the galaxies in our samples in a more systematic way, we fitted the observed Spectral Energy Distribution (SED) of each galaxy with sets of theoretical, as well as empirical SED models. To do this we used the *Le Phare* code[1] (see Arnouts *et al.*, 2007; Ilbert *et al.*, 2009), and the state-of-the-art physically motivated model of da Cunha *et al.* (2008), which is called MAGPHYS[2]. Using *Le Phare*, we predicted the IR theoretical SEDs of the galaxies in *sample I*. Later, by applying MAGPHYS, on the multi-wavelength HCG *sample II*, we estimated the total theoretical SEDs of the galaxies as well as several of their physical parameters (i.e. SFRs, A_V). Finally, to constrain some of the physical properties of the galaxies in our SDSS CG *sample III* for which SDSS optical spectra were available, Brinchmann *et al.* (2004) followed the methodology of Charlot *et al.* (2002) to model their emission lines.

3.2.1 LePHARE

Using multi-wavelength template libraries, *Le Phare* is able to perform a two-component galaxy SED modeling by decomposing the fit of each source into the contribution of its stellar populations and the contribution from dust emission. The near-IR observations are strongly dominated by stellar blackbody emission, with possibly a small contribution from very hot dust in the case of an AGN. In late-type star-forming galaxies, two of the IRAC bands, centered on 5.8 and 8μm, may contain the contribution of PAHs, while the 24μm luminosity traces thermal emission from dust mostly heated in embedded star-forming regions. Consequently the templates used to fit the data should be compatible with those characteristics. A first fit of the near-IR J, H, and Ks photometry of our galaxies was obtained using pure stellar templates taken from the library of SEDs used by Ilbert *et al.* (2009) to derive galaxy photometric redshifts. The goal of this initial step was to estimate the contribution of the underlying stellar component to the emission observed in the Spitzer bands at longer wavelengths. This contribution was subsequently subtracted from the IRAC and MIPS fluxes assuming an extrapolation of a typical stellar blackbody emission, and the resulting fluxes were fitted between 5 and 24μm using a separate library of IR SEDs. For the IR SEDs, we used a modified version of the IR template library of Chary & Elbaz (2001), which includes 105 star-forming galaxy IR SEDs over a broad range of total IR luminosities.

---

[1] For more information on *Le Phare* visit the web page of the package at http://www.cfht.hawaii.edu/∼arnouts/LEPHARE/cfht_lephare/lephare.html

[2] The da Cunha *et al.* (2008) model is publicly available at http://www.iap.fr/magphys.

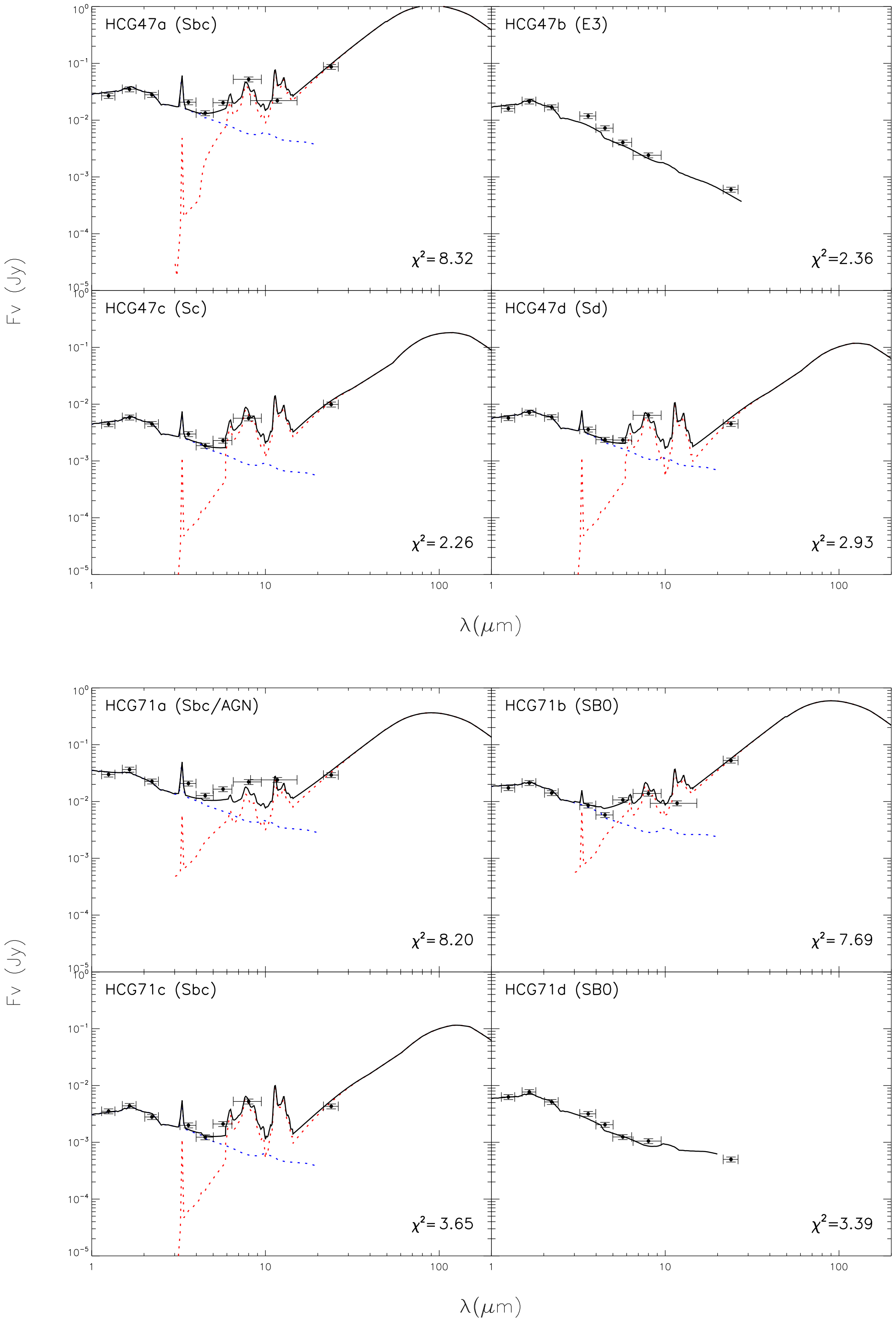

Figure 3.1: The observed and theoretical SEDs of HCG 47(top panel) and HCG 71 (bottom panel). The galaxies are labeled with their HCG number, type, and spectral classification, if known. The vertical error bars indicate the uncertainty of each measurement, while horizontal bars show the bandwidth of the corresponding filter.

These templates cover the optical to radio wavelength range, so their stellar component was systematically removed prior to the fitting with *Le Phare* to reproduce only the thermal dust component of our sources. For each galaxy of our *sample I*, the best total fit was then obtained by co-adding the fit derived for the stellar component and the one obtained in the mid-IR. Galaxies with very low 24μm emission, mostly early-type systems, were only fitted with a single stellar component, since subtracting it from the 24μm flux would introduce a large uncertainty to the final estimate of the thermal dust emission. In Fig. 3.1 we present an example of the infrared SEDs of two groups (HCG 47 & 71) along with the best-fit model from *Le Phare* (all the fitted mid-IR SEDs of *sample I* are presented in Fig. A.1. of Bitsakis *et al.* 2010). Each panel corresponds to one galaxy.

Most SED fits are fairly good as is evident from the plots in Fig. 3.1 and the corresponding reduced χ^2 values, which vary between 1 and 11 and are marked in each plot. A number of galaxies display mid-IR fluxes consistent with strong PAH emission and often warm dust, a sign of enhanced star formation activity. There are, though, some galaxies (such as 71a in Fig. 3.1) that are not fitted as well by the templates. These galaxies display an excess emission in the Ks-band and/or mid-IR, which is suggestive of some type of nuclear activity, possibly from an AGN. Even if star formation and thus PAH emission were present in these systems, the nuclear thermal dust emission would dominate the emitted flux, resulting in rather flat or rising mid-IR spectrum.

3.2.2 MAGPHYS

As discussed in detail by da Cunha *et al.* (2008) the Multiwavelength Analysis of Galaxy Physical Properties model (MAGPHYS) assumes that the source of energy in a galaxy is due to an ensemble of stellar populations (no AGN heating is included) whose emission is partially absorbed by dust and re-emitted at longer wavelengths. The model treats the complete SED from the UV to the far-IR and allows us to derive not simply best fit physical parameters to the data, but also to provide the range of their median-likelihood values which are consistent with the observations. To achieve this, the model adopts a Bayesian approach which draws from a large library of random models encompassing all plausible parameter combinations, such as star formation histories, metallicities, dust optical depths as well as dust masses and temperatures. Clearly the wider the wavelength coverage, the more robust the derived parameters. Thus to properly estimate the effect of dust extinction, the UV and optical range needs to be well sampled, while to estimate dust masses and luminosities mid- and far-IR coverage is essential. In addition to the HCG sample, we used the model to fit the interacting pairs of Smith *et al.* (AJ) and the results are presented in the Table 5 of Bitsakis *et al.* (2011). The galaxies of the SINGS sample had already been fit by da Cunha *et al.* (2008).

3.2.2.1 Description of the model

The da Cunha *et al.* (2008) model computes the emission by stars in galaxies using the latest version of the Bruzual & Charlot (2003) population synthesis code. This code predicts the spectral evolution of stellar populations in galaxies from the far-ultraviolet to infrared wavelengths and at ages between 1×10^5 and 1.37×10^{10} yr, for different metallicities, initial mass functions (IMFs) and star formation histories. In this work, we adopt the Chabrier (2003) Galactic-disc IMF. The model does not take in account the energy contribution of an active nucleus to the global SED. Since nearly 40% of our sources host an optically identified AGN one could consider that this could introduce a bias in our analysis. However, based on a number of mid-IR diagnostics, the influence of the active nucleus to the total infrared emission of the majority of our galaxies is insignificant, thus this limitation does affect seriously our conclusions (see details in Section 4.5.2).

The emission from stars is attenuated using a two component dust model of Charlot & Fall (2000). This model uses an “effective absorption” curve for each component. They use this prescription to compute the total energy absorbed by dust in the birth clouds (BC) and in the ambient interstellar medium (ISM); this energy is re-radiated by dust at infrared wavelengths (see Fig. 3.2). They define the total dust luminosity re-radiated by dust in the birth clouds and in the ambient ISM as L_d^{BC} and L_d^{ISM}, respectively. The total luminosity emitted by dust in the galaxy is then $L_d^{tot} = L_d^{BC} + L_d^{ISM}$. The value of L_d^{BC} and L_d^{ISM} is calculated over the wavelength range from 3 to 1000 μm using four main components:

- The emission from polycyclic aromatic hydrocarbons (PAHs; i.e. mid-infrared emission features).
- The mid-infrared continuum emission from hot dust with temperatures in the range 130-250 K.
- The emission from warm dust in thermal equilibrium with adjustable temperature in the range 30-60 K.
- The emission from cold dust in thermal equilibrium with adjustable temperature in the range 15-25 K.

A detail analysis of da Cunha *et al.* (2008) suggests that the above minimum number of components is required to account for the infrared spectral energy distributions of galaxies in a wide range of star formation histories.

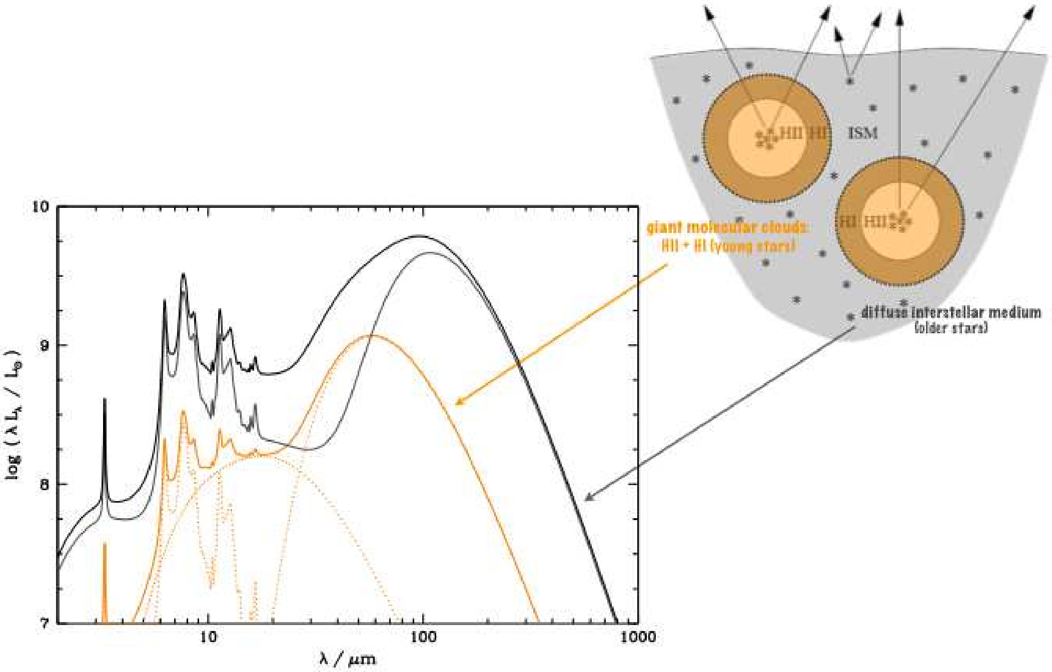

Figure 3.2: This figure presents the way that the emission from the stellar birth clouds (orange) and the diffuse interstellar medium (grey) are affecting the galaxy emission in the infrared wavelengths [Image from da Cunha *et al.* 2008]

3.2.2.2 Model library

We use a large random library of star formation histories and dust emission models presented in da Cunha *et al.* (2008). In this library, each star formation history is parameterized using a star formation rate that is exponentially declining with time, on top of which random bursts are superimposed. The metallicities of these models are sampled uniformly between 0.2 and 2 times solar, and the model ages are distributed uniformly between 0.1 and 13.5 Gyr. Each stellar emission model computed using these star formation histories, ages and metallicities is then attenuated by dust using the two-component description of Charlot & Fall (2000) described above, using a wide range of V-band dust optical depths in the birth cloud and ISM component. Each of these model spectra are then consistently connected to dust emission spectra spanning a wide range in dust temperatures and fractional contributions of each dust emission component to the total dust luminosity. In particular, dust emission models with the same dust luminosity and the same relative contributions to total dust luminosity from the birth cloud and ISM (i.e. $L_{d,tot}$ and $f\mu$) are assigned to each stellar emission model, as detailed in da Cunha *et al.* (2008).

For each ultraviolet to infrared model spectrum in this library, we compute the synthetic photometry in the GALEX FUV and NUV, SDSS ugriz, B, R, near-IR, Spitzer IRAC and MIPS-24, AKARI/FIS and IRAS 60 and 100μm bands at the redshifts of our galaxies to allow for a direct comparison between the observed and model broad-band SEDs as detailed below.

3.2.2.3 Spectral energy distribution fits

We compare the observed spectral energy distributions of the galaxies in our HCGs to every model in the stochastic library of models described above by directly comparing the observed and model broad-band fluxes and computing the χ^2 goodness of fit for each model in the library. This allows us to compute, for each galaxy in the sample, the full likelihood distributions of several model parameters, such as the star formation rate, stellar mass, V-band optical depth in the birth clouds and ISM, dust luminosity etc. We take our final estimate of each parameter to be the median of the likelihood distribution, and the associated confidence interval to be the 16th − 84th percentile range of that distribution.

As examples of our fits, we show in Fig. 3.3 the best-fit spectral energy distributions of two galaxies from our sample: a typical late-type galaxy (HCG2a, top panel); and one quiescent elliptical galaxy (HCG62a, bottom panel).

We note that, as discussed in Section 2.2.5, even though far-IR measurements are available for each HCG as a whole, most of the galaxies are not independently resolved in the far-IR, due to the large IRAS beam sizes. This presents a serious limitation to the sampling of our SEDs and consequently to the constraints on the dust temperature, total dust mass and luminosity of each galaxy. One of the strengths of this approach is that, by building the full likelihood distributions of the model parameters, we are able to take these uncertainties caused by the lack of far-IR observations into account (see also da Cunha *et al.*, 2008).

3.2.3 Modeling the emission lines of the SDSS CG sample

We can derive several of the physical parameters of the SDSS CG galaxies, which have available spectroscopy, by modeling their observed optical line emission. Brinchmann

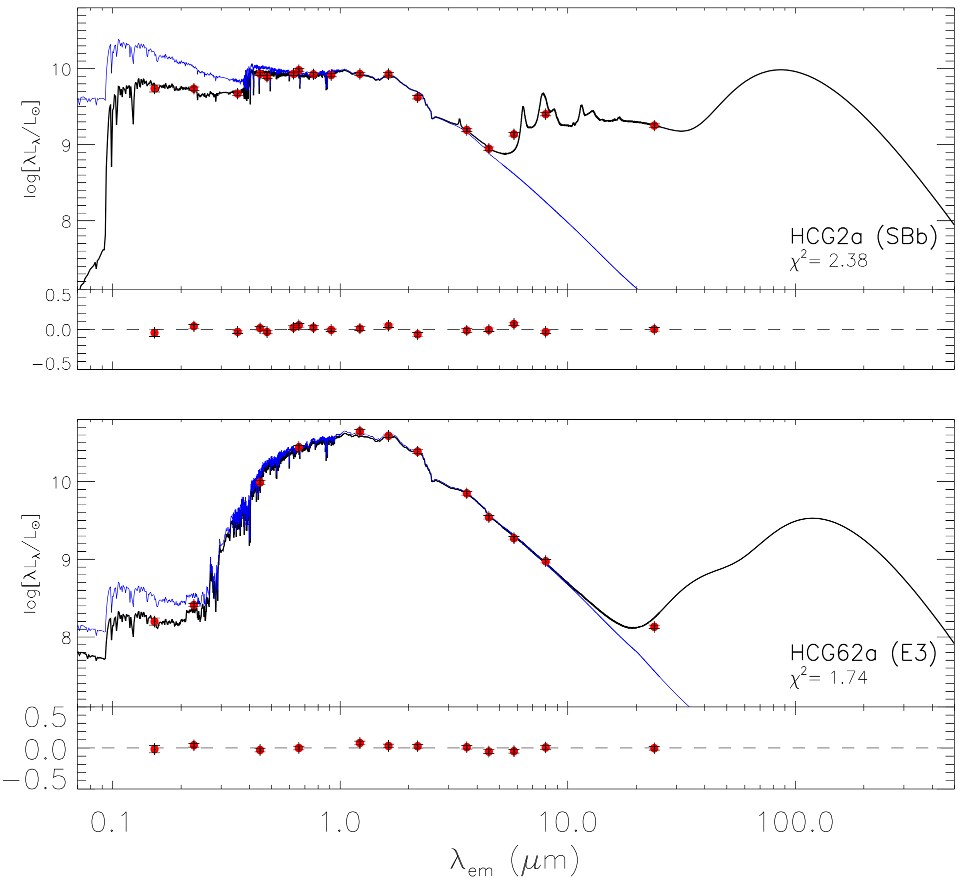

Figure 3.3: Example of best fit models (in black line) to the observed spectral energy distributions of two galaxies in *sample II*. One is a typical late-type galaxy (HCG2a; top panel) and the second is a quiescent elliptical galaxy (HCG62a; bottom panel). In each panel, the blue line shows the unattenuated stellar spectrum estimated by the model. The red circles are the observed broadband luminosities with their errors as vertical bars. The residuals, $(L_\lambda^{\rm obs} - L_\lambda^{\rm mod})/L_\lambda^{\rm obs}$, are shown at the bottom of each panel. Note the uncertainty in the far-IR shape of the SED due to lack of high spatial resolution data.

et al. (2004) published a catalog of ~10^5 galaxies with measurable star formation in the SDSS. They modeled the emission lines of the galaxies in their sample, which were classified as star forming (SF) in the BPT diagram (see Section 2.1.2.2), and they calculated the likelihood distributions of their physical parameters (such as the SFRs). To do this, they had generated a model grid using: the galaxy metallicity (Z), the ionization parameter in the edge of the Strömgren sphere (U), the total V-band dust attenuation (τ_V), and the dust-to-metal ratio of the ionized gas (ξ), in the way it is described in Charlot *et al.* (2002), with only difference that Brinchmann *et al.* (2004) used a Bayesian approach. On the other hand, they did not use parameters such as the stellar age, the star formation history, and the relative attenuation by dust in the stellar birth clouds and the ambient ISM, since they only wanted to model the relative line fluxes. For each model in their grid they had estimated a different dust extinction. Then, they estimated the attenuated line ratios (e.g. $H\alpha/H\beta$) and using these ratios they compared them directly with the observed spectra.

However, as we mentioned in Sect. 2.2.2, the diameter of the spectroscopic fiber of SDSS was 3arcsec. At the z of 0.091, where the most of the galaxies of *sample III* are found, 3arcsec in the fiber correspond to ~5kpc, which is relatively small to the typical diameters of spiral galaxies (5-50kpc). As a result, light coming from these sources is not totally measured, and their SFR is underestimated. Therefore, in order to estimate the total SFRs, and not only the ones within the fibre, Brinchmann *et al.* (2004) calculated the light outside the fibre of each galaxy, and then fitted the stochastic models. The basic advantage of their method is that it generates the likelihood distributions of the parameters, thus they are able to calculate the confidence of their estimates.

However, for the galaxies which may host an AGN or a transition object (TO), they could not use the model fits to determine their SFRs, since their optical line fluxes are possibly affected from the AGN component. However, they found that there is a correlation between the 4000-Å break index (or D4000) and the sSFRs in the SF sample (see Fig. 3.4). This break arises from the accumulation of absorption lines of ionized metals. In young hot stars the elements are multiply ionized and the opacity decreases, thus, the 4000-Å break will be small. The D4000 is the break index (Bruzual, 1983), and is defined as the average ratio between the 4050-4250Å and 3750-3950Å bands. Thus, D4000 is useful to investigate recent star formation activity in galaxies. Therefore, Brinchmann *et al.* (2004) using the correlation, mentioned above, derived the approximated SFRs for the AGN and TO galaxies. However, as they mention, these SFRs are only approaching the real values, due to large uncertainties, and they can be used only on average.

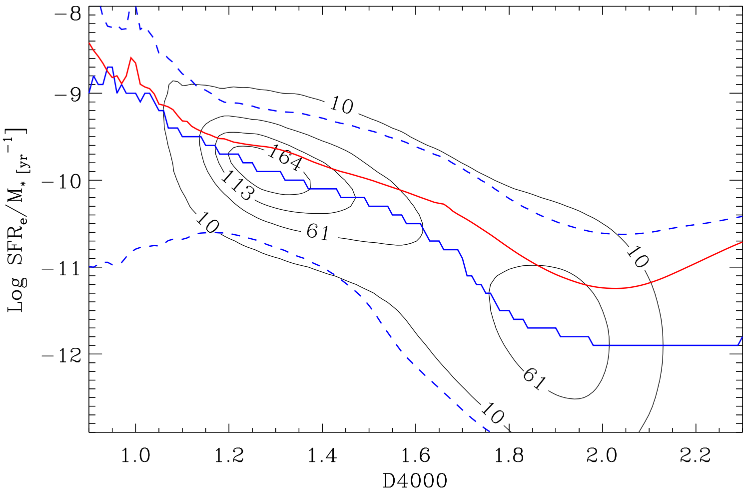

Figure 3.4: Correlation between the 4000-Å break and the sSFR of the galaxies, which were classified as AGN or TO (Brinchmann *et al.*, 2004). The contour lines are equally spaced from 10 galaxies per bin to the maximum. The upper solid line shows the average at a given D4000 and the lower solid line shows the mode of the distribution. The dashed lines show the limits containing 95 per cent of the galaxies at a given D4000. [Image from Brinchmann *et al.* 2004]

Brinchmann *et al.* (2004) used as stellar masses for their sample the ones derived by Kauffmann *et al.* (2003b), who developed a new method to constrain the stellar masses, dust extinction and star formation histories, based on two stellar absorption indices, the 4000-Å break and the Balmer absorption line index (Hδ_A). To do this they generated a large library of Monte Carlo realizations of different star formation histories. Using this library they calculated the likelihood distributions of several parameters, such as the dust attenuation and the stellar mass-to-light ratios. For each acceptable model, they multiplied the unattenuated luminosity of each galaxy with the stellar mass-to-light ratio of the model, and they estimated the stellar mass of the galaxy.

Therefore, by cross-correlating our *sample III* with the sample of Brinchmann *et al.* (2004), we find that: (*i*) for the 3374 galaxies, with optical SDSS spectra, there are 1961 star forming galaxies, for which they have estimated their M$_{stellar}$ and SFRs, using the emission lines modeling, and (*ii*) 1413 galaxies for which they estimated the SFRs using the more uncertain of 4000-Å break.

3.3 Comparison of the empirical and theoretical modeling results

3.3.1 Evaluating the LePhare estimates

We compared the galaxy classification for the *sample I*, which is based on the template fitting of their SEDs to existing optical morphology classification. Our data, indicate that some of the galaxies, classified as early-type based on their optical images, do have excess dust emission in the infrared. These are HCG26b, 37c, 37e, 55a, 55b, 55d, 56b, 56d, 56e, 71b, 79b, 95b, and 95d of *sample I*. This implies that either embedded star formation or accretion of gas-rich dwarf galaxies have fueled these systems with enough dust and gas to emit strongly in the mid-IR. All of them seem to have late-type galaxy SEDs in the infrared. Three (HCG37c, 56b, and 56d) are spectroscopically classified as AGN in the optical, while others exhibit a mid-IR SED that is suggestive of emission from an AGN. Interestingly, there are also galaxies that have IR SEDs consistent with that of an early-type galaxy. These include HCG38d and HCG95b, which are nonetheless classified as late-type in the optical. This could be due to the loss of a large fraction of their gas and dust, probably because of interactions, which would be the result of the absence of far-infrared emission. One of the galaxies in our sample, HCG 40f, which was not classified in the literature, has been fitted with an E1 galaxy template, consistent with its morphological appearance in the optical and infrared images.

As we already mentioned in Sect. 3.1.1, the Ks band luminosity is a good tracer of the stellar mass because light in this band is dominated by the emission of low-mass stars, which are responsible for the bulk of stellar mass in galaxies. Similarly, we showed that the 24μm emission is a good tracer of star formation because it originates in regions of dust mainly heated by young stars. We used the observed Ks-band and 24μm luminosities (L_K and $L_{24\mu m}$) to estimate the corresponding stellar mass and SFR for each galaxy. To obtain the galaxy mass, we used the Bell *et al.* (2003) relation (described in the Section 3.1.1), with systematic errors of $\sim 30\%$, dominated by the uncertainties in the star formation history and dust. The SFRs were estimated from the 24μm by the calibration developed by Calzetti *et al.* (2007) (described in detail in Section 3.1.2). Examples of our mass and SFR estimates is reported in Table 2 of Bitsakis *et al.* (2010) along with a measure of the sSFR of our sources defined as the ratio of SFR over the galaxy stellar mass.

3.3.2 Evaluating the MAGPHYS estimates

Given the available observations, the stellar mass and SFR of a galaxy are the two physical parameters which are constrained more accurately using our SED modeling. Since in *sample I*, we did not have the multi-wavelength data and the more sophisticated SED model, we used semi-empirical methods, relying on the K-band luminosity and the 24μm emission, to estimate the stellar mass and the SFR respectively. In this section, we compare the model derived parameters with those from the empirical methods, to better understand the uncertainties in the interpretation of the results. We also compare them with the methods of Salim *et al.* (2007) and Iglesias-Páramo *et al.* (2006), which use the NUV and FUV bands of GALEX, respectively, to estimate the SFR, in order to evaluate their consistency with the model results (see Section 3.1.2).

As we can see in Fig. 3.5, the masses estimated by the model (M_{model}) agree with the Zibetti *et al.* (2009) ones (described in Section 3.1.1). This was somewhat expected as the latter recipe was calibrated using the same models. However, there are some outliers such as HCG40f, for which the model was not able to estimate very well the stellar mass since there were not enough observations to well constrain its SED.

Using the formula of Calzetti *et al.* (2007), described in Section 3.1.2, we also estimated the SFR of the galaxies in *sample II* (they are displayed as red points in Fig. 3.6). As we can see the 24μm estimates and those from the model fit to the whole SED, agree fairly well, having a ratio with a median value of unity and a standard deviation of 0.51dex. The scatter does not seem to correlate with the galaxy mass or luminosity. To examine whether the scatter is due to the absence of far-IR measurements for a large fraction of the galaxies in our sample we selected 35 galaxies for which IRAS and Akari fluxes were available and fit them again with the model, removing this time the far-IR points. We then compared the new estimates of the SFRs with the ones when all data were used and found that they were very similar, their average ratio being 0.95 and the corresponding standard deviation 0.19. A possible explanation for the scatter between the SFRs estimates of the model and ones of the Calzetti *et al.* (2007) method could be related to variations in the metallicity of the galaxies (see Rosenberg *et al.*, 2008). Another factor which may influence the SFR values, related to the star formation history of the galaxies, is the fact that in the da Cunha *et al.* (2008) model the star formation rates are averaged over 100Myr, while Calzetti *et al.* (2007) assumes a timescale of 10Myr.

In addition, using the formula of Salim *et al.* (2007) (described in Section 3.1.2), we estimated the SFRs of the late-type galaxies of our *sample II* (see Fig. 3.6 with blue triangles). However, even for these galaxies, the FUV estimates of the SFR with the

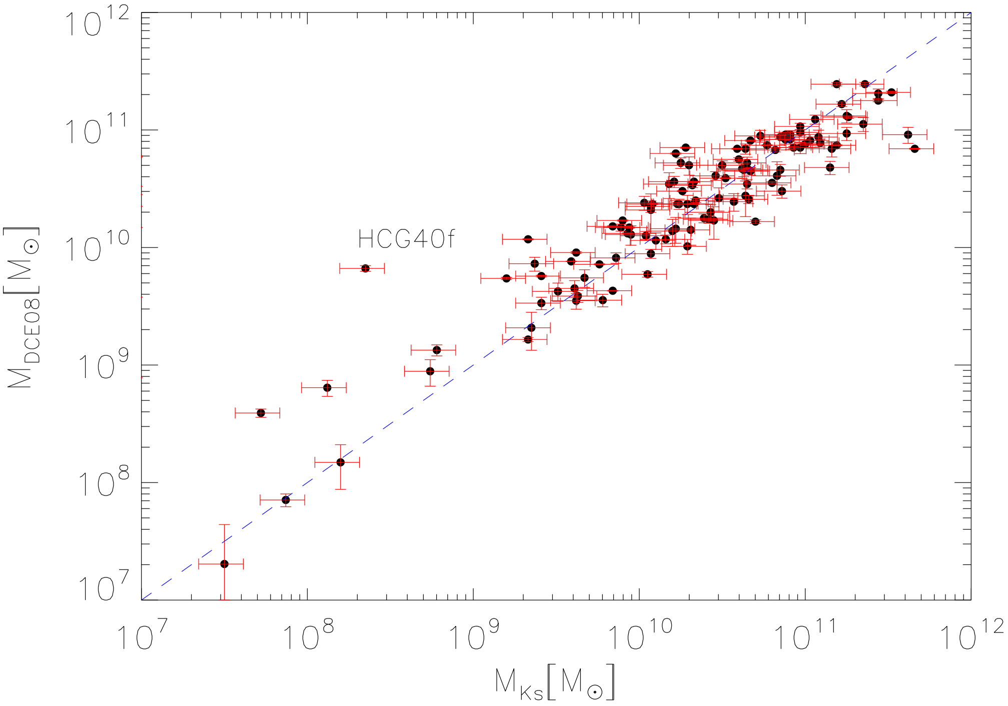

Figure 3.5: Stellar masses based on the da Cunha *et al.* (2008) model (hereafter M_{DCE08}) are plotted as a function of the ones derived from Bell *et al.* (2003) relation based on Ks luminosity (M_{Ks}) after applying the corrections discussed in the text. Vertical error bars indicate the 16-84 percentile ranges in the recovered probability distributions while the horizontal error bars are the 30% errors as described by Bell *et al.* (2003) determined from the scatter in the models. The blue dashed line represents the one-to-one relation.

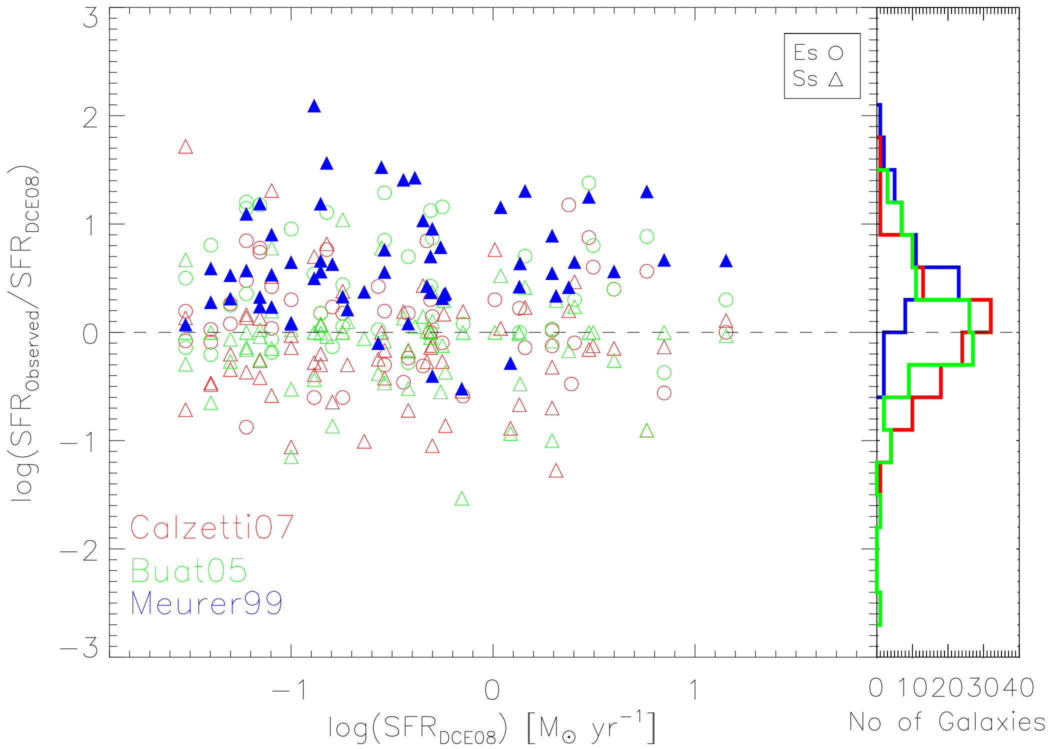

Figure 3.6: A plot of the ratio of the SFRs derived from the observed FUV or 24μm fluxes over the SFRs derived from the da Cunha *et al.* (2008) model as a function of the model SFR. Red open circles and red open triangles are the SFRs derived from the MIPS 24μm fluxes for early and the late-type galaxies respectively. Green open circles and green open triangles mark the estimates based on the FUV to infrared excess as described by Buat *et al.* (2005). Filled blue triangles indicate late-type galaxies for which the SFRs are derived from the FUV after estimating the extinction using the β slope method of Meurer *et al.* (1999). The dashed line is the one-to-one relation. The histogram of the ratios for each method is indicated on the right panel.

corresponding values obtained with the model we find that the former are overestimated by a factor of 0.56dex with a global scatter of 0.46dex. We attribute this to the calibration of the extinction correction of Meurer *et al.* (1999) who used a sample of local UV-selected starburst galaxies with high dust content, quite dissimilar to the HCG galaxies. As discussed in detail by Kong *et al.* (2004), this results in overestimating the UV corrected luminosities and consequently to an overestimate of the SFRs. Indeed, when we plot the FIR-to-UV luminosities of our galaxies against the spectral slope (β-slope) we notice that at a fixed β all the galaxies have systematically lower ratio of total to FIR-to-UV luminosities than the starburst galaxies of Meurer *et al.* (1999). On the other hand, the galaxies HCG16c and HCG16d which are infrared luminous (L_{IR} >$10^{11}L_{\odot}$), have SFRs which are very similar to those derived by the model (10.02 and 1.52$M_{\odot}yr^{-1}$, respectively).

Finally, we estimate the SFRs using the method of Buat *et al.* (2005). The results are presented in Fig. 3.6 with green. We notice that the ratios of the SFRs are uniformly distributed around ∼1.05 displaying a scatter of 0.56dex and also agree with the 24μm estimates. Given the success of the model in a variety of systems (see da Cunha *et al.*, 2008, 2010a,b)) we will base the remaining of the analysis in the SFRs derived using the da Cunha *et al.* (2008) model.

3.3.3 Evaluating the emission line modeling results

In order to estimate if there are any systematics between the two methods we used to calculate the stellar masses, the models of Kauffmann *et al.* (2003b) (described in Sect. 3.2.3) or the empirical method of Bell *et al.* (2003), we compare their ratios in Fig. 3.7. A similar comparison was published by Li & White (2009). These authors used the Blanton & Roweis (2007) stellar mass estimates to compare them with the two observational methods we describe above. As they present, in Fig. A.1 of their paper, the Kauffmann *et al.* (2003b) and Blanton & Roweis (2007) stellar masses are very similar and they display a dispersion of 0.1dex. Similarly, the comparison of the Bell *et al.* (2003) and Blanton & Roweis (2007) stellar masses (see Fig. A.2 of their paper) reveals that for stellar mass >$10^{10}M_{\odot}$, they remain very similar, having a standard deviation of 0.1dex. Yet, for lower stellar masses, the Bell *et al.* (2003) formula overestimates the stellar masses by a factor of 0.3dex. In Fig. 3.7 we present the ratio of the stellar masses estimated using the models of Kauffmann *et al.* (2003b) over the ones estimated using the Bell *et al.* (2003) relation. As we can see there is a global agreement between the two methods, and the median estimates (red diamonds) have values of ∼0.01dex and standard deviation of 0.28dex. However, at stellar masses lower than $10^{10}M_\odot$, the mean value of the ratio drops down to -0.25dex with a dispersion of 0.27dex, which is in contradiction to what Li & White (2009) concluded. However, the fact that we do not sample this low mass range sufficiently well, does not allow us to better evaluate the Li & White (2009) findings.

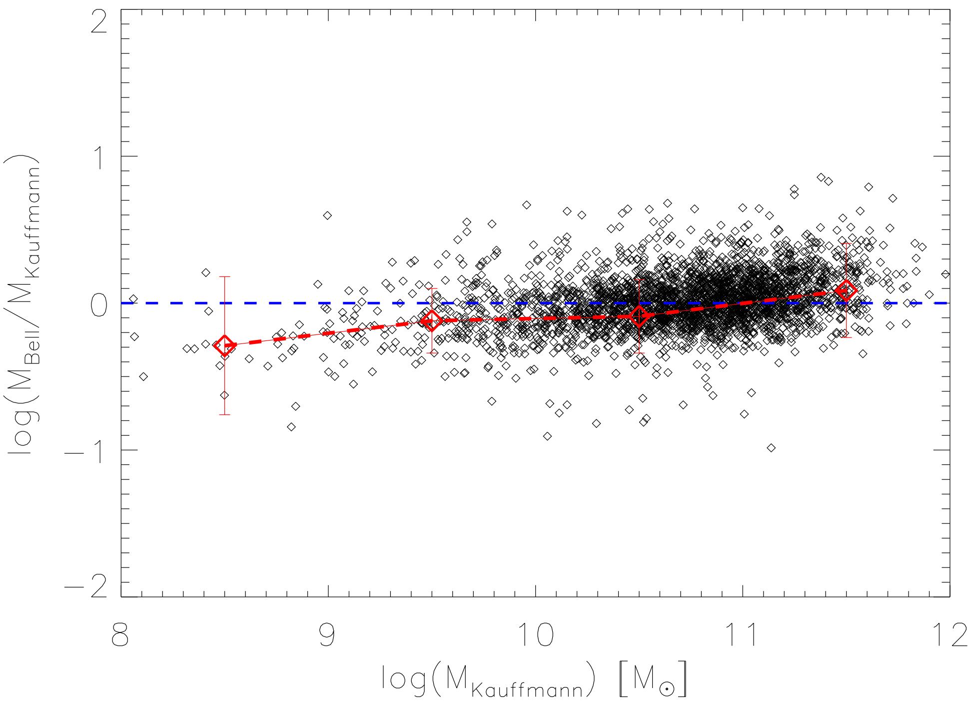

Figure 3.7: Ratios of the stellar masses which were estimated using the method of Kauffmann *et al.* (2003b) over the ones estimated using the empirical relation of Bell *et al.* (2003) versus the second. Red diamonds denote the median ratio of each bin of $1M_\odot$ size.

We also estimated the SFRs of the SDSS CG sample using emission line modeling, as well as several empirical methods. As we mentioned in Sect. 3.2.3, we can derive the SFRs of our galaxies based on the Hα luminosity. However, this can be achieved only for the 1961 SF galaxies which have available spectroscopy; for the remaining 1413 galaxies, classified as AGN or TOs, we can have rough estimations for the SFRs using the 4000-Å break. Moreover, we also used the infrared fluxes of the 5834 mostly late-type galaxies, which were not upper limits and their PSFs were not blended with those of other galaxies, to estimate their SFRs using the empirical relation 3.3. In addition, we can estimate the UV fluxes using the relations of 3.4, 3.5 and 3.6. Yet, this method can only be used for the 3422 late-type galaxies, since in early-type galaxies the β-slope is mainly determined by the old stellar population rather than the dust extinction, and thus their extinction corrected UV luminosities are completely overestimated (see the previous paragraph).

Therefore, in panel (a) of Fig. 3.8 we compare the SFRs which were derived using the WISE 22μm fluxes, to the ones estimated using the Hα fluxes. We can see that for the SF galaxies (blue diamonds) there is a global agreement between the two methods, having a median of unity and a standard deviation of 0.16 dex. However, if we now include the galaxies, which are classified as AGN or TOs (red stars) and their SFRs where estimated using D4000, they display a median of 0.05 dex and a dispersion of 0.60 dex. This is in agreement with Brinchmann *et al.* (2004) who found that these SFRs are just rough approximations. Moreover, we note that for the low-SFR galaxies ($<$1M$_\odot$ yr^{-1}) the scatter is larger ($\sim$0.72dex) since these galaxies are fainter and the uncertainty of their flux grows.

In Fig. 3.8b we compare the SFR$_{UV}$ estimates versus the Brinchmann *et al.* (2004) ones. As we already mentioned, the UV method can only be applied to late-type galaxies. As a consequence in this plot we present only the late-type galaxies which had available spectroscopy. We can notice that the UV emission overestimates the SFRs by a factor of 0.56 dex at SFR$>$1M$_\odot$yr^{-1}, and even higher at lower SFRs. This result is in agreement with those of Kong *et al.* (2004), and is also confirmed from Bitsakis *et al.* (2011) for the Hickson CG galaxies. Kong *et al.* (2004) showed that for a given β the formula of Meurer *et al.* (1999) overestimates the UV luminosity. As we move to higher L$_{UV}$, and thus higher SFRs, the extinction correction is closer to the real value. This is happening because Meurer *et al.* (1999) had used a sample of starburst galaxies to calibrate their method, and therefore it cannot be applied directly to normal star forming galaxies.

In conclusion, we can use both methods of Kauffmann *et al.* (2003b) and Bell *et al.* (2003) to estimate the stellar masses of the galaxies in our sample. The former method can provide as the stellar masses of the 3374 galaxies with available spectroscopy, and the latter can give us the stellar masses of all the galaxies in our sample (since it uses the 2MASS K-band magnitudes). Furthermore, we can rely on the empirical method of Rieke *et al.* (2009) to estimate the SFRs of the 1860 late-type galaxies from WISE 22μm, or the models of Brinchmann *et al.* (2004) to estimate the exact SFRs of 1961 galaxies, and have a rough estimation for the SFRs of the rest 1413 galaxies with available spectroscopy. Since the SFR estimates of Brinchmann *et al.* (2004) contain both late, as well as early-type galaxies, with fractions representative of the whole SDSS CG sample, they can be used for the comparison with other samples.

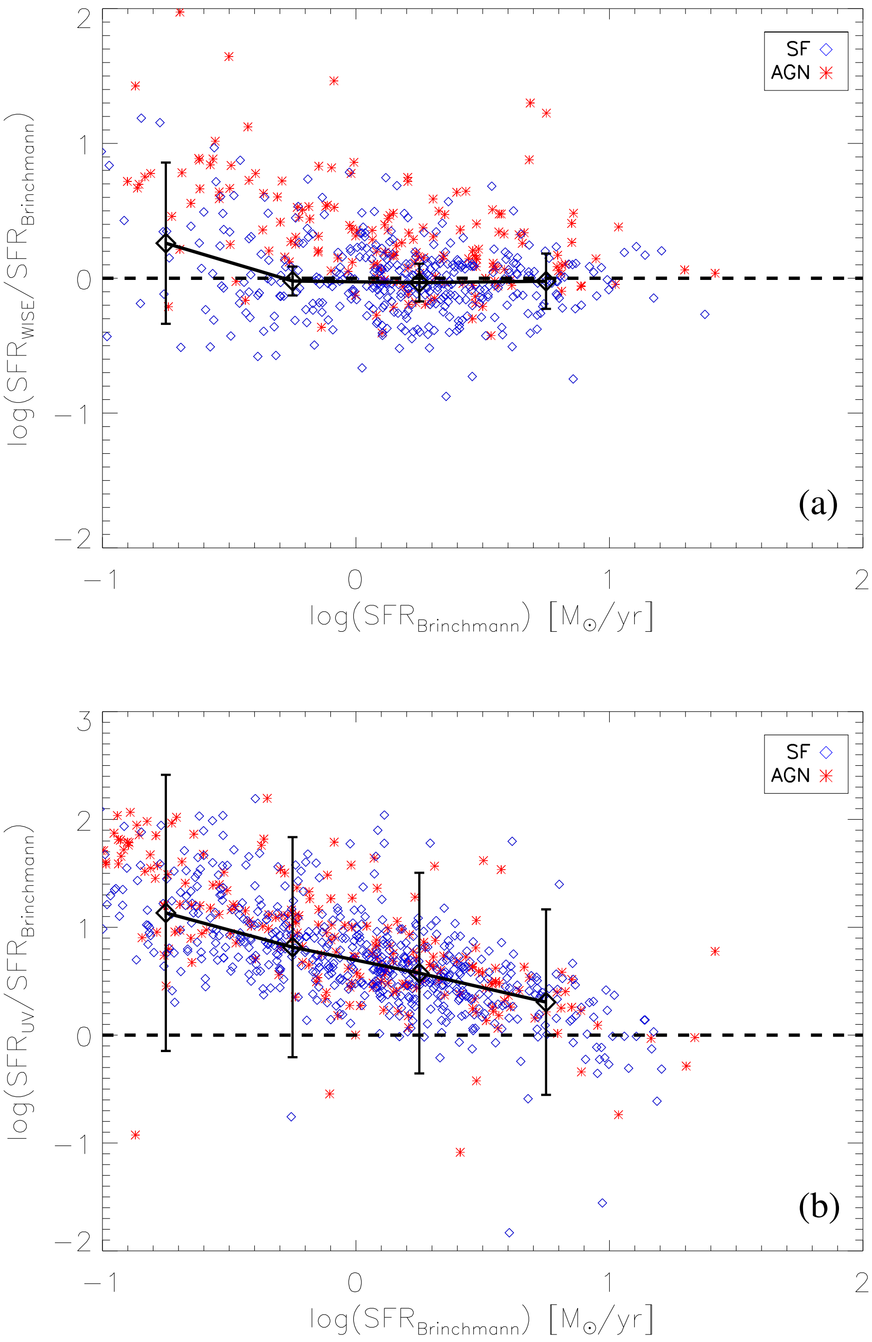

Figure 3.8: (a) The ratio of the SFRs derived from the WISE 22μm emission over the ones derived using the models from Brinchmann *et al.* (2004). With blue diamonds are presented the star forming galaxies and with red stars the AGN or TO galaxies. (b) The ratio of the SFRs derived using the relations of Meurer *et al.* (1999) and Salim *et al.* (2007) for the UV, over the ones from Brinchmann *et al.* (2004). The symbols are as in (a). In both cases the blue dashed line indicates a ratio of unity.

Chapter 4

Physical properties of the HCG galaxies

As we mentioned in the introduction, in order to answer a number of questions related to the nature of compact galaxy groups, one must study their physical properties, as well as the colors of their galaxies. Our initial motivation was to examine the star formation properties of compact groups. For this reason, we selected a sample of 14 HCGs (*sample I*; Sect. 2.1.1), for which we obtained deep high-resolution near- and mid-IR observations, and derived, for the first time in compact groups, the star formation rates and stellar masses of their galaxies (Sect. 3.1 and 3.2.1). However, as we showed in Chapter 3, to properly estimate the effects of the extinction and accurately account for the global energy production of a galaxy, additional observations are essential. Thus, using all the released data from the Spitzer archive, we obtained the UV-to-far-IR fluxes of 135 galaxies, in 32 HCGs (*sample II*). Using the state-of-the-art model of da Cunha *et al.* (2008), we fitted their observed SEDs, and we derived the likelihood distributions of their physical parameters (see Sect. 3.2.2). In the present chapter, we compare the estimated colors and properties of compact group galaxies with those of galaxies within other environments (field galaxies, early-stage interacting pairs, and galaxies in clusters).

4.1 Evolutionary state of compact galaxy groups

During our analysis of the star formation properties of galaxies in compact groups, we noticed that when we were separating the groups according to the fraction of late-type galaxies they host, several of their properties (which we will examine in the next sections) appeared to be bimodal. It is known that the sSFR is a tracer of the star formation history of a galaxy and galaxies in compact groups do experience multiple encounters with other group members. Consequently, we would expect that a “young” group is more likely to have a larger fraction of late-type galaxies, since its members would not have enough time to experience multiple interactions which would trigger star formation, consume the available gas and transform them into early-type systems. Furthermore, these late-type galaxies would have not built up much of their stellar mass. They would still have larger amounts of gas and dust, as well as higher SFRs and sSFR. On the other hand, if a group is dominated by early-type systems, it would be dynamically “old”, since interactions and possible merging of its members over its history would have led to the formation of some of those ellipticals. As a result, the spirals in these groups would have already built some of their stars and their sSFR would be lower. After a detailed study, we decided to classify a group as dynamically “young” if at least 75% of its galaxies are late-type. On the other hand, a group is dynamically “old” if more than 25% of its galaxies are early-type (see Fig. 4.1). The dynamical state of the groups in our samples are presented in Table 4.1.

Moreover, we noticed that in the majority of the groups (80%) classified as dynamically “old”, the most massive galaxy is an early-type galaxy with a median stellar mass of $1.2\times10^{11}\mathrm{M}_\odot$. In all dynamically “young” groups the dominant galaxy is late-type, with a median stellar mass of $5.1\times10^{10}\mathrm{M}_\odot$. These most massive galaxies of each group, are marked with a star in Table 4 of Bitsakis *et al.* (2011). Despite the fact that there are just 10 dynamically “young” groups in our sample and we could be affected by small number statistics, we note that dynamically “old” groups have on average 4.7 members, more than the “young” groups which only have 4 members.

A different classification of HCGs into three phases, 1, 2, and 3, using their atomic HI gas content was proposed by Verdes-Montenegro *et al.* (2001). In the first phase the HI gas of the groups is mainly associated with the disks of galaxies. In the second, only 40-70% of the HI is found in the disks of the galaxies and the rest is into the intragroup medium, as a result of tidal stripping. Finally, in the third phase are groups with almost all their HI located outside of member galaxies, or in a common envelope engulfing most group members. Using this classification Borthakur *et al.* (2010) classified 14 of the groups in our sample and the results are presented in Table 4.1. Both our, as well as Verdes-Montenegro *et al.* (2001) classification method, is based on how galaxy interactions and merging affect the morphology of the group members, thus it is related to their evolution. There is a global agreement between the two methods for 12 of the 14 groups in common. We will discuss these in more detail in Sect. 4.6.1.

Table 4.1: Evolutionary classifications of the groups of samples I and II.

HCG ID	Dynamical class.[a]	HI class.[b]	Group members
2	young	-	3
4	young[c]	-	3
6	old	-	4
7	young	1	4
15	old	3	6
16	young	2	4
19	old	-	3
22	old	-	3
25	old	2	4
26	old	-	7
33	old	-	4
37	old	3	5
38	young	-	3
40	old	3	6
42	old	-	4
44	young	3	4
47	young	-	4
54	young	-	4
55	old	-	4
56	old	-	5
57	old	-	8
59	young	-	4
61	old	-	3
62	old	-	4
67	old		4
68	old	1	5
71	young[c]	3	3
75	old	-	5
79	old	1	4
82	old	-	4
91	young	2	4
92	old	3	5
95	old	-	3
97	old	3	5
100	young	2	4

[a] The dynamically "young" and "old" classification as discussed in Section 4.1.

[b] The classification to Phase 1, 2, and 3, follows the definition of Verdes-Montenegro *et al.* (2001).

[c] See Section 4.4.

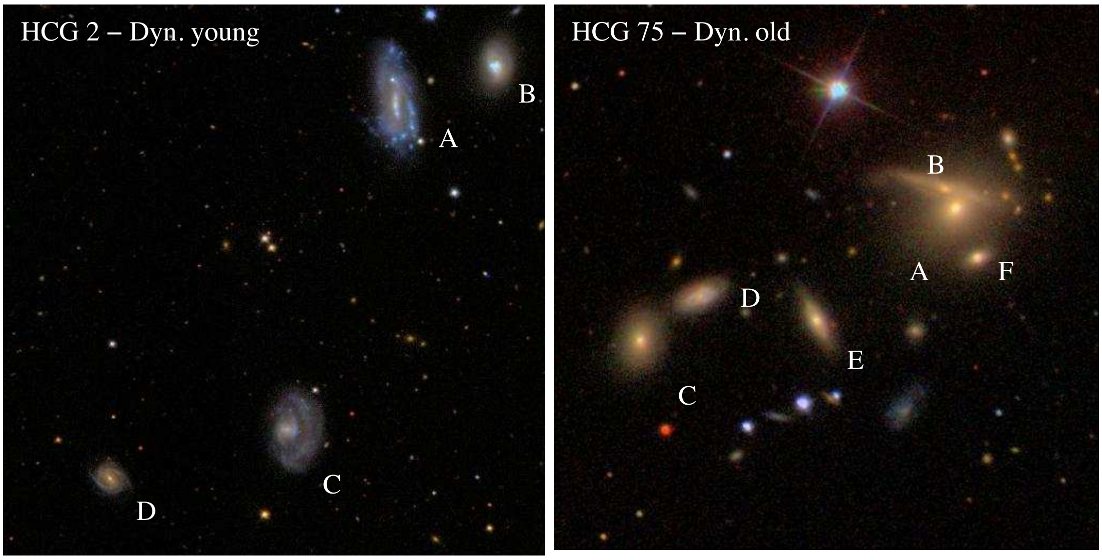

Figure 4.1: Examples of dynamically "young" and "old" groups. On the left, the SDSS "true" color optical image of the dynamically "young" group HCG 2, consisting of 4 late-type galaxies, and on the right, the SDSS image of the dynamically "old" group HCG 75, which contains 3 early-type members (A, C, F), and 3 late-type. [Image credit: SDSS]

4.2 Model derived physical properties

In the previous chapter, we used the empirical relations of Bell *et al.* (2003) and Calzetti *et al.* (2007) to estimate the stellar masses and SFRs of the 69 galaxies of *sample I*. Later, we expanded our original sample into 32 HCGs (*sample II*) and we estimated those parameters, as well as several others, using the model of da Cunha *et al.* (2008). Moreover, we showed in Sect. 3.3.2, that the estimates of the model are in very good agreement with those from Bell *et al.* (2003) and Calzetti *et al.* (2007). In this section we will present the physical parameters of the galaxies of *sample II* (which also includes *sample I*; see Sect. 2.1.1), as derived from the model fitting of the galaxy SEDs (see Fig. 4.2).

4.2.1 Stellar masses

In panel (a) of Fig. 4.2 we show the distributions of the stellar masses separated in early- (E's and S0's) and late-type (S's and Irr's) galaxies in groups, marked in red and blue respectively. We can see that the distributions are not too different as a two-sided Kolmogorov-Smirnov (KS-test) suggests that the probability (P_{KS}) that the two samples are drawn from the different populations is ∼0.04. The median stellar masses of the late and early-type galaxies in our sample are $1.78^{+4.64}_{-1.71}\times10^{10}M_{\odot}$ and

$4.07^{+11.0}_{-3.23}\times10^{10}M_{\odot}$ respectively. One might have expected that the late-type galaxies would have much lower stellar masses compared to the early-types since the latter had more time to increase their stellar mass as they converted their gas into star and/or resulted from the merging of late type systems . However, as we know tidal interactions play an important role in triggering star formation in galaxies (Struck, 1999). Compact groups have high galaxy density, display signs of interaction (i.e. Verdes-Montenegro *et al.*, 2001)) and contain galaxies which are actively forming young stars. Furthermore, as we showed in the previous section, most of the massive late-type galaxies are found in dynamically "old" groups. We, thus, believe that several of the HCG late-type galaxies have already increased their stellar mass, due to past tidal encounters. We will examine more specifically these galaxies and their properties in the Sect. 4.3.

4.2.2 Star formation rates

In Fig. 4.2b we present the distributions of the star formation rates of early and late-type galaxies in groups. As it was expected, most of the late-type galaxies have higher SFRs than the early-type systems, their median SFR being $0.60^{+3.24}_{-0.54}M_{\odot}yr^{-1}$ compared to $0.05^{+0.24}_{-0.04}M_{\odot}yr^{-1}$. The maximum SFR of our sample is $\sim26M_{\odot}yr^{-1}$, typical of starbursts in the Luminous Infrared Galaxy (LIRG) range. We should note that there are 8 early-type galaxies with relatively high SFRs ($\sim$1-5$M_{\odot}$/yr) which is more than an order of magnitude higher than what is observed in the rest of the sample. We will discuss these galaxies in more detail in Section 4.4.

4.2.3 Specific SFRs

In panel c of Fig. 4.2 we display the distributions of the sSFRs of the *sample II*. We can see that there are late-type galaxies with rather low sSFRs ($\sim10^{-12}yr^{-1}$). These galaxies, which belong to dynamically "old" groups, must have had already increased their stellar masses, thus decreasing their sSFRs, as a consequence of dynamically triggered star formation events due to past interactions. On the other hand, there are early-type galaxies which display rather high sSFRs ($\sim10^{-10}yr^{-1}$). One explanation is that accretion and merging of gas rich dwarf companions has increased the gas content of these galaxies and they are currently forming stars. However, it is also possible that these galaxies are misclassified, dust obscured, edge one late-type systems. In Sections 4.3 and 4.4 we examine in more detail the sSFR distribution as a function of the dynamical state of each group, study the mid-IR and optical colors of the galaxies and compare them with our control samples.

4.2.4 Infrared luminosities

In Fig. 4.2d we present, in red, the distribution of the infrared luminosities (L_{IR}) as estimated from the da Cunha *et al.* (2008) model. Since no far-IR observations were available for most of the galaxies (74%) of our sample, the L_{IR} can not be robustly constrained. Using for each galaxy the minimum and the maximum values of the probability distribution functions as reported by the model, we create two additional histograms corresponding to the low and high values respectively. We observe that the overall shape and median value of the distribution does not change substantially. The median L_{IR} of the sample is $5.0^{+3.0}_{-0.9}\times10^{9}L_{\odot}$ and most of the HCG galaxies are not IR luminous ($L_{IR} \geq 10^{11}\,L_{\odot}$). There are only 7 galaxies, HCG4a, HCG16c, HCG16d, HCG38b, HCG91a, HCG92c and HCG95a, with $L_{IR} > 10^{11}L_{\odot}$. Note that these are all late-type systems, they are detected in the far-IR, and the first 5 are found in dynamically "young" groups.

4.2.5 Dust extinction

As we discussed in Section 3.2.2.3 we can use the model-derived attenuated (observed) and unattenuated SEDs to estimate the V-band optical depth ($A_{V,obs}$) for each galaxy. Two histograms of these values, for the early and late-type systems, are presented in Fig. 4.2d. The median $A_{V,obs}$ is 0.23±0.17mag and 0.58±0.36mag for the early and late-type galaxies, respectively. We observe that there are 8 (∼14%) of the early-type galaxies, with extinctions similar to what is seen in dusty late-type galaxies (≥1mag). These are HCG4d, HCG55c, HCG56b, HCG56d, HCG56e, HCG71b, HCG79b, HCG100a. We should note that these galaxies are the ones forming the tail of early-type galaxies with high SFRs and sSFRs, mentioned above. The fact that they appear to have larger amounts of dust than what one may expect for early-type galaxies, as well as the fact that they display higher star formation activity, further supports the idea that these may indeed be misclassified late-type systems.

The model of da Cunha *et al.* (2008) also estimates the total effective V-band absorption optical depth of the dust seen by a young star ($\tau_V = \tau_{V,BC} + \tau_{V,ISM}$) inside the stellar birth clouds, and the fraction of the absorption (μ) contributed by dust found in the diffuse ISM along the line of sight. The emission from young stars is more attenuated than that from old stars. In young stars the extinction is dominated by the dust of the surrounding birth clouds with an additional component due to the dust in the diffuse ISM traversed by their light. Older stars ($>$ 100Myr), which have dispersed their birth clouds, are only affected from the dust found in the diffuse ISM.

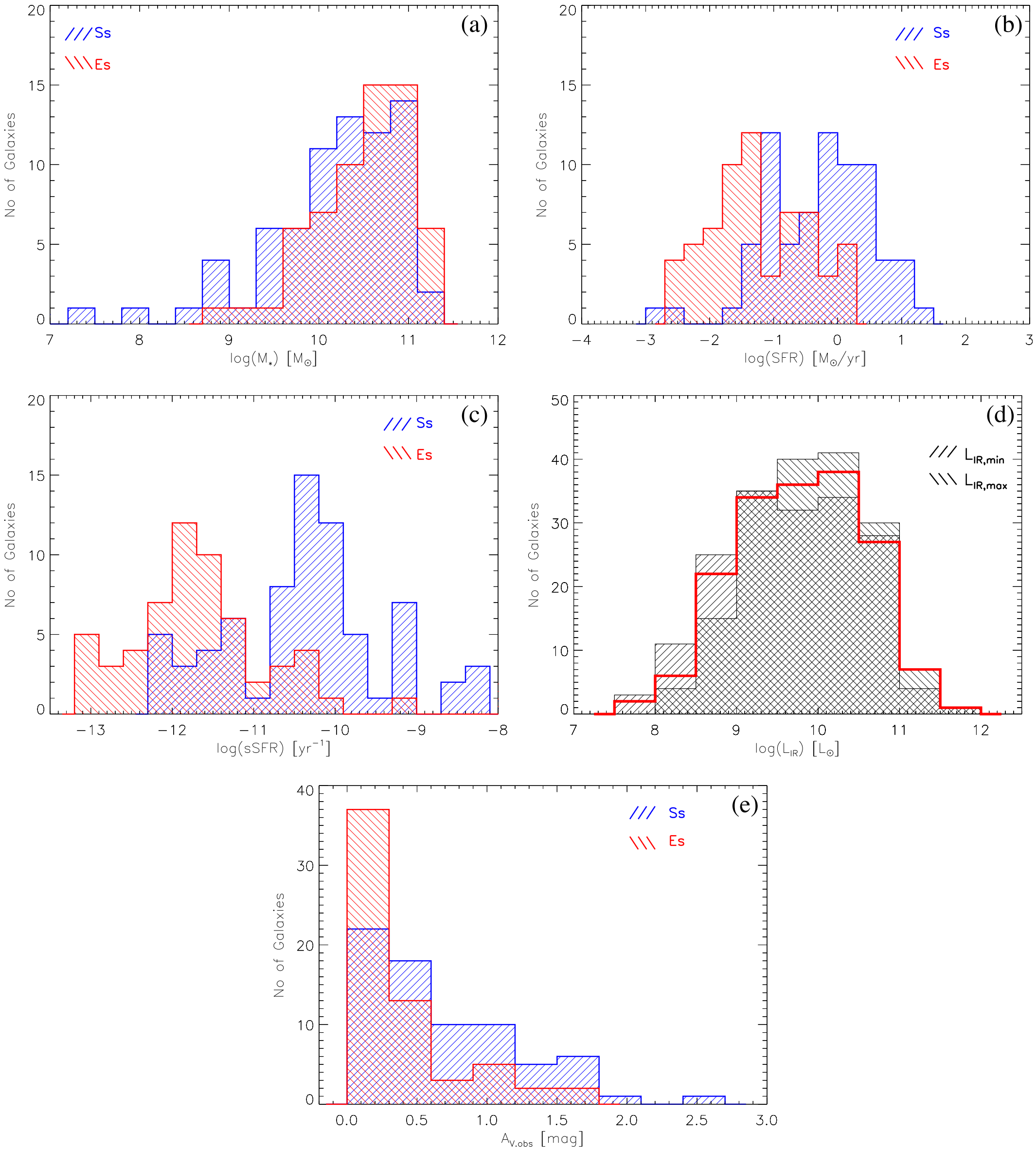

Figure 4.2: Histograms of several properties of our HCG *sample II*. Early type galaxies are marked in red and late type galaxies in blue a) the distributions of the stellar masses (M_*); b) the distributions of the star formation rates (SFR); c) the distributions of specific star formation rates (sSFR); d) the histogram of the infrared luminosities, L_{IR}, in red, as estimated by our SED modelling. Because of the absence of far-IR observations for most of the galaxies in the sample we overplot in hashed areas the histograms corresponding to the minimum and maximum L_{IR} of each galaxy, associated to the 16th and 84th percentile range of the best fit respectively; e) a histogram of the extinction inferred from the SED fit ($A_{V,obs}$) as measured model-derived atttenuated and unattenuated SED

Consequently, one would expect that in early-type galaxies, where currently no recent star formation is taking place, the optical light would be dominated by the old stars and therefore, the representative obscuration would be that of the ambient ISM. In late-type galaxies the total extinction would be the contribution of both components, BC and ISM. In that case, each component will contribute differently, depending on how much of the optical energy production in the galaxy is due to stars within the birth clouds. We would like to emphasize that since both components can contribute to a different extent at different wavelengths, the representative extinction of a galaxy varies also with wavelength, and that is why here we consider only optical light, instead of referring to the total energy output of the galaxy.

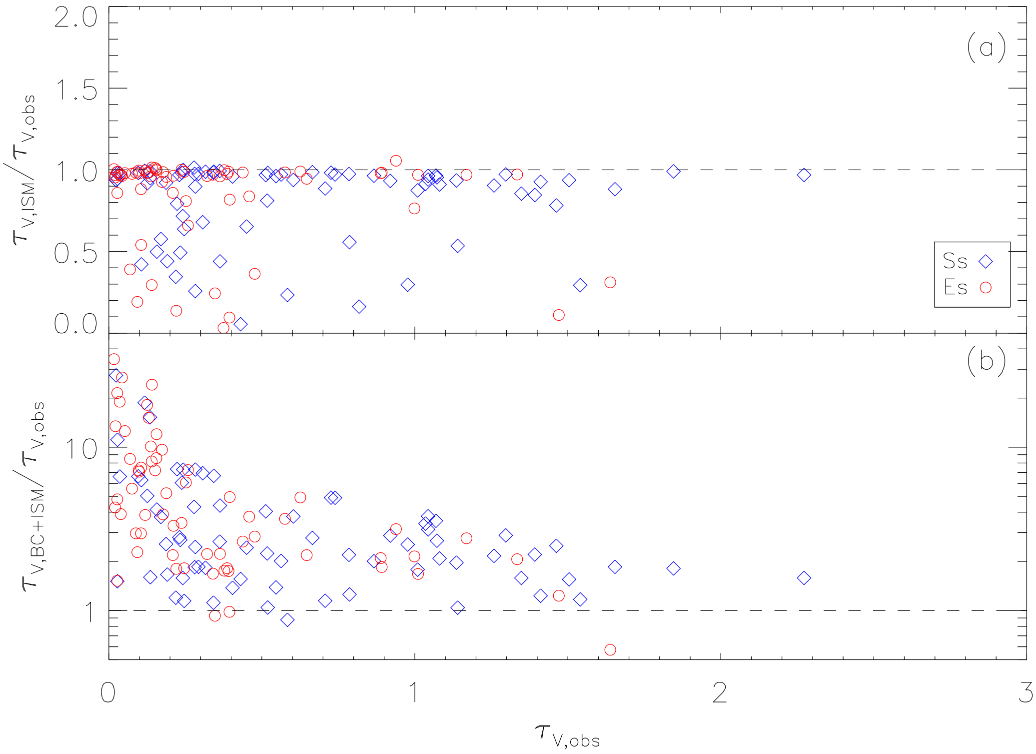

Figure 4.3: a) Ratio of the intrinsic optical depth ($\tau_{V,ISM}$) derived by the model over the observed (attenuated spectrum) $\tau_{V,obs}$ versus the $\tau_{V,obs}$. The dashed line is the one-to-one ratio. The red circles represent the early-type galaxies in HCGs and the blue diamonds the late-type ones. b) Ratio of the intrinsic τ_V for stars in birth clouds, derived by the model over the observed $\tau_{V,obs}$ versus the $\tau_{V,obs}$, using the same notation. We excluded from the plot 6 galaxies (HCG44a, HCG47a, HCG47b, HCG56b, HCG59a and HCG68a) since their χ^2 of model-fit was more than 9.00 and the derived τ fairly uncertain.

Using the output of the model, we can thus estimate the optical depth contributed from the diffuse ISM, $\tau_{V,ISM} = \mu\,\tau_V$, and the optical depth from the stellar birth clouds, $\tau_{V,BC} = (1-\mu)\,\tau_V$. In Table 2 of Bitsakis *et al.* (2011), we present the optical depth derived from the attenuated and unattenuated SED, $\tau_{V,obs}$, the $\tau_{V,ISM}$, as well as the total optical depth seen by young stars inside stellar birth clouds, τ_V=$\tau_{V,BC}$+$\tau_{V,ISM}$. In Fig. 4.3, we plot the ratios of the intrinsic, model-derived optical depth (ISM and BC+ISM components) versus the observed optical depth, $\tau_{V,obs}$, we measured from the SED. We note that in most galaxies the ratio of $\tau_{V,ISM}$ over $\tau_{V,obs}$ is very close to unity. For these galaxies, in particularly for those with low extinction values, it is the dust in the ISM which determines the overall absorption of the emitted radiation. The contribution of the BC component is a small fraction of the overall light. On the other hand there are 28 galaxies with ratios lower than unity. From these, 18 are classified as late-type, half of them belong to dynamically "young" groups, and 10 are classified as early-type, 6 of which we believe are likely misclassified late-type systems (see Section 4.4 and Appendix A of Bitsakis *et al.* 2011). In the bottom panel of the same figure we plot the ratio of total τ_V over the $\tau_{V,obs}$, versus the $\tau_{V,obs}$. We notice that there are galaxies with very high τ_V over $\tau_{V,obs}$ values at small $\tau_{V,obs}$, most of which are early-type systems. Even though these galaxies have had recent (<100Myr) star formation events, this does not dominate their global emission. We do note though, that as the $\tau_{V,obs}$ increase, the ratio converges towards unity, implying that the contribution of light from young stars in the BC component becomes a considerable fraction of the total emission, making the obscuration seen by the newly formed stars more representative of the observed obscuration of the galaxy.

4.3 Late-type galaxies in groups

In the previous section we presented a number of physical parameters of late, as well as early-type galaxies in HCGs, derived by fitting their SED. However, as we already mentioned in Sect. 4.1, during our preliminary investigation in the sSFRs of the galaxies of *sample I*, we noticed that their distributions appeared to be bimodal. This enabled us to propose a classification for the groups, depending on their early-type galaxy fraction. In this section we will present our preliminary results, as well as the more extensive analysis of *sample II*, which had improved our statistics.

4.3.1 Enhanced stellar mass in dynamically "old" late-type systems

It has been well established that interactions can trigger star formation in galaxies (Struck, 1999). During an interaction between two late-type galaxies their atomic gas, typically found in diffuse clouds, collide. Shocks are produced which in turn increase the local gas density thus triggering bursts of star formation. The fact that the group environment has played an important role in the evolution of its member galaxies, is evident since the fraction of early-type systems in groups is higher than what is found in the field. So one would expect that because of their proximity, the late-type galaxies in groups display different star formation properties from the ones in the field. However, in our preliminary analysis of the 14 groups of *sample I*, we found that overall there is no evidence that the SFR and sSFR in late-type galaxies of HCG is different from galaxies in the field or in early-stage interacting systems. Interestingly though, when we separated our *sample I* into two sub-samples, namely the dynamically "old" and dynamically "young" groups (see Section 4.1 for the definition), late-type galaxies in dynamically "old" HCGs showed lower sSFRs than those in dynamically "young" groups. This was attributed to the likely larger number of past interactions experienced in the dynamically "old" groups, which would lead to a faster increase of their stellar mass compared to galaxies in young groups. The higher stellar mass would reduce their current sSFR, even if subsequent gas accretion would result in star formation activity in them.

Later, we re-examined this issue, using the 32 HCGs of *sample II* which contains 73 late-type galaxies. This time we derived their sSFR, as well as the ones of the control samples, using the SED model of da Cunha *et al.* (2008). The results are shown in Fig. 4.4 and Table 2 of Bitsakis *et al.* (2011). Galaxies in dynamically "young" groups have a median sSFR of $8.51^{+4.07}_{-2.75}\times10^{-11}\mathrm{yr}^{-1}$, while for galaxies in the dynamically "old" groups of $2.75^{+2.03}_{-1.16}\times 10^{-11}\mathrm{yr}^{-1}$. Similarly, galaxies in interacting pairs have a sSFR of $11.20^{+3.67}_{-2.70}\times10^{-11}\mathrm{yr}^{-1}$ and in field galaxies of $15.30^{+5.65}_{-4.29}\times10^{-11}\mathrm{yr}^{-1}$. An analysis using two sided KS test indicates that there is no statistical difference between the samples of late-type galaxies in dynamically "young" HCGs and those of the SINGs and interacting pair samples ($P_{KS}>0.80$). However, the same KS-test reveals that the late-type galaxies in dynamically "old" groups, having a median sSFR which is more than three times lower, can not be drawn from same parent distribution as the other three samples ($P_{KS}\sim10^{-3}$). Investigating in more detail the reason for this disparity, we find that it cannot be attributed to depressed SFR but instead it is due to a substantially more massive stellar content ($\sim3\times10^{10}M_{\odot}$), similar to what is found early-type systems. This confirms our previous results and interpretation (Bitsakis *et al.*, 2010) based on semi-empirical estimates of the sSFR on a smaller galaxy sample. According to those findings one would also expect that due to their higher stellar mass, the late-type type galaxies in dynamically "old" groups should have redder UV and optical colors than late-type galaxies in the field. We will discuss this in Section 4.5.1.

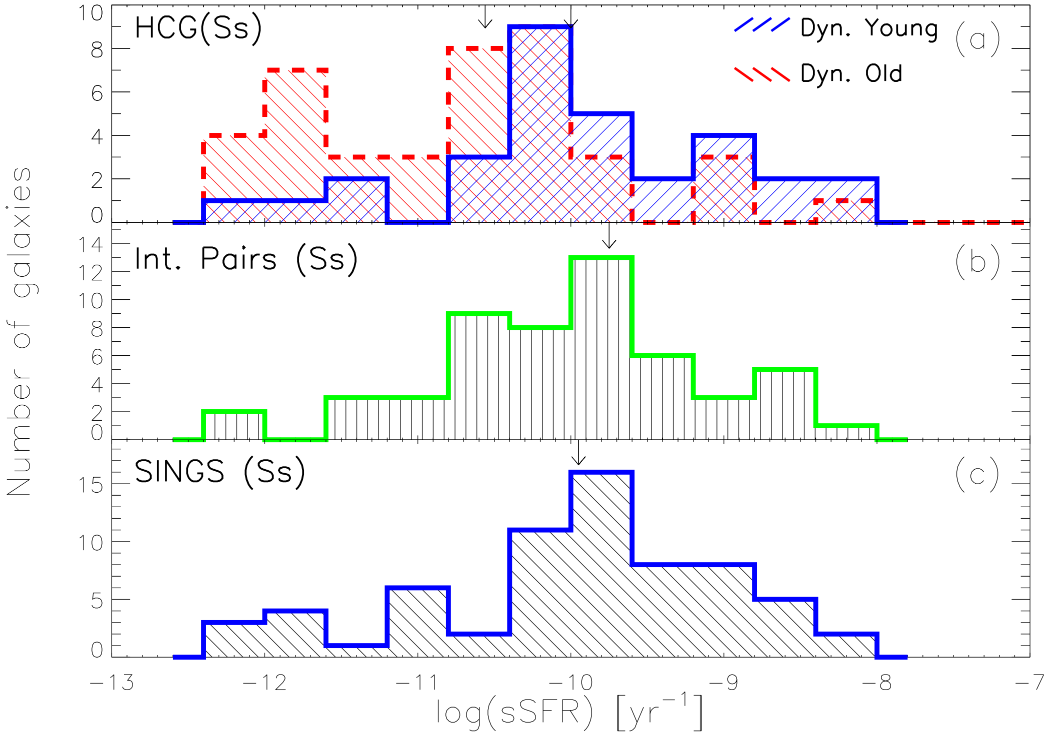

Figure 4.4: Histograms of our three samples, estimated by modeling their SED. The top plot displays in blue the histogram of the sSFR of the 31 late-type galaxies found in dynamically-young, spiral-dominated groups. Over-plotted in red is the corresponding histogram of the 42 galaxies in dynamically-old elliptically dominated groups. The middle and bottom plots present the histograms of the 52 late-type galaxies in the Smith *et al.* (AJ) interacting galaxy pairs, as well as the 71 SINGS late-type galaxies. The arrows indicate the median sSFR value of each distribution.

4.3.2 The Schmidt-Kennicutt law in HCG late-type galaxies

As we mentioned in the previous section, late-type galaxies in dynamically "old" groups are more massive than those in "young" groups. One would expect that in order to increase their stellar masses, these galaxies should consume large amounts of their available gas, and as a result, they should also display lower SFRs. In order to examine this, we separated the SFR distributions of the late-type galaxies in dynamically "young" and "old" groups, and we noticed that both distributions are very similar, having median values of 0.63±1.9$M_\odot$ yr^{-1} and 0.59±5.1$M_\odot$ yr^{-1}, respectively (P_{KS}=0.8; see Fig. 4.5a). There are two possibilities which could explain these results. One is that the late-type galaxies in dynamically "old" groups have comparable molecular gas masses to the ones found in "young" groups. This implies either that they had more gas in the past, or that they had increased it due to gas inflows from merging. To make this clear, we have used the published molecular hydrogen masses of 25 late-type galaxies (13 in dynamically "young" and 12 in dynamically "old" groups; Leon *et al.* 1998). We normalized those masses by dividing them with the stellar masses of the same galaxies as estimated from the model of da Cunha *et al.* (2008). We noticed that the distribution of the ratios of the M_{H2} to the $M_{stellar}$, for late-type galaxies in dynamically "old" groups is lower that the one of those found in "young" groups. Yet, the two distributions are not significantly different (P_{KS}~0.5), possibly due to small number statistics.

The other possibility is that the late-type galaxies in dynamically "old" groups use their existing gas in a more efficient manner to form stars. To examine this in detail, we plot in Fig. 4.5b the average surface densities of the SFR versus the ones of the M_{H2}. To estimate those values we used as sizes of the galaxies the apertures we used in the mid-IR photometry. The dashed lines indicate the total gas fractions which will be used to make stars after 100Myrs (Bigiel *et al.*, 2008). To make this easier to understand, consider a galaxy with molecular hydrogen surface density (Σ_{H2}) of about 10 $M_\odot$ pc^{-2}. If this galaxy, after 100Myr has a Σ_{SFR} of 0.01 $M_\odot$ yr^{-1} kpc^{-2}, it means that it has converted about 10% of its gas mass into stars. Galaxies with this fraction larger than 10% are very efficient to produce stars, using a certain amount of gas, and on the other hand, galaxies with that fraction less than 1% are very inefficient. As we can see in Table 4.2, late-type galaxies in dynamically "old" groups seem to be more efficient in producing stars than those found in "young" ones, even though they have lower gas-to-stellar mass fractions. Despite the fact that these results cannot be significant, due to small number statistics, they can be attributed to the dynamical state of those groups. As we mentioned before, dynamically "old" groups are more compact and with more members than "young" ones. Thus, late-type galaxies within them are experiencing more tidal interactions, which produce turbulence and shocks in their ISM, initiating the collapse of dense molecular clouds and inducing star formation. The end result is that even though these galaxies have less fuel to form stars, they are producing them more efficiently.

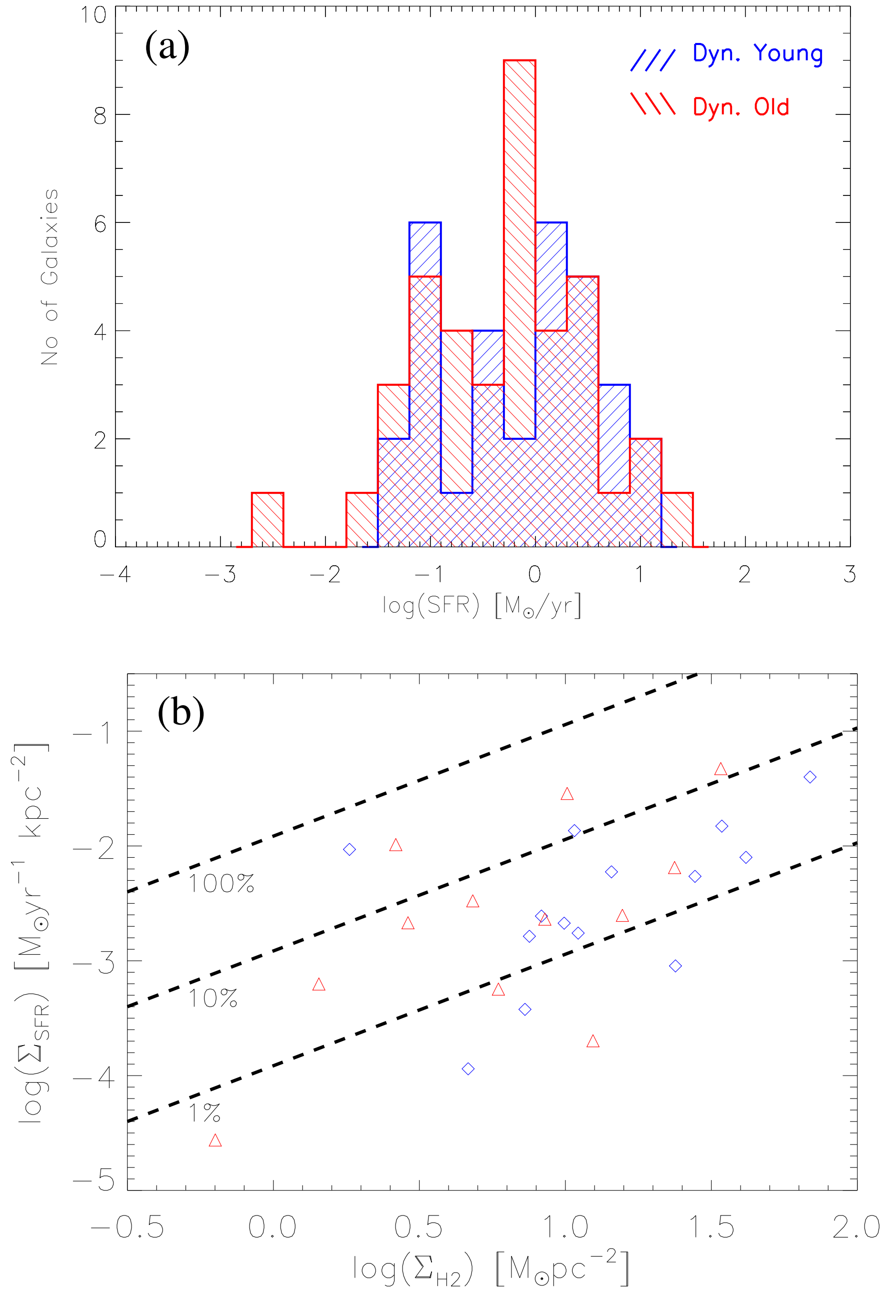

Figure 4.5: (a) The distributions of the SFRs of the late-type galaxies in dynamically "young" (in blue) and "old" (in red) groups. (b) The Schmidt-Kennicutt law in 25 HCG late-type galaxies, 13 of which are found in dynamically "young" (blue diamonds) and 12 are in dynamically "old" groups (red triangles). We plot their average SFR surface density versus the average molecular hydrogen surface density. The dashed lines indicate the fraction of total gas which is used in a period of 100Myr to form stars (1%, 10%, and 100%).

Table 4.2: Efficiencies of compact group galaxies in Fig. 4.5b.

Efficiency	Dyn. "Young" (%)	Dyn. "Old" (%)
Eff.>10%	8	25
10%>Eff.>1%	69	50
Eff.<1%	23	25

4.4 Early-type galaxies in groups

We showed in the previous section that the group environment affects the star formation history of the late-type members increasing their stellar mass in the process of transforming them into early-type systems. However, is there any evidence indicating that the early-type galaxies in groups are distinctly different from similar galaxies found in the field? To examine this, we initially fitted the mid-IR SEDs of the 32 early-type galaxies of *sample I* (see Fig.A.1 from Bitsakis *et al.* 2010) where we noticed that for 14 of them these SEDs were consistent with those expected for late-type galaxies. Later, based on our SED modeling in the galaxies of *sample II*, we derived the results shown in Fig. 4.2; nearly 15% of all early-type galaxies have SFRs and dust extinction similar to what is seen in late-type systems. We suggested that there are two possible explanations for this. One was that they were simply misclassified as Es or S0s, while in fact they are edge-on late-type systems. The second was that these galaxies even if they are early-type, based on their optical morphology, they have experienced minor merging with gas/dust rich dwarf companions in the groups, which has increased their gas content, star formation activity, and dust extinction.

According to Hickson (1982) the classification of the HCG galaxies was performed using their morphological features, optical colors, and sharpness of the edge of the image. For all groups of our samples though, we also have Spitzer mid-IR images which provide additional information on their properties. It is well known that the mid-IR spectra of the star forming galaxies in addition, to continuum emission due to warm dust, they are also filled with a series of broad emission features between 3 to 18μm, which can contribute up to 20% of their total IR luminosity (Dale *et al.*, 2005; Smith *et al.*, 2007). These features are the vibrational modes of PAHs, which absorb UV photons from newly born stars and re-emit them in the mid-IR. Typically only late-type galaxies with active star formation and dust emit strongly in these bands. Some PAHs have also been detected in some early-type systems, but they display peculiar PAH-band ratios (Bressan *et al.*, 2006; Kaneda *et al.*, 2008; Panuzzo *et al.*, 2011). To probe the properties of the early-type galaxies in the groups, we examine their mid-IR colors and compare them with isolated ellipticals in the field which are not expected to have PAH emission.

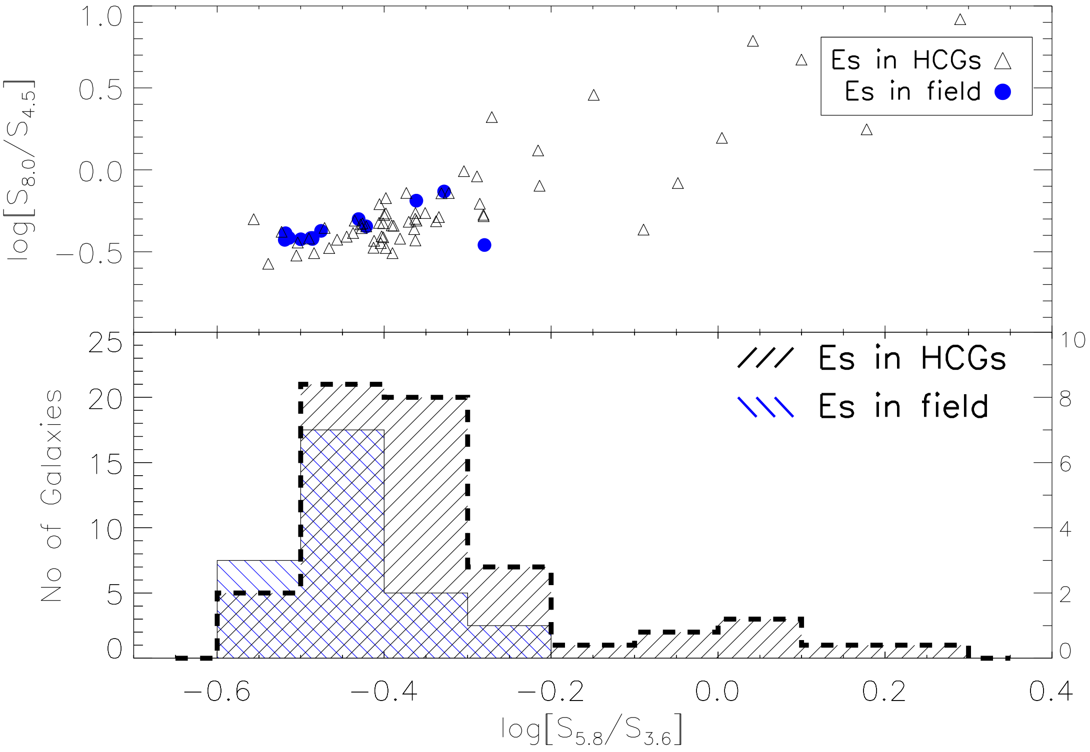

Figure 4.6: Top panel: IRAC color-color plot of the early-type galaxies in HCGs (black open triangles) and a sample of field ellipticals (blue filled circles). Bottom panel: The histograms of the log[$S_{5.8}/S_{3.6}$] color of the two samples. The early-type galaxies in the groups are marked with a black line (left axis) while the field elliptical are presented in blue (right axis).

In Fig. 4.6 we use our Spitzer/IRAC photometry and plot the 8.0 to 4.5 μm flux density ratio as a function of the 5.8 to 3.5μm ratio for the early-type galaxies of our HCG *sample II*, as well as the control sample of field ellipticals. Weak PAHs would result in low values of both ratios since the 6.2 and 7.7μm features, which contribute ~50% of the total PAH emission, are sampled by the 5.8 and 8.0μm IRAC filters (Smith *et al.*, 2007). Indeed, we observe that most of the early-type galaxies in groups, as well as in the field are concentrated in the lower left part of the color-color plot of Fig. 4.6. These galaxies are very close to the (-0.4, -0.5) locus of pure stellar photospheric emission where the flux density in the mid-IR scales with λ^{-2}. Consequently, they are expected to have very weak dust and PAH emission. On the other hand, the upper right quadrant of the figure should be populated by galaxies with strong PAH features and possibly some hot dust contribution, as a result of intense star formation and/or AGN activity. As expected, no field ellipticals are seen in this quadrant. However, there is a "tail" of 10 early-type HCG galaxies (∼16% of the total) extending to this part of the plot (for $\log[f_{5.8}/f_{3.6}]>-0.25$). Examining the 5.8 to 3.5μm IRAC color distributions of HCG and field with a KS-test, we find that they are different ($P_{KS}\sim0.005$). The early-type galaxies with red IRAC colors are: HCG4d, HCG40f, HCG55c, HCG56b, HCG56d, HCG56e, HCG68a, HCG71b, HCG79b & HCG100a. We note that HCG40f and HCG68a are at the left edge of the color selection and it is possible that contamination from a red nearby companion is affecting their mir-IR fluxes. All these galaxies are examined in more detail in the Appendix A of Bitsakis *et al.* (2011), where we display their SEDs, SDSS spectra, Ks-band contour plots and "true color" composites based on their Spitzer/IRAC mid-IR images. Based on this analysis and previous suggestions, we propose that 7 of them, HCG4d, HCG55c, HCG56d, HCG56e, HCG71b, HCG79b, and HCG100a are likely dust obscured late type systems. Furthermore, if HCG4d and HCG71b are indeed late-type galaxies, then their groups must be reclassified as dynamically "young" (instead of "old"). Thus, from now on we will consider them as such (see Table 7 from Bitsakis *et al.* 2011 and explanations therein).

4.5 The colors of HCG galaxies

Up to this point, we examined several of the physical parameters of the galaxies in our groups, and found them to be bimodal, depending on the dynamical state of their groups. Late-type galaxies in dynamically "old" groups display higher stellar masses and comparable SFRs to those in "young" groups. We suggested that these galaxies had increased their stellar mass due to tidal interactions, which had occured in the past and made them form stars. As a result one would expect that these galaxies, due to higher old stellar populations, they would display redder optical colors than normal star-forming field galaxies. Moreover, we have found that there is a fraction of early-type galaxies, which display higher SFRs, as well as warmer mid-IR colors. It is possible that these galaxies had increased their gas content, as result of past interactions and minor merging. We suggest that these galaxies should display bluer optical colors than normal ellipticals, due to the higher fraction of hot young stars they host. Thus, to inspect more thoroughly the evidence of evolution due to the group environment, we will now compare the UV, optical, as well as mid-infrared colors of the galaxies in our samples, with those found in the field and clusters.

4.5.1 The UV-optical color bimodality

4.5.1.1 Color bimodality in field and cluster galaxies

A number of studies of galaxies have revealed a bimodality in the UV-optical colors of galaxies in field and in clusters (i.e Haines *et al.*, 2008; Wyder *et al.*, 2007). This type of bimodality in the colors of the late- and early-type galaxies is real and directly connected to the original galaxy classification scheme by Hubble. It appears quite strongly in the NUV-r color distribution of a sample and consists of two peaks, called the "red sequence" and the "blue cloud", and a minimum in between them identified as the "green valley" (see Strateva *et al.*, 2001). Wyder *et al.* (2007) examined a sample of over 18,000 galaxies observed with GALEX and SDSS and showed that a NUV-r versus M_r color magnitude diagram can be used to separate them into (i) passively evolving, (ii) star-forming and (iii) AGN components. Passively evolving galaxies are well confined to the "red sequence" (NUV-r>5), with few showing blue UV-optical colors, while all blue galaxies, with NUV-r<3, are spectroscopically classified as star forming (see also Haines *et al.*, 2008). AGN seem to dominate the area of the green valley" (3<NUV-r<5). The small fraction of galaxies in the "green valley" can be understood from the fact that galaxies do not spend so much time at these colors. Using Starburst99 (Leitherer *et al.*, 1999) we simulated the evolution of a stellar population typical of a spiral galaxy assuming solar metallicity and either a continuous star formation (of $1M_{\odot}yr^{-1}$) or a single starburst (producing total stellar mass of 10^6 $M_{\odot}$). Depending on the assumptions, we find that the colors of the population place it within the "blue cloud" just for ∼5-7Myr and after spending only ∼1-5Myr transiting through the "green valley" it remains in the "red sequence" for the rest of its lifetime. Thus this color bimodality emerges from the nature of the galaxies as they evolve through time.

4.5.1.2 The UV-optical colors of HCG galaxies

As we already mentioned in the introduction of this section, we expect that the late-type galaxies in dynamically "old" groups will display redder colors, since the had increased their stellar masses and they contain a large number of old stars. On the other hand, some compact group early-type galaxies, display enhanced SFRs, a sign of recent star formation, thus, one would expect that these galaxies would have bluer colors than normal ellipticals. In Fig. 4.7 we plot the NUV-r colors of the *sample II*, as a black solid line, and compare them with the field and cluster galaxies of the Haines *et al.* (2008) sample, indicated in blue and red respectively. The three regions of the color space discussed by Wyder *et al.* (2007) are clearly visible. On the left, near NUV-r∼2, we identify the “blue cloud” where the field galaxy distribution peaks. Nearly 58% of the total number of field galaxies is found within 0.5mags of this color. Few of the galaxies in clusters (15%) are also seen in this area. To the right, near NUV-r$\sim$5.5, we observe the “red sequence” where most (51%) of the cluster galaxies are concentrated. Only 16% of the field galaxies are found in the “red sequence”. The “green valley” is between the two peaks and is mostly (34%) populated by cluster galaxies (Haines *et al.*, 2008). When we examine the HCG NUV-r color distribution, we note a clear difference. Only 17% of their galaxies are in the “blue cloud”, a fraction similar to what is found for galaxies in clusters. However, the majority (73%) of the HCG galaxies are concentrated in the “green valley” and “red sequence” areas. A likely explanation would be that most of the HCG galaxies are already passively evolving or they are in the process of moving from the star-forming region to the “red sequence”. This is consistent with the fact that compact groups have a higher fraction of elliptical galaxies than the field. Another possibility is that some of these galaxies are in fact late-type systems which have redder colors and hence move to the right on the plot, because of dust extinction and/or due to the presence of a substantial older stellar population (post starburst galaxies). This is expected from our earlier findings regarding the miss-classification of a fraction of the early-type galaxies in the HCG and the lower sSRF in dynamically “old” groups.

To study in more detail how the NUV-r color distribution of the HCG galaxies is affected by their morphology and nuclear activity, we present in Fig. 4.8 the corresponding histograms based on their optical morphologies, as well as their nuclear spectral classification. We note that only 36% of the late-type galaxies, indicated in blue, are found within the “blue cloud”. However the majority of the HCG galaxies, almost 60%, are located in the “green valley” and in the “red sequence” ($\sim$13%). In Fig. 4.8b we present the same plot as at the top, but only for the galaxies of our *sample II* who have an optically identified AGN. The whole distribution is shown with the black dashed line, while the distributions of early- and late-type AGN hosts are shown in red and blue. We performed a two sided KS-test between the distribution of galaxies hosting an AGN and the total distribution of the HCG galaxies and we conclude that there is no statistical difference in their NUV-r colors ($P_{KS}\sim0.25$). This suggests that the presence of an AGN does not affect substantially the UV-optical color of the galaxies in Hickson Compact Groups.

In order to explore the color variations as a function of the evolution state of the groups, we plot in Fig. 4.9 the histograms of the early-and late-type galaxies found in the dynamically “young” and “old” groups respectively. Observing the top panel we

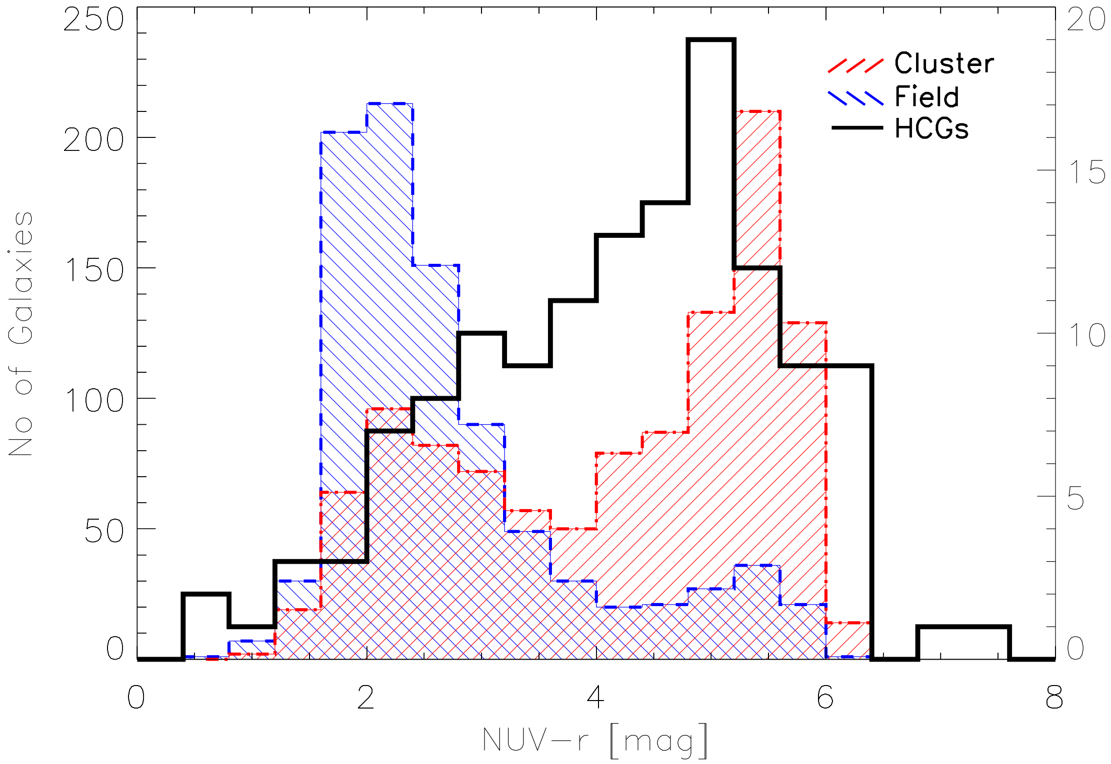

Figure 4.7: NUV-r histogram of HCG *sample II* shown in black (right Y-axis). The histograms of the field, in blue, and cluster galaxies, in red, from the Haines *et al.* (2008) control sample are also presented (left Y-axis).

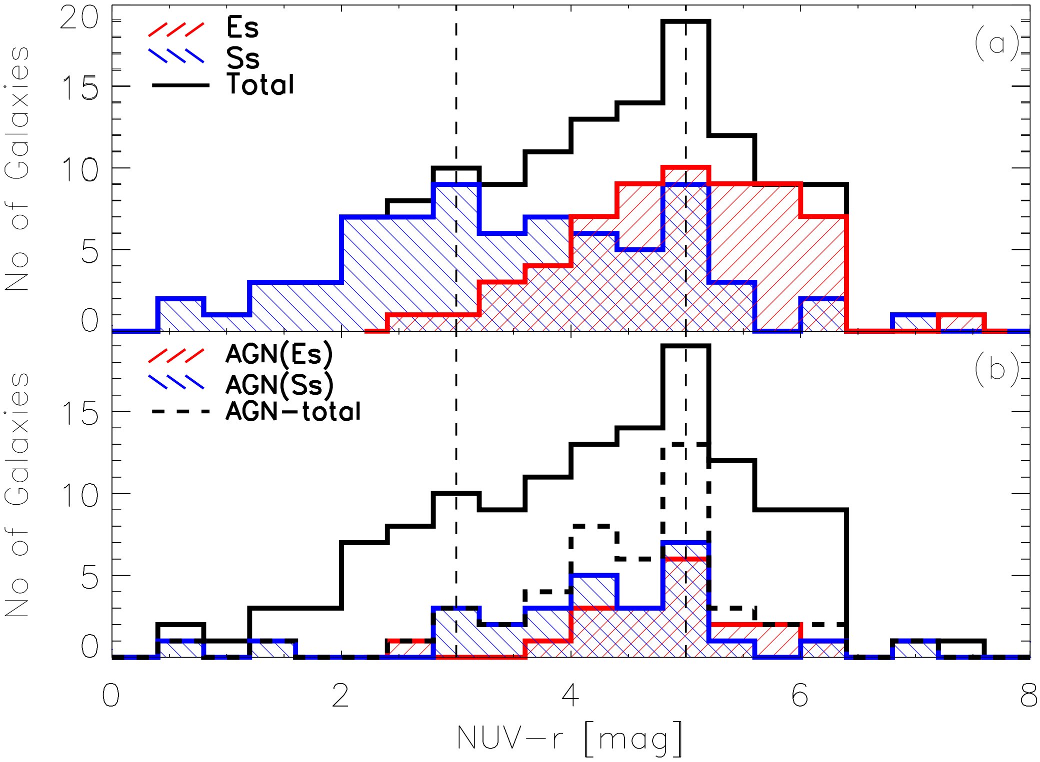

Figure 4.8: a) NUV-r histogram of the whole HCG galaxy sample is shown in black. The corresponding histograms of the early- and late-type galaxies of the sample, classified according to their optical morphology, are shown with the red and blue shaded areas. b) The NUV-r distribution of the galaxies hosting an AGN is indicated with the dashed dark line. As above, the early- and late-type hosts are indicated with the red and blue histograms. The region of 3<NUV-r<5, identified as "green valley", is marked with the vertical dashed lines.

find that almost 60% the late-type galaxies in dynamically "young" groups are located within the "blue cloud" and 43% of them, for which nuclear spectra were available, host an AGN in their nucleus. There are also three outlier galaxies (HCG16b, HCG44a and HCG59a) which have red NUV-r colors (>5mag). It is possible, that these systems have built up their stellar mass in the past and their UV/optical colors are currently dominated by emission from old stars. In addition, past tidal interactions probably stripped some of their gas in the intragroup medium decreasing the fuel necessary for current star formation. In dynamically "old" groups the late-type galaxies are redder and as we can see in Fig. 4.9b most of them (>63%) are located within the "green valley". As in dynamically "young" groups there are also four galaxies (HCG22b, HCG40d, HCG68c and HCG71a) in these groups which are found in the "red sequence".

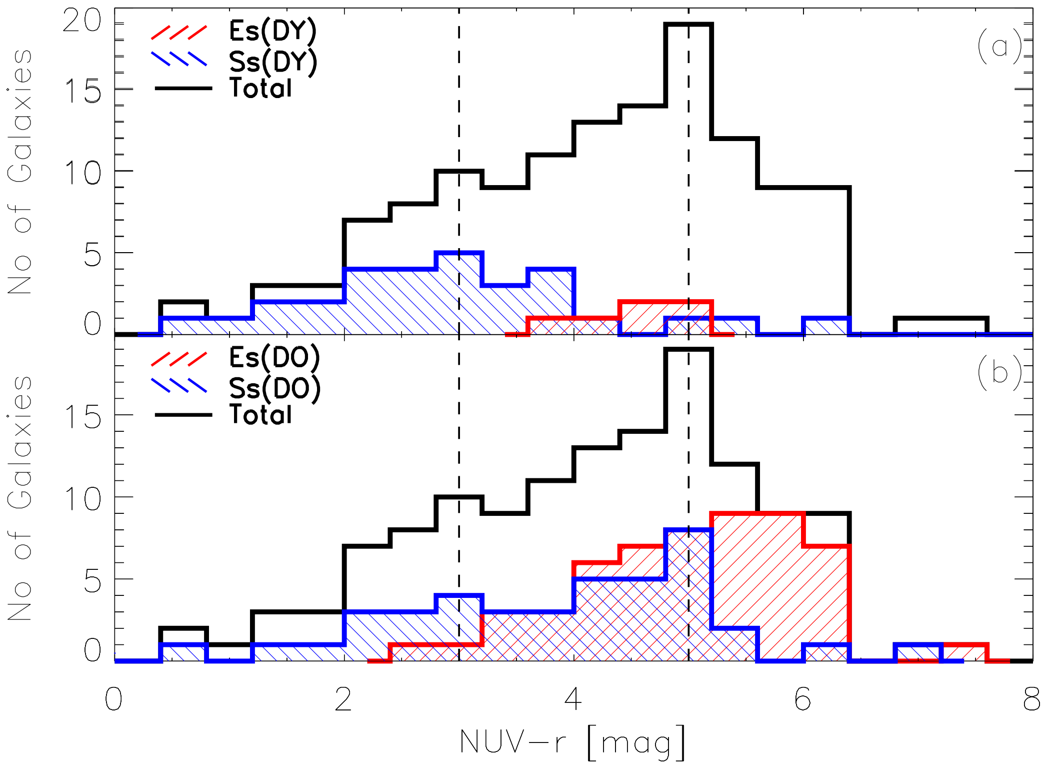

Figure 4.9: a) NUV-r histogram of our HCG *sample II* shown in black solid line. The corresponding histograms of the early- and late-type galaxies found in dynamically "young" groups are shown with the red and blue shaded areas respectively. b) Same as in a), but for the galaxies in dynamically "old" groups. The region of 3<NUV-r<5, identified as "green valley", is marked with the vertical dashed lines.

Overall 45% of the early-type galaxies, shown in red in Fig. 4.8, are located within the “red sequence” and the rest are along the “green valley”. As we mentioned earlier, these systems are expected to be passively evolving and thus, their colors should be dominated by old stellar populations. We find that this is the case for most of them, as only two are found in the “blue cloud”. We believe that these galaxies are misclassified late-type galaxies (see Section 4.4) and we examine them in more detail in the Appendix A of Bitsakis *et al.* (2011). From Fig. 4.9a we see that all early-type galaxies in the dynamically “young” groups are in the “green valley”. One could suggest that they were already early-type before reaching the group and the interactions and/or merging of dwarf companions in the group environment triggered the star formation activity and provide extra gas. However, the most likely explanation is that these are group galaxies which are currently migrating from the “blue cloud” to the “red sequence”. In that case, the morphological transformation should accompany the color transformation. Indeed, the galaxies located in bluer colors (around NUV-r∼4) are lenticulars, while the ones at NUV-r∼5 are ellipticals. Similarly, at the bottom panel of Fig. 4.9 we see that more than half of the early-type galaxies in dynamically “old” groups are located within the “green valley”. These galaxies are mostly (>70%) S0/SB0’s. However, there is a large fraction (∼25%) of elliptical galaxies which also have the same colors. We suggest that even though the morphology of a galaxy typically determines its colors, there are several of the group ellipticals which move back to bluer colors due to interactions and/or merging in the compact group environment.

4.5.1.3 Extinction and the effects of dust

As discussed before, we know that the UV-optical colors of a galaxy, are not only affected by its star formation history, but also from dust extinction. Thus, it would be useful to understand how much of the observed variation in colors is due to intrinsic extinction in the galaxies. Especially for the late-type galaxies which are located within the “green valley”, we have to examine if their colors are affected more from dust or because they contain a substantial old stellar population. Our SED model allows us to estimate and correct for dust attenuation, thus we plot in Fig. 4.10 the distributions of the corrected NUV-r colors of the early- and late-type galaxies in dynamically “young” (top panel) and dynamically “old” groups (bottom panel). We notice in panel (a) that almost all late-type galaxies in “young” groups move back to the “blue cloud”, suggesting that it is the dust which plays a dominant role in their apparent colors. On the other hand, 40% of the late-type galaxies in dynamically “old” groups still remain in the “green valley” after the extinction correction. It seems that in those it is the old red stars that dominate their UV/optical colors. This also agrees with the

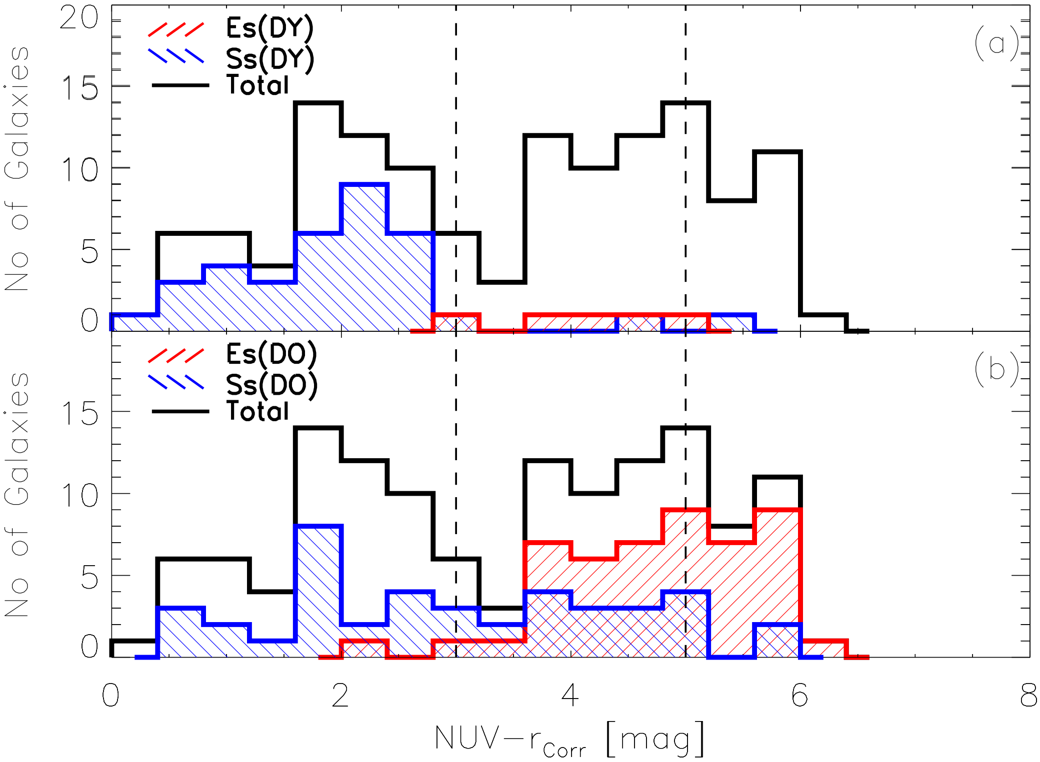

Figure 4.10: A histogram of the NUV-r colors of the HCG sample after correcting for dust extinction, in shown with the black solid line. The separation in two panels for "young" and "old" groups as well as the symbols follow the notation of Fig. 4.9

results of Section 4.3 where these galaxies display low sSFRs. Moreover, one can notice the large fraction of early-type galaxies which after the extinction correction move to the "green valley" (∼50% of the galaxies at these colors). These galaxies display high sSFRS ($\sim 0.21 \times 10^{-11}$yr^{-1}), so their bluer colors are possibly due higher levels of current star formation. We should note that even though for most galaxies the observed optical extinction derived from the SED model (A_V) is not very high (see Fig. 4.2e and Table 2 of Bitsakis *et al.* 2011), due to the steepness of the extinction curve this translates to over 2 mags of correction in the NUV.

4.5.2 IRAC colors and AGN diagnostics

As we know, stellar emission in the UV-to-mid-IR is a composite blackbody spectrum. Moreover, part of the UV light, which is produced by young stars, is absorbed by the PAHs and re-emitted some specific bands in the mid-IR. As a result, one would expect that the mid-IR spectra of normal ellipticals will be dominated by the stellar photospheric emission, and conversely, that of late-type galaxies will display strong PAH features. On the other hand, AGN are often deeply enshrouded in dust that may heavily absorb the emitted radiation, in particular in the UV, optical, and even in the X-rays in some extreme cases. The energy is then re-emitted isotropically at longer wavelengths in the mid- and far-IR (i.e. Charmandaris, 2008; Elitzur, 2008). As a result, active galaxies often display an excess of continuum emission at wavelengths $2\mu m < \lambda < 15\mu$m, compared to normal quiescent or starbursting galaxies. In addition, there is a weak PAH emission in their mid-IR spectrum, which is attributed to the destruction of their carriers by the strong radiation field surrounding the AGN (see Brandl *et al.*, 2006; Smith *et al.*, 2007; Weedman *et al.*, 2005).

As we already mentioned in Sect. 2.2.2, from the 103 galaxies in our samples I and II, with available optical spectroscopy, 38 are classified as AGN or transition objects (TOs; objects between the area of the BPT which is defined by the criteria of Kewley *et al.* 2006 and Kauffmann *et al.* 2003b). This in addition with the fact that the model of da Cunha *et al.* (2008) does not include the contribution of an AGN to the SED of a galaxy, could bias some of our results, and in particular the SFR, sSFR, and L_{IR}, of the galaxies for which the AGN dominates their mid-IR wavelengths. However, we can use our Spitzer infrared photometric measurements to examine the presence of dominant AGN among the galaxies in our sample.

Stern *et al.* (2005) have defined a locus in the IRAC [3.6-4.5] vs [5.8-8.0] colors which is populated by AGN which are dominant in the infrared. Their criteria provide a robust identification of dominant AGN with more than 80% completeness. We plot in Fig. 4.11 the Stern diagnostic for the galaxies of *sample II*. By construction, the galaxies located in the left of Fig. 4.11 are those dominated by the stellar photospheric emission. As a result, they are expected to have very weak dust or PAH emission, if any. Most of our early-type galaxies lie in this region. On the other hand, galaxies found in the right of this figure should have strong PAH features (at 3.3 and 7.8μm), as well as some hot dust contribution, because of intense star formation. Most galaxies in this area are late-type systems. Finally, galaxies found in the shaded area, are those which their mid-IR spectra are dominated by the AGN power-law. We can see that only at three galaxies their mid-IR SEDs are dominated by AGN emission (HCG 6b, HCG 56b, and HCG 92c).

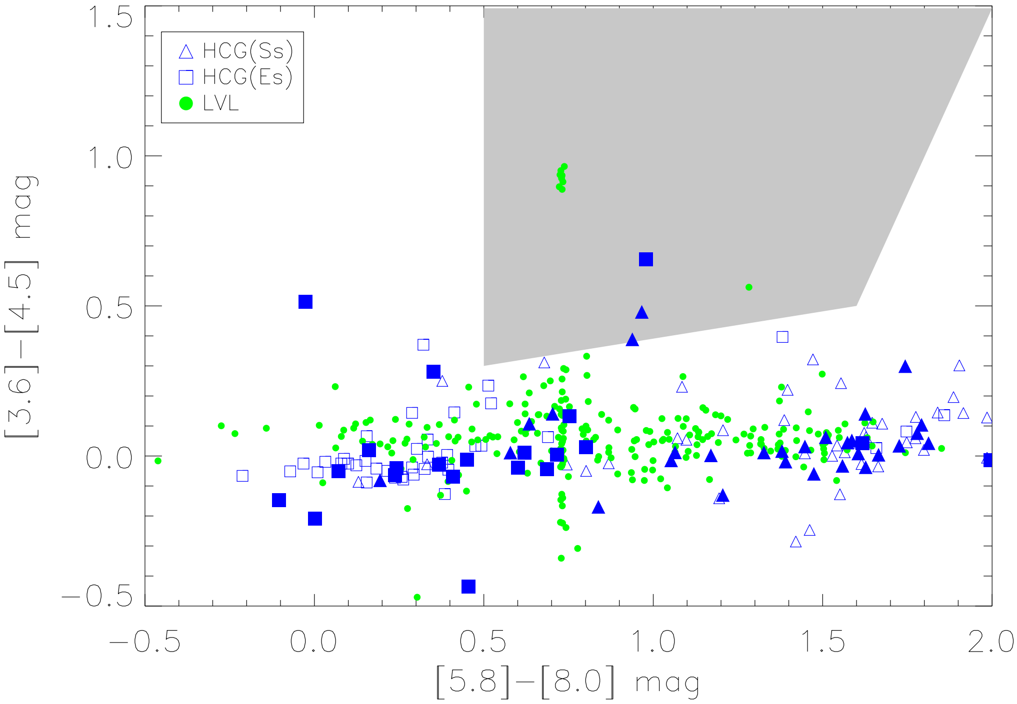

Figure 4.11: AGN diagnostic according to the criteria of Stern *et al.* (2005). Late and early-type galaxies, in HCGs, are marked with blue triangles and squares, respectively. With filled triangles and squares are marked the galaxies which were classified as AGN using optical spectroscopy, and, with green filled circles are the galaxies of the LVL sample. Only three candidates, HCG 6b ,HCG 56b, and HCG92c are found within the AGN candidate area.

To further examine the mid-IR colors of these galaxies, we plot in Fig. 4.12 their

IRAC colors. We notice that most of the late-type galaxies are located in the upper right quadrant of the plot, while most of the early-types are in the lower left. The 10 early-type galaxies which display red mid-IR colors are the ones we mentioned in Section 4.4. We observe that between the colors -0.1<log[$f_{8.0}/f_{4.5}$]<0.3 and -0.25<log[$f_{5.8}/f_{3.6}$] <-0.10 there is a lower density of galaxies. Johnson *et al.* (2007) and Tzanavaris *et al.* (2010) proposed that this "gap" is related to an accelerated migration of the galaxies from star forming to quiescent systems. Examining Fig. 4.10 we notice that the galaxies in the upper right quadrant of the IRAC color-color plot are the ones with NUV-r<2.5, while galaxies which are located in the lower left portion of the figure have NUV-r>3.5. We finally notice that the lower galaxy density area appears in both figures and actually separates the star forming ("blue cloud") from the passive evolving ("green valley" and "red sequence") galaxies. Therefore we suggest that the color bimodality observed in the extinction corrected UV-optical colors, is also observed in the mid-IR and possibly emerges from the same physical properties of the galaxies.

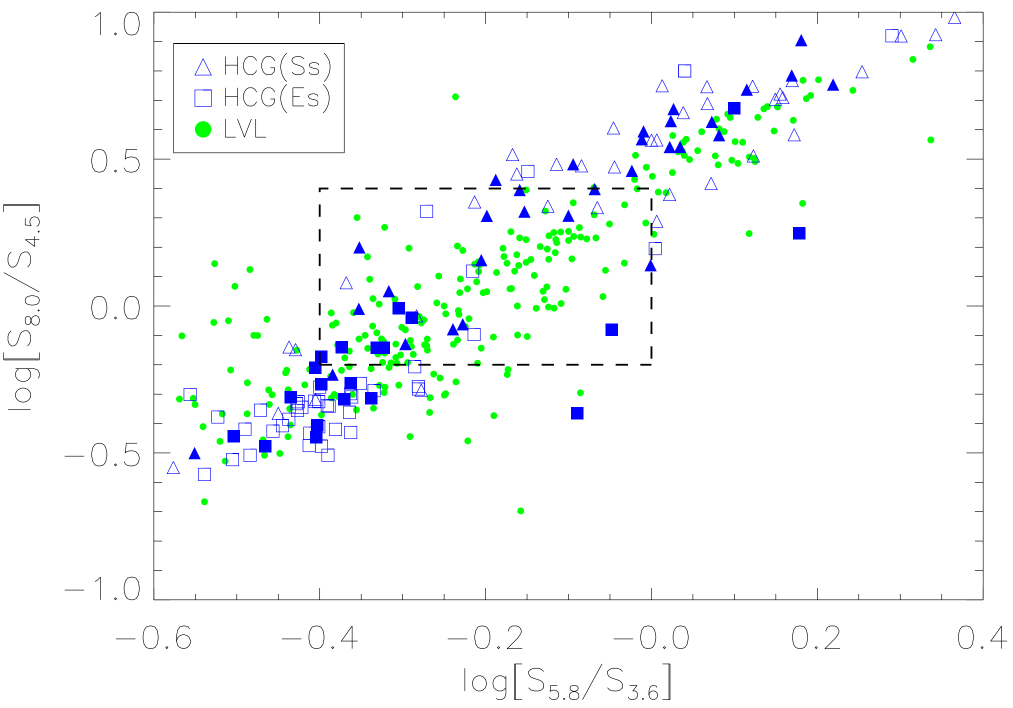

Figure 4.12: IRAC color-color plot of the galaxies in our *sample II*. The symbols are as in Fig. 4.11. According to Johnson *et al.* (2007) the "gap" is located in the area enclosed by the dashed lines.

How significant though is this "gap"? Walker *et al.* (2010) compared their sample of 12 HCGs with several control samples including the SINGS and interacting pair sample we used, as well as galaxies from the Coma cluster, and the Local Legacy Volume sample (LVL Dale *et al.*, 2009). They concluded that the mid-IR color distribution of HCG galaxies is not seen in the field but it is seen in galaxies of the Coma infall region. However, in their analysis they combined the SINGS and LVL galaxies as a single local galaxy sample. As we mentioned though in Section 2.1.3.1, the SINGS sample was selected to explore the mid-IR properties of various galaxy types seen in the local universe, but it is not representative of a flux or volume limited population (Kennicutt *et al.*, 2003). This selection biases the statistics of the colors of the sample. In contrast the LVL sample is volume limited, since it contains all known galaxies inside a sub-volume of 3.5Mpc and an unbiased sample of spiral and irregular galaxies within the larger, more representative, 11Mpc volume. The mid-IR colors of the LVL sample are plotted in Fig. 4.12 as green points. Performing a two sided KS-test between the distributions of the IRAC colors (log[$f_{8.0}/f_{4.5}$] and log[$f_{5.8}/f_{3.6}$]) of HCG and LVL samples, we find that the distributions are not significantly different displaying P_{KS} =0.035 and P_{KS} =0.028, respectively. This suggests that there is no strong evidence that an accelerated evolution of galaxies in HCG is responsible for a significant fast change in their global mid-IR colors.

4.6 Dynamical properties of HCGs

We examined so far the UV-to-mid-IR colors and the model derived physical parameters of HCG galaxies. We have presented that several of these parameters and colors are bimodal, depending on the dynamical state of their groups. However, we should also study in detail the dynamical properties of these galaxies. In the next paragraphs we examine the "strength" of interaction between the galaxies within groups, depending on the dynamical state of their groups, as well as we compare the total dynamical, stellar, and gas mass contents of the groups.

4.6.1 Virial radius and neighbors distance

As we mentioned in Section 4.1, we classified the dynamical state of our sample depending on the fraction of elliptical galaxies they contain. Our method is related to their evolution since it is known that galaxy interactions and merging, transform galaxies from late-type systems to ellipticals. Thus, groups with excess of early-type members, are likely to be older and more compact. In order to investigate this we have estimated the projected distance of each galaxy from the other members of the same group members, as well as the virial radius of each galaxy. To calculate the projected distance between the group members we used the great circle distance relation. Then, using the relation described in Park & Hwang (2009), we estimated the virial radius with the formula:

$$r_{vir}(\mathrm{Mpc}) = \left(\frac{3\gamma \mathrm{L}\Omega_{\mathrm{m}}}{800\pi\rho_{\mathrm{m}}}\right)^{1/3} \tag{4.1}$$

where $\mathrm{L}=10^{-0.4(\mathrm{M_r}+20.00)}$ is the r-band luminosity in $\mathrm{L}_\odot$ and M_r is the absolute r-band magnitude of the galaxy, γ is the mass to light ratio (1 or 2 for late- and early-type galaxies, respectively), and ρ_m=0.0223h^3Mpc^{-3} is the mean density of the universe, with h=0.72 and Ω_m=0.27. Keeping in mind that compact groups may not be fully virialized dynamical systems, we present our results in Table 6 of Bitsakis *et al.* (2011). We note that indeed, in dynamically "old" groups the member galaxies are statistically closer to their nearest neighbors, having a mean projected distance of 26 kpc compared to 37 kpc for the dynamically "young" groups.

However, galaxies in groups are interacting not only with their nearest neighbors, but also with all other group members since in all cases the virial radii of the galaxies are substantially larger than the linear size of their group (see Table 6 of Bitsakis *et al.* 2011). To better quantify this effect we have followed the approach of Hwang *et al.* (2010), introducing the parameter of the "strength" of the interaction ($<\mathrm{R}/\mathrm{r}_{vir,nei}>/\mathrm{n}$). This is estimated by averaging the ratios of the projected distances over the virial radii for all the neighbors of each galaxy and divide them by the total number of neighbors (n). This quantity provides an empirical measure of the interaction strength each galaxy experiences from its companions. The smaller this parameter is, the stronger the dynamical influence of the companions.

In Fig. 4.13, we plot the distributions of the distributions of the strengths according to the dynamical state of each group. Since we have SDSS data for only 74 galaxies and equation (4.1) relies on the SDSS r-band magnitude to compute the virial radius, we used the SED model fits to estimate the synthetic r-band magnitudes for the remaining of the *sample II*. We observe that the "strength" parameter of dynamically "old" groups is indeed smaller than in dynamically "young" groups, suggesting that in the former the gravitational effects are stronger. A KS-test between the two distributions confirms that the two distributions are significantly different ($\mathrm{P_{KS}}\sim10^{-5}$). Moreover, if we compare our results with the findings of Hwang *et al.* (2010) we see that the distances between the galaxies in groups and those of the centers of rich clusters are

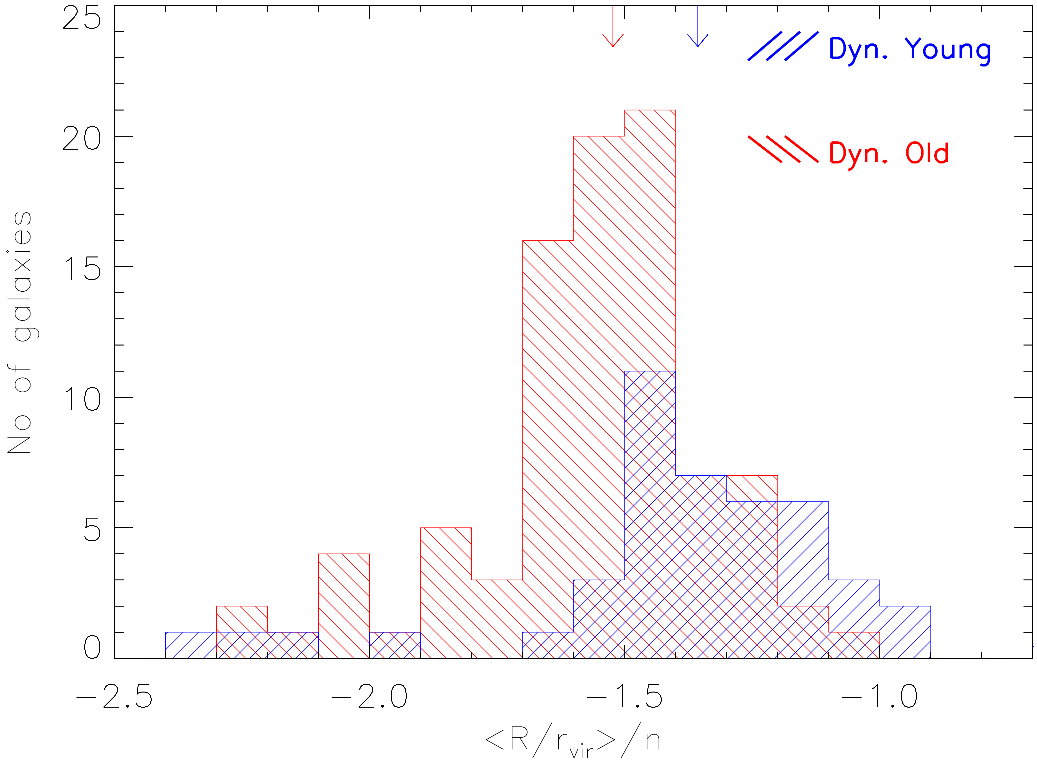

Figure 4.13: Histograms of the “strength” of the dynamical interaction felt by each group galaxy (<R/r$_{vir,nei}$>/n). As usual, we separate our sample into dynamically “young” (blue) and dynamically “old” (red) groups. The arrows indicate the median values of the two distributions.

similar (both have $R<0.5r_{vir}$). We can also estimate the velocity dispersion, σ_r, of each galaxy from the most massive-central galaxy of its group, using the published velocities from Hickson *et al.* (1992). Galaxies in dynamically "old" groups display mean velocity dispersion of 408±50km s^{-1}, which is the half of what is observed in the Virgo cluster, in contrast with those in dynamically "young" groups for which is about 132±39km s^{-1}. All these facts lead us to the conclusion that dynamically "old" groups, as their name implies, are indeed older, denser and more evolved systems, since their properties are intermediate between those of rich clusters and dynamically "young" groups.

4.6.2 The mass content of compact groups

To further examine the dynamical properties of these groups, we can calculate their dynamical masses using the projected mass estimator from Bahcall & Tremaine (1981):

$$\mathrm{M_{dyn}} = \frac{24}{\pi \mathrm{GN}} \sum_{\mathrm{i=1}}^{\mathrm{N}} \mathrm{u_i^2 R_i}, \tag{4.2}$$

where u_i is the difference in the recessional velocity between the group member i and the central massive object (see Table 2 of Bitsakis *et al.* 2011 where the most massive objects in each group are marked with a star), R_i is the projected distance from the central object, and N is the number of group members. This dynamical mass can be compared to the various components of the baryonic mass of the groups. The stellar mass is derived from our SED modeling while the total atomic hydrogen mass, M_{HI}, is available for 29 of the groups from Verdes-Montenegro *et al.* (2001). Unfortunately, the mass of the molecular hydrogen, M_{H_2}, is only available for 12 groups (Martinez-Badenes *et al.*, 2010). We note that even though the integrated masses of the molecular and atomic hydrogen of the groups are often similar, on average they are both ∼25 times less massive that the stellar component. These results are summarized in Table 7 of Bitsakis *et al.* (2011).

In Fig. 4.14 we separate the 32 groups, of the *sample II*, in the two subsamples of dynamically "young" and "old" groups and present the corresponding histograms of the distributions of their atomic hydrogen, stellar, and dynamical masses. We observe that the stellar mass distribution of dynamically "old" groups, shown in Fig. 4.14b is markedly different from that of dynamically "young" groups. A KS-test confirms this, as the probability that the two are drawn from the same parent distribution is $P_{KS}\sim0.009$. The median stellar mass of the dynamically "old" groups is $\sim1.95\times10^{11}M_\odot$, more than double of what is seen in the "young" group subsample ($\sim8.90\times 10^{10}M_\odot$). This is understood on the basis of our classification scheme; dynamically "old" groups do have more elliptical galaxies which are typically more massive than spirals. Furthermore, from the analysis of Section 4.3, we have shown that the late-type galaxies of these groups also have redder optical colors.

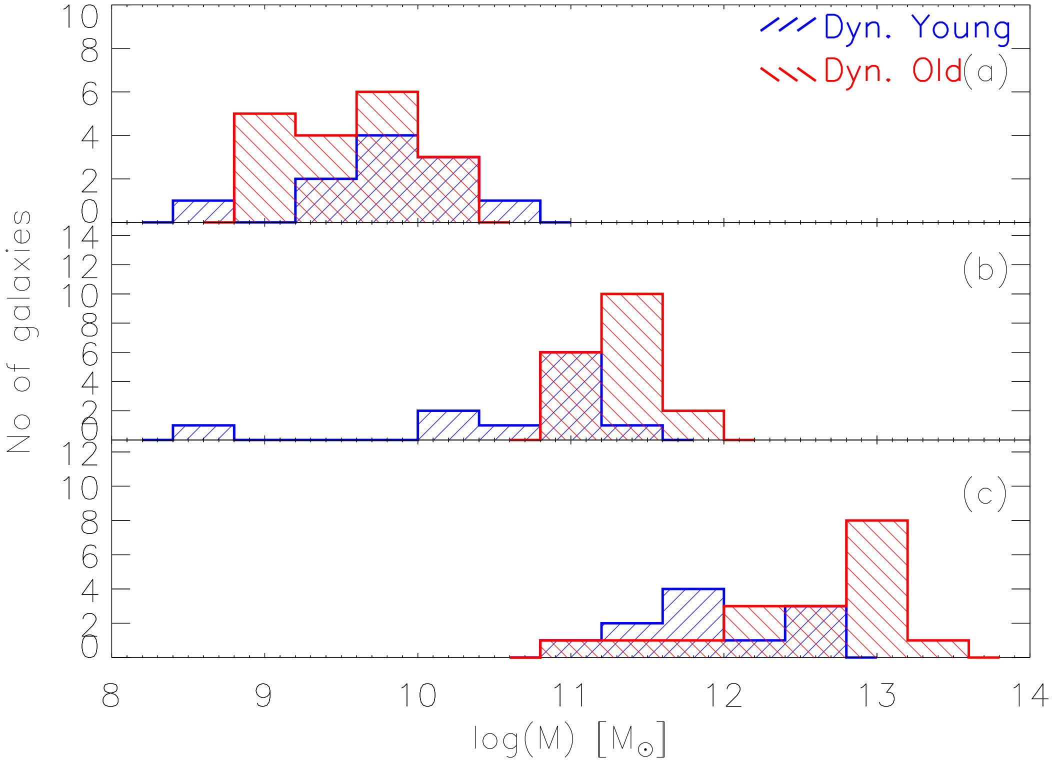

Figure 4.14: a) Distributions of the total HI masses in the dynamically "young" (in blue) and the dynamically "old" (in red) groups, of the total stellar masses (panel b) and the total dynamical masses (panel c).

Surprisingly though, in Fig. 4.14a we note that the HI mass distribution is fairly similar in both subsamples (P_{KS}~0.26), with a median value of HI mass $\sim 3.2\times10^{9}M_{\odot}$. In addition, in Sect. 4.3.2, we showed that the molecular gas mass distributions of the galaxies in dynamically "old" groups were found to be slightly lower than those found in "young" ones, the results were not significant, though. Yet, Verdes-Montenegro *et al.* (2001) showed that a fraction of the HI gas is expelled from the galaxies, mainly of our dynamically "old" groups, to the intragroup medium in the form of plumes and long filaments. However, we can observe such features only in few HCG, since only a dozen of them have high spatial resolution maps of their atomic gas component. In the next paragraph, we will try to investigate the existence of warm molecular gas in the intragroup medium of these galaxies, using the high-resolution Spitzer IRS mid-IR spectra.

Finally, examining the distributions of the dynamical masses of the two subsamples in panel (c) of the same figure, we find that, as was the case with the stellar mass, these are also different (P_{KS}~0.008). The dynamically "old" groups display a median dynamical mass of $6.46^{+1.28}_{-1.57}\times10^{12}$ $M_{\odot}$, nearly an order of magnitude higher from what is seen in the "young" ones ($4.67^{+1.29}_{-3.43}\times10^{11}M_{\odot}$). Note, that the dynamical masses do not simply scale with the stellar mass of the subsamples, which only differ by a factor of ~2. Furthermore, there is no indication of a variation in the ratio between the dark matter, as probed by the kinematics, and the baryonic matter in groups, or that there is a systematic error in the estimates of the dynamical mass due to one subsample being less virialized than the other. As a result, one could attribute the deficit in the observed baryons in the dynamically "old", to a component of hot intragroup gas, since there is clear evidence that groups with more early type systems have stronger X-ray emission (Mulchaey *et al.*, 2003; Ponman *et al.*, 1996).

As we showed in Sect. 4.1, in Table 7 of Bitsakis *et al.* (2011) we also present our classification of the 32 groups, of the *sample II*, based on the fraction of the early-type members, as well as the classification based on their HI morphology proposed by Verdes-Montenegro *et al.* (2001) for 13 groups where this was available. Despite the small number statistics, we note that there is an overall agreement. Groups which we consider as dynamically old are in Phase 3 or 2 according to their HI content, while groups which we consider dynamically "young" are in Phase 1 or 2. There are two exceptions in this. HCG79, the so called "Seyferts' Sextet" was classified by us as dynamically "old" but it is Phase 1 based on the distribution of its HI gas by Borthakur *et al.* (2010). Inspecting it closely we see that our definition is likely marginal as the system does not have an elliptical galaxy and its 2 early type members are peculiar S0s. The other case is HCG44, which was classified as Phase 3 by Borthakur *et al.* (2010). The group consists of 3 late type galaxies and NGC 3193, an E2 which Aguerri *et al.* (2006) argue that may be an interloper. Close inspection of the HI map of the group shown in Fig. 2 of Williams *et al.* (1991) reveals that nearly all gas emission is associated with the 3 late type systems, and only a small fraction is seen outside the galaxy disks. We would thus argue that this system is more likely in Phase 1 or 2, which would be consistent with our classification as dynamically "young". Therefore, as expected, a change in the galaxy morphology also carries a change in the distribution of the atomic hydrogen within the group, and vice-versa.

4.7 The impact of the compact group environment to the gas content

As we presented in the previous section, the atomic gas mass distribution of the galaxies in dynamically “old” groups is similar to the one in “young”. Moreover, in Sect. 4.3.2, we showed that the molecular gas mass distributions, do not depend significantly on the dynamical state. One would expect that the late-type galaxies in dynamically “old” groups, due to past star formation activity, have consumed part of their molecular gas to form stars, while tidal forces and interactions with a dense medium would strip the gas out of their disks. We already saw that Verdes-Montenegro *et al.* (2001) found that the galaxies which were more HI deficient (their observed HI mass is less than 1/3 of the predicted), were those found in the groups with the more massive diffuse-HI component. They suggested that the HI which is stripped out of the galaxies, due to tidal interactions, goes into the intragroup medium. In the most evolved groups (such as HCG 40), the intragroup gas can be heated up to X-ray emitting temperatures (Ponman *et al.*, 1996), due to gravitational interactions and shocks. In addition, Appleton *et al.* (2006) discovered very strong emission of warm H_2 in the intragroup medium of Stephan’s Quintet (HCG 92), which is produced by a shock wave, and is a direct evidence for the existence of molecular gas in the intragroup medium. This gas was possibly stripped out from the member galaxies due to past tidal interactions, and it is heated by the mechanical energy, which is deposited by the shock.

It is, thus, evident that tidal interactions and shocks can heat up the molecular gas both found inside the galaxies, as well as into the intragroup medium. However, UV light from hot young stars can also excite the molecular gas of the galaxies. Yet, as we already mentioned in Sect. 2.2.4, part of the UV light from these stars is absorbed by the PAHs, which re-emit it in the mid-IR. As a consequence, one could use these PAH features to derive, which fraction of the warm-H_2 is coming from the stars and how much from the mechanical/shock heating. To quantify this process Ogle *et al.* (2010) defined as molecular hydrogen emission-line galaxy (MOHEG), a galaxy where the ration of the integrated H_2 flux over the 7.7μm PAH is larger than 0.4.

To examine if there are MOHEGs among our compact groups, we performed mid-IR spectroscopy in 23 HCGs (7 dynamically “young” and 16 dynamically “old”), using the IRS spectrograph on-board on Spitzer space telescope (see Cluver *et al.*, 2012). Since our original aim was to search for extended warm molecular hydrogen emission, we had selected groups with intermediate HI deficiencies (for definition see Verdes-Montenegro *et al.*, 2001).These groups are more likely to have active gas stripping, as well obvious signs of tidal interactions, such as disturbed disks, tails etc. However, searching in the intragroup medium for warm H_2 emission, only two possible candidates were detected (HCG 40 and HCG 91), suggesting that shock-heated intragroup emission is rare in HCGs.

However, we did find evidence of enhanced warm H_2 emission in 13 galaxies, all in dynamically "old" groups (mostly S0's and Sa's) even though it is not clear if the elevated $H_2/7.7\mu$m ratio is due to enhanced warm molecular gas emission, for the reasons we describe above, or because of 7.7μm depletion due to AGN activity. However, as we showed in Fig. 4.11, there are only two galaxies at this sample, which's mid-IR spectra are dominated by an AGN (see Table 2 of Cluver *et al.* 2012). In Fig. 4.15a, we present again the Stern diagnostic diagram for the 74 galaxies in the spectroscopic analysis HCG sample, and separate them according to their mid-IR spectral features. As we can see the MOHEGs, are located in the lower left portion of the diagram. These systems are obviously not dominated by star formation and/or AGN emission. It seems that tidal interactions and/or shock-heating due to the interaction with the intragroup medium, are the most likely mechanisms that warm-up the molecular gas in these compact group galaxies.

In Sect. 4.5.2 we also showed that the observed under-density in the intermediate mid-IR colors is directly connected with the UV-optical color bimodality. Star forming galaxies, which are found in the "blue cloud", in the UV-optical colospace, dominate the warm mid-IR colors (upper right portion of Fig 4.15), while red quiescent galaxies are found in the cold area of the mid-IR colorspace (lower left). Thus, we expect that if we plot them depending on their UV-optical classification, the results will be similar with the previous figure. Therefore, in Fig. 4.15b we plot the $H_2/7.7\mu$m PAH values, this time separating the galaxies according to their extinction-corrected NUV-r colors. As we can see the MOHEGs are mostly located in the "green valley", with only few of them in the "blue cloud" and "red sequence". We believe that since these galaxies are mostly in the "green valley", they will also display lower star formation activity than the galaxies of the "blue cloud", and perhaps, slightly higher than those of the "red sequence". Thus, we plot the sSFRs of these galaxies versus their mid-IR colors (see Fig. 4.16). We can see that most of the MOHEG galaxies do display very low sSFRs, slightly larger, though, than those of group ellipticals not detected to have warm-H_2 emission. We could expect this result, since elliptical galaxies do not contain significant quantities of gas. On the other hand, galaxies of intermediate color and morphology in dynamically "old" groups, may still contain some amounts of gas. These galaxies have already experienced numerous interactions with other group members; there the tidal

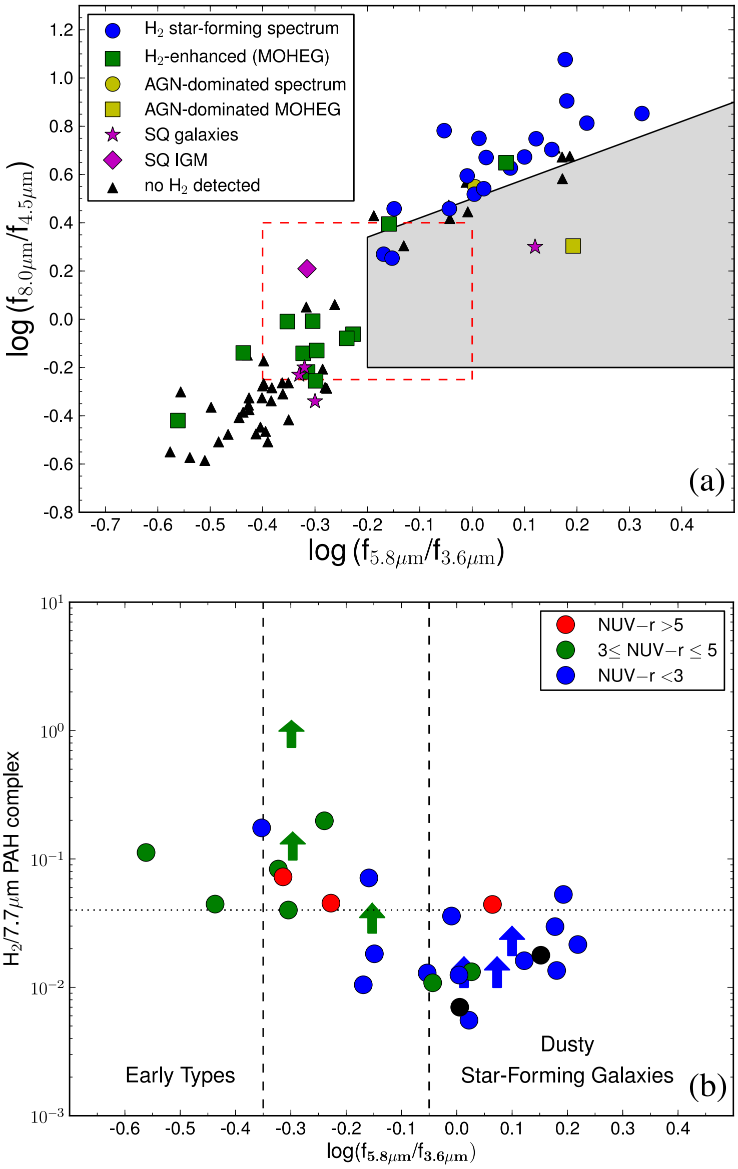

Figure 4.15: (a) IRAC color diagram of the sample of Cluver *et al.* (2012). Galaxies with no warm H_2 detection are marked with black triagles, H_2 detected in line with UV-heated PDR emission are marked with blue circles, MOHEGs with green squares, and AGN dominated spectra are in yellow. The red box shows the low density region, from Walker *et al.* (2010), and the grey region is where mid-IR dominant AGN should be found, according to Lacy *et al.* (2004) criteria. The purple diamond indicates the Stephan's Quintet IGM (Cluver *et al.*, 2010), with member galaxies shown in magenta stars. (b) The H_2/7.7μm PAH ratio according to NUV-r color for the galaxies with warm H_2 detected. The red symbols indicate the galaxies found in the "red sequence", the green symbols the ones of the "green valley" and the blue symbols are indicating the galaxies of the "blue cloud". The vertical dashed lines correspond to the intermediate mid-IR color region and over the vertical dotted line are found the MOHEG galaxies. With black point are marked the galaxies which were not included in our *sample II*.

torques and shocks could ignite star formation, which enhanced their stellar masses, but also exciting part of their gas content, and make them observed as MOHEGs.

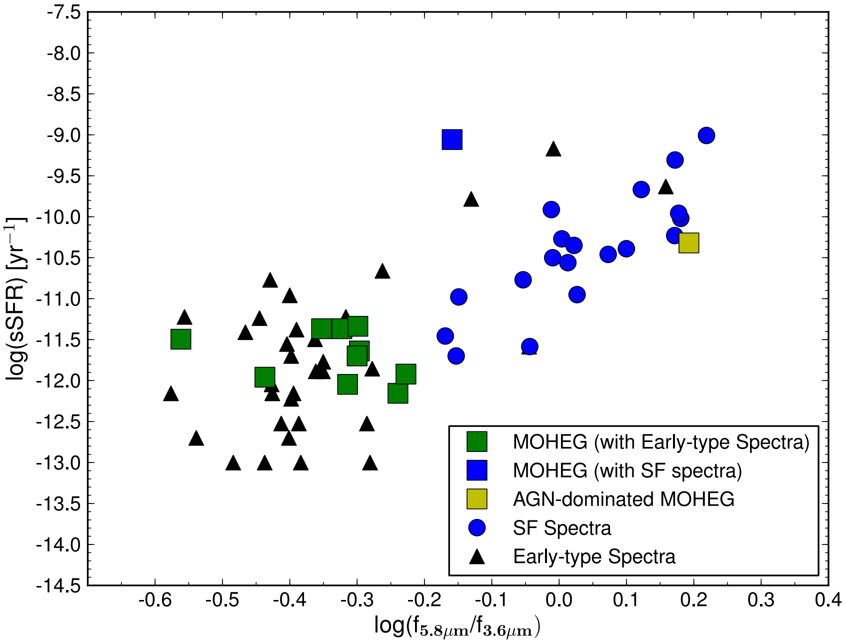

Figure 4.16: The sSFRs against the log[$f_{5.8}/f_{3.6}$] colors. MOHEGs are marked with squares (green for the early-type and blue for the star forming), in black are the galaxies with no warm-H_2 detection and in yellow is HCG 56b, which host a dominant AGN.

4.8 Cold dust in the intra-group medium

As we discussed in the introduction, dust is produced during the late stages of stellar evolution. The outflows from stellar winds and supernovae explosions enrich the ISM with dust grains of various sizes. Cold large dust grains (T∼20K) are well mixed with atomic gas in the ISM. Even though the gas-to-dust mass ratio varies depending on the metallicity and the radiation field its typical value is ∼600 (Sanders *et al.*, 1991). Dynamical interactions among galaxies pull not only gas from their disks to the intergalactic medium, but also the cold dust found in the disks. Several such cases of diffuse dust emission in the intergalactic space have already been observed, with a well known example the plume of about 15K dust outside the main body of the nearby elliptical galaxy Centaurus A. In order to be able to identify this cold dust and discern it from similar emission due to the cirrus clouds of our own Galaxy along the line of sight, high resolution far-IR observations are necessary.

Up to date, the low resolution IRAS maps were only capable to detect the total far-IR emission of each HCG group. However, using our sample of 32 HCGs (*sample II*) and the physical model of da Cunha *et al.* (2008), we can predict by extrapolation of the SED, the total far-IR fluxes of the galaxies of each group, and compare them to the integrated values for the whole group from IRAS. In Fig. 4.17 we plot the fraction of the integrated IRAS flux densities at 60 and 100μm for each group as measured by Allam *et al.* (1996) divided by the sum of the flux densities of all group members predicted by our SED model fit. The results are presented in Table 7 of Bitsakis *et al.* (2011). We identify 13 groups (HCG6, 7, 16, 25, 55, 57, 67, 68, 71, 75, 79, 91 & 95) where diffuse cold dust emission may be present. We note that, 10 of these groups are dynamically "old". This is in agreement with the notion that dynamically "old" groups are more evolved and their members have experienced more encounters enriching the intragroup medium. It is possible that part of the apparent far-IR excess is due to the uncertainties introduced by our SED fits. As we will discuss also in Sect. 6.3.2, high-resolution far-IR observations for 29 groups, will be soon available allowing us to reliably characterize the composition and structure of the intragroup medium as well as study the evolution of the cold dust in these systems.

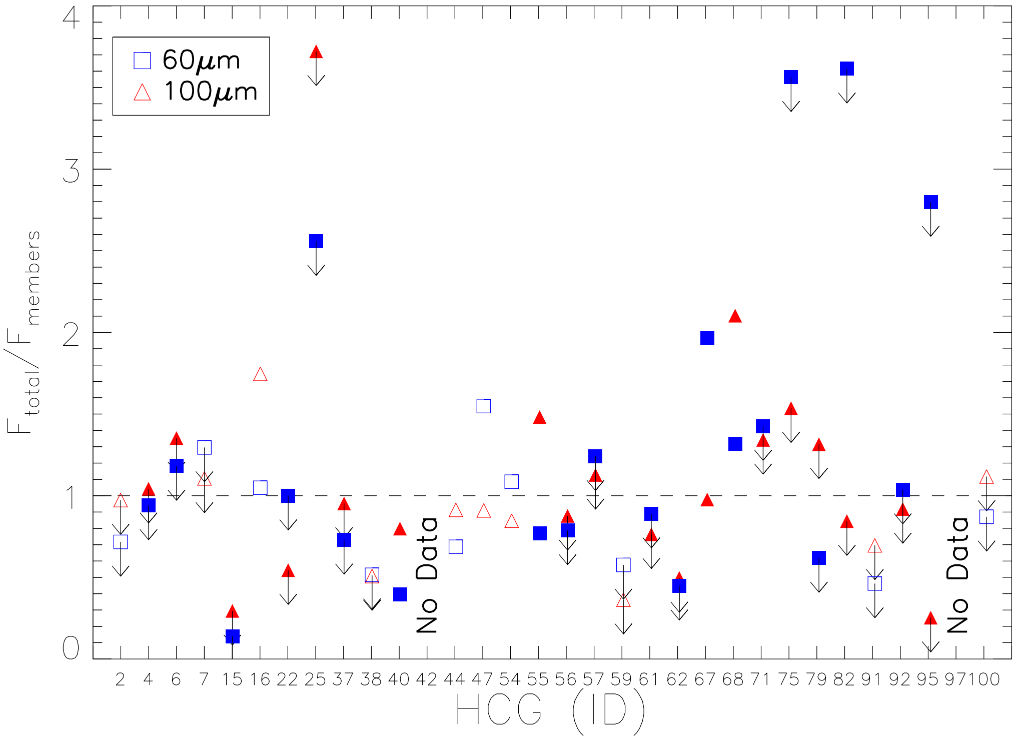

Figure 4.17: Plot of the ratio of the observed IRAS 60 and 100 μm fluxes of each group divided by the corresponding flux all group members as predicted by our model fits. Since IRAS did not resolve/detect all the members of each group, several of the ratios are indicated as upper limits. Filled symbols indicate dynamically "old" groups.

Chapter 5

The SDSS CG sample

In the previous chapters we presented our study on the effects of the group environment in galaxies using multiwavelength observations for a subsample of 32 of the original Hickson Compact Groups. This presented some limitations since the total number of galaxies studied was 135. Here we extend this analysis to a substantially larger number of galaxies for which similar type of data exist. More specifically, as we discussed in Sect. 2.1.2, McConnachie *et al.* (2009) applied the Hickson criteria to the whole SDSS DR6 catalogue. Based on simulations and mock catalogs they concluded that if they increase the minimum surface brightness of the group to 22 mags arcsec^{-2}, they can reduce the contamination of no-members to 25%. Their final catalog consists of 2297 compact groups. As we described in the same section, we performed GALEX/UV photometry, and also cross-correlated their catalog with 2MASS/near-IR and WISE/mid-IR surveys, and our final multiwavelength catalog (*sample III*) consists of 1770 compact groups, containing 7417 galaxies.

This new sample is the largest and most complete compact group catalogue to-date, since it resulted by applying to the whole SDSS survey the improved Hickson criteria. It increases the number of group galaxies by a factor of 55 and it samples groups out to z$\sim$0.3, sampling a volume nearly 16 times larger than our previous samples. Following the same methodology to the one used for our other samples we examine in this Chapter the properties of the galaxies in these groups and test with significantly better statistics the results we have obtained so far.

5.1 Evaluating the SDSS-HCG galaxy properties

As we presented in Sect. 2.1.2.2, we classified the galaxies of this sample into late and early-type from their fitted radial profiles, placing the separator at n_{Sersic}=3.3 according to the classification we did using the Hα EWs of the 3374 galaxies with available spectroscopy. From these galaxies 3985 (54%) are classified as early-types and 3422 (46%) as late-types. According to the group dynamical classification we describe in Sect. 4.1, from the 1770 groups of this sample, 482 groups (or 27%) are classified as dynamically "young", and 1288 groups (or 73%) are classified as dynamically "old". We can see that this sample is very similar to the HCG where the corresponding fractions were ∼20% and ∼80%.

5.1.1 Stellar masses

In Sect. 4.2 we presented the distributions of the stellar masses of the early and late-type galaxies in Hickson compact groups. As it is expected the early-type galaxies display usually higher masses that those of the late-type galaxies. We found that the two distributions were significantly different, and they displayed median values of $1.78^{+4.64}_{-1.71}\times10^{10}M_{\odot}$ and $4.07^{+11.0}_{-3.23}\times10^{10}M_{\odot}$ for the late and early-type galaxies, respectively.

In Chapter 3, we used the empirical formula of Bell *et al.* (2003), as well as the models of Kauffmann *et al.* (2003b) to estimate the stellar masses of the galaxies of *sample III*, and we found that they are in agreement (see Fig. 3.7). Here, we will use the first since they are estimated for the whole sample and not only for the galaxies with available optical spectroscopy. In Fig. 5.1a we present the distributions of the stellar masses of early (in red), as well as of late-type (in blue) galaxies in the SDSS CG sample. According to the KS-test, the two distributions are significantly different (displaying $P_{KS}\sim10^{-5}$). The median values they display are $3.09^{+8.87}_{-2.82}\times10^{10}M_{\odot}$ and $6.91^{+11.5}_{-5.13}\times10^{10}M_{\odot}$ for the late and early-type galaxies, respectively. In addition, the results of the model estimates, are also similar, having median values of $3.54^{+10.7}_{-2.66}\times10^{10}M_{\odot}$ and $8.60^{+14.0}_{-5.33}\times10^{10}M_{\odot}$ for the late and early-type galaxies, respectively.

However, one can notice that the stellar mass distributions of both the early, as well as the late-type galaxies in *sample III* are almost the double than those of the same galaxies in *sample II*. We cannot attribute this to the downsizing scenario, since these galaxies differ only by Δz of 0.07, which corresponds to 0.9 Gyr. Therefore, in order to built mass of $3\times10^{10}M_{\odot}$ within this period, galaxies would need a constant star formation of $\sim35M_{\odot}$ yr^{-1}. In Fig. 5.1b we plot the stellar masses of the late

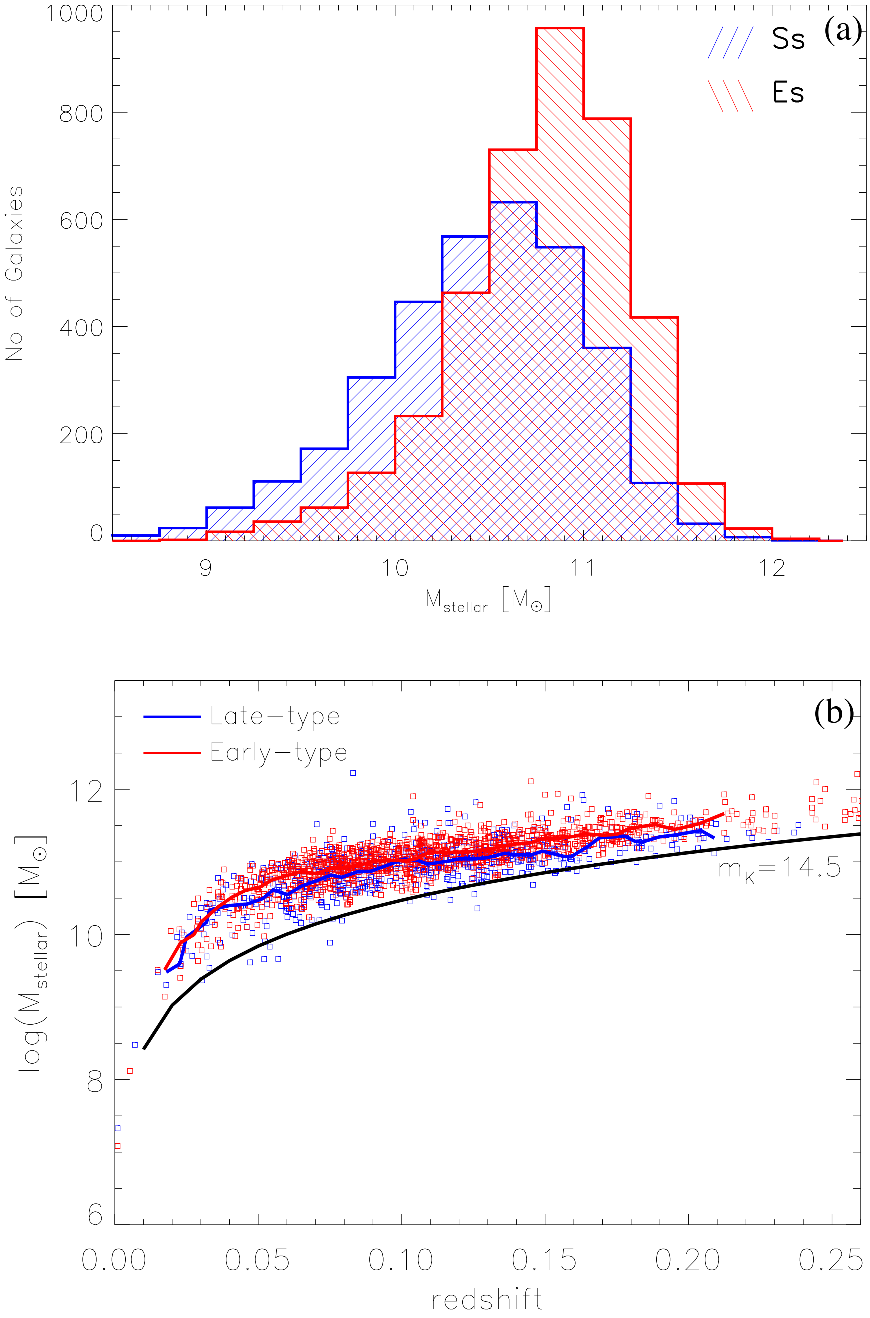

Figure 5.1: (a) Distribution of the stellar masses in our *sample III*. In red are the early-type galaxies and in blue are the late-type ones. (b) Stellar masses versus the redshift in late (blue) and early-type (red) galaxies in the SDSS CG sample. The red and blue lines indicate the running averages, and the black line in the stellar mass of a galaxy with K-band magnitude 14.5, in different redshifts.

and the early-type galaxies of our sample against their redshift. We can see that in both cases the stellar mass is getting higher as the z increases. We over-plot on the figure the stellar mass of a galaxy with magnitude in the K-band 14.5mag, which is the upper limit for the 2MASS in this band, in different redshifts (black solid line). We can conclude that the increase of the stellar mass with the redshift, is simply due to the fact that at higher-z the faintest sources are under the detection limit of 2MASS.

Finally, when we separate the late-type galaxies in HCGs depending on the dynamical state of their group, the ones found in dynamically "old" groups display higher stellar mass. We attributed this to the fact that the multiple past interactions, which those galaxies had experienced, induced star formation and had as a result to increase the stellar mass content of those galaxies. In Fig. 5.2, we plot the distributions of the stellar masses of the late-type galaxies of the *sample III*. We notice that here the two distributions are also statistically different ($P_{KS} \sim 10^{-7}$) and they display median values of $2.71^{+10.7}_{-2.66} \times 10^{10} M_{\odot}$ and $3.49^{+3.01}_{-2.63} \times 10^{10} M_{\odot}$ for "young" and "old" groups, respectively.

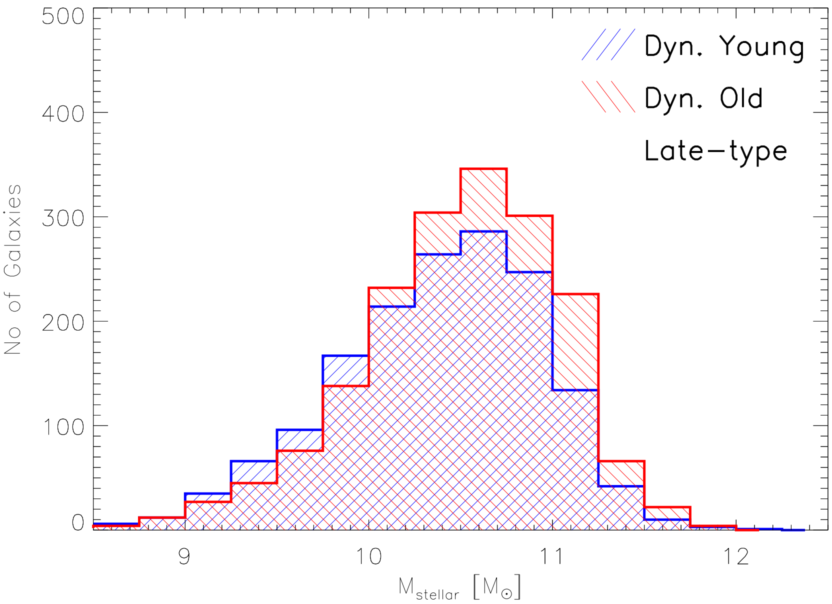

Figure 5.2: Distribution of the stellar masses of the late-type galaxies in dynamically "young" (in blue) and in dynamically "old" (in red) groups.

5.1.2 Star formations rates

In Sections 3.1.2 and 3.2.3, we described several methods (theoretical and empirical) to estimate the SFRs of the galaxies in our samples. Later we compared them in Section 3.3.3 and we concluded that we can use either those derived from the Hα fluxes (1961 galaxies which have no optically detected AGN into their nucleus) or those estimated using the WISE 22μm emission (1860 late-type galaxies which were not upper limits and their PSF were not blended with those of other group members). Since WISE was not sensitive enough to detect early-type galaxies, here will we use the ones derived from Hα, which are more representative of the total sample having early and late-type galaxy fractions of ~40% and ~60%, respectively.

Thus, in Fig. 5.3a, we present the distributions of the late (in blue) and the early-type (in red) galaxies in the SDSS CG sample. The median value of the late-type galaxies is $1.62^{+4.67}_{-1.20}$M$_\odot$ yr^{-1} and of the early-type is $0.14^{+0.20}_{-0.08}$M$_\odot$ yr^{-1}. The two distributions are statistically different according KS-test (P$_{KS}$~0). Moreover, when we separate the late-type galaxies of these groups, according to their dynamical state (Fig. 5.3b), we notice that, even if the late-type systems in dynamically "young" groups display slightly higher SFRs ($1.73^{+4.90}_{-1.27}$M$_\odot$ yr^{-1}) than those of the galaxies in "old" groups ($1.56^{+4.69}_{-1.16}$M$_\odot$ yr^{-1}), the two distributions are not different (displaying P$_{KS}$~0.3). In addition, when we compare the corresponding distributions of the SFRs as derived from the WISE, we see that they are also similar (P$_{KS}$ ~0.51), displaying also median values of 1.83±0.70M$_\odot$ yr^{-1}, and 1.81±0.65M$_\odot$ yr^{-1}, in dynamically "young" and "old" groups, respectively. These results are in agreement with those of Sect. 4.2.2, derived for the HCG galaxies. It seems that even if the star forming galaxies in dynamically "old" groups display higher masses, they do not seem to differentiate their star formation rates.

5.1.3 Specific SFRs

As we presented in the previous chapter, one of our very first discoveries in HCG late-type galaxies, was that their sSFRs varied depending on the dynamical state of their group. Moreover, we showed that dynamically "old" groups are more compact and with more members. As a result, late-type galaxies in these groups, had already experienced several tidal encounters, which had increased their stellar masses. In addition, we showed that their SFR remained similar, even if the late-type galaxies of dynamically "old" groups appeared to have slightly lower molecular gas masses. Yet, using the Schmidt-Kennicutt law, we found that the later were forming stars more efficiently

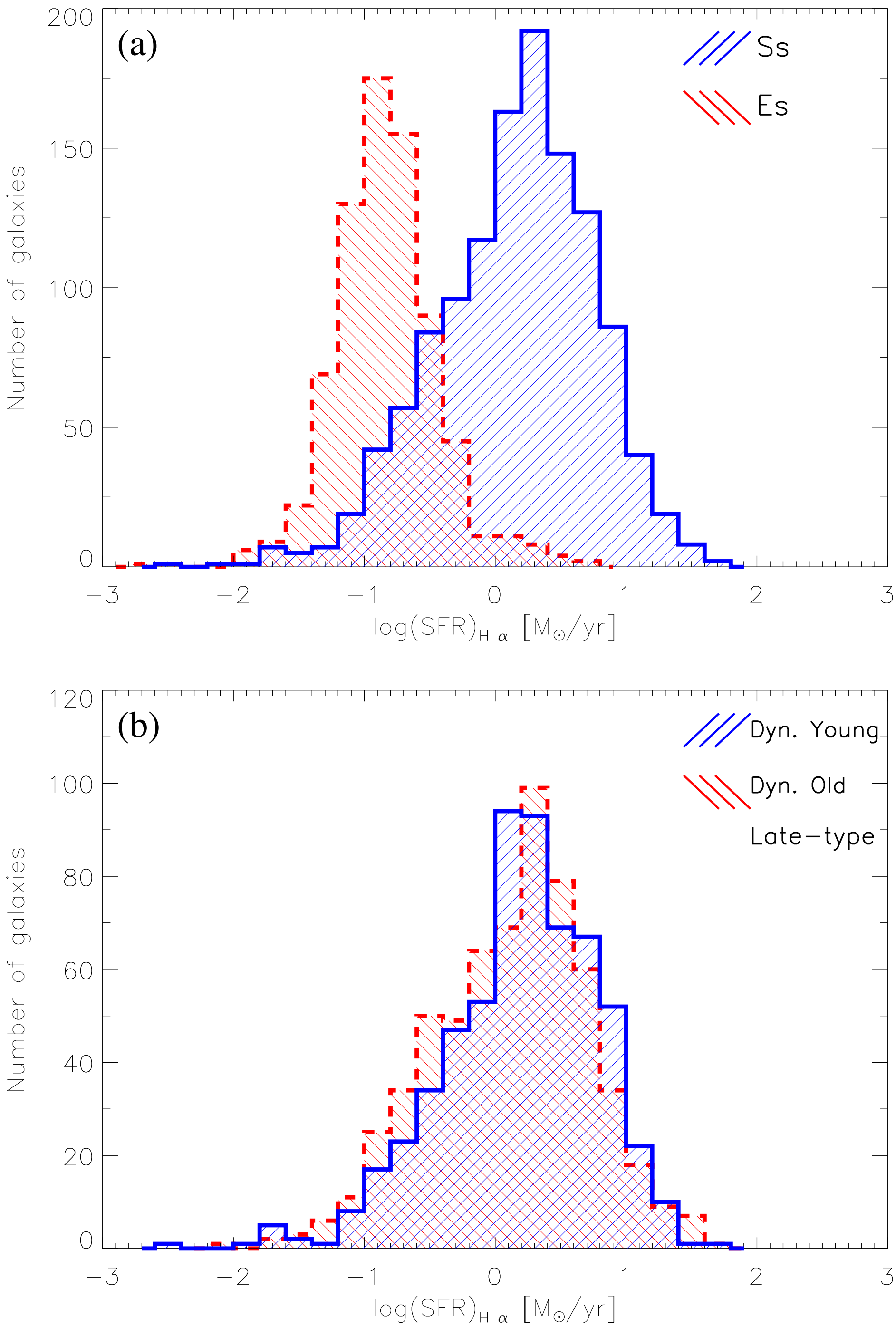

Figure 5.3: (a) Distributions of the star formation rates of the 1961 late (in blue) and early-type (in red) galaxies, as derived from the Hα line flux modeling. (b) Distributions of the SFRs of the same late-type galaxies in the same sample. This time we separate them according to their dynamical state (dynamically "young" and "old" in blue and red, respectively).

using the same amount of gas.

In the previous paragraphs, we presented the stellar masses, and SFRs of the galaxies in the SDSS CG sample, where we found that they appear to display large similarity with those found in HCG galaxies. Thus, we expect that this will be the case also for the sSFRs. In Fig. 5.4 we present the distributions of the late-type galaxies in dynamically "young" (top panel) and dynamically "old" (bottom panel) groups, where we can see that they are significantly different (having $P_{KS}\sim0.05\%$). The median values are $10.2^{+29.0}_{-7.54}\times10^{-11}\mathrm{yr}^{-1}$ for the "young" and $7.88^{+24.8}_{-5.98}\times10^{-11}\mathrm{yr}^{-1}$ for the "old" late-type galaxies. Finally, the early-type galaxies in both states are similar ($P_{KS}\sim4\%$) , and they display median values of $0.14^{+0.11}_{-0.06}\times10^{-11}\mathrm{yr}^{-1}$ and of $0.13^{+0.15}_{-0.07}\times10^{-11}\mathrm{yr}^{-1}$ for the dynamically "young" and "old" groups, respectively.

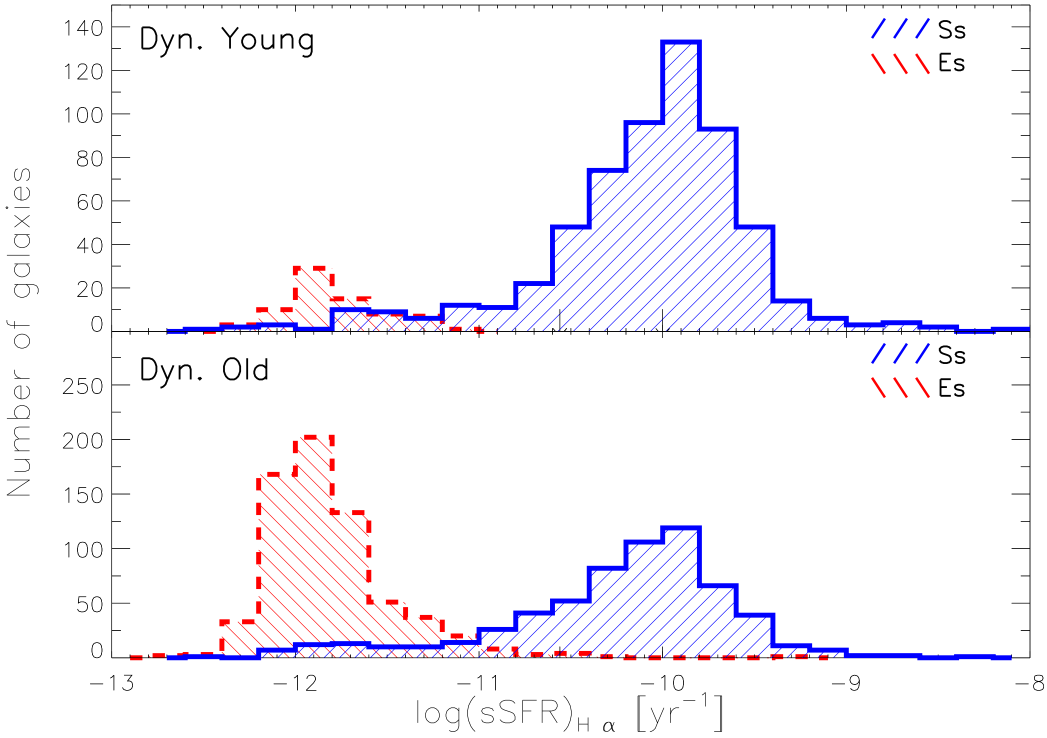

Figure 5.4: Distributions of the sSFRs of the 1961 late-type (blue) and early-type (red) galaxies in dynamically young (top panel) and dynamically old (bottom panel) groups, as derived from the Hα.

5.1.4 UV-optical colors

A number of studies (i.e. Haines *et al.*, 2008; Wyder *et al.*, 2007) revealed that there is a bimodality in the colors of field, as well as of galaxies in clusters. Using stellar population synthesis models (see Sect. 4.5.1) we showed that star forming galaxies are found in the blue edge of the NUV-r colorspace (the "blue cloud"), and on the other hand, quiescent systems are redder (the "red sequence"). Between these two there is an area with lower concentration of galaxies (the "green valley"), mostly found to host an AGN into their nuclei. However, as we saw in the previous Chapter, most HCG galaxies were found in this area. Further analysis revealed that the late-type systems in dynamically "young" groups were mostly populated the blue cloud, with the remaining been redder due to extinction by dust. Contrary, the large fraction of the late-type galaxies in dynamically "old" groups were observed in the "green valley", since they contain enhanced old stellar populations. On the other hand, about ∼25% of the early-type systems in these groups, have bluer colors. We suggested that tidal interactions and the merging of dwarf companions had increased their gas content, and as a result enhanced their SFRs.

We have seen , so far, in this Chapter that the SDSS CG galaxies display similar SFR and stellar mass distributions as do the corresponding HCG systems. Thus, one would expect that they will also display similar NUV-r colors. To examine this, we present in Fig. 5.5a the distributions of the late and the early-type galaxies in dynamically "young" groups of *sample III*. Similarly to what it was found in HCGs, more than half of the late-type galaxies (52%, see Table 5.1) are concentrated within the "blue cloud", with the rest to be within the green valley. We suggest that these galaxies are also extinct by dust. Moreover, the early-type galaxies in the same groups are mostly found within the "green valley" (76%). We believe that they are also following the normal color and morphological transformation, as the corresponding galaxies in HCG.

In Fig. 5.5b, we present the distributions of the late and the early-type galaxies in dynamically "old" groups. We notice that more than the half of the late-type galaxies (see Table 5.1) are concentrated within the "green valley". Similarly to the corresponding HCG galaxies, we suspect that a large number of these are found in the "green valley" because they had increased their stellar masses and they display redder colors. We will re-examine those galaxies in Sect. 5.2. Conversely, we can see that ∼75% of the early-type galaxies are placed within the same area. In HCGs we showed that after we correct the attenuation, about half of them remained there. These galaxies display higher sSFRs $\sim 0.16 \cdot 10^{-11} \mathrm{yr}^{-1}$ contrary to $\sim 0.21 \cdot 10^{-11} \mathrm{yr}^{-1}$ in HCGs and are consistent with the dynamically triggered star formation scenario.

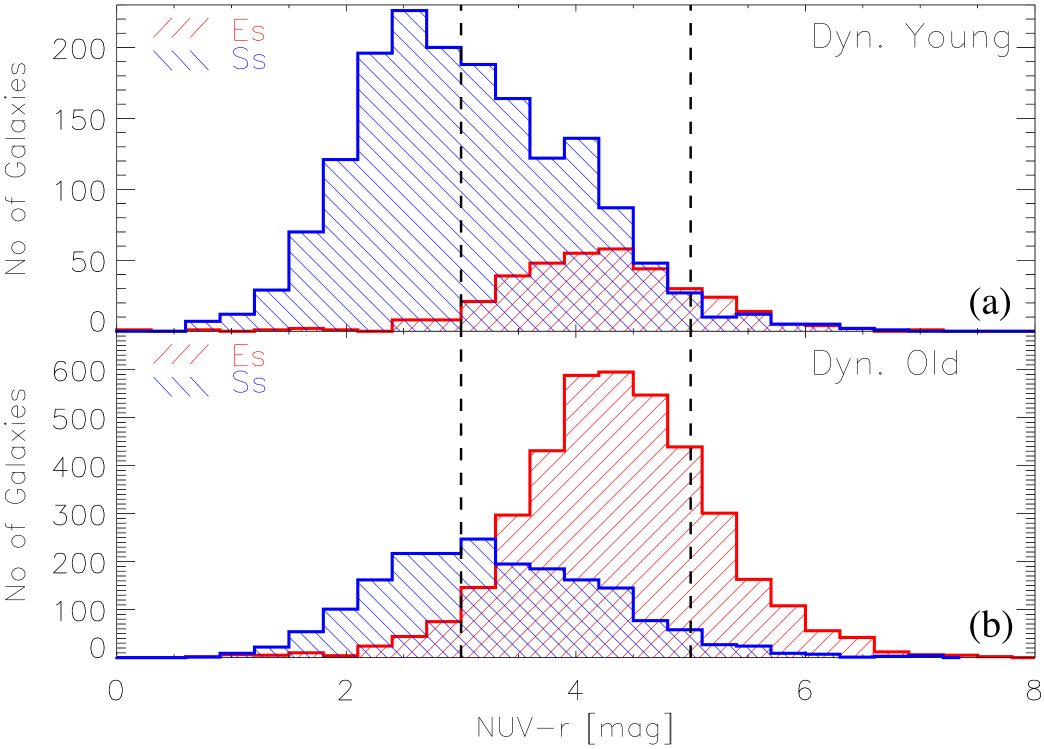

Figure 5.5: NUV-r color distribution of the galaxies in *sample III*. In the top panel (a) are the galaxies belong to the dynamically "young" groups and in the bottom (b) are the ones within "old" groups. The dashed lines separates the "blue cloud" (on the left), the "green valley" (in the middle), and the "red sequence" (in the right).

Table 5.1: Fractions of SDSS CG galaxies in the NUV-r colorspace.

	blue cloud (%)	green valley (%)	red sequence (%)
Dyn. Young S's	52(61)	45(37)	3(2)
Dyn. Young E's	7(15)	76(75)	17(10)
Dyn. Old S's	41(44)	54(53)	5(3)
Dyn. Old E's	5(8)	74(77)	21(15)

Within the parenthesis are presented the corresponding fractions of the HCG galaxies of *sample II*.

Finally, as we showed in the previous chapter, the presence of an AGN does not affect the NUV-r colors of galaxies in HCG. This is in contrast with what it was found in field and cluster galaxies (Wyder *et al.*, 2007), where the "green valley" is dominated by AGN hosts. Using our *sample III*, we compared the NUV-r distribution of the AGN-hosting galaxies to the whole distribution. We notice that the two distributions are significantly different ($P_{KS} \sim 0$), with the AGN-hosting galaxies being at slightly redder colors (NUV-r=4.2, instead of 3.9 of the total distribution). To further investigate this, we separate our sample according the galaxy morphology and the group dynamical state. Comparing the AGN-hosting with the total galaxy distributions, we find that they significantly differ only in the case of dynamically "young" late-type galaxies, where the AGN-hosting galaxies mostly populate the "green valley". This result was not observed in HCGs, probably due to the smaller number of galaxies. However, we cannot even confirm the results of the other studies (i.e. Haines *et al.*, 2008), where the AGN-hosting galaxies are preferentially found in the "green valley".

5.1.5 The fractions and properties of the AGN-hosting galaxies in compact groups

As we just showed, AGN-hosting galaxies do not seem to dominate any specific area of the NUV-r colorspace, but only in the case of dynamically "young" late-type systems which display a small excess in the "green valley". In Sect. 2.1.2.2 we presented that the AGN fraction is about 42%, for the galaxies with available optical spectroscopy (43% in HCGs). From them, 22% are found at late-type galaxies (38% of their total number), and the rest are found in early-type galaxies (47% of their total number). It is obvious that AGN seem to prefer early-type galaxies. This is expected, since AGN hosting systems are more possible that had already experienced various tidal interactions, which had also shaped their morphologies. In addition using numerical simulations, Mihos & Hernquist (1996) showed that such event lead to gas inflow towards the galaxies central regions, with result to fuel both an AGN and/or a central starburst. As a result, one would expect that AGN-hosting galaxies will be also more massive.

In Fig. 5.6a and b, we plot the distributions of the AGN-hosting and non-hosting late-type galaxies in dynamically "young" and "old" groups, respectively. In both cases we can see that the AGN hosting galaxies have significantly larger stellar masses ($P_{KS} \sim 0$), with a median value of $5.54^{+7.23}_{-3.12} \times 10^{10} M_{\odot}$ and $5.99^{+7.80}_{-3.39} \times 10^{10} M_{\odot}$, in "young" and "old" groups, respectively. In contrast, the non-hosting systems have $2.85^{+6.39}_{-1.37} \times 10^{10} M_{\odot}$ and $3.15^{+7.17}_{-2.19} \times 10^{10} M_{\odot}$, respectively. Yet, when we compared the distributions of the late-type galaxies with an AGN in dynamically "young" groups with those

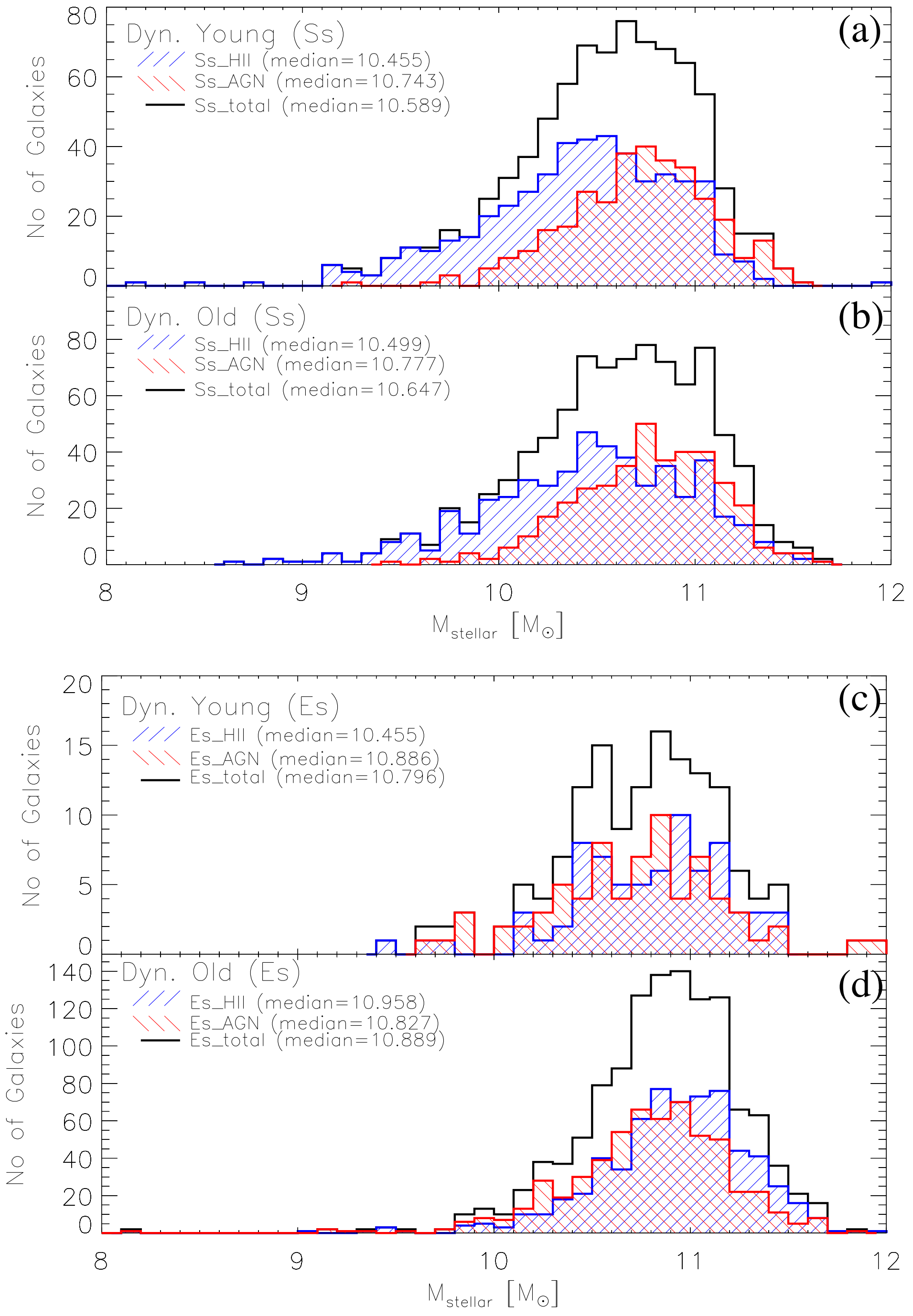

Figure 5.6: Distributions of the stellar masses of AGN hosting (with red) and non-hosting (HII, in blue), late-type galaxies in dynamically "young" groups (panel a), and in dynamically "old" groups (panel b), and in the early-type galaxies of dynamically "young" (panel c) and dynamically "old" groups (panel d). In all the cases the total distributions are indicating with the black solid line.

in dynamically “old”, we notice that they were not different (P_{KS} ∼28%). Moreover, as we showed in Sect. 5.1.1, dynamically “old” late-type galaxies were more massive. Thus, we could explain the above results, if we consider that the same processes, which had increased the stellar masses of the AGN-hosting late-type galaxies in dynamically “old” groups (e.g. tidal interactions and merging), had also the same effects to the corresponding galaxies of dynamically “young” groups. Yet, “young” groups contain much less of those galaxies, and as a result, their stellar mass distribution is not seriously affected.

Finally, in panels (c) and (d) of the same figure, we present the distributions of the stellar masses of the early-type galaxies with or without an optically identified AGN, in “young” and “old” groups, respectively. In both cases the AGN-hosting galaxies seem to have slightly lower stellar masses than those of non-hosting systems, yet this is not significant.

5.2 Examining the radial profiles of the galaxies

In the Sect. 2.1.2 we decided to separate the galaxies in our *sample III* into early or late-type depending if their published Sersic indices (Simard *et al.*, 2011) were larger or not than n_{Sersic}=3.3, respectively. To derive the value of the separator we used the the Hα EWs, of the 3374 galaxies of this sample with available optical spectra. Here, using the star formation properties we already estimated for our galaxies we will re-examine our previous morphological classification.

In Fig. 5.7 we plot the sSFRs of the galaxies in our sample, versus their Sersic indices. As it was expected, the star forming galaxies are mostly found at log(sSFR)>-11.2 yr^{-1} (see the distributions on the right of the same figure), with most of them having low n_{Sersic}. Conversely, the quiescent galaxies are found at log(sSFR)<-11.2 yr^{-1} and they mostly have n_{Sersic}>4. The green dashed line indicates the n_{Sersic}=3.3 separator, according to our previous classification. When we estimate the number of galaxies with log(sSFR)>-11.2 yr^{-1} at n_{Sersic} <3.3, we can see that the 79% of them are classified as late-types, according to our morphological classification. On the other hand, the fraction of the early-type galaxies which have log(sSFR)<-11.2 yr^{-1} at n_{Sersic} >3.3 are 80%. We can see that both methods we used to classify our galaxies into early and late-types are in agreement. This, is really important since using this classification we separated our groups into dynamically “young” and “old”, which is crucial for our analysis.

The existence of the fitted profile parameters of the galaxies in our sample, en-

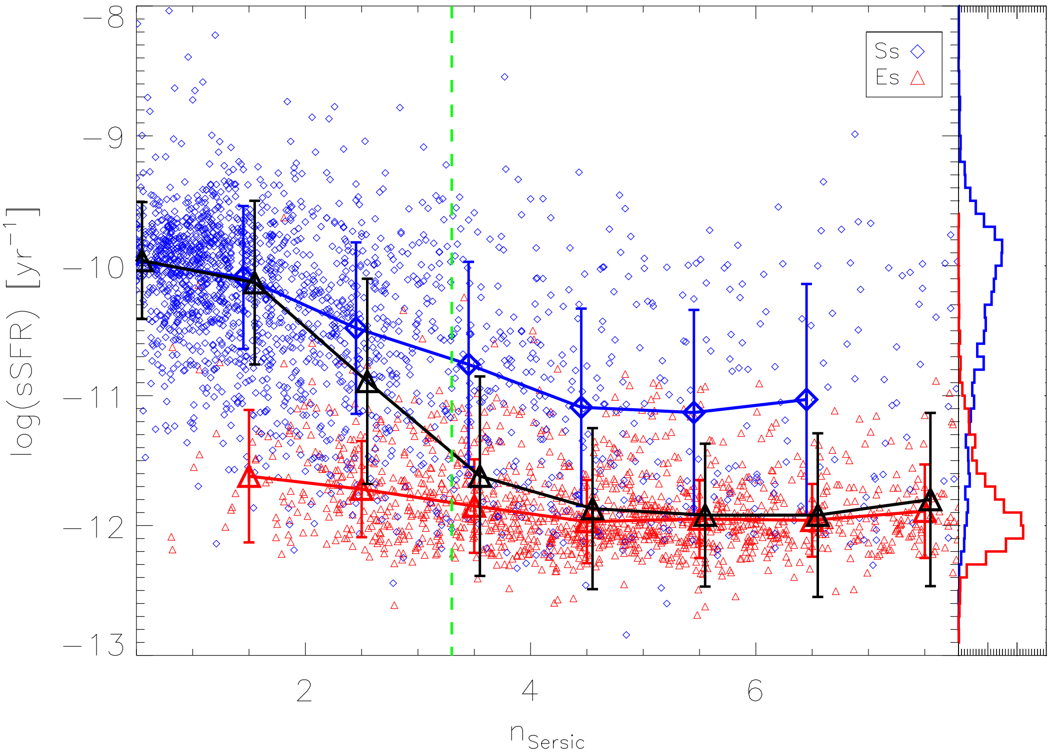

Figure 5.7: In this plot we check the validity of our morphological classification, based on the Hα EWs. With blue diamonds are presented the galaxies, which were classified as late-types, and with red triangles the ones classified as early-types, according to our previous classification. The black line indicates the median and standard deviation values in bins with size the unit, and the green dashed lines indicates the n_{Sersic}=3.3 (see Fig. 2.5). On the right panel are the distributions of the sSFRs of the late and early-type galaxies.

abled us to study in more detail the brightness profiles of these systems. We already showed that the late-type galaxies in dynamically "old" groups are more massive and preferentially found in the "green valley". One would expect that tidal interactions could also increase the random velocities of the stars in those galaxies, as well as fuel a central starburst (Mihos & Hernquist, 1996) with result to increase the size of their central bulge and make them appear more "spheroidal" (larger n_{Sersic}) than the corresponding galaxies of dynamically "young" groups. For that reason, we compared the normalized cumulative distributions of the late-type galaxies found in the "green valley" (in Fig. 5.8a). We can notice that the dynamically "old" galaxies appear to be more "spheroidal" than those found in "young" groups, having median values of 2.24±0.77 and 1.93±0.73, respectively (the distributions are significantly different, $P_{KS} \sim 0$). In addition, we plot in Fig. 5.8b the median values of the Sersic indices found in each bin of the NUV-r colorspace in dynamically "young" and "old" late-type galaxies. We can see that the latter display larger n_{Sersic} independent of their color, suggesting that indeed, those systems had increased their central bulges.

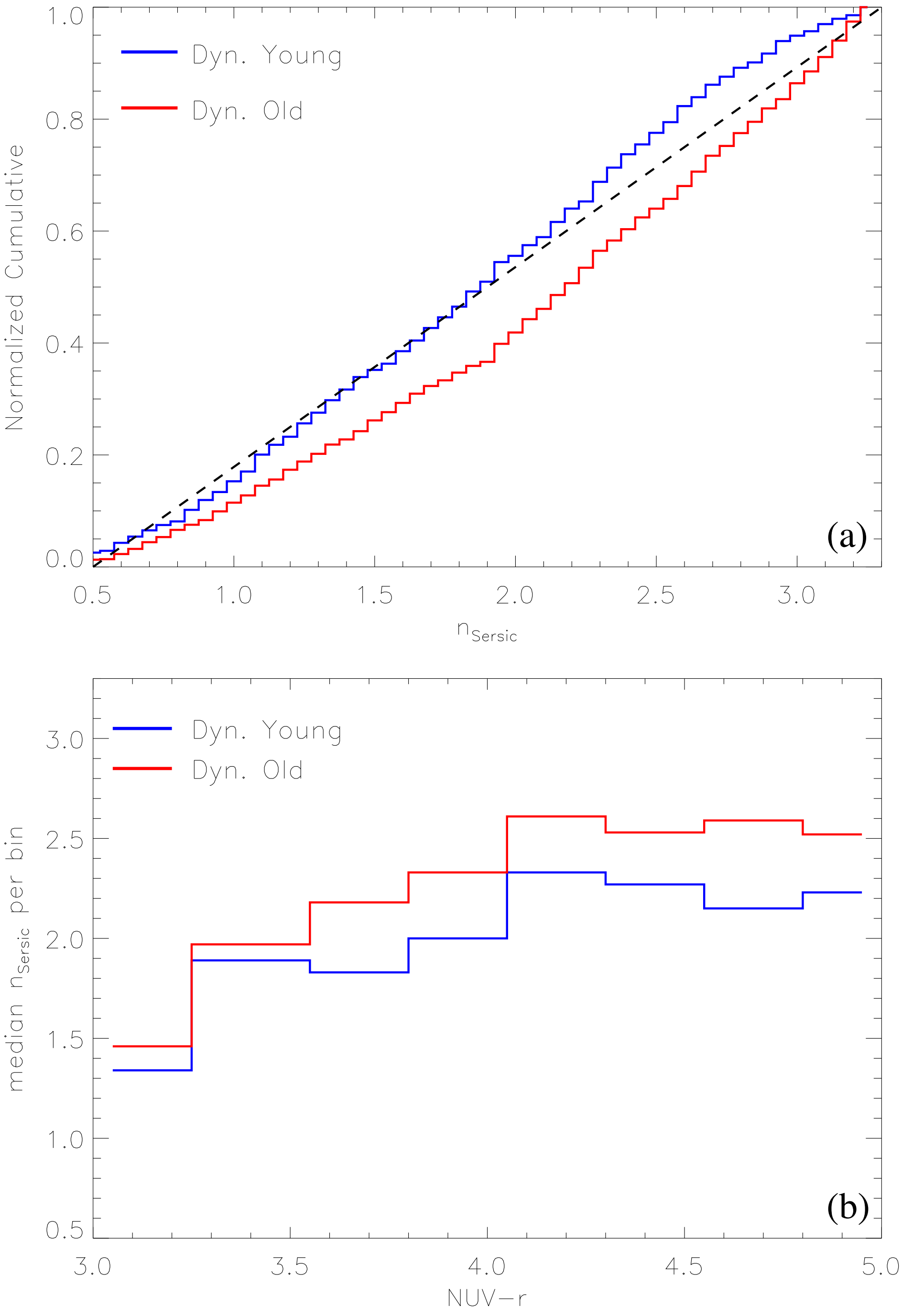

Figure 5.8: (a)Normalized cumulative distributions of the Sersic indices of dynamically "young" (in blue) and dynamically "old" (in red) late-type galaxies found in the "green valley". The black dashed line indicates a homogenous distribution. (b) The median value of n_{Sersic} in dynamically "young" in blue, and "old" in red, late-type galaxies, in each bin of the NUV-r colorspace.

Chapter 6

Conclusions and future perspectives

6.1 Summary of the conclusions

As we have discussed already, compact groups are ideal environments to study the impact of tidal interactions on galaxy properties. Despite the fact that groups had been studied extensively in the optical (i.e. Hickson, 1982; Verdes-Montenegro *et al.*, 2001), the lack of deep high-resolution infrared imaging, sensitive to probe the warm and cold dust content, made estimates of the star formation properties, as well as a census of the total energy balance of the galaxies in these systems challenging. In this thesis we address these limitations by identifying samples of Hickson Compact Groups for which high-resolution Spitzer mid-infrared (3.6 to 24μm) observations were available. The infrared observations were complemented with additional UV and near-IR imaging and the complete spectral energy distribution of the group members was fitted using theoretical models. Finally, to expand our analysis and improve our statistics by a factor of $\sim$50, we have used a larger, more complete, sample of 1770 compact groups, defined by applying the criteria of Hickson to the whole Sloan Digital Sky Survey database. For all the galaxies in this sample, we have performed GALEX/UV photometry and obtained the 2MASS/near-IR and WISE/mid-IR fluxes. Using empirical estimators, as well as theoretical modeling we estimated the stellar masses, star formation rates, dust extinction, infrared luminosities, and nuclear activity of the galaxies. For comparison we have used control samples of field and early-stage interacting pair galaxies, as well as galaxies in clusters. Based on the analysis of these results, we have reached the following conclusions:

- Our proposed classification of the evolutionary state of Hickson Compact Groups (HGCs) as dynamically “young” and “old” according to the fraction of their early-type members appears to be physical and is in general agreement with classifications based on the distribution of their atomic hydrogen. The study of their properties suggests that dynamically “old” groups are more compact and have higher velocity dispersions. They also display higher stellar masses than the “young” ones, while both have similar HI mass distributions. However, “old” groups have nearly an order of magnitude larger dynamical masses than “young” groups.

- In dynamically “young” groups, the late-type galaxies display similar star formation activity to spirals in the field and early-stage interacting pairs. The NUV-r color of most of them place them in the so called “blue cloud” star-forming sequence, while some display redder colors due to higher extinction by dust. The early-type galaxies in these groups appear to passively evolve and to migrate normally from the star-forming sequence to the quiescent one.

- On the other hand, the late-type galaxies in dynamically “old” groups display lower sSFRs. These galaxies show morphological evidence of past interactions with other group members with resulted in converting part of their H_2 gas to stars in a more efficient way than the corresponding galaxies in “young” groups. As a result they display redder NUV-r colors, and enhanced stellar masses. Tidal interactions must have also increased their central bulges and as a consequence these galaxies display more “spheroidal” radial profiles. Furthermore, there are few spiral galaxies which display even redder colors. They all have very small SFRs, similar to early-type systems. We speculate that tidal interactions must have stripped the gas out of their disks, suppressing their star formation activity.

- Most early-type galaxies in dynamically “old” groups, appear to migrate from the star-forming to the quiescent galaxy colors, even though a fraction of them ($\sim$25%) display bluer colors and higher star formation activity than normal field ellipticals. This is possibly due to gas accretion from other group members, as well as the merging of dwarf companions.

- Nearly 42% of HGCs members have an optically identified AGN. They are mostly found in the early-type galaxies, as well as in most massive spirals, which are preferentially located in dynamically “old” groups.

- Our analysis suggests that the reported lower density of galaxies in the IRAC

5.8μm/3.6μm versus 8.0μm/4.5μm diagram is caused by the morphological natural bimodality of galaxies and it is similar to what is also observed in the UV-optical colors.

- We identify two groups, HCG 40 and HCG 91, as possible candidates in which mechanical/shock heating of their intragroup molecular gas takes place. In addition we observe warm molecular gas, which cannot be explained by excitation via star formation, in 13 galaxies preferentially found in dynamically "old" groups. We suggest that the effects of tidal interactions on those galaxies, had as a result to excite their H_2 gas content.
- Modeling the complete SED of 32 HGCs suggests that in 17 groups (~50% of our HCG sample), extended cold dust emission may be present. All these groups are classified as dynamically "old".
- We compare the derived properties and colors of our SDSS CGs with those of the HCG samples. We conclude that even though we can not ascertain group membership for all the galaxies of the first sample, due to lack of redshift information, all the derived results are in excellent agreement.

6.2 The effects of tidal interactions in galaxies

In the introduction of this thesis (Sect. 1.4), we presented two outstanding questions concerning the effects of galaxy interactions and argued that compact groups are maybe the best environments to study the influence of such events. After our detailed study in the properties and colors of compact group galaxies, we present our interpretation.

- **How do the colors and properties of the galaxies within dense environments compare to those evolving in isolation?** – Early-on the influence of close companions to late-type galaxies in groups is negligible and these galaxies display similar properties and colors to those found in the field and early-stage interacting pairs. However, as the time progresses, the effects of tidal interactions and the minor merging increase their stellar mass content, as well as the random motions of their stars. As a result, these galaxies will display redder UV-optical colors and more "spherical" radial profiles. Even though interactions can also strip gas and dust out of the galaxy disks into the intra-group medium, mechanical/shock heating of this material is rare. Eventually, these interactions lead to an increase of the early-type galaxy fraction, as most of the gas in the late-type galaxies is consumed and they begin to transform into early-types.

- **Are tidal interactions enhancing the star formation rates of the galaxies in dense environments, due to turbulence and shocks, or do they reduce them, indirectly, due to gas loss?** – It seems that tidal interactions act in a more complex way in dense galaxy environments. In late-type systems, turbulence and shocks, which occur in their disks as a result of close encounters, make them to convert their gas into stars in a more efficient manner. However, the same interactions also strip part of this gas from the disk sending it into the intragroup medium. As a result late-type galaxies in groups display similar SFRs to those found in isolation, even though their sSFRs are significantly lower. On the other hand, it seems that part of the material which was stripped out of galactic disks, may be accreted by the early-type members of these groups. About 25% of these galaxies, display enhanced star formation activity and bluer colors.

6.3 Future perspectives

Despite our results and improved understanding on the properties of compact groups, there are a number of issues which still remain open. In the next paragraphs we present some future work, which may help clarify them.

6.3.1 Ascertain group membership in the SDSS CG sample

Since the discovery of the first such group, the Stephan's Quintet (or HCG 92) in 1877, hundreds of groups had been identified, using several criteria, with the most complete been that of Hickson (1982). However, the identification of real, physically dense groups, with only just a few members, is a difficult case. Ponman *et al.* (1996) showed that 75% of the HCGs contain warm intragroup gas, yet they could not confirm if some of the apparent members are interlopers; back- or foreground galaxies which are projected on the group. It was found that even in the prototypical such group, HCG 92, member A (NGC 7320) is a foreground galaxy. The best way to ascertain group membership is to obtain spectroscopic redshifts. Based on optical spectroscopy 16 HCG galaxies (11% of our group sample) have members with with discordant redshifts. These galaxies, if not excluded, can bias our results as the classification of the dynamical state of a group relies on the fraction of the "apparent" early-type members.

More recently the availability of SDSS enabled McConnachie *et al.* (2009) to identify 2297 compact groups, for 1770 of which we have produced the complete SED from the UV to 22μm. This sample is more complete than Hickson's in terms of selection. However, group membership is estimated using simulations and mock catalogs, with the possibility that 25% of these groups contain interlopers. The absence of spectroscopic redshifts for nearly 50% of the SDSS CG sample, places limitations on the robustness of our results.

For that reason, we have already proposed a pilot study and were successfully to obtain optical spectra for 20 galaxies, which will complete the spectroscopy in 10 SDSS CGs, using the FAST spectrograph of the FLWO telescope facility in Arizona. Having spectra for all our galaxies we will be able to ensure that these groups are real physically dense systems. In addition, we will be able to estimate the SFRs and identify the possible presence of an AGN into the nucleus of those galaxies.

6.3.2 Identify the presence of diffuse cold dust in the intragroup medium and complete the far-IR SEDs of HCG galaxies

We have presented a number of observational evidence for the existence of diffuse cold dust (T∼20K) in the intragroup medium of Hickson Compact Groups, emitting in the far-IR (see Sect. 4.8). To separate the emission of this dust from the diffuse emission of our Galactic cirrus along the line of sight, as well as to resolve what fraction originates from each galaxy of a group, high resolution far-IR imaging is essential. Currently such unique capabilities are only offered by Herschel Space Observatory. Herschel is a far-IR telescope with a 3.5m mirror which carries 2 photometer/spectrometer instruments (PACS and SPIRE), and a high-resolution spectrometer (HIFI). We have already proposed and were awarded observing time to image in the far-IR a total of 29 HCGs with Herschel. These observations will also help us to better estimate the total energy budget of HCG galaxies. To demonstrate this we use the model of da Cunha *et al.* (2008) and estimate the Herschel PACS (at 70 and 170μm) and SPIRE (at 250, 350, and 500μm) synthetic fluxes for HGC 2c, a sufficiently isolated SBc galaxy for which far-IR IRAS data were available (see Fig. 6.1a) as well as HCG 40b and HCG22a. Using the estimated Herschel fluxes and lower wavelength data we calculated the likelihood distributions of the physical parameters with the da Cunha model we present in Fig. 6.1b the likelihood estimations of the physical parameters with (in green) and without (in red) we included the Herschel bands. These histograms show a clear improvement in constraining the physical properties of the galaxies with Herschel, in particular the dust luminosity, the ISM and birth cloud temperatures, the extinction and the dust mass. In the future, the Space Infrared Telescope for Cosmology and Astrophysics (SPICA), currently scheduled to be launched in 2017 and will have a cryogenically cooled 3.5m mirror, can make it possible to observe a large number of such objects.

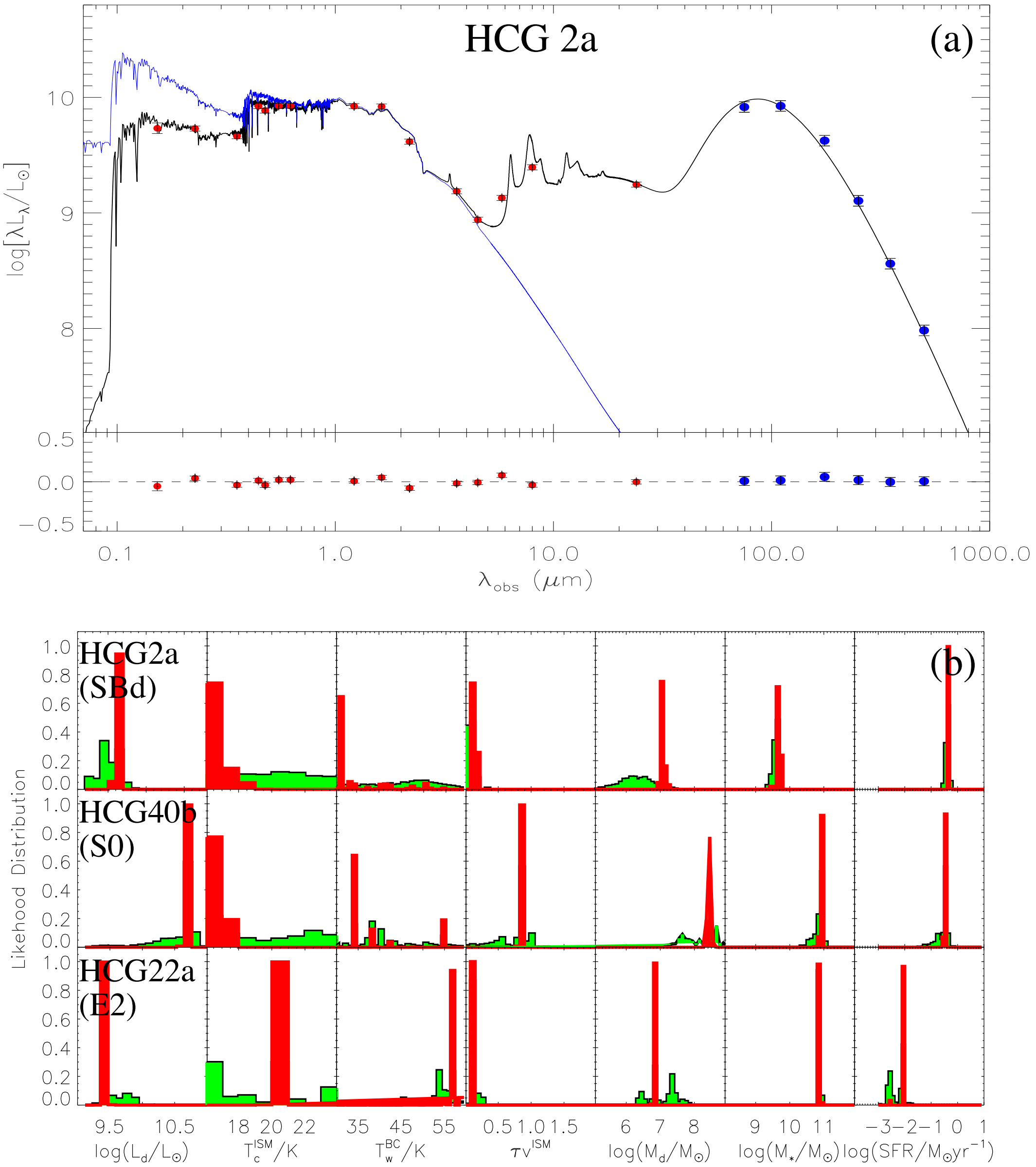

Figure 6.1: (a) In black is the best model fit of the observed SED of HCG 2c shown in red points. The blue line shows the unattenuated spectrum. The blue points are the expected Herschel PACS and SPIRE fluxes. (b) The likelihood distributions of several physical parameters derived from the fits to the observed UV to far-IR SEDs of HCG 2c (and SBc galaxy), HCG 40b (a S0), and HCG 22a (an E2). The light green histograms correspond to the observational constraints using data from UV to 24μm, and the dark red is what we obtain adding the synthetic Herschel fluxes to the fit.

6.3.3 Evolution of metallicity in the SDSS CG sample

One issue we did not explored in this work is the evolution of metallicity in the SDSS compact group galaxies. Galactic chemical evolution is crucial to derive the star formation histories (SFHs), based on the ages of the stellar populations, and can be used to constrain the gas accretion and outflow histories of galaxies. Galaxies in compact groups experience multiple tidal interactions and merging, which should differentiate their SFHs. Mendes de Oliveira *et al.* (2005) examined a sample of 16 compact group elliptical galaxies, and they suggested that according to numerical simulations (i.e. Athanassoula *et al.*, 1997), HCGs are old systems which avoided merging due to the fact that their galaxies are embedded under a common dark matter halo. In addition Proctor *et al.* (2004) found that the ages of the HCGs are closer to those of clusters than field galaxies, and there are indications of a correlation between the velocity dispersions of the compact groups and their ages. More recently, Plauchu-Frayn *et al.* (2012) examined the metallicities of a sample of 210 HCG galaxies. They found that the late-type galaxies can be split into two subclasses, "young" and "old", with the second having mostly intermediate and old stellar populations. Interestingly, the "young" late-type galaxies are preferentially found in late-type dominated compact groups – similar to our dynamically "young" groups– and, conversely, the "old" are found in early-type dominated groups –similar to our dynamically "old" groups. Using the published metallicities of the 3374 galaxies in our SDSS CG sample (Tremonti *et al.*, 2004), as well as the ones we will derive from the requested spectra (see Sect. 6.3.1), we will be able to systematically study the star formation histories of those galaxies, as well as the integrated metallicities for some of these groups.

Appendix A

Publications

.

A&A 517, A75 (2010)
DOI: 10.1051/0004-6361/201014102

Astronomy
&
Astrophysics

A mid-IR study of Hickson compact groups

I. Probing the effects of environment in galaxy interactions*

T. Bitsakis[1], V. Charmandaris[1,2,3], E. Le Floc'h[4], T. Díaz-Santos[1,2], S. K. Slater[5], E. Xilouris[6], and M. P. Haynes[7]

[1] Department of Physics, University of Crete, 71003 Heraklion, Greece
e-mail: `bitsakis@physics.uoc.gr`
[2] IESL/Foundation for Research and Technology-Hellas, 71110 Heraklion, Greece
[3] Chercheur Associé, Observatoire de Paris, 75014 Paris, France
[4] Laboratoire AIM, CEA/DSM – CNRS – Université Paris Diderot, DAPNIA/Service d'Astrophysique, 91191 Gif-sur-Yvette Cedex, France
[5] Department of Physics, Harvard-Smithsonian Center for Astrophysics, Harvard University, Cambridge, MA 02138, USA
[6] Institute of Astronomy & Astrophysics, National Observatory of Athens, 15236 Athens, Greece
[7] Astronomy Department, Cornell University, Ithaca, NY 14853, USA

Received 19 January 2010 / Accepted 12 April 2010

ABSTRACT

Hickson compact groups (HCGs) are among the densest galaxy environments of the local universe. To examine the effects of the environment on the infrared properties of these systems, we present an analysis of *Spitzer* and *ISO* mid-infrared imaging, as well as of deep ground-based near-infrared imaging of 14 HCGs containing a total of 69 galaxies. Based on mid-infrared color diagnostics we identify the galaxies that appear to host an active nucleus, while using a suite of templates, and fit the complete infrared spectral energy distribution for each group member. We compare our estimates of galaxy mass, star formation rate, total infrared luminosities, and specific star formation rates (sSFR) for our HCG sample to samples of isolated galaxies and interacting pairs and find that overall there is no discernible difference among them. However, HCGs that can be considered as dynamically "old" host late-type galaxies with a slightly lower sSFR than the one found in dynamically "young" groups. This could be attributed to multiple past interactions among the galaxies in old groups, that have led to the build up of their stellar mass. It is also consistent with our prediction of the presence of diffuse cold dust in the intergalactic medium of 9 of the dynamically "old" groups.

Key words. infrared: galaxies – galaxies: evolution – galaxies: interactions – galaxies: peculiar

1. Introduction

Compact groups of galaxies were identified as systems of several galaxies that, owing to their small projected separations and signs of tidal distortion, appear to be real physical entities of gravitationally interacting systems (Hickson 1997). Since the discovery in 1877 of Stephan's Quintet, the prototypical group, many others have been found by both visual and automated searches of the Palomar Observatory Sky Survey plates. Although the criteria for assigning group membership based only on imaging data have often been debated, it is now generally accepted that the most complete and better studied of these samples is the one compiled by Hickson (1982). His catalog of the so-called Hickson compact groups (hereafter HCGs) consists of 451 galaxies contained in 100 groups of four or more galaxies, that occupy compact configurations within relatively isolated regions where no excess of other surrounding galaxies can be seen (see Hickson 1982, for details on the criteria used). More recently, it has been revealed that the HCG catalog is incomplete because several compact groups are apparent associations of galaxies along the line of sight. However, compact group catalogs, produced with redshift information, to select galaxies that are physically close, are dense (Mamon & Diaz-Gimenez 2009).

Over the past 20 years, various detailed analyses of HCGs have been performed using multi-wavelength imaging and spectroscopy. Based on optical morphology alone, it is obvious that the overwhelming majority of HCGs display an excess of elliptical galaxies (~31% of the total) while their spiral fraction is just 43%, nearly a factor of two less than what is observed in the field (Hickson 1982). Rubin et al. (1991) have found that two thirds of HCG spirals display peculiar rotation curves, while Zepf & Whitmore (1993) report that ellipticals in compact groups are likely to have irregular isophotes and exhibit lower internal velocity dispersions for their luminosities, so that they do not lie on the fundamental plane of isolated field ellipticals. Interestingly, the luminosity function derived for HCG members is deficient at the faint end compared to other samples. All these clues are consistent with an evolutionary pattern of tidal encounters and the accretion of small companions by the group members. Furthermore, Mendes de Oliveira & Hickson (1994) also show that 43% of all HCG galaxies display morphological features of interactions and mergers, such as bridges, tails, and other distortions.

The HCGs appear to occupy a unique position in the range of galaxy environments found in the local universe. While their density enhancements are high, close to those seen in rich clusters, the overdensities appear to be more locally contained, with a much smaller population involved in the enhancement. Furthermore, the HCG velocity dispersions

---

* Appendix is only available in electronic form at `http://www.aanda.org`

are $\sigma_V \sim 250$ km s^{-1}, lower than what is seen in rich clusters but higher than that of typical loose groups. In addition, a clear correlation exists between the group velocity dispersion and the elliptical galaxy fraction, with the highest values of σ_V to be found in the most elliptical rich groups (Hickson et al 1988).

Despite this progress, several open questions remain. Are compact groups a transient phenomenon fading out after the merging of all their galaxies into a giant field elliptical? Were they more numerous in the early universe, and can they account for all, or most, present-day giant ellipticals? Are they dynamically closed systems, or can they replenish the intergalactic medium with reprocessed material in the form of diffuse tails and tidal dwarf galaxies?

A necessary step in determining of the evolutionary state of HCGs is the complete census and analysis of the member galaxies' stellar population, gas content, and star formation properties. Even though only a few HCGs have been mapped in detail in neutral hydrogen, single-dish measurements reveal that they are generally deficient in HI with a median mass of $M_{\rm HI} \sim 2.2 \times 10^{10}\,M_\odot$, two times less than what is observed in loose groups (Williams & Rood 1987; Verdes-Montenegro et al. 2001). However, the molecular gas content of their individual galaxies, as traced by the CO emission, is similar to that of interacting pairs and starburst galaxies (Leon et al. 1998). Nearly 40% of the HCG members for which nuclear spectroscopy has been obtained display evidence of active galactic nuclei (AGN), and it has been argued that those contain copious amounts of dust (Shimada et al. 2000). Up to now, however, there is scant information on the far-IR colors and luminosities of the individual galaxies of the groups, because the available IRAS measurements have typically not resolved the groups, especially at 60 and 100 μm, providing only a single value and color for the ensemble of their galaxies. Despite this limitation, it has been shown that compact groups have warm far-IR colors, similar to those of merging gas-rich galaxies (Zepf 1993). If one recalls that HCGs are in fact deficient in spirals and that the far-IR flux of field ellipticals is typically below the IRAS detection limit, one may speculate that vigorous star formation activity may actually take place in some locations within the groups. Could this activity be in circumnuclear regions of weak, enshrouded AGN because of the dynamical torques exerted in the gas from small nuclear bars funneling it to the center (Combes 2001)? Would it be possible instead that there is star formation due to shocked compressed gas outside the main bodies of galaxies as seen in Stephan's Quintet (Xu et al 1999; Appleton et al. 2006)?

A first analysis of the mid-infared properties of 12 HCG using Spitzer imagery has been presented by Johnson et al. (2007) and Gallagher et al. (2008). These authors use near- and mid-IR color diagnostics to reveal a possible excess thermal emission due to an active nucleus (AGN). They also separate the groups into three types based on the ratio of their neutral hydrogen to dynamical mass, and find that most groups are either gas-rich or gas-poor, while very few groups are found in an intermediate state. As expected, gas-rich groups are the ones that are more actively forming stars. In addition, an absence of intermediate stage groups is apparent, which would be consistent with a rapid evolution of the group members, probably the result of dynamical interactions.

In this paper we present the first results of our detailed analysis of the deep near-IR, mid-IR, and far-IR imagery of 14 HCGs and place them in the context of similar results for samples of isolated galaxies and early-stage interacting systems. In Sect. 2, we describe our data and reduction processes, along with the control samples used. In Sect. 3, we describe how we model the infrared spectral energy distribution (SED) of all galaxies in the groups. Our results on the physical properties of each galaxy such as star formation rate (SFR), stellar mass, dust content, and specific star formation rate (sSFR) are presented in Sect. 4. We discuss the implications of these findings in Sect. 5, and present our conclusions in Sect. 6.

2. Observations and data reduction

Our sample of 14 HCGs contains 69 galaxies, 31 of which are early-type and 38 late-type galaxies. It was selected in a random fashion from the original Hickson catalog (see Table 1 of Hickson 1982) and is presented in Table 1. The only constraint applied was that the group members had to be separated enough to allow more accurate photometry, but also contained enough within $\sim 5' \times 5'$ to be efficiently imaged by the Wide-field Infrared Camera (WIRC) at the Palomar 5m telescope. This constrains our sample to nearby groups typically with 5 or 6 members. Despite the small numbers, the sample can be considered representative of Hickson's catalog having an early-type galaxy fraction of ~40% and a spiral and irregular galaxy fraction of just ~60% of the total. Furthermore, as we discuss in Sect. 4.2, Kolmogorov-Smirnov (KS) tests indicate that the mass distribution of our subsample, estimated by their $K_{\rm s}$-band luminosites, is representative of the whole HCG sample. Nine galaxies of our sample are classified as AGN based on optical spectroscopy, even though this number is probalby a lower limit given the sparse spectroscopic coverage. In Figs. 1 and 2, we show typical images of one group of our sample, HCG 57, using the J, H, $K_{\rm s}$, and *IRAC* filters.

2.1. Near-infared observations

Deep near-IR observations were obtained with the Wide Field Infrared Camera (WIRC) of the 5m Hale telescope at Palomar, during several observing runs in the 2002 and 2003 observing periods. All groups were imaged in the J, H, and $K_{\rm s}$ bands for an on-source time of 20 min per filter (Slater et al. 2004). The 20 min exposures were taken in multiple shorter segments to avoid saturation by the sky brightness. The telescope was dithered in a 3- or 5-position pattern during the exposure. Due to sizable telescope nodding as well as dithering, it was necessary to perform astrometry on each of the shorter exposure images separately. This was done with the software-package WCSTools (Mink 2004), matching foreground stars to the USNO A2.0 and 2MASS point source catalogs. Once a World Coordinate System (WCS) was established for each image, they were pixel-resampled and coadded using the Swarp package (Bertin 2008). Source extraction was performed with SExtractor (Bertin & Arnouts 1996). The flux was calibrated to a level of 0.1 mag using near-IR standards, and it was bootstrapped to 2MASS foreground stars, which were detected in both our images. Our 1σ sensitivity limit was ~21.5 mag arcsec^{-2} in J and H bands and ~20.5 mag arcsec^{-2}. A near-IR image of the group HCG 57 is presented in Fig. 1.

2.2. Mid-infrared Spitzer observations

Observations of these groups were obtained between 2008 January and 2009 March in the 3.6, 4.5, 5.8, and 8.0 μm broad-band filters of the Spitzer Infrared Array Camera (IRAC, Fazio et al. 2004) and the 24 μm band of the Multiband Imaging Photometer for Spitzer (MIPS, Rieke et al. 2004) (PID: 40459).

Table 1. Near-IR and mid-IR photometry of our Hickson compact group sample.

HCG (ID)	Type	z	J (mJy)	H (mJy)	K_s (mJy)	3.6 μm (mJy)	4.5 μm (mJy)	5.8 μm (mJy)	8.0 μm (mJy)	12.0 μm (mJy)	24.0 μm (mJy)
19a	E2	0.014	43.7	43.4	33.0	21.3	13.5	7.5	4.3	3.8	1.8
19b	Scd	0.014	10.9	11.1	8.6	5.9	4.2	8.6	20.0	11.7	24.2
19c	Sdm	0.014	4.4	4.1	2.5	3.2	1.4	2.3	5.1	...	6.7
26a	Scd	0.032	12.8	13.9	23.0	12.1	8.5	16.8	43.5	12.5	29.2
26b	E0	0.031	10.1	11.0	11.0	5.6	3.6	2.7	3.3	...	9.0
26c	S0	0.032	4.8	5.3	4.6	2.3	1.5	0.9	1.0	...	0.9
26d	cI	0.030	1.9	2.2	2.5	1.2	0.9	0.6	0.8	...	...
26e	Im	0.032	0.5	0.6	1.1	0.7	0.5	0.9	2.6	...	4.0
26f	cI	0.032	0.3	0.2	0.4	0.2	0.1	...	...	...	0.3
26g	S0	0.031	0.9	1.1	1.3	0.7	0.6	0.3	0.2	...	...
33a	E1	0.025	41.7	45.5	36.5	27.6	17.9	10.3	6.6	...	2.6
33b	E4	0.026	40.9	44.0	34.9	24.8	15.5	9.4	7.1	...	2.3
33c	Sdm	0.026	29.6	25.0	16.8	21.2	15.2	21.4	58.6	16.3	41.2
33d	E0	0.026	12.1	13.0	9.7	5.5	4.0	1.7	0.9	...	0.1
37a	E7	0.022	64.7	79.6	72.1	61.7	37.2	19.3	13.1	...	4.8
37b	Sbc	0.022	33.2	43.3	43.6	22.9	14.4	14.5	29.2	14.1	36.7
37c	S0a	0.024	11.1	11.9	10.4	3.5	2.3	1.8	2.1	...	3.5
37d	SBdm	0.020	2.7	3.5	3.2	1.8	1.1	2.0	5.2	3.3	4.9
37e	E0	0.021	4.4	5.6	5.2	2.4	1.5	1.0	1.1	..	1.8
38a	Sbc	0.029	17.1	21.5	18.1	11.1	8.0	16.4	46.9	...	44.5
38b	SBd	0.029	15.4	18.8	14.7	12.3	8.5	16.3	27.6	8.3	45.2
38c	Im	0.029	9.2	11.1	8.4	6.5	4.4	8.4	24.2	5.6	67.8
38d	SBa	0.029	6.7	7.8	6.6	3.4	2.5	1.2	1.4	...	0.4
40a	E3	0.022	79.4	78.7	74.2	45.4	28.0	20.2	15.3	...	4.0
40b	S0	0.023	35.1	33.3	31.1	18.7	12.2	8.9	8.8	...	3.0
40c	Sbc	0.021	37.3	43.1	45.7	29.4	19.7	34.7	83.5	...	73.4
40d	SBa	0.022	31.7	32.0	30.7	21.3	14.3	22.7	66.9	...	88.1
40e	Sc	0.022	8.8	8.7	8.5	6.4	4.1	4.0	5.9	...	5.6
40f	E1	0.021	5.9	4.4	3.0	1.4	1.0	0.9	0.8	...	...
47a	Sbc	0.032	26.8	35.0	28.0	20.7	13.3	20.3	52.3	22.1	87.0
47b	E3	0.032	16.0	21.4	16.9	11.8	7.2	4.1	2.4	...	0.6
47c	Sc	0.032	4.5	5.9	4.5	3.0	1.9	2.3	2.4	...	9.9
47d	Sd	0.032	5.7	7.1	5.9	3.6	2.4	2.3	6.4	...	4.5
54a	Sdm	0.005	10.2	8.6	6.0	6.7	5.3	6.8	10.3	...	4.4
54b	Im	0.005	5.6	5.6	4.4	3.7	2.9	5.5	11.1	...	22.7
54c	Im	0.005	1.3	1.1	1.4	2.3	1.5	2.1	4.1	...	2.8
54d	Im	0.006	0.5	0.7	0.6	0.5	0.4	0.3	0.7	...	0.7
55a	E0	0.054	14.4	17.2	16.6	6.5	3.9	2.7	1.2	...	0.6
55b	S0	0.052	7.3	7.4	7.3	3.4	2.2	1.3	0.7	...	0.3
55c	E3	0.052	7.7	10.8	11.6	5.5	3.8	3.9	10.9	...	7.7
55d	E2	0.054	4.3	4.9	4.8	2.1	1.4	0.9	0.7	...	0.6
55e	Sc	0.054	1.2	2.2	2.2	1.8	1.3	0.9	4.0	...	6.3
56a	Sc	0.027	15.7	25.0	13.5	6.8	4.4	6.1	13.0	3.9	13.4
56b	SB0	0.026	35.0	52.9	29.5	25.9	30.4	39.0	53.7	49.8	185
56c	S0	0.027	18.8	24.8	15.0	7.7	3.3	3.8	3.2	...	0.9
56d	S0	0.028	9.3	13.8	7.8	4.7	3.1	5.9	14.8	5.4	20.2
56e	S0	0.027	5.7	7.2	4.4	2.0	1.4	2.1	4.2	1.8	6.6
57a	Sbc	0.029	56.7	62.2	67.9	33.8	18.5	15.0	18.1	12.5	13.8
57b	SBb	0.030	26.7	26.8	27.2	14.1	8.9	6.8	10.0	...	8.1
57c	E3	0.030	22.1	23.0	23.7	12.8	8.7	4.2	2.7	1.4	0.4
57d	SBc	0.030	13.1	13.4	14.1	7.6	4.9	7.4	18.1	6.6	24.0
57e	S0a	0.030	20.1	20.8	21.4	9.5	6.1	3.8	4.1	...	2.1
57f	E4	0.031	13.7	13.6	14.3	6.7	4.3	1.5	1.0	...	0.9
57g	SB0	0.032	11.7	11.8	12.0	5.4	3.3	1.5	0.7	...	...
57h	SBb	0.031	3.8	3.9	3.9	1.8	1.2	0.8	1.9	...	2.5
71a	Sbc	0.031	29.9	36.5	22.6	17.4	11.3	16.5	32.6	24.0	29.2
71b	SB0	0.032	17.3	21.2	14.1	8.5	5.8	10.6	9.1	9.3	52.7
71c	Sbc	0.029	3.5	4.4	2.8	2.0	1.2	2.1	5.2	...	4.3
71d	SB0	0.031	6.3	7.7	5.1	3.2	2.1	1.2	1.1	...	2.5

Table 1. continued.

HCG (ID)	Type	z	J (mJy)	H (mJy)	K_s (mJy)	3.6 μm (mJy)	4.5 μm (mJy)	5.8 μm (mJy)	8.0 μm (mJy)	12.0 μm (mJy)	24.0 μm (mJy)
79a	Sa	0.015	33.5	36.0	27.4	23.7	15.2	18.8	30.9	11.9	23.3
79b	S0	0.015	37.3	40.3	30.9	17.6	14.6	15.8	12.2	6.6	33.7
79c	S0	0.014	12.6	12.7	9.1	10.2	5.7	4.0	2.0	...	1.2
79d	Sdm	0.015	4.3	3.2	3.2	2.2	1.2	1.5	3.5	...	5.2
79e	Scd	0.015	5.7	6.1	5.3	4.3	3.3	4.0	17.5	5.8	0.5
95a	Sbc	0.040	30.5	33.5	28.6	18.0	11.0	6.7	7.8	...	1.3
95b	SB0	0.039	11.9	13.0	13.3	9.2	6.4	14.1	30.4	23.1	41.2
95c	Sbc	0.039	10.4	11.1	9.7	7.1	4.3	4.9	10.6	13.6	19.8
95d	SB0	0.041	7.7	8.5	9.4	4.8	3.1	2.6	6.7	4.7	5.6

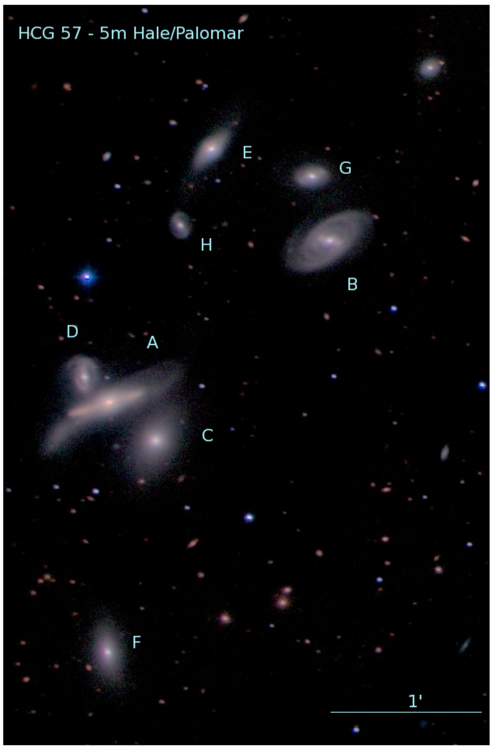

Fig. 1. A "true color" image of HCG57 based on the Palomar J, H, and K_s data (Slater et al. 2004). This is the largest group of our sample containing 4 early and 4 late-type galaxies. The galaxy triplet consisting of members A, C and D is also known as Arp 320. Galaxy A is classified as an AGN.

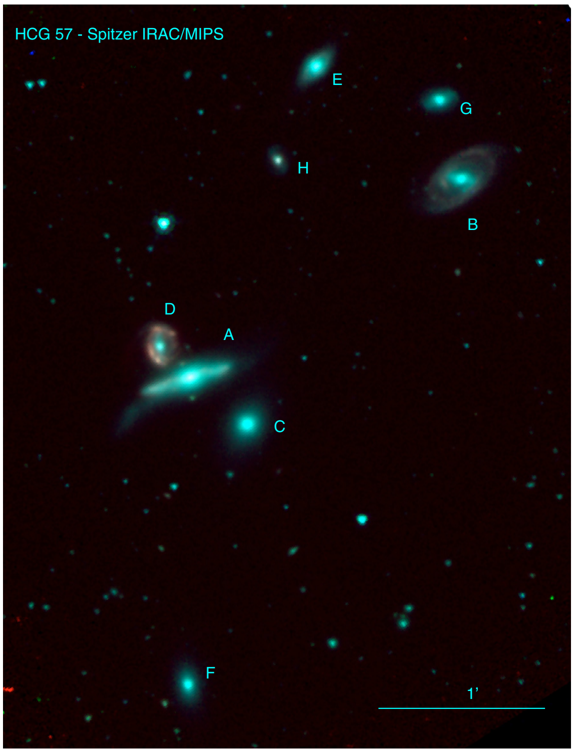

Fig. 2. A Spitzer/IRAC "true color" image of the same group. The blue channel traces the 3.6 μm emission, the green the 4.5 μm, and red the 8.0 μm. Galaxies A, B, and D have very luminous spiral arms, and when examined more closely, they appear to contain some bright mid-IR spots.

The IRAC observations were obtained with a 270 s exposure per filter for each set of cameras (see Fig. 2). All groups had an angular size small enough to fit within the 5′ × 5′ field of view of IRAC. The on-source time for the 24 μm MIPS observations was 375.4 s.

The IRAC postpipeline Basic Calibrated Data were downloaded and mosaicked onto the same grid with a pixel scale of 1.2″ × 1.2″. The 1σ sensitivity limits varyied slightly for each group owing to changes in the background. Typical 3σ limits were measured to be ~0.04 MJy sr^{-1}, ~0.05 MJy sr^{-1}, ~0.2 MJy sr^{-1}, and ~0.2 MJy sr^{-1}, for the 3.6, 4.5, 5.8, and 8.0 μm filters, respectively. Since most of the galaxies have disturbed morphologies, simple fixed aperture photometry was often not the most appropriate method of measuring the object flux. Thus, we carefully calculated the isophotal contours around each source to properly account for variations in the shape of the emitting region. Examining the local background for each galaxy we defined a limiting isophote 3σ above the overall background and measured the flux within this region, after subtracting the corresponding sky. Even this method was challenging in some cases, so we defined the physical extent of each galaxy by hand using a polygon, and performed the photometry accordingly. The fluxes we report are for the same regions for all IRAC, and MIPS, images. Finally, we applied an extended source correction to our photometry by multiplying our measured fluxes with a correction factor of 0.91, 0.94, 0.71, and 0.74 for the corresponding 1 to 4 IRAC bands as indicated in the IRAC data handbook.

The MIPS postpipeline images have a pixel scale of 2.45″ × 2.45″, and their depth was measured as ~0.3 MJy sr^{-1} or ~250 μJy for a point source. In several cases the nuclei of galaxies were saturated and the frames were corrected using the IDP3 of IDL[1]. We estimate that our final uncertainties in the IRAC and MIPS photometry are ~5%.

To ascertain variations between the nuclear and total mid-IR SED of each galaxy, we also performed nuclear photometry for our sources using the smallest aperture possible. The motivation behind this work was to examine whether the observed SEDs of some sources are dominated by the contribution of a strong nuclear emission, possibly due to the presence of an AGN. The apertures used were 3 pixels (3.6″) in diameter for the IRAC images and 5 pixels (12.2″) for the MIPS, based on the size of the corresponding point spread function (PSF).

2.3. Mid-infrared 12 μm ISO/CAM data

Archival observations for a fraction of the galaxies were retrieved from the Infrared Space Observatory (ISO) data archive. The observations were performed with the ISO/CAM instrument (Cesarsky et al. 1996), using the *LW10* filter (Program HCGROU-A). The *LW10* filter is centered on λ = 11.7 μm, and covers the 8.5–15.5 μm range so that it matches the IRAS 12 μm bandpass. The pixel size was 6″×6″, and it is larger than the PSF of the telescope at this wavelength. The total on-source exposure time for the galaxies varied between 200 and 300 s.

The ISO/CAM data were analyzed with the CIR data processing software, an implementation of the algorithms of Starck (1999) developed by P. Chanial. The standard ISO/CAM data reduction procedure was followed. First the data, were read into the CIR environment. Then the "correct-dark-vilspa" routine was applied to correct for the dark current. This was followed by applying the multiresolution algorithm "correct-glitch-mr". Next, the "correct-transient-fs" routine, based on the Fouks-Schubert transient correction method (Coulais & Abergel 2000), was applied to the data to remove transient effects. The frames were flat-fielded using the CIR's library flat field, and subsequently combined to produce a final image. Some masking on the edges of the images was performed to correct for bad pixels. Photometry was performed by selecting the regions of galaxies with emission greater than 3σ above the sky background noise. We estimate that the absolute uncertainty of our photometric measurements is ~10%, mainly owing to errors in the correction of the detector transient effect.

2.4. Comparison samples

We compare our findings to the published mid-IR data on the HCG of the Johnson et al. (2007) sample, as well as on two "control" samples, for which a similar type of data exist. One is the nearby "normal" sample of 75 field galaxies from the Spitzer Infrared Nearby Galaxies Survey (SINGS; Kennicutt et al. 2003; Dale et al. 2005). The SINGS sample was selected to cover a wide range in Hubble type and luminosity. Most objects are late-type systems that have angular sizes between 5′ and 15′. It also contains four early-type galaxies (NGC 855, 1377, 3773, and 4125) with the last one being a LINER. The second comparison sample contains the 36 nearby (v < 11 000 km s^{-1}) early stage interacting galaxy pairs of Smith et al. (2007a). The galaxies in the Smith sample are tidally disturbed and fairly extended, with linear sizes >3′. We note that 13 galaxies of this sample are classified as LINERs and 3 as Seyferts. The motivation behind the comparison of our HCG sample to these samples was to investigate how the group environment affects the infrared properties of galaxies, in contrast to isolated systems, because of a single companion galaxy. The basic properties of the three samples are presented in Fig. 3. The mid-IR activity in groups, as traced by the 24 μm and 8 μm luminosity, is similar in all three samples, suggestive that as samples there is no substantial difference in their SFR. This has already been pointed out by Smith et al. (2007a), who find that there was no more than a factor of two difference between the SFR in isolated (SINGS) galaxies and early stage interacting pairs. The K-band luminosities, hence the stellar mass distributions, are also similar with the exception of the interacting pairs, who do not extend to masses below ~10^8 $M_\odot$.

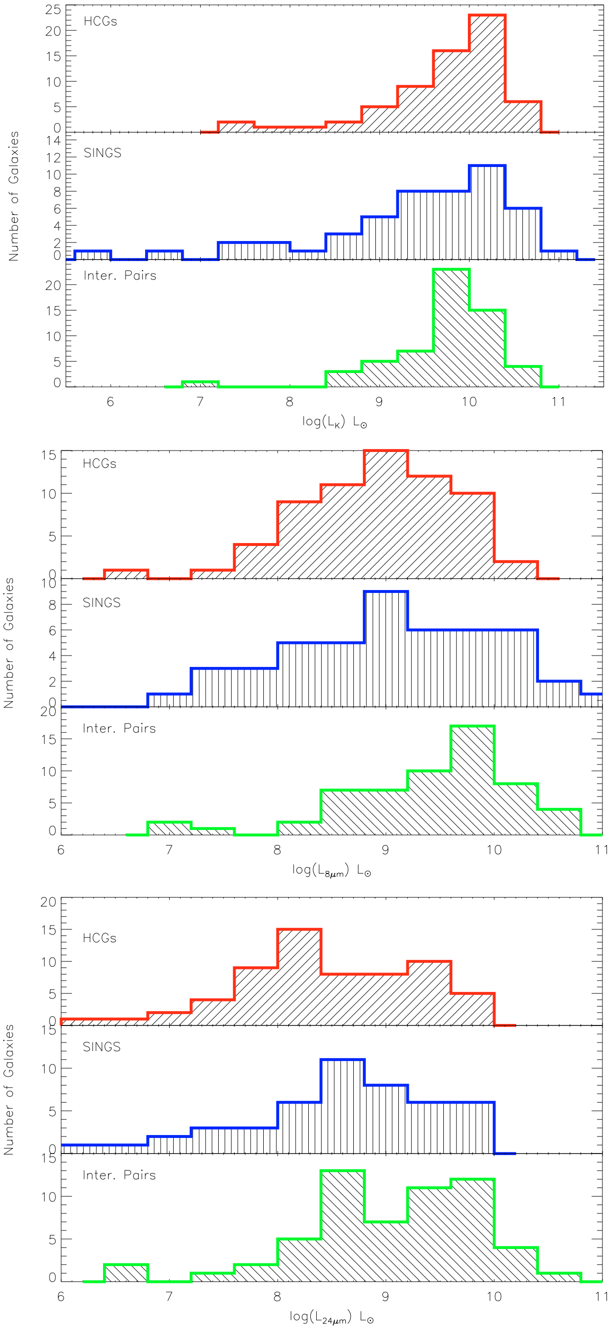

Fig. 3. Comparison of the K-band, 8 μm, and 24 μm luminosities of our samples: HCGs (*top panels*), field galaxies (*middle panels*), and interacting pair galaxies (*lower panels*).

---

[1] IDP3 is the Image Display Paradigm 3 package available for the Interactive Data Language (IDL).

3. Spectral energy distribution fitting

To estimate the physical properties of the galaxies in our sample in a systematic way, we first fit the observed SED of each galaxy with a set of theoretical and empirical SED models from *Le Phare*[2] (see Arnouts et al. 2007; Ilbert et al. 2009). We compared the observed near-IR J, H, and $K_{\rm s}$ fluxes, as well as the mid-IR fluxes from Spitzer and ISO to the ones predicted using the *Le Phare* template SEDs.

Using multi-wavelength template libraries, *Le Phare* is able to perform a two-component galaxy SED modeling by decomposing the fit of each source into the contribution of its stellar populations and the contribution from thermal dust emission. The near-IR observations is strongly dominated by stellar blackbody emission, with a possibly small contribution from very hot dust in the case of an active nucleus (AGN). In late-type, star-forming galaxies, two of the IRAC bands, centered on 5.8 and 8 μm, may contain the contribution of polycyclic aromatic hydrocarbons (PAHs), and finally the 24 μm luminosity traces thermal emission from dust mostly heated in embedded star-forming regions. Consequently the templates used to fit the data should be compatible with those characteristics. A first fit of the near-IR J, H, and $K_{\rm s}$ photometry was obtained using pure stellar templates taken from the library of SEDs used by Ilbert et al. (2009) to derive galaxy photometric redshifts. The goal of this initial step was to estimate the contribution of the underlying stellar component to the emission observed in the Spitzer bands at longer wavelengths. This contribution was subsequently subtracted from the IRAC and MIPS fluxes assuming an extrapolation of a typical stellar blackbody emission, and the resulting fluxes were fitted between 5 and 24 μm using a separate library of IR SEDs. For the IR SEDs, we used a modified version of the IR template library of Chary & Elbaz (2001), which includes 105 star-forming galaxy IR SEDs over a broad range of total IR luminosities. These templates cover the optical to radio wavelength range, so their stellar component was systematically removed prior to the fitting with *Le Phare* to reproduce only the thermal dust component of our sources. For each galaxy of our sample, the best total fit was then obtained by co-adding the fit derived for the stellar component and the one obtained in the mid-IR. Galaxies with very low 24 μm emission, mostly early-type systems, were only fitted with a single stellar component, since subtracting it from the 24 μm flux would introduce a large uncertainty to the final estimate of the thermal dust emission.

In Fig. A.1 of the appendix we present the infrared SEDs of each galaxy along with the best-fit model from *Le Phare*. Each panel corresponds to one group; groups with more than six members are plotted in two figures. The galaxies are labeled with their HCG number, type, and spectral classification, if known. The vertical error bars indicate the uncertainty of each measurement, while horizontal bars show the bandwidth of the corresponding filter.

Most SED fits are fairly good as is evident from the plots and the corresponding reduced χ^2 values, which vary between 1 and 11 and are marked in each plot. A number of galaxies display mid-IR fluxes consistent with strong PAH emission and often warm dust, a sign of enhanced star formation activity. There are, though, some galaxies (such as HCG26a, 26e, or 57a) that are not fitted as well by the templates. These galaxies display an excess emission in the $K_{\rm s}$-band and/or mid-IR, which is suggestive of some type of nuclear activity, possibly from an AGN. Even if star formation and thus PAH emission were present in these systems, the nuclear thermal dust emission would dominate the emitted flux, resulting in rather flat or rising mid-IR spectrum.

We also compared our galaxy classification based on the templates of the SED fit to existing optical morphology classification. Our data, as do the SED fits, indicate that some of the galaxies, classified as early-type based on the optical images, do have excess dust emission. These are HCG26b, 37c, 37e, 55a, 55b, 55d, 56b, 56d, 56e, 71b, 79b, 95b, and 95d. This implies that either embedded star formation or accretion of gas-rich dwarf galaxies have fueled these systems with enough dust and gas to emit strongly in the mid-IR. All of them seem to have late-type galaxy SEDs in the infrared. Three (HCG37c, 56b, and 56d) are spectroscopically classified as AGN in the optical, while others exhibit a mid-IR SED that is suggestive of emission from an AGN. Interestingly, there are also galaxies that have IR SEDs consistent with that of an early-type galaxy. These include HCG38d and HCG95b, which are nonetheless classified as late-type in the optical. This could be due to the loss of a large fraction of their gas and dust, probably because of interactions, which would be the result of the absence of far-infrared emission. One of the galaxies in our sample, HCG 40f, which did not have a classification in the literature, has been fitted with an E1 galaxy template, consistent with its morphological appearance in the optical and infrared images.

It is known that the $K_{\rm s}$ band luminosity is a good tracer of the stellar mass because light in this band is dominated by the emission of low-mass stars, which are responsible for the bulk of stellar mass in galaxies. Similarly, the 24 μm emission is a good tracer of star formation because it originates in regions of dust mainly heated by young stars. We used the observed $K_{\rm s}$-band and 24 μm luminosities (L_K and $L_{24\,\mu{\rm m}}$) to estimate the corresponding stellar mass and SFR for each galaxy. To obtain the galaxy mass, we used the Bell et al. (2003) relation where the mass, in $M_\odot$, is $(0.95 \pm 0.03) \times L_K(L_\odot)$, with systematic errors of ~30%, owing to uncertainties in the star formation history and dust. The SFR was estimated from the 24 μm by the calibration developed by Calzetti et al. (2007) for the SINGS sample:

$$SFR(M_\odot\,{\rm yr}^{-1}) = 1.27 \times 10^{-38} \left(L_{24\,\mu{\rm m}}({\rm erg\,s}^{-1})^{0.885}\right).$$

Our mass and SFR estimates are reported in Table 2 along with a measure of the sSFR of our sources defined as the ratio of SFR over the galaxy stellar mass.

4. Results

4.1. IRAC colors and AGN diagnostics

AGN are often deeply enshrouded in dust that may heavily absorb the emitted radiation, in particular in the UV, optical, and even in the X-rays in some extreme cases. The energy is then re-emitted isotropically at longer wavelengths in the mid- and far-IR (see Charmandaris 2008; Elitzur 2008, and references therein). As a result, active galaxies often display an excess of continuum emission at wavelengths 2 μm < λ < 15 μm, compared to normal or starbursting galaxies. In addition, there is a weak PAH emission in their mid-IR spectrum, which is attributed to the destruction of their carriers by the strong radiation field surrounding the AGN (i.e. see Weedman et al. 2005; Brandl et al. 2006; Smith et al. 2007b). We can use our Spitzer infrared photometric measurements to probe for an AGN among the galaxies in our sample. Lacy et al. (2004) have defined a locus in the IRAC [8.0–4.5] vs. [5.8–3.6] color–color plot populated by

---

[2] For more information on *Le Phare* visit the web page of the package at `http://www.cfht.hawaii.edu/~arnouts/LEPHARE/cfht_lephare/lephare.html`

Table 2. Stellar mass, IR luminosity, SFRs, and sSFRs for the sample.

HCG (ID)	log(M) $M_\odot$	log($L_{\rm IR}$) $L_\odot$	SFR $M_\odot$ yr^{-1}	sSFR 10^{-11} yr^{-1}
19a	10.57	...	...	...
19b	9.99	9.38	0.24	2.54
19c	9.46	8.84	0.08	2.75
26a	10.91	10.34	1.28	0.92
26b	10.81	9.65	0.44	0.68
26c	10.45	...	...	...
26d	10.12	8.73	0.08	0.40
26e	9.83	9.46	0.23	3.34
26f	9.12	8.49	0.02	0.85
26g	9.87	...	...	...
33a	11.13	...	...	...
33b	11.15	...	...	...
33c	10.93	10.18	1.21	1.79
33d	10.59	...	...	...
37a	11.32	...	...	...
37b	11.10	9.91	0.81	0.65
37c	10.55	9.23	0.12	0.33
37d	9.88	9.09	0.12	1.52
37e	10.13	8.60	0.05	0.38
38a	10.96	10.42	1.55	1.73
38b	10.87	10.21	1.57	2.17
38c	10.63	10.37	2.25	5.40
38d	10.55	...	...	...
40a	11.33	...	...	...
40b	10.99	...	...	...
40c	11.08	10.34	1.35	1.15
40d	10.95	10.41	1.78	2.00
40e	10.39	9.25	0.16	0.63
40f	9.89	...	...	...
47a	11.21	10.59	3.19	2.00
47b	11.02	...	...	...
47c	10.45	9.72	0.51	1.81
47d	10.57	9.49	0.26	0.68
54a	9.09	7.97	0.01	1.02
54b	8.79	8.46	0.04	5.99
54c	8.33	7.81	0.01	3.49
54d	8.09	7.37	0.002	1.91
55a	11.37	8.92	0.12	0.04
55b	11.10	8.59	0.06	0.04
55c	11.30	10.18	1.05	0.50
55d	10.95	8.99	0.12	0.12
55e	10.64	10.02	0.91	2.18
56a	10.77	9.68	0.48	0.82
56b	11.08	10.71	4.44	3.85
56c	10.82	...	...	...
56d	10.56	9.86	0.73	2.02
56e	10.28	9.18	0.26	1.35
57a	11.54	9.99	0.58	0.16
57b	11.14	9.69	0.39	0.26
57c	11.11	...	...	...
57d	10.88	9.96	0.97	1.28
57e	11.07	9.17	0.11	0.10
57f	10.92	...	...	...
57g	10.87	...	...	...
57h	10.36	9.22	0.15	0.62
71a	11.11	10.10	1.25	0.94
71b	10.93	10.34	2.11	2.53
71c	10.16	9.39	0.21	1.42
71d	10.49	...	...	...
79a	10.56	9.44	0.27	0.75
79b	10.61	9.36	0.38	0.93
79c	10.07	...	...	...
79d	9.62	8.79	0.07	1.71
79e	9.87	9.37	0.21	2.65
95a	11.44	...	...	...
95b	11.09	10.49	2.60	2.06
95c	10.95	10.12	1.32	1.48
95d	10.99	9.70	0.48	0.05

Table 2. continued.

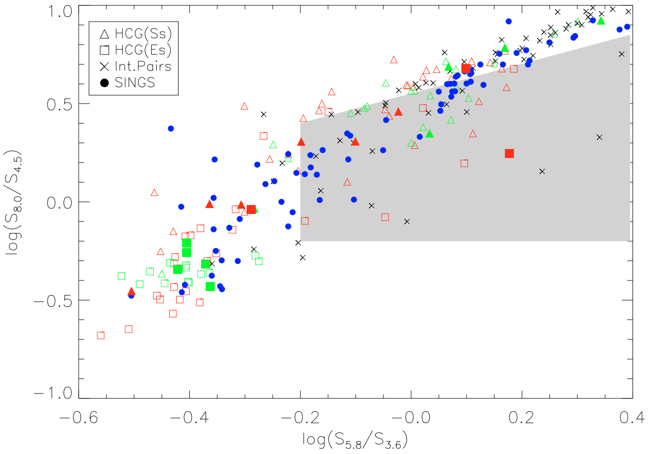

Fig. 4. The Lacy et al. (2004) IRAC color diagnostic. Red symbols indicate the galaxies of our HCG sample, green those of the Johnson et al. (2007) sample, black crosses the interacting pairs of the Smith et al. (2007a), and blue filled circles the SINGS galaxies. Late-type galaxies (spirals) are marked with triangles, while squares denote early-type galaxies (ellipticals). Filled squares and filled triangles denote that the corresponding galaxy is classified as an AGN based on optical spectroscopy. According to the mid-IR colors, the AGN candidates are those found in the gray shaded area. The gap in the distribution of the galaxies between those on the lower left side of the plot and those on the upper right side, mentioned by Johnson et al. (2007), may also be present in data, but it is not as clear.

AGN which are dominant in the infrared. Similarly, Stern et al. (2005) propose using of the IRAC [3.6–4.5] vs. [5.8–8.0] colors to identify their AGN candidates. Among our galaxies optical spectra were available for 24 Shimada et al. (2000), with 15 classified as H II galaxies and 9 as AGNs, (3 as Sy2 and 3 as LINERs).

In Fig. 4, we present the IRAC colors for our sample following the Lacy et al. (2004) criteria. We separate our sample in early and late-type galaxies, and identify the galaxies that we already know from optical spectroscopic observations host an active nucleus. We also include in Fig. 4 the galaxies from the Johnson et al. (2007) HCG sample, as well as the SINGS and interacting galaxy samples. By construction, the galaxies located in the lower left of the color−color plot are those dominated by the stellar photospheric emission. As a result, they are expected to have very weak dust or PAH emission, if any. Most of our early-type galaxies lie in this region. On the other hand, galaxies found in the upper right quadrant of the figure should have strong PAH features, as well as some hot dust contribution, because of intense star formation, and/or AGN activity. Furthermore, as we discuss in Sect. 4.4, most of the galaxies in this quadrant are spirals found in spiral-rich groups. According to Lacy et al. (2004), galaxies located within the shaded area are AGN candidates. A total of 16 galaxies in our sample (~23%) are AGN candidates based on this criterion, almost half of which are found in previous optical spectroscopy studies (Shimada et al. 2000; Coziol et al. 2000). These are 11 late-type systems (HCG 37b, 38b, 38c, 47c, 54abcd, 57d, 71a, 79a) and 5 early-type systems (HCG 40f, 56b, 56e, 71b, and 95b). Of those galaxies, four are spectroscopically classified as AGN, while eight are classified as H II galaxies. In addition, as we can see from their mid-IR SEDs in Fig. A.1, several of them do show signs of active nuclei, such as a flat rising continuum. It is possible, though, that either because of obscuration or because some may harbor low-luminosity AGNs (LLAGNs), the colors of the AGN are diluted when we perform the photometry over the whole galaxy. To better probe the properties of the nuclear emission, we can examine the nuclear SEDs of our sample, which was obtained using circular apertures with a diameter of 3.6″ in the IRAC images and 12.2″ in the MIPS 24 μm band. Among the AGN candidates based on the Lacy plot, the ratio of the nuclear to their total flux is not constant in all mid-IR bands, in five galaxies, HCG 37b, 47c, 56b, 71a, and 79a, but it peaks at 4.5 μm. This suggests that the nuclear contribution which possibly caused by hot dust heated in near sublimation temperatures by an AGN, contributes substantially in this band. On the other hand, nine galaxies, HCG 38b, 38c, 54abcd, 56e, 71b, and 95b, have a rising nuclear SED and a constant ratio of nuclear to total flux in all IRAC bands. This would be consistent with their being star-forming H II galaxies.

Contrary to SINGS galaxies, which are distributed fairly uniformly along the diagonal of the color-color plot in Fig. 4 and the interacting galaxy pairs which are located in the upper right quadrant due to the fact that they contain only late-type galaxies, there might be a small gap in the distribution of the HCG galaxies at the position log($S_{5.8}/S_{3.6}$) ≃ −0.2 and log($S_{8.0}/S_{4.5}$) ≃ 0. This gap is identified in Fig. 11 of Johnson et al. (2007), even though it is more obvious there. These authors combine the mid-IR colors with estimates of the neutral hydrogen mass and dynamical mass of the their HCG sample and suggest that this small gap separates the gas-rich and gas-poor groups. The explanation is consistent with the notion that gas-poor groups will mostly contain early-type galaxies where PAH emission will be suppressed by low star formation activity; and they will populate the lower left part of the plot, while late-type gas-rich galaxies will be found on the upper right. The absence of HCG galaxies with intermediate mid-IR colors would imply that their evolution from the gas-rich to the gas-poor state is more rapid than what is observed in field galaxies, and it could be understood as the result of more frequent dynamical interactions between galaxies in groups. As a result of the interactions, tidal forces drive the gas in their nuclei and create instabilities in their disk, forcing them to use their gas in a more accelerated fashion.

In Fig. 5, we also examine how the Stern et al. (2005) color−color diagnostic is applied in our data. As was the case in Fig. 4, galaxies located in the lower left region of the plot have SEDs dominated by the stellar photospheric emission, while the galaxies found on the right should display strong PAH and hot dust emission. The shaded area denotes the colors of potential AGN candidates. When we compare this to Fig. 4, we notice that only one galaxy, HCG56b, is identified as an AGN candidate. However, as discussed in the detail by Donley et al. (2008) the Stern criteria may suffer in low-z because of contamination from star-forming galaxies. Consequently, in this work we adopt the ones fulfilling the Lacy criteria as mid-IR identified AGN.

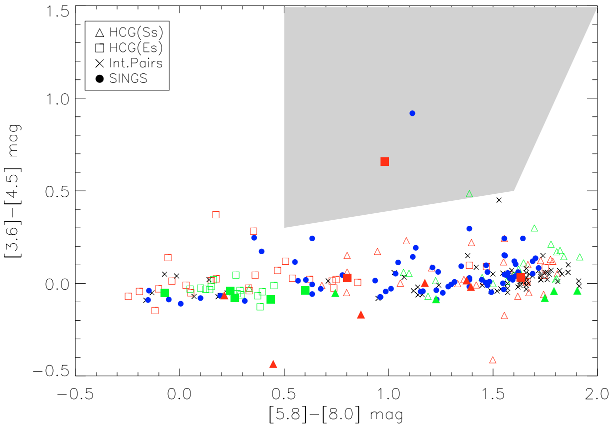

Fig. 5. The Stern et al. (2005) IRAC color diagnostic. The symbols are as in Fig. 3. The gas-poor galaxies are located in the lower left portion and the gas-rich in the lower right. Only one candidate, HCG 56b (a Seyfert 2), is found within the AGN candidate area.

4.2. Star formation activity in Hickson compact groups

As mentioned in the previous section, one would expect that galaxies in groups would have enhanced SFR, because of tidal interactions. The 24 μm emission is a good tracer of the SFR and following the approach of (Calzetti et al. 2007), we calculated the SFR for each galaxy of our groups in Sect. 3. In Fig. 6a, we plot the sSFR as a function of the mass of each galaxy, which was estimated using the observed K-band luminosity (Bell et al. 2003). We include 57 the galaxies of our sample that were detected in 24 μm. In the same figure 61 normal galaxies of the SINGS sample are presented, along with 30 of the interacting pairs of Smith et al. (2007a) for which integrated K-band 2MASS photometry was available. For the interacting pairs, the average sSFR of the two components is given. Galaxies found over the dashed line, have SFRs greater than 1 $M_{\odot}$ yr^{-1}. Galaxies in interacting pairs display a median sSFR of ~$2.96^{+2.70}_{-1.41}\times10^{-11}$ yr^{-1}. This is slightly higher than what is found in HCGs and field galaxies, which have a corresponding value of ~$1.68^{+1.41}_{-1.16}\times10^{-11}$ yr^{-1}. However, given the scatter seen in each population there is no strong statistical difference among them. As mentioned in Sect. 2.3, the interacting pair sample does not extend to the lower galaxy masses of the two other samples. However, even when we restrict the galaxy masses to a range that is identical in all three samples, an analysis using Kolmogorov-Smirnov test still indicates that there is no statistical difference between the samples. In Fig. 6b, we plot the sSFRs as a function of the total infrared luminosity ($L_{\rm IR}$). For similar infrared luminosities, HCG members seem to have sSFRs similar to field galaxies and slightly lower than interacting pairs. How is this understood given that HCGs are also interacting systems?

To better address this issue, we decided to separate the late-type galaxies of the HCGs into two categories depending on whether the group they belong to has a high or low fraction of late-type galaxies. We classify a group as "spiral-rich" if fewer than 25% of its galaxies are early-type. Conversely, a group is

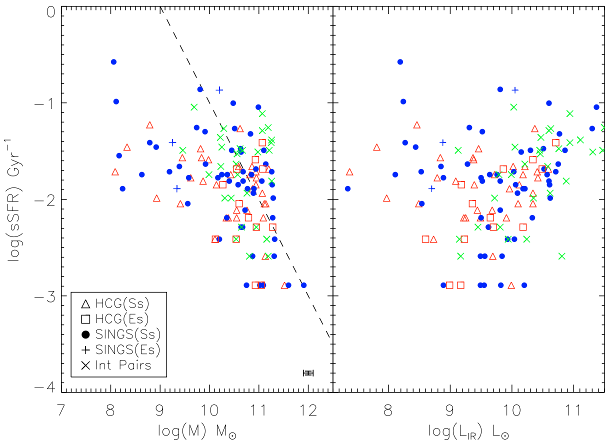

Fig. 6. a) Specific star formation rate as a function of stellar mass. The red triangles are HCG late-type galaxies and the red squares are the HCG early-type galaxies detected at 24 μm. Galaxies found in “spiral-rich” groups are marked with filled symbols. Blue filled circles and blue crosses indicate SINGS late- and early-type galaxies, respectively. The green x’s indicate the interacting galaxy pairs of Smith et al. (2007a). Galaxies to the right of the dashed line have SFR greater than 1 $M_\odot$ yr^{-1}. **b)** Specific star formation rate as a function of $L_{\rm IR}$. Symbols as before.

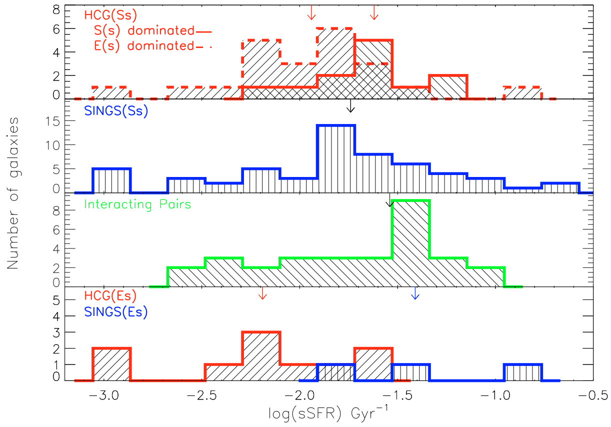

Fig. 7. Histograms of the sSFRs in the samples used. The top plot displays a histogram of the late-type galaxies found in spiral-rich groups marked with the solid line, as well as a histogram of the late-type galaxies in elliptically dominated groups marked with the dashed line. The second is a histogram of the SINGS late-type galaxies, and the third is the corresponding one for the interacting galaxy pairs. Finally, the bottom plot displays the histogram of the early-type galaxies found in HGCs (in red), as well as the SINGS early-type galaxies (in blue), which are detected at 24 μm. The arrows indicate the median sSFR value of each distribution.

“spiral-poor”, or elliptically dominated, if fewer than 75% of its galaxies are late-type. The sSFR is a tracer of the star formation history of a galaxy, and galaxies in compact groups do experience multiple encounters with the various group members. Consequently we would expect that if the group is dynamically “young” (that is, its galaxies are gravitationally interacting for the first time) it is more likely to be dominated by late-type galaxies. Furthermore, these spiral galaxies would have not built up much of their stellar mass, but would have larger amounts of gas and dust, as well as higher SFRs and sSFR. On the other hand, if the group is dominated by ellipticals, it could be dynamically “old”, since interactions and possible merging of its members over its history would have led to the formation of some of those ellipticals. As a result, the spirals in these groups could have already built some of their stars, and their sSFR would be lower.

We thus present in Fig. 7 histograms of the sSFR distribution of the samples. We notice that spirals in elliptically dominated groups have a median sSFR that is lower than in spiral-rich groups. However, when we examine their distribution in detail, we see that they have a median of $\sim 1.29^{+3.86}_{-3.47} \times 10^{-11}$ yr^{-1}, while galaxies in spiral-rich groups have a median of $\sim 2.71^{+2.45}_{-1.29} \times 10^{-11}$ yr^{-1}. As explained above, this minor difference could be attributed to the possibility that, in dynamically “old” groups, spiral galaxies have already interacted several times in the past with the other members of their groups and as a result had more time to increase their stellar mass. Also their SFR is much lower than in the past, since they have consumed most of their gas. These galaxies are located in the lower left part of Lacy’s plot.

It is interesting to note that the sSFR of spirals in spiral-rich groups is similar to the sSFR of interacting pair spirals. This appears to contrast to the fact that galaxies in compact groups do experience more interactions from their close neighbors, either major or minor mergers, than a single galaxy by its companion. A possible explanation could be that the higher velocity dispersion of compact groups (~330 km s^{-1}, Hickson et al. 1992), compared to typical values seen in near parabolic prograde encounters of galaxy pairs, reduces the gravitational impulse exerted on each galaxy. Furthermore, the complex geometry and orbits of the group members could strip some of the gas out of these galaxies rather than funnel it to the central part, thereby increasing the SFR. This is consistent with the observed morphology of the group members, since ~43% of them display features such as tidal tails, bridges, etc. (Mendes de Oliveira & Hickson 1994). Another explanation for this similarity could be that spiral-rich compact groups are simply chance alignments of interacting pairs (Mamon 2008). In this scenario, two or more interacting galaxy pairs at different redshifts have a projected separation that makes them appear as a compact group. However, this is not the case for our sample, as only real group members were considered in our analysis.

4.3. Cold dust in Hickson compact groups

For estimating the total amount of dust in a galaxy, far-IR observations are essential, since the bulk of the dust mass in galaxies is at low temperatures (<20 K). The only far-IR data available for our sample are based on IRAS (see Allam et al. 1996), since the Akari all-sky maps have not yet been released. However, the IRAS data suffer from poor spatial resolution and in nearly all cases one cannot resolve the emission of individual group members. Even though there is no high spatial-resolution, far-IR imagery for groups, one would expect that gas and dust could be stripped from the group members during their tidal interactions. This material could remain outside the areas of the galaxies and would have low temperature (see Xilouris et al. 2006). Such a case has been detected in the nearby giant elliptical galaxy Centaurus A, where ~15 K dust has been detected outside the main body of the galaxy (see Stickel et al. 2004). This was understood as a consequence of the accretion by a number of gas-rich dwarf companion galaxies that surround Centaurus A and have led to the formation of its dust lane, as well as to the filaments of atomic and molecular gas that surrounds it (see Schiminovich et al. 1994; Charmandaris et al. 2000). Based on our Spitzer data, warm dust in the intragroup environment has been seen

Table 3. Observed and predicted IRAS 60 μm and 100 μm fluxes.

HCG group	IRAS 60 μm Observed mJy	Predicted mJy	IRAS 100 μm Observed mJy	Predicted mJy
19	300	246.8	1110	673
26	540	450.6	1496	976
33	<660	339.6	<1140	752
37	~560	449.5	<2000	665
38	~1430	1439	<3160	2076
40	<1090	1478	3850	3686
47	<580	880.9	<1510	1336
54	300	278.2	710	675
55	200	139.4	1630	322
56	<690	1860	<1510	2637
57	<460	437.5	<1380	917
71	1640	736.9	<3070	1069
79	~960	584.4	<2320	1137
95	941	616.2	2390	898

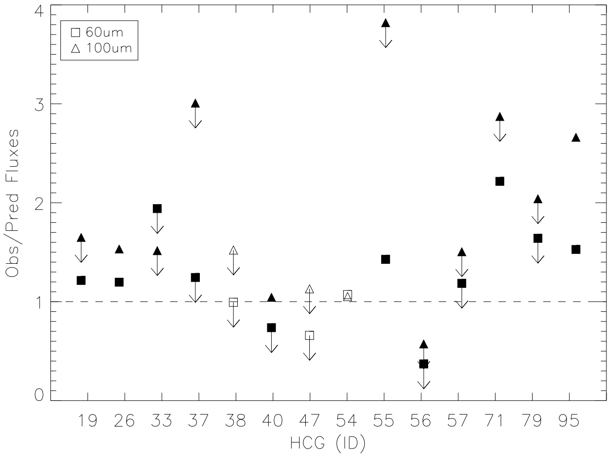

Fig. 8. Plot of the ratio of the observed IRAS 60 and 100 μm fluxes of each group divided by the corresponding flux predicted by our SED fits. Since IRAS did not resolve/detect all the members of each group, several of the ratios are indicated as upper limits. Filled symbols indicate spiral-poor groups.

in some groups (HCG40, 54, 55, and 79) in the form of diffuse mid-IR light or an extended halo around groups members.

Using the mid-IR imaging and extrapolating to the far-IR by the SED fits in this work, we can estimate the fraction of the far-infrared luminosity that is contributed by each group member to the total far-IR luminosity of the whole group. We can calculate the "synthetic" IRAS 60 μm and 100 μm flux densities of each group and compare them to the ones deduced by Allam et al. (1996). The results are presented in Table 3 and Fig. 8. In most cases, IRAS could not detect all the members of each group, so upper limits were used for then. Consequently, our total flux estimate is an upper limit. We observe that there are 9 groups, HCG19, HCG26, HCG33, HCG37, HCG55, HCG57, HCG71, HCG79, and HCG95, where the emission detected by IRAS is clearly higher than the total emission estimated using our galaxy SED fits. Most of these groups display evidence of strong tidal encounters and merging. This agrees with half or more of their members are early-type or peculiar galaxies and are classified as dynamically "old", while only one (HCG55) has the form of a compact chain. It is thus likely that these groups have diffuse cold dust in the intragroup region. Part of this excess could also be caused by the uncertainties introduced by our SED fits when we extrapolated to the 60 and 100 μm flux of the galaxies. This uncertainty is real and can be seen if we notice that, in most groups, the 100 μm flux ratio is higher than the 60 μm one, possibly because it is farther away than our last anchor point at 24 μm. A more detailed analysis of the SEDs from the UV to the mid-IR for all these groups using the models developed by da Cunha et al. (2008), along with observations with PACS and SPIRE instrument onboard the Herschel Space Telescope, will address this issue conclusively.

5. Conclusions

In this paper we have presented our first analysis of the near- and mid-infrared SED of 69 galaxies contained in 14 Hickson compact groups, and found the following:

- Nearly half of the galaxies in the groups, 14 out of the 32, which are optically classified as ellipticals, have mid-IR emission and colors consistent with those expected for late-type systems. We suggest that this stems from enhanced star formation as a result of recent gas accretion from companion galaxies in the groups.
- Based on their integrated mid-IR color, 16 galaxies (23%) are AGN candidates. Detailed nuclear photometry reveals that 6 of these have nuclear mid-IR SEDs, which are inconsistent with a mid-IR spectrum dominated by star formation.
- We find no evidence of the SFR and build up of stellar mass, which would substantially differentiate late-type galaxies in groups from galaxies in early-stage interacting pairs, or spiral galaxies in the field. This is a surprise given that the group environment has played an important role in the evolution of the galaxies, shown by the fact that most groups contain a large fraction of early-type systems. However, late-type galaxies in dynamically "old" HCGs might have a lower, though not statistically significant, sSFR than those in dynamically "young" groups, which could be attributed to multiple past interactions.
- We investigated the contribution of each galaxy to the total far-IR emission of its group, and identify 9 groups where extended cold dust emission may be present.

Acknowledgements. We would like to thank E. da Cunha, D. Elbaz and G. Magdis for useful discussions, an anonymous referee for the detailed comments that improved this paper. T.B., V.C., and T.D.S., would like to acknoledge partial support from the EU ToK grant 39965 and FP7-REGPOT 206469.

References

Allam, S., Assendorp, R., Longo, G., Braun, M., & Richter, G. 1996, A&AS, 117, 39
Appleton, P. N., Xu, K. C., Reach, W., et al. 2006, ApJ, 639, L51
Arnouts, S., Walcher, C. J., Le Fèvre, O., et al. 2007, A&A, 476, 137
Bell, E. F., McIntosh, D. H., Katz, N., Weinberg, M. D. 2003, ApJS, 149, 289
Bertin, E. 2008, SWarp, `http://astromatic.iap.fr/software/swarp`
Bertin, E., & Arnouts, S. 1996, A&AS, 117, 393
Brandl, B. R., Bernard-Salas, J., Spoon, H. W. W., et al. 2006, ApJ, 653, 1129
Calzetti, D., Armus, L., Bohlin, R. C., et al. 2000, ApJ, 533, 682
Calzetti, D., Kennicutt, R. C., Engelbracht, C. W., et al. 2007, ApJ, 666, 870
Cesarsky, C. J., Abergel, A., Agnese, P., et al. 1996, A&A, 315, L32
Charmandaris, V. 2008, Infrared Diagnostics of Galaxy Evolution, 381, 3
Charmandaris, V., Combes, F., & van der Hulst, J. M. 2000, A&A, 356, L1
Chary, R., & Elbaz, D. 2001, ApJ, 556, 562
Coziol, R., Iovino, A., & de Carvalho, R. R. 2000, AJ, 120, 47
Combes, F. 2001, Fueling the AGN. In Lectures on the Starburst-AGN Connection, NAOE, ed. D. Kunth, & I. Aretxaga `[arXiv:astro-ph/0010570]`
Coulais, A., & Abergel, A. 2000, A&AS, 141, 533
da Cunha, E., Charlot, S., Elbaz, D. 2008, MNRAS, 388, 1595
Dale, D. A., Bendo, G. J., Engelbracht, C. W., et al. 2005, ApJ, 633, 857
Donley, J. L., Rieke, G. H., Pérez-González, P. G., & Barro, G. 2008, ApJ, 687, 111

Elitzur, M. 2008, New Astron. Rev., 52, 274
Fazio, G. G., Hora, J. L., Allen, L. E., et al. 2004, ApJS, 154, 10
Gallagher, S. C., Johnson, K. E., Hornschemeier, A. E., Charlton, J. C., & Hibbard, J. E. 2008, ApJ, 673, 730
Hickson, P. 1982, ApJ, 255, 382
Hickson, P. 1997, ARA&A, 35, 357
Hickson, P., Kindl, E., & Huchra, J. P. 1988, ApJ, 329, L65
Hickson, P., Mendes de Oliveira, C., Huchra, J. P., & Palumbo, G. G. 1992, ApJ, 399, 353
Ilbert, O., Capak, P., Salvato, M., et al. 2009, ApJ, 690, 1236
Johnson, K. E., Hibbard, J. E., Gallagher, S. C., et al. 2007, AJ, 134, 1522
Kennicutt, R. C., Jr., Armus, L., Bendo, G., et al. 2003, PASP, 115, 928
Lacy, M., Storrie-Lombardi, L. J., Sajina, A., et al. 2004, ApJS, 154, 166
Leon, S., Combes, F., & Menon, T. K. 1998, A&A, 330, 37
Lupton, R., Blanton, M. R., Fekete, G., et al. 2004, PASP, 116, 816, 133
Mamon, G. A. 1986, ApJ, 307, 426
Mamon, G. A. 2008, A&A, 486, 113
Mamon, G. A., & Diaz-Gimenez, E. 2009
Mendes de Oliveira, C., & Hickson, P. 1994, ApJ, 427, 684
Mink, D. J. 2002, in Astronomical Data Analysis Software and Systems VIII, ed. D. Mehringer, R. Plante, & D. Roberts, ASP Conf. Ser., 172, 498
Polletta, M., Tajer, M., Maraschi, L., et al. 2007, ApJ, 663, 81
Rieke, G. H., Young, E. T., Engelbracht, C. W., et al. 2004, ApJS, 154, 25
Rubin, V. C., Hunter, D. A., & Ford, W. K. J. 1991, ApJS, 76, 153
Schiminovich, D., van Gorkom, J. H., van der Hulst, J. M., & Kasow, S. 1994, ApJ, 423, L101
Shimada, M., Ohyama, Y., Nishiura, S., Murayama, T., & Taniguchi, Y. 2000, AJ, 119, 2664
Slater, S. K., Charmandaris, V., & Haynes, M. P. 2004, BAAS, 36, 728
Smith, B. J., Struck, C., Hancock, M., et al. 2007a, AJ, 133, 791
Smith, J. D. T., Draine, B. T., Dale, D. A., et al. 2007b, ApJ, 656, 770
Starck, J. L., Abergel, A., Aussel, H., et al. 1999, A&AS, 134, 135
Stern, D., Eisenhardt, P., Gorjian, V., et al. 2005, ApJ, 631, 163
Stickel, M., van der Hulst, J. M., van Gorkom, J. H., Schiminovich, D., & Carilli, C. L. 2004, A&A, 415, 95
Verdes-Montenegro, L., Yun, M. S., Williams, B. A., et al. 2001, A&A, 377, 812
Weedman, D. W., Hao, L., Higdon, S. J. U., et al. 2005, ApJ, 633, 706
Williams, B. A., & Rood, H.J. 1987, ApJS, 63, 265
Xilouris, E., Alton, P., Alikakos, J., et al. 2006, ApJ, 651, L107
Xu, C., Sulentic, J. W., & Tuffs, R. 1999, ApJ, 512, 178
Zepf, S. E. 1993, ApJ, 407, 448
Zepf, S. E., & Whitmore, B. C. 1993, ApJ, 418, 72

Pages 12 to 21 are available in the electronic edition of the journal at http://www.aanda.org

Appendix A: Infrared morphology

In this section we briefly describe the overall appearance of groups in the Spitzer mid-IR images. A detailed analysis of the mid-IR and near-IR color profiles of the galaxies will be the subject of a future paper.

- HCG19: Galaxy a is faint in the mid-IR displaying only a luminous core at 8 μm. Member b is very bright in all mid-IR bands, and its spiral arms are clearly visible at 5.8, and 8 μm, likely due to associated PAH emission. Finally, galaxy c has faint extended emission in all bands.
- HCG26: This is a very dense group. Members a, b, d, and g are merging with a and e the brightest. There is also a feature similar to a tidal tail over galaxy g which is visible in the optical images but not in the mid-IR.
- HCG33: Galaxies a, b, and d are early-type and so are very faint in the mid-IR; however, galaxy c is classified as type Sdm and is very bright in all Spitzer bands.
- HCG37: Member a displays a very bright extended halo in the first IRAC band, but it is not so bright in the other bands. Member b presents strong nuclear emission at 8 and 24 μm. Member d is also bright in these wavelengths. Finally, member c has an IR-bright nucleus, and it is spectroscopically classified as a low-luminosity AGN.
- HCG38: Galaxies b and c form an interacting pair both displaying very luminous extended tails with bright spots, possibly because of giant HII regions. Galaxy a is also luminous in the mid-IR.
- HCG40: There is a 3.6 μm extended halo around the group. Galaxies c and d are very bright, especially at 24 μm. We can also clearly see the spiral arms of member e, as well as nuclear emission in a and b.
- HCG47: Galaxy a has a very bright nucleus and spiral arms while a mid-IR luminous bridge connects it to member b, which only has faint emission away from its nucleus. Galaxy c is also bright. Finally, member d is also rather faint in the mid-IR emission.
- HCG54: Member b is a very bright galaxy, in particular at 24 μm. Member a appears to have two cores. One is bright at 24 μm and the other is so the 5.6 and 8 μm bands.
- HCG55: An extended halo at 3.6 μm, is seen around the group. Galaxies c and e are most luminous especially at 24 μm.
- HCG56: Member b is the brightest galaxy of this group and one of the brightest of our sample. Galaxies a, d, and e are mid-IR luminous, while c has a bright nucleus visible only in the four IRAC bands. Finally, there is a bridge between members b and c seen only in 3.6 μm, suggesting that it contains mostly stars.
- HCG57: Galaxies a and d have very luminous spirals, also presenting some mid-IR bright spots. They also seem to have a common halo at 24 μm. Member b also has bright spiral arms with two bright spots on them seen at 24 μm. The latter coincide with the location of two identified supernovae (SN-2002AR and SN-2005BA).
- HCG71: Member a has a bright nucleus and very extended luminous spiral arms. The nucleus of galaxy b is bright, and c is also mid-IR bright.
- HCG79: There is an extended halo around the group seen in the 3.6 μm band. Galaxies a, b, d, and e are very luminous in mid-IR. There are also a tidal tail in member b and an extended feature over galaxy c. Finally, it seems that there is a bridge between a and d.
- HCG95: There is a bridge connecting galaxies a and c, observed in all wavelengths with bright spots on it. Members c and d are mid-IR bright. Galaxy a only has a luminous nucleus, while the spiral arms of galaxy d are seen in the IRAC images.

As seen from the above descriptions, the mid-IR morphology of the galaxies in the compact groups displays clear evidence of tidal interactions and shows the effects of the dynamically induced star formation activity in them.

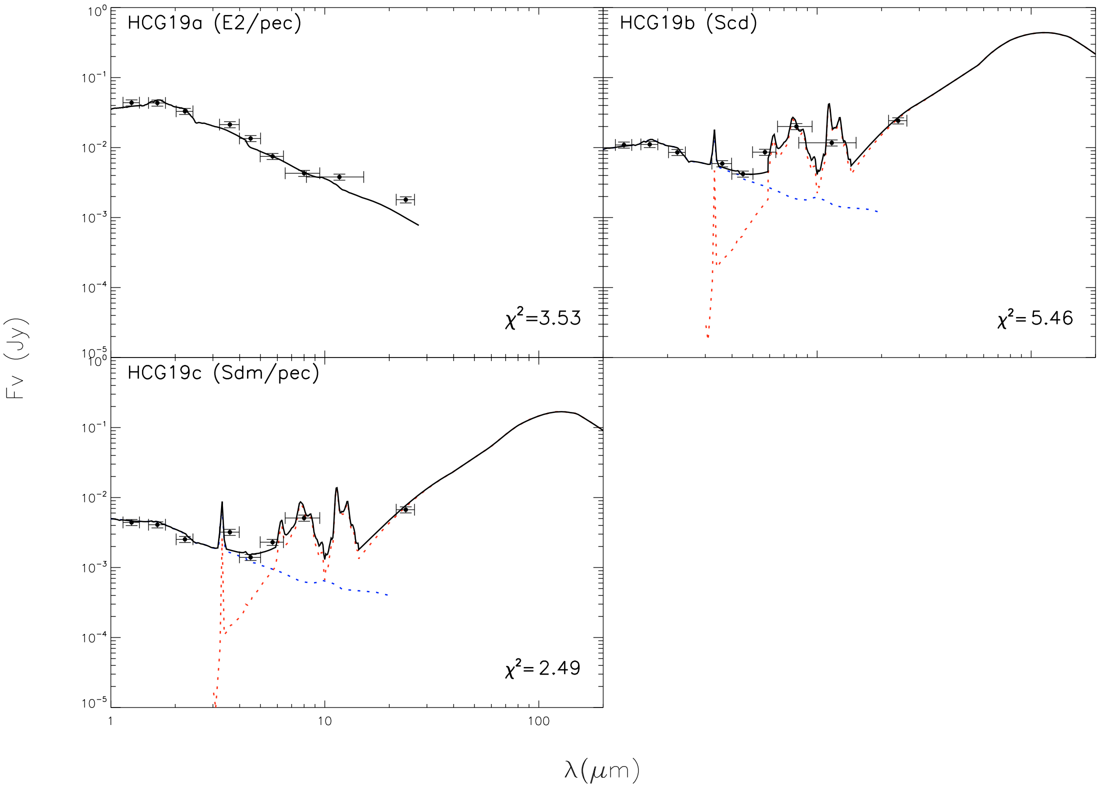

Fig. A.1. Infrared SEDs of the HCG galaxies. The name of each galaxy and its optical classification by Hickson (1982) is marked at the top left of each plot. The vertical error bars show the uncertainty of the flux, while the horizontal ones indicate the bandwidth of the corresponding filter. The reduced χ^2 value of each fit is marked in the bottom right of each plot.

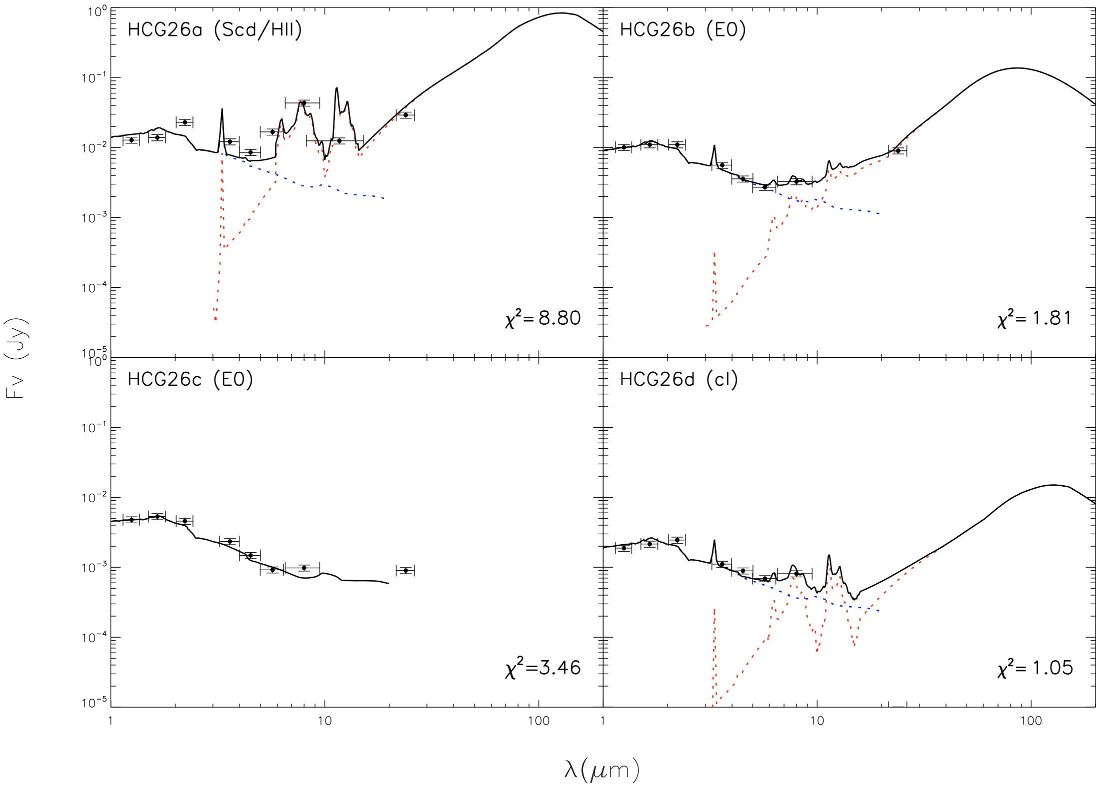

Fig. A.1. continued.

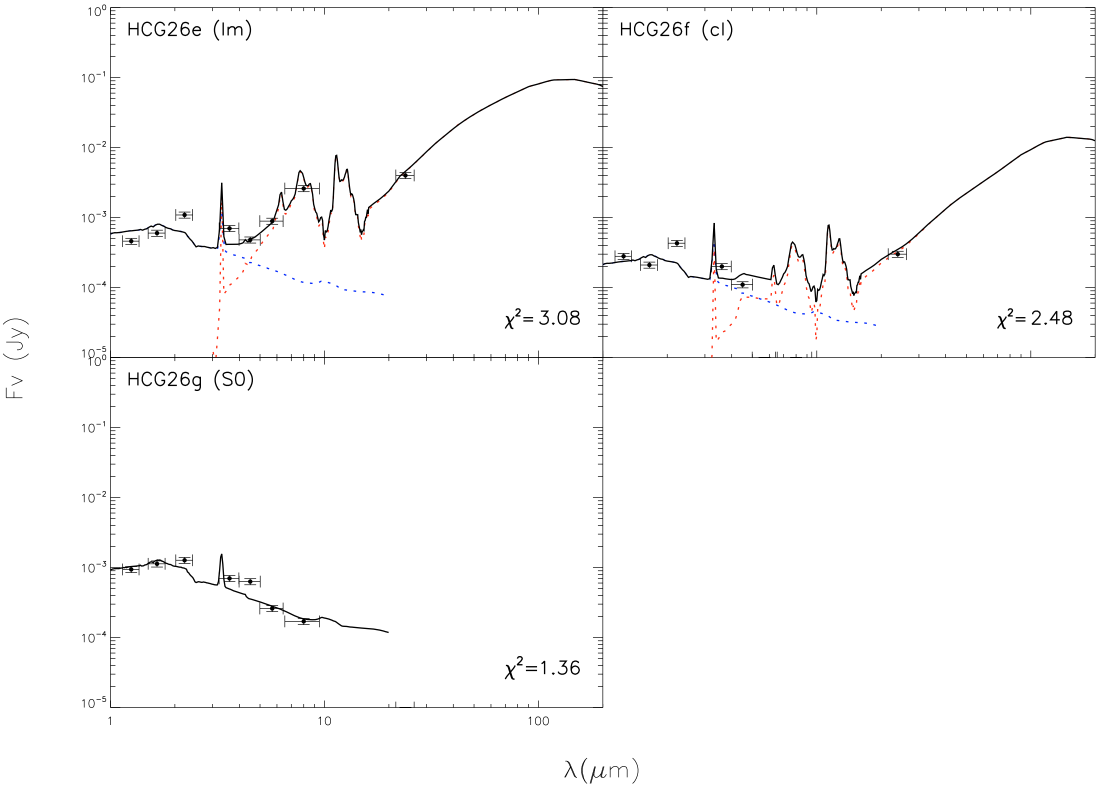

Fig. A.1. continued.

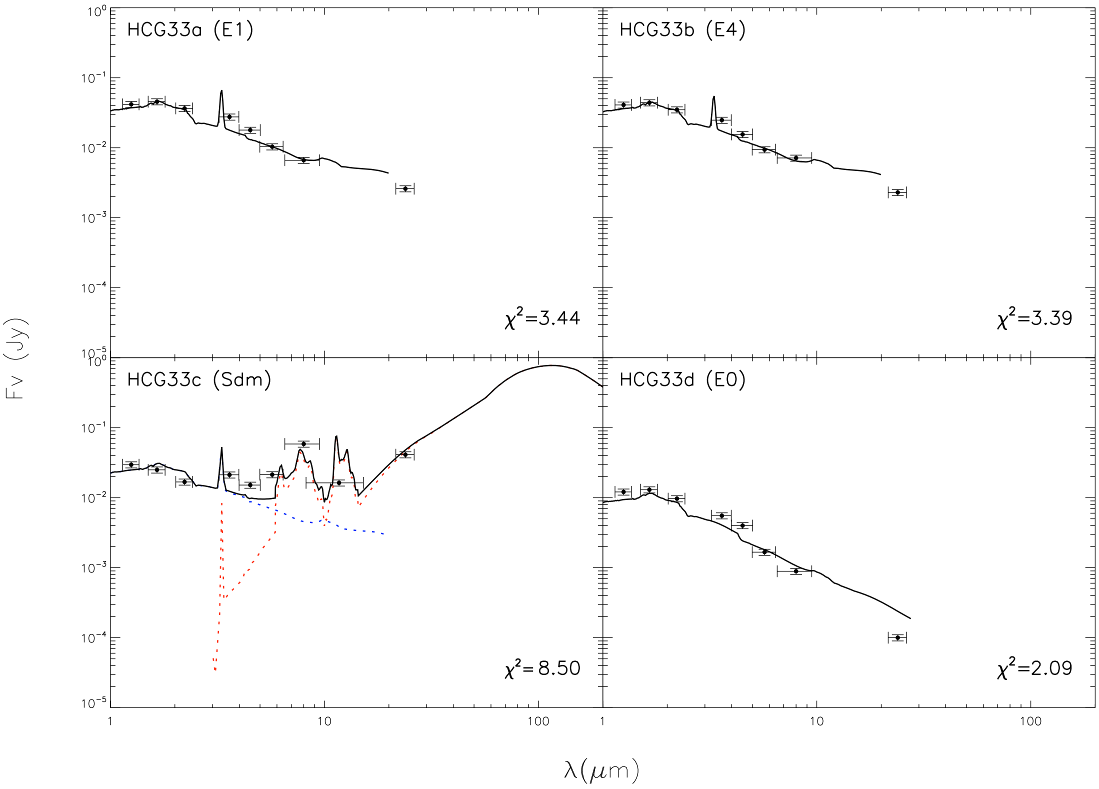

Fig. A.1. continued.

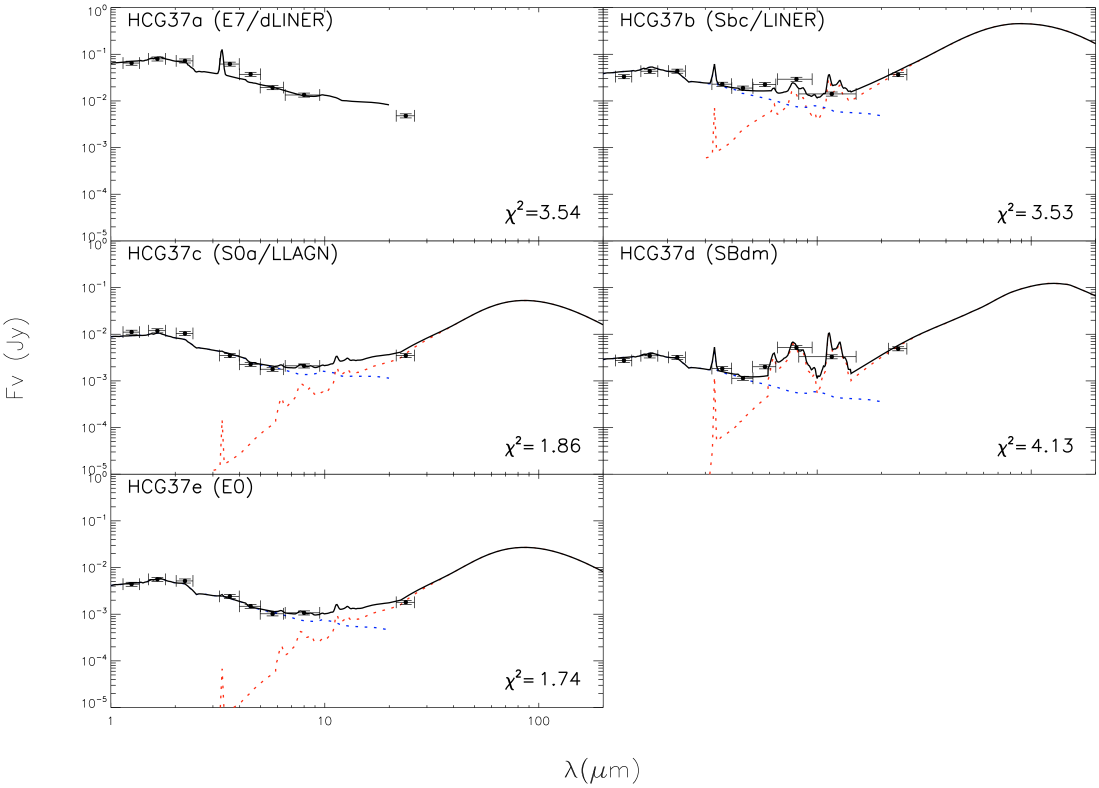

Fig. A.1. continued.

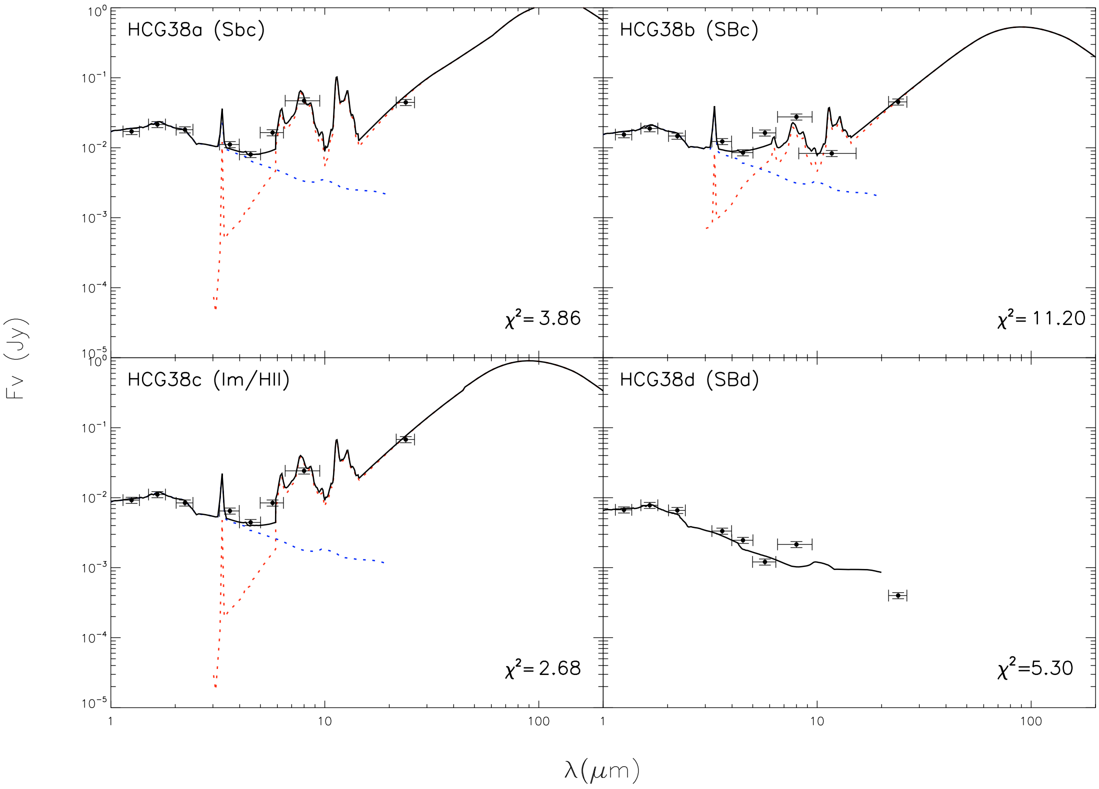

Fig. A.1. continued.

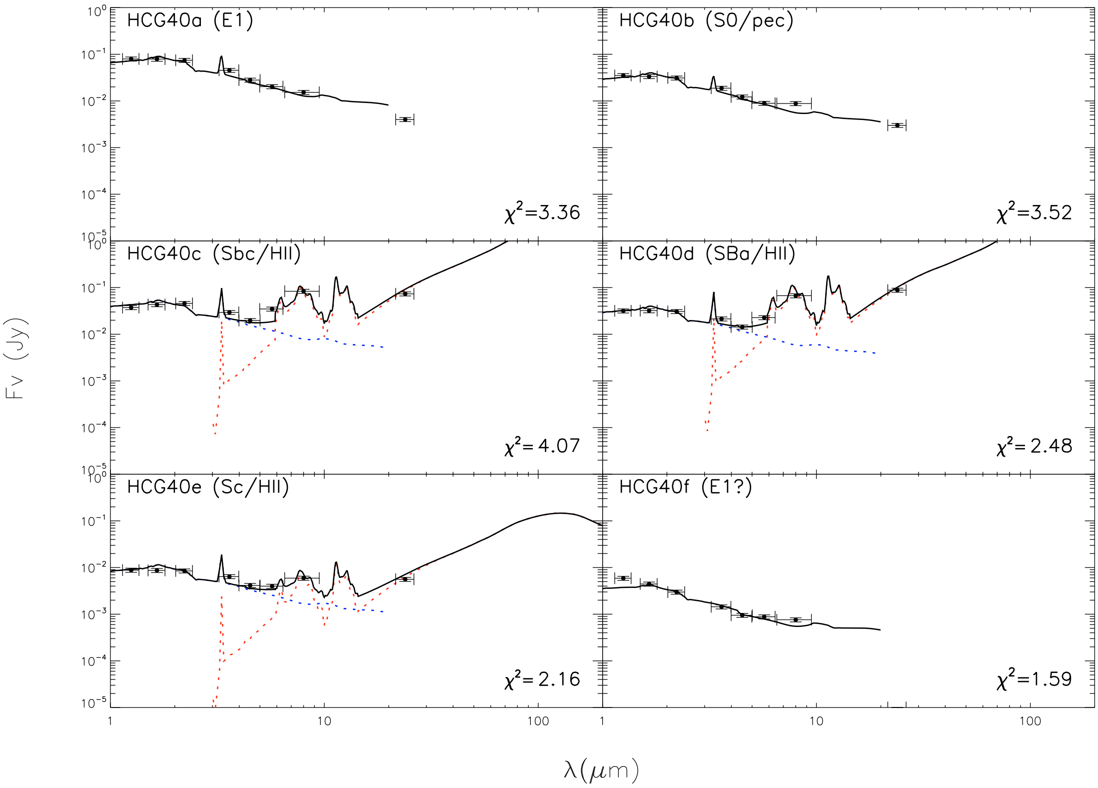

Fig. A.1. continued.

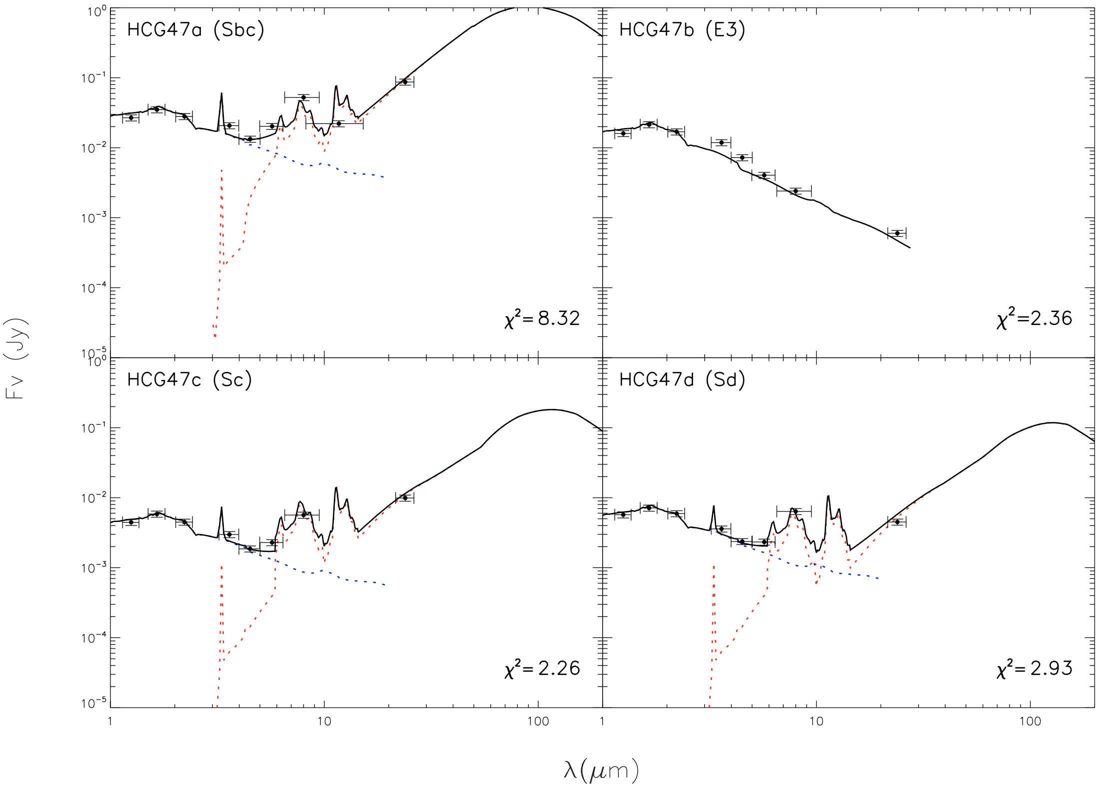

Fig. A.1. continued.

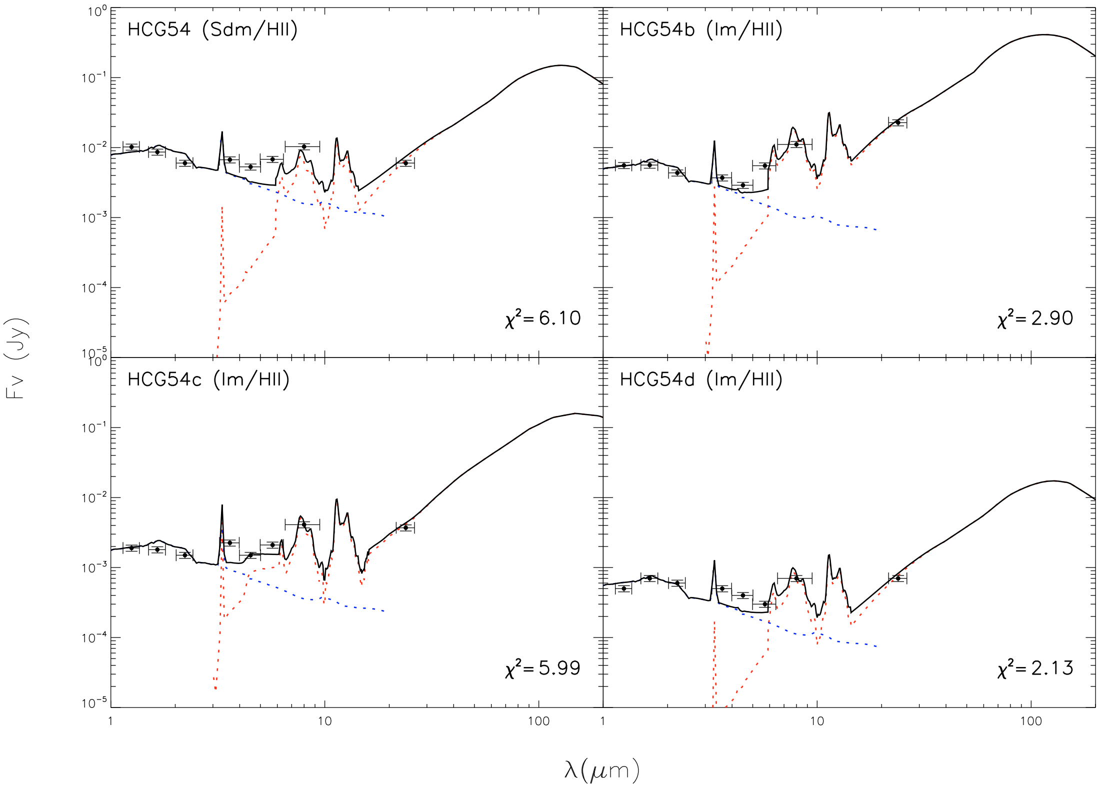

Fig. A.1. continued.

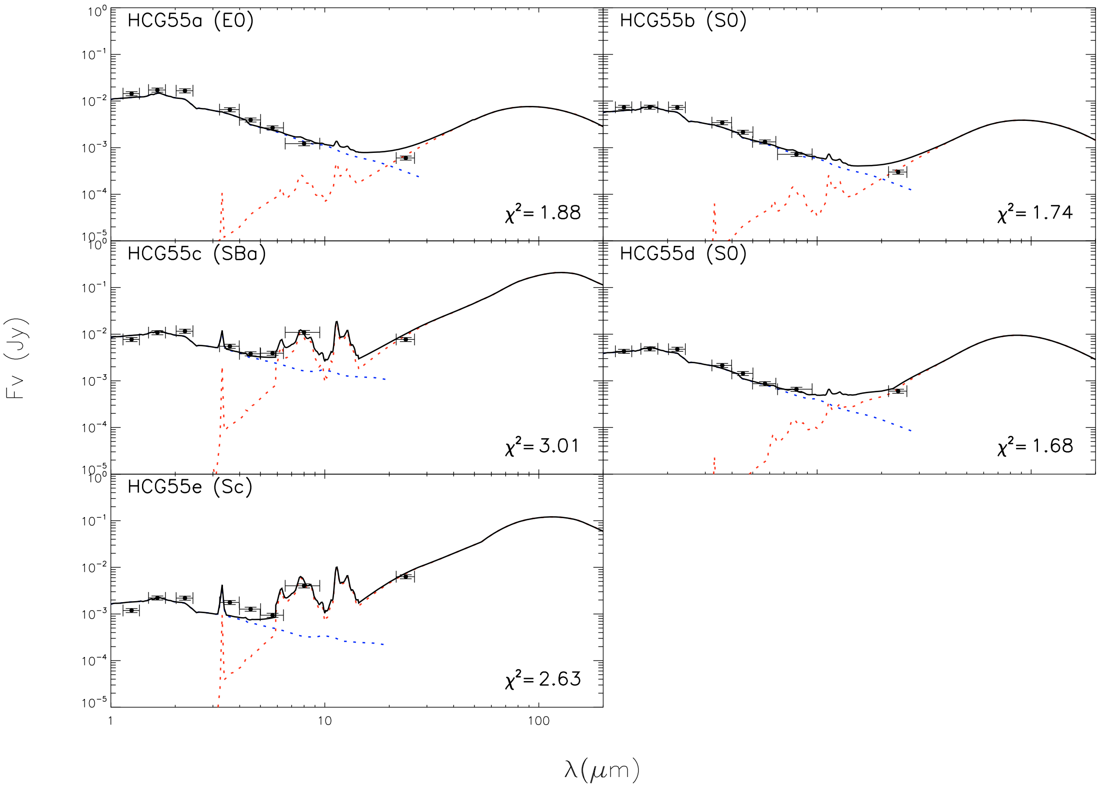

Fig. A.1. continued.

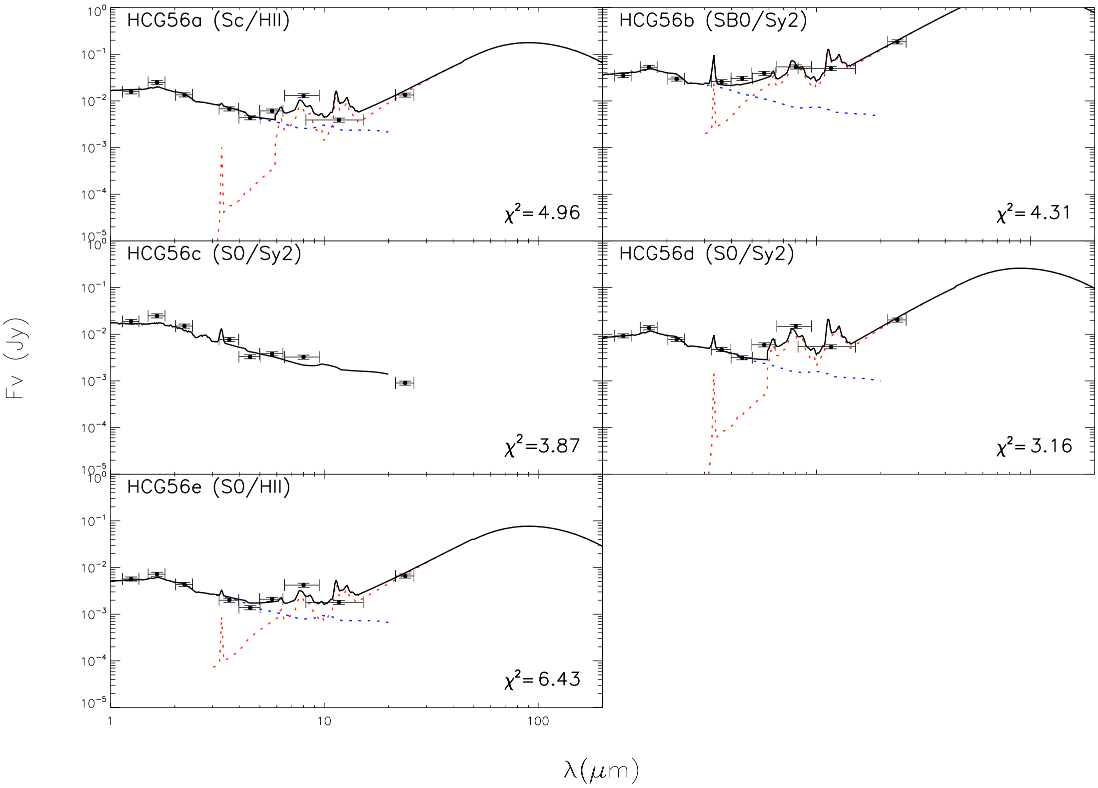

Fig. A.1. continued.

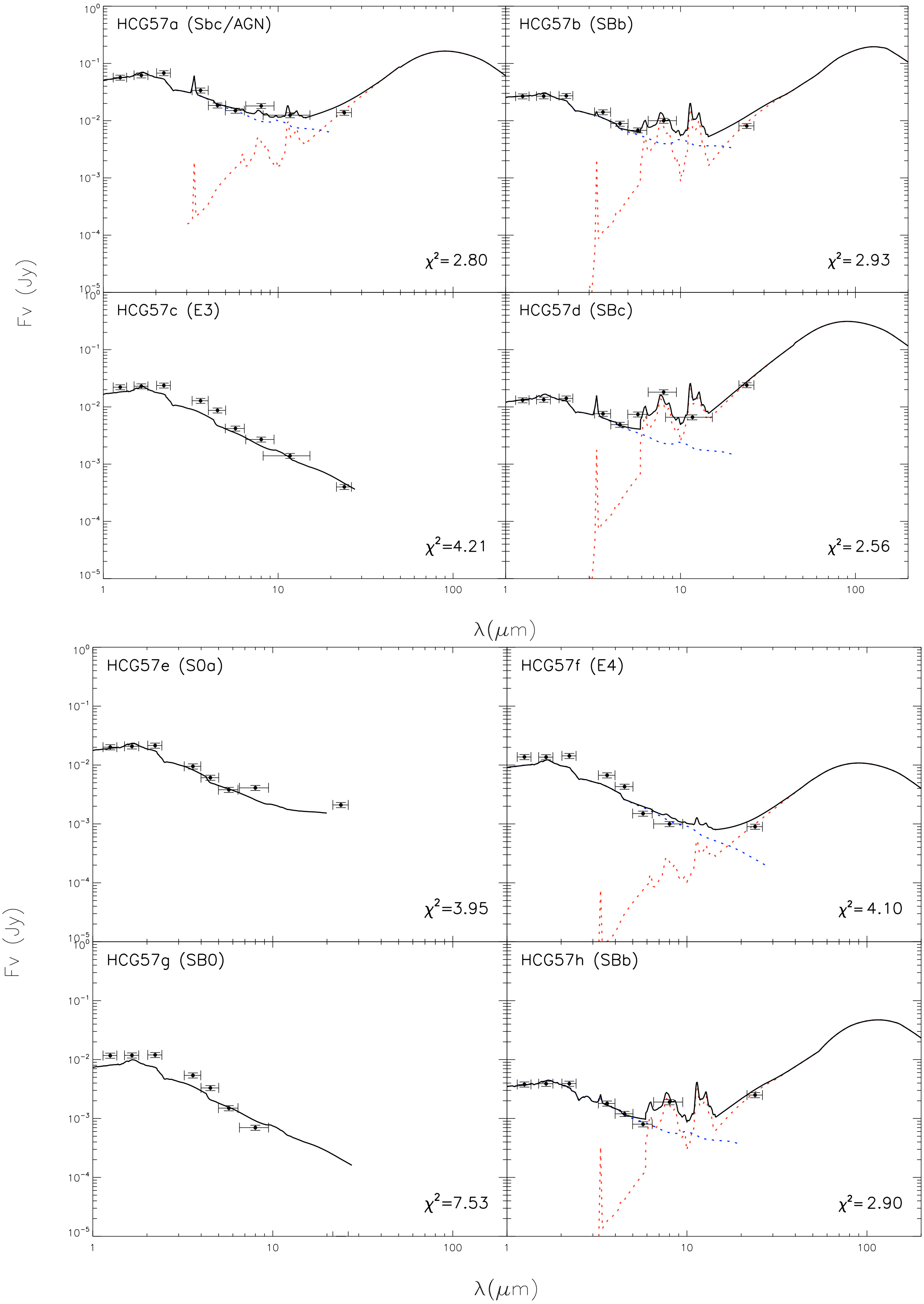

Fig. A.1. continued.

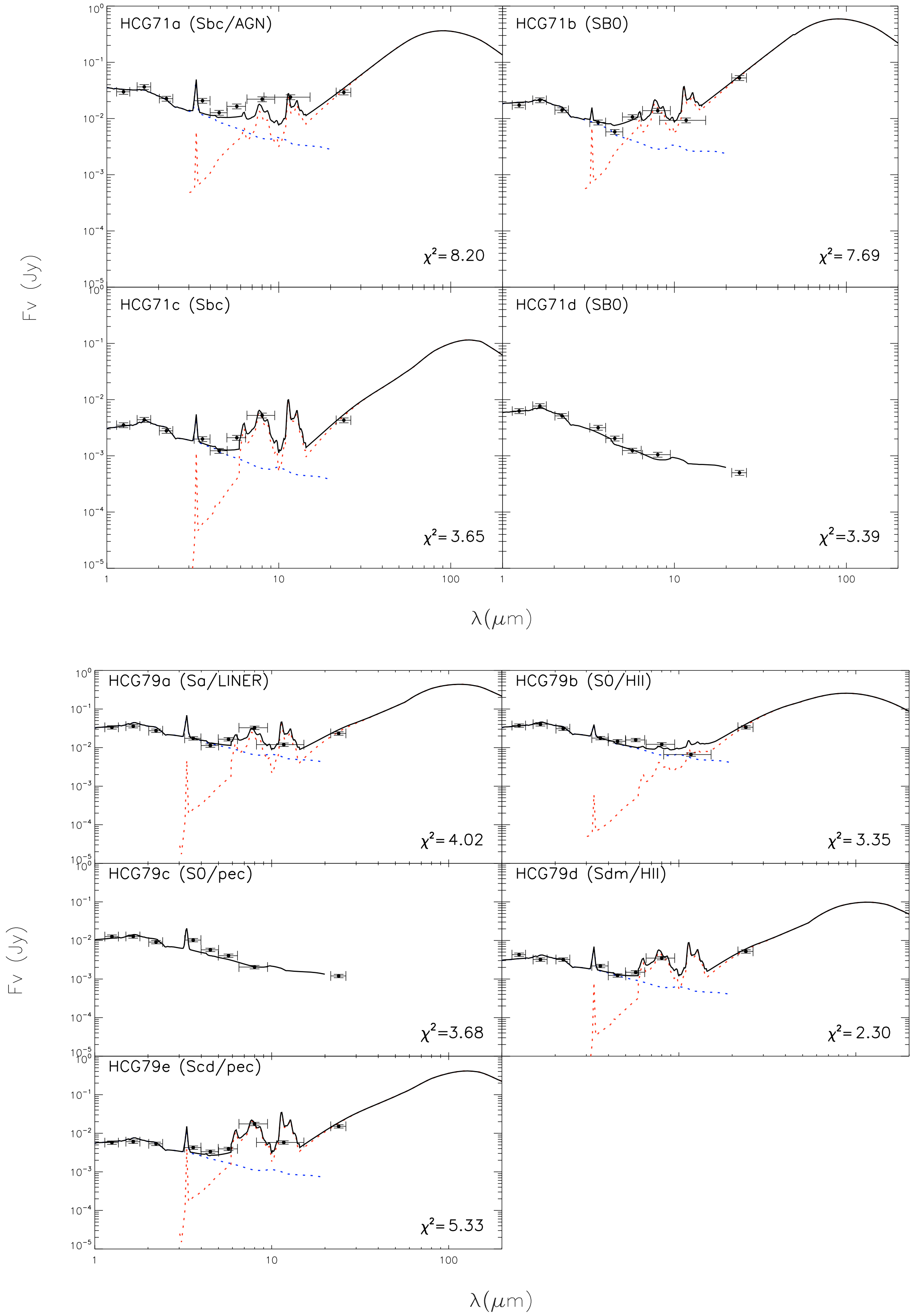

Fig. A.1. continued.

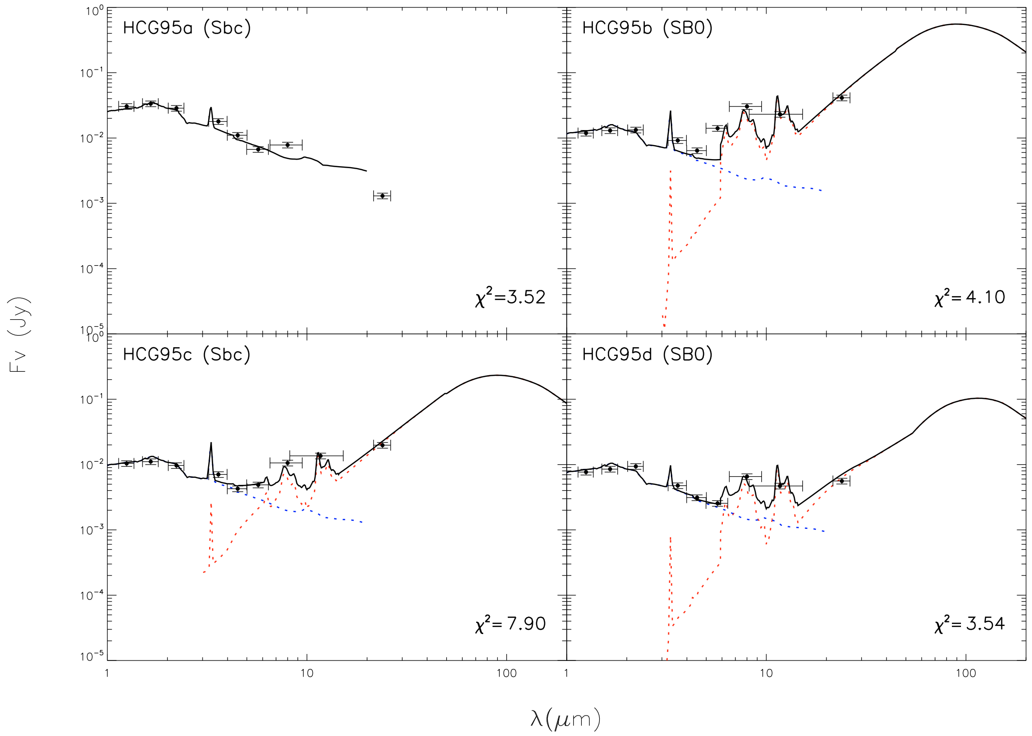

Fig. A.1. continued.

.

A&A 533, A142 (2011)
DOI: 10.1051/0004-6361/201117355

Astronomy & Astrophysics

A mid-IR study of Hickson compact groups

II. Multiwavelength analysis of the complete GALEX-*Spitzer* sample[⋆,⋆⋆]

T. Bitsakis[1], V. Charmandaris[1,2,3], E. da Cunha[4], T. Díaz-Santos[1], E. Le Floc'h[5], and G. Magdis[6]

[1] Department of Physics & ICTP, University of Crete, 71003 Heraklion, Greece
e-mail: `bitsakis@physics.uoc.gr`
[2] IESL/Foundation for Research & Technology-Hellas, 71110 Heraklion, Greece
[3] Chercheur Associé, Observatoire de Paris, 75014 Paris, France
[4] Max Planck Institute für Astronomie, 69117 Heidelberg, Germany
[5] Laboratoire AIM, CEA/DSM – CNRS – Université Paris Diderot, IRFU/Service d'Astrophysique, 91191 Gif-sur-Yvette Cedex, France
[6] University of Oxford, Department of Physics, Keble Road, Oxford OX1 3RH, UK

Received 27 May 2011 / Accepted 15 July 2011

ABSTRACT

We present a comprehensive study of the impact of the environment of compact galaxy groups on the evolution of their members using a multiwavelength analysis from the ultraviolet to the infrared, for a sample of 32 Hickson compact groups (HCGs) containing 135 galaxies. Fitting the spectral energy distributions (SEDs) of all galaxies with the state-of-the-art model of da Cunha et al. (2008, MNRAS, 388, 1595) we can accurately calculate their mass, SFR, and extinction, as well as estimate their infrared luminosity and dust content. We compare our findings with samples of field galaxies, early-stage interacting pairs, and cluster galaxies with similar data. We find that classifying the groups as dynamically "old" or "young", depending on whether at least one quarter of their members are early-type systems, is physical and consistent with past classifications of HCGs based on their atomic gas content. Dynamically "old" groups are more compact and display higher velocity dispersions than "young" groups. Late-type galaxies in dynamically "young" groups have specific star formation rates (sSFRs), NUV-r, and mid-infrared colors that are similar to those of field and early-stage, interacting pair spirals. Late-type galaxies in dynamically "old" groups have redder NUV-r colors, because they have likely experienced several tidal encounters in the past, thereby building up their stellar mass, and display lower sSFRs. We identify several late-type galaxies that have sSFRs and colors similar to those of elliptical galaxies, since they lost part of their gas due to numerous interactions with other group members. Also, 25% of the elliptical galaxies in these groups have bluer UV/optical colors than normal ellipticals in the field, probably due to star formation as they accreted gas from other galaxies of the group or via merging of dwarf companions. Finally, our SED modeling suggests that in 13 groups, ten of which are dynamically "old", there is diffuse cold dust in the intragroup medium. All this evidence points to an evolutionary scenario in which the effects of the group environment and the properties of the galaxy members are not instantaneous. Early on, the influence of close companions to group galaxies is similar to the one of galaxy pairs in the field. However, as the time progresses, the effects of tidal torques and minor merging shape the morphology and star formation history of the group galaxies, leading to an increase in the fraction of early-type members and a rapid build up of the stellar mass in the remaining late-type galaxies.

Key words. infrared: galaxies – galaxies: evolution – galaxies: interactions – galaxies: star formation

1. Introduction

It has become increasingly evident that interactions and merging of galaxies have contributed substantially to their evolution, in terms of both their stellar population and their morphological appearance. Compact galaxy groups, with their high galaxy density and signs of tidal interactions among their members, are ideal systems for studying the impact of the environment on the evolution of galaxies. The Hickson compact groups (HCGs) are 100 systems of typically four or more galaxies in a compact configuration on the sky (Hickson 1982). They contain a total of 451 galaxies and are mostly found in relatively isolated regions where no excess of surrounding galaxies can be seen, which reflects a strong local density enhancement.

The HCGs occupy a unique position in the framework of galaxy evolution, which bridges the range of galaxy environments from field and loose groups to cores of rich galaxy clusters. At the original selection of the HCG members did not include redshift information, led to including interlopers among them, the most famous being NGC 7320 in Stephan's Quintet (HCG 92). This led to a debate as to whether compact groups are line-of-sight alignments of galaxy pairs within loose groups or filaments seen end-on (Mamon 1986; Hernquist et al. 1995). However, the detection of hot X-ray gas in ~75% of the HCGs by Ponman et al. (1996) implies that they reside in a massive dark matter halo and thus are indeed physically dense structures. Numerical simulations indicate that in the absence of velocity information, raising the minimum surface brightness criterion for the group used by Hickson would help eliminate interlopers (see McConnachie et al. 2008).

[⋆] Tables 4–7 and Appendix are available in electronic form at `http://www.aanda.org`

[⋆⋆] Full Table 2 is only available at the CDS via anonymous ftp to `cdsarc.u-strasbg.fr (130.79.128.5)` or via `http://cdsarc.u-strasbg.fr/viz-bin/qcat?J/A+A/533/A142`

Because of the nature of these groups, the high-density enhancements, in addition to the low velocity dispersions (~250 km s^{-1}), make them ideal for studying the effects of galaxy interactions. Hickson (1982) found that the majority of HCGs display an excess of elliptical galaxies, which are ~31% of all members compared to the field, while the fraction of spiral and irregular galaxies is only 43%, nearly a factor of two less than what is observed in the field. Optical imaging by Mendes de Oliveira & Hickson (1994) showed that 43% of all HCG galaxies display morphological features of interactions and mergers, such as bridges, tails, and other distortions. Similar indications of interactions are seen in maps of the atomic hydrogen distribution in selected groups by Verdes-Montenegro et al. (2001). Moreover, Hickson (1989) found that the fractional distribution of the ratio of far-infrared (far-IR) to optical luminosity in HCG spiral galaxies is significantly wider than that of isolated galaxies, suggesting that for a given optical luminosity, spiral galaxies in groups have higher IR luminosities. Comparison of HCG spirals with those in clusters of galaxies from Bicay & Giovanelli (1987) reveals that both the distributions of the IR to optical luminosity, and the 60 to 100 μm far-IR color are similar. Finally, nuclear optical spectroscopy studies indicate that almost 40% of the galaxies within these groups display evidence of an active galactic nucleus (AGN, Martinez et al. 2010; Shimada et al. 2000). All these clues are consistent with an evolutionary pattern where tidal encounters and the accretion of small companions by the group members redistribute the gas content of the groups and affect the morphology of their members.

Verdes-Montenegro et al. (2001) and Borthakur et al. (2010) have proposed an evolutionary sequence for the HCGs based on the amount and spatial distribution of their neutral atomic gas. Using HI maps they classified the groups into three phases based on the ratio of the gas content within the galaxies over the total observed in the group. According to their scenario, a loose galaxy group starts to contract under the gravity to form a more compact one. During this first phase the HI gas is still mostly found in the individual galaxies. Then as the group evolves, it enters the second phase and a fraction of the atomic hydrogen is extracted from the galaxy disks into the intragroup medium, probably from tidal forces, and part of it becomes fully ionized. Finally, in the third phase, the dynamical friction leads to a decrease in the separation between the group members and the group becomes more compact. More than 80% of the HI originally in the disks of the galaxies has been displaced. Some of it is seen redistributed in a common envelope surrounding all groups members, and a fraction has likely been converted into molecular gas fueling star formation and/or accretion onto an AGN. A similar classification has been proposed by Johnson et al. (2007) and Tzanavaris et al. (2010). These authors separated the groups using the ratio of the $M_{\rm HI}$ over the dynamical mass of the group, the so-called "HI richness", and find that it is correlated to the specific star formation (sSFR) of their galaxies. They also find that galaxies in gas-poor groups display colors that are representative of a normal stellar population and observed a bimodality in both the mid-IR colors, and in the sSFRs of their members. They suggest that this is caused by enhanced the star formation activity that leads the galaxies in groups to evolve faster. Walker et al. (2010) conclude that a similar bimodality in the mid-IR is also observed in the colors of galaxies in the Coma Infall region.

A necessary step in determining the evolutionary state of HCGs is to analyze the morphology not just of the group members, but also of their stellar population and star formation history. In our first paper (Bitsakis et al. 2010), we commenced exploring the properties of an initial sample of 14 HCGs in mid-IR wavelengths and found that a large fraction of the early type galaxies in groups have mid-IR colors and spectral energy distributions (SEDs) consistent with those of late-type systems. We suggested that this possibly stems from an enhanced star formation, as a result of accretion of gas rich dwarf companions. We found no evidence that the star formation rate (SFR) and build up of stellar mass of late-type galaxies in groups is different from what is observed in early-stage interacting pairs, or spiral galaxies in the field. However, when we separated the groups according to the fraction of their early type members, they appear to stand out from the control samples. This would suggests an evolutionary separation of HCGs and can provide better insight into the nature of these groups.

Despite the progress in analyzing the properties of these groups, there are still several open questions. Is the bimodality of the mid-IR colors and sSFRs indeed linked with the evolutionary sequence of these galaxies, or is it also observed in other galaxies? How do the properties of HCG galaxies compare to those of galaxies in other environments? Is it really physical to classify the evolutionary stages of these groups also according to the fraction of their early-type systems? Is this classification meaningful in terms of galaxy properties and colors, and does it agree with the other classifications? To answer these questions we need multiwavelength data, as well as a theoretical model, to fit their global SED, in order to obtain the best possible constraints on the physical parameters. In this paper we present the first such analysis for a large sample, nearly one third of all Hickson groups, for which we have retrieved observations from the UV to the IR part of the spectrum.

The structure of the paper is the following. We present our samples, the observations, and the data reduction in Sect. 2. In Sect. 3, we describe the model used to fit the data, the basic physical parameters we can derive, and their uncertainties. Our results are shown in Sect. 4, and our conclusions are summarized in Sect. 5. In an Appendix we provide additional information on ten early-type galaxies that have peculiar mid-IR colors and SEDs.

2. Observations and data reduction

Our sample was constructed from the original Hickson (1982) catalog of 100 groups, using as criterion the availability of high spatial resolution 3.6 to 24 μm mid-IR imagery from the *Spitzer* Space Telescope archive, as well as UV imaging from GALEX. The infrared data are essential for probing the properties of the energy production in the nuclei of galaxies, some of which may be enshrouded by dust, while the UV is needed to properly estimate the effects of extinction and accurately account on the global energy balance when we model their SED. These constraints resulted in a sample of 32 compact groups containing 135 galaxies, 62 (46%) of which are early types (E's & S0's), and 73 (54%) are late types (S/SB's & Irr's). This nearly triples the sample of 14 HCGs we studied in Bitsakis et al. (2010). We verified that all galaxies of the groups are separated enough to be able to obtain accurate photometry from the UV to the mid-IR and that the average group properties, such as type of galaxy, stellar mass, and SFRs, are representative of the whole Hickson sample. We should note that seven groups contain interlopers along the line of sight. For these groups the number of physical members is three, below the lower limit of four members introduced by Hickson (1982). In Table 1 we present a summary of all observations available. The complete photometry is presented in Table 2.

Table 1. Summary of available observations.

Filters	No. of galaxies	Comments
GALEX FUV, NUV	105, 135	AIS, MIS, and Guest Investigator maps.
B, R	129	from Hickson (1982).
SDSS	79	Model magnitudes of all Sloan filters (*ugriz*) DR7.
J, H, Ks	128	63 galaxies from Palomar Obs., 4 from Skinakas Obs., and 68 from 2MASS.
Spitzer/IRAC	135	No maps at 3.6 and 5.8 μm for HCG44b. No maps at 4.5 and 8.0 μm for HCG68c.
Spitzer/MIPS 24 μm	124	No maps or undetected: HCG25f, 40f, 57g, 68d, 68e, 75b, 75e, 92d, 92e, 97b and 97e.
IRAS 60, 100 μm	31	from Allam et al. (1996).
AKARI FIS	26	AKARI FIS source catalogue includes the 65, 90, 140, and 160 μm photometry.
Optical Spectra	94	from Martinez et al. (2010), Shimada et al. (2000), Hao et al. (2005) and Véron-Cetty & Véron (2006).

2.1. GALEX data

The UV data presented in this paper were obtained from the Galaxy Evolution Explorer (GALEX) All Sky Survey (AIS), the Medium Imaging Survey (MIS), and from Guest Investigator Data data publicly available in the GALEX archive. GALEX is a 50 cm diameter UV telescope that images the sky simultaneously in both FUV and NUV channels, centered at 1540 Å and 2300 Å, respectively. The field of view (FOV) is approximately circular with a diameter of 1.2° and a resolution of about 5.5″ (*FWHM*) in the NUV. The data sets used in this paper are taken from the GALEX sixth data release (GR6). More technical details about the GALEX instruments can be found in Morrissey (2005). We performed aperture photometry and carefully calculated the isophotal contours around each source to account for variations in the shape of the emitting region, since most of the sources have disturbed morphologies. By examining the local overall background for each galaxy, we defined a limiting isophote 3σ above it and measured the flux within the region, after subtracting the corresponding sky. Finally, the conversion from counts to UV fluxes was done using the conversion coefficients given in the headers of each file. Our measurements are presented in Table 2.

2.2. SDSS-optical data

We compiled the B and R band images of all the galaxies in our sample as reported in Table 2 of Hickson (1989), who had observed the groups for 200s in both B and R bands using FOCAS1 on the Canada French Hawaii telescope resulting in images of 0.42″ pixel^{-1} and a typical resolution of 1.2″ (*FWHM*). In addition, imaging data of 74 galaxies in the u, g, r, i, z bands, centered at 3557, 4825, 6261, 7672, and 9097 Å, respectively, were recovered from the Sloan Digital Sky Survey (SDSS). We used the SDSS DR7 "model magnitudes", which reflect the integrated light from the whole galaxy and are best suited for comparisons with total photometry from UV to IR wavelengths.

Furthermore, optical spectra were available for 94 galaxies, 70% of our sample. Using the BPT diagram, Martinez et al. (2010) classified the nuclei of 67 galaxies in our sample, while the rest were obtained from Shimada et al. (2000), Hao et al. (2005) and Véron-Cetty & Véron (2006). The results are shown in Table 2. Galaxies without emission are referred as "unclas." (unclassified), as they display only stellar absorption features, "HII" are the galaxies with a starburst nucleus, and "AGN" (or LINER & Sy2) are the ones with an active nucleus. A number of galaxies are classified as transition objects (TO) since their emission line ratios are intermediate between Kauffmann et al. (2003) and Kewley et al. (2006) criteria. Based on these results for the galaxies in our sample where nuclear classification was available, 37% host an AGN, which is close to the 40% which Martinez et al. (2010) and Shimada et al. (2000) found for their samples.

2.3. Near-infrared observations

Deep near-IR observations were obtained for 15 of the groups, using the Wide Field Infrared Camera (WIRC) of the 5 m Hale telescope at Palomar. As we discussed in Bitsakis et al. (2010) all groups were imaged in the J, H, and Ks bands for an onsource time of 20 min per filter (Slater et al. 2004). Source extraction was performed with SExtractor (Bertin & Arnouts 1996). Our 1σ sensitivity limit was ~21.5 mag arcsec^{-2} in J and H bands and ~20.5 mag arcsec^{-2} for Ks. For the remaining 17 groups of our sample, the near-IR fluxes were obtained from the Two Micron All Sky Survey (2MASS; Skrutskie et al. 2006). In cases where the proximity of galaxy pairs was affecting the reliability of the 2MASS photometry, we used the reduced 2MASS images and performed aperture photometry ourselves by defining the same aperture we used in other wavelengths. However, for HCG6, the 2MASS photometry was problematic, and we observed the group using the wide-field near-IR camera of the 1.3 m telescope at Skinakas Observatory in Crete (Greece). The observations were carried out between 21 and 23 September 2010. The group was imaged in the J, H, and Ks bands for an onsource time of 30 min per filter, and flux calibration was performed using the a set of near-IR standard stars. Data reduction and aperture photometry was performed using IDL specialized routines. All near-IR photometry for our sample is available in Table 2.

2.4. Mid-infrared Spitzer observations

Mid-IR observations for 11 of the groups were performed by us using *Spitzer* Space Telescope between 2008 January and 2009 March. We used the Infrared Array Camera (IRAC, Fazio et al. 2004) and obtained 270 s onsource exposures with the 3.6, 4.5, 5.8, and 8.0 μm broadband filters. Each group was also imaged with the Multiband Imaging Photometer for *Spitzer* (MIPS, Rieke et al. 2004) with a 375.4 s on source exposure at 24 μm. Details on the analysis of these data were presented in Bitsakis et al. (2010). The *Spitzer* mid-IR fluxes for eight more groups of the sample were obtained from Johnson et al. (2007). In brief, the IRAC observations were taken in high dynamic range with 270 or 540 s exposures depending on the group. MIPS 24 μm images were obtained by the same authors with exposures of 180 or 260 s duration for the same reason. Finally, for 13 groups we recovered the IRAC and MIPS 24 μm data from the *Spitzer* archive (PIDs: 159; 198; 50764; 40385) and reduced them as in Bitsakis et al. (2010). The details of these observations are presented in Table 3, and the compilation of all mid-IR measurements is included in Table 2.

2.5. Far-infrared data

Integrated far-IR photometry at 60 and 100 μm data for each group as a whole was obtained from Allam et al. (1996). However, because of the compact environment and small angular separation of the galaxies in the HCGs, the coarse angular resolution of IRAS at the 60 and 100 μm (~100″), enabled us to resolve only 31 individual galaxies of our sample that were sufficiently isolated and bright.

Using the recently released AKARI data we retrieved far-IR observations for 26 galaxies of our sample (22 of them were common with the IRAS sample), which were obtained with the Far-IR Surveyor (FIS) and processed with the AKARI official pipeline software version 20080530 (Okada et al. 2008). The photometry using N60, WIDE-S, WIDE-L, and N160 filters, centered at 65, 90, and 140, and 160 μm was downloaded from the AKARI online archive and is reported along with the IRAS data on Table 2. We should note that the *FWHM*s of the AKARI PSF are ~45″ at 65 and 90 μm and ~60″ at 140 and 160 μm. Even though this is better than IRAS, as we will discuss in more detail later, it places restrictions on interpreting the far-IR properties of the groups and the spatial distribution of their cold dust content.

2.6. Comparison samples

To put the properties and evolution of the group galaxies into context, we must compare their observables and derived physical parameters with other control samples. Since dynamical interactions are the main drivers of galaxy evolution, we examined isolated field galaxies, as well as systems that are dynamically interacting, such as galaxy pairs and galaxies found in clusters for which we could obtain data of similar wavelength coverage. The samples we used in our analysis are the following.

2.6.1. Isolated field galaxies

A well-studied sample with superb data coverage is the 75 "normal", mostly isolated field galaxies from the *Spitzer* Infrared Nearby Galaxies Survey (SINGS; Kennicutt et al. 2003; Dale et al. 2005). We should note that the SINGS sample was selected explicitly to cover a wide range in Hubble type and luminosity, and as a result it is not characteristic of a volume or flux-limited population. Most objects are late-type systems that have angular sizes between 5′ and 15′. It also contains four early-type galaxies (NGC 855, NGC 1377, NGC 3773, and NGC 4125) with the last one being a LINER. Since the SINGS sample does not have many early type galaxies, we used the nine isolated early-type galaxies with available mid-IR imaging described in Temi et al. (2004) and expanded it with another four isolated galaxies (NGC 1404, NGC 1199, NGC 5363, & NGC 5866), for which *Spitzer* mid-IR imaging was also available.

2.6.2. Interacting galaxy pairs

This sample is drawn from the 35 nearby (v < 11.000 km s^{-1}) early stage interacting galaxy pairs of Smith et al. (2007a). The galaxies are tidally disturbed and fairly extended, with linear sizes >3′. For the purposes of this work only 26 pairs from the initial sample were used, in which all the data were available. As

Table 2. The UV to IR photometry of our sample.

HCG galaxy	Morphology	Nuclear classification	Distance Mpc	FUV mJy	NUV mJy	*B* mJy	*R* mJy	*u* mJy	*g* mJy	*r* mJy	*i* mJy	*z* mJy	*J* mJy
37a	E7	dLINER	95.8	0.10 ± 0.01	0.38 ± 0.04	11.2 ± 0.56	44.5 ± 2.23	3.26 ± 0.09	18.0 ± 0.54	38.0 ± 1.14	54.5 ± 1.63	71.8 ± 2.15	80.7 ± 2.42
37b	Sbc	LINER	95.8	0.04 ± 0.04	0.11 ± 0.01	2.58 ± 0.13	13.7 ± 0.69	0.58 ± 0.02	3.40 ± 0.10	8.87 ± 0.27	12.9 ± 0.39	19.6 ± 0.59	33.2 ± 1.00
37c	S0a	LLAGN	104.7	0.01 ± 0.00	0.04 ± 0.00	1.03 ± 0.05	4.92 ± 0.25	0.33 ± 0.01	1.64 ± 0.05	3.56 ± 1.07	5.20 ± 0.16	6.92 ± 0.21	8.10 ± 0.24
37d	SBdm	–	87.0	0.10 ± 0.01	0.15 ± 0.01	1.13 ± 0.06	1.32 ± 0.07	0.31 ± 0.01	1.08 ± 0.03	1.67 ± 0.05	2.13 ± 0.06	2.54 ± 0.08	2.74 ± 0.08
37e	E0	TO	91.4	0.01 ± 0.00	0.03 ± 0.00	0.65 ± 0.03	1.20 ± 0.06	0.19 ± 0.00	0.76 ± 0.02	1.19 ± 0.04	1.43 ± 0.04	1.59 ± 0.05	4.00 ± 0.12

HCG galaxy	*H* mJy	*Ks* mJy	3.6 μm mJy	4.5 μm mJy	5.8 μm mJy	8.0 μm mJy	24 μm mJy	60 μm mJy	100 μm mJy	65 μm mJy	90 μm mJy	140 μm mJy	160 μm mJy	References
37a	79.6 ± 2.39	88.1 ± 2.64	61.7 ± 1.85	37.2 ± 1.12	19.3 ± 0.58	13.4 ± 0.40	4.80 ± 0.24	490 ± 49	2000 ± 200	–	–	–	–	a2, b1, c1
37b	43.3 ± 1.30	43.6 ± 1.30	22.9 ± 0.68	14.4 ± 0.43	14.5 ± 0.44	29.1 ± 0.87	36.7 ± 1.84	561 ± 56	–	675 ± 34	725 ± 36	2156 ± 107	2445 ± 122	a2, b1, c1
37c	8.90 ± 0.27	7.40 ± 0.22	3.50 ± 0.11	2.30 ± 0.07	1.80 ± 0.05	2.10 ± 0.06	3.50 ± 0.18	190 ± 19	–	–	–	–	–	a2, b1, c1
37d	3.45 ± 0.10	3.19 ± 0.10	1.84 ± 0.06	1.14 ± 0.03	2.01 ± 0.06	5.19 ± 0.16	4.90 ± 0.25	–	–	–	–	–	–	a2, b1, c1
37e	5.18 ± 0.15	4.77 ± 0.14	2.41 ± 0.07	1.48 ± 0.04	1.02 ± 0.03	1.07 ± 0.03	1.80 ± 0.09	–	–	–	–	–	–	a1, b1, c1

Notes. [a1,2,3,4] The nuclear classification obtained from Martinez et al. (2010), Shimada et al. (2000), Hao et al. (2005) and Véron-Cetty & Véron (2006) respectively. [b1,2,3] The near-IR photometry from Palomar, 2MASS and Skinakas respectively. [c1,2,3,4,5,6] The mid-IR photometry from Bitsakis et al. (2010), Johnson et al. (2007), and the *Spitzer* archive (PIDs: 50764, 159, 40385, 198) respectively. The full table is available at the CDS.

Table 3. Observational parameters of *Spitzer* archival data.

HCG ID	RA (J2000)	Dec (J2000)	z	IRAC^a s	MIPS$_{24}$^{a} s	Observer PID
HCG4	00h34m15.9s	–21d26m48s	0.0269	10.0	18.3	40385
HCG6	00h39m10.1s	–08d23m43s	0.0379	150.0	375.4	50764
HCG15	02h07m39.0s	+02d08m18s	0.0228	300.0	375.4	50764
HCG25	03h20m43.7s	–01d03m07s	0.0212	300.0	375.4	50764
HCG44	10h18m00.5s	+21d48m44s	0.0046	360.0	917.5	159
HCG67	13h49m03.5s	–07d12m20s	0.0245	300.0	375.4	50764
HCG68	13h53m40.9s	+40d19m07s	0.0080	75.0	375.4	50764
HCG75	15h21m33.8s	+21d11m00s	0.0416	150.0	375.4	50764
HCG82	16h28m22.1s	+32d49m25s	0.0362	150.0	375.4	50764
HCG91	22h09m10.4s	–27d47m45s	0.0238	300.0	375.4	50764
HCG92	22h35m57.5s	+33d57m36s	0.0215	432.0	627.5	198
HCG97	23h47m22.9s	–02d19m34s	0.0218	300.0	375.4	50764
HCG100	00h01m20.8s	+13d07m57s	0.0178	300.0	375.4	50764

Notes. $^{(a)}$ On source integration time for each of the four IRAC filters and MIPS 24 μm filter.

discussed in Bitsakis et al. (2010), the stellar mass distributions are similar between this sample as well as ours, and the SINGS.

2.6.3. Field, group, and cluster galaxies

To compare in more detail the UV-optical colors of the galaxies in HCGs with the colors of galaxies found in the field, as well as in other groups and clusters, we used the volume-limited sample of Haines et al. (2008). This sample contains 1994 galaxies in redshift range $0.005 \leq z \leq 0.037$, selected by cross-correlating the SDSS-DR4 sample with the GALEX GR3 photometric catalogs. Using the Hα equivalent widths of $M_r < -18$ galaxies, the authors were able to separate the galaxies into passively evolving and star-forming, having $EW(\mathrm{H}\alpha) < 2$ and $EW(\mathrm{H}\alpha) > 2$, respectively. To quantify the effects of local mass density and environment the authors calculated the local galaxy number density, ρ, in units of projected area, in Mpc^2, around a central galaxy and within a radial velocity bin of 500 km s^{-1}. They found that for $\rho < 0.5$ Mpc^{-2} (500 km s^{-1})$^{-1}$ they can produce a pure field sample. If a galaxy has $\rho > 4.0$ Mpc^{-2} (500 km s^{-1})$^{-1}$ there is a 90% probability that it lies within the virial radius of a group or a cluster.

3. Estimating the physical parameters of the galaxies

3.1. Fitting the UV, optical, and IR SEDs

We used the state-of-the-art physically motivated model of da Cunha et al. (2008)[1] to fit the SEDs of the galaxies in our sample. As discussed in detail by da Cunha et al. (2008), the model assumes that the source of energy in a galaxy comes from an ensemble of stellar populations (no AGN heating is included) whose emission is partially absorbed by dust and re-emitted at longer wavelengths. The model treats the complete SED from the UV to the far-IR and allows us not only to derive best-fit physical parameters to the data, but also to provide the range of their median-likelihood values, which are consistent with the observations. To achieve this, the model adopts a Bayesian approach which draws from a large library of random models encompassing all plausible parameter combinations, such as star formation histories, metallicities, dust optical depths, and dust masses and temperatures. Clearly the wider the wavelength coverage, the more robust the derived parameters. Thus to properly estimate the effect of dust extinction, the UV and optical range needs to be well sampled, while estimating dust masses and luminosities mid- and far-IR coverage is essential. In addition to the HCG sample, we used the model to fit the interacting pairs of Smith et al. (2007a), and the results are presented in the Table 5. The galaxies of the SINGS sample had already been fit by da Cunha et al. (2008).

3.1.1. Description of the model

The da Cunha et al. (2008) model computes the emission by stars in galaxies using the latest version of the Bruzual & Charlot (2003) population synthesis code. This code predicts the spectral evolution of stellar populations in galaxies from far-UV to IR wavelengths and at ages between 1×10^5 and 1.37×10^{10} yr, for different metallicities, initial mass functions (IMFs) and star formation histories. In this work, we adopt the Chabrier (2003) Galactic-disk IMF. The model does not take the energy contribution of an active nucleus to the global SED into account. Since nearly 40% of our sources host an optically identified AGN one could consider that this could introduce a bias in our analysis. However, based on a number of mid-IR diagnostics the influence of the active nucleus on the total IR emission of the majority of our galaxies is insignificant, thus this limitation does affect our conclusions seriously (see details in Sect. 4.5).

The emission from stars is attenuated using a two component dust model of Charlot & Fall (2000). This model uses an "effective absorption" curve for each component. They use this prescription to compute the total energy absorbed by dust in the birth clouds (BC) and in the ambient interstellar medium (ISM), and this energy is re-radiated by dust at IR wavelengths. They define the total dust luminosity reradiated by dust in the birth clouds and in the ambient ISM as $L_{\mathrm{d}}^{\mathrm{BC}}$ and $L_{\mathrm{d}}^{\mathrm{ISM}}$, respectively. The total luminosity emitted by dust in the galaxy is then $L_{\mathrm{d}}^{\mathrm{tot}} = L_{d}^{\mathrm{BC}} + L_{\mathrm{d}}^{\mathrm{ISM}}$. The value of $L_{\mathrm{d}}^{\mathrm{BC}}$ and $L_{\mathrm{d}}^{\mathrm{ISM}}$ is calculated over the wavelength range from 3 to 1000 μm using four main components:

- the emission from polycyclic aromatic hydrocarbons (PAHs; i.e. mid-IR emission features);
- the mid-IR continuum emission from hot dust with temperatures in the range 130–250 K;

---

[1] The da Cunha et al. (2008) model is publicly available at `http://www.iap.fr/magphys`

- the emission from warm dust in thermal equilibrium with adjustable temperature in the range 30–60 K;
- the emission from cold dust in thermal equilibrium with adjustable temperature in the range 15–25 K.

A detailed analysis of da Cunha et al. (2008) suggests that the above minimum number of components is required to account for the IR SEDs of galaxies in a wide range of star formation histories.

3.1.2. Model library

We use a large random library of star formation histories and dust emission models presented in da Cunha et al. (2008). In this library, each star formation history is parameterized using a SFR that is exponentially declining with time, on top of which random bursts are superimposed. The metallicities of these models are sampled uniformly between 0.2 and 2 times solar, and the model ages are distributed uniformly between 0.1 and 13.5 Gyr. Each stellar emission model computed using these star formation histories, ages, and metallicities is then attenuated by dust using the two-component description of Charlot & Fall (2000) described above, using a wide range of V-band dust optical depths in the birth cloud and ISM component. Each of these model spectra is then consistently connected to dust emission spectra spanning a wide range in dust temperatures and fractional contributions of each dust emission component to the total dust luminosity. In particular, dust emission models with the same dust luminosity and the same relative contributions to total dust luminosity from the birth cloud and ISM (i.e. $L_{\mathrm{d,\,tot}}$ and $f\mu$) are assigned to each stellar emission model, as explained in da Cunha et al. (2008).

For each UV to IR model spectrum in this library, we compute the synthetic photometry in the GALEX FUV and NUV, SDSS *ugriz, B, R*, near-IR, *Spitzer* IRAC, MIPS-24, AKARI/FIS, and IRAS 60 and 100 μm bands at the redshifts of our galaxies to allow for direct comparison between the observed and model broad-band SEDs as detailed below.

3.1.3. Spectral fits

We compared the observed SEDs of the galaxies in our HCGs to every model in the stochastic library of models by directly comparing the observed and model broad-band fluxes and computing the χ^2 goodness of fit for each model in the library. This allows us to compute, for each galaxy in the sample, the full likelihood distributions of several model parameters, such as the SFR, stellar mass, V-band optical depth in the birth clouds, ISM, and dust luminosity. We take our final estimate of each parameter to be the median of the likelihood distribution, and the associated confidence interval to be the 16th–84th percentile range of that distribution.

As examples of our fits, we show in Fig. 1 the best-fit SEDs of two galaxies from our sample: one quiescent, moderately dusty galaxy (HCG48a, bottom panel) and one actively star-forming, relatively dusty galaxy (HCG7a, top panel).

We note that, as discussed in Sect. 2, even though far-IR measurements are available for each HCG as a whole, most of the galaxies are not independently resolved in the far-IR, due to the large IRAS beam sizes. This seriously restricts the sampling of our SEDs and consequently to the constraints on the dust temperature, total dust mass, and luminosity of each galaxy. One of the strengths of this approach is that, by building the full likelihood distributions of the model parameters, we are able to take these uncertainties caused by the lack of far-IR observations into account (see also da Cunha et al. 2008).

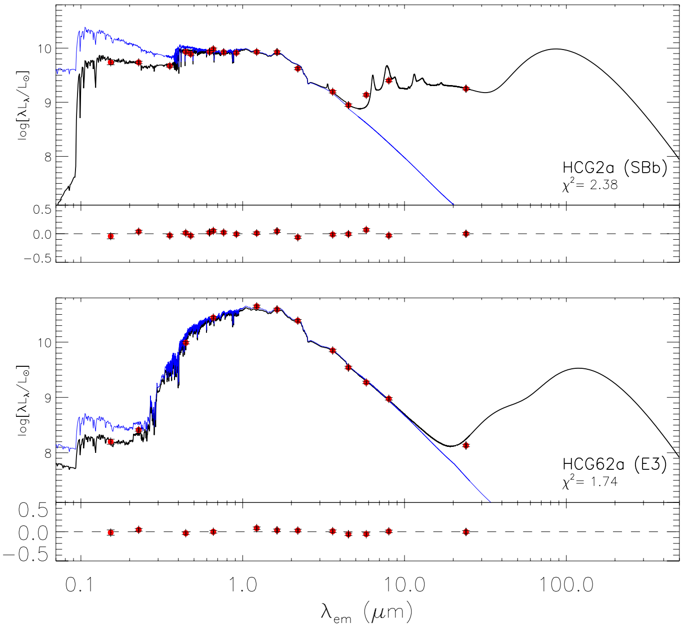

Fig. 1. Example of best-fit models (in black line) to the observed spectral energy distributions (SEDs) of two galaxies of our sample. One is a typical late-type galaxy (HCG2a; *top panel*) and the second is a quiescent elliptical galaxy (HCG62a; *bottom panel*). In each panel, the blue line shows the unattenuated stellar spectrum estimated by the model. The red circles are the observed broadband luminosities with their errors as vertical bars. The residuals, $(L_\lambda^{\mathrm{obs}} - L_\lambda^{\mathrm{mod}})/L_\lambda^{\mathrm{obs}}$, are shown at the bottom of each panel. Note the uncertainty in the far-IR shape of the SED due to lack of high spatial resolution data.

3.2. Comparison of empirical to model results

Given the available observations, the stellar mass and SFR of a galaxy are the two physical parameters that are constrained more accurately using our SED modeling. Since in Bitsakis et al. (2010) we did not had the multiwavelength data and the model, we used semi-empirical methods, relying on the K-band luminosity, to estimate the stellar mass, and the 24 μm emission for the SFR. In this section, we compare the model derived parameters with those from the empirical methods to better understand the uncertainties in the interpretation of the results. We also compare them with the methods of Salim et al. (2007) and Iglesias-Páramo et al. (2006), which use the NUV and FUV bands of GALEX, respectively, to estimate the SFR, in order to evaluate their consistency with the model results.

The stellar mass of a galaxies can be estimated using the Bell et al. (2003) prescription which was calibrated using a large sample of galaxies in the local universe. Their formula, based on the K-band luminosity, is

$$M(M_\odot) = 10^{a+b(B-R)} \times L_{Ks}(L_{Ks,\odot}) \tag{1}$$

where B and R are the B- and R-band magnitudes of the galaxy, L_{Ks} its Ks-band luminosity in units of solar luminosities ($L_{Ks,\odot} = 4.97 \times 10^{25}$ W), $a = -0.264$, and $b = 0.138$, with systematic errors of ~30% due to uncertainties in the star formation history and dust. Because these authors used "diet" Salpeter IMF, we corrected it to a Chabrier IMF (which our model uses, scaling down their M/L by −0.093 dex as described in Zibetti et al. 2009). Finally, since Bell et al. (2003) relation uses BC03 models (Bruzual & Charlot 2003), which do not take into account

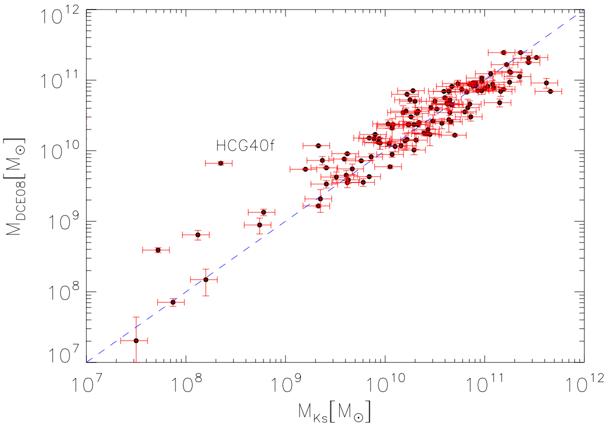

Fig. 2. Stellar masses based on the da Cunha et al. (2008) model (hereafter $M_{\rm DCE08}$) are plotted as a function of the ones derived from Bell et al. (2003) relation based on Ks luminosity ($M_{\rm Ks}$) after applying the corrections discussed in the text. Vertical error bars indicate the 16–84 percentile ranges in the recovered probability distributions, while the horizontal error bars are the 30% errors as described by Bell et al. (2003) determined from the scatter in the models. The blue dashed line represents the one-to-one relation.

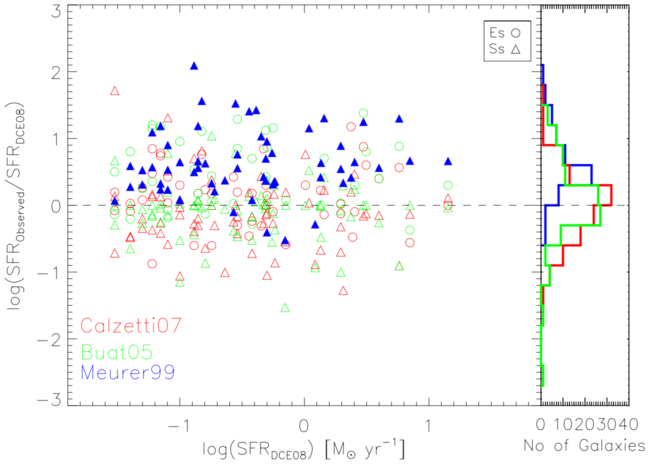

Fig. 3. A plot of the ratio of the SFRs derived from the observed FUV or 24 μm fluxes over the SFRs derived from the da Cunha et al. (2008) model as a function of the model SFR. Red open circles and red open triangles are the SFRs derived from the MIPS 24 μm fluxes for early and the late-type galaxies respectively. Green open circles and green open triangles mark the estimates based on the FUV to IR excess as described by Buat et al. (2005). Filled blue triangles indicate late-type galaxies for which the SFRs are derived from the FUV after estimating the extinction using the β slope method of Meurer et al. (1999). The dashed line is the one-to-one relation. The histogram of the ratios for each method is indicated in the right panel.

the contribution of thermally pulsing AGB stars, we applied the color correction as described in Zibetti et al. (2009) for the CB07 (Charlot & Bruzual 2007 libraries), where a is −1.513 and b is 0.750 for the same colors. As we can see in Fig. 2, the masses estimated by the model ($M_{\rm model}$) agree with the Zibetti et al. (2009) ones. This was somewhat expected as this recipe was calibrated using the same models. However, there are some outliers, such as HCG40f, for which the model was not able to estimate the stellar mass very well since there were not enough observations to constrain its SED well.

The rate at which a galaxy forms stars is one of its most important properties, especially in interacting systems, which evolve very rapidly as they are consuming the available gas. In the absence of narrow-band imaging of the hydrogen recombination lines (i.e. Hα), two of the most common ways to estimate the SFR rely on prescriptions using their UV broad band emission from GALEX or the 24 μm thermal dust emission from *Spitzer*/MIPS.

Since a significant fraction of the bolometric luminosity of a galaxy is absorbed by interstellar dust and re-emitted in the thermal IR, mid-IR observations can probe the dusty interstellar medium and dust-enshrouded SFRs. The efficiency of the IR luminosity as a SFR tracer depends on the contribution of young stars to heating of the dust and the optical depth of the dust in the star-forming regions. Calzetti et al. (2007) using a wealth of multiwavelength observations for 33 SINGs galaxies provided the recipe

$$SFR_{24}\left(M_\odot, {\rm yr}^{-1}\right) = 1.27\times10^{-38}\left(L_{24}({\rm erg\ s}^{-1})\right)^{0.885} \tag{2}$$

to calculate the SFR from the 24 μm luminosities obtained with *Spitzer*. We used this formula to estimate the SFR of the galaxies in our sample and display them in Fig. 3. As we can see, the 24 μm estimates and those from the model fit to the whole SED agree fairly well, because they have a ratio with a median value of unity and a standard deviation of 0.51dex. The scatter does not seem to correlate with the galaxy mass or luminosity. To examine whether the scatter is due to the absence of far-IR measurements, for a large fraction of the galaxies in our sample we selected 35 galaxies for which IRAS and Akari fluxes were available and fit them again with the model, this time removing the far-IR points. We then compared the new estimates of the SFRs with the ones when all data were used and found that they were very similar, their average ratio being 0.95 and the corresponding standard deviation 0.19. A possible explanation for the scatter between the results of the model and the Calzetti et al. (2007) method could be related to variations in the metallicity of the galaxies (i.e. Rosenberg et al. 2008). Another factor that may influence the SFR values, related to the star formation history of the galaxies, is that in the da Cunha et al. (2008) model the SFRs are averaged over 100 Myr, while the Calzetti et al. (2007) assumes a timescale of 10 Myr.

In the UV the integrated spectrum is dominated by young stars, so the SFR scales linearly with luminosity; however, in order to use the UV to trace SFR, we have to correct the attenuated UV fluxes for dust extinction. One method to do this is to use the β-slope correction,

$$\beta({\rm GALEX}) = \frac{\log(f_{\rm FUV}) - \log(f_{\rm NUV})}{\log(\lambda_{\rm FUV}) - \log(\lambda_{\rm NUV}))} \tag{3}$$

where $f_{\rm FUV}$ and $f_{\rm NUV}$ are the flux densities per unit wavelength in the FUV and NUV bands respectively, $\lambda_{\rm FUV}$ = 1520 Å, and $\lambda_{\rm FUV}$ = 2310 Å. Then we can apply the relation of Meurer et al. (1999) to starburst galaxies,

$$L_{\rm FUV,\,cor} = 10^{0.4(4.43+1.99\beta)}L_{\rm FUV,\,obs}, \tag{4}$$

where $L_{\rm obs}$ and $L_{\rm cor}$ are the observed and extinction corrected FUV luminosities. Finally, we can derive the SFRs using the relation of Salim et al. (2007):

$$SFR_{\rm FUV}(M_\odot\,{\rm yr}^{-1}) = 6.84\times10^{-29}\,L_{\rm FUV,\,cor} \tag{5}$$

for Chabrier IMF.

The SFRs of the early-type galaxies cannot be estimated using this method since the β-slope is mainly determined by the old stellar population rather than the dust extinction and thus their extinction-corrected UV luminosities are completely overestimated. Even for late-type galaxies, though, when we compare in Fig. 3 the FUV estimates of the SFR with the corresponding values obtained with the model, we find that the former are overestimated by a factor of 0.56 dex with a global scatter of 0.46 dex. We attribute this to the calibration of the extinction correction of Meurer et al. (1999), who used a sample of local UV-selected starburst galaxies with high dust content, quite dissimilar to the HCG galaxies. As discussed in detail by Kong et al. (2004), this leads to overestimating the UV corrected luminosities and consequently to an overestimate of the SFRs. Indeed, when we plot the FIR-to-UV luminosities of our galaxies against the spectral slope (β-slope), we notice that at a fixed β all the galaxies have systematically lower ratio of total to FIR-to-UV luminosities than the starburst galaxies of Meurer et al. (1999). On the other hand, galaxies HCG16c and HCG16d, which are IR luminous ($L_{\rm IR} > 10^{11}\ L_{\odot}$), have SFRs that are very similar to those derived by the model (10.02 and 1.52 $M_{\odot}\ {\rm yr}^{-1}$, respectively).

Since, the previous method overestimates the SFR, we can also use the relation of Buat et al. (2005). These authors used the IR-to-UV luminosity ratio to quantify the dust attenuation in the FUV band of GALEX for a wider sample consisted of more quiescent galaxies. The formula they derived to correct for dust extinction is described by the relation

$$A_{\rm FUV} = 0.0333y^3 + 0.3522y^2 + 1.1960y + 0.4967 \quad (6)$$

where $y = \log(F_{\rm dust}/F_{\rm FUV})$ is the ratio of the IR-to-UV flux densities. To derive these ratios for our galaxies we used the IR luminosities estimated by our SED modeling, as well the observed UV luminosities, and estimated the SFR using the formula (4) of Iglesias-Páramo et al. (2006):

$$\log[SFR_{\rm FUV}(M_{\odot}\ {\rm yr}^{-1}) = 0.63 \times (\log[L_{\rm FUV,\,corr}(L_{\odot})] - 9.51) \quad (7)$$

where the $L_{\rm FUV,\,corr}$ is the extinction-corrected FUV luminosity (in $L_{\odot}$), and the factor of 0.63 has been introduced to correct for the Chabrier IMF (Chabrier 2003; da Cunha et al. 2008). The results are presented in Fig. 3 in green. We notice that the ratios of the SFRs are uniformly distributed around ~1.05 displaying a scatter of 0.56 dex and also agree with the 24 μm estimates. Given the success of the model in a variety of systems (see da Cunha et al. 2008, 2010a,b) we base the remaining of the analysis in the model derived SFRs.

4. Results

4.1. Evolutionary state of the groups

To study the star formation properties of HCGs groups, Bitsakis et al. (2010) separated them into dynamically "young" and dynamically "old". We classified a group as dynamically "young" if at least 75% of its galaxies are late-type. Conversely, a group is dynamically "old" if more than 25% of its galaxies are early-type. It is known that the sSFR is a tracer of the star formation history of a galaxy, and galaxies in compact groups do experience multiple encounters with the various group members. Consequently, we would expect that a young group is more likely to have more late-type galaxies, since its members would not have enough time to experience multiple interactions that would trigger star formation, consume the available gas, and transform them into early-type systems. Furthermore, these late-type galaxies would not get built up much of their stellar mass. They would still have larger amounts of gas and dust, as well as higher SFRs and sSFR. On the other hand, if a group is dominated by early-type systems, it would be dynamically "old", since interactions and possible merging of its members over its history would have led to the formation of some of those ellipticals. As a result, the spirals in these groups would have already built some of their stars, and their sSFR would be lower. In our present sample, ten groups (HCG2, 7, 16, 38, 44, 47, 54, 59, 91, & 100) are classified as dynamically "young" and the remaining 22 as dynamically "old" (see Table 7).

We notice that in the majority of the groups (80%) that are classified as dynamically "old", the most massive galaxy that dominates is an early-type galaxy displaying a median stellar mass of $1.2 \times 10^{11}\ M_{\odot}$. In all dynamically "young" groups, the dominant galaxy is late-type, with a median stellar mass of $5.1 \times 10^{10}\ M_{\odot}$. These most massive galaxies of each group, are marked with a star in Table 4. Even though there are just ten dynamically "young" groups in our sample and we could be affected by small number statistics, we note that dynamically "old" groups have on average 4.7 members in each, more than the "young" groups, which only have four members.

A different classification of the HCGs into three phases, 1, 2, and 3, based on their HI gas content has been proposed by Verdes-Montenegro et al. (2001). In the first phase, the HI gas is mainly associated with the disks of galaxies. In the second, 40–70% of the HI is found in the disks of the galaxies, and the rest has been stripped out, due to tidal stripping, into the intragroup medium. Finally, in the third phase are groups with almost all their HI located outside of member galaxies, or in a common envelope engulfing most group members. Using this classification, Borthakur et al. (2010) classify 14 of the groups in our sample, and the results are presented in Table 7. Both ours, as well as the Verdes-Montenegro et al. (2001) classification method, are based on how galaxy interactions and merging affect the morphology of the group members, thus they are related to their evolution. There is global agreement between the two methods for 12 of the 14 groups we have in common. We discuss these in more detail in Sect. 4.6.

4.2. The physical properties of HCG galaxies

We now use the results of the SED modeling, described in the previous section, to examine the physical parameters of the galaxies in our sample and compare them with the ones derived for the comparison samples. The large number of galaxies, a total of 135 in 32 groups, is enough to produce statistically significant results in order to explore these parameters.

In panel a of Fig. 4 we present the distributions of the stellar masses separated in early- (E's and S0's) and late-type (S's and Irr's) galaxies in groups. We can see that the distributions are not too different because a two-sided Kolmogorov-Smirnov (KS) suggests that the probability ($P_{\rm KS}$) that the two samples are drawn from the different populations is ~0.04. The median stellar masses of the late and early-type galaxies in our sample are $1.78^{+0.79}_{-0.55} \times 10^{10}\ M_{\odot}$ and $4.07^{+0.72}_{-0.60} \times 10^{10}\ M_{\odot}$ respectively. One might have expected that the late-type galaxies would have much lower stellar masses than the early-types since the latter have had more time to increase their stellar mass as they converted their gas into star and/or resulted from the merging of late type systems. However, as we know tidal interactions play an important role in triggering star formation in galaxies (Struck 1999). Compact groups have high galaxy density, display signs of interaction (e.g. Verdes-Montenegro et al. 2001), and contain galaxies that are actively forming young stars. Furthermore, as

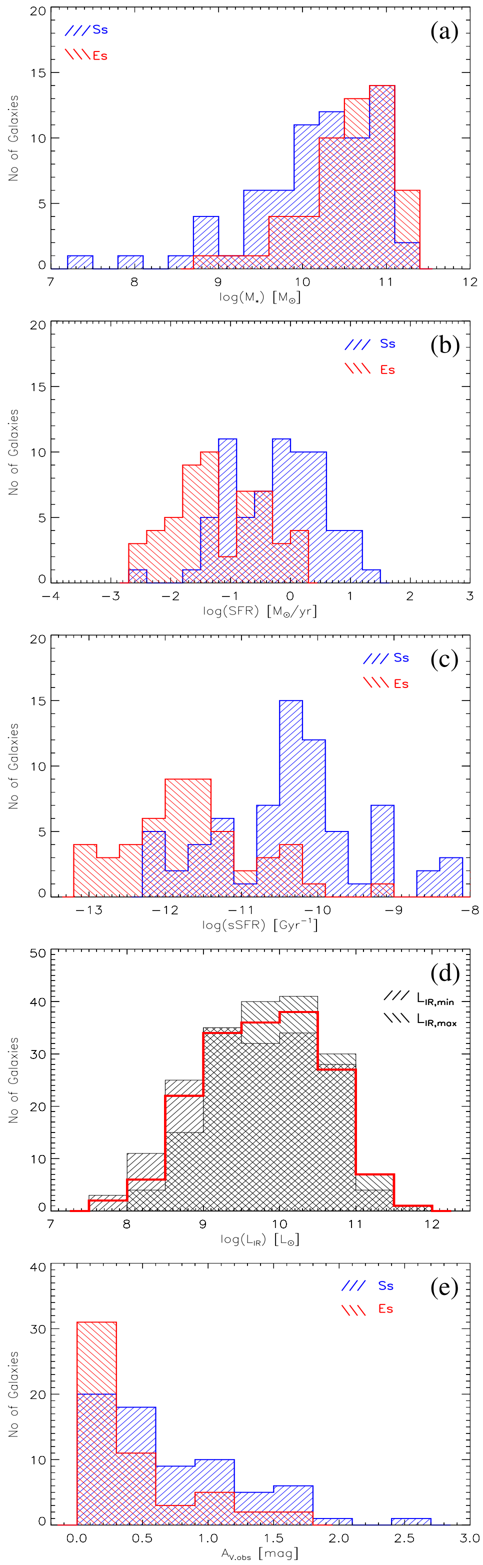

Fig. 4. Histograms of several properties of our HCG sample. Early type galaxies are marked in red and late type galaxies in blue: **a)** the distributions of the stellar masses (M_*), **b)** the distributions of the star formation rates (SFR), **c)** the distributions of specific SFR (sSFR), and **d)** the histogram of the IR luminosities, $L_{\rm IR}$, in red, as estimated by our SED modeling. Because of the absence of far-IR observations for most of the sample, we overplot in hashed areas the histograms corresponding to the minimum and maximum $L_{\rm IR}$ of each galaxy, associated to the 16th and 84th percentile ranges of the best fit, respectively, **e)** a histogram of the extinction inferred from the SED fit ($A_{V,\rm obs}$) as measured model-derived atttenuated and unattenuated SED (see Sect. 3.1.3).

we showed in the previous section, most of the massive late-type galaxies are found in dynamically “old” groups. We thus believe that several of the HCG late-type galaxies have already increased their stellar mass, thanks to past tidal encounters. We examine these galaxies and their properties more specifically in the next section.

In Fig. 4b we present the distributions of the SFRs of early and late-type galaxies in groups. As expected, most of the late-type galaxies have higher SFRs than the early-type systems, their median SFR being $0.60^{+0.12}_{-0.14}$ $M_\odot$ yr^{-1} compared to $0.05^{+0.02}_{-0.01}$ $M_\odot$ yr^{-1}. The maximum SFR seen in our sample is ~26 $M_\odot$ yr^{-1}, typical of starbursts in the luminous IR galaxy (LIRG) range. We should note that there are eight early-type galaxies with relatively high SFRs (~1–5 $M_\odot$/yr), which is more than an order of magnitude higher than what is observed in the rest of the sample. We discuss these galaxies in more detail in Sect. 4.4.

In panel c of Fig. 4 we display the distributions of the sSFRs of our sample. We can see that there are late-type galaxies with rather low sSFRs (~10^{-12} yr^{-1}). These galaxies, which belong to dynamically “old” groups, must have had already increased their stellar masses, thus decreasing their sSFRs, as a consequence of dynamically triggered star formation events due to past interactions. On the other hand, there are early-type galaxies that display rather high sSFRs (~10^{-10} yr^{-1}). One explanation is that accretion and merging of gas rich dwarf companions has increased the gas content of these galaxies, and they are currently forming stars. However, it is also possible that these galaxies are misclassified, dust obscured, edge-on late-type systems. In Sects. 4.3 and 4.4 we examine the sSFR distribution in more detail as a function of the dynamical state of each group, study the mid-IR and optical colors of the galaxies and compare them with our control samples.

In Fig. 4d we present the distribution of the $L_{\rm IR}$ as estimated from the da Cunha et al. (2008) model. Since no far-IR observations were available for most of the galaxies (74%) in our sample, the $L_{\rm IR}$ cannot be robustly constrained. Using the minimum and the maximum values of the probability distribution functions for each galaxy as reported by the model, we create two additional histograms corresponding to the low and high values. We observe that the overall shape and median value of the distribution does not change substantially. The median $L_{\rm IR}$ of the sample is $5.0^{+3.0}_{-0.9} \times 10^9 L_\odot$ and most of the HCG galaxies are not IR luminous ($L_{\rm IR} \geq 10^{11} L_\odot$). There are only seven galaxies, HCG4a, HCG16c, HCG16d, HCG38b, HCG91a, HCG92c and HCG95a, with $L_{\rm IR} > 10^{11} L_\odot$. These are all late-type systems, and they are detected in the far-IR, and the first five are found in dynamically “young” groups.

As we discussed in Sect. 3.1.3 we can use the model-derived attenuated (observed) and unattenuated SEDs to estimate the V-band optical depth ($A_{V,\rm obs}$) for each galaxy. Two histograms of these values, for the early and late-type systems, are presented in Fig. 4d. The median $A_{V,\rm obs}$ is 0.23 ± 0.17 mag and 0.58 ± 0.36 mag for the early and late-type galaxies, respectively. We observe that there are eight (~14%) of the early-type galaxies, with extinctions similar to what is seen in dusty late-type galaxies (≥1 mag). These are HCG4d, HCG55c, HCG56b, HCG56d, HCG56e, HCG71b, HCG79b, and HCG100a. We should note that these galaxies are the ones forming the tail of early-type galaxies with high SFRs and sSFRs, mentioned above. That they appear to have larger amounts of dust than what one may expect for early-type galaxies, as well as the fact that

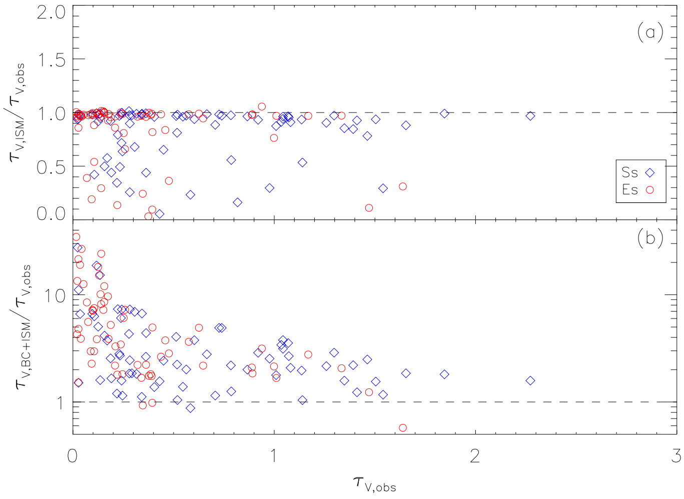

Fig. 5. a) Ratio of the intrinsic $\tau_{V,\mathrm{ISM}}$ derived by the model over the observed (attenuated spectrum) $\tau_{V,\mathrm{obs}}$ versus the $\tau_{V,\mathrm{obs}}$. The dashed line is the one-to-one ratio. The red circles represent the early-type galaxies in HCGs, and the blue diamonds the late-type ones. **b)** Ratio of the intrinsic τ_V for stars in birth clouds, derived by the model over the observed $\tau_{V,\mathrm{obs}}$ versus the $\tau_{V,\mathrm{obs}}$, using the same notation. We excluded 6 galaxies from the plot (HCG44a, HCG47a, HCG47b, HCG56b, HCG59a, and HCG68a) since their χ^2 of model-fit was more than 9.00 and the derived τ fairly uncertain (see Table 3).

they display higher star formation activity, further supports the idea that these may indeed be misclassified as late-type systems.

The model of da Cunha et al. (2008) also estimates the total effective V-band absorption optical depth of the dust seen by a young star ($\tau_V = \tau_{V,\mathrm{BC}} + \tau_{V,\mathrm{ISM}}$) inside the stellar birth clouds, and the fraction of the absorption (μ) contributed by dust found in the diffuse ISM along the line of sight. The emission from young stars is more attenuated than from old stars. In young stars the extinction is dominated by the dust of the surrounding birth clouds with an additional component due to the dust in the diffuse ISM traversed by their light. Older stars (>100 Myr), which have dispersed their birth clouds, are only affected by the dust found in the diffuse ISM. Consequently, one would expect that in early-type galaxies, where currently no recent star formation is taking place, the optical light would be dominated by the old stars, and therefore, the representative obscuration would be that of the ambient ISM. In late-type galaxies the total extinction would be the contribution of both components, BC and ISM. In that case, each component will contribute differently, depending on how much of the optical energy production in the galaxy is due to stars within the birth clouds. We would like to emphasize that since both components can contribute to a different extent at different wavelengths, the representative extinction of a galaxy also varies with wavelength, and that is why we consider only optical light here, instead of referring to the total energy output of the galaxy.

Using the output of the model, we can thus estimate the optical depth contributed from the diffuse ISM, $\tau_{V,\mathrm{ISM}} = \mu\,\tau_V$, and the optical depth from the stellar birth clouds, $\tau_{V,\mathrm{BC}} = (1-\mu)\,\tau_V$. In Table 4 we present the optical depth derived from the attenuated and unattenuated SED, $\tau_{V,\mathrm{obs}}$, the $\tau_{V,\mathrm{ISM}}$, as well as the total optical depth seen by young stars inside stellar birth clouds, $\tau_V = \tau_{V,\mathrm{BC}} + \tau_{V,\mathrm{ISM}}$. In Fig. 5, we plot the ratios of the intrinsic, model-derived optical depth (ISM and BC+ISM components) versus the observed optical depth, $\tau_{V,\mathrm{obs}}$, that we measured from the SED. We note that in most galaxies the ratio of $\tau_{V,\mathrm{ISM}}$ over $\tau_{V,\mathrm{obs}}$ is very close to unity. For these galaxies, in particular for those with low extinction values, it is the dust in the ISM that determines the overall absorption of the emitted radiation. The contribution of the BC component is a small fraction of the overall light. On the other hand, there are 28 galaxies with ratios lower than unity. From these, 18 are classified as late-type, half of them belong to dynamically "young" groups, and ten are classified as early-type, six of which we believe are likely misclassified late-type systems (see Sect. 4.4 and Appendix). In the bottom panel of the same figure we plot the ratio of total τ_V over the $\tau_{V,\mathrm{obs}}$, versus the $\tau_{V,\mathrm{obs}}$. We notice that there are galaxies with very high τ_V over $\tau_{V,\mathrm{obs}}$ values at small $\tau_{V,\mathrm{obs}}$, most of which are early-type systems. Even though these galaxies have had recent (<100 Myr) star formation events, this does not dominate their global emission. We do note, though, that as the $\tau_{V,\mathrm{obs}}$ increase, the ratio converges towards unity, implying that the contribution of light from young stars in the BC component becomes a considerable fraction of the total emission, making the obscuration seen by the newly formed stars more representative of the observed obscuration of the galaxy.

4.3. HCG late-type galaxies

It is well established that interactions can trigger star formation in galaxies (i.e. Struck 1999). During an interaction between two late-type galaxies, their atomic gas, as is typically found in diffuse clouds, collide. Shocks are produced that in turn increase the local gas density, thus triggering bursts of star formation. That the group environment has played an important role in the evolution of its member galaxies is evident since the fraction of early-type systems in groups is higher that what is found in the field, so one would expect that, because of their proximity, the late-type galaxies in groups would display different star formation properties from the ones in the field. However, in a preliminary analysis of 14 groups, Bitsakis et al. (2010) found that overall there is no evidence that the SFR and sSFR in late-type galaxies of HCG is different from galaxies in the field or in early-stage interacting systems. Interestingly though, when they separated their HCG sample into two subsamples, namely the dynamically "old" and dynamically "young" groups (see Sect. 4.1 for the definition), late-type galaxies in dynamically "old" HCGs showed lower sSFRs than those in dynamically "young" groups. This was attributed all the likely past interactions experienced in the dynamically "old" groups, which would lead to a faster increase in their stellar mass compared to galaxies in young group. The higher stellar mass would reduce their current sSFR, even if subsequent gas accretion would result in star formation activity in them.

We re-examined this issue using our larger sample of 32 groups that contains 73 late-type galaxies and derived their sSFR, as well as the one of the control samples, using the SED model of da Cunha et al. (2008). The results are shown in Fig. 6 and Table 3. Galaxies in dynamically "young" groups have a median sSFR of $8.51^{+4.07}_{-2.75} \times 10^{-11}\ \mathrm{yr}^{-1}$, while s$SFR$ = $2.75^{+2.03}_{-1.16} \times 10^{-11}\ \mathrm{yr}^{-1}$ for galaxies in the dynamically "old" groups. Similarly, galaxies in interacting pairs have an sSFR = $11.20^{+3.67}_{-2.70} \times 10^{-11}\ \mathrm{yr}^{-1}$ and in field galaxies sSFR = $15.30^{+5.65}_{-4.29} \times 10^{-11}\ \mathrm{yr}^{-1}$. An analysis using a two-sided KS test indicates that there is no statistical difference between the samples of late-type galaxies in dynamically "young" HCGs and those of the SINGs and interacting pair samples ($P_{\mathrm{KS}} > 0.80$). However, the same KS test reveals that the late-type galaxies in dynamically "old" groups, with a median sSFR that is more than three times lower,

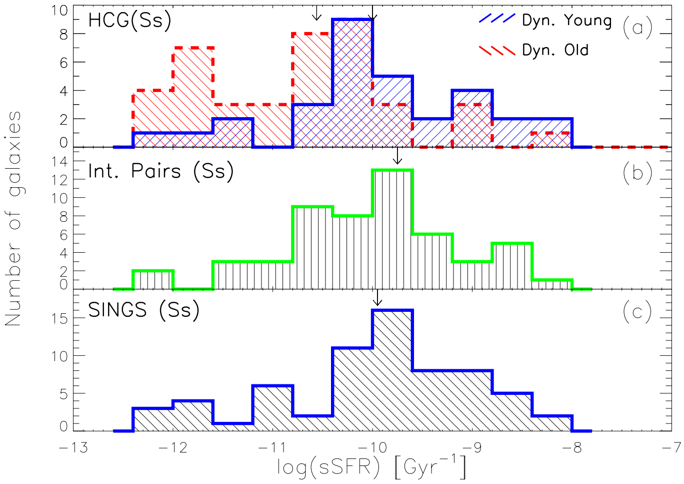

Fig. 6. Histograms of the sSFR of the late-type galaxies our three samples, estimated by modeling their SED. The top plot displays in blue the histogram of the sSFR of the 31 late-type galaxies found in dynamically-young, spiral-dominated groups. Overplotted in red is the corresponding histogram of the 42 galaxies in dynamically-old elliptically dominated groups. The middle and bottom plots present the histograms of the 52 late-type galaxies in the Smith et al. (2007a) interacting galaxy pairs, as well as the 71 SINGS late-type galaxies. The arrows indicate the median sSFR value of each distribution.

cannot be drawn from the same parent distribution as the three other samples ($P_{\rm KS} \sim 10^{-3}$). Investigating in more detail the reason for this disparity, we find that it cannot be attributed to depressed SFR, but instead it is due to a substantially more massive stellar content (~$3 \times 10^{10}\ M_{\odot}$), similar to what is found in early-type systems. This confirms the results and interpretation of Bitsakis et al. (2010), who relies on semi-empirical estimates of the sSFR on a smaller galaxy sample. Based on those findings one would also expect that owing to their higher stellar mass, the late-type type galaxies in dynamically "old" groups should have redder UV and optical colors than late-type galaxies in the field. We examine this in Sect. 4.5.

4.4. HCG early-type galaxies

We showed in the previous section that the group environment affects the star formation history of the late-type members by increasing their stellar mass in the process of transforming them into early-type systems. However, is there any evidence that the early-type galaxies in groups are distinctly different from similar galaxies found in the field? Based on our SED modeling, we have already shown in Fig. 4 that nearly 15% of all early-type galaxies have SFRs and dust extinction similar to what is seen in late-type systems. We suggested that there are two possible explanations for this. One was that they were simply misclassified as Es or S0s, while they are edge-on in fact late-type systems. The second was that even if they are early-type, based on their optical morphology, these galaxies they have experienced minor merging with gas/dust rich dwarf companions in the groups, which has increased their gas content, star formation activity, and dust extinction.

According to Hickson (1982) the classification of the HCG galaxies was performed using their morphological features, optical colors, and sharpness of the edge of the image. For all groups of our sample, though, we also have *Spitzer* mid-IR images that provide additional information on their properties. It is well known that the mid-IR spectra of the star-forming

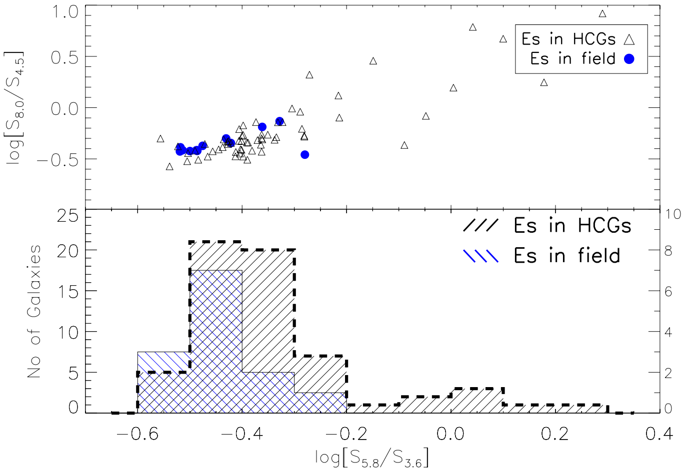

Fig. 7. *Top panel*: IRAC color–color plot of the early-type galaxies in HCGs (black open triangles) and a sample of field ellipticals (blue filled circles). *Bottom panel*: the histograms of the log[$S_{5.8}/S_{3.6}$] color of the two samples. The early-type galaxies in the groups are marked with a black line (left axis), while the field ellipticals are presented in blue (right axis).

galaxies, in addition to continuum emission due to warm dust, are also filled with a series of broad emission features between 3 and 18 μm, which can contribute up to 20% of their total IR luminosity (Dale et al. 2005; Smith et al. 2007b). These features are the vibrational modes of polycyclic aromatic hydrocarbons (PAHs), which absorb UV photons from newly born stars and re-emit them in the mid-IR. Typically only late-type galaxies with active star formation and dust emit strongly in these bands. Some PAHs have also been detected in some early-type systems, but they display peculiar PAH-band ratios (Bressan et al. 2006; Kaneda et al. 2008; Panuzzo et al. 2011).

To probe the properties of the early-type galaxies in the groups, we examined their mid-IR colors and compare them with isolated ellipticals in the field, which are not expected to have PAH emission. In Fig. 7 we use our *Spitzer*/IRAC photometry and plot the 8.0 to 4.5 μm flux density ratio as a function of the 5.8 to 3.5 μm ratio for both the early-type galaxies of our HCG sample, and the control sample of field ellipticals. Weak PAHs would result in low values of both ratios since the 6.2 and 7.7 μm features, which contribute ~50% of the total PAH emission, are sampled by the 5.8 and 8.0 μm IRAC filters (Smith et al. 2007b). Indeed, we observe that most of the early-type galaxies in groups, as well as in the field, are concentrated in the lower left hand part of the color–color plot of Fig. 7. These galaxies are very close to the (−0.4, −0.5) locus of pure stellar photospheric emission where the flux density in the mid-IR scales with λ^{-2}. Consequently, they are expected to have very weak dust and PAH emission. On the other hand, the upper right quadrant of the figure should be populated by galaxies with strong PAH features and possibly some hot dust contribution, as a result of intense star formation and/or AGN activity. As expected, no field ellipticals are seen in this quadrant. However, there is a "tail" of ten early-type HCG galaxies (~16% of the total) extending to this part of the plot (for log[$f_{5.8}/f_{3.6}$] > −0.25). Examining the 5.8 to 3.5 μm IRAC color distributions of HCG and field with a KS test, we find that they are different ($P_{\rm KS} \sim 0.005$). The early-type galaxies with red IRAC colors are HCG4d, HCG40f, HCG55c, HCG56b, HCG56d, HCG56e, HCG68a, HCG71b, HCG79b, and HCG100a. We note that HCG40f and HCG68a are at the left hand edge of the color selection, and it is possible that contamination from a red nearby companion is affecting their mir-IR fluxes. All these galaxies are examined in more detail in the Appendix, where we display their SEDs, Ks-band contour plots, and "true color" composites based on their *Spitzer*/IRAC mid-IR images. Based on this analysis and previous suggestions, we propose that seven of them, HCG4d, HCG55c, HCG56d, HCG56e, HCG71b, HCG79b, and HCG100a are likely dust-obscured late-type systems. Furthermore, if HCGd and HCG71b are indeed late-type galaxies, then their groups must be reclassified as dynamically "young" (instead of "old"). In the rest of this paper we consider them as such (see Tables 6 and A.1).

4.5. Bimodality in HCG galaxy colors

In the previous sections, we have examined several of the physical parameters of our HCG sample as derived by the SED modeling. To examine the evidence of evolution due to the group environment more thoroughly, we now compare all our results based on the UV, optical, and IR imaging, as well as the available spectroscopic diagnostics.

Several studies of galaxies have revealed a bimodality in the UV-optical colors of galaxies in field and in clusters (e.g. Wyder et al. 2007; Haines et al. 2008). This type of bimodality in the colors of the late- and early-type galaxies is real and directly connected to the original galaxy classification scheme by Hubble. It appears quite strongly in the NUV-r color distribution of a sample and consists of two peaks, called the "red sequence" and the "blue cloud", and a minimum in between them identified as the "green valley" (see Strateva et al. 2001). Wyder et al. (2007) have examined a sample of over 18 000 galaxies observed with GALEX and SDSS and showed that an NUV-r versus M_r color magnitude diagram can be used to separate them into (i) passively evolving, (ii) star-forming and (iii) AGN components. Passively evolving galaxies are confined to the "red sequence" (NUV-r $>$ 5), with few showing blue UV-optical colors, while all blue galaxies, with NUV-r $<$ 3, are spectroscopically classified as star forming (see also Haines et al. 2008). AGN seem to dominate the area of the green valley" (3 $<$ NUV-r $<$ 5). The small fraction of galaxies in the "green valley" can be understood from the fact that galaxies do not spend so much time at these colors. Using Starburst99 (see Leitherer et al. 1999) we simulated the evolution of a stellar population typical of a spiral galaxy assuming solar metallicity and either a continuous star formation (of 1 $M_\odot$ yr^{-1}) or a single starburst (producing total stellar mass of 10^6 $M_\odot$). Depending on the assumptions, we find that the colors of the population place it within the "blue cloud" just for ~5–7 Myr, and after spending only ~1–5 Myr transiting through the "green valley", it remains in the "red sequence" for the rest of its lifetime. Thus this color bimodality emerges from the nature of the galaxies as they evolve through time.

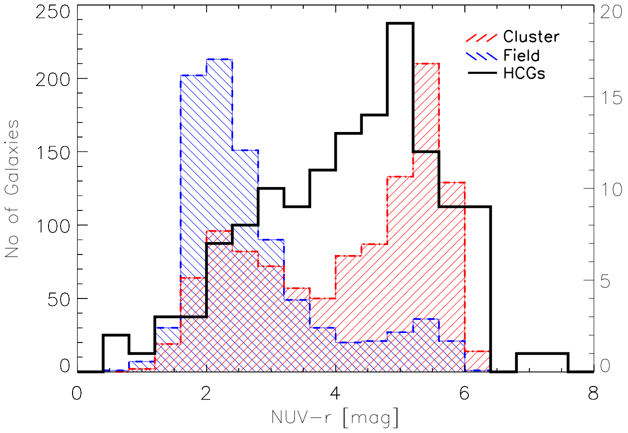

Fig. 8. NUV-r histogram of our HCG galaxy sample shown in black (right *Y*-axis). The histograms of the field, in blue, and cluster galaxies, in red, from the Haines et al. (2008) control sample are also presented (left *Y*-axis).

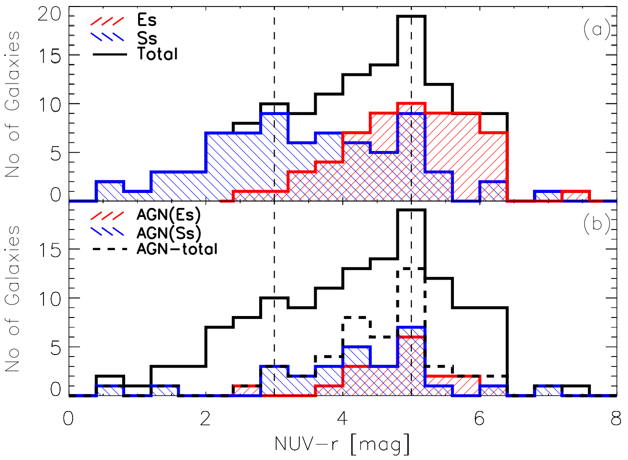

Fig. 9. a) NUV-r histogram of the whole HCG galaxy sample is shown in black. The corresponding histograms of the early- and late-type galaxies of the sample, classified according to their optical morphology, are shown with the red and blue shaded areas. **b)** The NUV-r distribution of the galaxies hosting an AGN is indicated with the dashed dark line. As above, the early- and late-type hosts are indicated with the red and blue histograms. The region of 3 $<$ NUV-r $<$ 5, identified as "green valley", is marked with the vertical dashed lines.

In Fig. 8 we plot the NUV-r colors of our HCG sample, and compare them with the field and cluster galaxies of the Haines et al. (2008) sample. The three regions of the color space discussed by Wyder et al. (2007) are clearly visible. On the left, near NUV-r ~ 2, we identify the "blue cloud" where the field galaxy distribution peaks. Nearly 58% of the total number of field galaxies is found within 0.5 mags of this color. Few of the galaxies in clusters (15%) are also seen in this area. To the right, near NUV-r ~ 5.5, we observe the "red sequence" where most (51%) of the cluster galaxies are concentrated. Only 16% of the field galaxies are found in the "red sequence". The "green valley" is between the two peaks and is mostly (34%) populated by cluster galaxies (Haines et al. 2008). When we examine the HCG NUV-r color distribution, we note a clear difference. Only 17% of their galaxies are in the "blue cloud", a fraction similar to what is found for galaxies in clusters. However, the majority (73%) of the HCG galaxies are concentrated in the "green valley" and "red sequence" areas. A likely explanation would be that most of the HCG galaxies are already passively evolving or that they are in the process of moving from the star-forming region to the "red sequence". This is consistent with compact groups having a higher fraction of elliptical galaxies than the field. Another possibility is that some of these galaxies are in fact late-type systems that have redder colors so move to the right on the plot, because of dust extinction or the presence of a substantial older stellar population (post starburst galaxies), or both. This is expected from our earlier findings regarding the missclassification of a fraction of the early-type galaxies in the HCG and the lower sSRF in dynamically "old" groups.

To study in more detail how the NUV-r color distribution of the HCG galaxies is affected by their morphology and nuclear activity, we present in Fig. 9 the corresponding histograms based on their optical morphologies, as well as their nuclear spectral

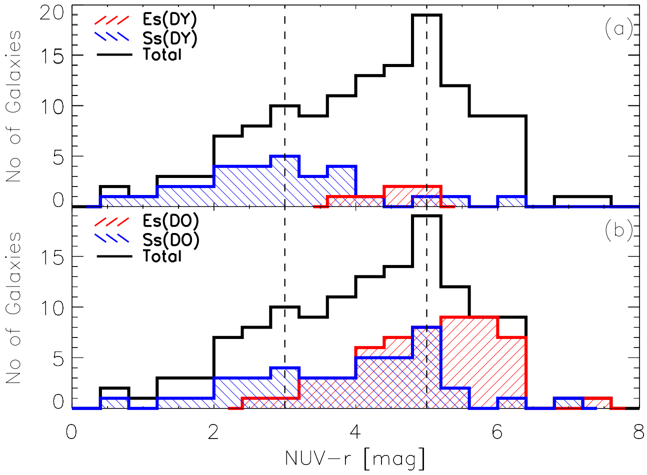

Fig. 10. **a)** NUV-r histogram of our HCG galaxy sample shown as a black solid line. The corresponding histograms of the early- and late-type galaxies found in dynamically "young" groups are shown with the red and blue shaded areas, respectively. **b)** Same as in **a)**, but for the galaxies in dynamically "old" groups. The region of 3 < NUV-r < 5, identified as "green valley", is marked with the vertical dashed lines.

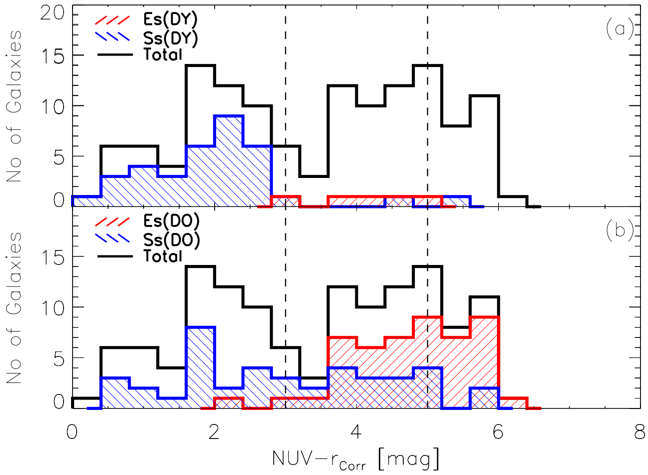

Fig. 11. A histogram of the NUV-r colors of the HCG sample after correcting for dust extinction, in shown with the black solid line. The separation in two panels for "young" and "old" groups as well as the symbols follow the notation of Fig. 10.

classification. We note that only 36% of the late-type galaxies are found within the "blue cloud"; however, the majority of the HCG galaxies, almost 60%, are located in the "green valley" and in the "red sequence" (~13%). In Fig. 9b we present the same plot as at the top, but only for the galaxies of our sample that have an optically identified AGN. The whole distribution is shown, while the distributions of early- and late-type AGN hosts. We performed a two-sided KS test between the distribution of galaxies hosting an AGN and the total distribution of the HCG galaxies, and we conclude that there is no statistical difference in their NUV-r colors ($P_{\rm KS} \sim 0.25$). This suggests that the presence of an AGN does not substantially affect the UV-optical color of the galaxies in HCGs.

As we described earlier, more than 40% of the galaxies in our sample host an AGN in their nucleus. This, in addition to the code of da Cunha et al. (2008) not including the contribution of an AGN to the SED of a galaxy, could bias some of our results, in particular the SFR, sSFR, and the $L_{\rm IR}$. Using the IRAC color–color AGN diagnostics introduced by Stern et al. (2005), we investigated the influence of the AGN to the mid-IR SED of the galaxies in our sample. Only three systems, HCG6b, HCG56b, and HCG92c, have mid-IR SEDs that are consistent with a strong power-law continuum emission, which indicates a strong AGN in their nucleus. For all remaining galaxies, the optically identified AGN does not dominate their SED, so that their physical parameters estimated by our model are considered reliable.

To explore the color variations as a function of the evolution state of the groups, we plot in Fig. 10 the histograms of the early- and late-type galaxies found in the dynamically "young" and "old" groups, respectively. Observing the top panel we find that almost 60% of the late-type galaxies in dynamically "young" groups are located within the "blue cloud", and 43% of them, for which nuclear spectra were available, host an AGN in their nucleus. There are also three outlier galaxies (HCG16b, HCG44a, and HCG59a) that have red NUV-r colors (>5 mag). It is possible that these systems have built up their stellar mass in the past and that their UV/optical colors are currently dominated by emission from old stars. In addition, past tidal interactions probably stripped some of their gas in the intragroup medium, thereby decreasing the fuel necessary for current star formation. In dynamically "old" groups, the late-type galaxies are redder, and as we can see in Fig. 10b, most of them (>63%) are located within the "green valley". As in dynamically "young" groups there are also four galaxies (HCG22b, HCG40d, HCG68c, and HCG71a) in these groups, which are found in the "red sequence".

Overall 45% of the early-type galaxies, shown in red in Fig. 9, are located within the "red sequence" and the rest are along the "green valley". As we mentioned earlier, these systems are expected to be passively evolving and thus, their colors should be dominated by old stellar populations. We find that this is the case for most of them, as only two are found in the "blue cloud". We believe that these galaxies are misclassified, as late-type galaxies (see Sect. 4.4), and we examine them in more detail in the Appendix. From Fig. 10a we see that all early-type galaxies in the dynamically "young" groups are in the in the "green valley". One could suggest that they were already early-type before reaching the group, and the interactions and/or merging of dwarf companions in the group environment triggered the star formation activity and provide extra gas. However, the most likely explanation is that these are group galaxies that are currently migrating from the "blue cloud" to the "red sequence". In that case, the morphological transformation should accompany the color transformation. Indeed, the galaxies located in bluer colors (around NUV-r ~ 4) are lenticulars, while the ones at NUV-r ~ 5 are ellipticals. Similarly, in the bottom panel of Fig. 10 we see that more than half of the early-type galaxies in dynamically "old" groups are located within the "green valley". These galaxies are mostly (>70%) S0/SB0's. However, there is a large fraction (~25%) of elliptical galaxies that have the same colors. We suggest that, even though the morphology of a galaxy typically determines its colors, there are several of the group ellipticals that move back to bluer colors due to interactions and/or merging in the compact group environment.

As discussed before, we know that the UV-optical colors of a galaxy, are not only affected by its star formation history, but also by dust extinction. Thus, it would be useful to understand how much of the observed variation in colors is due to intrinsic extinction in the galaxies. Especially for the late-type galaxies, which are located within the "green valley", we have to examine whether their colors are affected more from dust or whether it is because they contain a substantial old stellar population. Our

SED model allows us to estimate and to correct for dust attenuation, so we plot in Fig. 11 the distributions of the corrected NUV-r colors of the early- and late-type galaxies in dynamically "young" (top panel) and dynamically "old" groups (bottom panel). We notice in panel a) that almost all late-type galaxies in "young" groups move back to the "blue cloud", suggesting that it is the dust that plays a dominant role in their apparent colors. On the other hand, 40% of the late-type galaxies in dynamically "old" groups still remain in the "green valley" after the extinction correction. It seems that in those it is the old red stars that dominate their UV/optical colors. This also agrees with the results of Sect. 4.3 where these galaxies display low sSFRs. Moreover, one can notice the large fraction of early-type galaxies that, after the extinction correction, move to the "green valley" (~50% of the galaxies at these colors). These galaxies display high sSFRS ($\sim 0.21 \times 10^{-11}$ yr^{-1}), so their bluer colors are possibly due to higher levels of current star formation. We should note that even though for most galaxies the observed optical extinction derived from the SED model (A_V) is not very high (see Fig. 4e and Table 3), this translates to over 2 mags of correction in the NUV due to the steepness of the extinction curve.

Since dust appears to affect the UV colors of HCG galaxies, one could suggest the use of their mid-IR colors, because they trace the light that was originally absorbed by the dust grains in the UV-optical. In Fig. 12 we present the IRAC color–color diagram, also shown in Bitsakis et al. (2010), using our new, larger sample. The physical meaning of this plot was described extensively in Fig. 7. We notice that most of the late-type galaxies are located in the upper right quadrant of the plot, while most of the early-types are in the lower left. The ten early-type galaxies that display red mid-IR colors are the ones we mentioned in Sect. 4.3. We observe that between the colors $-0.1 < \log[f_{8.0}/f_{4.5}] < 0.3$ and $-0.25 < \log[f_{5.8}/f_{3.6}] < -0.10$, there is a lower density of galaxies. Johnson et al. (2007) and Tzanavaris et al. (2010) propose that this "gap" is related to an accelerated migration of the galaxies from star forming to quiescent. When we compare this result to Fig. 11 we notice that the galaxies in the upper right quadrant of the IRAC color–color plot are the ones with NUV-r < 2.5, while galaxies located in the lower left portion of the figure have NUV-r > 3.5. We finally notice that the lower galaxy density area appears in both figures and actually separates the star forming ("blue cloud") from the passive evolving ("green valley" and "red sequence") galaxies. Therefore we suggest that the color bimodality observed in the extinction-corrected UV-optical colors is also observed in the mid-IR and possibly emerges from the same physical properties of the galaxies.

How significant is this "gap"? Walker et al. (2010) compared their sample of 12 HCGs with several control samples including the SINGS and interacting pair sample we used, as well as galaxies from the Coma cluster, and the local legacy volume sample (LVL Dale et al. 2009). They conclude that the mid-IR color distribution of HCG galaxies is not seen in the field, but it is seen in galaxies of the Coma infall region. However, in their analysis they combine the SINGS and LVL galaxies as a single local galaxy sample. As we mentioned, though, in Sect. 2.6.1, the SINGS sample was selected to explore the mid-IR properties of various galaxy types seen in the local universe, but it is not representative of a flux or volume limited population (Kennicutt et al. 2003). This selection biases the statistics of the colors of the sample. In contrast, the LVL sample is volume limited, since it contains all known galaxies inside a subvolume of 3.5 Mpc and an unbiased sample of spiral and irregular galaxies within the larger, more representative, 11 Mpc volume. The mid-IR colors of the LVL sample are plotted in Fig. 12. Performing a two-sided KS-test between the distributions of the IRAC colors ($\log[f_{8.0}/f_{4.5}]$ and $\log[f_{5.8}/f_{3.6}]$) of HCG and LVL samples, we find that the distributions are not significantly different displaying $P_{\mathrm{KS}} = 0.035$ and $P_{\mathrm{KS}} = 0.028$, respectively. This suggests that there is no strong evidence that an accelerated evolution of galaxies in HCG is responsible for a significant fast change in their global mid-IR colors.

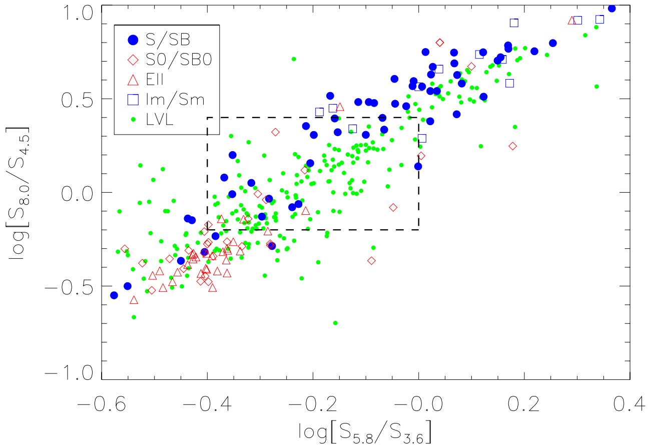

Fig. 12. The IRAC color–colors plot, originally presented in Fig. 7. Blue circles indicate the spiral galaxies of our HCG sample, blue squares are the irregulars, red triangles are the elliptical galaxies, and red diamonds the lenticular ones. Green dots indicate the LVL galaxies. According to Johnson et al. (2007) the "gap" is located in the area enclosed by the dashed lines.

4.6. Dynamical properties of HCG galaxies

As we mentioned in Sect. 4.1 we classified the dynamical state of our sample depending on the fraction of elliptical galaxies they contain. Our method is related to their evolution since it is known that galaxy interactions and merging, transform galaxies from late-type systems to ellipticals. Thus, groups with excess of early-type members are likely to be older and more compact. To investigate this, we estimated the projected distance of each galaxy from the other members of the same group members, as well as the virial radius of each galaxy. To calculate the projected distance between the group members we used the great circle distance relation. Then, using the relation described in Park & Hwang (2009), we estimated the virial radius with the formula

$$r_{\mathrm{vir}}(\mathrm{Mpc}) = \left(\frac{3\gamma L \Omega_{\mathrm{m}}}{800\pi\rho_{\mathrm{m}}}\right)^{1/3}, \tag{8}$$

where $L = 10^{-0.4(\mathrm{M_r}+20.00)}$ is the r-band luminosity in $L_\odot$, M_r the absolute r-band magnitude of the galaxy, γ the mass to light ratio (1 or 2 for late- and early-type galaxies, respectively), and $\rho_{\mathrm{m}} = 0.0223\, h^3$ Mpc^{-3} is the mean density of the universe, with $h = 0.72$ and $\Omega_{\mathrm{m}} = 0.27$. Keeping in mind that compact groups may not be fully virialized dynamical systems, we present our results in Table 6. We note that, indeed, the member galaxies are statistically closer to their nearest neighbors in dynamically "old" groups, having a mean projected distance of 26 kpc compared to 37 kpc for the dynamically "young" groups.

However, galaxies in groups are interacting not only with their nearest neighbors, but also with all other group members, since in all cases the virial radii of the galaxies are substantially

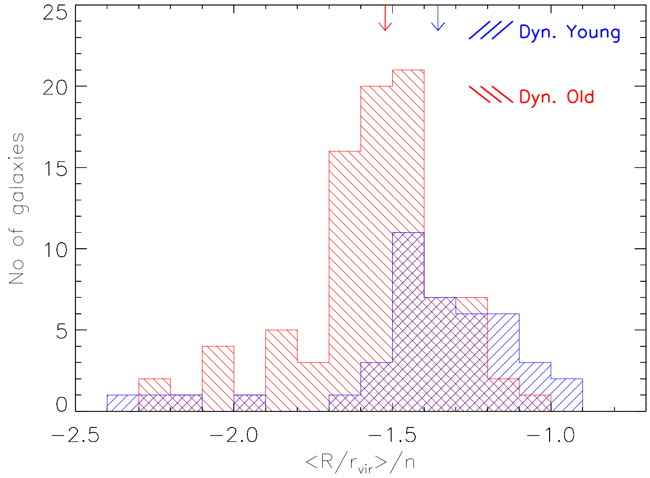

Fig. 13. Histograms of the "strength" of the dynamical interaction felt by each group galaxy ($\langle R/r_{\rm vir,nei}\rangle/n$). As usual, we separate our sample into dynamically "young" (blue) and dynamically "old" (red) groups. The arrows indicate the median values of the two distributions.

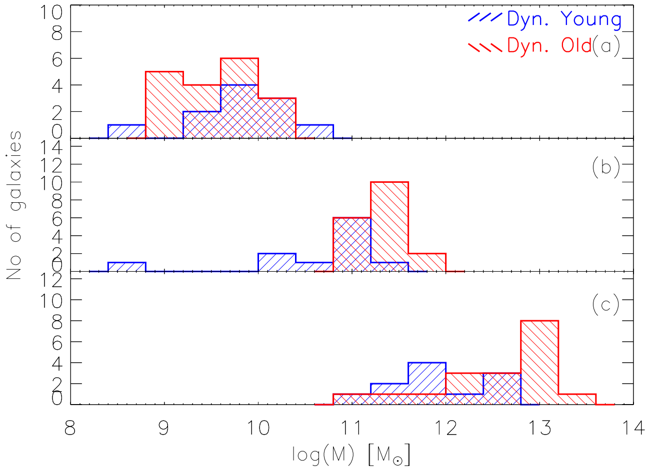

Fig. 14. a) Distributions of the total HI masses in the dynamically "young" (in blue) and the dynamically "old" (in red) groups, of the total stellar masses (panel **b)**) and the total dynamical masses (panel **c)**).

larger than the linear size of their group (see Table 6). To better quantify this effect we followed the approach of Hwang et al. (2010) by introducing the parameter of the "strength" of the interaction ($\langle R/r_{\rm vir,nei}\rangle/n$). This is estimated by averaging the ratios of the projected distances over the virial radii for all the neighbors of each galaxy and divide them by the total number of neighbors (n). This quantity provides an empirical measure of the interaction strength each galaxy experiences from its companions. The smaller this parameter, the stronger the dynamical influence of the companions.

In Fig. 13, we plot the distributions of the strengths according to the dynamical state of each group. Since we have SDSS data for only 74 galaxies and Eq. (6) relies on the SDSS r-band magnitude to compute the virial radius, we used the SED model fits to estimate the synthetic r-band magnitudes for the remaining of the sample. We observe that the "strength" parameter of dynamically "old" groups is indeed smaller than in dynamically "young" groups, suggesting that in the former the gravitational effects are stronger. A KS test between the two distributions confirms that the two distributions are significantly different ($P_{\rm KS} \sim 10^{-5}$). Moreover, if we compare our results with the findings of Hwang et al. (2010), we see that the distances between the galaxies in groups and those of the centers of rich clusters are similar (both have $R < 0.5$ $\rm r_{vir}$). We can also estimate the velocity dispersion, σ_r, of each galaxy from the most massive-central galaxy of its group, using the published velocities from Hickson et al. (1992). Galaxies in dynamically "old" groups display mean velocity dispersion of 408 ± 50 km s^{-1}, which is the half of what is observed in the Virgo cluster, in contrast to those in dynamically "young" groups which is about 132 ± 39 km s^{-1}. All these facts lead us to the conclusion that dynamically "old" groups, as their name implies, are older, denser, and more evolved systems, since their properties are intermediate between those of rich clusters and dynamically "young" groups.

To further examine the dynamical properties of these groups, we can calculate their dynamical masses using the projected mass estimator from Bahcall & Tremaine (1981):

$$M_{\rm dyn} = \frac{24}{\pi {\rm GN}} \sum_{i=1}^{N} u_i^2 R_i, \qquad (9)$$

where u_i is the difference in the recessional velocity between the group member i and the central massive object (see Table 4 where the most massive objects in each group are marked with a star), R_i is the projected distance from the central object, and N is the number of group members. This dynamical mass can be compared to the various components of the baryonic mass of the groups. The stellar mass is derived from our SED modeling, while the total atomic hydrogen mass, $M_{\rm HI}$, is available for 29 of the groups from Verdes-Montenegro et al. (2001). Unfortunately, the mass of the molecular hydrogen, $M_{\rm H_2}$, is only available for 12 groups (Martinez-Badenes et al. 2011). We note that, even though the integrated masses of the molecular and atomic hydrogen of the groups are often similar, on average they are both ~25 times less massive that the stellar component. These results are summarized in Table 7. In Fig. 14 we separate our 32 groups in the two subsamples of dynamically "young" and "old" groups and present the corresponding histograms of the distributions of their atomic hydrogen, stellar, and dynamical masses.

We observe that the stellar mass distribution of dynamically "old" groups, shown in Fig. 14b is markedly different from for dynamically "young" groups. A KS test confirms this, as the probability that the two are drawn from the same parent distribution is $P_{\rm KS} \sim 0.009$. The median stellar mass of the dynamically "old" groups is $\sim 1.95 \times 10^{11}$ $M_\odot$, more than double what is seen in the "young" group subsample ($\sim 8.90 \times 10^{10}$ $M_\odot$). This is understood on the basis of our classification scheme; dynamically "old" groups do have more elliptical galaxies, which are typically more massive than spirals. Furthermore, from the analysis of Sect. 4.3, we have shown that the late-type galaxies of these groups also have redder optical colors.

Surprisingly, though, in Fig. 14a we note that the HI mass distribution is fairly similar in both subsamples ($P_{\rm KS} \sim 0.26$), with a median value of HI mass $\sim 3.2 \times 10^9$ $M_\odot$. Assuming that dynamically "old" groups are older structures, with more early-type members that have already converted during a merging process a fraction of their gas into stars, it is not clear that what we see is a real "conspiracy", given the difference in star formation properties and relative amount of old stellar populations of the two subsamples. We know that a fraction of the HI gas is expelled from the galaxies to the intragroup medium in the form of plumes, and long filaments as a group evolve progressively, transforming the morphology of its members from late- to early-type (Verdes-Montenegro et al. 2001). However, the lifetime of these structures before they either change phase, as they interact with the hot intragroup gas, or are accreted back to the group members is not well constrained, since only a dozen of HCGs have high spatial resolution maps of their gas component.

Examining the distributions of the dynamical masses of the two subsamples in panel c of the same figure, we find that, as was the case with the stellar mass, these are also different ($P_{\rm KS} \sim 0.008$). The dynamically "old" groups display a median dynamical mass of 6.46×10^{12} $M_{\odot}$, nearly an order of magnitude higher from what is seen in the "young" ones (4.77×10^{11} $M_{\odot}$). The dynamical masses do not simply scale with the stellar mass of the subsamples, which only differ by a factor of ~2. Furthermore, there is no indication of a variation in the ratio between the dark matter, as probed by the kinematics, and the baryonic matter in groups, or that there is a systematic error in the estimates of the dynamical mass due to one subsample being less virialized than the other. As a result, one could attribute the deficit in the observed baryons in the dynamically "old" to a component of hot intragroup gas, since there is clear evidence that groups with more early type systems have stronger X-ray emission (Ponman et al. 1996; Mulchaey et al. 2003).

In Table 7 we also present our classification of the 32 groups, based on the fraction of the early-type members, as well as the classification based on their HI morphology proposed by Verdes-Montenegro et al. (2001) for 13 groups where this was available. Despite the small number statistics, we note that there is overall agreement. Groups that we consider as dynamically old are in Phase 3 or 2 according to their HI content, while groups that we consider dynamically "young" are in Phase 1 or 2. There are two exceptions in this. HCG79, the so-called "Seyferts' Sextet" was classified by us as dynamically "old", but it is Phase 1 based on the distribution of its HI gas by Borthakur et al. (2010). Inspecting it closely we see that our definition is probably marginal as the system does not have an elliptical galaxy and its two early-type members are peculiar S0s. The other case is HCG44, which was classified as Phase 3 by Borthakur et al. (2010). The group consists of three late-type galaxies and NGC 3193, an E2 which Aguerri et al. (2006) argue that may be an interloper. Close inspection of the HI map of the group shown in Fig. 2 of (Williams et al. 1991) reveals that nearly all gas emission is associated with the three late-type systems, and only a small fraction is seen outside the galaxy disks. We would thus argue that this system is more likely in Phase 1 or 2, which would be consistent with our classification as dynamically "young". Therefore, as expected, a change in the galaxy morphology also carries a change in the distribution of the atomic hydrogen within the group, and vice versa.

4.7. Diffuse cold dust in the intragroup medium

We mentioned earlier that by using the model of da Cunha et al. (2008) we were able to derive several of the physical properties of the galaxies in our sample. Even though a number of parameters, such as stellar mass and SFR, can be estimated with good accuracy, the lack of deep high spatial resolution wide field far-IR imaging, makes it very challenging to constrain the $L_{\rm IR}$ and accurately estimate the amount of cold dust in each galaxy.

As described in Bitsakis et al. (2010), there are several reasons to expect that the interactions among group members have expelled diffuse cold dust along with atomic gas in the intragroup medium. In this preliminary work we had investigated the contribution of each galaxy to the total far-IR emission of its group and identified nine of the 14 groups, in which extended cold dust emission may be present. In the present work, using our larger sample of 32 groups and the physical model of da Cunha et al. (2008), we have repeated the same analysis. In Fig. 15 we plot the fraction of the integrated IRAS flux densities at 60 and 100 μm for each group as measured by Allam et al. (1996) divided by the sum of the flux densities of all group members predicted by our SED model fit. The results are presented in Table 7. We identify 13 groups (HCG6, 7, 16, 25, 55, 57, 67, 68, 71, 75, 79, 91, and 95) where diffuse cold dust emission may be present. These results agree with the previous of Bitsakis et al. (2010) with HCG37 be the only exception. Moreover, ten of these groups are dynamically "old". This agrees with the notion that dynamically "old" groups are more evolved and their members have experienced more encounters enriching the intragroup medium. It is possible that part of the apparent far-IR excess is due to the uncertainties introduced by our SED fits. Only far-IR imaging with the *Herschel* Space Telescope will enable us to reliably characterize the composition and structure of the intragroup medium, as well as study the evolution of the cold dust in these systems.

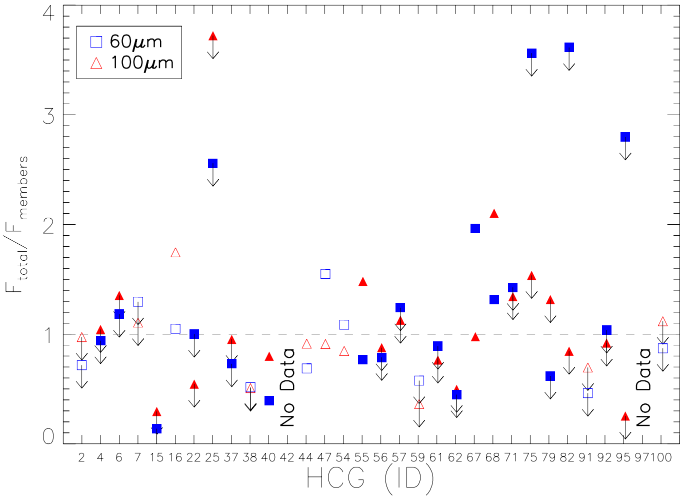

Fig. 15. Plot of the ratio of the observed IRAS 60 and 100 μm fluxes of each group divided by the corresponding flux all group members as predicted by our model fits. Since IRAS did not resolve/detect all the members of each group, several of the ratios are indicated as upper limits. Filled symbols indicate dynamically "old" groups.

5. Conclusions

In this paper we have presented the first multiwavelength analysis, from the UV to the IR, of the 135 galaxies that are members of 32 HCGs and studied the influence of the group environment in their evolution. Based on the theoretical modeling of their SEDs we conclude the following

- The classification of the evolutionary state of HCGs according to the fraction of their early-type members appears to be physical and is in general agreement with previous classifications. The study of their properties suggest that dynamically "old" groups are more compact and have higher velocity dispersions. They also display higher stellar masses than the "young" ones, while both have similar HI mass distributions. However, "old" groups have nearly an order of magnitude higher dynamical masses than "young" groups.
- The late-type galaxies in dynamically "old" groups display lower sSFRs since the multiple past interactions have already converted a fraction of their gas into stars, thereby increasing their stellar masses. This is also the main reason for these galaxies showing redder NUV/optical colors than field spirals. However, there are few spiral galaxies in these groups

that display even redder colors. They all have very low SFRs, similar to early-type systems. We speculated that tidal interactions must have stripped the gas out of their disk suppressing their star formation activity.

- Most early-type galaxies in dynamically "old" groups, seem to migrate from the star-forming to the quiescent galaxy colors, even though a fraction of them (~25%) display bluer colors and higher star formation activity than normal field ellipticals, possibly owing to gas accretion from other group members, as well as, to the merging of dwarf companions.
- Late-type galaxies in dynamically "young" groups have similar star formation properties to field, and early-stage interacting pair spiral galaxies.
- Even though nearly 46% of the HCG members have an optically identified AGN, we find no evidence either of enhanced AGN activity at any stage of the group's evolution or of the optical/mid-IR colors of the galaxies.
- Our analysis suggests that the reported lower density of galaxies in the IRAC color–color diagram is caused by the morphological natural bimodality of galaxies, and it is similar to what is also observed in the UV-optical colors.
- Our SED model suggests that in 13 groups, ten of which are dynamically "old", there is diffuse cold dust in the intragroup medium.
- There are ten galaxies with mid-IR colors, SEDs, and star formation properties that are inconsistent with their optical classification as early-type systems. We suggest that seven of them are likely to be nearly edge-on late-type galaxies that were misclassified owing to their small size and dust extinction.

Acknowledgements. T.B., V.C., and T.D.S. would like to acknowledge partial support from the FP7-REGPOT 206469 grant. We would like to thank H. S. Hwang, D. Elbaz, and P.-A. Duc (CEA/Saclay, France) for useful discussions that improved the paper, as well as U. Lisenfeld (Univ. of Granada) for providing the CO data for a number of groups prior to publication.

References

Aguerri, J. A. L., Castro-Rodríguez, N., Napolitano, N., Arnaboldi, M., & Gerhard, O. 2006, A&A, 457, 771
Allam, S., Assendorp, R., Longo, G., Braun, M., & Richter, G. 1996, A&AS, 117, 39
Bahcall, J. N., & Tremaine, S. 1981, ApJ, 244, 805
Bell, E. F., McIntosh, D. H., Katz, N., & Weinberg, M. D. 2003, ApJS, 149, 289
Bertin, E. 2008, SWarp, http://astromatic.iap.fr/software/swarp
Bertin, E., & Arnouts, S. 1996, A&AS, 117, 393
Bitsakis, T., Charmandaris, V., Le Floc'h, E., et al. 2010, A&A, 517, A75
Bressan, A., Panuzzo, P., Buson, L., et al. 2006, ApJ, 639, L55
Bicay, M. D., & Giovanelli, R. 1987, ApJ, 321, 645
Bruzual, G., & Charlot, S. 2003, MNRAS, 344, 1000
Borthakur, S., Yun, M. S., & Verdes-Montenegro, L. 2010, ApJ, 710, 385
Buat, V., Iglesias-Páramo, J., Seibert, M., et al. 2005, ApJ, 619, L51
Calzetti, D., Kennicutt, R. C., Engelbracht, C. W., et al. 2007, ApJ, 666, 870
Chabrier, G. 2003, PASP, 115, 763
Charlot, S., & Fall, S. M. 2000, ApJ, 539, 718
da Cunha, E., Charlot, S., & Elbaz, D. 2008, MNRAS, 388, 1595
da Cunha, E., Eminian, C., Charlot, S., & Blaizot, J. 2010a, MNRAS, 403, 1894
da Cunha, E., Charmandaris, V., Díaz-Santos, T., et al. 2010b, A&A, 523, A78
Dale, D. A., Bendo, G. J., Engelbracht, C. W., et al. 2005, ApJ, 633, 857
Dale, D. A., Cohen, S. A., Johnson, L. C., et al. 2009, ApJ, 703, 517
Fazio, G. G., Hora, J. L., Allen, L. E., et al. 2004, ApJS, 154, 10
Haines, C. P., Gargiulo, A., La Barbera, F., et al. 2007, MNRAS, 381, 7
Haines, C. P., Gargiulo, A., & Merluzzi, P. 2008, MNRAS, 385, 1201
Hernquist, L., Katz, N., & Weinberg, D. H. 1995, ApJ, 442, 57
Hao, L., Strauss, M. A., Tremonti, C. A., et al. 2005, AJ, 129, 1783
Hickson, P. 1982, ApJ, 255, 382
Hickson, P., Kindl, E., & Auman, J. R. 1989, ApJ, 70, 687
Hickson, P., Mendes de Oliveira, C., Huchra, J. P., & Palumbo, G. G. 1992, ApJ, 399, 353
Hwang, H. S., Elbaz, D., Lee, J. C., et al. 2010, A&A, 522, A33
Iglesias-Páramo, J., Buat, V., Takeuchi, T. T., et al. 2006, ApJS, 164, 38
Johnson, K. E., Hibbard, J. E., Gallagher, S. C., et al. 2007, AJ, 134, 1522
Kaneda, H., Onaka, T., Sakon, I., et al. 2008, ApJ, 684, 270
Kauffmann, G., Heckman, T. M., Tremonti, C., et al. 2003, MNRAS, 346, 1055
Kennicutt, R. C., Jr., Armus, L., Bendo, G., et al. 2003, PASP, 115, 928
Kewley, L. J., Groves, B., Kauffmann, G., & Heckman, T. 2006, MNRAS, 372, 961
Kong, X., Charlot, S., Brinchmann, J., & Fall, S. M. 2004, MNRAS, 349, 769
Leitherer, C., Schaerer, D., Goldader, J. D., et al. 1999, ApJS, 123, 3
Mamon, G. A. 1986, ApJ, 307, 426
Martinez, M. A., Del Olmo, A., Coziol, R., & Perea, J. 2010, AJ, 139, 1199
Martinez-Badenes, V., Lisenfeld, U., Espada, D., et al. 2011, A&A, submitted
McConnachie, A. W., Ellison, S. L., & Patton, D. R. 2008, MNRAS, 387, 1281
Mendes de Oliveira, C., & Hickson, P. 1994, ApJ, 427, 684
Meurer, G. R., Heckman, T. M., & Calzetti, D. 1999, ApJ, 521, 64
Morrissey, P., & GALEX Science Team 2005, A&AS, 20717903M
Mulchaey, J. S., Davis, D. S., Mushotzky, R. F., & Burstein, D. 2003, ApJS, 145, 39
Okada, Y., Murakami, N., Yasuda, A., et al., AKARI FIS Data Users Manual, Version 1.3, http://www.ir.isas.jaxa.jp/ASTRO-F/Observation/
Panuzzo, P., Rampazzo, R., Bressan, A., et al. 2011, A&A, 528, A10
Park, C., & Hwang, H. S. 2009, ApJ, 699, 1595
Ponman, T. J., Bourner, P. D. J., Ebeling, H., & Bohringer, H. 1996, MNRAS, 283, 690
Rieke, G. H., Young, E. T., Engelbracht, C. W., et al. 2004, ApJS, 154, 25
Rosenberg, J. L., Wu, Y., Le Floc'h, E., et al. 2008, ApJ, 674, 814
Salim, S., Rich, R. M., Charlot, S., et al. 2007, ApJS, 173, 267
Shimada, M., Ohyama, Y., Nishiura, S., Murayama, T., & Taniguchi, Y. 2000, AJ, 119, 2664
Skrutskie, M. F., Cutri, R. M., Stiening, R., et al. 2006, AJ, 131, 1163
Slater, S. K., Charmandaris, V., & Haynes, M. P. 2004, BAAS, 36, 728
Smith, B. J., Struck, C., Hancock, M., et al. 2007a, AJ, 133, 791
Smith, J. D. T., Draine, B. T., Dale, D. A., et al. 2007b, ApJ, 656, 770
Stern, D., Eisenhardt, P., Gorjian, V., et al. 2005, ApJ, 631, 163
Strateva, I., Ivezić, Ž., Knapp, G. R., et al. 2001, AJ, 122, 1861
Struck, C. 1999, Phys. Rep., 321, 1
Temi, P., Brighenti, F., & Mathews, W. G. 2004, AJ, 633, L25
Tzanavaris, P., Hornschemeier, A. E., Gallagher, S. C., et al. 2010, ApJ, 716, 556
Verdes-Montenegro, L., Yun, M. S., Williams, B. A., et al. 2001, A&A, 377, 812
Véron-Cetty, M.-P., & Véron, P. 2006, A&A, 455, 773
Walker, L. M., Johnson, K. E., Gallagher, S. C., et al. 2010, Galaxy Wars: Stellar Populations and Star Formation in Interacting Galaxies, 423, 88
Williams, B. A., McMahon, P. M., & van Gorkom, J. H. 1991, AJ, 101, 1957
Wyder, T., Martin, D. C., Schiminovich, D., et al. 2007, ApJ, 173, 293
Zibetti, S., Charlot, S., & Rix, H.-W. 2009, MNRAS, 400, 1181

Pages 18 to 29 are available in the electronic edition of the journal at http://www.aanda.org

Table 4. The morphological type and derived physical parameters based on the SED modeling of the HCG galaxies.

HCG galaxy	Morphological type	χ^2	$\tau_{V,\mathrm{obs}}$	$\tau_{V,\mathrm{ISM}}$	$\tau_{V,\mathrm{BC+ISM}}$	M_{star} $\times 10^9\ M_\odot$	SFR $M_\odot\ \mathrm{yr}^{-1}$	sSFR $\times 10^{-11}\ \mathrm{yr}^{-1}$	L_{IR} $\times 10^9\ L_\odot$
2a*	SBd	2.38	0.11	0.05	0.67	3.86	2.18	57.81	14.45
2b	cI	2.96	0.52	0.42	1.16	3.56	1.75	48.64	32.35
2c	SBc	1.66	0.17	0.10	0.64	4.24	0.43	10.28	3.17
4a*	Sc	5.47	0.36	0.16	1.60	69.18	7.29	10.52	169.8
4b	Sc	5.22	0.13	0.11	0.63	7.62	0.41	5.37	4.09
4d	E4	5.96	0.53	0.51	0.94	12.88	0.96	7.41	1.46
6a*	S0a	2.65	0.13	0.14	1.98	87.1	0.01	0.01	15.84
6b$^{\clubsuit}$	Sab	5.69	0.24	0.23	1.45	77.62	0.05	0.07	21.87
6c	E5	5.49	0.10	0.10	0.70	58.88	0.01	0.01	4.38
6d	Sbc	1.38	0.19	0.09	0.32	3.78	0.07	2.19	6.05
7a*	Sb	2.07	0.61	0.57	2.27	74.13	1.65	2.19	2.40
7b	SB0	3.58	0.17	0.17	1.68	38.90	0.14	0.36	0.77
7c	SBc	4.37	0.34	0.33	0.38	23.44	1.61	6.92	33.88
7d	SBc	8.61	0.03	0.02	0.65	8.85	0.32	3.16	4.38
15a	Sa	5.59	0.09	0.10	0.64	81.28	0.10	0.11	14.45
15b	E0	4.60	0.24	0.24	0.82	40.74	0.05	0.11	2.40
15c*	E0	8.73	0.07	0.08	0.42	107.15	0.02	0.02	3.86
15d	E2	2.06	0.48	0.18	1.35	24.55	0.01	0.32	8.64
15e	Sa	7.30	0.44	0.03	0.67	25.70	0.06	0.22	3.99
15f	Sbc	7.65	0.81	0.14	0.30	2.07	0.28	14.03	2.67
16a	Sba	5.95	0.92	0.85	2.65	50.12	4.14	7.76	0.63
16b*	Sab	3.41	0.12	0.11	2.19	63.10	0.04	0.07	1.78
16c	Im	2.11	1.09	0.99	2.25	11.75	8.18	69.5	72.4
16d	Im	6.86	1.26	1.14	2.72	30.20	1.45	4.79	2.61
22a*	E2	2.19	0.10	0.09	0.31	70.79	0.01	0.07	100.0
22b	Sa	2.55	0.24	0.17	0.38	5.52	0.01	0.06	89.12
22c	SBc	4.02	0.22	0.08	0.26	3.37	0.19	7.76	1.48
25a	SBc	5.86	0.29	0.54	1.13	13.18	9.61	71.94	3.48
25b*	SBa	5.62	0.03	0.03	0.31	69.18	0.16	0.23	0.85
25d	S0	3.58	0.14	0.14	3.40	11.48	0.05	0.58	3.06
25f$^{\spadesuit}$	S0	4.24	0.04	0.04	0.15	8.17	0.05	0.60	0.17
37a*	E7	5.26	0.24	0.24	0.45	128.82	0.18	0.14	1.38
37b	Sbc	4.15	0.74	0.73	3.63	74.13	0.58	0.78	26.91
37c	SBd	3.86	0.73	0.71	3.56	17.38	0.08	0.46	1.41
37d	SBdm	4.70	0.24	0.25	1.77	0.89	0.15	17.66	75.85
37e	E0	5.26	0.21	0.20	0.70	1.65	0.03	1.95	1.20
38a	Sbc	3.40	1.03	0.95	3.53	46.77	2.18	4.68	23.44
38b*	SBd	7.82	1.06	1.17	3.07	50.12	4.60	8.51	0.34
38c	Im	2.49	1.07	1.03	2.87	23.44	1.40	5.62	0.75
40a*	E3	0.85	0.57	0.57	2.10	165.96	0.22	0.13	38.90
40b	S0	2.30	0.89	0.87	1.65	83.18	0.36	0.43	12.88
40c	Sbc	4.24	1.46	1.13	3.64	69.18	2.39	3.47	3.21
40d	SBa	3.02	1.07	1.02	3.79	52.48	0.59	1.12	45.70
40e	Scd	3.65	1.50	1.40	2.33	14.13	0.66	4.27	5.03
40f$^{\spadesuit}$	E1	5.13	0.02	0.02	0.58	6.64	0.01	0.01	1.00
42a*	E3	3.38	0.15	0.15	1.09	245.47	0.05	0.02	2.58
42b	SB0	7.92	0.16	0.15	1.09	25.12	0.01	0.01	16.21
42c	E2	2.66	0.46	0.15	1.87	20.89	0.02	0.09	20.89
42d	E2	2.54	0.35	0.03	0.67	3.52	0.01	0.13	77.62
44a*	Sa	11.89	0.34	0.34	2.29	36.31	0.07	0.20	7.62
44b	E2	7.09	0.38	0.38	0.66	19.95	0.03	0.17	17.78
44c	SBc	3.93	0.29	0.29	0.54	5.46	0.11	2.09	22.90
44d	Sd	8.52	0.31	0.31	0.57	0.64	0.63	98.17	7.53
47a*	Sbc	10.46	0.54	0.53	0.76	95.5	3.07	3.16	1.74
47b	E3	9.66	0.34	0.33	0.57	75.86	0.30	0.39	0.70
47c	Scd	3.33	1.04	1.01	3.27	15.14	0.93	6.03	43.65
47d	Sdm	3.63	0.14	0.13	0.22	16.98	0.48	2.75	104.71
54a*	Sdm	7.78	1.84	1.84	3.34	0.39	3.07	16.53	34.67
54b	Im	5.67	1.41	1.31	1.74	0.07	0.20	49.26	0.78
54c	Im	2.35	1.13	0.61	1.19	0.02	0.08	23.44	40.73
54d	Im	4.36	0.98	0.30	2.48	0.01	0.03	32.51	33.88
55a	E0	5.80	0.36	0.35	0.81	93.33	0.40	0.42	64.56
55b	S0	4.03	0.26	0.17	1.87	70.79	0.02	0.03	36.30
55c*	E3	1.68	0.94	1.01	2.96	112.2	1.17	1.05	14.45
55d	E2	2.89	0.18	0.18	0.98	30.20	0.08	0.26	0.07
56a	Sc	4.68	0.52	0.51	0.54	17.78	0.70	3.89	12.58
56b$^{*\clubsuit}$	SB0	17.21	1.34	1.29	2.75	34.67	1.69	4.79	2.17
56c	S0	8.28	0.22	0.03	0.40	26.30	0.05	0.20	4.69

Notes. $^{(*)}$ The most massive galaxy of each group, used in the calculations of the dynamical masses in Table 5. $^{(\spadesuit)}$ Galaxies with no 24 μm data. The SFRs, sSFRs, and L_{IR} of these systems are not well constrained. $^{(\clubsuit)}$ An AGN in their nucleus dominates their mid-IR emission.

Table 4. continued.

HCG galaxy	Morphological type	χ^2	$\tau_{V,\mathrm{obs}}$	$\tau_{V,\mathrm{ISM}}$	$\tau_{V,\mathrm{BC+ISM}}$	M_{star} $\times 10^9\ M_\odot$	SFR $M_\odot\ \mathrm{yr}^{-1}$	sSFR $\times 10^{-11}\ \mathrm{yr}^{-1}$	L_{IR} $\times 10^9\ L_\odot$
56d	S0	5.05	1.01	0.98	1.69	10.23	0.42	4.07	0.08
56e	S0	4.91	0.32	0.31	0.71	4.29	0.23	5.37	4.04
57a[*]	Sbc	7.75	0.28	0.29	1.20	177.83	0.76	0.43	4.33
57b	SBb	4.15	0.28	0.28	0.52	83.18	0.49	0.60	1.43
57c	E3	4.00	0.06	0.05	0.66	87.10	0.01	0.01	1.80
57d	SBc	2.31	0.22	0.18	1.64	13.80	1.77	12.22	46.77
57e	S0a	4.74	0.89	0.87	1.86	91.20	0.19	0.20	11.48
57f	E4	3.28	0.40	0.33	1.96	52.48	0.03	0.05	27.54
57g[♠]	SB0	2.66	0.09	0.09	0.26	44.67	0.05	0.10	3.40
57h	SBb	6.18	0.30	0.21	2.13	12.59	0.09	0.71	3.36
59a[*]	Sa	19.03	0.28	0.25	2.06	14.79	0.06	0.43	4.75
59b	E0	7.77	0.03	0.03	0.59	7.19	0.01	0.06	0.88
59c	Sc	1.92	0.23	0.11	0.63	1.34	0.10	8.13	0.77
59d	Im	6.48	1.47	0.16	1.81	0.78	0.57	72.78	0.65
61a[*]	S0a	4.37	0.63	0.62	3.08	89.13	0.16	0.17	11.22
61c	Sbc	2.30	1.30	1.23	3.74	45.71	1.79	3.80	2.99
61d	S0	1.58	0.02	0.02	0.29	23.44	0.04	0.17	0.33
62a[*]	E3	1.74	0.16	0.16	1.33	91.20	0.03	0.03	0.55
62b	S0	4.60	0.10	0.10	0.70	35.48	0.01	0.01	0.68
62c	S0	5.48	0.17	0.17	0.69	22.39	0.02	0.07	22.90
62d	E2	4.89	0.39	0.39	0.68	5.92	0.03	0.48	7.03
67a[*]	E1	6.70	0.12	0.12	0.46	245.47	0.02	0.07	2.09
67b	Sc	8.25	1.13	1.07	2.23	23.99	1.13	4.47	1.22
67c	Scd	4.25	0.58	0.14	0.51	14.45	0.55	3.98	0.50
67d	S0	0.19	0.10	0.06	0.79	14.79	0.05	0.32	23.98
68a	S0	14.93	0.02	0.02	0.09	67.61	0.31	0.46	4.48
68b	E2	6.05	0.13	0.11	2.28	60.26	0.06	0.09	42.65
68c[*]	SBbc	4.95	0.36	0.36	0.96	70.79	0.05	0.07	3.73
68d[♠]	E3	6.22	0.14	0.05	1.15	9.06	0.01	0.10	54.95
68e[♠]	S0	3.83	0.07	0.03	0.59	5.71	0.01	0.06	10.23
71a[*]	Sbc	5.22	0.25	0.16	0.28	69.18	1.65	2.34	77.62
71b	SB0	7.41	1.17	1.13	3.23	40.74	1.34	3.31	1.30
71c	Sbc	4.74	0.18	0.17	0.48	7.28	0.53	7.24	15.48
75a[*]	E4	6.84	0.14	0.14	1.39	204.17	0.26	0.13	4.18
75b[♠]	Sb	8.62	0.03	0.03	0.04	33.11	0.01	0.01	23.44
75c	S0	6.18	0.21	0.18	0.46	56.23	0.02	0.06	13.80
75d	Sd	4.39	0.45	0.29	1.09	23.44	0.65	2.75	1.80
75e[♠]	Sa	1.72	0.01	0.04	0.24	45.71	0.06	0.14	19.05
79a[*]	Sa	6.76	0.66	0.65	1.85	36.31	0.10	0.26	30.90
79b	S0	5.90	0.99	0.77	2.14	34.67	0.14	0.35	9.59
79c	S0	6.83	0.44	0.43	1.16	4.49	0.01	0.28	1.61
79d	Sdm	3.36	1.34	1.15	2.13	0.74	3.74	48.08	1.98
82a[*]	E3	5.11	0.39	0.38	0.70	208.93	0.07	0.03	8.35
82b	SBa	4.75	0.78	0.76	1.72	123.03	0.15	0.12	0.12
82c	Im	4.86	1.04	0.99	3.94	33.88	3.25	9.55	0.86
82d	S0a	8.11	0.05	0.05	1.15	28.18	0.03	0.10	54.95
91a[*]	SBc	7.59	0.41	0.39	0.56	91.2	10.16	11.02	26.91
91b	Sc	2.41	1.01	0.88	1.80	27.54	5.22	18.49	53.70
91c	Sc	4.73	0.16	0.08	0.65	14.79	3.22	21.48	0.41
91d	SB0	0.95	0.40	0.04	0.39	22.39	0.26	1.10	4.33
92a	Sc	3.74	0.23	0.23	0.65	11.75	0.79	6.76	1.40
92b	SBbc	5.97	0.71	0.62	0.81	38.02	2.23	5.89	1.84
92c[*♣]	SBbc	5.05	2.27	2.20	3.60	39.81	26.42	64.86	1.48
92d[♠]	E2	5.94	0.35	0.08	0.32	34.67	0.12	0.35	7.19
92e[♠]	E4	3.72	0.37	0.01	0.07	64.57	0.01	0.01	43.66
95a[*]	Sbc	8.10	0.87	0.83	1.73	131.83	2.25	1.70	5.78
95c	Sbc	5.08	1.66	1.47	3.06	16.6	14.52	87.5	0.89
95d	SB0	2.25	0.64	0.61	1.41	45.71	0.96	2.14	1.22
97a[*]	E5	2.89	0.03	0.03	0.04	81.28	0.01	0.02	2.96
97b[♠]	Sc	1.95	0.78	0.44	0.99	16.98	0.55	2.75	11.22
97c	Sa	6.61	0.14	0.14	2.05	23.44	0.02	0.07	0.23
97d	E1	1.46	0.03	0.02	0.13	47.86	0.04	0.09	0.20
97e[♠]	S0a	5.10	0.09	0.02	0.21	9.82	0.02	0.17	15.84
100a[*]	S0a	2.54	0.25	0.20	1.53	61.66	1.05	1.70	60.25
100b	S	3.56	0.52	0.50	2.08	5.65	0.34	5.89	4.86
100c	S	3.78	1.54	0.45	1.80	2.44	1.67	67.92	5.98
100d	Scd	1.96	0.29	0.08	0.69	0.57	0.11	20.28	10.96

Notes. (*) The most massive galaxy of each group, used in the calculations of the dynamical masses in Table 5. (♠) No 24 μm observations were available, so their SFRs, sSFRs, and L_{IR} are not well constrained. (♣) An AGN in their nucleus dominates their IR emission.

Table 5. Derived physical parameters based on the SED modeling of the interacting pair's galaxy sample.

Galaxy	z	$\tau_{V,\mathrm{obs}}$	$\tau_{V,\mathrm{ISM}}$	$\tau_{V,\mathrm{BC+ISM}}$	M_{star} $\times10^9\ M_\odot$	SFR $M_\odot\ \mathrm{yr}^{-1}$	sSFR $\times10^{-11}\ \mathrm{yr}^{-1}$	L_{IR} $\times10^9\ L_\odot$
Arp24a	0.0069	0.21	0.06	0.59	0.05	0.05	74.47	0.17
Arp24b	0.0069	0.46	0.49	1.29	0.68	5.22	948.4	48.98
Arp34a	0.0157	0.32	0.16	0.81	4.90	1.50	30.20	12.3
Arp34b	0.0157	0.62	0.21	1.26	30.20	0.34	1.23	6.64
Arp65a	0.0179	0.95	0.90	2.81	34.67	1.12	3.16	39.81
Arp65b	0.0179	0.23	0.20	1.13	19.50	0.35	1.82	5.78
Arp72a	0.0109	0.89	0.17	0.96	2.28	3.98	165.9	30.9
Arp72b	0.0109	0.44	0.06	0.34	0.21	0.33	164.8	2.44
Arp82a	0.0136	0.23	0.26	1.85	18.62	2.39	12.59	29.51
Arp82b	0.0136	0.66	0.18	0.93	3.09	0.67	23.01	6.56
Arp84a	0.0115	1.12	1.16	2.47	9.33	3.56	36.31	51.29
Arp84b	0.0115	0.40	0.48	1.73	61.66	3.82	6.31	57.54
Arp85a	0.0015	0.31	0.48	2.07	9.12	0.05	0.60	3.61
Arp85b	0.0015	0.45	0.47	1.68	8.71	2.39	25.82	27.54
Arp86a	0.0172	0.29	0.34	1.79	114.82	4.09	3.63	63.1
Arp86b	0.0172	1.45	0.88	3.03	2.95	4.14	120.23	41.69
Arp87a	0.0235	0.86	0.90	2.00	9.77	3.98	38.90	54.95
Arp87b	0.0235	0.26	0.22	1.14	16.60	2.28	13.80	22.91
Arp89a	0.0068	0.21	0.17	1.44	0.66	0.16	23.28	1.31
Arp89b	0.0068	1.26	0.63	2.02	41.69	0.16	0.40	18.62
Arp120a	0.0026	0.25	0.25	1.75	11.20	0.09	0.08	1.75
Arp120b	0.0026	0.44	0.38	1.52	17.80	0.16	0.91	5.4
Arp181a	0.0315	0.72	0.29	1.20	97.72	2.24	2.40	37.15
Arp181b	0.0315	0.96	0.86	2.00	52.48	3.33	6.31	81.28
Arp202a	0.0102	1.00	0.30	1.04	0.66	1.67	234.4	11.75
Arp202b	0.0102	0.87	0.17	0.75	0.89	1.40	363.1	29.51
Arp242a	0.0220	1.03	0.93	3.00	43.65	3.03	7.24	50.12
Arp242b	0.0220	0.14	0.23	1.25	39.81	1.12	2.88	12.3
Arp244a	0.0054	0.29	0.30	1.56	26.3	4.45	16.29	54.95
Arp244b	0.0054	0.99	0.81	2.60	89.13	2.44	3.80	83.18
Arp271a	0.0087	0.08	0.19	0.96	12.88	7.19	54.95	58.88
Arp271b	0.0087	0.43	0.29	1.54	6.03	3.65	61.66	32.36
Arp280a	0.0024	0.93	0.72	2.00	0.02	0.15	916.2	1.57
Arp280b	0.0024	0.08	0.05	2.62	2.09	0.17	8.13	1.52
Arp282a	0.0154	0.49	0.48	2.20	85.11	0.42	0.54	19.05
Arp282b	0.0154	0.45	0.26	1.31	7.24	0.43	6.03	5.65
Arp283a	0.0055	0.07	0.11	0.82	1.23	0.17	15.38	1.52
Arp283b	0.0055	1.19	1.11	2.91	12.02	1.91	15.85	35.48
Arp284a	0.0092	0.80	0.10	0.55	0.81	0.07	8.13	0.56
Arp284b	0.0092	1.14	0.49	2.12	2.04	6.46	275.4	57.54
Arp285a	0.0087	0.76	0.81	2.32	18.62	1.14	5.75	26.3
Arp285b	0.0087	0.31	0.41	1.94	8.71	0.85	9.55	11.48
Arp290a	0.0121	0.29	0.21	1.41	29.51	0.44	1.51	5.92
Arp290b	0.0121	1.01	0.65	2.58	28.18	0.02	0.09	7.19
Arp295a	0.0220	1.06	0.89	3.30	7.76	11.48	144.5	114.82
Arp295b	0.0220	0.76	0.71	2.22	26.92	0.54	2.29	30.2
Arp297a	0.0322	0.17	0.12	0.68	31.62	1.23	3.72	12.02
Arp297b	0.0322	0.74	0.58	1.67	5.62	0.63	11.27	10.47
Arp298a	0.0163	0.85	1.02	2.77	14.79	2.09	13.80	33.88
NGC 4567a	0.0163	1.92	1.14	3.35	114.82	28.84	25.12	1047.13
NGC 4567b	0.0074	1.06	0.88	3.05	58.88	6.03	11.22	138.04

Notes. We calculate the two components of τ_V using $\tau_{V,\mathrm{ISM}} = \mu\tau_V$ and $\tau_{V,\mathrm{BC}} = (1 - \mu)\tau_V$.

Table 6. Distance to, virial radius, and morphology of the nearest neighbor, as well as “strength” of interaction for the HCG galaxies.

HCG galaxy	R^a kpc	$r_{\rm vir}{}^b$ kpc	$\langle R/r_{\rm vir,\,nei}\rangle/n^c$	Type of^d nearest neighbor
2a	24	404	0.092	late
2b	24	357	0.108	late
2c	76	255	0.673	late
4a	62	662	0.085	late
4b	28	467	0.041	early
4d	28	399	0.070	late
6a	37	745	0.047	early
6b	13	571	0.023	late
6c	13	528	0.025	late
6d	35	293	0.028	late
7a	36	523	0.043	late
7b	21	458	0.038	late
7c	76	452	0.058	late
7d	21	551	0.032	early
15a	101	736	0.055	early
15b	64	529	0.028	late
15c	49	868	0.030	early
15d	14	507	0.034	late
15e	64	591	0.043	early
15f	14	406	0.020	early
16a	16	563	0.032	late
16b	16	488	0.038	late
16c	37	462	0.034	late
16d	37	611	0.047	late
22a	37	555	0.070	late
22b	17	267	0.034	late
22c	17	285	0.034	late
25a	57	552	0.059	early
25b	9	667	0.032	early
25d	46	334	0.041	late
25f	9	310	0.029	late
37a	17	932	0.037	early
37b	20	455	0.039	late
37c	29	449	0.032	early
37d	20	245	0.037	late
37e	30	150	0.037	late
38a	87	437	0.104	late
38b	9	511	0.056	late
38c	9	399	0.060	late
40a	14	795	0.008	late
40b	12	685	0.008	late
40c	12	774	0.007	early
40d	20	760	0.012	early
40e	13	491	0.006	early
42a	21	998	0.034	early
42b	81	583	0.067	early
42c	21	510	0.041	early
42d	31	288	0.031	early
44a	26	335	0.044	late
44b	26	393	0.069	late
44c	54	348	0.078	late
44d	26	213	0.044	late
47a	34	778	0.052	early
47b	34	554	0.034	late
47c	15	389	0.028	late
47d	15	405	0.025	late
54a	1	147	0.007	late
54b	1	152	0.011	late
54c	1	110	0.005	late
54d	1	87	0.006	late
55a	23	929	0.015	early
55b	17	710	0.019	early
55c	17	790	0.015	early
55d	23	588	0.019	early
56a	59	476	0.046	early

Notes. [(a)] Projected distance to the nearest neighbor. [(b)] Virial radius. [(c)] “Strength” of interaction as described in Sect. 4.6. [(d)] Morphology of the nearest neighbor.

Table 6. continued.

HCG galaxy	R^a kpc	$r_{\rm vir}{}^b$ kpc	$\langle R/r_{\rm vir,\,nei}\langle/n^c$	Morphology of^d nearest neighbor
56b	31	622	0.027	early
56c	12	580	0.021	early
56d	12	402	0.022	early
56e	27	436	0.030	early
57a	13	669	0.031	late
57b	26	748	0.020	early
57c	26	583	0.031	late
57d	13	252	0.020	late
57e	32	516	0.028	late
57f	86	641	0.060	early
57g	26	463	0.022	late
57h	32	421	0.025	early
59a	13	368	0.036	late
59b	33	298	0.066	late
59c	26	232	0.046	late
59d	13	182	0.035	late
61a	43	705	0.043	early
61c	24	805	0.033	early
61d	24	400	0.023	late
62a	6	745	0.023	early
62b	6	500	0.025	early
62c	19	518	0.028	early
62d	56	354	0.035	early
67a	17	1032	0.028	early
67b	99	635	0.054	late
67c	25	624	0.031	early
67d	17	486	0.028	early
68a	10	710	0.032	early
68b	10	629	0.030	early
68c	33	532	0.038	early
68d	49	370	0.027	early
68e	47	337	0.037	early
71a	68	799	0.082	early
71b	68	502	0.066	late
71c	76	431	0.064	early
75a	3	920	0.033	early
75b	3	534	0.033	late
75c	23	498	0.032	late
75d	23	533	0.025	early
75e	41	453	0.023	late
79a	4	168	0.006	late
79b	8	523	0.013	early
79c	4	366	0.009	early
79d	5	229	0.009	late
82a	47	789	0.054	late
82b	66	819	0.097	early
82c	44	171	0.028	early
82d	44	440	0.053	late
91a	15	1047	0.039	early
91b	82	662	0.057	late
91c	15	553	0.031	early
91d	15	527	0.032	late
92a	5	629	0.019	late
92b	1	649	0.013	early
92c	4	925	0.020	late
92d	1	663	0.013	late
92e	5	801	0.024	early
95a	20	914	0.032	late
95c	20	726	0.030	late
95d	48	510	0.031	late
97a	37	757	0.031	early
97b	112	568	0.054	early
97c	75	528	0.043	early
97d	37	682	0.034	early
97e	41	442	0.038	early
100a	28	621	0.036	late
100b	34	506	0.056	early
100c	43	394	0.047	late
100d	28	254	0.031	early

Notes. [(a)] Projected distance to the nearest neighbor. [(b)] Virial radius. [(c)] “Strength” of interaction as described in the text. [(d)] Morphology of the nearest neighbor.

Table 7. Observed and predicted 60 μm and 100 μm IRAS fluxes for each group, as well as total HI, H_2, stellar, and dynamical masses.

HCG ID	Evolve Class[a]	HI Class[c]	Group members	$f_{60,\mathrm{pred}}$ Jy	$f_{60,\mathrm{obs}}$ Jy	$f_{100,\mathrm{pred}}$ Jy	$f_{100,\mathrm{obs}}$ Jy	$\log(M_{\mathrm{HI}})$[d] $M_\odot$	$\log(M_{\mathrm{star}})$ $M_\odot$	$\log(M_{\mathrm{H_2}})$[e] $M_\odot$	$\log(M_{\mathrm{dyn}})$ $M_\odot$	$(M_{\mathrm{bar}}/M_{\mathrm{dyn}})$[f]
2	young	-	3	6.33	6.16	4.03	2.89	10.33	10.07	-	11.67	0.07
4	young[b]	-	3	8.21	8.56	4.35	4.09	10.31	10.95	-	11.96	0.12
6	old	-	4	0.34	0.46	0.11	0.13	9.69	11.36	-	12.66	0.05
7	young	1	4	8.32	9.20	3.42	4.43	9.68	11.16	<9.88	11.64	0.35
15	old	3	6	1.29	0.38	0.94	0.13	9.41	11.14	<9.73	13.24	0.01
16	young	2	4	35.72	62.37	24.04	25.21	>10.42	11.19	10.41	12.57	>0.06
22	old	-	3	2.72	1.48	1.0	1.05	9.13	10.90	-	11.33	0.38
25	old	2	4	1.4	5.21	0.68	1.74	9.90	11.00	<9.61	11.13	0.83
37	old	3	5	2.73	2.60	1.22	0.89	9.19	11.34	9.88	13.01	0.02
38	young	-	3	7.09	3.60	3.16	1.63	9.69	11.08	-	11.31	0.61
40	old	3	6	4.82	3.85	3.42	1.35	9.14	11.59	10.07	12.29	0.21
42	old	-	4	5.14	-	1.66	0.0	9.40	11.47	-	13.17	0.02
44	young	3	4	15.68	14.32	8.28	5.69	9.23	10.79	<9.17	12.70	0.01
47	young	-	4	1.66	1.51	0.82	1.27	9.93	11.30	-	11.63	0.48
54	young	-	4	2.02	1.71	0.35	0.38	8.75	8.69	-	11.25	0.01
55	old	-	4	1.1	1.63	0.26	0.2	-	11.47	-	12.53	0.09
56	old	-	5	2.59	2.27	1.13	0.89	9.36	10.97	-	12.81	0.02
57	old	-	8	3.14	3.54	1.16	1.44	9.71	11.75	-	12.58	0.15
59	young	-	4	13.3	4.83	6.91	3.98	9.49	10.38	-	12.25	0.02
61	old	-	3	16.3	12.45	7.18	6.39	9.96	11.20	-	12.33	0.08
62	old	-	4	1.45	0.72	0.29	0.13	<9.06	11.19	-	12.85	<0.02
67	old	1	4	2.98	2.91	1.15	2.26	10.03	11.48	<10.04	12.16	0.21
68	old	3	5	4.97	10.45	2.08	2.74	9.62	11.33	<9.23	12.82	0.03
71	young[b]	-	3	2.75	3.69	1.29	1.84	-	11.07	-	11.55	0.33
75	old	-	5	1.4	2.15	0.16	0.57	-	11.56	-	12.74	0.07
79	old	1	4	2.89	3.80	2.28	1.41	9.30	10.88	<9.31	11.72	0.15
82	old	-	4	3.92	3.31	0.96	3.47	<9.69	11.60	-	13.04	<0.04
91	young	2	4	8.78	6.11	5.0	2.31	10.32	11.19	-	12.67	0.04
92	old	3	5	7.15	6.57	1.34	1.39	10.02	11.28	-	12.82	0.03
95	old	-	3	9.44	2.39	2.48	6.94	>10.10	11.29	-	12.70	>0.04
97	old	3	5	5.28	-	2.12	0.0	9.10	11.25	<9.80	13.02	0.02
100	young	2	4	5.78	6.46	2.71	2.36	9.74	10.85	<9.37	11.16	0.54

Notes. [a] The dynamically "young" and "old" classification as discussed in Sect. 4.1 and in Bitsakis et al. (2010). [b] The original classifications of HCG4 and HCG71 were dynamically "old", but changed as explained in Sect. 4.3. [c] The classification to Phases 1, 2, and 3, follows the definition of Verdes-Montenegro et al. (2001). [d] The upper and lower limits, in HI masses, taken into account by means of survival analysis. [e] The H_2 masses were obtained from Martinez-Badenes et al. (2011). [f] Ratio of the total baryonic mass $M_{\mathrm{bar}} = M_{\mathrm{star}} + M_{\mathrm{HI}} + M_{\mathrm{H_2}}$ over the dynamical mass M_{dyn}.

Appendix A: Peculiar early type systems

As mentioned in Sect. 4.4, there are ten peculiar early-type galaxies that display “red” mid-IR colors. It was suggested that they could either be misclassified late-type systems or that they are indeed early types that have increased their gas and dust owing to interactions and merging with companion galaxies. As discussed in Sect. 4.2, some of them display high A_v, SFR, and sSFR. In this section we present all available evidence and discuss their properties in detail.

To better probe their morphology, we first examine how the old stellar populations, traced by their near-IR emission, as well as the warm dust seen in the mid-IR are distributed in each galaxy. In Fig. A.1 we present the “true color” images constructed using the *Spitzer*/IRAC 3.6, 4.5, and 8.0 μm maps as the blue, green, and red channels, respectively. We also include contour maps of the Ks emission for these galaxies. Bona fide early-type systems should be relaxed dynamically with an $R^{1/4}$ radial profile and elliptical structure in their stellar light emission. Furthermore, they should not display star formation or color gradients, so no variation would be expected in their mid-IR “true color” images. Indeed, when one observes the “true color” image of NGC1404 (a typical field elliptical galaxy), no obvious mid-IR color gradient is seen, while the contours of the Ks-band emission, dominated by the old stellar population, are concentric ellipses. HCG40f and HCG68a also display similar mid-IR colors and profiles with the second having Ks contours consistent with a lenticular galaxy; however, the rest of the early-type HGC galaxies show either color gradients or patchy emission in their “true color” mid-IR images, which indicate possible on-going star formation warming up the dust and exciting the PAH molecules in these wavelengths. In particular the galaxies HCG4d, HCG55c, HCG56d, HCG71b, and HCG79b display reddish colors that imply stronger 8 μm emission. In HCG100a the 8.0 μm emission seems to emerge from two spiral-like structures, yet it appears relaxed when we closely examine the distribution of their old stellar population. With the exception of HCG56b and HCG71b, which display a barred-like structure, no other system shows obvious signs of spiral or irregular structure, even though it would have been challenging to identify such features in edge-on late type systems.

An additional tool that can help us classify these galaxies is their global SEDs and current star formation activity. In Fig. A.2 we present their SEDs and contrast it with the NGC 1404, a typical E1 galaxy whose SED was also fitted with the da Cunha et al. (2008) model. We note that HCG40f and HCG68a display SEDs that are consistent with those of an elliptical galaxy. It is very possible that HCG68a has “red” mid-IR colors because of the existence of an AGN in its nucleus (see Table A.1). HCG40f was not classified by Hickson (1982) but by us (Bitsakis et al. 2010), since its morphology and SED were consistent with an early-type galaxy. However, this galaxy is very close to its neighbor (HCG40d), and it is possible that this could slightly affect its mid-IR colors. The SED of HCG56b is strongly affected by the emission of its Sy2 nucleus that dominates its mid-IR colors. Since our model cannot account for emission due to an AGN we cannot draw a firm conclusion on its nature. Among the galaxies for which nuclear optical spectra were available, four systems, HCG56d, HCG68a, HCG79b, and HCG100a display signatures of an AGN or a transition object, while HCG56e and HCG71b are classified as purely star forming. The remaining galaxies display SEDs that are similar to those of late-type galaxies. They have strong mid-IR fluxes that are consistent with the presence of PAH emission.

With the exception of HCG40f, all nine galaxies have high sSFRs similar to those of late-type systems (see Table A.1). More specifically HCG4d, HCG55c, HCG56b, HCG56d, HCG56e, HCG71b, and HCG100a have sSFRs that are two orders of magnitude higher than what is seen in normal ellipticals, while HCG68a and HCG79b have sSFRs that are just a factor of ten higher. Finally, as mentioned in Sect. 4.5, if these galaxies were passively evolving, they would display “red” NUV-r colors (>5 mag). However, the observed NUV-r colors of HCG4d and HCG56b are blue. After correcting for the dust extinction, seven of the remaining of the galaxies also move to the “blue cloud”. It is thus possible that these galaxies are dust-obscured, late types with some ongoing star formation activity. As a result they display higher sSFRs, “bluer” colors in the UV-optical and “redder” in the mid-IR wavelengths. Even after extinction correction HCG40f remains in the “red sequence” while HCG68a is found in the “green valley”. These galaxies are early-type galaxies that display red mid-IR colors probably because they increased their dust content thanks to interactions with their neighbors (HCG40d and HCG68b).

Taking in account all the evidence mentioned above we suggest that HCG4d, HCG55c, HCG56d, HCG56e, HCG71b, HCG79b, and HCG100a could be misclassified as edge-on, late-type systems.

Table A.1. Properties of the 10 peculiar early-type HCG galaxies and the typical elliptical NGC 1404.

Galaxy	Type [a]	Optical feature	Nuclear type	SED type	$\tau_{V,\mathrm{obs}}$	SFR $M_\odot$ yr^{-1}	sSFR $\times 10^{-11}$ yr^{-1}	(NUV-r)$_{\mathrm{corr}}$ [mag]	Proposed type
HCG4d	E4	-	-	late-type	0.53	0.96	7.41	2.01	late-type
HCG40f[b]	-	-	-	early-type	0.02	0.01	0.01	5.11	early-type
HCG55c	E3	-	-	late-type	0.94	1.17	1.05	2.90	late-type
HCG56b[c]	SB0	bar	Sy2	AGN dom.	1.34	1.69	4.79	2.04	-
HCG56d	S0	-	Sy2	late-type	1.01	0.42	4.07	2.81	late-type
HCG56e	S0	-	HII	late-type	0.89	0.19	5.37	2.78	late-type
HCG68a	S0	-	AGN	early-type	0.02	0.31	0.46	3.81	early-type
HCG71b	SB0	bar	HII	late-type	1.17	1.34	3.31	2.74	late-type
HCG79b	S0	-	TO	late-type	0.99	0.10	0.35	2.95	late-type
HCG100a	S0	-	TO	late-type	0.25	1.05	1.70	2.24	late-type
NGC 1404	E1	-	-	early-type	0.02	0.15	0.08	5.49	-

Notes. [a] Based on Hickson (1982). [b] Galaxy HCG40f is not detected at 24 μm, thus its SFR and sSFR are not well constrained. [c] Galaxy HCG56b emission is dominated by the presence of an AGN.

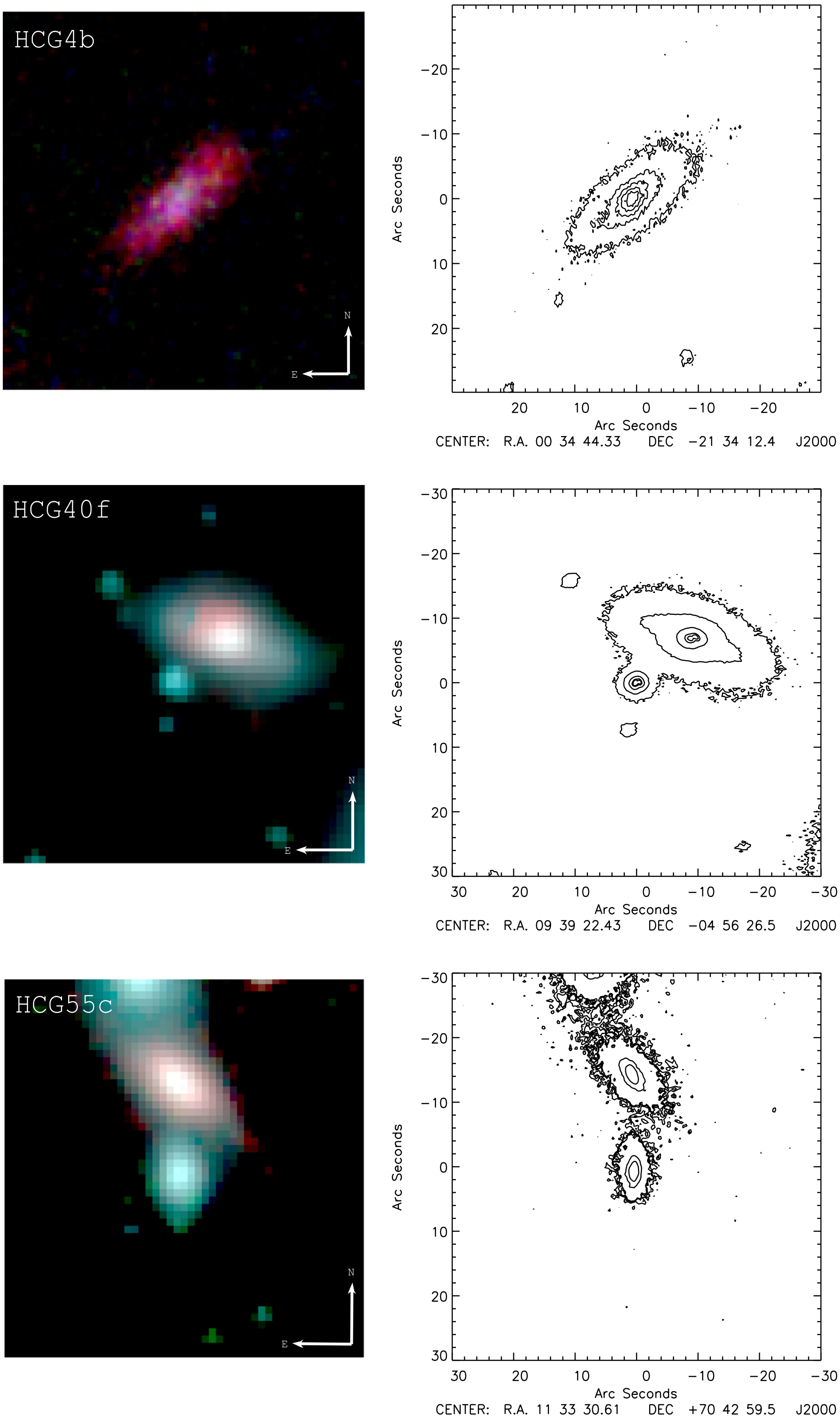

Fig. A.1. *Left column*: the "true color" images, created using the 3.6, 4.5, and 8.0 μm *Spitzer*/IRAC mosaics, of the 10 galaxies discussed in Sect. 4.3. The images are aligned northeast, and they are 1.5 × 1.5 arcmin in size. *Right column*: contour maps of the same fields observed in Ks-band with WIRC at the Palomar 5 m telescope. The five contours correspond to 3, 5, 8, 10, and 30σ. Since all images had similar exposure times the noise was $\sigma \sim 19.6$ mag arcsec^{-2}. For two galaxies not imaged with WIRC, HCG68a and HCG100a, we used the shallower Ks-band data from 2MASS (σ = 15.7 mag arcsec^{-2}).

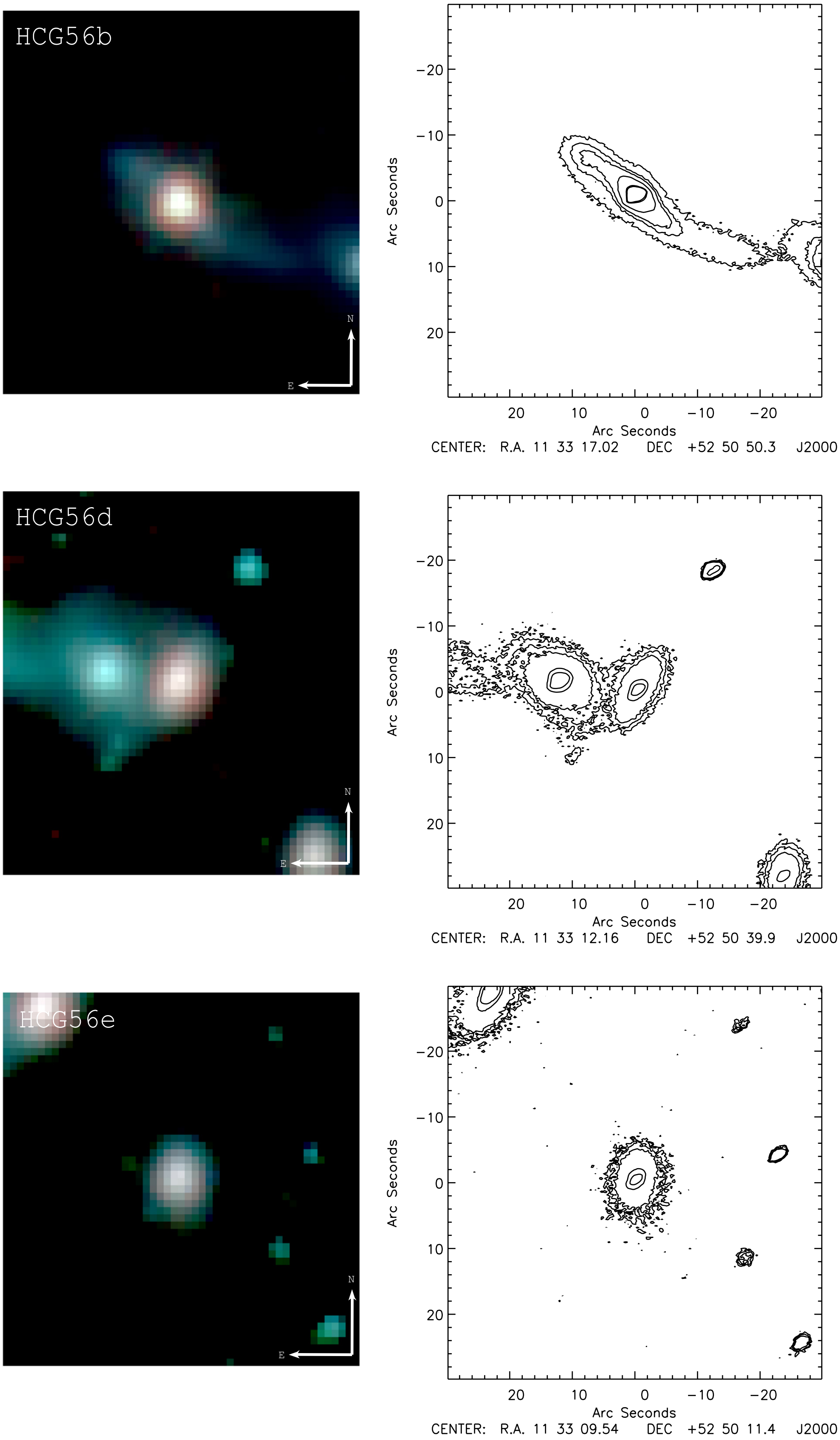

Fig. A.1. continued.

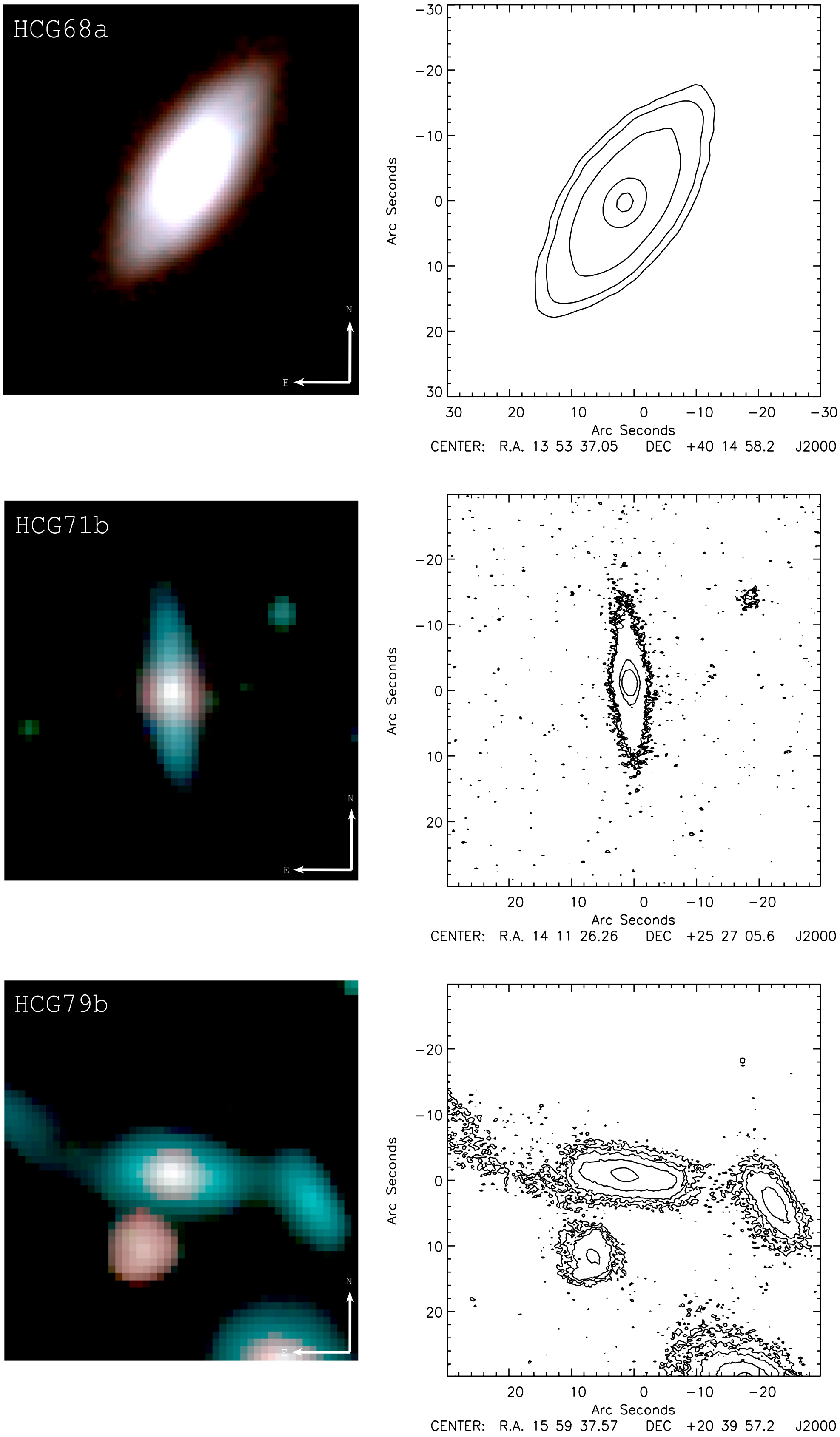

Fig. A.1. continued.

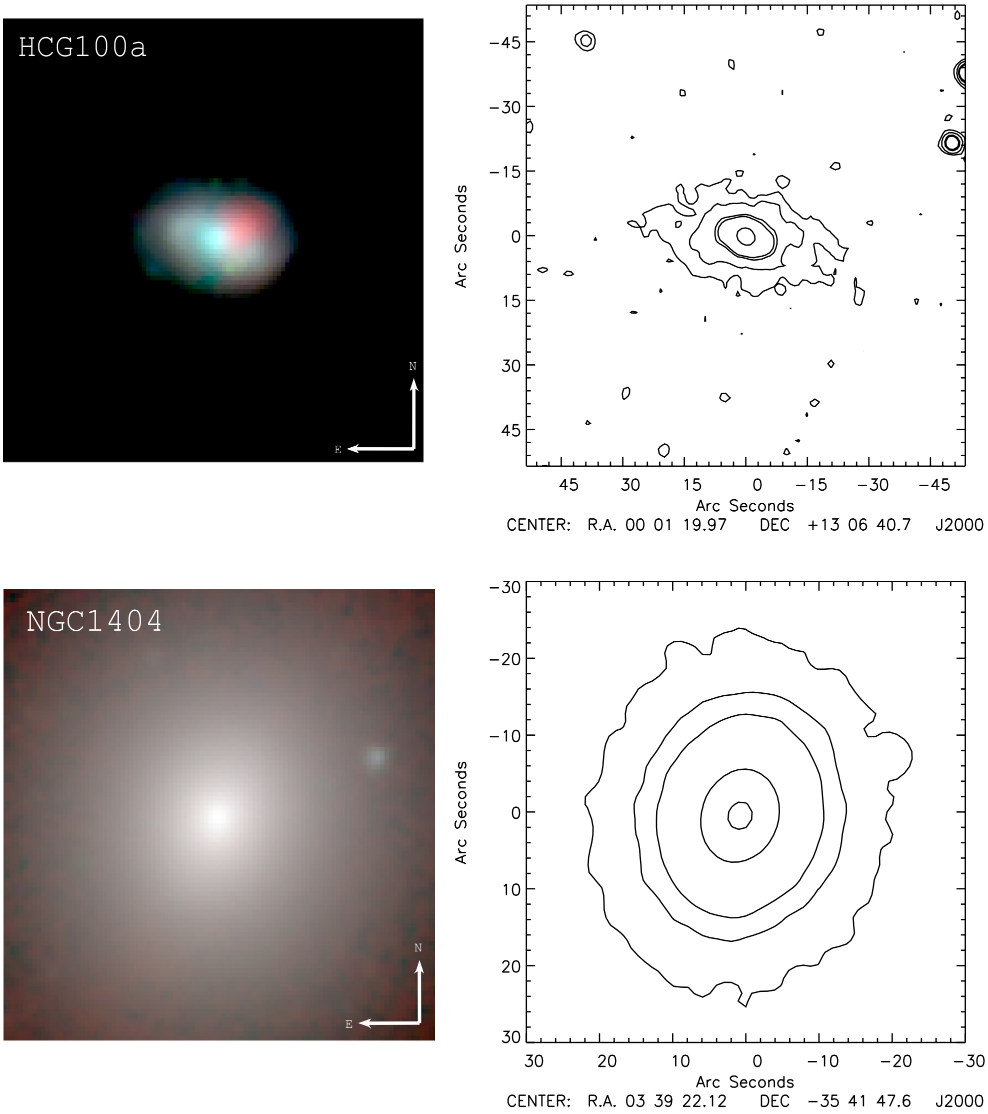

Fig. A.1. continued.

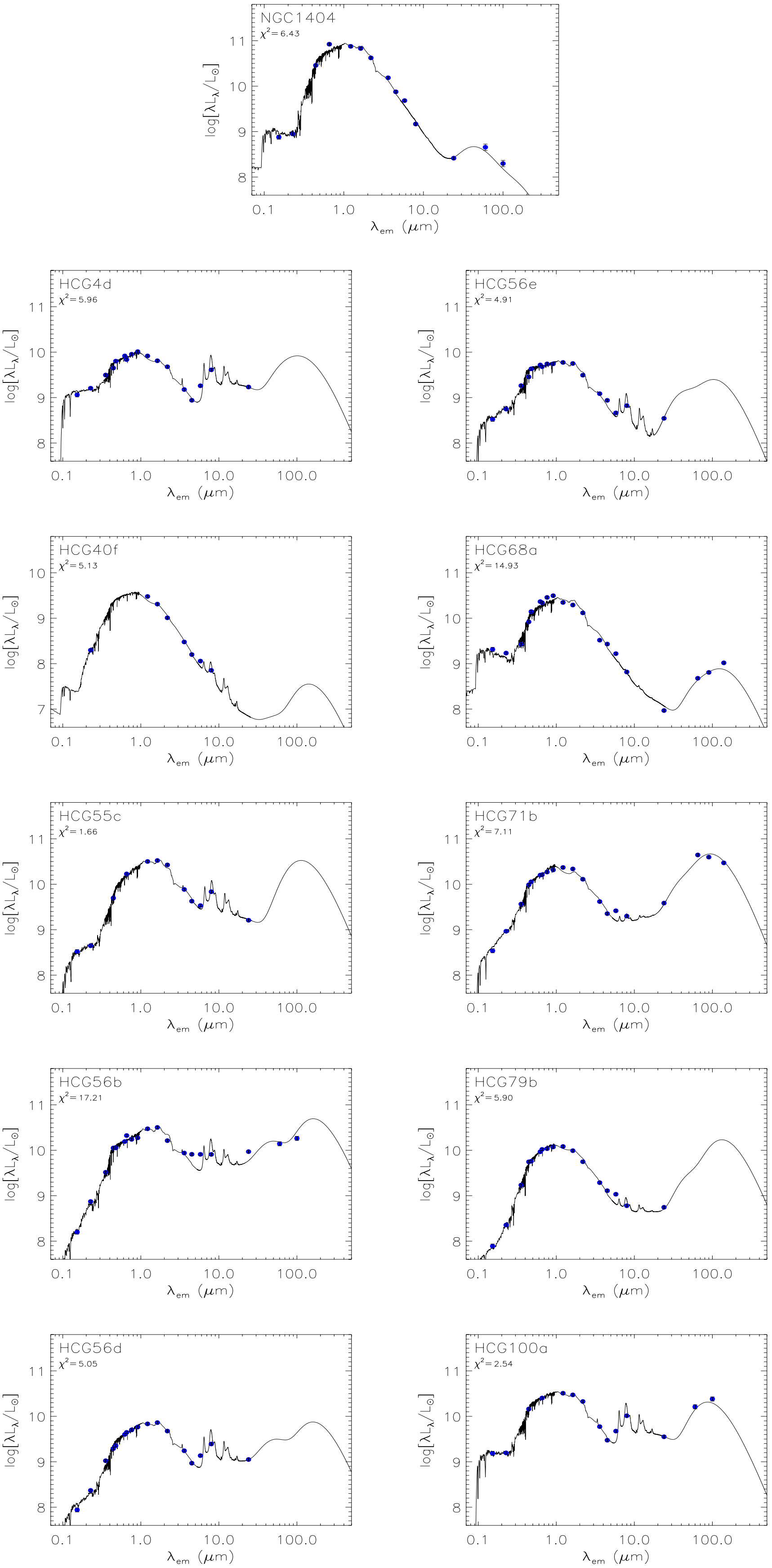

Fig. A.2. We display the observed SEDs (blue points) along with the da Cunha model fits (in black) of the 10 peculiar early-type galaxies mentioned in the Appendix. At the top panel we present the SED of a typical field elliptical galaxy, NGC 1404, for comparison. The name of each HCG galaxy is presented along with the χ^2 of the model fit to the data.

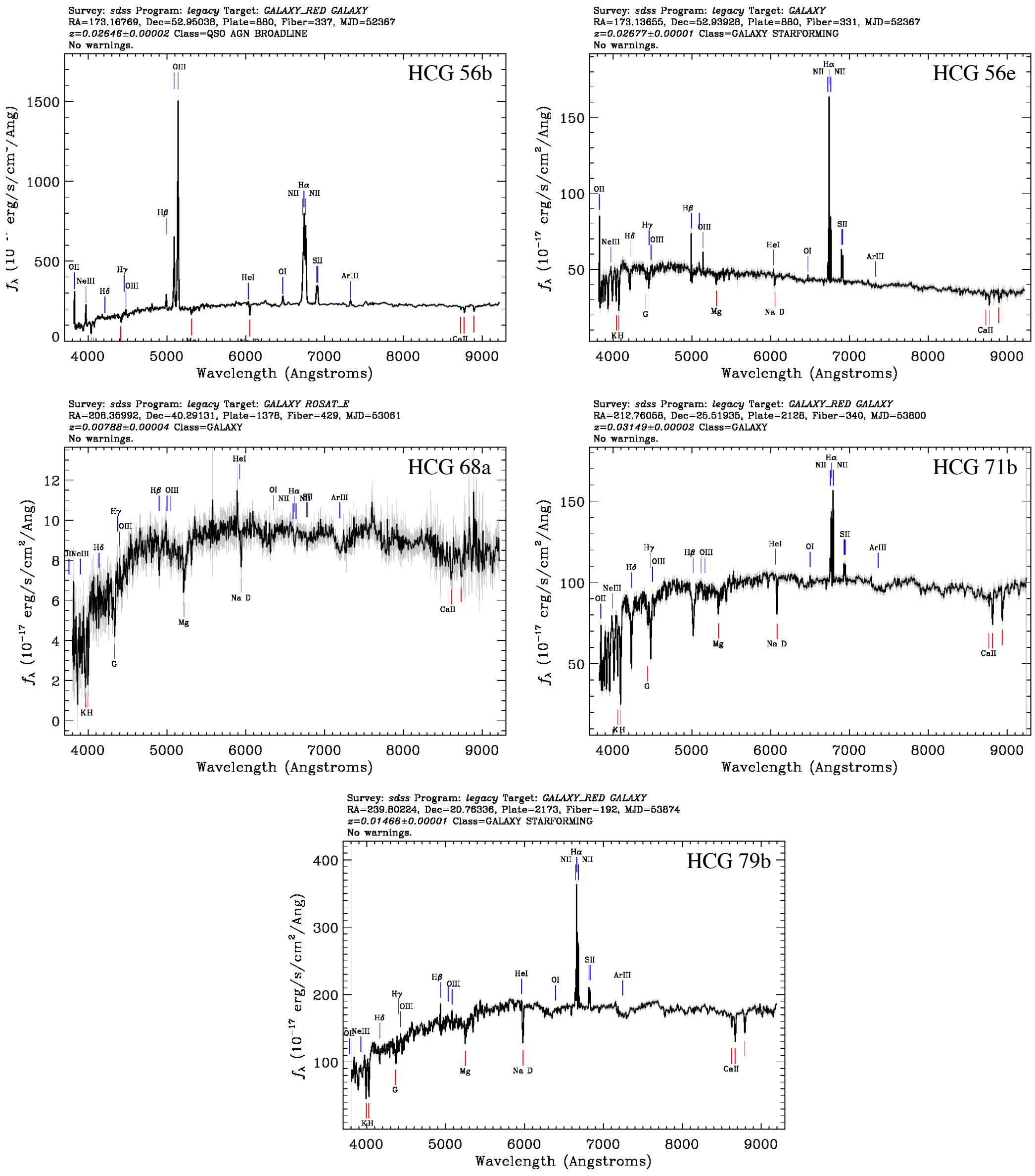

Figure A.1: The SDSS spectra of 5 of the 10 misclassified spiral galaxies. As we can see, the optical spectra of these galaxies are consistent with those of late-type galaxies.

Draft version October 12, 2012
Preprint typeset using LaTeX style emulateapj v. 08/22/09

ENHANCED WARM H_2 EMISSION IN COMPACT GROUP GALAXIES: EVOLUTION IN THE MID-INFRARED GREEN VALLEY

M.E. Cluver[1,2], P.N. Appleton[3], P. Ogle[1],, T.H. Jarrett[4], J. Rasmussen[4], U. Lisenfeld[6], P. Guillard[1], L. Verdes-Montenegro[7], R. Antonucci[8], T. Bitsakis[9], V. Charmandaris[9,10,11], F. Boulanger[12], E. Egami[13], C.K. Xu[2], M.S. Yun[14]

Draft version October 12, 2012

ABSTRACT

We present results from a *Spitzer* mid-infrared spectroscopy study of a sample of 74 galaxies located in 23 Hickson Compact Groups, chosen to be at a dynamically-active stage of H I depletion. We find evidence for enhanced warm H_2 emission (i.e. above that associated with UV excitation from young stars) in 13 galaxies (∼20%), with 8 of them having extreme values in excess of L(H_2 S(0)-S(3))/L(7.7μm PAH)$>$ 0.07. Such emission has been seen previously in HCG 92 (Stephan's Quintet), and was shown to be associated with the turbulent cascade from a large-scale shock caused when one group member collided, at high velocity, with tidal debris in the intragroup medium. Shock excitation or turbulent heating is likely responsible for the H_2 emission since other sources of heating (UV or X-ray excitation from star formation or AGN) is insufficient to explain the results. The galaxies exhibiting the enhanced H_2 emission in our sample fall predominantly in the optical "green valley" between the blue cloud and red-sequence, and are mainly of lenticular morphology (S0/a). Furthermore, they also lie in a region of mid-infrared color-color space that has been identified by previous studies as being connected to rapid transformations in HCG galaxy evolution. We argue that the H_2-enhanced systems may represent a specific phase in the evolution of galaxies in dense environments. These warm H_2 systems may provide new insight into mechanisms which may transform galaxies from the blue cloud to the red sequence.

Subject headings: galaxies: groups: compact groups – galaxies: evolution – galaxies: interactions – galaxies: ISM – galaxies: mid-infrared

1. INTRODUCTION

Compact Groups provide a convenient laboratory for studying morphological transformations, as they represent the highest density enhancements outside of clusters, and their relatively low velocity dispersions prolong gravitational interactions (Hickson et al. 1992). In addition, there is growing evidence that cluster galaxies have been "pre-processed" in groups, and then subsequently assimilated into larger systems (e.g. Cortese et al. 2006). Simulations show that spirals in a group environment are strongly influenced by repetitive slow encounters. This may build bulge mass as gas is funnelled into the central regions, transforming them into S0 galaxies with young, metal-rich stellar populations in the inner regions of their bulges (Bekki & Couch 2011). Galaxy interactions in groups may differ from isolated binary interactions because they can exhibit a broader range of behaviours, including tidal stripping and interactions with the intragroup medium (IGM; e.g. Allen & Sullivan 1980).

Hickson (1982) identified a uniform sample of 100 nearby compact groups (Hickson Compact Groups; hereafter HCG) using the Palomar Sky Survey, and applied the criterion of 4 or more members within a 3 magnitude range (δm_B) that also satisfied an isolation constraint. These groups have been the subject of extensive follow-up and study. Radial velocities (Hickson et al. 1992) have led to the identification of true associations of galaxies, with 92 groups consisting of at least three accordant members. That many of the groups are real physical associations is further attested by the presence of hot intragroup gas in many of them (Ponman et al. 1996). Signs of interactions within these groups include peculiar rotation curves and disturbed morphologies of group members (Rubin et al. 1991; Mendes de Oliveira & Hickson 1994), as well as the presence of intragroup light (Da Rocha et al. 2008).

H I deficiency in compact groups has long been suspected (Williams & Rood 1987; Huchtmeier 1997). A

[1] Spitzer Science Center, IPAC, California Institute of Technology, Pasadena, CA 91125, USA
[2] ARC Super Science Fellow, Australian Astronomical Observatory, PO Box 915, North Ryde, NSW 1670, Australia
[3] NASA Herschel S Center, California Institute of Technology, Pasadena, CA 91125, USA
[4] IPAC, California Institute of Technology, Pasadena, CA 91125, USA
[5] Dark Cosmology Centre, Niels Bohr Institute, University of Copenhagen, Juliane Maries Vej 30, DK-2100 Copenhagen, Denmark
[6] Departmento de Fìsica Teórica y del Cosmos, Facultad de Ciencias, Universidad de Granada, Spain
[7] Instituto de Astrofísica de Andalucía (IAA/CSIC), Apdo. 3004, 18080 Granada, Spain
[8] University of California Santa Barbara, Department of Physics, Santa Barbara, CA 93106, USA
[9] Department of Physics, University of Crete, GR-71003, Heraklion, Greece
[10] IESL/Foundation for Research & Technology-Hellas, GR-71110, Heraklion, Greece
[11] Chercheur Associé, Observatoire de Paris, F-75014, Paris, France
[12] Institute d'Astrophysique Spatiale, Universite Paris Sud 11, Orsay, France
[13] Steward Observatory, University of Arizona, 933 N. Cherry Avenue, Tucson, AZ 85721, USA
[14] Department of Astronomy, University of Massachusetts, Amherst, MA 01003, USA

larger study led to the idea that compact groups follow an evolutionary sequence in which the groups become increasingly deficient in neutral hydrogen (Verdes-Montenegro et al. 2001). Multiple tidal interactions, and possible gas stripping (via interaction with the IGM) may be the cause of H I depletion. More recent observations using the Green Bank Telescope, sensitive to extended, faint H I emission, have revealed a diffuse H I component in all the groups studied (Borthakur et al. 2010), explaining in part the "missing H I" reported by Verdes-Montenegro et al. (2001). Groups containing galaxies with the largest H I deficiencies are found to have a more massive diffuse-H I component (Borthakur et al. 2010). These observations have led to the conclusion that H I-deficient group galaxies lose H I into the IGM, primarily through tidal interactions. In the most evolved groups, gravitational heating may eventually create a hot X-ray emitting medium (see Ponman et al. 1996).

Leon et al. (1998) observed that the most compact group galaxies have more molecular gas concentrated in their nuclei, as expected from the effects of tidal forcing within the disk gas. However, the link between molecular gas and star formation properties in these interacting systems is less obvious. Studies of far-infrared and CO emission of galaxies in HCGs indicated no enhanced star formation, but 20% of spiral galaxies were tentatively found to be deficient in CO emission compared to isolated and weakly interaction systems (Verdes-Montenegro et al. 1998). A recent, more extensive CO study of HCGs also show that the specific star formation rate (SFR per unit stellar mass or sSFR) is lower in H I- and CO-deficient (as compared to isolated systems) HCG galaxies, but that the star formation efficiency (SFR per unit H_2 mass) in these galaxies appears unaffected compared to isolated galaxies (Martínez-Badenes 2012). Similar conclusions about the star formation efficiency is also supported by observations in the mid-infrared (Bitsakis et al. 2011).

The question of whether galaxies are stripped by interaction with a dense medium, or by tidal forces, still remains unclear. X-ray observations of 8 HCGs by Rasmussen et al. (2008) showed no obvious correlation between the presence of detectable hot intragroup gas and H I deficiency. Furthermore, in groups where X-ray emitting gas was strongly detected, it was shown that it was not of sufficient density to significantly strip H I from the group members, thus calling into question whether gas stripping by the hot X-ray medium is a viable stripping mechanism within compact groups.

Observations in the infrared with the *Spitzer* Space Telescope have led to potentially new evidence of evolutionary effects in HCGs. Johnson et al. (2007) observe a correlation in the IRAC color-color diagram of HCG galaxies, and argue for an evolutionary sequence – from groups dominated by dusty spirals with "red" IRAC colors, to groups containing evolved stellar-dominated galaxies with "blue" IRAC colors. These colors appear to correlate with the degree of H I depletion, supporting the idea of group evolution. Johnson et al. (2007) discuss a "gap" in the IRAC colour space between dusty/gas-rich and dust-free/gas-poor galaxies; this apparent absence of intermediate mid-infrared colours suggested a rapid evolution from gas-rich to H I-depleted systems (Walker et al. 2010). The role of environment is further investigated in Walker et al. (2012) using a sample of 37 compact groups. They find a statistically significant deficit of galaxies in the gap region with similarities to that found for the Coma Infall region. Accelerated transformation, possibly preceded by enhanced star formation in some galaxies, is also suggested by the significant bimodality in specific star formation rate (sSFR) seen in the HCG sample of Tzanavaris et al. (2010).

Bitsakis et al. (2011) performed a UV to mid-infrared analysis of a sample of 32 Hickson Compact Groups. They find that dynamically "old" groups (>25% are early-type galaxies) are more compact and display higher velocity dispersions, with late-type galaxies in these groups having more stellar mass and lower sSFR compared to dynamically "young" systems (>75% are late-type galaxies). The lower sSFR was attributed to a faster increase in stellar mass due to past interactions compared to the dynamically young groups. In addition they find that the majority (73%) of galaxies lie in either the "green valley" or the "red sequence" as defined by their NUV−r colors. More than half of the early-type galaxies in dynamically "old" groups were found to be located in the "green valley" and these are mostly (>70%) S0/SB0's. The authors also note that although 46% of their sample have optically identified AGN from nuclear spectra, they find no evidence of enhanced AGN activity at any stage of a group's evolution. This is consistent with the findings of (Martínez et al. 2010) where the median HCG AGN (Active Galactic Nuclei) luminosity corresponds to a low luminosity AGN (LLAGN) likely caused by gas depletion resulting in relatively low accretion rates

Our current paper is motivated by a possible new diagnostic of HCG evolution which uses mid-infrared spectroscopy from the *Spitzer* Space Telescope as a probe of the warm molecular gas in galaxies. Our team (Appleton et al. 2006; Cluver et al. 2010) discovered evidence for active transformation with the discovery of powerful ($L_{H_2} > 10^{35}$ W) mid-infrared H_2 line emission from an intergalactic shock wave in Stephan's Quintet (HCG 92). The emission was found to be spatially associated with a 40 kpc-long X-ray and radio-continuum filament believed to be formed as a result of a high-speed collision ($\sim 1000\ \mathrm{km\,s^{-1}}$) between a group member and tidal debris from a previous encounter within the group. In this case, the high power of the H_2 relative to both the infrared continuum and very faint PAH (polycyclic aromatic hydrocarbon) emission, and the close association with a known group-wide shock wave, makes a strong case for shock-heating as a viable mechanism in that compact group (Appleton et al. 2006; Cluver et al. 2010). Models demonstrate that driving a shock into a multiphase medium, such as a pre-existing H I tidal arm are capable of explaining many of the observed properties of the H_2 emission in SQ (Guillard et al. 2009). The group members are known to be H I and CO depleted (see Yun et al. 1997; Gao & Xu 2000), and may be one of the best candidates for hydrodynamic stripping effects as much of the molecular gas appears to reside in the IGM (Guillard et al. 2012a) based on deep IRAM CO observations. The discovery of H I and molecular gas between galaxies in HCG 92, as well as in the bridge between the Taffy galaxies (Peterson et al. 2012) – a system which has recently experienced a head-on collision similar to those ex-

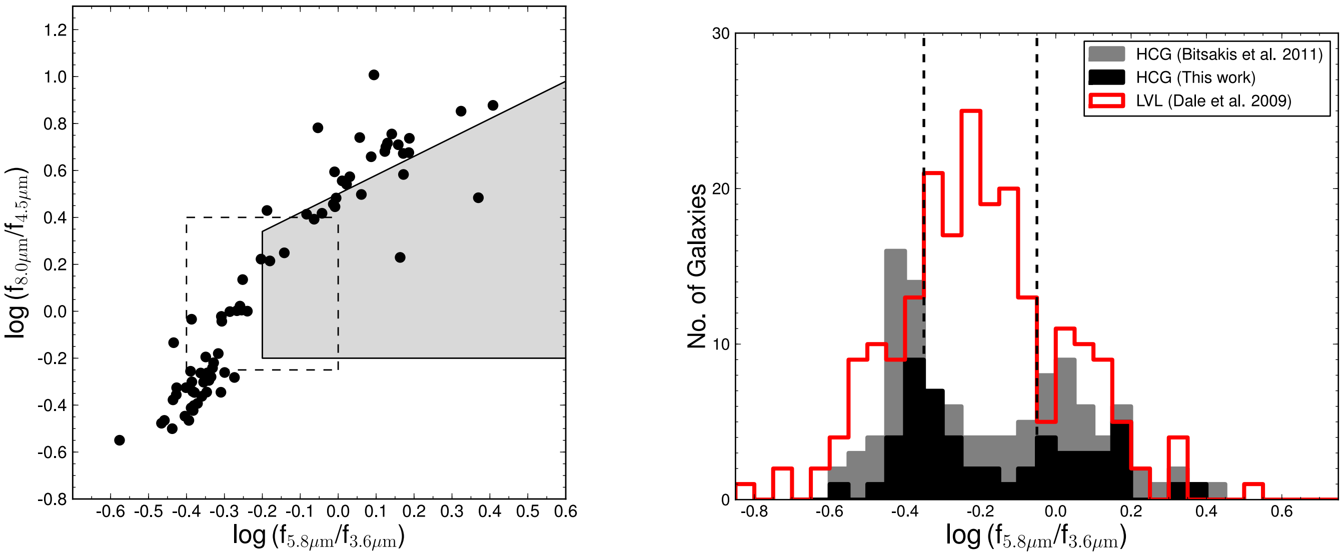

(a)

(b)

FIG. 1: a) The IRAC color-color diagram of the galaxies in our sample showing that the mid-infrared colours of our chiefly intermediate H I-deficiency groups span the colour space found in the larger samples of, for example, Walker et al. (2012) and Bitsakis et al. (2011). The shaded grey region is the AGN zone, as defined by Lacy et al. (2004), and the black dashed region shows the Johnson et al. (2007) "gap" region. b) A histogram comparing the IRAC [f$_{5.8\mu m}$/f$_{3.6\mu m}$] colors within our sample (grey filled; $z < 0.035$ galaxies only to avoid colors affected by redshifted spectral features), versus the larger HCG sample of Bitsakis et al. (2011, black filled; also excluding galaxies at $z > 0.035$), as well as the distribution from the Local Volume Limited (LVL) sample of nearby galaxies of Dale et al. (2009, red unfilled). The grey dashed lines indicate galaxies with intermediate mid-infrared colours, as determined from the distribution of Bitsakis et al. (2011).

pected in dense environments – led to our present study of a much larger sample of 23 HCGs with *Spitzer*.

The discovery of a class of powerful H_2-emitting radio galaxies with similar *Spitzer* IRS spectra to SQ led to the coining of the term MOHEG (MOlecular Hydrogen Emission-line Galaxies) and are defined as having large H_2 to 7.7μm PAH emission ratios ($= 0.04 - 4$) indicating excitation above that expected from UV heating (Ogle et al. 2010). In this paper we focus on the warm H_2 properties of the HCG sample in particular those that show H_2-enhancement as defined for a MOHEG. A subsequent paper will focus on the cold molecular gas properties of H_2-enhanced systems through IRAM CO observations and comparisons of the cold versus warm H_2 masses (and temperatures of the excited H_2). In Section 2 we outline the sample, observations and data reduction. Section 3 focuses on the results of the H_2 line emission survey and Section 4 presents our discussion. Conclusions are summarised in Section 5. Throughout this paper we assume a cosmology with Hubble constant $H_o = 73\,\mathrm{km\,s^{-1}Mpc^{-1}}$, matter density parameter $\Omega = 0.3$, and dark energy density $\Omega_\Lambda = 0.7$.

2. THE SAMPLE

We have selected 23 compact groups from the HCG catalog of Hickson (1982), representing 25% of the physically associated groups, as targets for probing active transformation. The aim of the project was to search for evidence of extended molecular hydrogen emission so groups were selected to have intermediate H I deficiencies (like SQ) which we reasoned were more likely to be in an active phase of gas stripping. From the study of Verdes-Montenegro et al. (2001), the deficiencies in HCGs range between $1 \leq \frac{M(\mathrm{HI})_{\mathrm{pred}}}{M(\mathrm{HI})_{\mathrm{obs}}} \leq 9.33$ (i.e. $0 \leq \log[M(\mathrm{HI})_{\mathrm{pred}}] - \log[M(\mathrm{HI})_{\mathrm{obs}}] \leq 0.97$). Thus we isolated 27 groups with H I deficiencies in the range $1.2 < \frac{M(\mathrm{HI})_{\mathrm{pred}}}{M(\mathrm{HI})_{\mathrm{obs}}} < 8$, based on Verdes-Montenegro et al. (2001). To further maximize the chances of finding dynamically active systems, we only considered those depleted groups that showed visible signs of tidal interaction (disturbed optical disks and tidal tails) in two or more of the members. This resulted in 22 groups. We added one extra group, HCG 40, which has the highest H I deficiency in the sample studied by Verdes-Montenegro et al. (2001), but shows an X-ray morphology similar to that of Stephan's Quintet, possibly indicating a shocked IGM. The final sample of 23 groups is listed in Table 1; galaxies that are not group members (i.e. with discordant redshifts) are not included in this analysis.

Although our primary selection criterion is based on the groups exhibiting intermediate H I-depletion (based on the original definition of Verdes-Montenegro et al. 2001), the sample spans a large range of galaxy properties shared by the more complete samples of HCG groups (e.g. Bitsakis et al. 2011; Walker et al. 2012). As shown in Figure 1a, the intermediate H I-depletion in these groups is not biased towards mid-infrared blue or red populations, but perhaps not surprisingly, spans the entire range of mid-infrared colour.

TABLE 1: HCG Sample

Group	z [a]	$\frac{M(\mathrm{HI})_{\mathrm{pred}}}{M(\mathrm{HI})_{\mathrm{obs}}}$ [b]	Galaxies Sampled	Designation [c]
HCG 6	0.0379	2.14	4	A, B, C, D[◇]
HCG 8	0.0545	> 1.10	3	A, C, D
HCG 15	0.0228	4.17	3	A, C, D
HCG 25	0.0212	1.82	4	B, C[†], D, F
HCG 31	0.0135	1.51	2	A+C[•], B
HCG 40	0.0223	9.33	4	A, B, C, D
HCG 44	0.0046	4.90	3	A, B, D
HCG 47	0.0317	1.91	3	A, B, D
HCG 54	0.0049	3.09	3	A, B, C
HCG 55	0.0526	–	5	A, B, C, D, E[†]
HCG 56	0.0270	5.37	4	B, C, D[⋆], E
HCG 57	0.0304	7.24	5	A, B, C[◇], D[◇], E
HCG 62	0.0137	> 2.88	3	A, B, C
HCG 67	0.0245	1.86	3	A, B, D[◇]
HCG 68	0.0080	3.02	3	A, B, C
HCG 75	0.0416	–	4	A, C, D[◇], E
HCG 79	0.0145	2.57	4	A, B, C, E[†]
HCG 82	0.0362	> 5.75	3	A, B, C
HCG 91	0.0238	1.74	3	A, C, D
HCG 95	0.0396	> 1.62	3	A, B[‡], C
HCG 96	0.0292	> 1.48	3	A, B, C
HCG 97	0.0218	7.76	3	A, C, D
HCG 100	0.0170	3.16	3	A, B, C

[a] From NED
[b] From Verdes-Montenegro et al. (2001)
[c] From Hickson (1982)
[†] Discordant redshift (from Hickson et al. 1992)
[‡] Discordant redshift (from Iglesias-Páramo & Vílchez 1998)
[•] Merging Object; Blended
[⋆] SL coverage only
[◇] LL coverage only

This color-color space has been shown to separate late-type, star-forming galaxies (top right) from early-type galaxies (bottom left). The dashed box shows the region of the "gap" found in the smaller samples of HCGs (Johnson et al. 2007; Walker et al. 2010). Bitsakis et al. (2011) also observe a lower density of galaxies at intermediate mid-infrared colors; this they interpret as separating the star-forming galaxies from the "green valley" and "red sequence" galaxies. They attribute the distribution in IRAC colors as the natural result of morphological transformation as galaxies evolve from star forming to passively evolving systems. We will show later in this paper that galaxies which fall within this intermediate region of mid-infrared color preferentially show signs of shocked molecular hydrogen emission. This may support the idea that the "gap galaxies" represent a transitional population.

The mid-infrared color properties of our sample, both in the context of the larger HCG group population and general galaxy populations, is shown in Fig. 1b. Here we compare the IRAC colors of our intermediate H I-deficient sample, to the larger Bitsakis HCG sample (which was not selected for deficiency), and galaxies taken from the Local Volume-Limited (LVL) sample of Dale et al. (2009), as a comparison control sample. The LVL sample consists of 256 galaxies within 11 Mpc and is dominated by spirals and irregulars. It is clear that both HCG sample galaxies have a deficiency of galaxies of intermediate color compared with a volume-limited sample of nearby galaxies, i.e. between

$$-0.35 \leq \log \mathrm{f}_{5.8\mu\mathrm{m}}/\mathrm{f}_{3.6\mu\mathrm{m}} \leq -0.05, \qquad (1)$$

the distribution of Bitsakis et al. (2011) indicates a lowering in the density of galaxies compared to the LVL galaxy colours. This deficiency, although not a complete "gap", is what led Walker et al. (2010) to suggest HCG galaxies rapidly evolved through this intermediate color region. Alternatively, one could argue that, unlike the LVL sample, the HCG group galaxies have a well-defined red and blue sequence in this color space.

3. OBSERVATIONS AND DATA REDUCTION

3.1. *Spitzer IRS Spectroscopy*

The galaxies and groups listed in Table 1 were targeted by the *Spitzer* IRS instrument (Houck et al. 2004) using the low-resolution Short-Low ($R \sim 60 - 127$; $5.2 - 14.5$ μm) and Long-Low ($R \sim 57 - 126$; $14.0 - 38.0$ μm) modules. Observations were carried out as part of GO-5 PID 50764 and taken between 2008, June 29 and 2009, January 19.

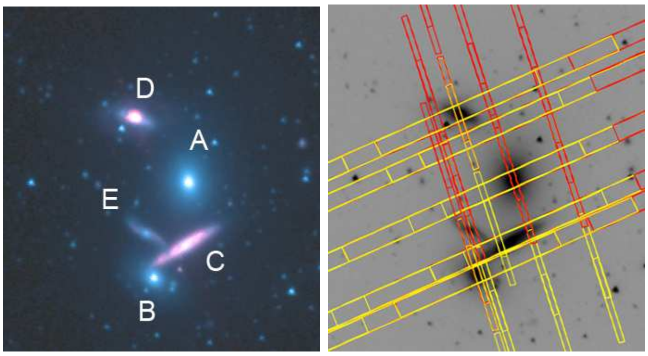

FIG. 2: The IRS sampling (Long-Low; $\sim$ 10.5″ and Short-Low; $\sim$ 3.6″ slits) shown on HCG 40 (IRAC four-color image is $\sim$4′× 4′). 1st order spectral coverage is shown in yellow with 2nd order in red. As can be seen, the mapping combined with staring strategy probes the intragroup region, as well as the galaxies themselves.

Since it was not known apriori where in the group environment shock-excited H_2 emission may be located, the primary observations employed a sparse mapping strategy – centering the most disturbed member of the group on a 3-leg grid[15] (see Figure 2). The scales were adjusted for each group to provide good coverage of the inner group in both modules. The typical coverage was linear ∼70 kpc for SL and ∼180 kpc for LL. In addition, a further two member galaxies were targeted in IRS "Staring Mode", where the target center is placed at the $\frac{1}{3}$ and $\frac{2}{3}$ position along the length of the slit. Because of the way that the IRS performs a staring mode observation (by sampling first the 2nd order spectrum followed by a similar observation in first order), this increases the coverage of the group, further providing information about

---

[15] In most cases this was a 2×3 sparse map with typical step sizes of 30″ parallel (to the slit) steps and 35″ perpendicular for SL, and 70″ and 35″ parallel and perpendicular in the LL module.

potential extended emission in the groups, as well as often intersecting by chance (depending on the roll-angle of the focal plane at the time of the observations) additional group members. As a result, the SL and LL slits typically sampled $\sim$800 kpc^2 and $\sim$6000 kpc^2, respectively, with some of this area covering the galaxies themselves.

Primary data reductions were performed by the *Spitzer* Science Center (SSC) pipeline, version S18.0.2-18.7.0, which performs standard spectral reductions such as wavelength and flux calibration, ramp fitting, dark current subtraction and detector droop and non-linearity linearity corrections. The observing strategy discussed above provides a sparse map across the group. Basic Calibrated Data (BCDs) frames, output from the pipeline, were combined within the SSC tool CUBISM (Smith et al. 2007a), optimised for extended sources, with each AOR forming one spectral cube. This was done to ensure proper background subtraction, using backgrounds taken close in time to the observations. This was achieved using either dedicated backgrounds or from the “off” position BCDs with coverage outside of the group.

Pixel outlier rejection was done using the CUBISM algorithm (with a conservative 8σ clipping) and then by visual inspection of the spectral cubes to ensure that no weak signals are lost. The cubes were inspected for any H_2 emission in the IGM and spectra extracted for each galaxy with coverage. Since we are particularly interested in emission from the disk, we were careful to extract spectra along the slit with an aperture large enough to capture most of the source’s light while still maximising signal to noise. Extraction areas for SL and LL for each galaxy are listed in Table A5. Due to the coverage obtained through the sparse mapping mode, several galaxies have “off-nuclear” coverage where the slits have not been centered on the nucleus; these are indicated in Table A5 and treated separately to those that cover the nuclear region.

Spectra were extracted for all but 4 galaxies in the sample (HCG 6A, 6C, 6D and 79C) where no signal above the noise was detected. Spectra were converted to flux densities (mJy) using the extraction areas, and SL scaled to LL to match continuum levels in cases that required it (see Table A5). This accounts for beam resolution differences between the long and short order; here we make the assumption that the emission in each slit is uniform. The scaling of spectra is further discussed in Section A of the Appendix.

We used PAHFIT to characterize our spectra, but visually inspected each spectrum one by one to determine which lines were detected reliably and which were marginal detections (i.e. between 2 and 3 σ). PAHFIT is a spectral decomposition package (Smith et al. 2007b) that fits emission lines, bands and dust continua to stitched LL and SL spectra.

The spectra rms (root mean square) for determining upper limits were measured using ISO Spectral Analysis Package (ISAP)[16].

3.2. *Spitzer IRAC and MIPS Photometry*

The *Spitzer* IRAC (Fazio et al. 2004) and MIPS (Rieke et al. 2004) instruments were used to obtain imaging at 3.6, 4.5, 5.8 and 8.0μm, and 24μm, respectively, of our sample and observed as part of PID 50764 (P.I. Appleton), PID 40459 (P.I. Le Floc’h), PID 631 (P.I. Mazzarella) and PID 101 (P.I. Kennicutt).

IRAC photometric measurements (to obtain colours) for 21 galaxies in our sample are taken from Bitsakis et al. (2011) as indicated in Table A1. Fluxes for the remainder of galaxies were carefully measured to improve the deblending systematics where contamination from nearby stars and galaxies may affect the photometry. For these systems, the data was reduced using the SSC science pipeline version S18.5.0 and 18.7.0. Galaxy photometry was performed using a matched elliptical aperture, determined by the 1σ isophote in IRAC 3.6μm, after foreground contaminating stars were masked from all images and replaced by the corresponding isophotal value of the source. Nearby contaminating galaxies were similarly masked. The local background was determined from the median pixel value distribution within a surrounding annulus. Aperture corrections were applied as specified by the IRAC Handbook. The formal photometric uncertainties are $\sim$5% for the IRAC calibration error.

Potentially saturated sources, particularly in IRAC 3.6μm and 4.5μm, namely HCG 56B, 91A, 96A and 100A were investigated. HCG 96A was saturated in the cBCDs at IRAC 3.6μm, 4.5μm and 5.8μm. For this system the short HDR (High Dynamic Range) exposures were used for measuring fluxes instead. For HCG 100A the source counts for all bands was nominal, although at their full well capacity. For 56B and 91A the source counts for IRAC 5.8μm and 8.0μm were nominal and below the saturation limit at 3.6μm and 4.5μm. However, since the peak pixel flux is within the non-linear regime at 3.6μm and 4.5μm, the integrated fluxes may be slightly underestimated (as indicated in Table A1), but the mid-infrared colors, however, are likely unaffected.

For galaxies located at a redshift greater than 0.035 the shifting features, in particular the 6.2μm PAH, affect the observed colours of a galaxy. For the groups in our sample affected by this (HCG 6, 8, 55, 75, 82 and 95) we have corrected the IRAC fluxes for redshift (i.e. “k-corrected”) using the empirical template library, 125 galaxy templates in total, of local well-studied and morphologically diverse galaxies (e.g. SINGS, the *Spitzer* Infrared Nearby Galaxy Survey) from M. Brown et al. (in prep.). These are combined using optical and *Spitzer* spectroscopy with matched aperture photometry from *GALEX*, *XMM* UV, SDSS, 2MASS, *Spitzer* and WISE, synthesized with MAGPHYS (da Cunha et al. 2008). For galaxies with velocities $< 9000\,\mathrm{km\,s^{-1}}$, k-corrections do not appreciably affect the mid-infrared colours, or analysis derived thereof, presented in this work.

MIPS 24μm data was processed through SSC science pipeline versions 18.1.0, 18.12.0 and 18.13.0, achieving a spatial resolution of $\sim 6''$. The LL spectral extraction areas output from CUBISM were used to make matched aperture photometric measurements using the IRAF[17] task, POLYPHOT. For star-forming and

---

[16] The ISO Spectral Analysis Package (ISAP) is a joint development by the LWS and SWS Instrument Teams and Data Centers. Contributing institutes are CESR, IAS, IPAC, MPE, RAL and SRON.

[17] IRAF is distributed by the National Optical Astronomy Ob-

AGN-dominated spectra showing continua with a strong power-law dependence, we applied colour corrections as recommended in the MIPS Handbook. This correction is of the order of ∼5%. The MIPS calibration error is of the order of ∼10 – 20%. .

In the cases of 31AC, 40C, 44A and 75D we have H_2 detections in LL coverage without matching SL coverage. In order to measure the 7.7μm PAH emission, we use the prescription of Helou et al. (2004) and measured matched (to the LL extraction) apertures of the IRAC 3.6μm and IRAC 8μm bands. By subtracting a scaled version of IRAC 3.6μm from IRAC 8μm we can compensate for the stellar light contamination in the band and use this as a measure of the strength of the aromatic emission within the band i.e. the 7.7μm PAH (see, for example, Roussel et al. 2007). This was also done for the IGM detections discussed in Section 4.1.1.

4. RESULTS

4.1. *Emission from Warm Molecular Hydrogen*

The pure rotational transitions of molecular hydrogen covered by the SL and LL spectral windows at the redshifts of the HCGs, are the 0-0 S(0), S(1), S(2), S(3), S(4) and S(5) lines at 28.22, 17.03, 12.28, 9.67, 8.03 and 6.91μm, respectively. These can be excited in a variety of astrophysical processes including UV pumping and collisional heating in photodissociation regions associated with star formation (e.g. Hollenbach & Tielens 1997), X-ray heating in XDRs (X-ray dominated regions) -especially near AGN (e.g. Draine & Woods 1992), cosmic ray heating (e.g. Dalgarno et al. 1999) and heating by turbulence or shocks (e.g. Shull & Hollenbach 1978). We detect ($> 2\sigma$) two or more lines of warm H_2 in 32/74 galaxies in our sample; this includes marginal detections, but we do not include these in the analysis that follows. In addition, we have two tentative detections of excited H_2 in the group IGM.

Many of the galaxies located in HCGs are star forming systems, generating a UV radiation field capable of heating very small grains (VSGs) and exciting PAH molecules, thus producing distinctive dust features in the mid-infrared. We wish to focus on systems where the H_2 emission is shock-excited. In order to separate mechanical heating of H_2 from UV-heating within photodissociation regions (PDRs) associated with active star formation, we use the 7.7μm PAH emission band as a discriminator (described by Ogle et al. 2010). By using the ratio of H_2 luminosity (summed over the 0-0 S(1)–S(3) lines) to the 7.7μm PAH luminosity we can determine which systems have enhanced or "MOHEG-type" emission. A MOHEG (MOlecular Hydrogen Emission Galaxies), by definition, has a H_2/7.7μm PAH ratio ≥ 0.04 (Ogle et al. 2010) i.e. strongly H_2-emitting compared to SINGS star-forming galaxies (Roussel et al. 2007). The value of H_2 S(0)-S(3)/PAH (7.7μm) ratio separating PDR-dominated H_2 heating from other heating sources has been demonstrated by radiation modeling (Guillard et al. 2012b).

4.1.1. *H_2 in the Group IGM*

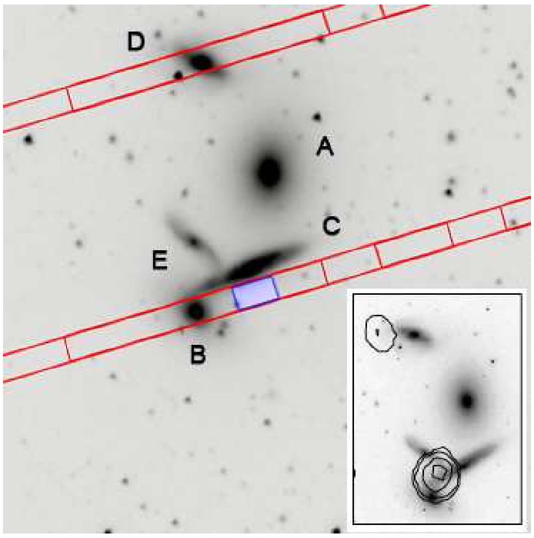

(a) HCG 40 IRAC 3.6μm image with LL slit coverage overlaid; the blue box shows the position of the extraction. Inset: The VLA H I distribution from Verdes-Montenegro et al. (2001). Image reproduced with kind permission from the authors.

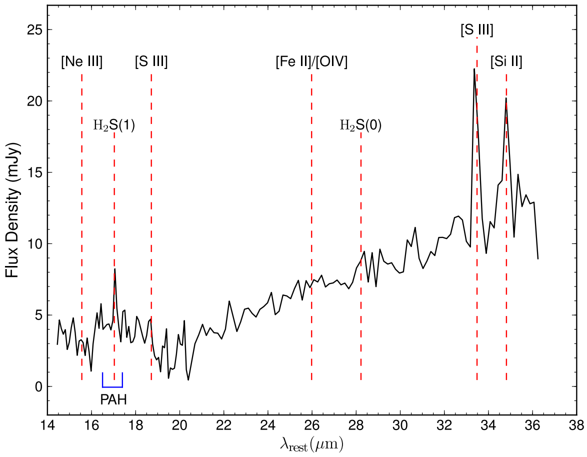

(b) LL Extraction centered on 09^{h}38^{m}53.45^s, -04°51′47.2″

FIG. 3: Due to a latent-induced flux bias in the first set of BCDs, the signal-to-noise of the S(1) line is diminished.

A key aim of this project was to determine how common IGM warm H_2 (as in SQ) is in compact groups. From the sample of 23 groups, we have discovered two locations showing warm H_2 detections in the IGM. These are both detected in the LL spectra and appear to come from the edge of the disks. Figure 3 and 4 show detections in HCG 40 and HCG 91, respectively. We consider these detections to be preliminary, demanding follow-up observations for confirmation.

In HCG 40, we detect the S(1) line (Figure 3) outside the Sb galaxy HCG 40C (the positions of the IRS slits are shown in 2), fitting an approximate velocity of 5700 km^{-1}, offset from that in NED (6406±6 km s^{-1}), but well within the uncertainties given the LL spectral resolution of 3350 km s^{-1} at 17μm. Using the IRAC 3.6μm and 8.0μm coverage to provide an estimate of the 7.7μm PAH emission (4.771×10^{-16} W.m^{-2}) and the

---

servatory, which is operated by the Association of Universities for Research in Astronomy, Inc., under cooperative agreement with the National Science Foundation

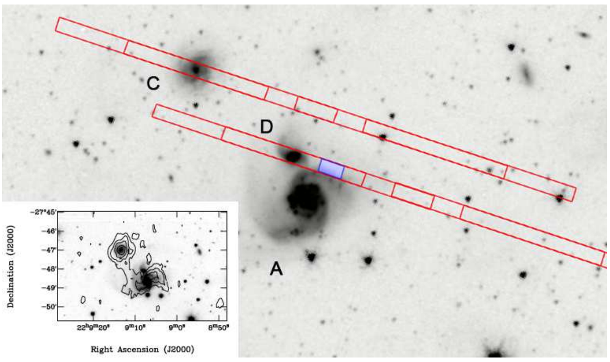

(a) HCG 91 IRAC 3.6μm image with LL slit coverage overlaid; the blue box shows the position of the extraction. Inset: The ATCA H I distribution from Barnes & Webster (2001). Image reproduced with kind permission from the authors.

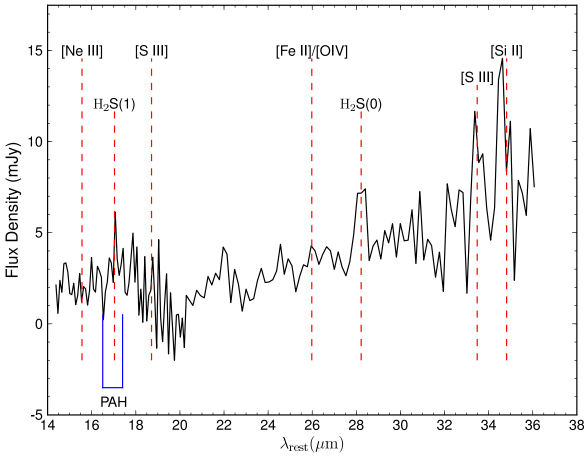

(b) LL extraction centered on $22^{h}09^{m}06.20^{s}$, -27°48′09.1″.

FIG. 4: Due to a latent effect in the first set of BCDs, the signal-to-noise of the S(1) line is diminished.

combined S(0) and S(1) flux of 1.017×10^{-17} W.m^{-2}, we find a $H_2$7.7μm PAH ratio of > 0.021; it is a lower limit due to missing SL coverage, as well as the poor signal to noise of the S(1) line due to the latent-induced flux bias in the first set of BCDs.

The VLA H I distribution (shown as an inset of Fig. 3a) indicates the presence of H I in the IGM between 40B, 40C and 40E, made all the more unusual by the fact that this system suffers the greatest H I-deficiency of the HCGs studied by Verdes-Montenegro et al. (2001). Interactions with a tidal tail associated with 40E could account for this emission, and would also explain the (albeit weak) warm H_2 signal from 40B presented in the next section. Follow-up IRAM CO observations (Lisenfeld et al., in prep.) find indications for extended CO emission at the location of the IGM detection within the group.

In HCG 91, we find a detection at what appears to be the edge of the disk of 91A, a star-forming galaxy (Figure 4). The LL2 spectrum suffers from a similar latent effect as above (due to observing a bright target prior to this observation) and the first BCD is contaminated, resulting in a lower signal to noise for the S(1) detection, but we see a strong S(0) detection. In spite of this, the estimated $H_2$7.7μm PAH ratio (calculated as above with an H_2 flux of 1.430×10^{-17} W.m^{-2} and 7.7μm dust estimate of 3.511×10^{-16} W.m^{-2}) is $>$0.041 and therefore would be classified as a MOHEG even without SL coverage.

Barnes & Webster (2001) find two H I knots centered around HCG 91A and 91C with a connection between the two through a gas bridge (shown in the inset of Fig. 4a), since there is a common velocity between the southern part of HCG 91C and the northern part of HCG 91A. Amram et al. (2003) find that the Hα distribution shows a tidal arm pointing from HCG 91A towards HCG 91C. They also find a double gaseous component for HCG 91C strongly suggestive of a past interaction. They suggest a possible scenario where HCG 91C is passing through the group forming the tail of HCG 91A.

The location of these two detections suggest a possible connection with disks interacting with the group IGM.

4.1.2. *H_2 in Individual Group Galaxies*

In Table A1 of the Appendix, we summarise the IRAC fluxes for all galaxies in our sample and indicate whether a warm H_2 detection was made in an individual galaxy. The fluxes determined for the H_2 emission lines are presented in Table A2; we note that several systems have their SL and LL lines presented separately due to the regions sampled by the IRS not overlapping (and therefore not joined together). In addition, spectra that are not centered on the nucleus (therefore dominated by emission from the disk) are indicated. Extraction areas for H_2-detected galaxies are listed in Table A5. The strengths of the PAH complexes and atomic emission lines for the H_2-detected systems are presented in Tables A3 and A4, respectively. Upper limits for the H_2 S(0)–S(3) emission for galaxies without H_2 detections, and measurements of their PAH features, are included in the Appendix.

In Table 2 we summarise the summed H_2 fluxes (upper limits and marginal detections are not included), H_2 (S(0)-S(3))/PAH (7.7μm) ratio and MIPS 24μm fluxes (measured within a matched aperture). We find 13 MOHEG galaxies (H_2/7.7μm PAH $\geq$ 0.04) and 19 non-MOHEGs, i.e. with H_2 emission in line with star formation. We note, however, that HCG 44A only has LL coverage with detected H_2 (the SL slits sampled only a small section of the outer disk) and we thus have a lower limit for its H_2/7.7μm PAH ratio (see Fig. 10). However, from the SINGS study, we know it has a H_2/7.7μm PAH value of 0.042 (Roussel et al. 2007) and is therefore a weak MOHEG.

We find 13 MOHEGs in our sample. As shown in Section 2, the distribution of Bitsakis et al. (2011) indicates a lowering in the density of galaxies between

$$-0.35 \leq \log f_{5.8\mu m}/f_{3.6\mu m} \leq -0.05, \qquad (2)$$

compared to the LVL galaxy colors. If we separate the MOHEGs according to mid-infrared color, we find 11 located between $-0.35 \leq \log[f_{5.8\mu m}/f_{3.6\mu m}] \leq -0.05$ (i.e. intermediate mid-infrared colors); these systems have enhanced H_2 relative to their star formation, and their mid-infrared colors reflect that globally they are not dominated by star formation (or AGN emission); this is a clear indication that the warm H_2 is not UV-excited. This is discussed further in Section 4.1.4.

The morphological types of the H_2-detected systems are given in Table 3, where de Vaucouleurs et al. (1991)

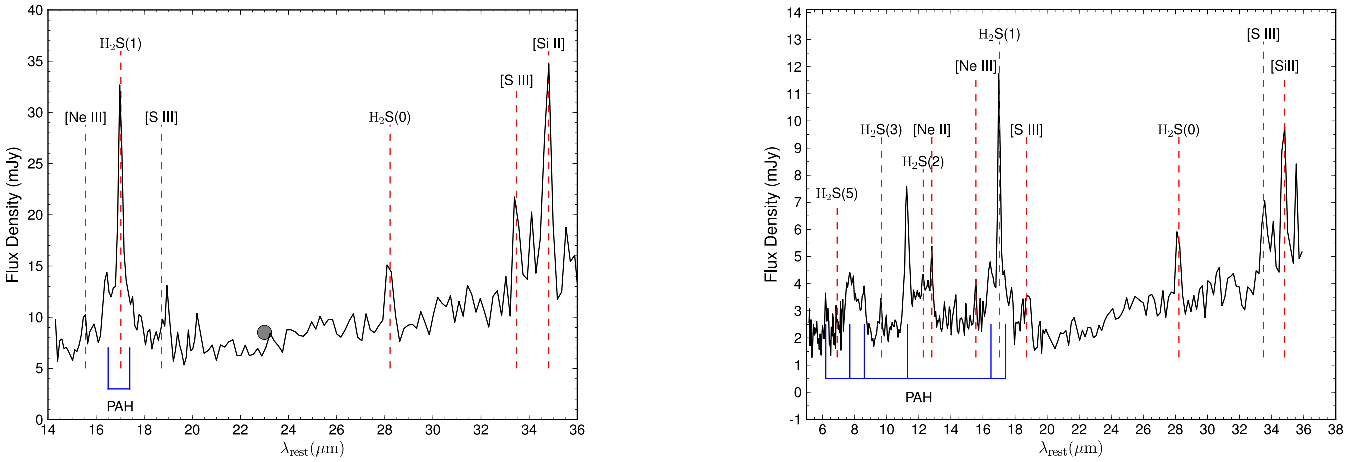

(a) HCG 57A - including the nuclear region

(b) HCG 57A - off-nuclear extraction

FIG. 5: Spectra of HCG 57A. The matched MIPS 24μm photometry is shown as a grey point.

TABLE 2: H_2-detected Galaxies: H_2 and 24μm Data

Source	H_2 S(0)–S(3) ($\mathrm{W\,m^{-2}}$)	log $L(H_2)$ ($L_\odot$)	H_2/7.7μm	$F_{24\mu\,\rm m}$ mJy	log L_{24} ^{a} $L_\odot$
6B	1.633e-17	7.093	0.198	2.14	8.31
15A	8.012e-18	6.321	0.044	3.46	8.05
15D	2.280e-17	6.776	0.112	3.25	8.03
25B*	3.299e-18	5.883	0.098	–	
25B$^{\diamond\dagger}$	1.159e-17	6.429	–	3.08	7.95
31A+C$^\diamond$	2.004e-17	6.289	0.002	286.87	9.54
40B	5.619e-18	6.227	0.083	4.72	8.25
40C$^\diamond$	9.166e-17	7.439	0.010	46.52	9.24
40D	4.707e-17	7.150	0.013	67.71	9.40
44A$^\diamond$	1.338e-16	6.355	0.027	98.74	8.32
44D	6.202e-17	6.021	0.021	35.22	7.87
47A	2.556e-17	7.181	0.035	31.96	9.38
55C	8.395e-18	7.126	0.018	5.31	9.02
56B	1.829e-17	6.885	0.053	138.52	9.86
56C	1.205e-17	6.704	0.037	^{b}3.59	8.27
56D*	1.338e-17	6.749	0.018	6.03	8.50
56E	3.169e-18	6.124	0.012	4.88	8.41
57A†	2.501e-17	7.140	–	–	–
57A$^\diamond$	8.385e-17	7.665	0.174	8.52	8.77
67B	2.330e-17	6.920	0.006	20.84	8.97
68A	4.275e-17	6.228	0.741	13.63	7.83
68B	8.100e-18	5.505	0.073	6.77	7.52
68C	1.311e-16	6.714	0.044	137.13	8.83
75D$^\diamond$	9.676e-18	6.985	0.010	8.59	9.03
79A	2.693e-17	6.503	0.011	15.13	8.35
79B	1.045e-17	6.092	0.010	18.11	8.43
82B	8.947e-18	6.821	0.045	3.26	8.48
82C	5.567e-17	7.614	0.014	62.51	9.76
91A	5.931e-17	7.227	0.030	159.93	9.75
91C	1.770e-17	6.702	0.016	13.35	8.68
95C	3.354e-17	7.438	0.071	13.35	9.14
96A	8.378e-17	7.553	0.007	914.78	10.69
96C	3.928e-17	7.224	0.018	30.45	9.21
100A	5.459e-17	6.910	0.013	102.11	9.28

[a] $L_{24} \equiv \nu L_\nu(24\mu\mathrm{m})$

* $S(2)$, $S(3)$ lines (SL coverage)

$^\diamond$ $S(0)$, $S(1)$ lines (LL coverage)

† Off nuclear extraction

[b] Contamination from 56B and 56D

classifications are given; where these are absent or assigned a ? symbol, classifications from Hickson et al. (1989) are given. We include the nuclear classifications from Coziol et al. (2004), Brinchmann et al. (2004), Martínez et al. (2010), as well as the T-Type from the RC3 catalogue of de Vaucouleurs et al. (1992).

We include the spectra for the non-MOHEG H_2 galaxies in Section B of the Appendix, as well as any discussion pertaining to individual systems. Spectra for the MOHEG galaxies are presented in the following section.

4.1.3. *Spectra of MOHEG Sources*

The power in H_2 lines compared to the mid-infrared continuum is particularly noticeable in several MOHEGs. For example, in Figure 5 we show two spectra of HCG 57A, one centered on the nuclear region (LL only) and a matched, off-nuclear extraction in the disk of the galaxy, made possible by the sparse mapping strategy employed (see Section 3.1). The nuclear extraction shows powerful H_2 S(1) and S(0) emission and, although we have no coverage of the PAH bands, we do not see a steeply rising mid-infrared continuum typical of star-forming systems.

The off-nuclear extraction shows powerful H_2 emission with relatively weak 6.2 and 7.7μm PAH emission. This spectrum suggests a non-star-forming mechanism able to excite the H_2 in the disk of galaxy, away from the nucleus.

In Figure 6 and 7 we plot the spectra the other HCG galaxies classified as MOHEGs that lie at intermediate mid-infrared color ($-0.35 \leq \log[f_{5.8\mu m}/f_{3.6\mu m}] \leq -0.05$). In particular, HCG 6B (Fig. 6a) and HCG 15D (Fig. 6c) show the distinctive H_2 S(1) emission line dominating the spectrum, with little 6.2 and 7.7μm PAH emission, reflected in Figure 10.

HCG 25B has SL coverage of the nuclear region (Fig. 6e) and we see clear H_2 S(2), S(3) and S(5) emission (the weaker S(4) transition is not seen above the PAH emission at 8μm). Similar to HCG 57A, 25B has coverage of the disk region – it covers a larger region compared to the SL extraction, and is noiser, yet we see the S(1) clearly above the weak mid-infrared continuum, again suggestive of a mechanism influencing regions away from the nucleus.

For HCG 68A and 68B, we see the strong contribution

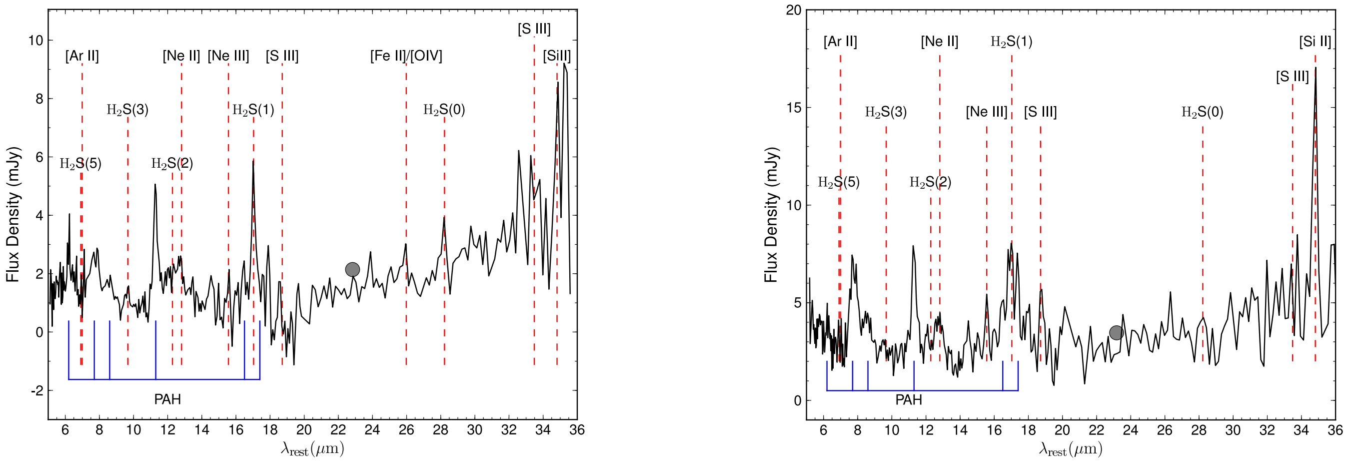

(a) HCG 6B

(b) HCG15A

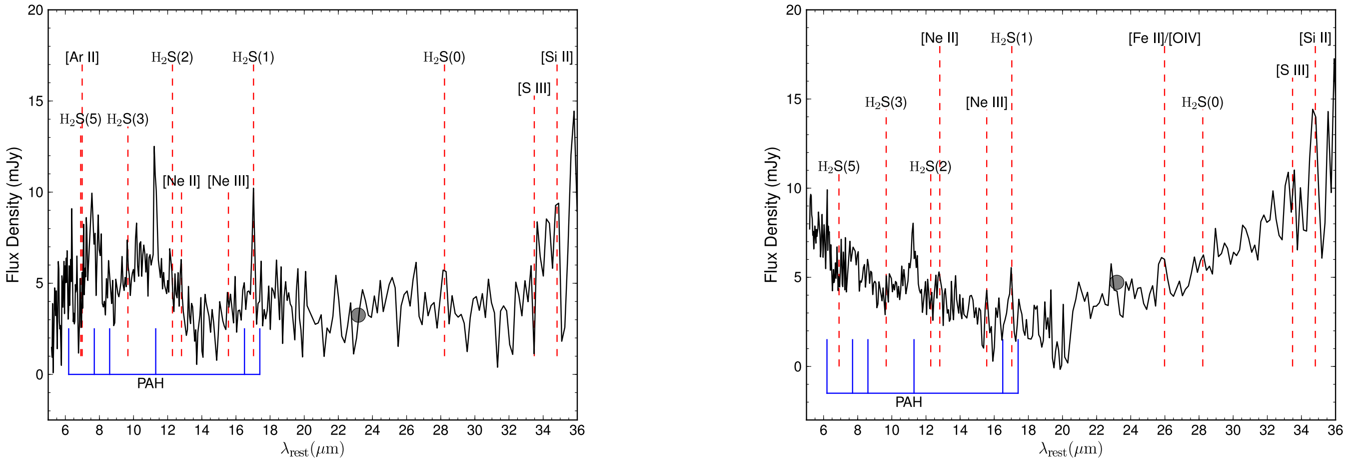

(c) HCG15D

(d) HCG 40B

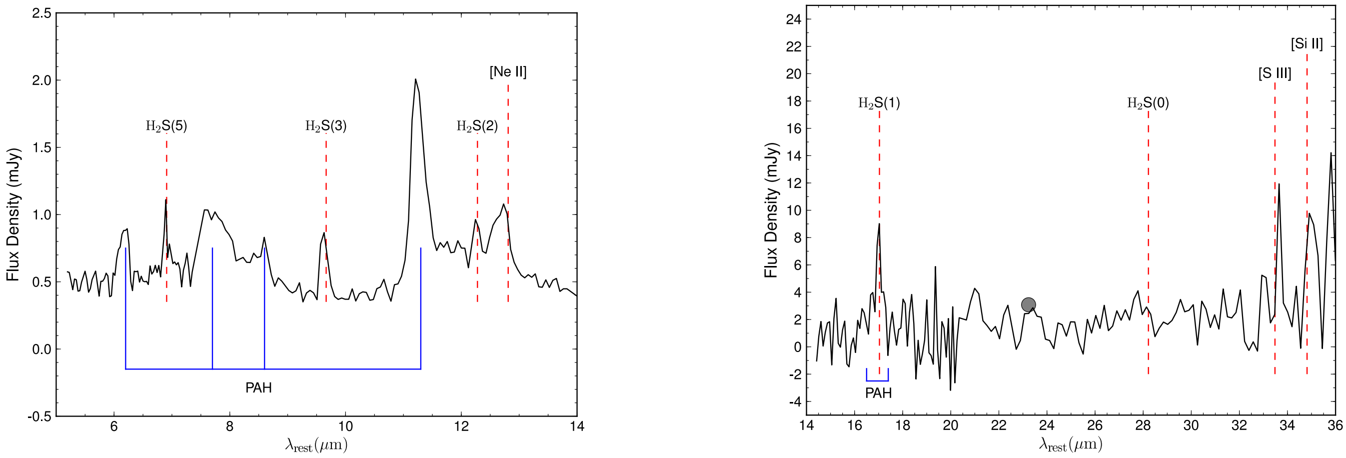

(e) HCG25B - including the nuclear region

(f) HCG25B - off-nuclear extraction

FIG. 6: MOHEGs with Intermediate Mid-infrared Colours. The matched MIPS 24μm photometry is shown as a grey point.

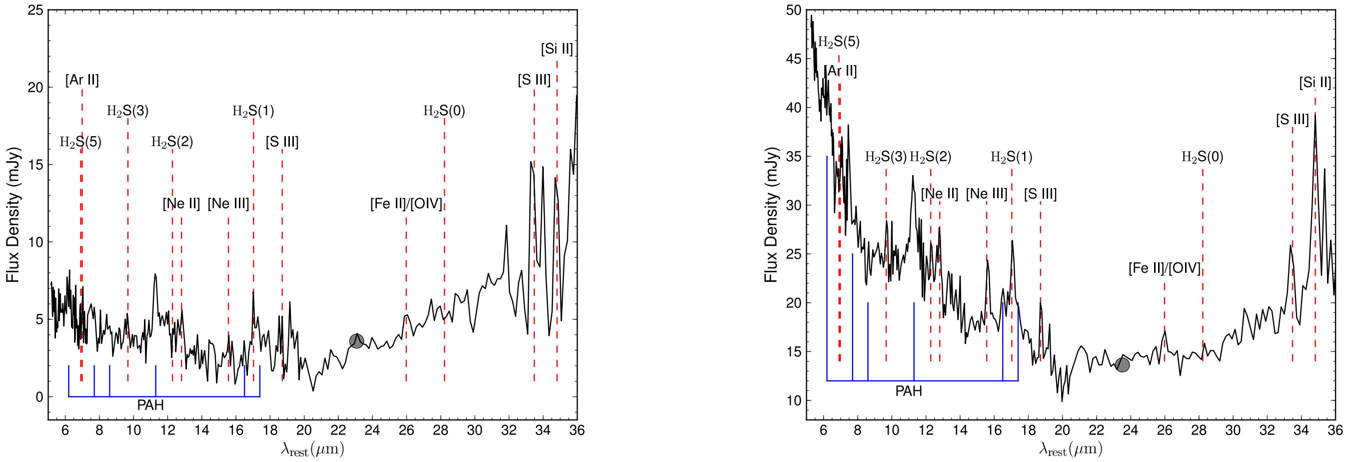

(a) HCG 56C

(b) HCG 68A

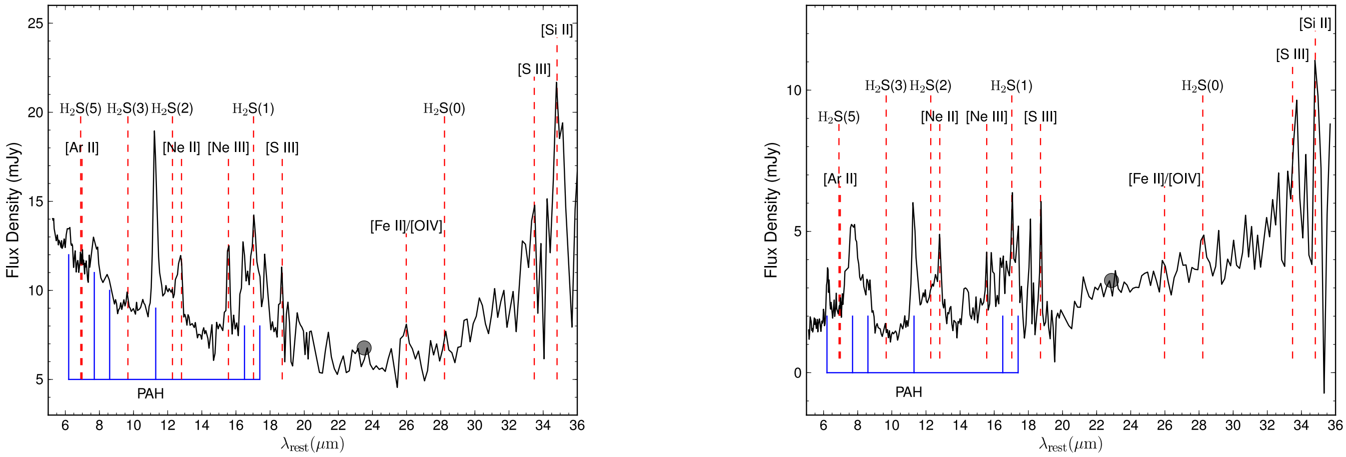

(c) HCG 68B

(d) HCG 82B

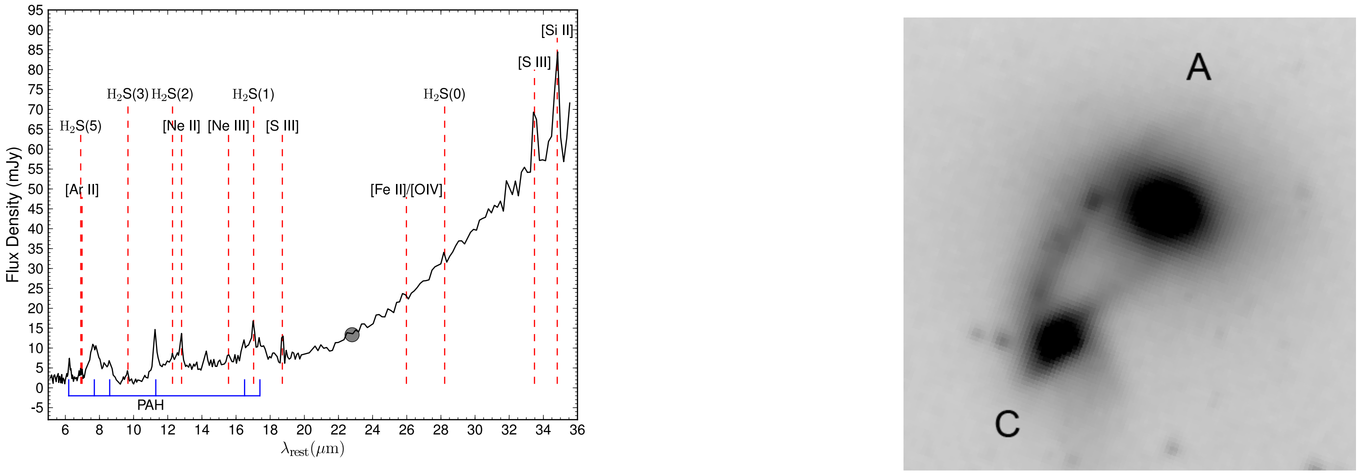

(e) HCG 95C

(f) HCG 95C - IRAC 3.6μm image ($\sim 1' \times 1'$)

FIG. 7: MOHEGs with Intermediate Mid-Infrared Colours (cont.). The matched MIPS 24μm photometry is shown as a grey point.

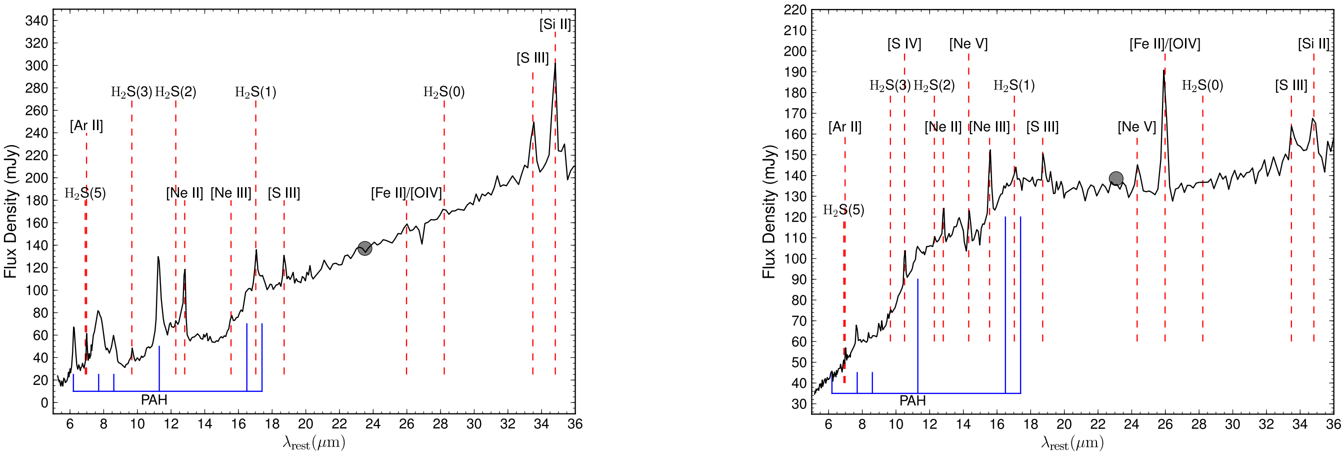

(a) HCG 68C – Star Formation-dominated spectrum

(b) HCG 56B – AGN-dominated spectrum

FIG. 8: MOHEGs with Star Formation-/AGN-Dominated Colours. The matched MIPS 24μm photometry is shown as a grey point.

from the stellar continuum ($\lambda < 18\mu$m), indicative of their early type morphology (S0), yet the H_2 S(1) and S(3) ortho transitions feature clearly.

In contrast, the galaxies HCG 40B (Fig. 6d) has a spectrum where the warm H_2 emission does not appear to be very strong – the S(1) line is weakly detected – and we note that the 7.7μm PAH is very weak.

The fact that the 11.3μm PAH often features prominently in these spectra is not surprising as the large, neutral PAHs can be excited by soft radiation from evolved stars (Kaneda et al. 2008) and this would be consistent with their early-type morphologies.

We note that HCG 95C (Fig. 7e) appears discrepant compared to the spectra shown in Figures 6 and 7. The strong PAH emission and steeply rising 24μm continuum is indicative of a system dominated by star formation. Figure 7f shows that the galaxy is highly disrupted due to an interaction with 95A, and its current state is classified as having an Sm morphology. The galaxy appears to have two nuclei and is either part of an ongoing merger between two galaxies or is seen in projection with each system having interacting with 95A individually to produce the the bridges and tails (Iglesias-Páramo & Vílchez 1998).

However, the mid-infrared color of this system (95C) is not strongly star-forming and indeed, the $\log[f_{5.8\mu m}/f_{3.6\mu m}]$ color of -0.08 places it within the intermediate region (Fig. 10).

Within our sample, there are two galaxies that show MOHEG-like emission with global mid-infrared colours that suggest they are dominated by star formation, or AGN activity ($\log[f_{5.8\mu m}/f_{3.6\mu m}] > -0.05$); their spectra are included in Figure 8. The spectrum of HCG 68C appears typical of a star-forming galaxy, with a steeply rising mid-infrared continuum and clear 6.2 and 7.7μm PAH emission. HCG 56B is a known Seyfert 2 galaxy and shows a power law continuum combined with high ionisation lines typical of an AGN-dominated mid-infrared spectrum.

4.1.4. *Comparison to Mid-Infrared Color*

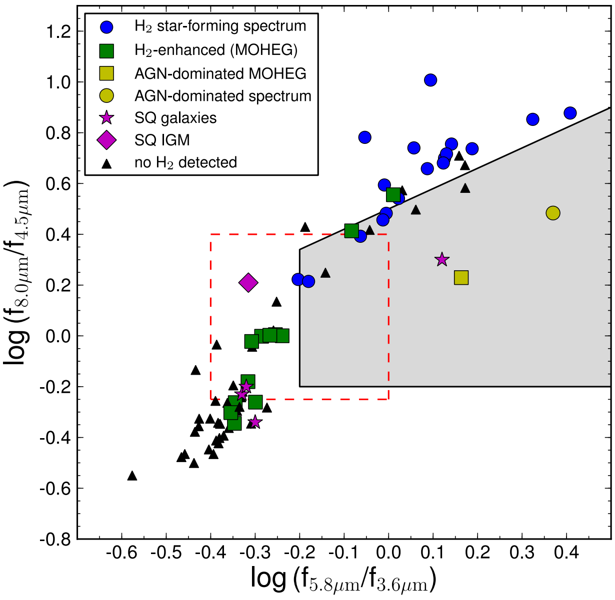

FIG. 9: IRAC colour-colour diagram for the sample; H_2-bright galaxies are shown as green squares, H_2-detected galaxies are shown as blue circles. The red box shows the gap in color-color space from Walker et al. (2010). The shaded region corresponds to the AGN colour selection criteria of Lacy et al. (2004); AGN-dominated systems are in yellow. The purple diamond is the location of the shocked IGM in SQ (from Cluver et al. 2010), with member galaxies shown as magenta stars.

In Figure 9 we plot the IRAC color-color diagram ($\log[f_{8.0\mu m}/f_{4.5\mu m}]$ vs $\log[f_{5.8\mu m}/f_{3.6\mu m}]$) for our entire sample of 74 galaxies, color-coded according to their mid-infrared spectral features as follows: no warm H_2 detected (black triangles), H_2 detected in line with UV-heated PDR emission (blue circles), H_2 detected in a galaxy with an AGN-dominated spectrum in the mid-infrared (yellow circle), H_2-enhanced galaxies i.e.

TABLE 3: Morphologies and Nuclear Classifications

Galaxy	Morphology	Nuclear class.	T-Type†
MOHEGs with $-0.35 \leq \log[\mathrm{f}_{5.8\mu\mathrm{m}}/\mathrm{f}_{3.6\mu\mathrm{m}}] \leq -0.05$			
6B	S?$^\diamond$, Sab*	TO^a	–
15A	S0$^\diamond$	dLINER^b	-2
15D	S0$^\diamond$	LINER^b	-3
25B	SBa*	HII^c	-2
40B	SA0(r) pec$^\diamond$	No emission^b	-3
56C	S0/a pec$^\diamond$	No emission^b	0
57A	Sab? pec$^\diamond$, Sb*	AGN^a	2
68A	S0?$^\diamond$, S0*	No emission^b	-2
68B	S0$^\diamond$	TO^a, dLINER^b	-2
82B	SB0?$^\diamond$, Sa*	TO^a	-2
95C	Sm*	AGN^a	–
MOHEGs with $\log[\mathrm{f}_{5.8}/\mathrm{f}_{3.6}] > -0.05$			
68C	SB(r)b$^\diamond$	TO^a, LINER^b	3
56B‡	SB0*	AGN^a, Sy 2^b	–
non-MOHEG H_2-galaxies			
31AC	Sm/Im*	H II^a	–
40C	SB(rs)b pec$^\diamond$	TO^a, H II^b	3
40D	SB(s)0/a pec$^\diamond$	TO^a, H II^b	0.3
44A	SA(s)a pec$^\diamond$	AGN^a	1
44D	SB(s)c pec$^\diamond$	TO^a	5
47A	SA(r)$^\diamond$	AGN^a	–
55C	SBa pec?$^\diamond$, E*	–	1
56D	SA(s)0/a pec?$^\diamond$, S0*, •	TO^a, H II^b	0
56E	SB0 pec?$^\diamond$, S0*, •	H II^a, H II?^{b}	-2.1
67B	Sb$^\diamond$	H II^a	3
75D	Sd*	HII^c	7
79A	Sa pec$^\diamond$	TO^a, LINER^b	1
79B	S0 pec$^\diamond$	H II?^{b}	-2
82C	S?$^\diamond$, Im*	TO/AGN^a	–
91A	SB(s)bc pec?$^\diamond$, SBc*	AGN^a	4.3
91C	S?$^\diamond$, Sc*	–	–
96A‡	SA(r)bc pec$^\diamond$	AGN^a	4
96C	S?$^\diamond$, Sa*	TO^a	–
100A	S0/a$^\diamond$	TO^a	0

Note. — TO indicates line ratio's intermediate between AGN and H II, dLINER designation indicates a LL (low luminosity) AGN

† From the RC3 Catalogue of de Vaucouleurs et al. (1992) * From the Optical Classification of Hickson et al. (1989)

$^\diamond$ From the Classification of de Vaucouleurs et al. (1991)

• Misclassification Bitsakis et al. (2011)

‡ AGN-dominated Mid-Infrared Spectrum

[a] Martínez et al. (2010)

[b] From Coziol et al. (2004)

[c] Brinchmann et al. (2004)

MOHEGs (green squares), and MOHEGs with AGN-dominated mid-infrared spectra (yellow squares). For reference, we include the region defined by Walker et al. (2010) as the gap in color-color space. We note that our mid-infrared spectra sample the nuclear and disk regions and reflect the galaxies' global properties – optical nuclear classifications from the literature are provided in Table 3.

For comparison, we also plot in Figure 9 the IRAC colors of the shocked region in SQ and the SQ member galaxies – a system undergoing very powerful interaction. The H_2-enhanced systems (green squares) systems are located preferentially in and around the lower left part of the red box, which suggests a possible connection to transformation from blue star-forming to "red sequence", passively evolving systems.

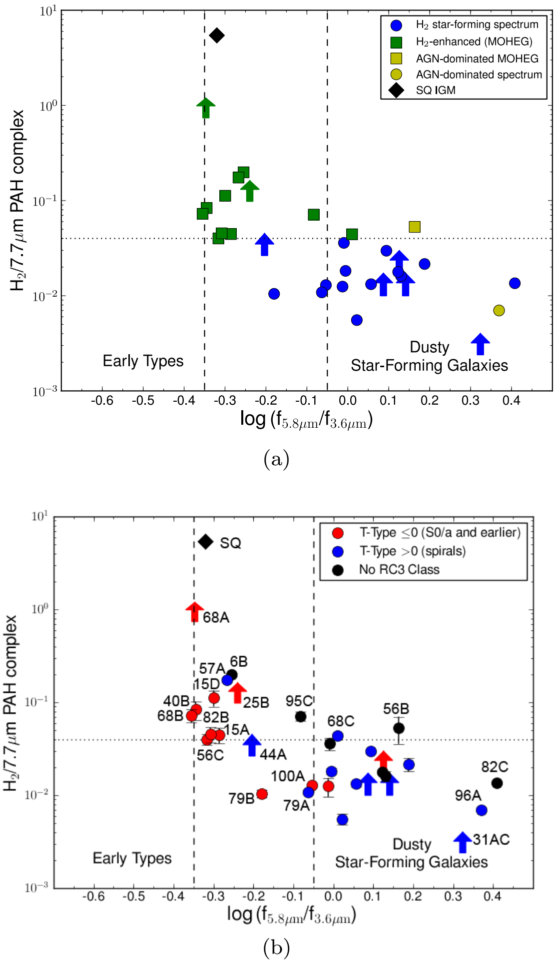

(a)

(b)

FIG. 10: a) H_2 S(0)-S(3)/7.7μm PAH ratio as a function of IRAC color ($\mathrm{f}_{5.8\mu m}/\mathrm{f}_{3.6\mu m}$) with the same symbols as in Figure 9. Lower limits (arrows) and the location of the IGM shock in SQ (diamond) are shown. The dashed line indicates the intermediate mid-infrared colours (determined in Section 2) and the dotted line indicates MOHEG H_2-enhancement from Ogle et al. (2010). b) H_2 S(0)-S(3)/7.7μm PAH ratio as a function of [$\mathrm{f}_{5.8\mu m}/\mathrm{f}_{3.6\mu m}$] color color-coded according to T-Type. Error bars from the combined line measurements are indicated, although for several systems they are comparable to the size of the marker.

To explore this further, we plot in Figure 10, the H_2/7.7μm PAH ratio as a function of mid-infrared color (*Spitzer* IRAC 5.8μm/3.6μm bands); here H_2 represents the sum of S(0)-S(3) lines, as per the definition of MOHEG, as listed in Table 2. We note that HCG 68A has an upper limit for its 7.7μm PAH detection,the other upper limits are due to not having a complete spectrum to determine the total warm H_2 emission. The dashed lines indicate the $\log[\mathrm{f}_{5.8\mu m}/\mathrm{f}_{3.6\mu m}]$ colour limits of the "intermediate-color" systems as shown in Figure 1b i.e.

$$-0.35 \leq \log \mathrm{f}_{5.8\mu m}/\mathrm{f}_{3.6\mu m} \leq -0.05, \qquad (3)$$

This region we define as the mid-infrared "green valley". A discussion of the link between the optical and mid-infrared green valley is included in Section 5.3.

HCG 31AC has the lowest H_2/7.7μm PAH ratio within the sample, likely due to powerful PAH emission arising from a triggered starburst in this merging system (Gallagher et al. 2010). Apart from the AGN-dominated systems (in yellow), the H_2/7.7μm PAH ratios appear to increase towards more negative IRAC color, with MOHEGs predominately found at intermediate color in what we now term the mid-infared green valley.

4.1.5. *H_2 and the Mid-Infrared Continuum*

VSGs reprocess UV radiation to give rise to the mid-infrared continuum at 24μm. Since a UV radiation field can be produced by star formation, AGN emission and radiative shocks (Dopita & Sutherland 1996), a paucity of 24μm emission relative to that from excited H_2 is a strong indicator of non-radiative (e.g. shock) heating of H_2. In star-forming galaxies, $L(H_2)/L_{24}$ appears to decrease with increasing L_{24} (Roussel et al. 2007). This effect is similar to the decreasing L(PAH)/L_{24} with L_{24} observed in starbursts and ULIRGS that may be due to increasing AGN heating in these systems (e.g. Desai et al. 2007). Depletion of VSGs due to shocks may also be a factor.

We plot in Fig 11a the ratio of H_2 to 24μm luminosity as a function of $\log[f_{5.8\mu m}/f_{3.6\mu m}]$ color and we see a similar distribution to that of the H_2/7.7μm PAH ratio. The increased $L(H_2)/L_{24}$ values compared to star-forming systems indicates the importance of non-radiative heating, most likely due to shocks. We find that the systems with AGN-dominated mid-infrared colors (HCG 56B and HCG 96A) to have low $L(H_2)/L_{24}$ values, but the highest L_{24} luminosities in the sample, lying within the locus found for radio galaxies (Ogle et al. 2010). This is in agreement with their mid-infrared spectra. The lowest $L(H_2)/L_{24}$ value is found for the HCG 31AC complex and its associated starburst Gallagher et al. (2010).

Fig 11b plots H_2/7.7μm PAH versus $L(H_2)/L_{24}$, which shows that H_2 emission and 7.7μm PAH emission decrease together relative to $L(H_2)/L_{24}$, i.e. 7.7μm PAH emission decreases in line with a decrease in L_{24}. Omitting lower limits and mid-infrared AGN-dominated systems, we show a least-squares fit to the data as the grey dashed line in Fig 11b. The clear outlier is HCG 56B with a large L_{24}, but high H_2/7.7μm PAH emission. The deficit of 24μm continuum relative to H_2 emission in the HCG MOHEGs (except for HCG 56B) strongly suggests shock heating.

4.2. *Atomic Emission Lines*

In this section we discuss the ionic emission of several few key systems, as well as the sample overall. In Figure 12 we plot the H_2/7.7μm PAH ratios as functions of [NeIII] 15.56μm/[NeII] 12.81μm and [SIII] 33.48μm/[SiII] 34.82μm, respectively. We note that for the majority of HCG MOHEGs, the [NeII] 12.81μm, [NeIII] 15.56μm, [SIII] 33.48μm and [SiII] 34.82μm are upper limits or marginal detections and are not shown.

The [NeIII] 15.56μm/[NeII] 12.81μm ratios shown in Fig. 12a occupy the same range as what is found in the SINGS sample (Dale et al. 2009) and starburst systems (Bernard-Salas et al. 2009). HCG 56B shows a distinctive AGN-dominated spectrum (Fig. 8c) with a substantial warm dust continuum and the high ionisation [NeV] 24.32μm and [OIV] 25.89μm (blended with [FeII] 25.98μm in LL) emission lines. This galaxy is classified as a Seyfert 2 (Khachikian & Weedman 1974) and we determine a [NeIII] 15.56μm/[NeII] 12.81μm ratio of ~ 1.86 signifying a hard radiation field. Given the powerful continuum emission, the warm H_2 lines do not appear very strong, but the weak 7.7μm PAH band gives rise to the enhancement of H_2. This system may be exhibiting excited H_2 produced within the XDR associated with the AGN (Maloney et al. 1996) or, alternatively, due to jet interactions with the ISM (Ogle et al. 2010). Based on its L_{H_2}/L_X ratio (see section D of the Appendix) we can rule out XDR-heating and, in combination with its radio luminosity (Table D2), a jet-ISM interaction appears a more likely mechanism.

HCG 68B and 15A have high ratios of [NeIII] 15.56μm/[NeII] 12.81μm (3.1 and 2.6, respectively), but are classified as low-luminosity LINERS from their optical spectra (Coziol et al. 2004). We note that 68B and 15A are NVSS catalogued radio sources (see Table D2). HCG 68A also has a relatively high ratio, but Coziol et al. (2004) assign it as having no clear optical emission lines, however, it is an NVSS source (see Table D2). Since [NeIII] 15.56μm and [NeII] 12.81μm can also be shock-excited (Allen et al. 2008) and is observed associated with the shock in SQ (Cluver et al. 2010) and in supernovae remnants (Neufeld et al. 2007), we may be seeing evidence of this. For HCG 57A's off-nuclear extraction, the [NeIII] 15.56μm/[NeII] 12.81μm ratio is ~ 0.77 indicating a radiation field typical of star-forming and Seyfert sources (Dale et al. 2006).

The nebular line [SIII] 33.48μm can be used to determine relative enhancement of the [SiII] 34.82μm in active galaxies with hard radiation fields, or associated with XDR emission and, finally, due to shocks returning Si to the gas phase (as seen in SQ; Cluver et al. 2010). In Fig. 12b, [SIII] 33.48μm/[SiII] 34.82μm ratios of between 0.5 and and 2 are expected for star-forming regions (Dale et al. 2009), with an average of $\sim$0.8. [SIII] 33.48μm/[SiII] 34.82μm values of < 0.4 generally indicates enhanced [SiII] 34.82μm emission, indicate of the presence of an AGN or shocks. Very few HCG MOHEGS can be plotted on this figure, mostly due to the [SIII] 33.48μm line having only an upper limit (see Table A4). However, HCG 68A has a [SIII] 33.48μm/[SiII] 34.82μm value of 0.36, significantly lower than SINGS ratios. This may be an indication of silicon atoms being liberated from dust grains driven by shocks. The galaxy is an NVSS source, but is not classified as an AGN optically (Coziol et al. 2004). HCG 57A's off-nuclear spectrum has a [SiII] 34.82μm/[SIII] 33.48μm of ~ 1.71, which is marginally higher than the average found for normal galaxies (~ 1.2, Dale et al. 2006) despite not incorporating the nucleus. The galaxy may host an AGN (see Table 3), but the [SIII] 18.71μm/[SIII] 33.48μm ratio is ~ 0.58, corresponding to an electron density of $100 - 200\mathrm{cm}^{-3}$, close to the low-density limiting value for this diagnostic (Smith et al. 2009).

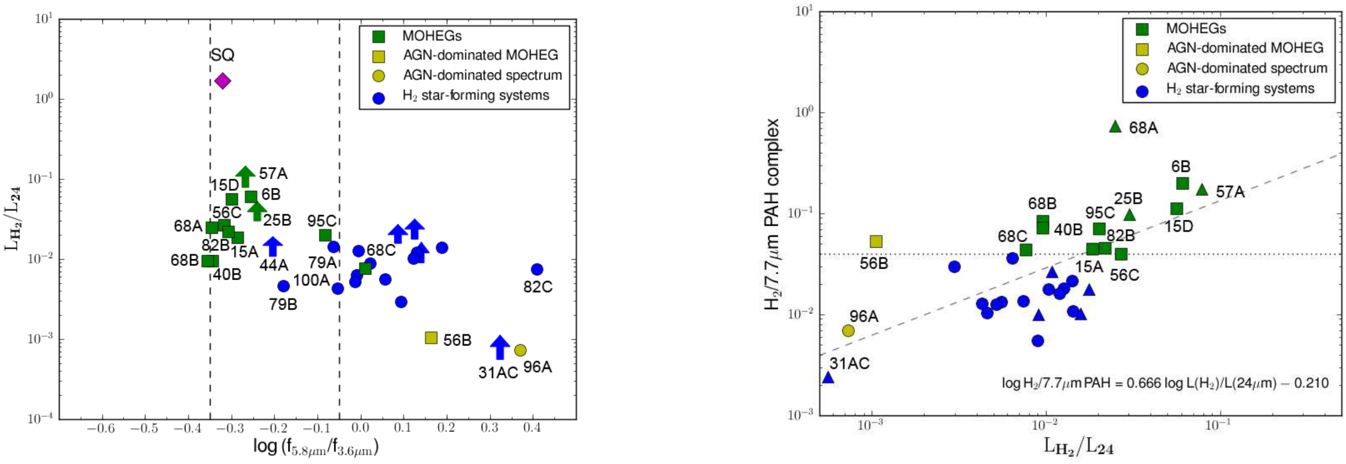

(a) (b)

FIG. 11: a) $L_{H_2\,S(0)-S(3)}/L_{24}$ luminosity ratio for H_2 detected systems as a function of log[$f_{5.8}/f_{3.6}$] color. MOHEGs are shown in green, MOHEGs with AGN-dominated spectra are shown as yellow squares and H_2-detected systems with AGN-dominated spectra as yellow circles. Arrows represent systems where the H_2 luminosity is a lower limit and the vertical dashed lines are from Equation 1. The diamond shows the location of the shock sub-region of SQ (from Cluver et al. 2010). b) H_2 S(0)-S(3)/7.7μm PAH ratio as a function of $L_{H_2\,S(0)-S(3)}/L_{24}$ with the same color-coding as on the left. The dotted line indicates MOHEG H_2-enhancement (Ogle et al. 2010). Systems shown as triangle only have lower limits for their H_2 fluxes (due to not having the full SL+ LL coverage) and are not included in the best fit line (grey dashed).

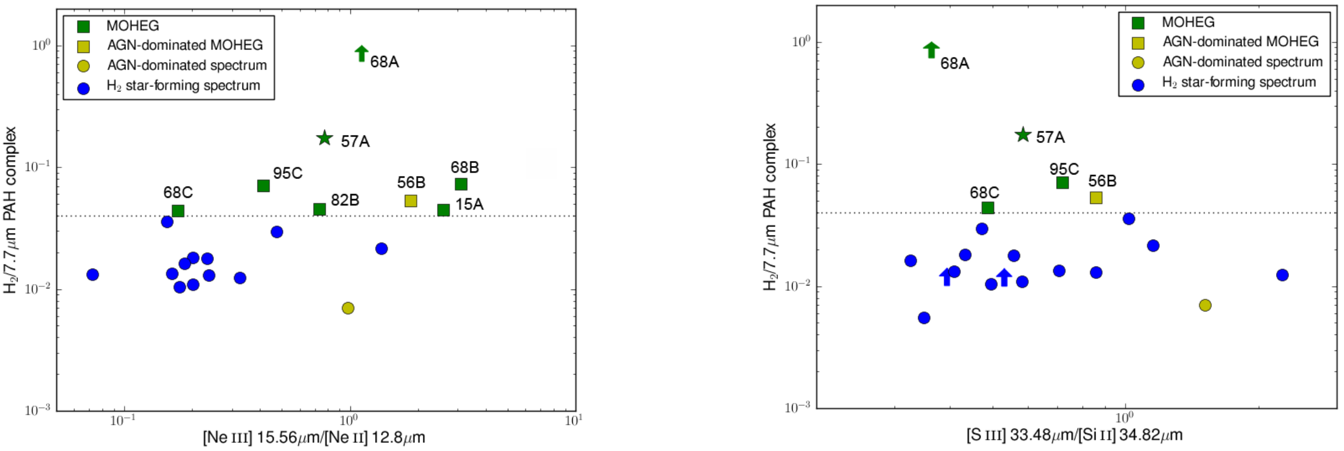

(a) (b)

FIG. 12: a) H_2/7.7μm PAH plotted as a function of [NeIII] 15.56μm/[NeII] 12.81μm with the same color-coding as Figure 10a. The off-nuclear extraction of HCG 57A is shown as a star. b) H_2/7.7μm PAH plotted as a function of [SIII] 33.48μm/[SiII] 34.82μm with the same color designation as on the left.

5. DISCUSSION

5.1. *Source of Excitation in HCG MOHEGs*

5.1.1. *AGN and X-ray Excitation of H_2*

Previous studies of the AGN content of HCGs have found most to be low luminosity AGNs, or LLAGNs (Coziol et al. 2004; Martínez et al. 2010), with a ratio of broad-to narrow-line AGNs of only 3%. As shown by Coziol et al. (2004), the LLAGN are either LINERS or Seyfert 2 systerms based on their emission line diagnostics. From the optical classifications of Coziol et al. (2004) and Martínez et al. (2010) of the H_2-detected galaxies (shown in Table 3), 42% have H II classifications and 26% have AGN designations. By contrast, the H_2-enhanced systems are dominated by LINERS (31%), Transitional Objects (31%) and 23% with no detectable emission. Only three indicate the presence of an AGN based on optical spectra of their nuclear regions.

Powerful AGN in our sample, as measured by the shape of the IRS spectrum, are rare. Only two galaxies, HCG 56B and 96A (classified as Seyfert 2 optically, Coziol et al. 2004), have a clear power-law mid-infrared spectrum.

Tidal interactions are expected to trigger nuclear activity. However, since galaxies are being stripped, their neutral gas reservoir rapidly becomes depleted causing relatively low accretion rates onto the black hole (Martínez et al. 2010).

Ogle et al (2007; 2010) explained the powerful excited H_2 emission in their sample of 3CR radio galaxies to be the result of shocks associated with radio jets from these generally low-luminosity AGN interacting with the host galaxy (see also Guillard et al. 2012b). However, in our sample, this mechanism is unlikely (except in the case of HCG 56B) since very few are known radio sources and those that are, are weak (see Table D2).

Molecular hydrogen can be excited directly by X-ray heating (Lepp & McCray 1983), either in the form of XDRs associated with AGN (Maloney et al. 1996), or due to the presence of hot, diffuse intragroup gas. We know from SQ that the collision of a group galaxy with previously stripped tidal material can produce hot plasma and copious X-ray emission (Trinchieri et al. 2005; Guillard et al. 2009). However, the role of the hot IGM in the most H I-deficient groups has been shown to be less dominant, notably compared to clusters, with half the groups undetected and no clear evidence of ram-pressure stripping in X-ray detected systems (Rasmussen et al. 2008). Thus the IGM is heated as the group evolves, but gas stripping due to the hot plasma does not appear to be effectual.

We present data for X-ray detections for groups in our sample in Appendix D. In addition, X-ray heating is investigated using archival Chandra and *XMM* data for 9/13 MOHEGs (HCG 15A, 15D, 40B, 56B, 56C, 57A, 68A, 68B and 68C). We show that the X-ray emission is insufficient to excite the amount of enhanced warm H_2 we observe and we therefore do not believe it to be a dominant mechanism.

Likewise, by analogy with SQ (Guillard et al. 2009) and the Taffy galaxies (Peterson et al. 2012) and the available radio data (see Appendix D), H_2 excitation due to cosmic rays in these systems is unlikely, which leaves the possibility of collisional excitation due to shocks.

5.1.2. *Collisional Excitation by Interaction of Galaxies with Group IGM*

We have ruled out X-ray heating from within MOHEG galaxies as a mechanism for producing the observed enhanced H_2 emission. However, could interactions with the group IGM produce shock-heating of the molecular hydrogen? Possible processes are ram pressure stripping due to a hot IGM, collisions with previously stripped tidal material (i.e. cold IGM), and finally material being accreted onto galaxies from the IGM.

Rasmussen et al. (2008) investigated the X-ray properties of H I-deficient groups and found the effect of ram pressure stripping to be small, only capable of removing small amounts of cold gas from group members. Unlike clusters, the relatively shallow gravitational potential well does not produce copious X-ray emission (see Section D). By comparison, they find viscous stripping (e.g. Nulsen 1982) to be more efficient at removing gas, but the efficiency may be overestimated (because such processes may not be well treated by SPH schemes, Kawata & Mulchaey 2008). In terms of H I-stripping mechanisms in compact groups, tidal interactions appear to be the dominant, with viscous stripping potentially having a significant contribution, but ram-pressure stripping being virtually insignificant (Rasmussen et al. 2008). Since tidal stripping would produce the material required for viscous stripping, is there evidence for this material within the MOHEG groups?

Recent H I observations of HCGs have shown that even though the galaxies themselves are H I-deficient (Williams & Rood 1987; Verdes-Montenegro et al. 2001), a large diffuse-H I component exists in their IGM (Borthakur et al. 2010).

**** Several groups with $10''$ resolution VLA H I observations contain MOHEGS (6/8) and many of them show evidence for clumpy streams and clouds in the IGM (L. Verdes-Montenegro; private comm). This number is significant given that not all galaxies in each group were targeted and some MOHEG emission may be missed due to the orientation of the slits on the galaxy (see section 3).

As galaxies travel through this clumpy IGM, we could expect stochastic collisions between the inhomogeneous tidal H I and the disks of the galaxies that would lead to shocks in the ISM of the galaxies. Gas disks disrupted and heated due to the turbulent energy created in the collision would be more prone to viscous stripping (Nulsen 1982) due to hydrodynamic drag or hydro-instabilities, and would therefore lose gas in a similar way to traditional ram-pressure stripping by a hot medium. This mechanism would effectively suppress star formation and may be powerful enough to speed up color evolution, accelerating blue cloud galaxies across the green valley.

If this is the case, the physical process producing the HCG H_2-enhanced galaxies are similar to what is observed in Stephan's Quintet, with the difference that the relative velocities would be much lower than the high-velocity collision occurring in SQ. Inspection of the groups included in this study show that groups with H_2-enhanced galaxies have velocity dispersions ranging from $\sim 100\,\mathrm{km\,s^{-1}}$ to $500\,\mathrm{km\,s^{-1}}$ (Hickson et al. 1992), whilst the broad H I profiles of the HCGs (Borthakur et al. 2010) indicate that high-velocity dispersion ($\sim 500\,\mathrm{km\,s^{-1}}$) cold gas is available in the IGM (with column densities $> 10^{19}\,\mathrm{cm^{-2}}$) in addition to tidal streams and clouds. This means lower kinetic energy in the interaction and thus we wouldn't expect the warm H_2 to be as luminous. Nevertheless, the surface area of the leading disk edge and the distribution of broad H I clouds could produce significant warm H_2 mass. The limitations of slit coverage prevent us from making a definitive statement about the spatial distribution of shock-excited H_2, but the extraction areas (particularly LL) cover large parts of the disk, so even though we may have missed stronger emission towards the edges of galaxies, we were able to maximise obtaining a detection of H_2. Follow-up IRAM CO mapping (Lisenfeld et al, in prep.) in combination with optical AGN and shock diagnostics using VIRUS-P (Freeland et al, in prep.) and *Herschel* far-infrared spectral mapping will shed light on the mechanisms contributing to the observed evolution.

An alternative possibility to a viscous stripping mechanism removing gas is that tidal debris in the IGM forms coherent gas streams that fall back onto the galaxies at low-to-medium velocity, thus fueling new star formation activity. If the gas is being decelerated abruptly, this would produce shock excitation and the increased star formation would shift the galaxy from the red sequence to intermediate mid-infrared colours. Given the velocity dispersions in compact groups (Hickson et al. 1992) and complex gravitational interactions, it is not clear how common such events would be and how much gas could be added in this way.

Bitsakis et al. (2011) find that in dynamically old groups, 25% of the elliptical galaxies have bluer UV/optical colors than field ellipticals. This they attribute to star formation facilitated by accretion of intragroup gas by, or merging of dwarf companions. In a sample of local early-type, red sequence galaxies, Shapiro et al. (2010) find two modes of star formation occurring within fast rotating systems, one associated with gas external in origin and one representing rejuvenation in previously quiescent stellar populations. Star formation in fast rotators is believed to be common and therefore present in a wide range of environments.

The only HCG MOHEGs in this study that show significant star formation (based on their mid-infrared spectra) are 95C and 68C. HCG 95C has the intriguing combination of intermediate mid-infrared colours and a star forming spectrum that may indicate a recent increase in star formation relative to the galaxy's stellar mass. This may be due to tidal interactions or possibly a significant gas accretion event enhancing star formation. There may be a threshold of gas mass that must be accreted to generate enough excited H_2 and consequently an associated amount of star formation expected to be seen in these systems; detailed modelling is required to investigate this threshold. In the majority of HCG systems, however, no enhancement in star formation is found (Iglesias-Páramo & Vílchez 1998; Martínez et al. 2010) and instead evidence of truncation in early-type HCG galaxies (de la Rosa et al. 2007) and relatively low star formation rates (Bitsakis et al. 2011).

5.2. *Could AGN activity be responsible?*

The presence of weak AGNs are capable of influencing the chemistry and composition of nuclear regions within galaxies. The spectra of the inner few square kiloparsecs of 59 nearby galaxies (Smith et al. 2007b) suggest that the radiation from AGN may be modifying the grain distribution and exciting unusual PAH emission, i.e. where 5-8μm features are diminished. However, shocks can also destroy PAHs (Micelotta et al. 2010). Alternatively, the low star formation intensities in the center modify the form of PAH emission compared to star forming systems. However, it is a possibility AGN activity in our study could produce a somewhat artificial enhancement of the $H_2/7.7\mu$m PAH ratio.

Since we have extracted large areas (see Table A5) that nominally include the nuclear region, but are not limited to it, the effect of AGN radiation that may be present will be lessened compared to the study of Smith et al. (2007b) which focused specifically on the nuclear region. The majority of HCG MOHEGs with detected optical nuclear activity are LINERS (57%) with only one Seyfert galaxy (HCG 56B, Sy2) and two optically classified as AGN (HCG 57A and HCG 95C; Table 3). For HCG 57A, however, an extraction in the disk, well away from the nucleus, clearly shows the H_2-enhancement (Fig. 5b). We note that the sources of LINER emission in galaxies is still under debate (see e.g. Yan & Blanton 2012), but recent work by Rich et al. (2011) find widespread LINER-like emission due to shocks in late-stage mergers.

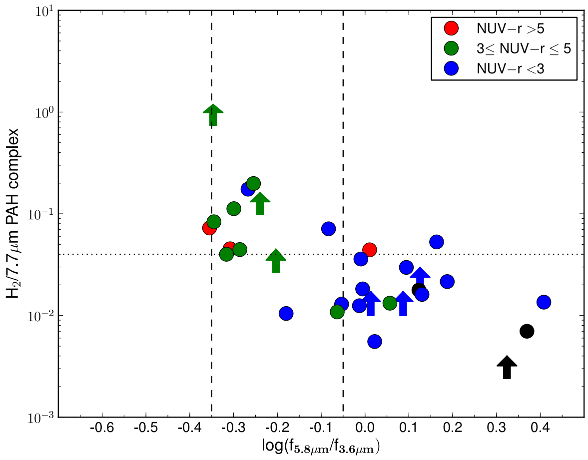

FIG. 13: $H_2/7.7\mu$m PAH ratio color-coded according to NUV-r color. The galaxies are divided into red sequence systems (red), blue cloud galaxies (blue) and green valley members (green) with black points representing galaxies with absent data. The vertical dashed lines are from Equation 1.

Also, if the 7.7μm PAH is tracing star formation (and not being depleted) in the HCG MOHEGS, we would expect it to scale approximately with the 24μm continuum emission (unless there is a strong contribution from AGN). Indeed, we show in Fig. 11b that elevated $H_2/7.7\mu$m PAH ratio's map to elevated $H_2/24\mu$m emission, except in the case of HCG 56B where the MOHEG emission may be due to jet-ISM interactions in this Seyfert galaxy.

The evidence presented here is most consistent with shock-excitation through dynamical interaction; nevertheless our current data does not allow us to definitively distinguish between shock excitation of H_2 (via H I cloud collisions or gas infall) or PAH depletion due to AGN, although the latter appears unlikely for the majority of cases.

5.3. *The Mid-Infrared "Green Valley": An Evolutionary Connection?*

The observed underdensity of HCG galaxies at intermediate mid-IR colors HCG hints at active evolution from dusty star-forming to early type (as originally suggested by Johnson et al. 2007). The location of warm H_2-enhanced galaxies (as shown in Figs 9 and 10) appearing to lie at intermediate mid-infrared colours provides a tantalising element to the overall picture of transformation within HCGs.

The UV-optical colors of the local universe has uncovered an intermediate population of "green valley" galaxies (Blanton et al. 2003), speculated to be undergoing active transformation. In addition, Bitsakis et al. (2011) find that over 50% of early-type and more than 60% of late-type galaxies in "dynamically old" groups are located in the optical green valley. Is there a possible connection between HCG MOHEGS and the optical green valley?

Using the NUV and r-band photometry from Bitsakis et al. (2011), we determine extinction-corrected NUV−r colors for the HCG MOHEGs with available data. In Figure 13 we plot the $H_2/7.7\mu$m PAH values color-coded with NUV−r colors i.e. 3 ≤NUV−r≤ 5 lies in the optical green valley, NUV−r> 5 belongs to the red sequence and NUV−r< 3 designates the blue cloud. We note that a large fraction of the galaxies with enhanced $H_2/7.7\mu$m PAH ratios lie either in the green valley or the red-cloud, with only two galaxies with blue NUV−r colors. The predominance of green NUV−r optical colors in the MOHEG sample is suggestive of a connection between the H_2 enhancement and star formation properties of the systems.

Using intermediate mid-infrared colors to define a mid-infrared “green valley” has the advantage of mitigating dust obscuration, which affects the NUV−r color heavily. In environments and interactions where gas and dust is being stripped from galaxies, this may be a key tracer of transformation and therefore using this emission (particularly to select dusty early-type galaxies) may help uncover its ubiquity.

To investigate this further, we look at the specific star formation rates (sSFR) of galaxies in our sample in common with that of Bitsakis et al. (2011). Their sSFR (SFR per unit old stellar mass) is based on SED fitting and K_s-band luminosity.

As shown in Figure 14a we see that the HCG MOHEGs occupy a narrow range in sSFR (−12.3 <log(sSFR)[Gyr^{-1}]< −11.3). Figure 14b plots our entire sample with sSFR taken from Bitsakis et al. (2011). The observed trend is due to the $\log[f_{5.8\mu m}/f_{3.6\mu m}]$ color acting as a proxy of sSFR, similar to $\log[f_{8.0\mu m}/f_{4.5}\mu m]$. As can be seen, the majority of HCG MOHEGS lie at intermediate sSFR i.e. between the blue cloud population of spirals and the evolved (low sSFR) early-types. This suggests that these galaxies may form a transitional population between the two main populations, and that the warm H_2 emission is connected to the mechanism driving the apparent evolution from blue to red or, alternatively, the migration of systems from the red sequence to intermediate sSFR.

5.4. *Comparison with other samples containing MOHEGs*

Ogle et al. (2010) have shown that jet-ISM interactions can efficiently produce excited H_2 in radio loud galaxies. Since, we have ruled out this mechanism in the majority of HCG MOHEGs, we now consider whether the phenomenon of enhancement in warm H_2 emission could be linked to the environment of the host. For example, several nearby dusty early type galaxies reveal strong H_2 emission associated with almost negligible star formation (Kaneda et al. 2008; Vega et al. 2010). Recent accretion events have been suggested as a mechanism, particularly since some systems show star/gas counter-rotation. The shocks believed to give rise to the observed 11μm PAH and warm H_2 emission could arise from a mechanism such as gas infall or a minor merger delivering additional gas, that then fuels a rejuvenation event (Vega et al. 2010). The ellipticals in Kaneda et al. (2008) were chosen to be X-ray-bright, dusty systems, with some having known jets (making jet-ISM interactions a possible mechanism) and other containing LLAGN.

A connection between H_2-enhanced systems and LINER-like optical emission is not clear. All four of the early types in the sample of Vega et al. (2010) are classified as LINERs, and, within the SINGS sample, galaxies classified as LINERs as well as Seyfert galaxies show enhanced H_2 emission (Roussel et al. 2007; Ogle et al. 2010).

In Figure 15a we plot 6 of the Kaneda et al. (2008) systems (with archival IRAC photometry) and the SINGS sample, as a function of $\log[f_{5.8\mu m}/f_{3.6\mu m}]$ color. We see that the dusty ellipticals from Kaneda et al. (2008) and several SINGS LINERs occupy a similar phase space compared to the HCG MOHEGs. However, the SINGS sample was not chosen to be uniform, but instead representative of nearby galaxies; several systems are located in dense environments such as clusters. In Figure 15b we plot the SINGS galaxies as a function of T-type and we notice more spiral systems inhabit the start of the mid-infrared green valley, compared to HCGs where this region is dominated by S0/a types. In addition, we have plotted galaxies in SINGS that are located in a dense or interacting environment (Virgo, Fornax, Dorado clusters, compact group, pair or triple) as an open circle. Intriguingly, the distribution appears somewhat similar to the HCG distribution in $H_2/7.7\mu$m PAH space. However, we cannot rule out AGN being the source of excitation in the Kaneda et al. (2008) and SINGS MOHEG systems.

5.5. *Transformation in Groups and Clusters*

The effect of environment on the evolution of a galaxy is still contentiously debated. Compact groups are relatively rare, but given their strong gravitational interactions, and relatively shallow potential-wells, may provide an opportunity to understand related mechanisms at work in high-density clusters, as well as loose groups.

Comparisons with several different control samples led Walker et al. (2010, 2012) to conclude that the observed IRAC color bimodality in their sample of HCGs was a direct consequence of environment and appeared most similar to the distribution found for the Coma infall region.

Cluster galaxies undergoing active ram-pressure stripping can show excited H_2 emission (e.g. ESO 137-01 in Abell 3627; Sivanandam et al. 2010). Murphy et al. (2009) have shown that in the Virgo cluster, interactions of the intracluster medium with the ISM of cluster galaxies produces a deficit of radio emission at the leading edge, but galaxies show globally enhanced radio-to-far-infrared emission which may be tracing current stripping.

It is plausible that similar transformations within non-cluster environments can occur without ram-pressure stripping, but instead through a combination of tidal interactions, collisions with tidal debris and viscous stripping within groups. *Chandra* and VLA data of the NGC 2563 galaxy group finds H I-deficient galaxies, likely due to galaxy-galaxy interactions, and possible evidence of ram pressure (or viscous) stripping of cold gas in several group galaxies (Rasmussen et al. 2012a). Westmeier et al. (2011) find asymmetries in the H I disk of NGC 300 in the Sculptor group to be consistent with ram-

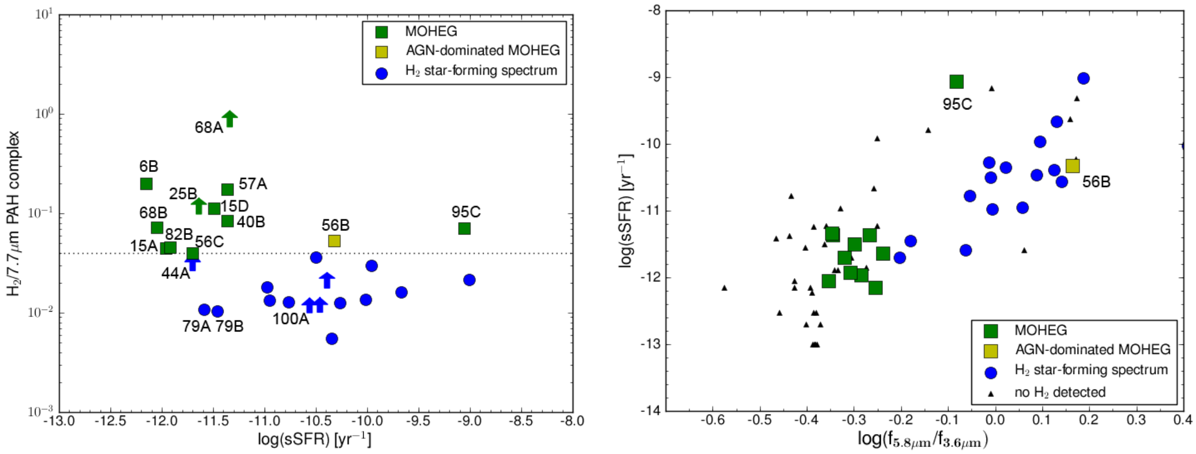

(a) (b)

FIG. 14: a) $H_2/7.7\mu m$ PAH as a function of log sSFR (sSFR data from Bitsakis et al. 2011). b) Plotting log sSFR (sSFR data from Bitsakis et al. 2011) against $\log[f_{5.8\mu m}/f_{3.6\mu m}]$ shows that the majority of MOHEGS may form a transitional population between star-forming spectra in blue and early-type systems.

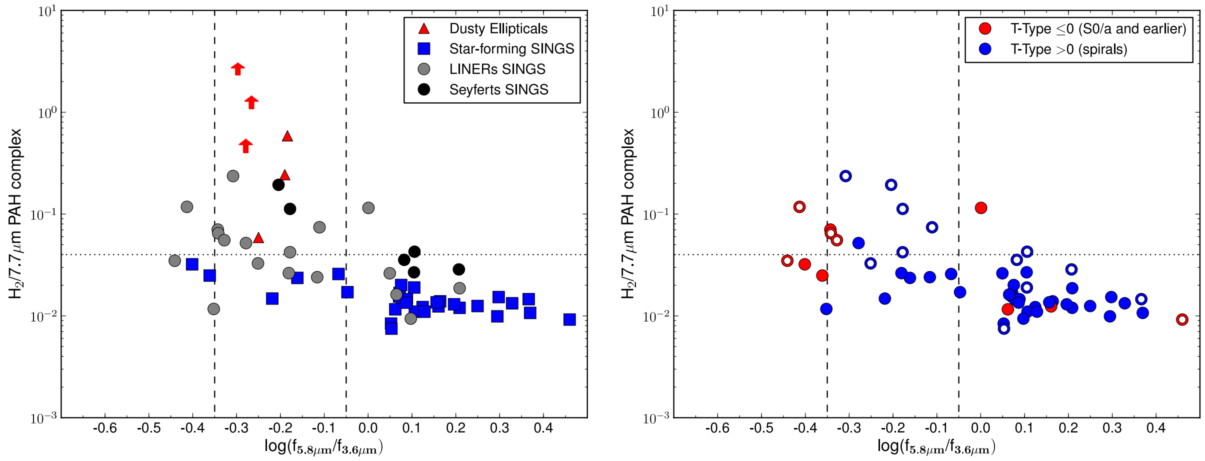

(a) (b)

FIG. 15: a) The Kaneda et al. (2008) dusty ellipticals (red) and SINGS H_2-detected galaxies are plotted as a function of $\log[f_{5.8\mu m}/f_{3.6\mu m}]$ color, where the vertical dashed line indicates the start of the mid-infrared green valley (from equation 1). SINGS star-forming systems are shown in blue (squares), LINER systems are grey (circles) and Seyferts are in black (circles). b) The SINGS sample is plotted in terms of T-type (late-type in blue, early type in red), with open circles indicating galaxies in dense/interacting environments.

pressure stripping by the IGM, but may also be due to cold-mode accretion. In the Pegasus I cluster, evidence of H I-deficiency and truncated H I disks cannot be explained by simple ram pressure arguments as the level of X-ray emission in the system are too low (Levy et al. 2007). Rose et al. (2010) observe the same correlation between sSFR and H I-deficiency in the lower density, low velocity dispersion Pegasus I Cluster as is observed in Virgo. They find that sSFR within H I-depleted disks is lower, but that the sSFR of the nucleus relative to the global value actually increases with H I deficiency.

Rasmussen et al. (2012b) find evidence for suppression of star formation in low-redshift galaxy groups. Using *GALEX* imaging they find that on average the sSFR of star-forming galaxies in groups is suppressed by ∼40% relative to the field.

5.6. *Gas Stripping and the Formation of S0 Galaxies*

Recent studies have explored the connection between dense environments and the formation of lenticular galaxies. HCGs may be the ideal laboratory to study how galaxies are being “pre-processed” and transformed by mechanisms within groups and clusters. Coziol & Plauchu-Frayn (2007) studied the observed asymmetries and nuclear activity in several Hickson groups. They propose three evolutionary phases for group galaxies: (1) galaxy-group tidal interactions, stripping most of the gas, (2) galaxy-galaxy tidal interactions and (3) mergers. The latter occurring under chiefly dry conditions. Thus late types transform into early types (S0 and elliptical) via tidal interactions and merging.

The simulations of Bekki & Couch (2011) indicate that the compact group environment, causing gas stripping and bulge building via tidal interactions, preferentially form S0's from spirals. They predict long tidal streams, broken rings and seemingly isolated massive clouds of neutral gas within the IGM. Deep H I observations are uncovering these kind of features (e.g. in HCG 44, Serra et al. 2012b), as well as the strong dependence of the H I morphology of early-type galaxies on environment (Serra et al. 2012a). The pre-processing mechanisms occurring in groups may be key to reconciling the morphology-density relation (Postman & Geller 1984).

Observationally, Bitsakis et al. (2011) find that S0's dominate dynamically evolved HCGs, as well as preferentially occupying the optical green valley. If we believe that these systems are not passively evolving, but instead show accelerated evolution from the blue cloud to red sequence, there may be quenching of star formation due to viscous stripping and heating by the (now enriched) IGM which further strips gas, as well as prevents further gas accretion. The interactions of the gaseous components could lead to the formation of bow shocks (Nulsen 1982) and may also play a role in transforming star-forming disk galaxies into S0 systems (Quilis, Moore & Bower 2000).

Are other dense environments pre-processing galaxies by effecting how the galaxy evolves? In a study of the mid-infrared colours of galaxies in the Shapley supercluster core, Haines et al. (2011) find that cluster galaxies undergoing star-formation quenching are all either S0 or Sa and surmise that late-type spirals are morphologically transformed from late-type spirals into S0/a and subsequently quenched of star formation once the lenticulars encounter the dense cluster core. They also determine that star-formation in cluster galaxies is being quenched both before and after morphological transformation from spiral to lenticular. This argues against morphological quenching where the transformation from spiral to lenticular makes gas more stable against collapse into molecular clouds, thus quenching star formation for a constant gas/dust fraction (Martig et al. 2009). The alternative to morphological quenching would be ram-pressure stripping and starvation where the accretion of pristine gas is shut down.

Compact groups provide evidence of galaxy transformation being an ongoing process (Barnes 1989) and the dynamical evolution of loose groups may maintain the supply of compact ones. The endpoint of compact group evolution may be a "dry merger" i.e. a merger in the absence of large amounts of cold gas, and the formation of massive elliptical galaxies. However, "isolated" ellipticals are rare since the first compact groups to completely evolve must now be located in larger structures as groups have merged into dense groups and clusters (Mihos et al. 2005; Coziol et al. 2009). We argue that interactions in the group environment are an important process in the overall evolution of a galaxy.

6. CONCLUSIONS

In this paper we have presented the results of a mid-infrared spectral and photometric study of 74 galaxies in 23 Hickson Compact Groups using the *Spitzer Space Telescope* with the goal of searching for enhanced H_2 emission and its possible connection to evolution within HCGs. We highlight here our primary conclusions:

- Searching for excited H_2 in the intragroup medium have led to two tentative detections, located at the edges of two disk galaxies in HCG 40 and 91, respectively. Large-scale intergroup warm H_2 emission like that seen in Stephans' Quintet, appears to be rare.

- We have detected warm H_2 in 32 galaxies with 13 MOHEG (Molecular Hydrogen Emission Galaxies) systems, i.e. H_2 emission in excess of what is expected from UV excitation associated with star formation. The observed $H_2/7.7\mu$m PAH ratios may be due to either shock-induced excitation of H_2 or, in a small minority of systems, possible PAH depletion due to AGN activity.

- The luminosity of X-rays detected in the MOHEG galaxies with archival data is insufficient to heat the warm H_2 and AGN activity is an unlikely explanation in all but one system. Instead shock-excitation through interaction with the IGM is the most plausible mechanism for producing the observed emission.

- The presence of copious intragroup H I suggests that collisional excitation may be due to galaxies passing through this debris, thus experiencing shock heating of their disks – analogous to what is seen in the SQ shock. The heated gas disks undergoing viscous stripping may accelerate evolution from the blue cloud across the green valley. The previously stripped material may also accrete back onto the galaxies, shock-heating the disk gas and providing fuel for "new" star formation.

- The H_2-bright systems are mainly S0 and lie chiefly within a mid-infrared "green valley", between the population of dusty star formers and relatively dust-free early types. The optical colours of most of these systems lie in the NUV−r green valley. In specific star formation, they appear to form a transitional population between the blue cloud and red sequence.

- Interactions within a group, pair or triple environment may be producing similar H_2-enhancement accompanied by non-passive evolution in mid-infrared or optical colour, as seen in the SINGS sample.

- Transformations in groups and clusters may be connected to the processes causing the observed evolution in compact groups.

Although the mechanisms governing the processing of galaxies in the (compact) group environment are still being disentangled, it appears that they may play a significant role in galaxy evolution.

We thank the referee for helpful comments and suggestions that improved this paper. Thank you to Michael

Brown (Monash University) for the use of his galaxy template library. This work is based on observations made with the *Spitzer* Space Telescope, which is operated by the Jet Propulsion Laboratory, California Institute of Technology under NASA contract 1407. MEC acknowledges support from the Australian Research Council (FS110200023). Support for this work was provided by NASA through an award issued by JPL/Caltech. UL acknowledges support by the research projects AYA2007-67625-C02-02 and AYA2011-24728 from the Spanish Ministerio de Ciencia y Educaci ón and the Junta de Andaluc ía (Spain) grant FQM108. This research has made use of the NASA/IPAC Extragalactic Database (NED) which is operated by the Jet Propulsion Laboratory, California Institute of Technology, under contract with the National Aeronautics and Space Administration. This research has made use of data obtained from the Chandra Source Catalog, provided by the Chandra X-ray Center (CXC) as part of the Chandra Data Archive.

REFERENCES

Allen, M.G., Groves, B.A., Dopita, M.A., Sutherland, R.S., & Kewley, L.J. 2008, ApJ, 178, 20

Allen, R.J., & Sullivan, W.T., III. 1980, A&A, 84, 181

Amram, P., Plana, H., Mendes de Oliveira, C., Balkowski, C., & Boulesteix, J. 2003, A&A, 402, 865

Appleton, P.N. et al. 2006, ApJ, **639**, L51

Barnes, D. G., & Webster, R. L. 2001, MNRAS, 324, 859

Barnes, J. E. 1989, Nature, 338, 123

Bekki, K., & Couch, W. J. 2011, MNRAS, 415, 1783

Bernard-Salas, J., Spoon, H. W. W., Charmandaris, V., et al. 2009, ApJS, 184, 230

Bitsakis, T., Charmandaris, V., da Cunha, E., et al. 2011, A&A, 533, A142

Blanton, M. R., Hogg, D. W., Bahcall, N. A., et al. 2003, ApJ, 594, 186

Borthakur, S., Yun, M., & Verdes-Montenegro, L. 2010, ApJ, 710, 385

Brinchmann, J., Charlot, S., Heckman, T. M., et al. 2004, arXiv:astro-ph/0406220

Cluver, M. E., Appleton, P. N., Boulanger, F., et al. 2010, ApJ, 710, 248

Condon, J. et al. 1998, AJ, 115, 1693

Cortese, L., Gavazzi, G., Boselli, A., Franzetti, P., Kennicutt, R. C., O'Neil, K., & Sakai, S. 2006, A&A, 453, 847

Coziol, R., Andernach, H., Caretta, C. A., Alamo-Martínez, K. A., & Tago, E. 2009, AJ, 137, 4795

Coziol, R., & Plauchu-Frayn, I. 2007, AJ, 133, 2630

Coziol, R., Brinks, E., & Bravo-Alfaro, H. 2004, AJ, 128, 68

da Cunha, E., Charlot, S., & Elbaz, D. 2008, MNRAS, 388, 1595

Dale, D. A., Cohen, S. A., Johnson, L. C., et al. 2009, ApJ, 703, 517

Dale, D. A., Smith, J. D. T., Armus, L., et al. 2006, ApJ, 646, 161

Dalgarno, A., Yan, M., & Liu, W. 1999, ApJS, 125, 237

Da Rocha, C., Ziegler, B. L., & Mendes de Oliveira, C. 2008, MNRAS, 388, 1433

de la Rosa, I. G., de Carvalho, R. R., Vazdekis, A., & Barbuy, B. 2007, AJ, 133, 330

Desai, V., Armus, L., Spoon, H. W. W., et al. 2007, ApJ, 669, 810

de Vaucouleurs, G., de Vaucouleurs, A., Corwin, H. G., Jr., Buta, R. J., Paturel, G., & Fouque, P. 1991, Volume 1-3, XII, 2069 pp. 7 figs.. Springer-Verlag Berlin Heidelberg New York

de Vaucouleurs, G., de Vaucouleurs, A., Corwin, H. G., Jr., et al. 1992, VizieR Online Data Catalog, 7137, 0

Dopita, M. A., & Sutherland, R. S. 1996, ApJS, 102, 161

Draine, B. T., & Woods, D. T. 1992, ApJ, 387, 732

Durbala, A., del Olmo, A., Yun, M. S., et al. 2008, AJ, 135, 130

Evans, I. N., Primini, F. A., Glotfelty, K. J., et al. 2010, ApJS, 189, 37

Fazio, G. G., Hora, J. L., Allen, L. E., et al. 2004, ApJS, 154, 10

Forbes, D. A. et al. 2006, PASA, 23, 38

Gallagher, S. C., Durrell, P. R., Elmegreen, D. M., et al. 2010, AJ, 139, 545

Gao, Y., & Xu, C. 2000, ApJ, 542, L83

Governato, F., Tozzi, P., & Cavaliere, A. 1996, ApJ, 458, 18

Guillard, P., Boulanger, F., Pineau Des Forêts, G., & Appleton, P. N. 2009, A&A, 502, 515

Guillard, P., Boulanger, F., Pineau des Forêts, G., et al. 2012, ApJ, 749, 158

Guillard, P., Ogle, P. M., Emonts, B. H. C., et al. 2012, ApJ, 747, 95

Haines, C. P., Merluzzi, P., Busarello, G., et al. 2011, MNRAS, 417, 2831

Helou, G., Roussel, H., Appleton, P., et al. 2004, ApJS, 154, 253

Hickson, P. 1982, ApJ, 255, 382

Hickson, P., Kindl, E., & Auman, J. R. 1989, ApJS, 70, 687

Hickson, P., Mendes de Oliveira, C., Huchra, J. P., & Palumbo, G. G. 1992, ApJ, 399, 353

Ho, L. C. 2008, ARA&A, 46, 475

Hollenbach, D. J., & Tielens, A. G. G. M. 1997, ARA&A, 35, 179

Houck, J. R., Roellig, T. L., Van Cleve, J., et al. 2004, Proc. SPIE, 5487, 62

Huchtmeier, W. K. 1997, A&A, 325, 473

Iglesias-Páramo, J., & Vílchez, J. M. 1998, AJ, 518, 94

Iglesias-Páramo, J., & Vílchez, J. M. 1998, AJ, 115, 1791

Johnson, K.E., Hibbard, J.E., Gallagher, S.C., Charlton, J.C., Hornschemeier, A.E., Jarrett, T.H.& Reines, A.E. 2007, AJ, 134, 1522

Kaneda, H., Onaka, T., Sakon, I., Kitayama, T., Okada, Y., & Suzuki, T. 2008, ApJ, 684, 270

Kawata, D., & Mulchaey, J. S. 2008, ApJ, 672, L103

Khachikian, E. Y., & Weedman, D. W. 1974, ApJ, 192, 581

Lacy, M., Storrie-Lombardi, L. J., Sajina, A., et al. 2004, ApJS, 154, 166

Leon, S., Combes, F., & Menon, T. K. 1998, A&A, 330, 37

Lepp, S., & McCray, R. 1983, ApJ, 269, 560

Levy, L., Rose, J. A., van Gorkom, J. H., & Chaboyer, B. 2007, AJ, 133, 1104

Maloney, P. R., Hollenbach, D. J., & Tielens, A. G. G. M. 1996, ApJ, 466, 561

Martig, M., Bournaud, F., Teyssier, R., & Dekel, A. 2009, ApJ, 707, 250

Martínez, M. A., Del Olmo, A., Coziol, R., & Perea, J. 2010, AJ, 139, 1199

Martínez-Badenes, V., Lisenfeld, U., Espada, D., et al. 2012, A&A, 540, A96

Mendes de Oliveira, C., & Hickson, P. 1994, ApJ, 427, 684

Micelotta, E. R., Jones, A. P., & Tielens, A. G. G. M. 2010, A&A, 510, A36

Mihos, J. C., Harding, P., Feldmeier, J., & Morrison, H. 2005, ApJ, 631, L41

Mulchaey, J. S., Davis, D. S., Mushotzky, R. F., & Burstein, D. 2003, ApJS, 145, 39

Murphy, E. J., Kenney, J. D. P., Helou, G., Chung, A., & Howell, J. H. 2009, ApJ, 694, 1435

Neufeld, D. A., Hollenbach, D. J., Kaufman, M. J., et al. 2007, ApJ, 664, 890

Nulsen, P.E.J. 1982, MNRAS, 198, 1007

Ogle, P., Antonucci, R., Appleton, P., & Whysong, D. 2007, ApJ, 668, 699

Ogle, P., Boulanger, F., Guillard, P., Evans, D.A., Antonucci, R., Appleton, P.N, Nesvadba, N. & Leipski, C. 2010, ApJ, 724, 1193

Osmond, J. P. F., & Ponman, T. J. 2004, MNRAS, 350, 1511

Osterbrock, D. E., & Martel, A. 1993, ApJ, 414, 552

Peterson, B., Appleton, P., Helou, G., Jarrett, T., Cluver, M., Ogle, P., Guillard, P., Struck, C., Boulanger, F., 2011, ApJ, 751, 11

Ponman, T. J., Bourner, P. D. J., Ebeling, H., Böhringer, H. 1996, MNRAS, 283, 690

Postman, M., & Geller, M. J. 1984, ApJ, 281, 95

Quilis, V., Moore, B. & Bower 2000, Science, 288, 1617

Radovich, M., Rafanelli, P., & Barbon, R. 1998, A&A, 334, 124

Rasmussen, J., Ponman, T. J., Verdes-Montenegro, L., Yun, M. S., & Borthakur, S. 2008, MNRAS, 388, 1245

Rasmussen, J., Bai, X., Mulchaey, J.S., et al. 2012, ApJ, 757, 122

Rasmussen, J., Mulchaey, J.S., et al. 2012, arXiv:1208.1762

Rieke, G. et al., 2004, ApJS, 154, 204

Rich, J. A., Kewley, L. J., & Dopita, M. A. 2011, ApJ, 734, 87

Rose, J. A., Robertson, P., Miner, J., & Levy, L. 2010, AJ, 139, 765

Roussel, H., et al. 2007, ApJ, 669, 959

Rubin, V.C., Hunter, D.A., & Ford, W.K.J. 1991, ApJS, 76, 153

Sanders, D. B., Mazzarella, J. M., Kim, D.-C., Surace, J. A., & Soifer, B. T. 2003, AJ, 126, 1607

Serra, P., Oosterloo, T., Morganti, R., et al. 2012, MNRAS, 422, 1835

Serra, P. et al. 2012, arXiv:1209.4107

Shapiro, K. L., Falcón-Barroso, J., van de Ven, G., et al. 2010, MNRAS, 402, 2140

Shull, J. M., & Hollenbach, D. J. 1978, ApJ, 220, 525

Sivanandam, S., Rieke, M.J. & Rieke, G.H. 2010, ApJ, 717, 147

Smith, J.D.T. et al. 2009, ApJ, 693, 713

Smith, J. D. T., Armus, L., Dale, D. A., et al. 2007, PASP, 119, 1133

Smith, J. D. T., Draine, B. T., Dale, D. A., et al. 2007, ApJ, 656, 770

Tang et al. 2011

Trinchieri, G., Sulentic, J., Pietsch, W., & Breitschwerdt, D. 2005, A&A, 444, 697

Tzanavaris, P., Hornschemeier, A. E., Gallagher, S. C., et al. 2010, ApJ, 716, 556

Vega, O. et al. 2010, ApJ, 721, 1090

Verdes-Montenegro, L., Yun, M. S., Williams, B. A., Huchtmeier, W. K., Del Olmo, A., & Perea, J. 2000, IAU Colloq. 174, Small Galaxy Groups, ed. M. Valtonen & C. Flynn (San Francisco: ASP), 167.

Verdes-Montenegro, L., Yun, M.S., Williams, B.A., Huchtmeier, W.K., Del Olmo, A., & Perea, J. 2001, A&A, 377, 812

Verdes-Montenegro, L., Yun, M. S., Perea, J., del Olmo, A., & Ho, P. T. P. 1998, ApJ, 497, 89

Walker, L. M., Johnson, K. E., Gallagher, S. C., et al. 2012, AJ, 143, 69

Walker, L. M., Johnson, K. E., Gallagher, S. C., Hibbard, J. E., Hornschemeier, A. E., Tzanavaris, P., Charlton, J. C., & Jarrett, T. H. 2010, AJ, 140, 1254

Westmeier, T., Braun, R., & Koribalski, B. S. 2011, MNRAS, 410, 2217

Williams, B. A., & Rood, H. J. 1987, ApJS, 63, 265

Yan, R., & Blanton, M. R. 2012, ApJ, 747, 61

Yun, M. S., Verdes-Montenegro, L., del Olmo, A., & Perea, J. 1997, ApJ, 475, L21

APPENDIX

A. THE HCG SAMPLE AND ASSOCIATED DATA

In this section we list all the galaxies that formed part of the parent HCG galaxy sample and the IRAC photometry measurements of each (as outlined in Section 3.2). Table A1 provides the photometry for each galaxy in the sample and if an H_2 detection was made.

TABLE A1: Measured Fluxes of HCG Sample

Galaxy	H_2-detected	3.6μm (mJy)	4.5μm (mJy)	5.8μm (mJy)	8.0μm (mJy)
6A	no	6.71	4.28	2.70	1.63
6B	yes	7.78	5.12	4.10	4.93
6C	no	5.81	3.72	2.37	1.64
6D	no	0.95	0.68	0.50	0.68
8A	no	11.37	7.42	4.65	3.04
8C	no	5.99	3.86	2.73	2.14
8D	no	5.72	3.72	2.45	2.25
15A	yes	18.32	11.63	9.49	11.59
15C	no	13.79	8.72	5.87	3.53
15D	yes	8.13	5.49	4.08	3.01
25B	yes	18.33	12.09	10.56	12.10
25D	no	3.72	2.44	1.53	1.22
25F	no	2.86	1.82	1.25	0.79
31AC	yes	13.54	10.37	28.55	73.86
31B	no	2.46	1.69	2.23	4.42
40A	no	35.53	22.12	16.21	11.22
40B	yes	10.11	6.41	4.57	3.50
40C	yes	23.77	16.22	29.04	73.88
40D	yes	16.61	11.15	18.93	61.31
44A	yes	292.17	185.70	182.89	309.77
44B	no	–	96.29	–	38.56
44D	yes	13.46	9.11	20.74	49.71
47A†	yes	20.71	13.31	20.26	52.28
47B†	no	11.84	7.23	4.05	2.41
47D†	no	3.59	2.37	2.33	6.37
54A	no	1.14	0.78	0.82	1.39
54B†	no	3.70	2.90	5.50	11.10
54C†	no	1.25	0.80	1.80	4.10
55A†	no	6.53	3.93	2.66	1.22
55B†	no	3.44	2.15	1.33	0.72
55C†	yes	5.51	3.80	3.91	10.91
55D†	no	6.76	4.36	6.10	12.97
56B	yes	◇25.36	◇30.84	36.94	52.30
56C	yes	5.82	3.71	2.81	2.45
56D	yes	4.08	2.90	5.45	14.53
56E	yes	2.12	1.43	2.06	4.08
57A	yes	31.11	20.04	16.82	20.15
57B	no	14.36	9.14	8.04	12.47
57C	no	10.88	6.99	4.51	2.64
57D	no	7.83	5.26	8.40	19.69

Galaxy	H_2-detected	3.6μm (mJy)	4.5μm (mJy)	5.8μm (mJy)	8.0μm (mJy)
57E	no	8.98	5.77	4.43	5.23
62A	no	94.42	58.58	38.77	54.16
62B	no	15.16	9.36	6.27	4.26
62C	no	14.69	9.46	5.93	3.24
67A[†]	no	54.40	34.10	20.40	16.10
67B[†]	yes	30.70	20.80	32.30	72.30
67D[†]	no	5.30	3.30	2.30	1.80
68A	yes	226.63	136.56	101.99	61.77
68B	yes	108.76	66.57	48.04	33.19
68C	yes	111.70	69.21	114.44	248.81
75A[†]	no	13.10	10.40	5.70	5.10
75C[†]	no	4.00	2.40	1.60	1.30
75D[†]	yes	3.30	2.10	3.40	11.80
75E	no	3.70	2.37	1.51	0.93
79A	yes	16.09	10.58	13.91	26.10
79B	yes	14.53	9.15	9.60	15.00
79C[†]	no	10.22	5.71	4.03	2.04
82A	no	15.69	10.06	6.56	3.94
82B	yes	12.78	8.02	5.98	6.96
82C	yes	8.54	6.24	15.12	47.75
91A	yes	[⋆]74.57	[◇]59.87	92.65	608.84
91C	yes	8.68	5.88	11.71	30.63
91D	no	10.97	7.21	5.15	4.35
95A[†]	no	18.00	11.01	6.70	7.82
95C[†]	yes	7.05	4.27	4.89	10.60
96A[a]	yes	80.15	107.86	187.72	328.56
96B	no	17.71	12.09	8.69	5.46
96C[b]	yes	8.86	6.21	11.76	29.78
97A[†]	no	19.90	12.70	7.90	6.0
97C[†]	no	13.20	7.80	3.50	2.20
97D[†]	no	15.50	9.30	5.80	4.10
100A	yes	40.38	25.93	35.70	156.89
100B	no	5.49	3.95	8.15	18.58
100C	no	3.65	2.56	3.58	7.14

[a] Measured using short exposure (1.2s) HDR image
[b] Contamination from 96A
[◇] Flux may be underestimated by ∼5% due to peak pixel non-linearity
[⋆] Flux may be underestimated by ∼10% due to peak pixel non-linearity
[†] Photometry from Bitsakis et al. (2011)

For systems with detected excited H_2 emission lines, the measured fluxes presented in Table A2. Several systems have their SL and LL lines presented separately due to the regions sampled by the IRS not overlapping (and therefore not joined together). In addition, spectra that are not centered on the nucleus (therefore dominated by emission from the disk) are indicated. The strengths of the PAH complexes and atomic emission lines for the H_2-detected systems are presented in Tables A3 and A4. For galaxies without SL coverage, the IRAC inferred 7.7μm PAH values are: $8.771\times10^{-15}\,\mathrm{W.m^{-2}}$, $1.327\times10^{-14}\,\mathrm{W.m^{-2}}$ and $1.684\times10^{-15}\,\mathrm{W.m^{-2}}$ for 40C, 44A and 75D, respectively.

The extracted areas of the H_2-detected galaxies are listed in Table A5, as well as any scaling factors employed to match the LL and SL spectral orders. The scaling between modules makes the assumption that the emission lines scale with the continuum i.e. the SL spectrum is scaled to bring it in line with the LL spectrum continuum. An independent check is to use the 7.7μm PAH and 11.3μm PAH emission features compared to the matched 24μm photometry. For systems not dominated by AGN heating, these measures should scale similarly with star formation. We plot these comparisons in Figure A1 for systems where the respective PAH emission lines are well-determined and the spectra (and global mid-IR colors) are not AGN-dominated. Since systems that have been scaled show the same behaviour as those that have not, the scaling does not appear to have produced inconsistent fluxes. Uncertainties in the SL scaling factor (due to noise of the continuum) are estimated to be <0.02, corresponding to a flux uncertainty of <5%.

B. SPECTRA OF NON-MOHEG H_2 DETECTIONS

The spectra of the non-MOHEG H_2-detected HCG galaxies are shown in Figure B1 and B2. As expected, the majority of spectra appear consistent with star-forming systems, consistent with warm H_2 associated with PDRs and UV excitation. The spectrum of HCG 96A indicates the presence of a powerful AGN given the prominent hot and warm dust and strong high excitation lines (Fig. B2g), also reflected in its mid-infrared colors. This galaxy is a known LIRG (Sanders et al. 2003) and Seyfert 2 galaxy (Osterbrock & Martel 1993).

The HCG 31AC complex has an irregular morphology and high levels of star formation; it is likely experiencing a triggered starburst due to the mutual interaction between the two parent systems (Gallagher et al. 2010). HCG 91A appears strongly star forming, but has an optically-identified active nucleus (Sy1.2, Radovich et al. 1998); we note

TABLE A2: Observed H_2 Fluxes in units of $\mathrm{W\,m^{-2}}$

Source	H_2 0-0 S(0) $\lambda 28.21\mu$m	H_2 0-0 S(1) $\lambda 17.03\mu$m	H_2 0-0 S(2) $\lambda 12.28\mu$m	H_2 0-0 S(3) $\lambda 9.66\mu$m	H_2 0-0 S(4) $\lambda 8.03\mu$m	H_2 0-0 S(5) $\lambda 6.91\mu$m
6B	1.710e-18 (5.093e-19)	8.440e-18 (8.113e-19)	1.251e-18 (5.748e-19)$^{\square}$	6.185e-18 (1.739e-18)	<3.751e-18	<3.151e-18†
15A	<2.605e-18	4.796e-18 (8.951e-19)	<2.446e-18	3.216e-18 (1.186e-18)	<5.385e-18	6.149e-18 (1.819e-18)
15D	2.920e-18 (1.019e-18)	1.107e-17 (1.864e-18)	3.750e-18 (1.719e-18)$^{\square}$	8.811e-18 (2.345e-18)	<2.367e-17	<6.414e-18 †
25B*	–	–	7.643e-19 (4.799e-20)	2.535e-18 (1.202e-19)	<8.727e-19	2.012e-18 (2.728e-19)†
25B$^{\diamond\bullet}$	<1.853e-18	1.159e-17 (1.979e-19)	–	–	–	–
31A+C$^{\star\bullet}$	–	–	1.731e-19 (3.424e-20)$^{\square}$	1.329e-19 (5.397e-20)$^{\square}$	<3.332e-19	< 7.815e-19
31A+C$^{\diamond}$	<1.423e-17	2.004e-17 (3.924e-20)	–	–	–	–
40B	<2.673e-18	5.619e-18 (1.081e-18)	<9.519e-19	3.457e-18 (1.063e-18)$^{\square}$	4.550e-18 (1.920e-18)$^{\square}$	<1.631e-18†
40C$^{\star\bullet}$	–	–	<1.966e-19	3.932e-19 (1.611e-19)$^{\square}$	<6.603e-19	4.335e-19 (2.012e-19)$^{\square\dagger}$
40C$^{\diamond}$	1.857e-17 (1.602e-18)	7.308e-17 (1.093e-19)	–	–	–	–
40D	9.173e-18 (3.047e-18)$^{\square}$	2.697e-17 (2.675e-18)	1.084e-17 (1.256e-18)$^{\square}$	2.009e-17 (1.693e-18)	<8.889e-18	6.978e-18 (2.348e-18)$^{\square}$
44A$^{\star\bullet}$	–	–	2.124e-18 (2.083e-19)$^{\square}$	3.245e-18 (2.542e-19)$^{\square}$	4.527e-18 (1.047e-18)$^{\square}$	7.281e-18 (9.326e-19)$^{\square\dagger}$
44A$^{\diamond}$	2.693e-17 (5.940e-18)	1.069e-16 (3.014e-20)	–	–	–	–
44D	9.598e-18 (3.674e-18)	5.243e-17 (8.442e-18)	<1.261e-17	<3.129e-16	<7.616e-17	3.302e-17 (1.337e-17)$^{\square\dagger}$
47A	<8.042e-18	2.556e-17 (3.100e-18)	7.745e-18 (3.100e-18)$^{\square}$	<1.769e-17	1.928e-17 (8.152e-18)$^{\square}$	<1.534e-17†
55C	1.056e-18 (1.718e-19)	3.927e-18 (3.630e-19)	1.445e-18 (3.084e-19)$^{\square}$	3.411e-18 (5.093e-19)	3.035e-18 (6.191e-19)$^{\square}$	<5.632e-18†
56B	<6.768e-18	5.973e-18 (3.035e-18)	1.231e-17 (3.704e-18)	<1.575e-17	<3.544e-18	8.222e-18 (3.403e-18)$^{\square}$
56C	<1.143e-18	4.915e-18 (8.659e-19)	<4.024e-18	7.139e-18 (1.290e-18)	<7.657e-18	5.764e-18 (1.706e-18)$^{\square\dagger}$
56D*	–	–	1.892e-17 (8.559e-19)$^{\square}$	1.338e-17 (2.767e-18)	8.456e-18 (2.124e-18)$^{\square}$	1.136e-17 (1.441e-18)$^{\square}$
56E	<3.736e-18	3.169e-18 (7.172e-19)	<1.122e-18	1.027e-18 (4.599e-19)$^{\square}$	<2.200e-18	2.641e-18 (7.172e-19)$^{\square\dagger}$
57A$^{\bullet}$	3.521e-18 (4.759e-19)	1.311e-17 (5.390e-19)	2.622e-18 (5.269e-19)	5.754e-18 (4.856e-19)	1.343e-18 (6.313e-19)$^{\square}$	2.792e-18 (6.507e-19)$^{\square\dagger}$
57A$^{\diamond}$	7.728e-18 (1.699e-18)	7.612e-17 (2.456e-19)	–	–	–	–
67B	5.306e-18 (1.044e-18)	1.800e-17 (2.793e-18)	1.036e-17 (1.655e-18)$^{\square}$	1.528e-17 (3.829e-18)$^{\square}$	2.852e-17 (4.397e-18)$^{\square}$	<2.102e-17
68A	<1.642e-18	1.212e-17 (9.984e-19)	1.037e-17 (9.887e-19)	2.026e-17 (1.115e-18)	<1.193e-17	<1.605e-17 †
68B	<1.709e-18	4.415e-18 (9.170e-19)	<2.312e-18	3.685e-18 (8.024e-19)	<3.436e-18	<7.999e-18†
68C	7.839e-18 (8.386e-19)	3.919e-17 (1.540e-18)	2.625e-17 (2.388e-18)	5.779e-17 (3.792e-18)	<1.566e-17	<2.433e-17
75D$^{\diamond}$	2.163e-18 (6.665e-19)	7.513e-18 (1.533e-18)	–	–	–	–
79A	3.830e-18 (4.552e-19)	1.248e-17 (1.053e-18)	5.138e-18 (3.508e-19)$^{\square}$	1.062e-17 (7.780e-19)	<5.298e-18	< 3.660e-18
79B	1.028e-18 (2.694e-19)	6.854e-18 (5.797e-19)	1.867e-18 (5.214e-19)$^{\square}$	2.563e-18 (7.620e-19)	<5.196e-18	1.783e-17 (2.512e-18)$^{\square}$
82B	1.684e-18 (3.707e-19)	4.619e-18 (8.734e-19)	<2.300e-18	2.644e-18 (1.024e-18)	<4.643e-18	<1.333e-18†
82C	1.026e-17 (8.441e-19)	3.333e-17 (1.375e-18)	9.751e-18 (7.786e-19)$^{\square}$	1.208e-17 (1.113e-18)	<6.353e-18	1.528e-17 (2.511e-18)$^{\square}$
91A	1.346e-17 (1.010e-18)	4.585e-17 (1.844e-18)	1.078e-17 (1.468e-18)$^{\square}$	1.831e-17 (1.662e-18)$^{\square}$	<1.186e-17	2.959e-17 (5.604e-18)$^{\square\dagger}$
91C	<2.228e-18	1.028e-17 (1.750e-18)	2.327e-18 (7.695e-19)$^{\square}$	7.423e-18 (1.079e-18)	<7.423e-18	<7.430e-18
95C	2.249e-18 (7.984e-19)	8.838e-18 (1.317e-18)	5.388e-18 (7.923e-19)	1.707e-17 (1.975e-18)	<5.144e-18	7.497e-18 (2.633e-18)
96A	3.337e-17 (2.346e-18)	5.041e-17 (3.424e-18)	5.085e-17 (1.418e-18)$^{\square}$	<3.897e-18	5.609e-17 (3.380e-18)$^{\square}$	1.472e-16 (4.225e-18)$^{\square\dagger}$
96C	2.954e-18 (9.037e-19)	1.795e-17 (1.498e-18)	7.339e-18 (8.066e-19)	1.104e-17 (1.407e-18)	<5.604e-18	1.462e-17 (3.051e-18)$^{\square}$
100A	5.569e-18 (9.621e-19)	3.240e-17 (1.723e-18)	6.564e-18 (5.994e-19)	1.662e-17 (9.197e-19)	<9.418e-18	2.584e-17 (2.536e-18)$^{\square}$

Note. — Uncertainties are listed in parentheses. Marginal detections are low signal to noise lines as determined by visual inspection.

† Blended with [ArII] 6.98μm

$^{\square}$ Marginal Detection

* SL coverage

$^{\diamond}$ LL coverage

$^{\bullet}$ Off nuclear extraction

TABLE A3: Observed PAH Fluxes in units of W m^{-2}

Source	6.2μm	7.7μm	8.6μm	11.3μm	12.0μm	12.6μm	17μm
6B	4.887e-17 (4.680e-18)	8.243e-17 (1.297e-17)	2.040e-17 (4.442e-18)	5.249e-17 (3.756e-18)	1.523e-17 (2.321e-18)	2.342e-17 (2.536e-18)	3.676e-17 (2.710e-18)
15A	3.540e-17 (7.305e-18)$^{\square}$	1.801e-16 (8.771e-18)	4.074e-17 (5.875e-18)	6.837e-17 (2.427e-18)	<1.070e-17	2.597e-17 (3.200e-18)	7.251e-17 (4.287e-18)
15D	<6.174e-17	2.032e-16 (2.877e-17)	<2.337e-17	6.964e-17 (5.563e-18)	1.485e-17 (6.701e-18)	<8.418e-18	2.192e-17 (7.626e-18)
25B*	7.689e-18 (7.358e-19)	3.357e-17 (1.538e-18)	6.939e-18 (5.788e-19)	1.848e-17 (1.940e-19)	7.228e-18 (2.091e-19)	9.607e-18 (1.871e-19)	–
25B$^{\diamond\bullet}$	–	–	–	–	–	–	6.379e-16 (1.166e-18)
31A+C$^{\star\bullet}$	1.365e-17 (3.994e-19)	3.780e-17 (8.320e-19)	7.066e-18 (3.023e-19)	1.278e-17 (1.103e-19)	4.095e-18 (1.370e-19)	7.486e-18 (1.484e-19)	–
31A+C$^{\diamond}$	–	–	–	–	–	–	2.376e-16 (4.624e-19)
40B	7.170e-17 (5.749e-18)$^{\square}$	6.738e-17 (7.512e-18)	1.622e-17 (4.595e-18)	4.554e-17 (3.003e-18)	<3.919e-18	1.491e-17 (4.326e-18)	<1.469e-17
40C$^{\star\bullet}$	1.319e-17 (5.119e-19)	3.887e-17 (1.208e-18)	9.010e-18 (5.650e-19)	1.555e-17 (3.918e-19)	3.898e-18 (2.845e-19)	9.877e-18 (2.920e-19)	–
40C$^{\diamond}$	–	–	–	–	–	–	1.524e-15 (2.062e-18)
40D	1.033e-15 (1.337e-17)	3.561e-15 (2.860e-17)	6.633e-16 (9.244e-18)	9.058e-16 (1.484e-17)	2.417e-16 (5.517e-18)	4.741e-16 (6.437e-18)	4.988e-16 (1.937e-17)
44A$^{\star\bullet}$	<1.051e-17	1.037e-16 (5.614e-18)$^{\square}$	2.189e-17 (1.916e-18)	3.914e-17 (4.805e-19)	1.815e-17 (6.773e-19)	9.427e-18 (3.950e-19)	–
44A$^{\diamond}$	–	–	–	–	–	–	1.857e-15 (4.175e-19)
44D	7.656e-16 (5.555e-17)	2.879e-15 (2.036e-16)	1.021e-15 (1.427e-16)	1.255e-15 (1.397e-16)	<1.529e-16	2.680e-16 (4.162e-17)	7.096e-16 (7.267e-17)
47A	3.529e-16 (2.302e-17)	7.118e-16 (6.860e-17)	9.348e-17 (2.120e-17)	3.640e-16 (1.234e-17)	1.126e-16 (1.318e-17)	1.650e-16 (1.282e-17)	1.179e-16 (1.423e-17)
55C	1.302e-16 (3.253e-18)	4.601e-16 (8.403e-18)	1.027e-16 (2.327e-18)	1.293e-16 (2.369e-18)	2.390e-17 (1.269e-18)	5.445e-17 (1.442e-18)	7.819e-17 (2.511e-18)
56B	<7.599e-17	3.457e-16 (6.633e-17)	<1.439e-17	2.538e-16 (1.399e-17)	1.972e-16 (1.630e-17)	1.330e-16 (1.568e-17)	2.918e-16 (1.856e-17)
56C	4.972e-17 (9.903e-18)	3.228e-16 (1.748e-17)	6.813e-17 (5.966e-18)	1.218e-16 (1.496e-18)	5.649e-17 (2.109e-18)	2.935e-17 (1.229e-18)	<1.666e-17
56D*	3.337e-16 (1.170e-17)	7.553e-16 (2.350e-17)	1.618e-16 (1.319e-17)	1.914e-16 (1.259e-17)	<9.407e-18	3.028e-17 (1.515e-18)	–
56E	6.294e-17 (2.653e-18)	2.540e-16 (6.618e-18)	4.730e-17 (2.157e-18)	5.496e-17 (1.055e-18)	1.294e-17 (1.323e-18)	2.286e-17 (1.447e-18)	2.499e-17 (3.501e-18)
57A$^{\bullet}$	3.918e-17 (1.651e-18)	1.433e-16 (5.967e-18)	2.508e-17 (2.045e-18)	5.307e-17 (1.507e-18)	1.823e-17 (2.041e-18)	2.444e-17 (2.253e-18)	5.068e-17 (2.757e-18)
57A$^{\diamond}$	–	–	–	–	–	–	4.564e-16 (1.887e-18)
67B	1.104e-15 (1.766e-17)	4.201e-15 (6.808e-17)	7.128e-16 (1.455e-17)	9.034e-16 (1.341e-17)	2.917e-16 (7.759e-18)	5.261e-16 (8.408e-18)	2.416e-16 (9.284e-18)
68A	1.168e-16 (5.306e-18)	<8.205e-17	<3.644e-17	1.442e-16 (2.168e-18)	3.786e-17 (3.059e-18)	3.908e-17 (3.000e-18)	9.871e-17 (4.280e-18)
68B	5.253e-17 (6.416e-18)	1.117e-16 (6.815e-18)	1.542e-17 (3.073e-18)	1.028e-16 (1.665e-18)	2.346e-17 (2.352e-18)	4.577e-17 (3.457e-18)	1.060e-16 (4.077e-18)
68C	1.045e-15 (2.108e-17)	2.964e-15 (7.289e-17)	4.906e-16 (1.552e-17)	1.046e-15 (7.681e-18)	3.649e-16 (8.636e-18)	5.015e-16 (7.960e-18)	7.284e-16 (9.992e-18)
75D$^{\diamond}$	–	–	–	–	–	–	1.844e-16 (2.583e-17)
79A	6.546e-16 (5.593e-18)	2.483e-15 (1.268e-17)	3.424e-16 (3.394e-18)	4.291e-16 (2.668e-18)	1.281e-16 (2.033e-18)	2.652e-16 (1.990e-18)	2.608e-16 (6.256e-18)
79B	2.760e-16 (6.515e-18)	9.979e-16 (2.698e-17)	1.606e-16 (3.098e-18)	2.040e-16 (4.496e-18)	7.498e-17 (2.311e-18)	1.327e-16 (2.878e-18)	9.559e-17 (4.119e-18)
82B	4.659e-17 (5.080e-18)	1.977e-16 (1.941e-17)	3.197e-17 (3.731e-18)	5.797e-17 (2.708e-18)	9.219e-18 (2.504e-18)	2.647e-17 (2.714e-18)	4.386e-17 (5.425e-18)
82C	1.157e-15 (9.503e-18)	4.116e-15 (2.664e-17)	6.894e-16 (7.531e-18)	7.082e-16 (7.277e-18)	2.260e-16 (3.150e-18)	4.615e-16 (3.427e-18)	4.445e-16 (1.119e-17)
91A	7.837e-16 (1.712e-17)	1.996e-15 (5.703e-17)	2.009e-16 (7.835e-18)	6.046e-16 (4.341e-18)	1.983e-16 (5.965e-18)	2.840e-16 (6.344e-18)	6.052e-16 (8.812e-18)
91C	3.142e-16 (7.112e-18)	1.098e-15 (2.869e-17)	2.135e-16 (5.177e-18)	2.488e-16 (3.136e-18)	6.280e-17 (3.899e-18)	1.510e-16 (4.302e-18)	1.586e-16 (9.371e-18)
95C	1.081e-16 (8.582e-18)	4.714e-16 (2.685e-17)	9.415e-17 (4.675e-18)	1.364e-16 (4.887e-18)	4.481e-17 (3.553e-18)	8.102e-17 (3.839e-18)	1.477e-16 (1.020e-17)
96A	2.593e-15 (1.179e-17)	1.197e-14 (4.933e-17)	7.595e-16 (8.759e-18)	1.736e-15 (4.418e-18)	1.007e-15 (6.902e-18)	1.410e-15 (6.369e-18)	2.030e-15 (2.042e-17)
96C	7.005e-16 (1.056e-17)	2.209e-15 (3.928e-17)	4.341e-16 (7.732e-18)	5.684e-16 (1.190e-17)	1.558e-16 (4.062e-18)	2.825e-16 (4.642e-18)	2.439e-16 (1.070e-17)
100A	1.226e-15 (7.659e-18)	4.220e-15 (2.289e-17)	6.740e-16 (3.410e-18)	1.209e-15 (2.044e-18)	2.752e-16 (2.881e-18)	6.563e-16 (3.496e-18)	6.432e-16 (7.450e-18)

Note. — Uncertainties are listed in parentheses. Marginal detections are low signal to noise lines as determined by visual inspection.

$^{\square}$ Marginal Detection

* SL coverage

$^{\diamond}$ LL coverage

$^{\bullet}$ Off nuclear extraction

TABLE A4: Observed Forbidden Line Fluxes in units of W m^{-2}

Source	[ArII] 6.98μm	[NeII] 12.81μm	[NeIII] 15.56μm	[SIII] 18.71μm	[OIV] 25.89μm/ [FeII] 25.98μm	[SIII] 33.48μm	[SiII] 34.82μm
6B	<3.400e-18†	1.364e-18 (4.693e-19)$^{\square}$	2.568e-18 (4.584e-19)$^{\square}$	<1.306e-18	1.575e-18 (4.075e-19)	<3.423e-18	3.674e-18 (1.066e-18)
15A	5.290e-18 (1.470e-18)	2.452e-18 (6.782e-19)	6.353e-18 (7.423e-19)	4.737e-18 (7.139e-19)	<2.554e-18	<4.0479e-18	1.033e-17 (2.001e-18)
15D	<1.072e-17†	4.369e-18 (1.704e-18)$^{\square}$	<4.799e-18	<3.546e-18	<6.896e-18	<3.141e-18	4.005e-18 (1.893e-18)$^{\square}$
25B*	9.752e-19 (2.419e-19)$^{\square\dagger}$	5.534e-19 (4.702e-20)	–	–	–	–	–
25B$^{\diamond\bullet}$	–	–	1.772e-18 (1.979e-20)	<4.689e-18	<2.629e-18	<4.047e-18	<4.604e-18
31AC$^{\diamond}$	–	–	3.737e-16 (6.930e-20)	2.718e-16 (1.148e-19)	<1.690e-17	2.786e-16 (1.446e-17)	1.269e-16 (1.366e-17)
40B	<3.457e-18	3.542e-18 (1.002e-18)$^{\square}$	3.353e-18 (1.045e-18)$^{\square}$	<2.196e-18	3.748e-18 (6.926e-19)$^{\square}$	<3.748e-18	<7.405e-18
40C$^{\star\bullet}$	4.938e-19 (1.332e-19)$^{\square\dagger}$	5.706e-19 (7.023e-20)	–	–	–	–	–
40C$^{\diamond}$	–	–	2.452e-17 (2.294e-20)	8.971e-17 (1.469e-19)	3.861e-18 (1.208e-18)	6.325e-17 (1.651e-20)	1.602e-16 (2.331e-20)
40D	5.886e-17 (2.446e-18)	1.114e-16 (1.431e-18)	8.048e-18 (1.824e-18)	3.385e-17 (2.402e-18)	1.365e-17 (1.376e-18)	4.870e-17 (5.056e-18)	1.190e-16 (4.805e-18)
44A$^{\star\bullet}$	2.621e-18 (8.208e-19)$^{\square}$	1.849e-18 (2.263e-19)	–	–	–	–	–
44A$^{\diamond}$	–	–	5.692e-17 (1.718e-20)	3.348e-17 (4.615e-20)	2.096e-17 (9.390e-18)	3.348e-17 (7.745e-18)	1.863e-16 (6.930e-18)$^{\square}$
44D	4.933e-17 (1.245e-17)$^{\square\dagger}$	4.149e-17 (8.400e-18)	5.717e-17 (7.080e-18)	1.540e-16 (1.346e-17)	7.843e-18 (3.406e-18)	9.845e-17 (5.490e-18)	8.545e-17 (5.903e-18)
47A	3.295e-17 (5.367e-18)$^{\square\dagger}$	3.745e-17 (3.049e-18)	5.792e-18 (2.624e-18)	1.928e-17 (2.403e-18)	<9.792e-18	4.433e-17 (2.369e-18)	4.356e-17 (2.998e-18)
55C	<5.808e-18†	1.002e-17 (2.574e-19)	2.021e-18 (4.941e-19)	3.873e-18 (7.648e-19)	<1.045e-18	6.434e-18 (4.134e-19)	1.487e-17 (7.770e-19)
56B	2.725e-17 (4.189e-18)	3.636e-17 (4.169e-18)	6.748e-17 (3.365e-18)	1.813e-17 (2.695e-18)	8.377e-17 (2.220e-18)	1.377e-17 (2.569e-18)	1.610e-17 (3.423e-18)
56C	8.005e-18 (1.469e-18)$^{\square\dagger}$	4.830e-18 (1.316e-18)$^{\square}$	2.555e-18 (9.593e-19)$^{\square}$	2.581e-18 (5.985e-19)$^{\square}$	<4.609e-18	6.053e-18 (1.783e-18)$^{\square}$	<7.828e-18
56D*	3.089e-17 (1.583e-18)	2.381e-17 (8.803e-19)	–	–	–	–	–
56E	3.111e-18 (7.657e-19)$^{\square\dagger}$	5.185e-18 (3.979e-19)	1.682e-18 (4.357e-19)	4.846e-18 (5.428e-19)	<2.224e-18	5.767e-18 (1.502e-18)	2.559e-18 (1.575e-18)
57A$^{\bullet}$	1.216e-18 (5.026e-19)$^{\square\dagger}$	4.006e-18 (5.876e-19)	3.084e-18 (5.026e-19)	1.585e-18 (3.229e-19)	1.148e-18 (5.099e-19)	2.719e-18 (7.600e-19)	4.637e-18 (8.110e-19)
57A$^{\diamond}$	–	–	1.184e-17 (2.592e-20)	3.971e-18 (7.379e-20)	<1.875e-18	1.010e-17 (2.515e-18)	2.845e-17 (2.864e-18)
67B	4.092e-17 (7.869e-18)	7.530e-17 (1.715e-18)	3.404e-18 (1.672e-18)$^{\square}$	8.065e-18 (1.426e-18)	<5.662e-18	1.825e-17 (2.334e-18)	5.212e-17 (3.192e-18)
68A	1.706e-17 (2.472e-18)$^{\square\dagger}$	1.270e-17 (7.531e-19)	1.435e-17 (7.590e-19)	6.979e-18 (9.325e-19)	4.381e-18 (5.709e-19)	6.465e-18 (1.202e-18)	1.774e-17 (1.338e-18)
68B	4.644e-18 (2.089e-18)$^{\square\dagger}$	3.880e-18 (6.767e-19)	1.206e-17 (6.631e-19)	5.383e-18 (7.310e-19)	<3.986e-18	2.921e-18 (8.830e-19)$^{\square}$	8.915e-18 (1.155e-18)$^{\square}$
68C	9.516e-17 (7.711e-18)	1.207e-16 (2.188e-18)	2.078e-17 (1.134e-18)	3.974e-17 (1.464e-18)	8.149e-18 (9.425e-19)	3.573e-17 (1.721e-18)	7.328e-17 (1.969e-18)
75D$^{\diamond}$	–	–	<1.730e-18	1.666e-17 (2.527e-18)	1.763e-18 (7.331e-19)	1.309e-17 (1.569e-18)	2.460e-17 (1.939e-18)
79A	2.106e-17 (1.427e-18)	3.949e-17 (4.816e-19)	7.949e-18 (6.939e-19)	1.639e-17 (9.172e-19)	2.293e-18 (4.442e-19)	3.040e-17 (1.113e-18)	5.215e-17 (1.384e-18)
79B	9.151e-18 (2.436e-18)	2.363e-17 (5.177e-19)	4.156e-18 (3.445e-19)	9.698e-18 (6.162e-19)	3.719e-18 (3.252e-19)	1.371e-17 (6.089e-19)	2.767e-17 (8.313e-19)
82B	<4.450e-18†	4.770e-18 (6.114e-19)	3.503e-18 (6.453e-19)	5.095e-18 (8.831e-19)	<1.618e-18	2.829e-18 (1.058e-18)$^{\square}$	4.949e-18 (1.271e-18)$^{\square}$
82C	5.974e-17 (2.780e-18)	1.179e-16 (9.169e-19)	1.921e-17 (1.077e-18)	3.471e-17 (2.088e-18)	8.369e-18 (2.263e-18)	6.899e-17 (1.761e-18)	9.751e-17 (3.246e-18)
91A	3.796e-17 (5.058e-18)$^{\square\dagger}$	5.676e-17 (1.286e-18)	2.693e-17 (1.504e-18)	4.185e-17 (1.468e-18)	2.474e-17 (3.857e-18)	5.955e-17 (2.402e-18)	1.261e-16 (2.511e-18)
91C	1.376e-17 (3.007e-18)	2.140e-17 (9.767e-19)	3.949e-18 (1.580e-18)	1.469e-17 (2.013e-18)	<7.169e-18	1.418e-17 (2.166e-18)	4.348e-17 (3.185e-18)
95C	6.705e-18 (3.206e-18)	1.481e-17 (7.070e-19)	6.089e-18 (1.085e-18)	9.996e-18 (1.201e-18)	1.792e-18 (7.802e-19)	1.195e-17 (1.268e-18)	1.664e-17 (1.810e-18)
96A	7.912e-17 (4.590e-18)$^{\square\dagger}$	2.506e-16 (1.260e-18)	2.448e-16 (2.681e-18)	1.544e-16 (2.346e-18)	3.031e-16 (1.923e-18)	2.506e-16 (3.744e-18)	1.661e-16 (4.866e-18)
96C	2.650e-17 (3.245e-18)	5.489e-17 (1.007e-18)	1.274e-17 (1.225e-18)	1.528e-17 (1.322e-18)	4.755e-18 (1.134e-18)	2.638e-17 (2.117e-18)	4.719e-17 (2.942e-18)
100A	6.115e-17 (2.560e-18)	1.080e-16 (7.013e-19)	2.548e-17 (1.359e-18)	9.609e-17 (1.274e-18)	1.003e-17 (1.614e-18)	1.164e-16 (2.293e-18)	1.359e-16 (2.269e-18)

Note. — Uncertainties are listed in parentheses. Marginal detections are low signal to noise lines as determined by visual inspection.

† Blended with H_2 S(5) 6.91μm

$^{\square}$ Marginal Detection

* SL coverage

$^{\diamond}$ LL coverage

$^{\bullet}$ Off nuclear extraction

TABLE A5: H_2-detected Extraction Areas

Galaxy	SL Area (arcsec^2)	LL Area (arcsec^2)	SF^a
6B	27.3	154.8	1
15A	75.3	309.6	1
15D	47.9	309.8	2.50
25B	82.3	–	
25B$^\bullet$ –	516.5		
31AC	–	722.7	
31AC$^\bullet$	82.3	–	
40B	47.8	258.5	3.37
40C	–	516.5	
40C$^\bullet$	77.8	–	
40D	95.6	464.6	1.96
44A	–	619.4	
44A$^\bullet$	116.0	–	
44D	93.5	878.1	5.90
47A	75.0	361.3	3.79
55C	68.4	258.2	1
56B	61.9	412.5	1.59
56C	54.7	361.2	4.09
56D	54.8	–	
56E	41.0	206.2	1
57A	–	413.1	
57A$^\bullet$	67.9	103.3	1
67B	170.4	361.2	1
68A	61.7	412.4	5.33
68B	75.4	361.2	1
68C	308.6	775.6	2.24
75D	–	257.8	
79A	61.6	361.3	1.58
79B	68.6	155.1	1.24
82B	34.3	206.4	1
82C	54.7	309.6	1.60
91A	225.1	516.0	1.53
91C	47.8	361.3	2.36
95C	82.7	259.3	1
96A	130.9	619.9	1.64
96C	41.4	258.0	1.61
100A	68.4	516.2	1

^{a} Scale Factor
$^\bullet$ Off-nuclear extraction

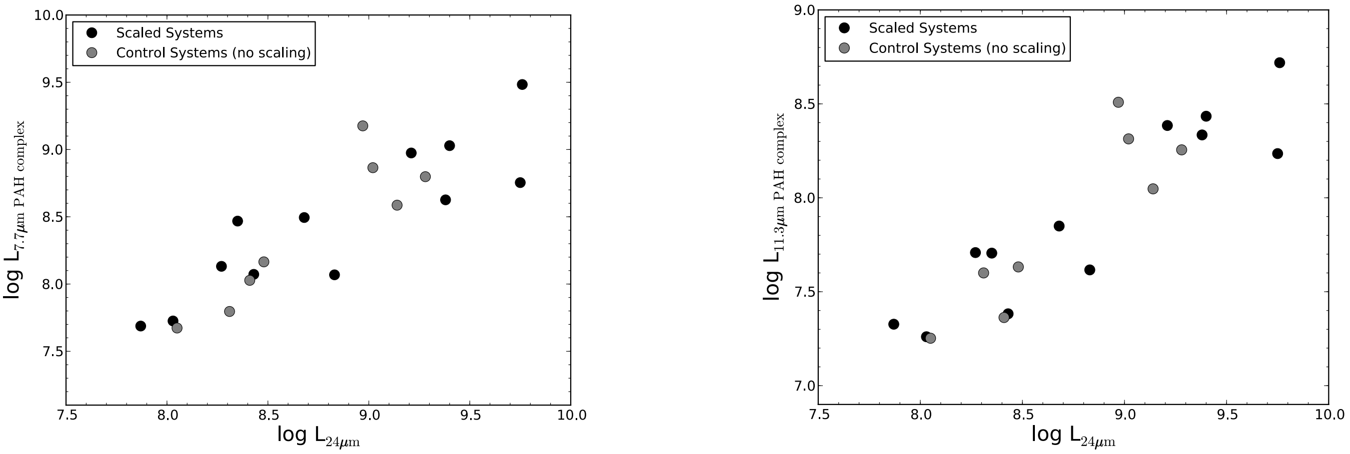

(a) Comparison of 7.7μm PAH and 24μm Luminosity

(b) Comparison of 11.3μm PAH and 24μm Luminosity

FIG. A1: Comparison of scaled and unscaled continuum and emission features our extraction is optimised to include the disk.

HCG 44A only has LL coverage, so we have a lower limit for its $H_2/7.7\mu m$ PAH (see Fig. 10), however, from its SINGS data, we know it has a $H_2/7.7\mu m$ PAH value of 0.042 (Roussel et al. 2007) and is therefore a weak MOHEG. With a $\log[f_{5.8\mu m}/f_{3.6\mu m}]$) of -0.20, it is also located within the green valley and appears to have an asymmetrical disk (see Fig. B3a).

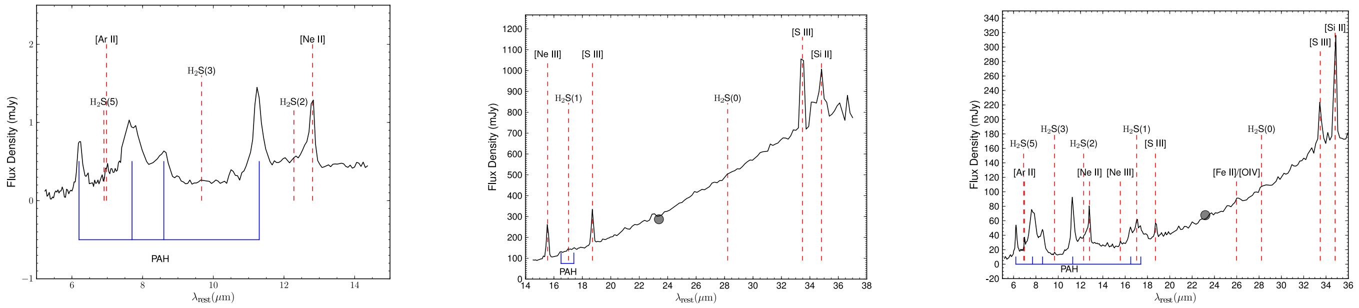

(a) HCG 31AC – SL (Off-Nuclear)
(b) HCG 31AC – LL (Nuclear)
(c) HCG 40D (Nuclear)

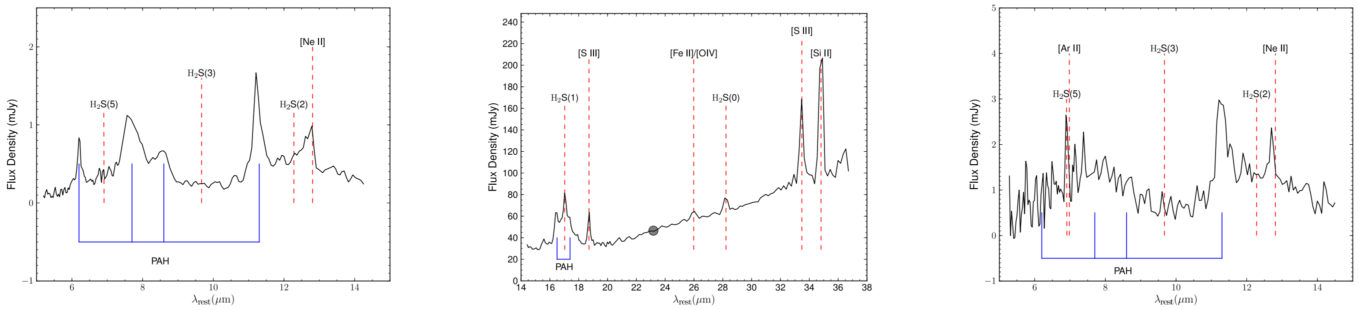

(d) HCG 40C – SL (Off-Nuclear)
(e) HCG 40C – LL (Nuclear)
(f) HCG 44A – SL (Off-Nuclear)

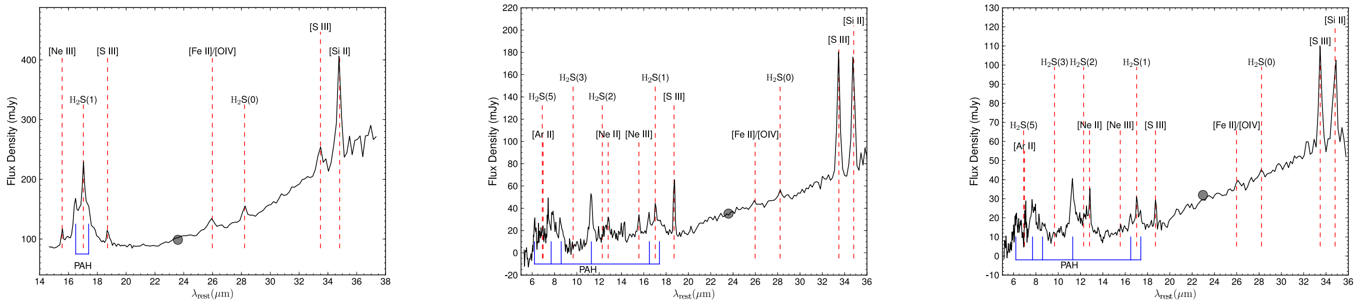

(g) HCG 44A – LL (Nuclear)
(h) HCG 44D (Nuclear)
(i) HCG 47A (Nuclear)

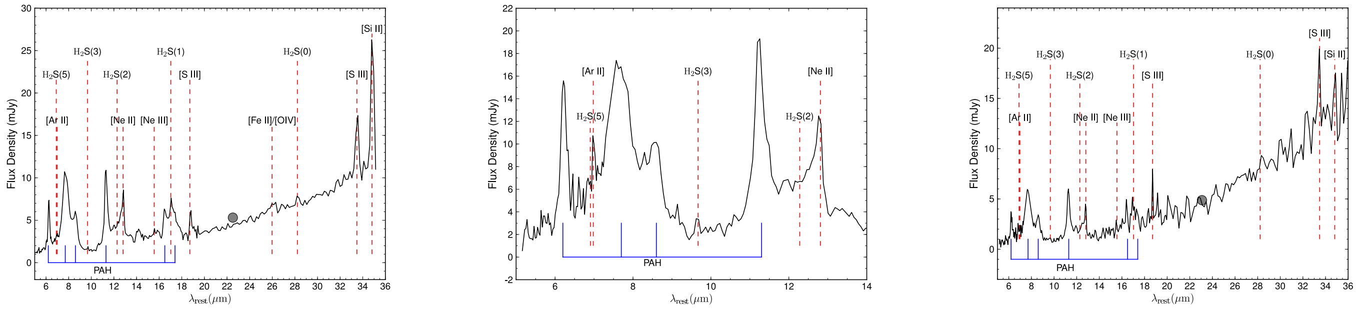

(j) HCG 55C (Nuclear)
(k) HCG 56D – SL (Nuclear)
(l) HCG 56E (Nuclear)

FIG. B1: Non-MOHEG, H_2-detected HCG Galaxies. The matched MIPS $24\mu m$ photometry is shown as a grey point.

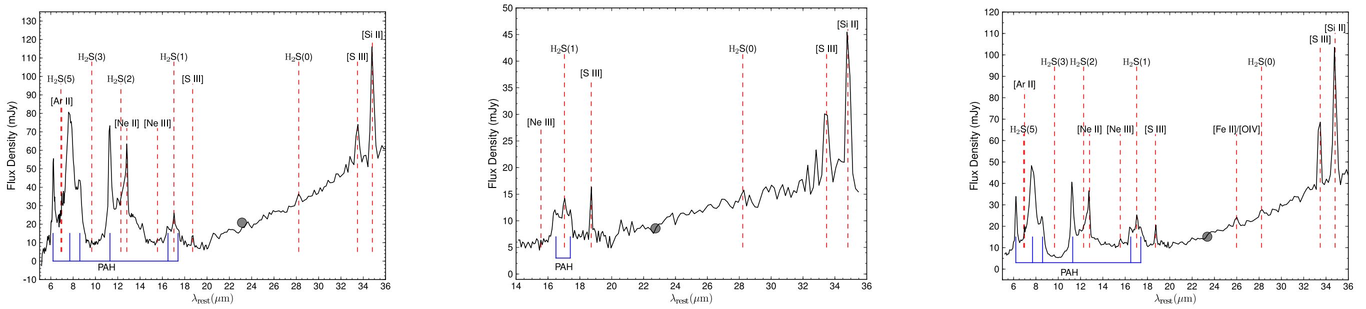

(a) HCG 67B (Nuclear) (b) HCG 75D – LL (Nuclear) (c) HCG 79A (Nuclear)

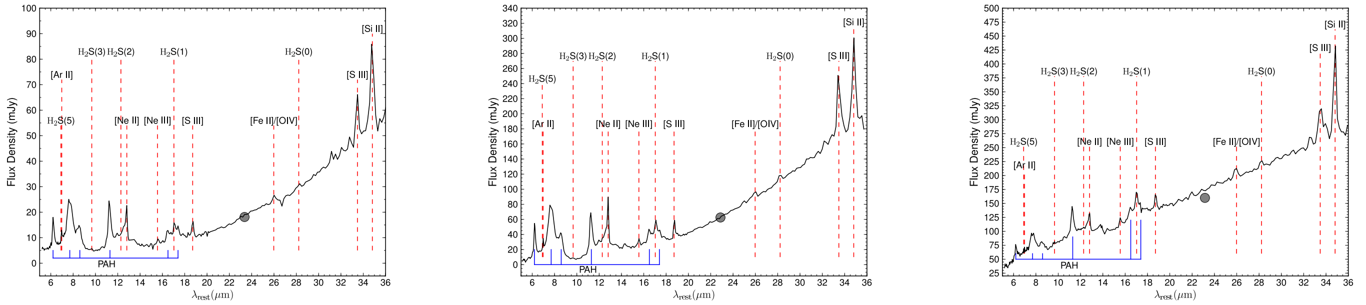

(d) HCG 79B (Nuclear) (e) HCG 82C (Nuclear) (f) HCG 91A (Nuclear)

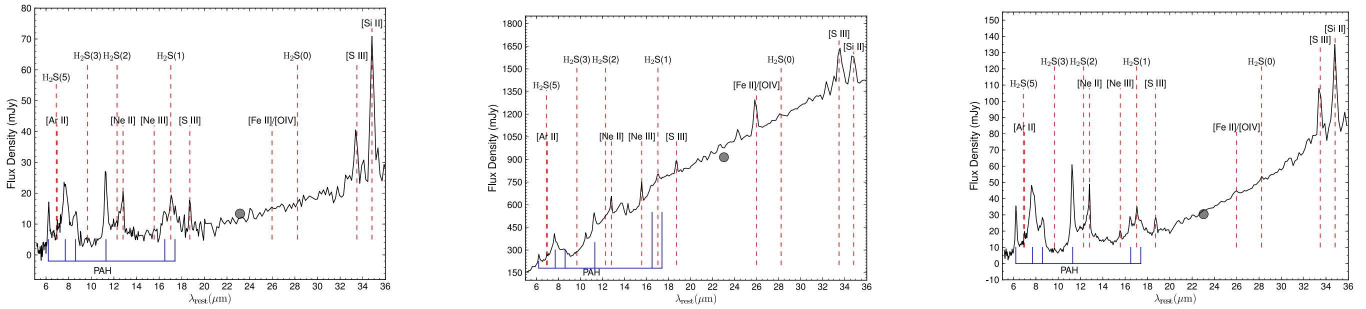

(g) HCG 91C (Nuclear) (h) HCG 96A (Nuclear) (i) HCG 96C (Nuclear)

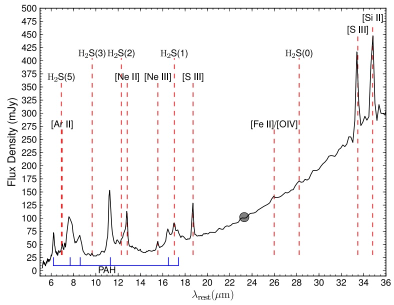

(j) HCG 100A (Nuclear)

FIG. B2: Non-MOHEG, H_2-detected HCG Galaxies. The matched MIPS 24μm photometry is shown as a grey point.

If we consider the morphological types of the non-MOHEG H_2 galaxies listed in Table 3, they are mainly classified as peculiar early type galaxies (Sa/b or S0). However, these galaxies have spectra consistent with current star formation (strong PAH emission and a sharply rising mid-infrared continuum). Bitsakis et al. (2011) have suggested that several systems are misclassified (due to orientation and dust obscuration). For the galaxies 55C, 56D and 56E (see Fig. B1) our spectra don't rule out this possibility, as proposed by Bitsakis et al. (2011) based on their SEDs and IRAC mid-infrared morphology. In addition, their global mid-infrared colors are consistent with late type systems ($\log[f_{5.8\mu m}/f_{3.6\mu m}] > 0$) and their nuclear classifications suggest they are star-forming systems (Coziol et al. 2004).

HCG 79A has a star-forming spectrum, but a mid-infrared color of $\log[f_{5.8\mu m}/f_{3.6\mu m}]$ = -0.06, putting it at the start of the mid-infrared green valley. Inspection of its IRAC image (included as Figure B3d) suggests that 79A is an S0/a type. The star formation seen in its spectrum could be the result of a minor merger or gas accretion that has introduced star forming fuel and is expected to further build the lenticular bulge (Shapiro et al. 2010). The Hα velocity field determined by Durbala et al. (2008) suggests a cross-fueling (discrete infall or fueling event rather than a continuous flow) from HCG 79D. Evidence for a minor merger in HCG 79A were also see by Coziol & Plauchu-Frayn (2007) based on the asymmetry seen in their near-infrared images.

Within our sample, Bitsakis et al. (2011) have also suggested 79B and 100A are late type galaxies (i.e. misclassified as early types). Inspection of their spectra indicates star formation is occurring (Figures B2d and B2j, respectively). We note that their SEDs (Bitsakis et al. 2011) show warm dust continuum superimposed on a substantial stellar component. However, we draw attention to these galaxies since they have IRAC colors ($\log[f_{5.8\mu m}/f_{3.6\mu m}]$) of -0.18 and -0.05, for HCG 79B and 100A, respectively. This places them at intermediate mid-infrared color. We show these galaxies in Figure B3 and draw attention to their disturbed morphologies. HCG 79B displays a magnificent tidal feature and there is evidence that it has accreted a dwarf (Durbala et al. 2008). These galaxies are all classified as early types (S0/a), but we may be seeing the effect of minor mergers or gas accretion producing star formation and giving rise to the combination of relatively dusty mid-infrared colours with mid-infrared spectra indicative of star formation. Alternatively star formation is being actively shut off or "starved" by some mechanism. It is therefore not clear that these galaxies are misclassifications.

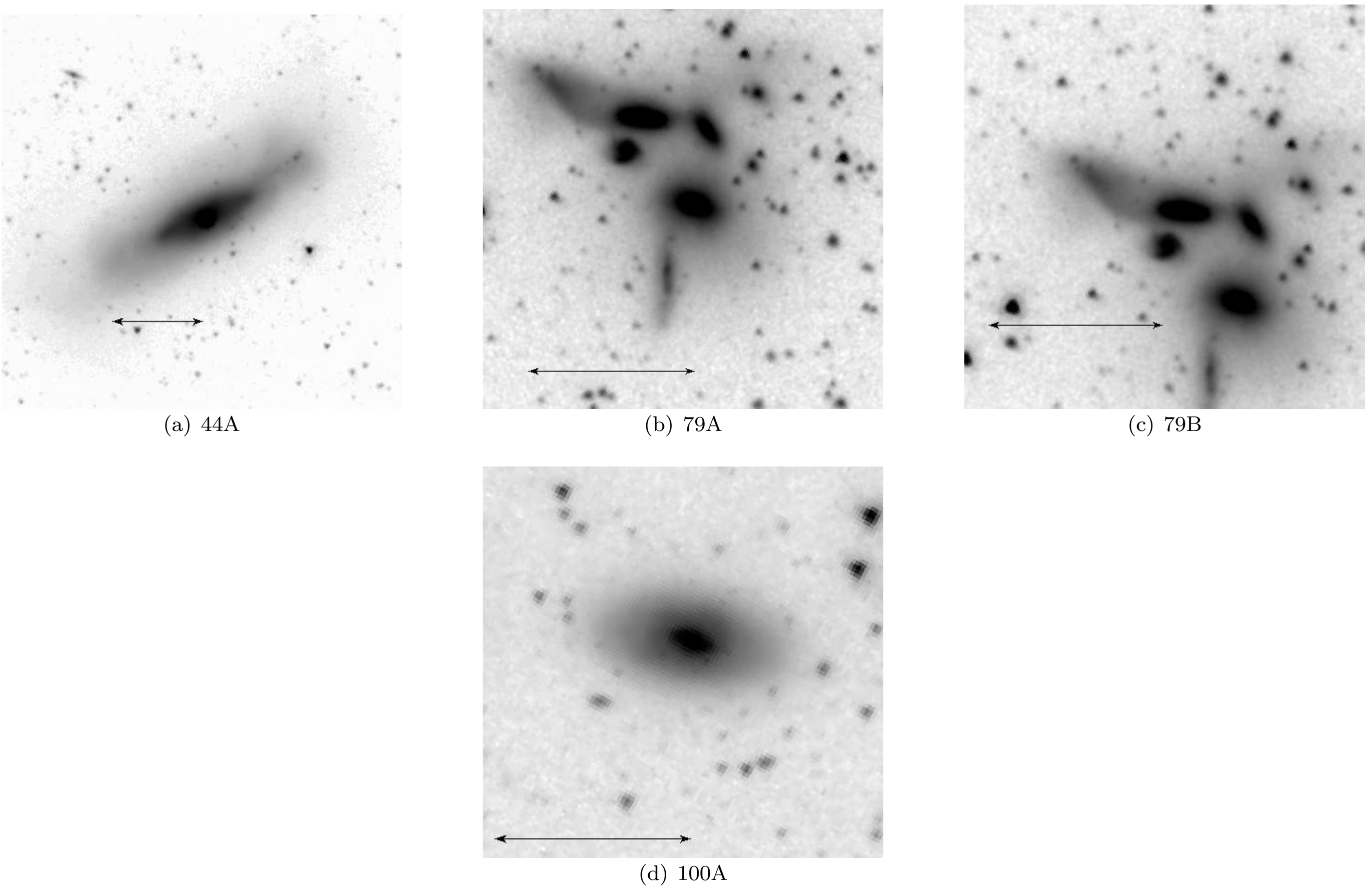
(a) 44A
(b) 79A
(c) 79B
(d) 100A

FIG. B3: IRAC images of the non-MOHEG H_2-detected galaxies which lie within the green valley. These systems all have spectra that indicate active star formation. The galaxy in question lies at the center of the 3.6μm IRAC image; the arrow is $1'$ in length.

C. H_2 UPPER LIMITS FOR NON-DETECTIONS IN THE REST OF THE SAMPLE

In this section we give the H_2 upper limits for the S(0), S(1), S(2) and S(3) lines and measured PAH values for galaxies in the sample with an extracted spectrum.

TABLE C1: H_2 Upper Limits for the Remainder of Sample in units of $\mathrm{W\,m^{-2}}$

Galaxy	H_2 0-0 S(0) $\lambda 28.21\mu$m	H_2 0-0 S(1) $\lambda 17.03\mu$m	H_2 0-0 S(2) $\lambda 12.28\mu$m	H_2 0-0 S(3) $\lambda 9.66\mu$m
8A	<1.513e-18	<2.286e-18	<5.699e-19	<1.142e-18
8C	<1.897e-18	<2.509e-18	<7.261e-19	<1.566e-18
8D	<1.752e-18	<3.618e-18	<1.298e-18	<1.592e-18
15C	<1.506e-18	<3.299e-18	<1.196e-18	<2.198e-18
25D	<1.650e-18	<2.958e-18	<1.161e-18	<1.252e-18
25F	<1.864e-18	<3.186e-18	<9.264e-19	<1.825e-18
40A	<1.415e-18	<2.303e-18	<7.692e-19	<1.173e-18
31B	< 2.864e-18	< 2.383e-18	< 3.292e-18	< 4.508e-18
44B	<1.976e-18	<3.267e-18	<1.883e-18	<6.087e-18
47B	<1.284e-18	<1.454e-18	<1.342e-18	<2.156e-18
47D	<4.018e-18	<5.080e-18	<3.122e-18	<3.052e-18
54A	<1.415e-18	<4.105e-18	<1.108e-18	<2.264e-18
54B	<2.152e-18	<2.184e-18	<2.537e-18	<6.094e-18
54C	<1.564e-18	<2.643e-18	<8.198e-19	<1.662e-18
55A	<7.940e-19	<9.644e-19	<3.727e-19	<5.379e-19
55B[⋆]	–	–	<6.945e-19	<5.913e-19
55D[⋆]	–	–	<2.814e-19	<4.005e-19
57B[◇]	<1.108e-18	<2.865e-18	–	–
57B[⋆]	–	–	<1.709e-19	<1.994e-19
57C	<1.945e-18	<2.728e-18	–	–
57D	<2.085e-18	–	–	–
57E	<1.361e-18	<2.108e-18	<6.653e-19	<9.469e-19
62A[◇]	<9.610e-19	<1.881e-18	–	–
62A[⋆]	–	–	<1.776e-18	<3.169e-18
62B	<1.082e-18	<1.588e-18	<1.578e-18	<3.723e-18
62C	<9.707e-19	<1.422e-18	<9.435e-19	<2.819e-18
67A	<2.099e-18	<3.888e-18	<4.141e-18	<7.609e-18
67D	<1.704e-18	<2.371e-18	–	–
75A	<2.375e-18	<2.323e-18	<2.861e-18	<6.098e-18
75C	<9.559e-19	<1.815e-18	<1.804e-18	<2.296e-18
75E	<1.333e-18	<1.768e-18	<6.877e-19	<1.205e-18
82A	<1.331e-18	<2.363e-18	<3.547e-19	<7.162e-19
91D	<2.280e-18	<5.068e-18	<5.111e-19	<1.894e-18
95A	<1.506e-18	<2.906e-18	<1.561e-18	<3.768e-18
96B	<1.241e-18	<3.459e-18	<1.041e-18	<2.242e-18
97A	<1.798e-18	<2.312e-18	<1.042e-18	<1.490e-18
97C	<1.510e-18	<3.099e-18	<1.357e-18	<2.160e-18
97D	<1.988e-18	<2.146e-18	<1.450e-18	<3.818e-18
100B	<2.716e-18	<5.954e-18	<1.867e-18	<4.176e-18
100C	<1.965e-18	<3.052e-18	<1.643e-18	<2.809e-18

[⋆] SL coverage only

[◇] LL coverage only

TABLE C2: Measurements for Main PAH features for Remainder of Sample in units of $\mathrm{W\,m^{-2}}$

Galaxy	6.2μm	7.7μm	11.3μm
8A	<6.014e-18	<7.630e-18	9.170e-18 (1.826e-18)
8C	<7.029e-18	<7.961e-17	1.754e-17 (2.363e-18)
8D	<7.180e-18	5.434e-17 (4.884e-18)	2.076e-17 (8.858e-19)
15C	<1.788e-17	<5.850e-17	<5.884e-18
25D	<7.194e-18	<2.707e-17	<4.555e-18
25F	<4.319e-18	<3.667e-17	<2.530e-18
31B	2.269e-16 (1.306e-17)	6.022e-16 (5.166e-17)	2.119e-16 (6.787e-18)
40A	<7.947e-18	1.058e-17 (2.645e-18)	1.242e-17 (5.437e-19)
44B	<1.912e-17	<1.127e-16	<9.197e-18
47B	<1.214e-17	<6.908e-17	<6.273e-18
47D	<4.196e-17	<4.482e-17	2.309e-17 (3.805e-18)
54A	<1.180e-17	6.653e-17 (6.314e-18)	1.318e-17 (1.314e-18)
54B	9.182e-17 (9.197e-18)	1.764e-16 (1.756e-17)	6.839e-17 (7.564e-18)
54C	<8.366e-18	6.307e-17 (6.260e-18)	1.568e-17 (2.409e-18)
55A	<9.556e-18	<7.376e-18	1.248e-18 (3.539e-19)
55B	<4.214e-18	<1.768e-17	<1.422e-18
55D	<2.492e-18	<4.115e-18	2.180e-18 (6.428e-19)
57B	<3.270e-18	4.168e-18 (1.015e-18)	2.027e-18 (3.227e-19)
57C$^\diamond$	–	–	–
57D$^\diamond$	–	–	–
57E	<5.498e-18	<7.503e-17	1.541e-17 (3.929e-18)
62A	3.606e-17 (7.201e-18)	< 6.775e-17	8.293e-18 (2.755e-18)
62B	<1.723e-17	<6.527e-17	<1.132e-17
62C	<1.735e-17	< 9.991e-17	<4.573e-18
67A	<5.361e-17	< 1.850e-16	<2.205e-17
67D$^\diamond$	–	–	–
75A	<2.737e-17	3.330e-17 (6.426e-18)	2.916e-17 (1.506e-18)
75C	2.154e-17 (6.270e-18)	8.114e-17 (2.569e-17)	3.254e-17 (2.010e-18)
75E	<2.183e-17	<1.652e-17	<6.830e-18
82A	<6.455e-18	<4.775e-17	<2.735e-18
91D	<1.781e-17	3.659e-17 (7.704e-18)	7.828e-18 (2.189e-18)
95A	<2.470e-17	<2.100e-17	<6.839e-18
96B	<1.568e-17	<7.431e-17	<4.826e-18
97A	<1.236e-17	<8.951e-17	<5.459e-18
97C	<1.510e-17	<2.646e-17	<2.602e-18
97D	<2.322e-17	<1.220e-16	<6.714e-18
100B	2.164e-16 (9.738e-18)	5.821e-16 (4.674e-17)	1.361e-16 (7.608e-18)
100C	1.999e-17 (7.049e-18)	5.320e-17 (8.919e-18)	2.929e-17 (2.515e-18)

$^\diamond$ LL coverage only

D. X-RAY AND RADIO PROPERTIES OF THE HCG SAMPLE

The X-ray distribution and luminosity in our HCG MOHEGs is an important consideration since XDRs (X-ray dominated regions) associated with AGN may excite H_2. It is therefore necessary to rule out photo-heating of H_2 from within the galaxies.

First we consider the amount and distribution of X-ray emission (including diffuse plasma) in the MOHEG groups to explore any connections to the H_2-enhanced systems. We have X-rays detected in 5 groups and we list the diffuse X-ray measurements obtained from the literature in Table D1. The MOHEGs, HCG 15A and D appear to have some X-ray structure associated with them, in particular HCG 15D appears connected to 15F (Rasmussen et al. 2008). In HCG 40, B is H_2-enhanced, but the strongest X-ray sources are C and D, which are only H_2-detected systems (Rasmussen et al. 2008). However, HCG 40B and C appear connected in X-ray emission, particularly interesting as we detect H_2 outside 40C (see section 4.1.1). In HCG 68, the map of Forbes et al. (2006) indicates emission around MOHEGs HCG 68A and C show emission and it appears that the emission from A connects to B (also a MOHEG).

TABLE D1: MOHEG Compact Group X-ray Data

Group	MOHEGs	X-ray Luminosity	
		L_X (erg s^{-1})	$L_\odot$
HCG 6	1	$<2.7\times10^{41}$ (3σ, a)	$<7.0\times10^{7}$
HCG 15	2	$3.2\pm0.2\times10^{41}$ (b)	8.3×10^{7}
HCG 25	1	–	–
HCG 40	1	$3.1\pm0.5\times10^{40}$	8.1×10^{6}
HCG 56	1	$<1.7\times10^{42}$ (3σ, a)	$<4.4\times10^{8}$
HCG 57	1	$8.3{+}3.2{-}3.5\times10^{41}$ (c)	2.2×10^{8}
HCG 68	3	$3.3\pm0.3\times10^{41}$ (d)	8.6×10^{7}
HCG 82	1	$1.9\pm0.8\times10^{42}$ (a)	4.9×10^{8}
HCG 95	1	$<2.7\times10^{42}$ (3σ, a)	$<7.0\times10^{8}$

(a) From Ponman et al. (1996)
(b) From Rasmussen et al. (2008)
(c) From Mulchaey et al. (2003)
(d) From Osmond & Ponman (2004)

Unlike SQ, X-ray emission from a shock-front is not clearly distinguishable from the diffuse emission in the groups. Of course, that system is impressive due to the high relative velocity (~ 1000 km/s) of the collision of the intruder with the intragroup H I. Collisions of the group galaxies with tidal material would be occurring at far lower relative velocities ($100 - 1000$ km/s), thus the kinetic energy would be far less compared to SQ, resulting in weaker X-ray emission.

We have seen, however, that several galaxies appear to have nuclear enhancements in the X-ray data. Searching the archives for suitable coverage of the HCG MOHEGs, we have determined that HCG 6B, 25B, 82B and 95C have not been covered by *Chandra/XMM* and were not detected by *ROSAT*. All other available measurements (from the literature and data, as specified) are listed in Table D2. We include the radius of the measurement, the luminosity of the H_2 in relation to the X-ray. In addition, archival radio data is presented. The galaxies are listed in order of decreasing $H_2/7.7\mu$m PAH.

H_2 heating by X-rays via photoelectrons in XDR models leads to $\sim$2% of the total gas cooling via the pure rotational lines of H_2 (Maloney et al. 1996). Assuming all of the X-ray flux is absorbed by an XDR, the maximum $L(H_2\,0\text{-}0\ S(0)\text{-}S(3))/L_X(2\text{-}10\ \text{keV}) < 0.01$ (Ogle et al. 2010). Assuming a power-law spectrum typical of an AGN (as in Ogle et al. 2010), we scale the fluxes in the energy bands listed in Table D2 to the L_X(2-10 keV) band. Given that our IRS spectra have only sampled a fraction of the HCG galaxies, we do not have a measure of the total amount of warm H_2 and hence the L_{H_2}/L_X values are lower limits, but still illustrative. We note that all the HCG MOHEGS have $L_{H_2}/L_X > 0.01$, usually having H_2 luminosities more than an order of magnitude greater than what can be generated by X-rays (except HCG 15D, although this measurement is contaminated by diffuse emission). We can thus rule out XDRs as being responsible for the enhanced H_2 seen in the HCG MOHEGs. This is not unexpected as even though HCG galaxies have increased AGN activity (likely due to tidal interactions), they are dominated by low luminosity AGN.

Archival radio data is also included in Table D2. The highest 1.4 GHz luminosity is associated with the Seyfert 2 galaxy HCG 56B, a candidate MOHEG for jet-ISM interactions producing the excited H_2 (see Ogle et al. 2010).

TABLE D2: MOHEG Nuclear X-ray and Radio Data

	X-ray Luminosity				Radio Data			
	$\mathrm{L_X}$ $(\mathrm{erg\,s^{-1}})$	Radius	$\mathrm{L_X}$ $(\mathrm{L_\odot})$	$\frac{\mathrm{L_{H_2}}}{\mathrm{L_X}}$ †		$F_{1.4\mathrm{GHz}}$ (mJy)	$\mathrm{L_{1.4GHz}}$ $(\mathrm{erg\,s^{-1}})$	$\log \mathrm{L_{1.4GHz}}$ $[\mathrm{W\,Hz^{-1}}]$
68A	1.6×10^{40} ^{a,b}	4.7″	4.1×10^{6}	>0.53	NVSS$^{\diamond}$	40.5 (1.3)	8.7×10^{37}	21.6
6B	–	–	–	–	–			
57A	4.1×10^{39} ^{c,d}	15″	1.1×10^{6}	>28.9	–			
40B	1.8×10^{39} ^{c,e}	2.1″	4.7×10^{5}	>2.42	–			
25B	–	–	–	–	–			
15D	$6.7\times10^{41}(\star)$ ^{c,e}	25″	1.7×10^{8}	>0.03	NVSS	4.6 (0.5)	6.6×10^{37}	21.7
68B	9.0×10^{39} ^{a,b}	2.3″	2.3×10^{6}	>0.18	NVSS	8.0 (0.5)	1.7×10^{37}	21.1
95C	–	–	–	–	–			
15A	$2.6\times10^{40}(\star)$ ^{c,e}	25″	6.8×10^{6}	>0.22	NVSS	3.6 (0.6)	5.1×10^{37}	21.6
56B	$<1.5\times10^{40}$ ^{c,f}	3″	$<3.8\times10^{6}$	>1.42	NVSS	26.7 (1.2)	6.1×10^{38}	22.6
68C	6.9×10^{39} ^{a,b}	1.2″	1.8×10^{6}	>3.70	NVSS	16.8 (1.7)	3.6×10^{37}	21.4
82B	–	–	–	–	–			
56C	$<1.5\times10^{40}$ ^{c,f}	3″	$<3.8\times10^{6}$	>1.69	–			

[†] $L(\mathrm{H_2}$ 0-0 S(0)-S(3)$)/L_X$(2-10 keV)

[◇] NRAO VLA Sky Survey; Condon et al. (1998)

($\star$) *XMM* – Can't discern point-like from diffuse emission

[a] 0.5-7 keV

[b] From Chandra Source Catalogue; Evans et al. (2010)

[c] 0.3-2 keV

[d] Derived from *XMM* pn data

[e] From Rasmussen et al. (2008)

[f] Upper limit: not detected in Chandra Source Catalogue

.

Appendix B

HCG infrared morphology

In this appendix we present the “true” color images (in blue, green and red are presented the IRAC 3.6, 4.5, and 8.0μm bands) of the 35 HCG groups, of our samples I and II. As we mentioned in Chapter 2, near-IR light of galaxies is dominated by the emission of old stellar populations. Conversely, hot new stars emit in the UV. This light is absorbed by the interstellar dust and re-emitted in the mid-IR wavelengths. Thus, with the appropriate selection of filters, we can see early-type galaxies as very blue objects, containing only old stars, while spiral galaxies been very bright in the red, since they contain large amounts of warm dust. Moreover, one can see other features, such as the red bridge, between members B and C of HCG 92, which is dust warmed due to excitation from the tidal interaction of these galaxies with the intragroup medium of their group.

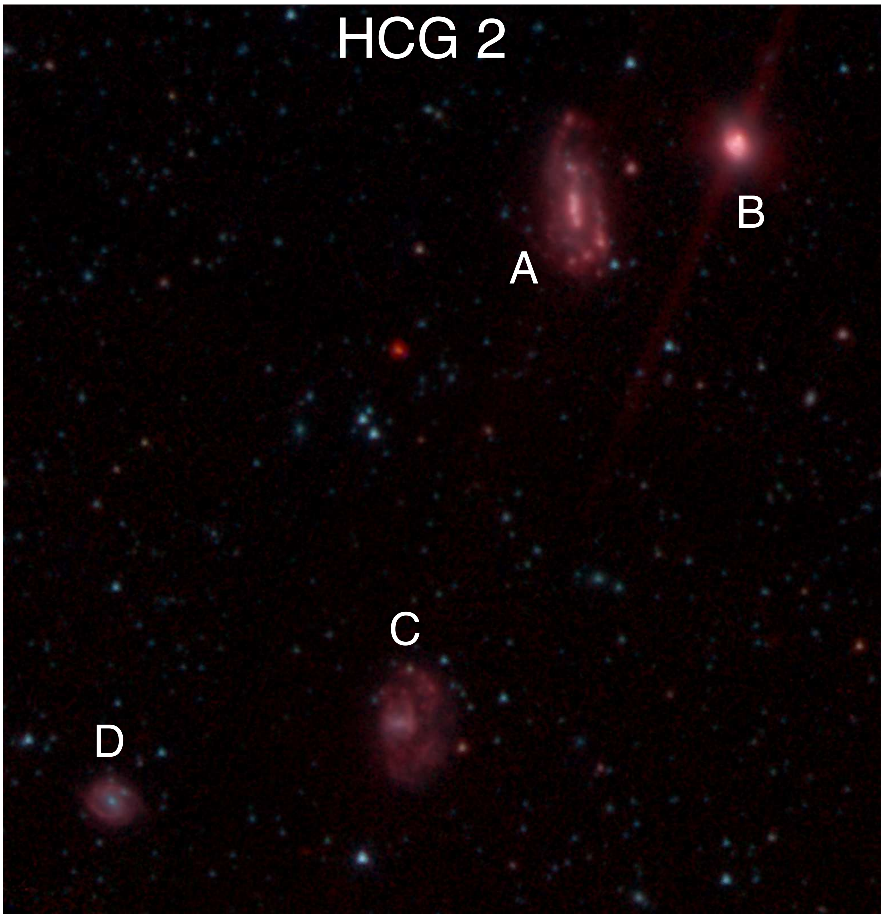

Figure B.1: IRAC true color image. Blue, green and red colors correspond to 3.6, 4.5 and 8.0μm bands, respectively.

group id	apparent members	outliers	Dynamical state
HCG 2	4	1	Young

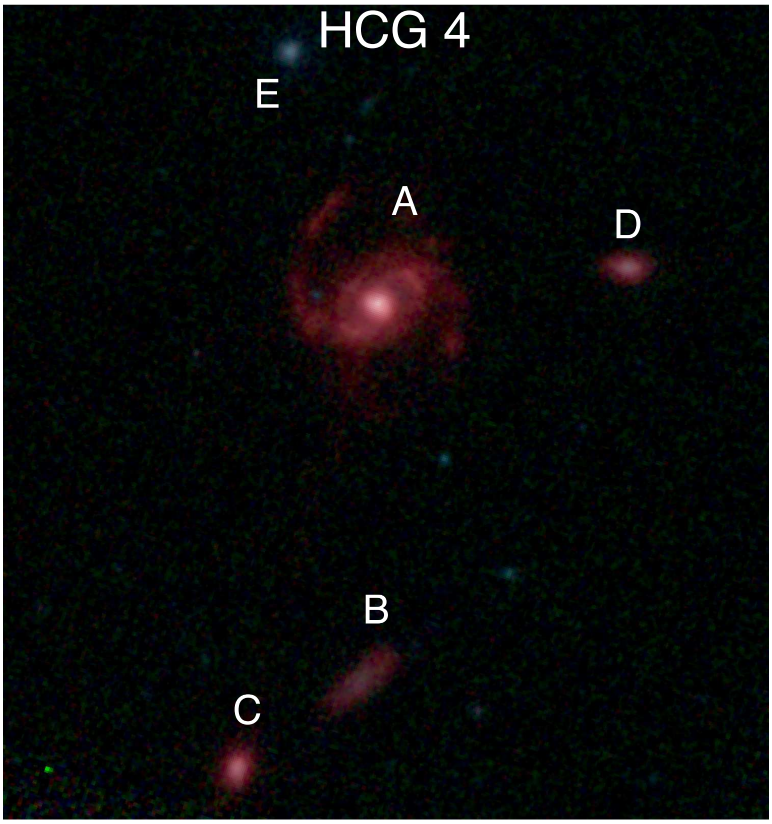

Figure B.2: IRAC true color image. Blue, green and red colors correspond to 3.6, 4.5 and 8.0μm bands, respectively.

group id	apparent members	outliers	Dynamical state
HCG 4	5	1	Old

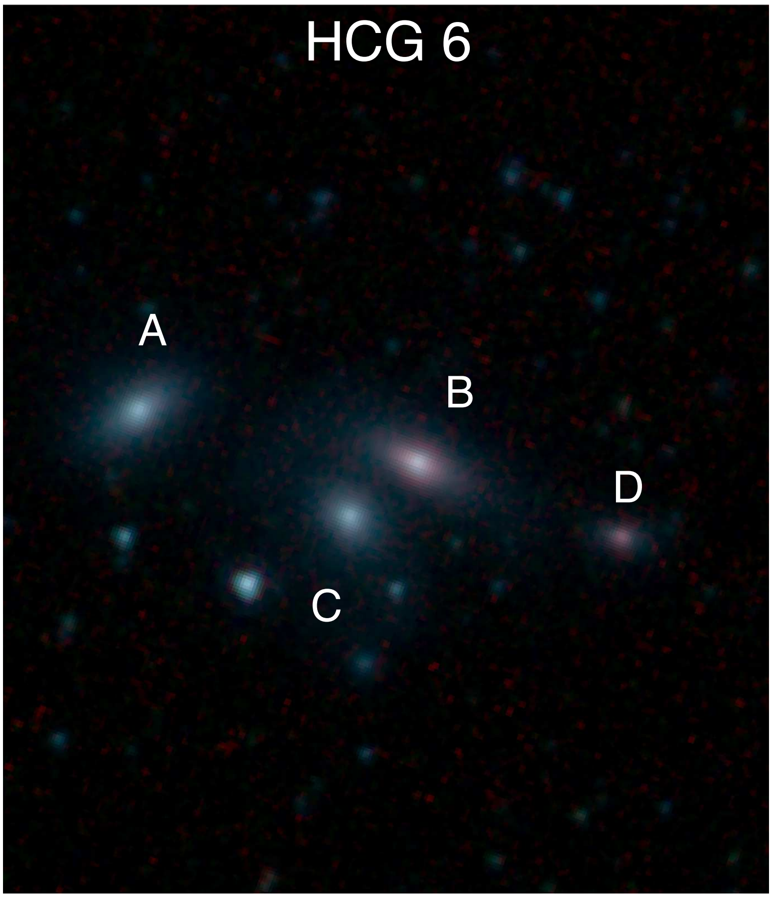

Figure B.3: IRAC true color image. Blue, green and red colors correspond to 3.6, 4.5 and 8.0μm bands, respectively.

group id	apparent members	outliers	Dynamical state
HCG 6	4	-	Old

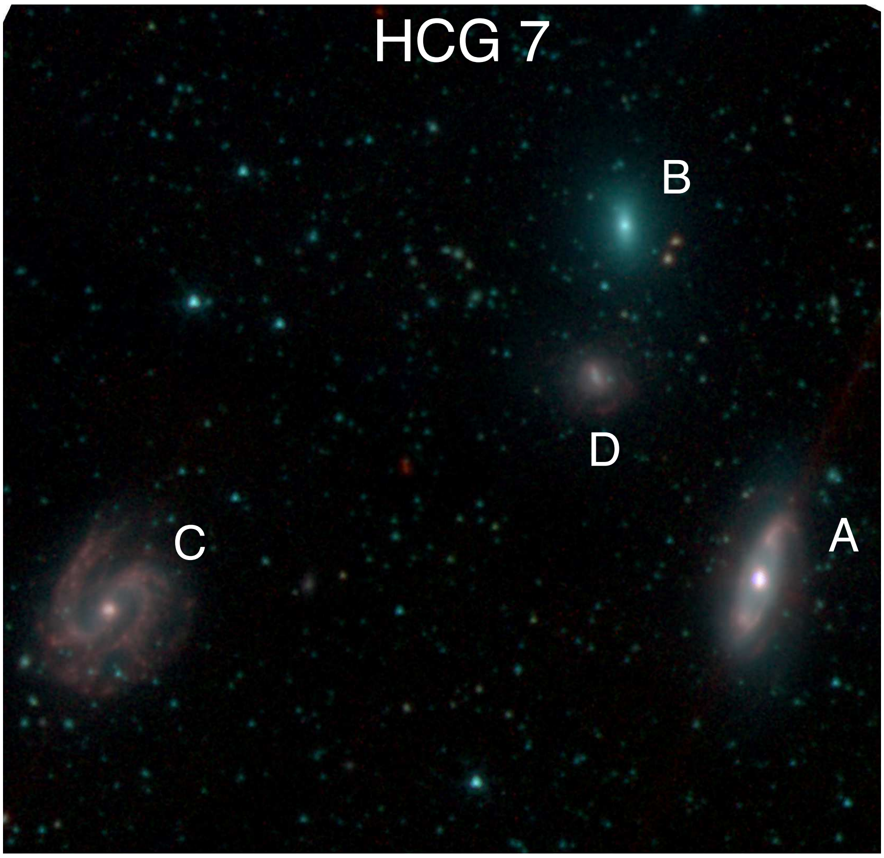

Figure B.4: IRAC true color image. Blue, green and red colors correspond to 3.6, 4.5 and 8.0μm bands, respectively.

group id	apparent members	outliers	Dynamical state
HCG 7	4	-	Young

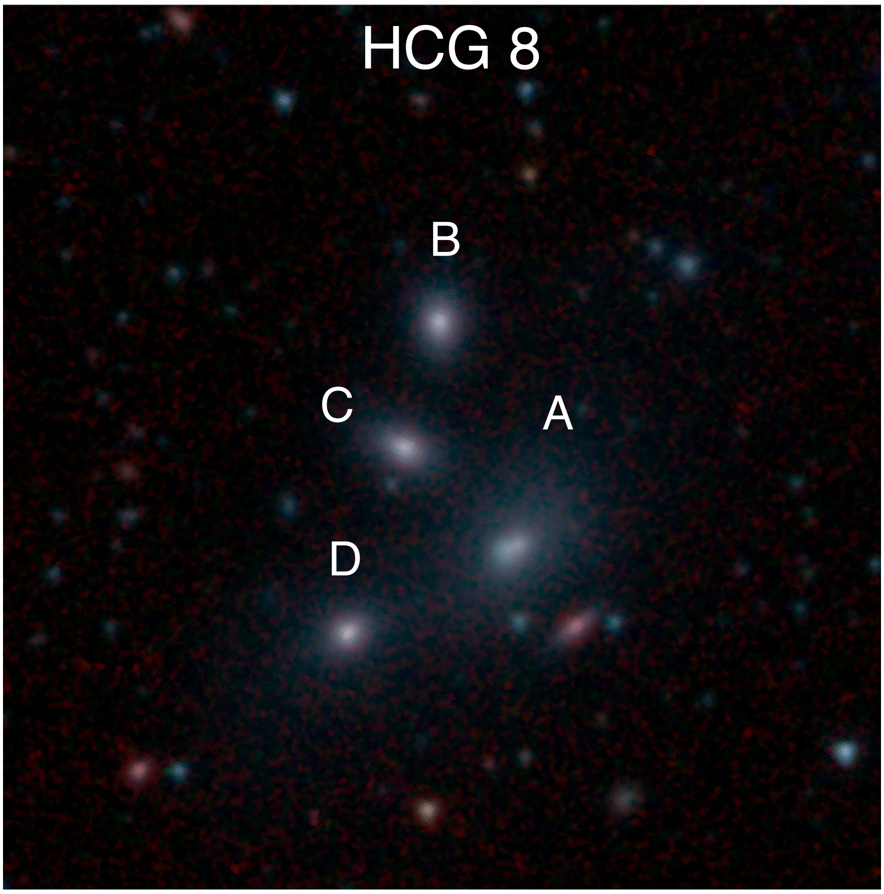

Figure B.5: IRAC true color image. Blue, green and red colors correspond to 3.6, 4.5 and 8.0μm bands, respectively.

group id	apparent members	outliers	Dynamical state
HCG 8	4	-	Old

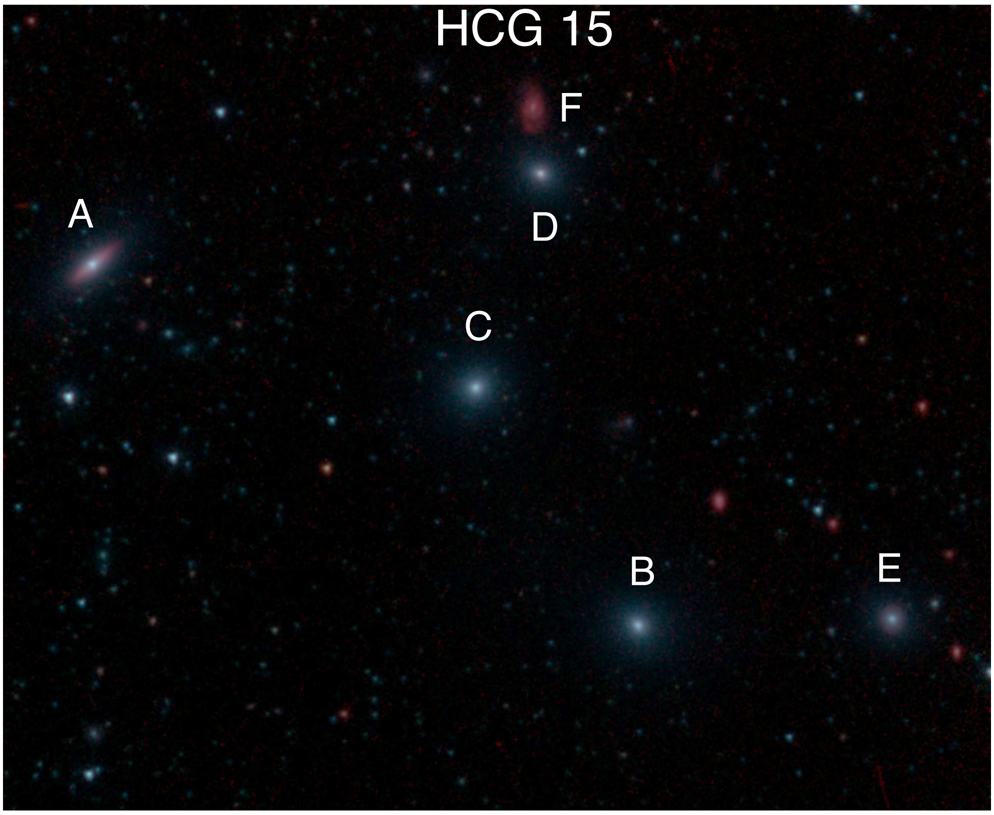

Figure B.6: IRAC true color image. Blue, green and red colors correspond to 3.6, 4.5 and 8.0μm bands, respectively.

group id	apparent members	outliers	Dynamical state
HCG 15	6	-	Old

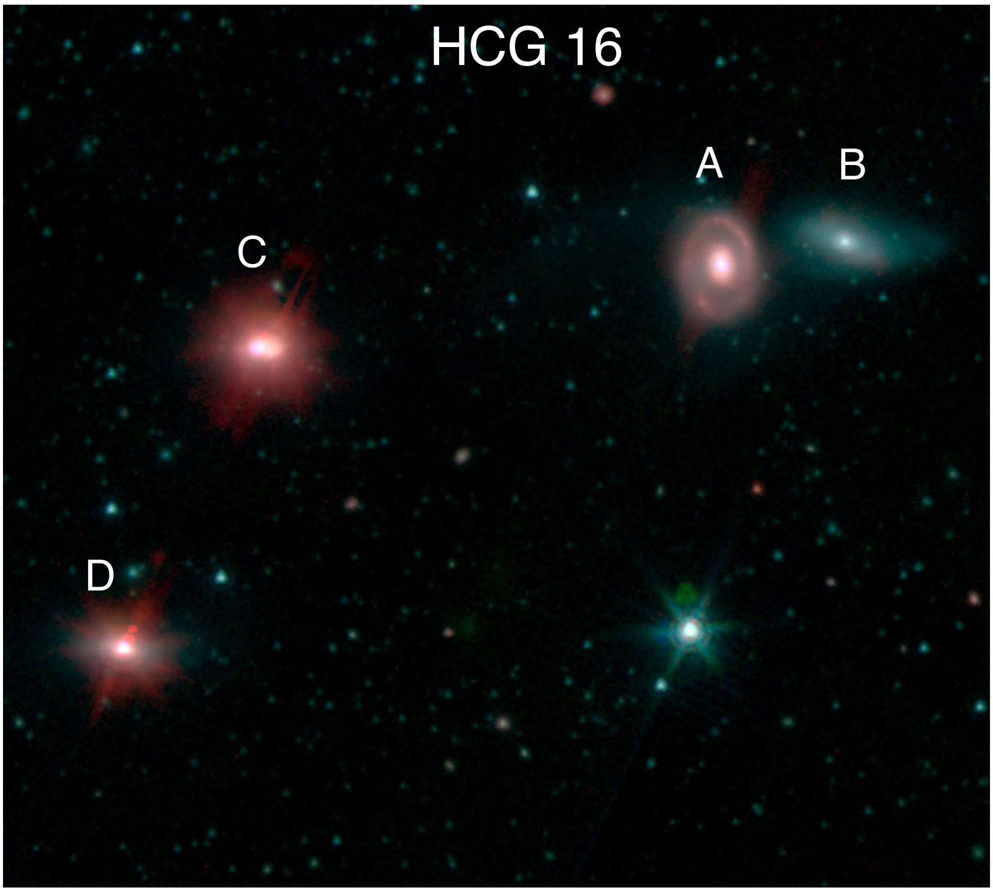

Figure B.7: IRAC true color image. Blue, green and red colors correspond to 3.6, 4.5 and 8.0μm bands, respectively.

group id	apparent members	outliers	Dynamical state
HCG 16	4	-	Young

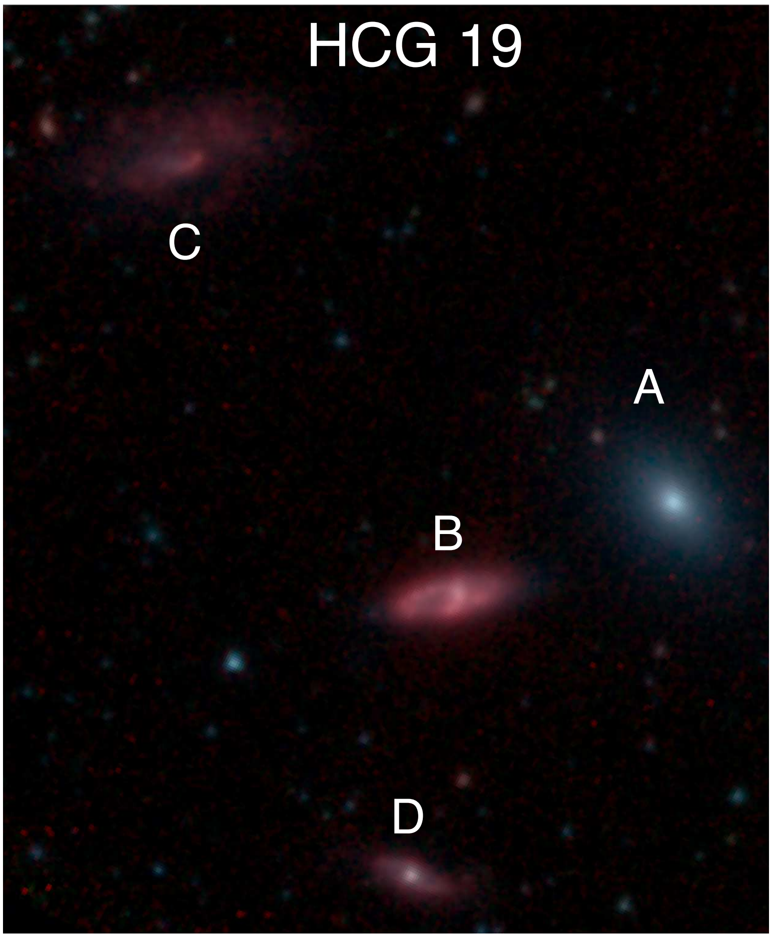

Figure B.8: IRAC true color image. Blue, green and red colors correspond to 3.6, 4.5 and 8.0μm bands, respectively.

group id	apparent members	outliers	Dynamical state
HCG 19	4	1	Old

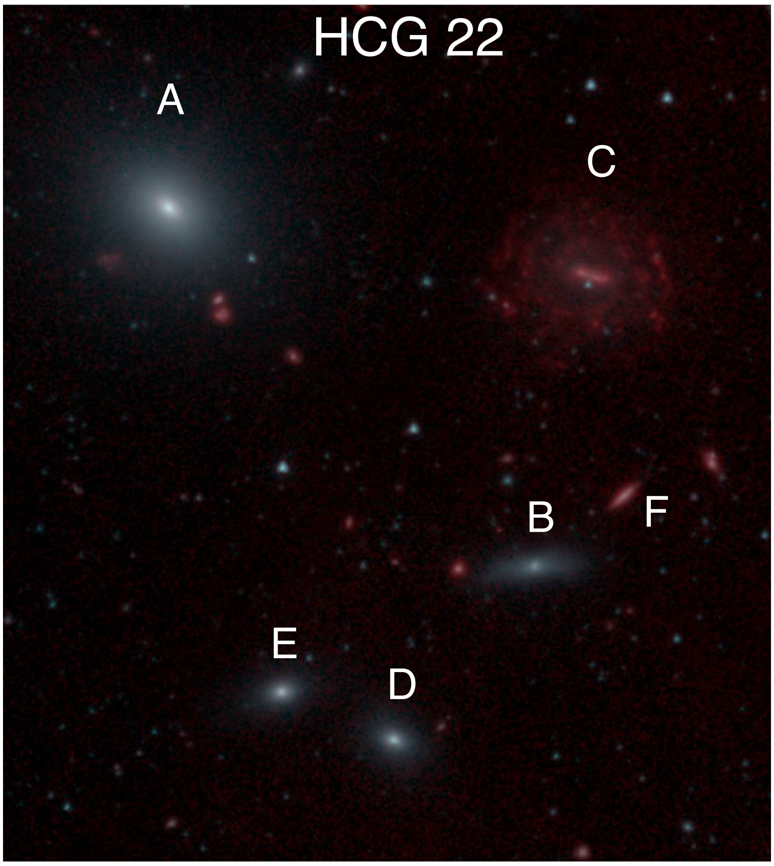

Figure B.9: IRAC true color image. Blue, green and red colors correspond to 3.6, 4.5 and 8.0μm bands, respectively.

group id	apparent members	outliers	Dynamical state
HCG 22	6	3	Old

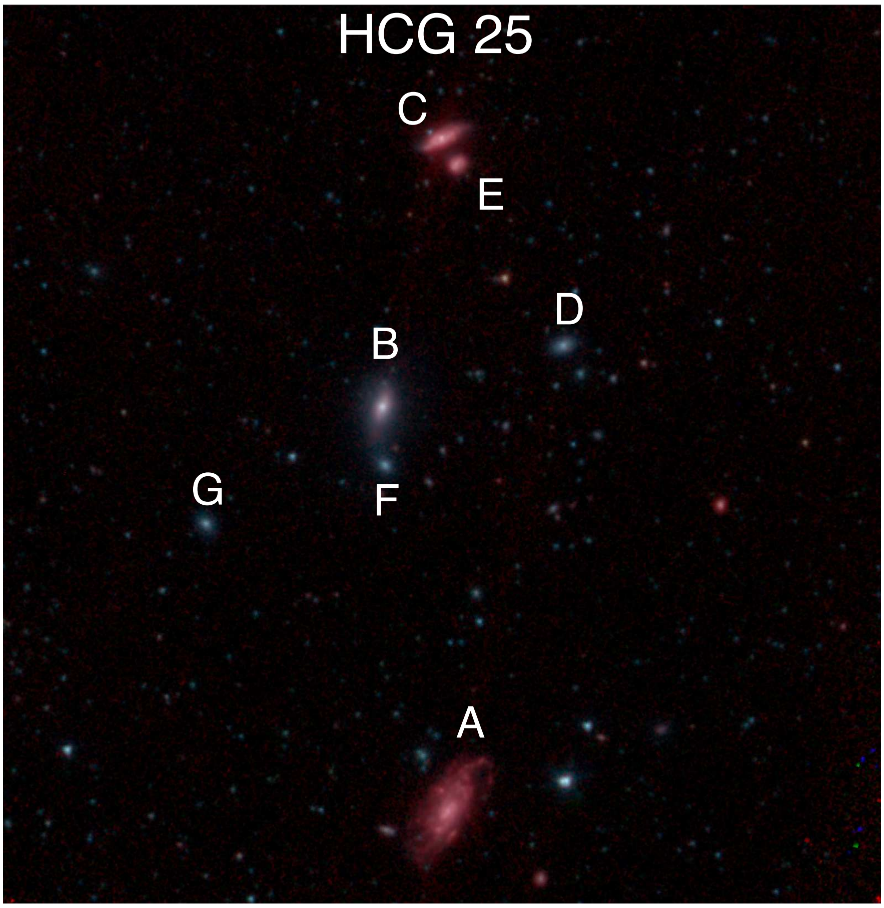

Figure B.10: IRAC true color image. Blue, green and red colors correspond to 3.6, 4.5 and 8.0μm bands, respectively.

group id	apparent members	outliers	Dynamical state
HCG 25	7	2	Old

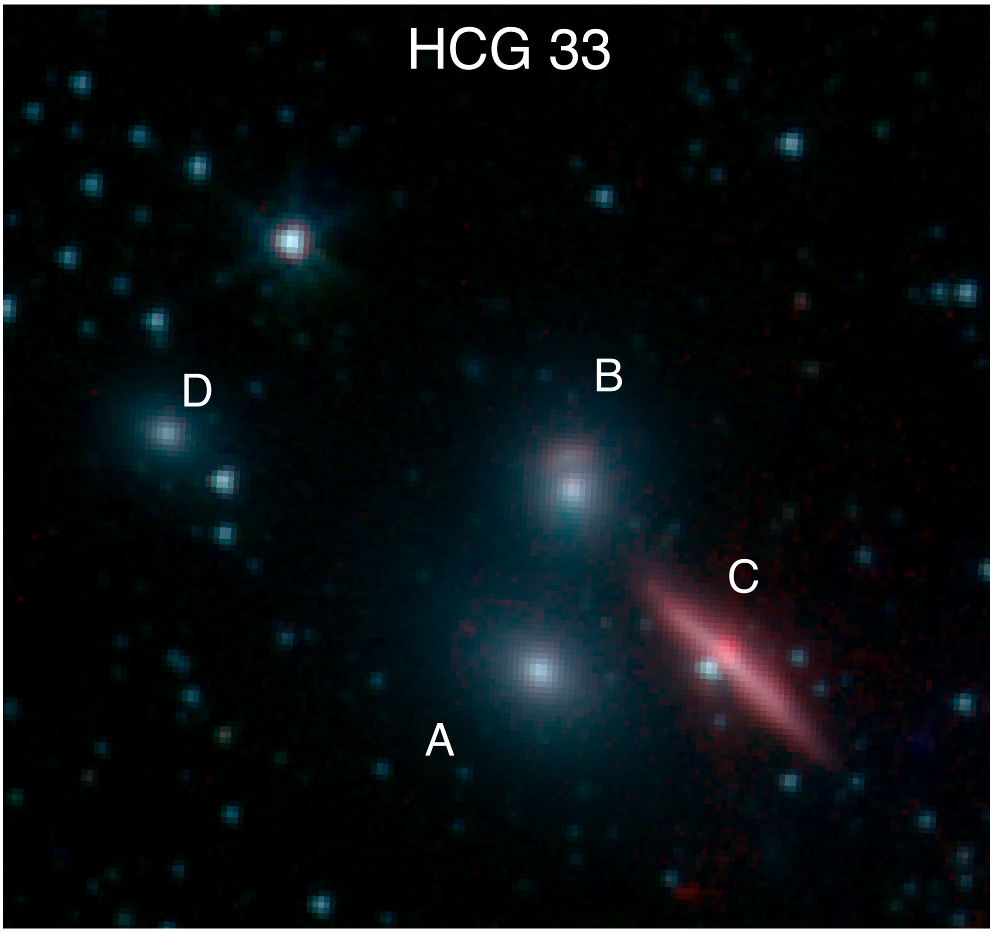

Figure B.11: IRAC true color image. Blue, green and red colors correspond to 3.6, 4.5 and 8.0μm bands, respectively.

group id	apparent members	outliers	Dynamical state
HCG 33	4	-	Old

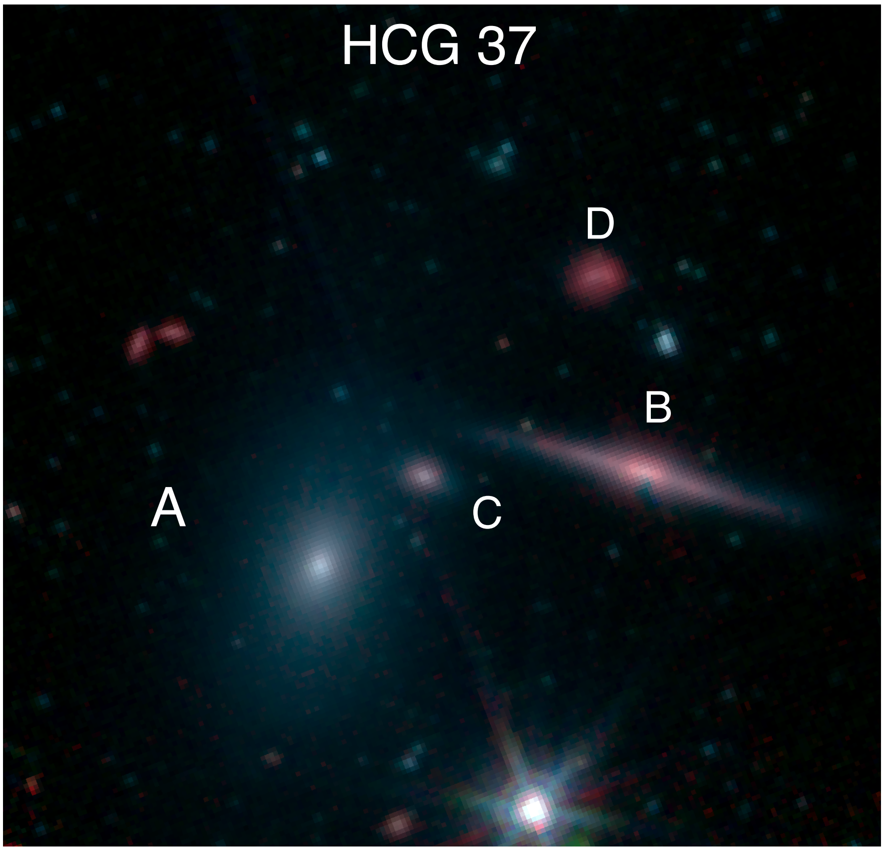

Figure B.12: IRAC true color image. Blue, green and red colors correspond to 3.6, 4.5 and 8.0μm bands, respectively.

group id	apparent members	outliers	Dynamical state
HCG 37	4	-	Old

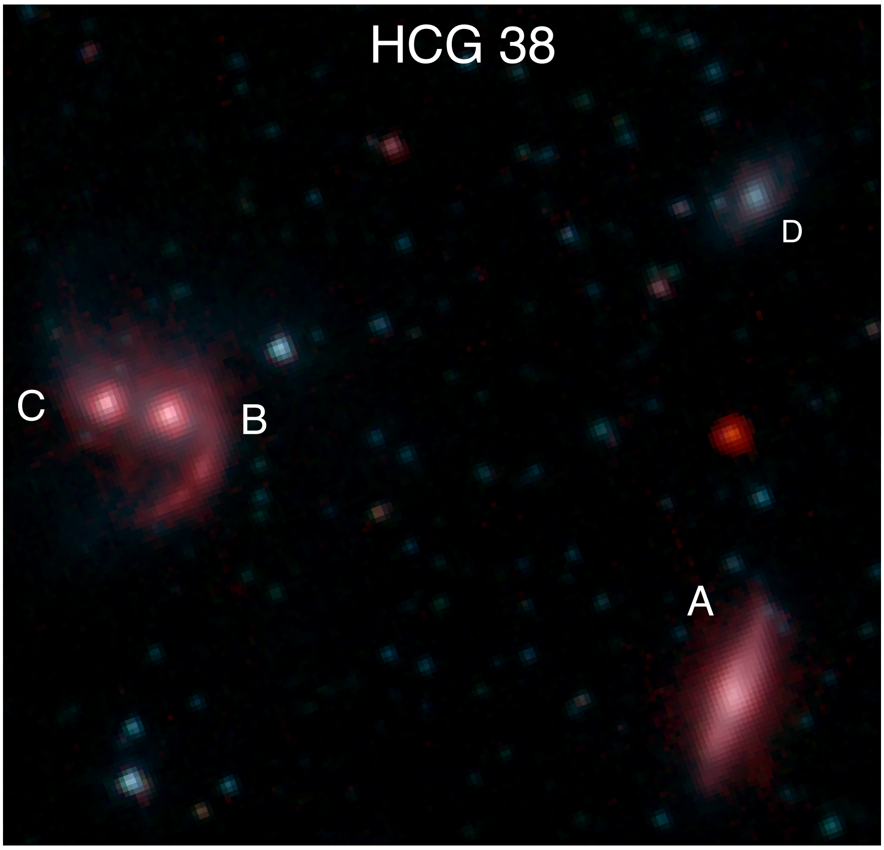

Figure B.13: IRAC true color image. Blue, green and red colors correspond to 3.6, 4.5 and 8.0μm bands, respectively.

group id	apparent members	outliers	Dynamical state
HCG 38	4	1	Young

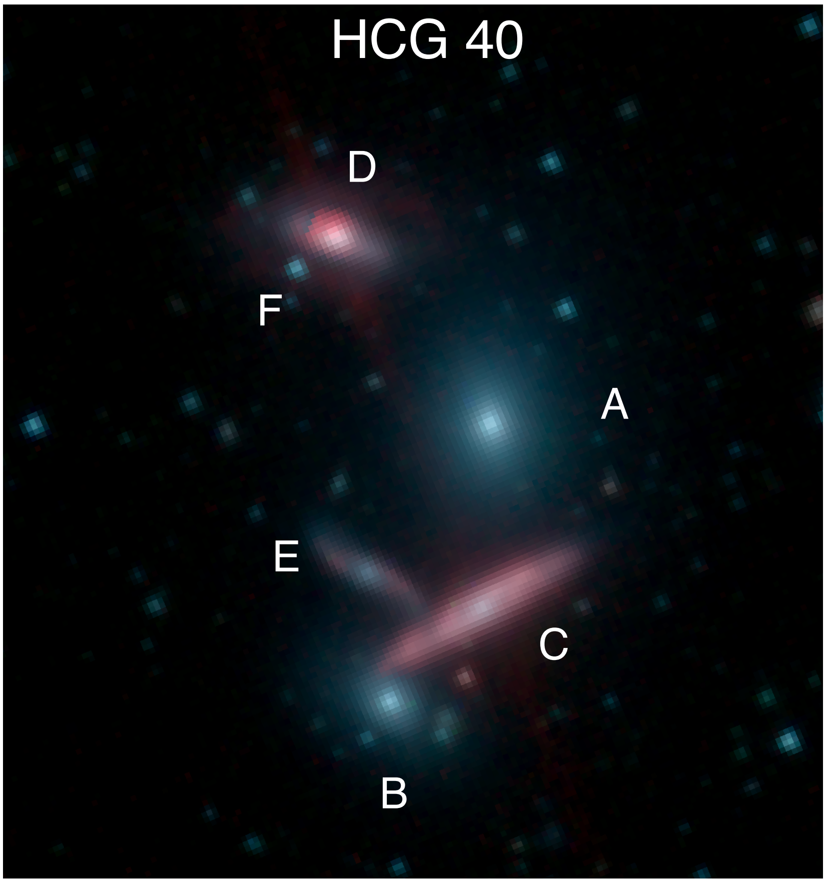

Figure B.14: IRAC true color image. Blue, green and red colors correspond to 3.6, 4.5 and 8.0μm bands, respectively.

group id	apparent members	outliers	Dynamical state
HCG 40	5	-	Old

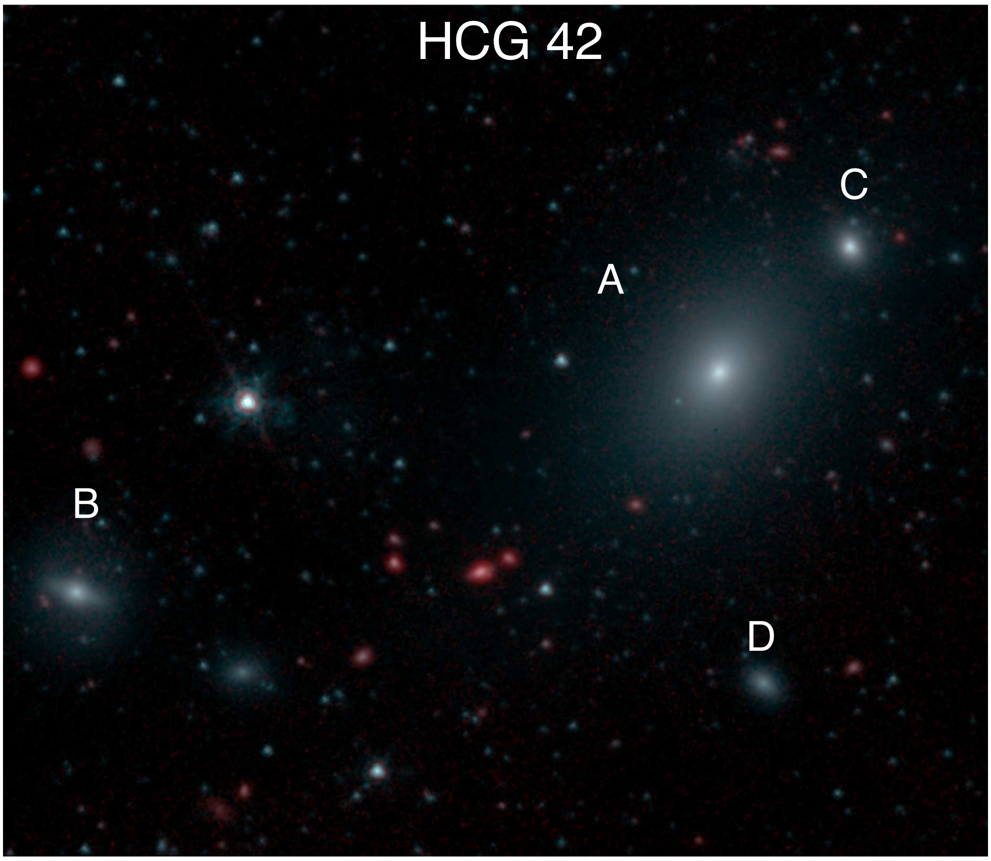

Figure B.15: IRAC true color image. Blue, green and red colors correspond to 3.6, 4.5 and 8.0μm bands, respectively.

group id	apparent members	outliers	Dynamical state
HCG 42	4	-	Old

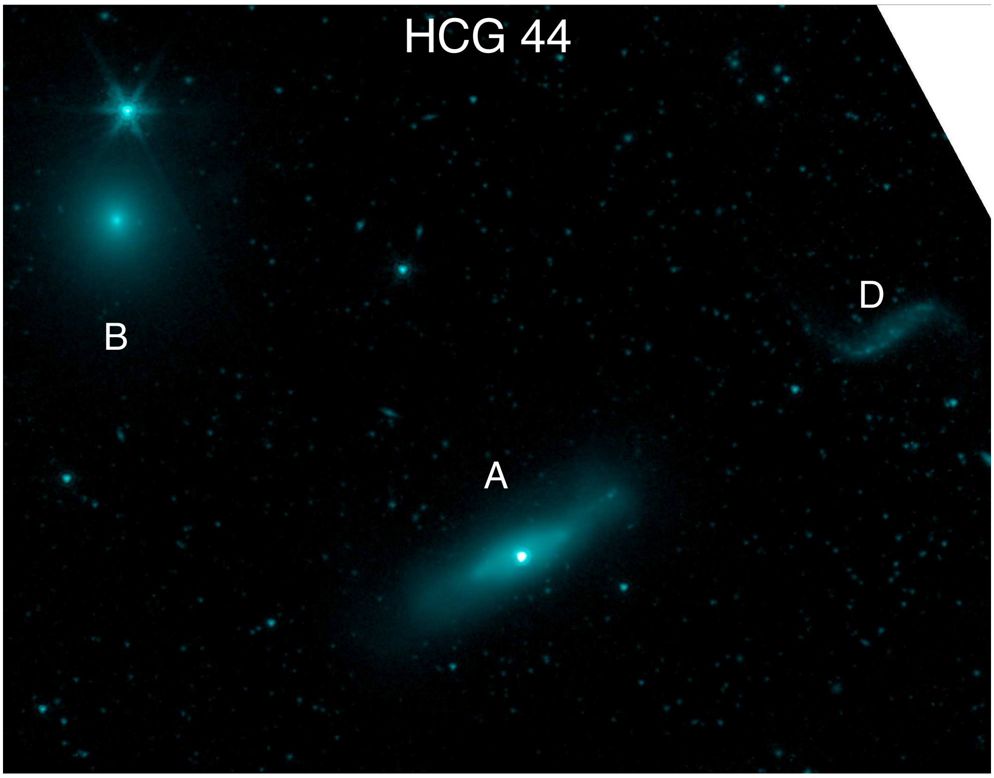

Figure B.16: IRAC true color image. Blue, green and red colors correspond to 3.6, 4.5 and 8.0μm bands, respectively.

group id	apparent members	outliers	Dynamical state
HCG 44	4	-	Young

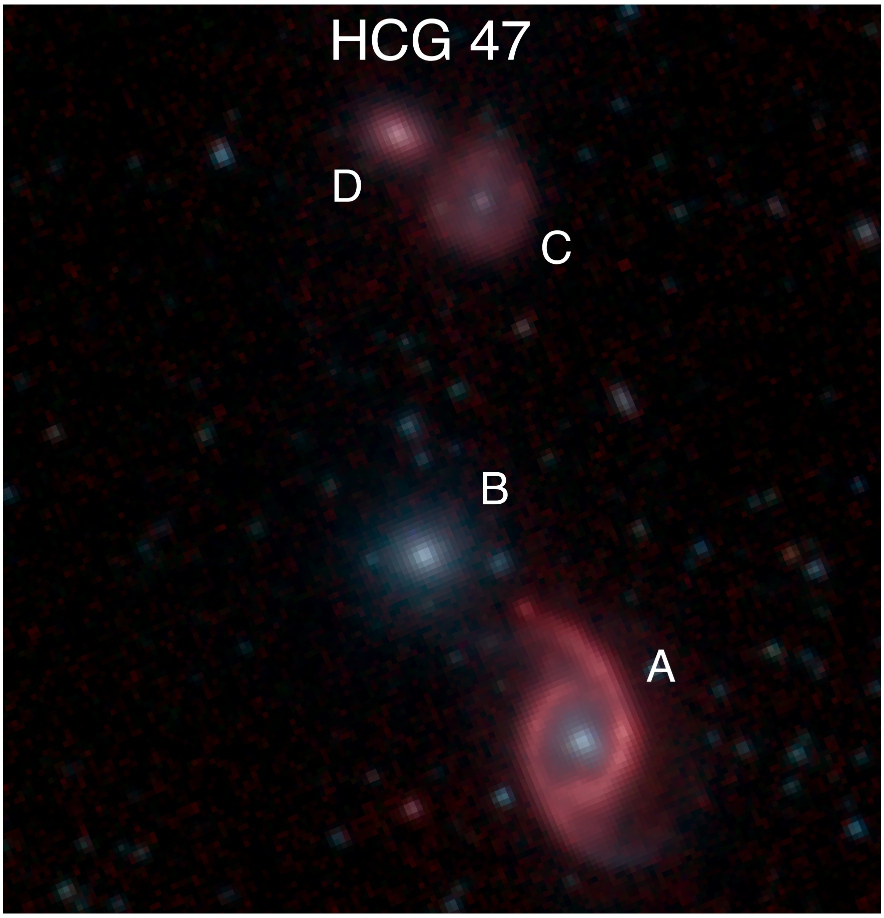

Figure B.17: IRAC true color image. Blue, green and red colors correspond to 3.6, 4.5 and 8.0μm bands, respectively.

group id	apparent members	outliers	Dynamical state
HCG 47	4	-	Young

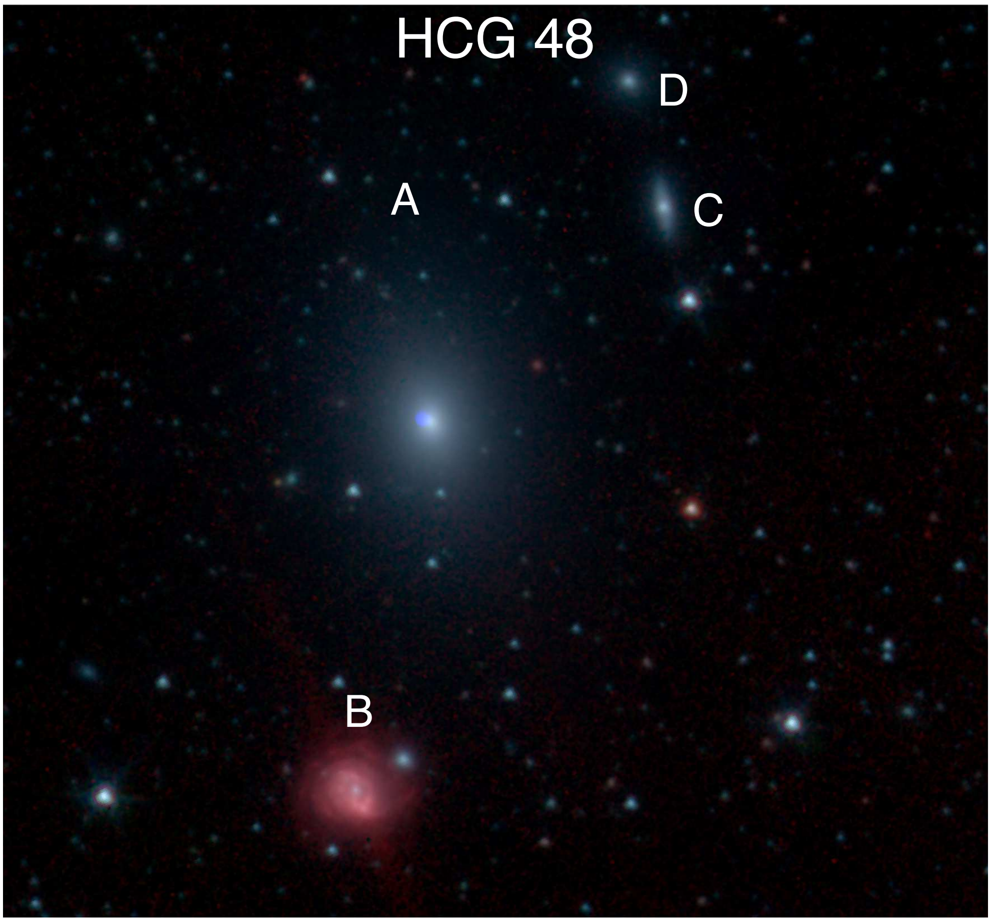

Figure B.18: IRAC true color image. Blue, green and red colors correspond to 3.6, 4.5 and 8.0μm bands, respectively.

group id	apparent members	outliers	Dynamical state
HCG 48	4	-	Old

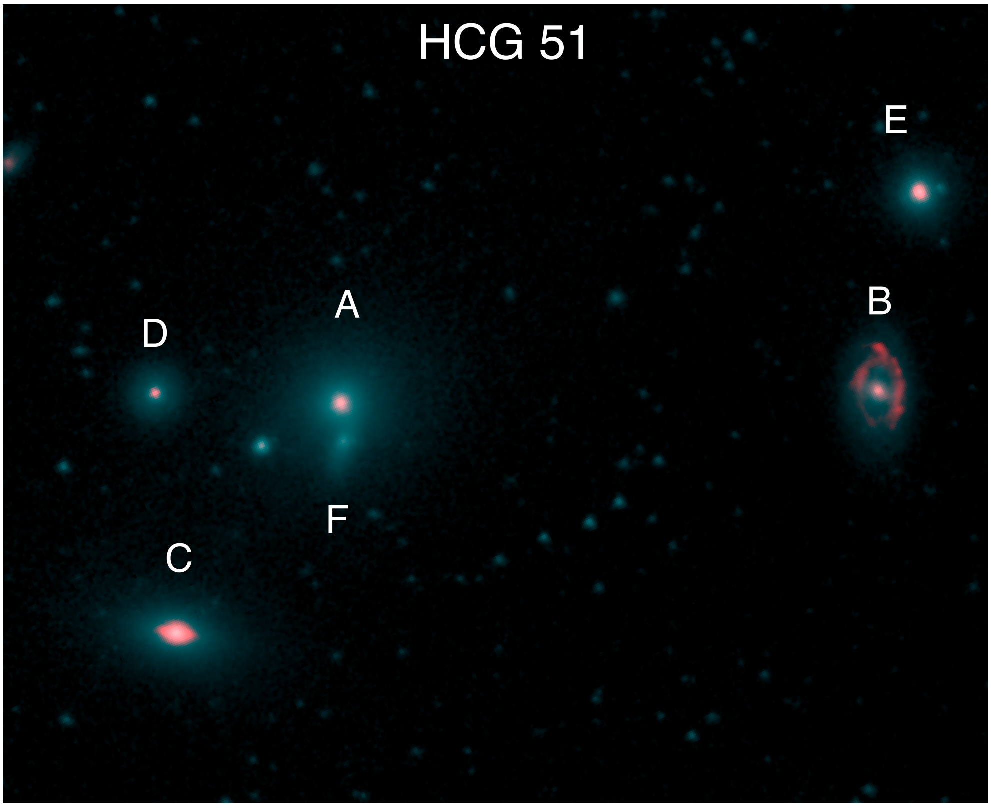

Figure B.19: IRAC true color image. Blue, green and red colors correspond to 3.6, 4.5 and 8.0μm bands, respectively.

group id	apparent members	outliers	Dynamical state
HCG 51	6	-	Old

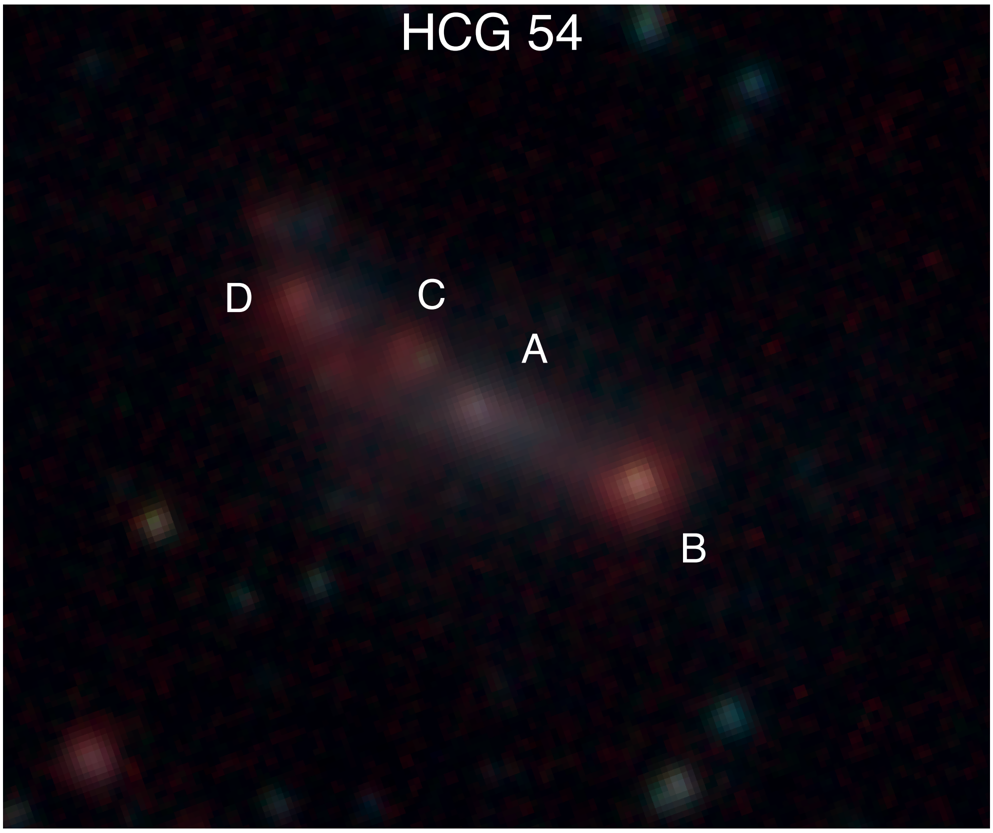

Figure B.20: IRAC true color image. Blue, green and red colors correspond to 3.6, 4.5 and 8.0μm bands, respectively.

group id	apparent members	outliers	Dynamical state
HCG 54	4	-	Young

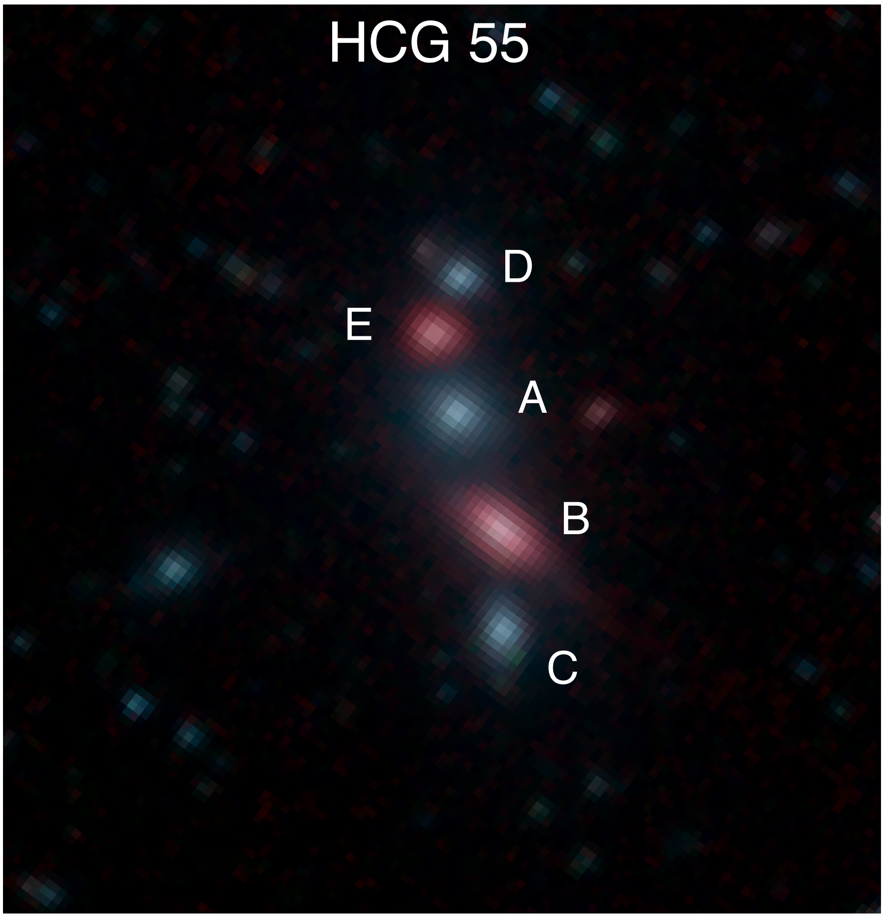

Figure B.21: IRAC true color image. Blue, green and red colors correspond to 3.6, 4.5 and 8.0μm bands, respectively.

group id	apparent members	outliers	Dynamical state
HCG 55	5	-	Old

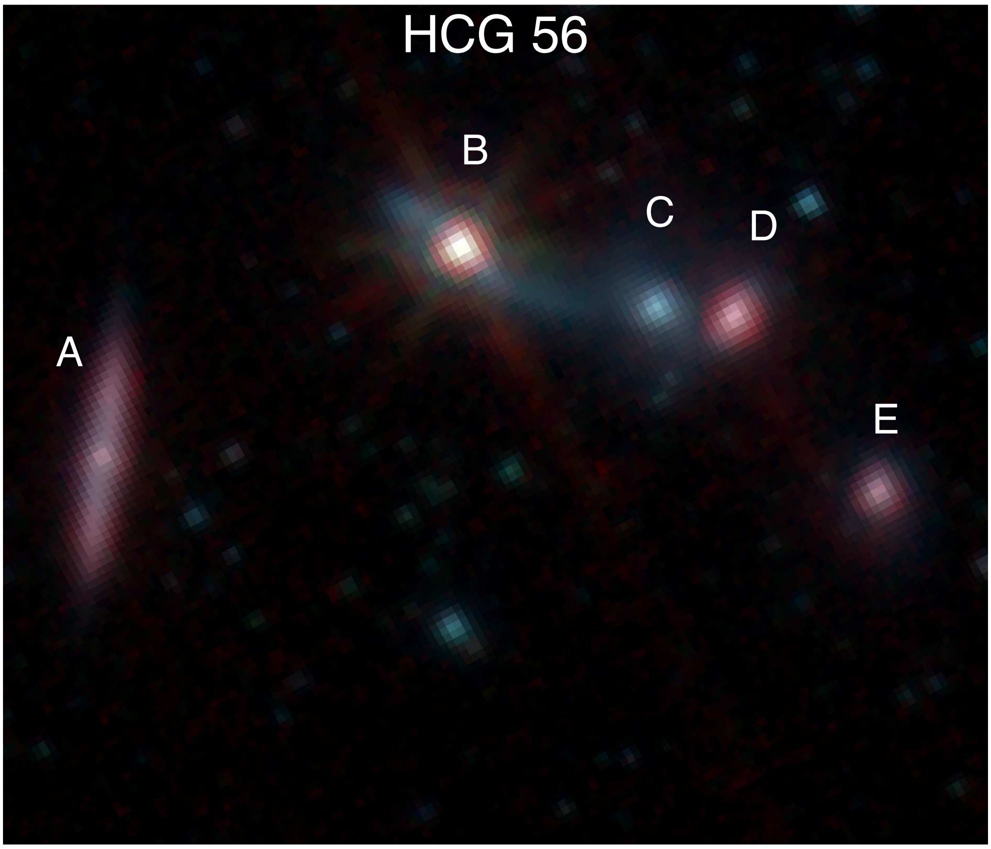

Figure B.22: IRAC true color image. Blue, green and red colors correspond to 3.6, 4.5 and 8.0μm bands, respectively.

group id	apparent members	outliers	Dynamical state
HCG 56	5	-	Old

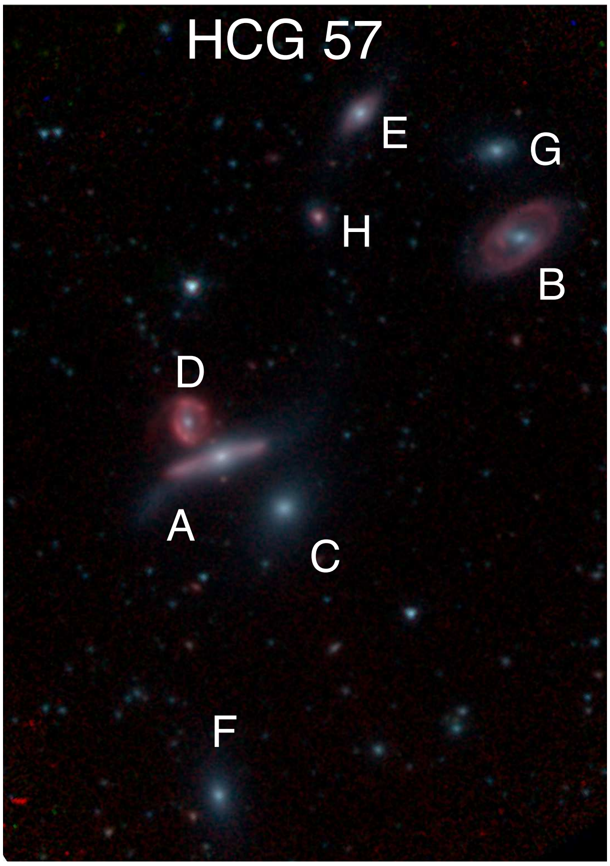

Figure B.23: IRAC true color image. Blue, green and red colors correspond to 3.6, 4.5 and 8.0μm bands, respectively.

group id	apparent members	outliers	Dynamical state
HCG 57	8	-	Old

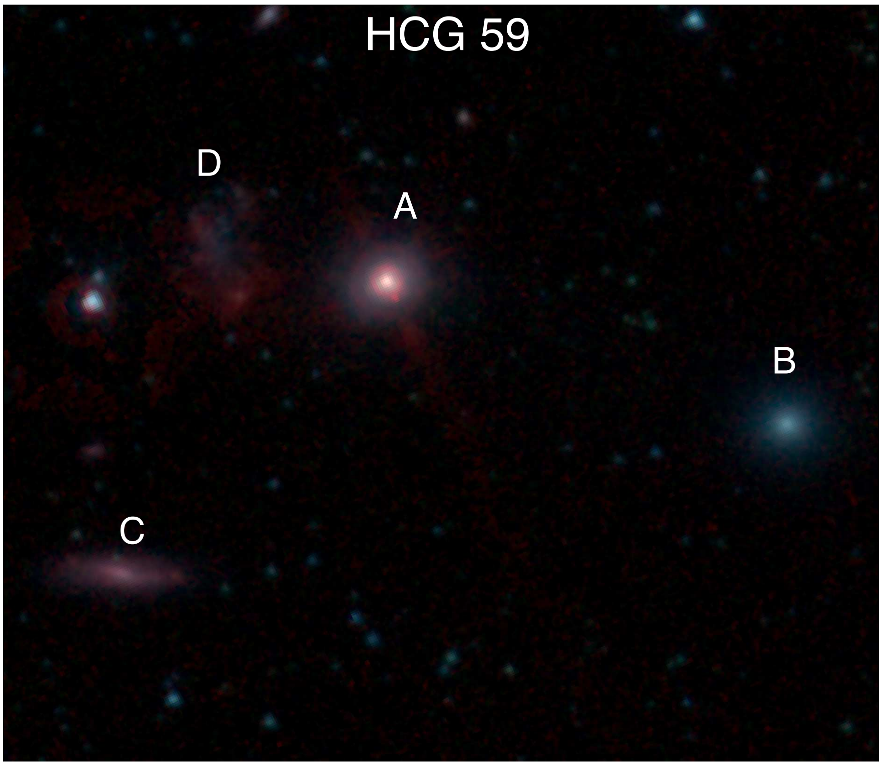

Figure B.24: IRAC true color image. Blue, green and red colors correspond to 3.6, 4.5 and 8.0μm bands, respectively.

group id	apparent members	outliers	Dynamical state
HCG 59	4	-	Young

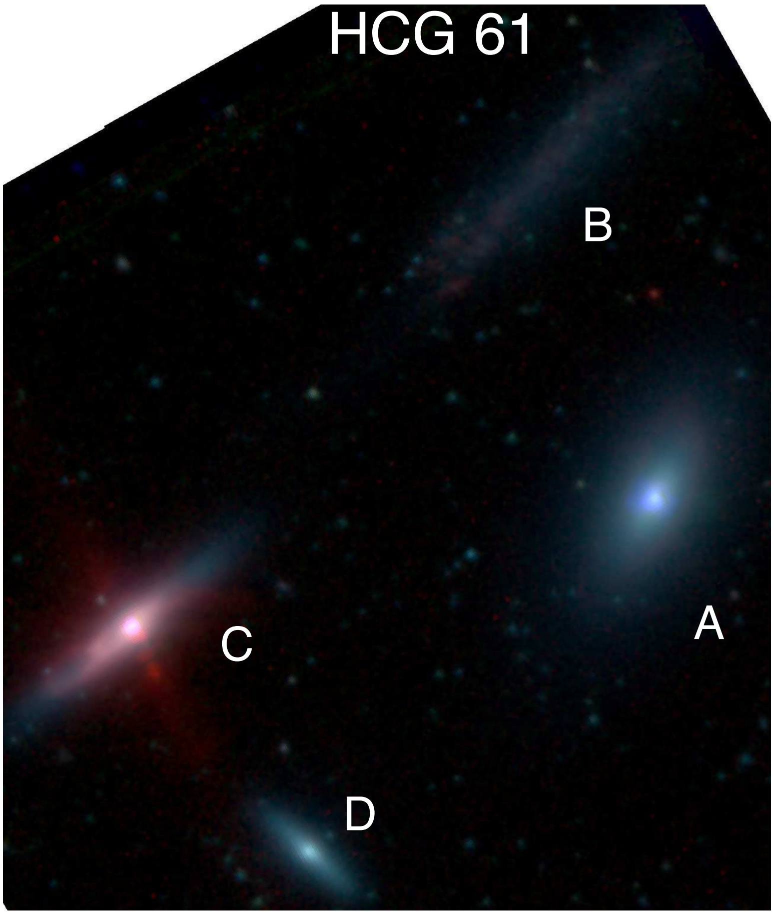

Figure B.25: IRAC true color image. Blue, green and red colors correspond to 3.6, 4.5 and 8.0μm bands, respectively.

group id	apparent members	outliers	Dynamical state
HCG 61	4	1	Old

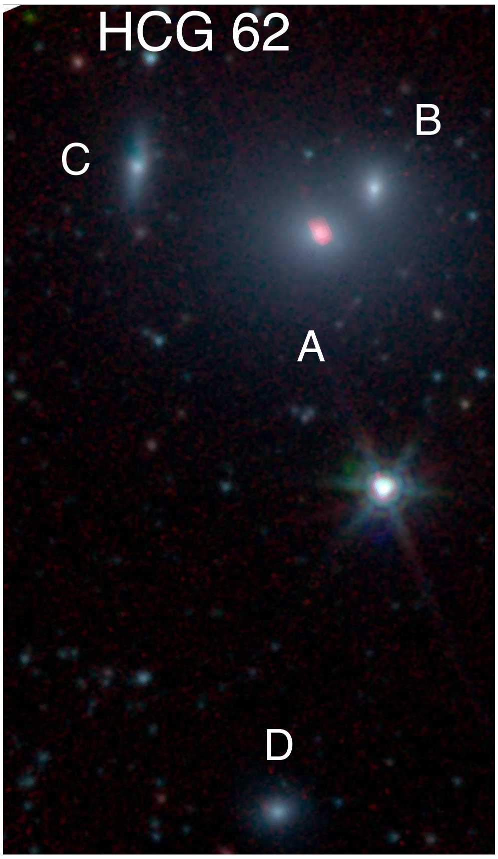

Figure B.26: IRAC true color image. Blue, green and red colors correspond to 3.6, 4.5 and 8.0μm bands, respectively.

group id	apparent members	outliers	Dynamical state
HCG 62	4	-	Old

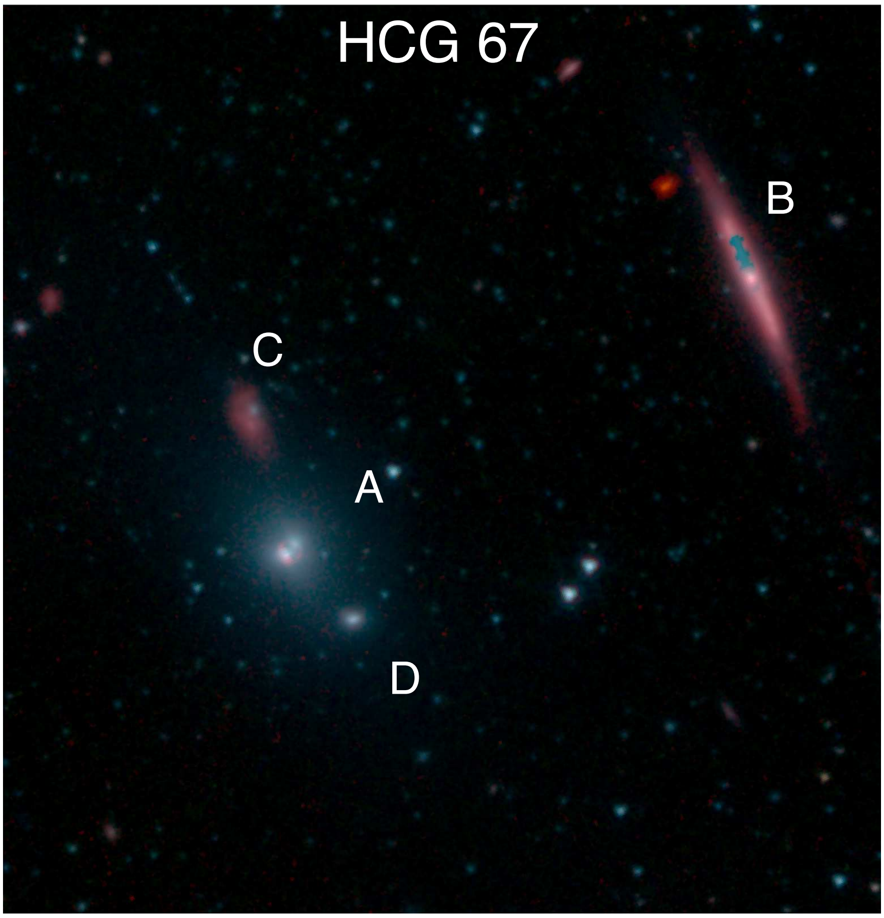

Figure B.27: IRAC true color image. Blue, green and red colors correspond to 3.6, 4.5 and 8.0μm bands, respectively.

group id	apparent members	outliers	Dynamical state
HCG 67	4	-	Old

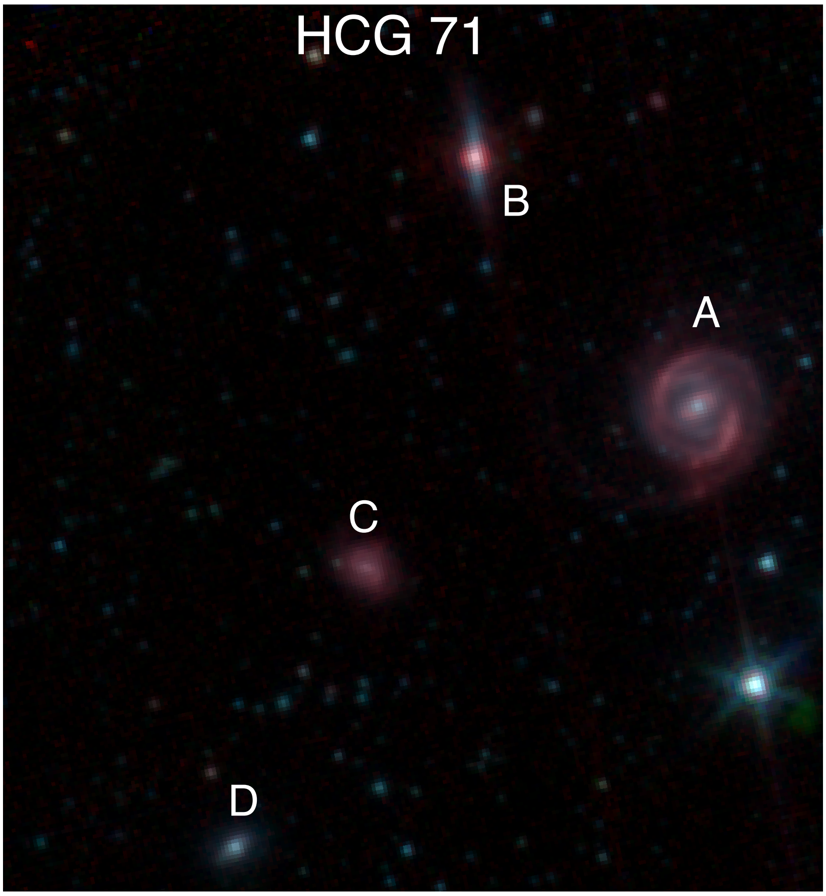

Figure B.28: IRAC true color image. Blue, green and red colors correspond to 3.6, 4.5 and 8.0μm bands, respectively.

group id	apparent members	outliers	Dynamical state
HCG 71	4	1	Old/Young

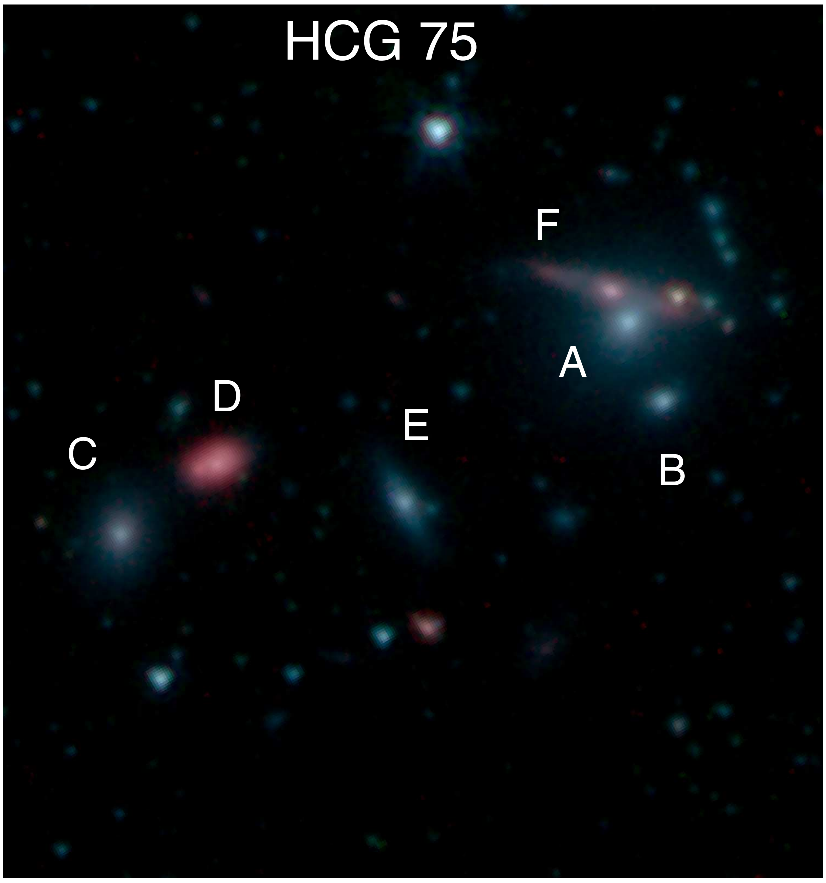

Figure B.29: IRAC true color image. Blue, green and red colors correspond to 3.6, 4.5 and 8.0μm bands, respectively.

group id	apparent members	outliers	Dynamical state
HCG 75	7	-	Old

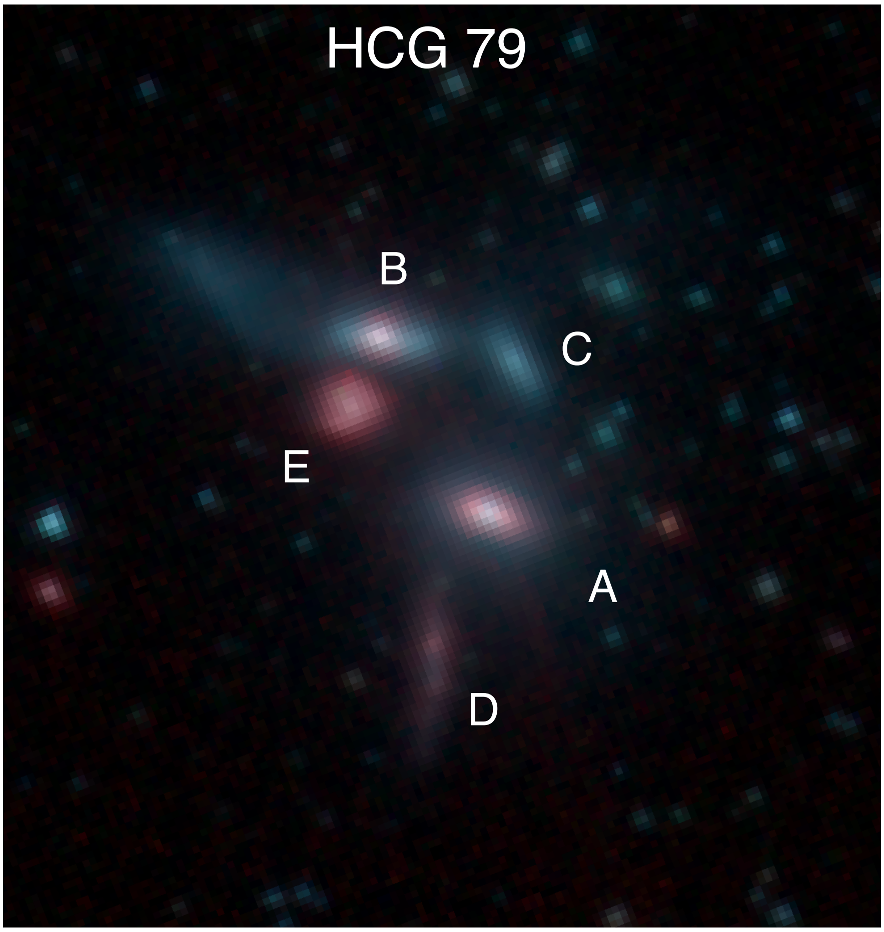

Figure B.30: IRAC true color image. Blue, green and red colors correspond to 3.6, 4.5 and 8.0μm bands, respectively.

group id	apparent members	outliers	Dynamical state
HCG 79	5	1	Old

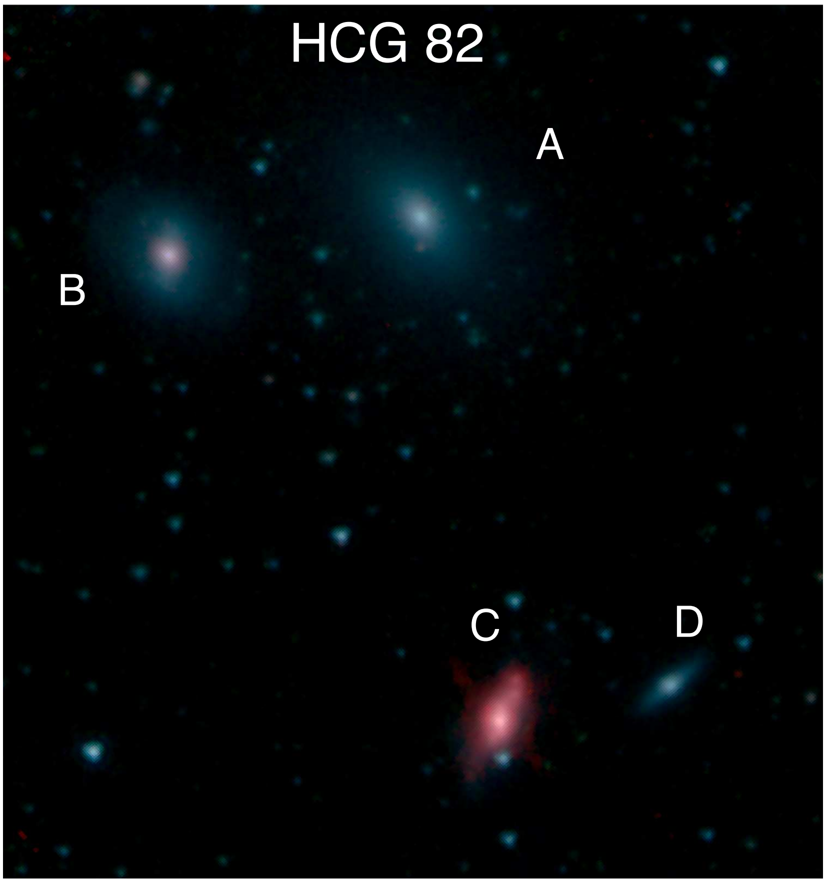

Figure B.31: IRAC true color image. Blue, green and red colors correspond to 3.6, 4.5 and 8.0μm bands, respectively.

group id	apparent members	outliers	Dynamical state
HCG 82	4	-	Old

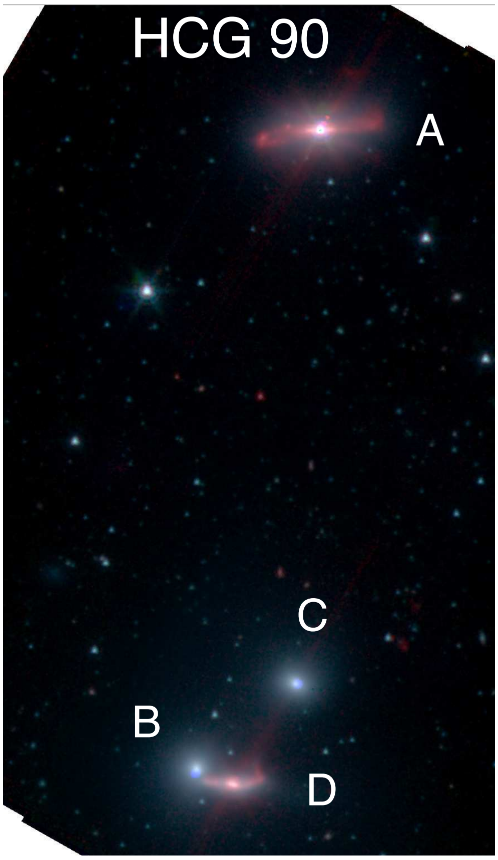

Figure B.32: IRAC true color image. Blue, green and red colors correspond to 3.6, 4.5 and 8.0μm bands, respectively.

group id	apparent members	outliers	Dynamical state
HCG 90	4	-	Old

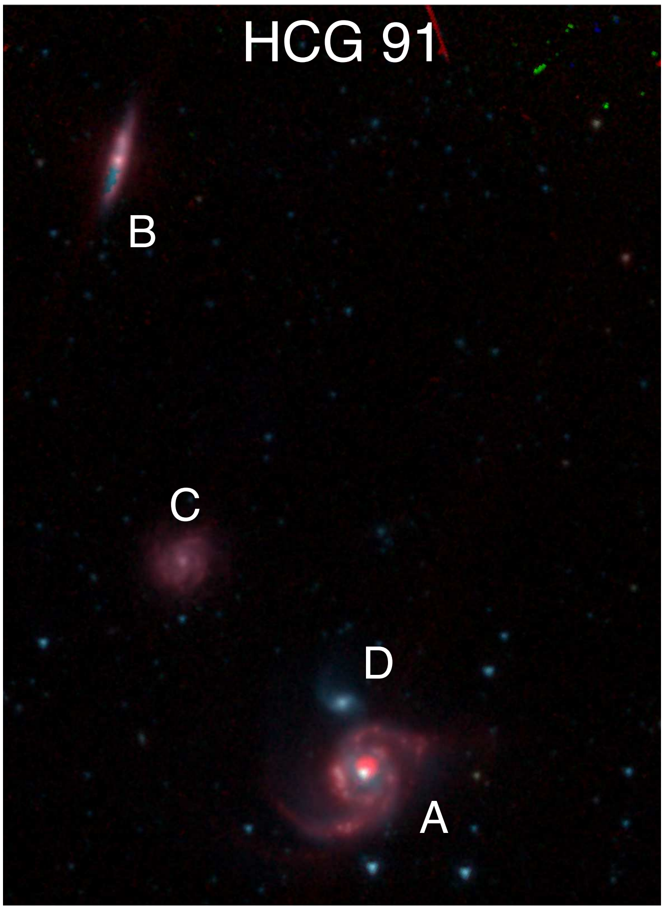

Figure B.33: IRAC true color image. Blue, green and red colors correspond to 3.6, 4.5 and 8.0μm bands, respectively.

group id	apparent members	outliers	Dynamical state
HCG 91	4	-	Young

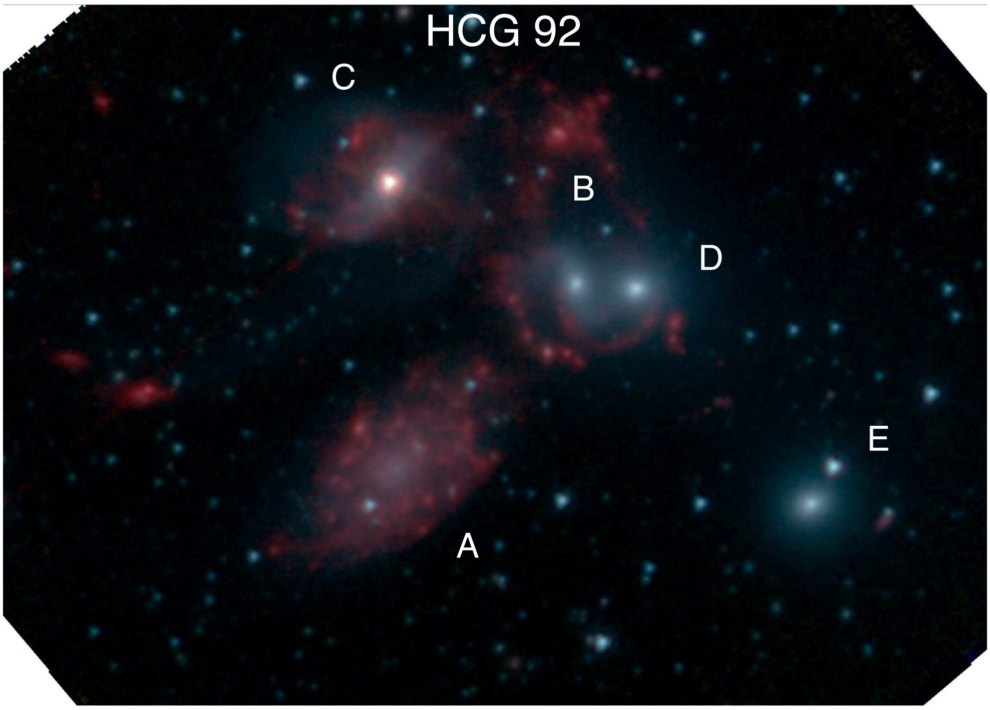

Figure B.34: IRAC true color image. Blue, green and red colors correspond to 3.6, 4.5 and 8.0μm bands, respectively.

group id	apparent members	outliers	Dynamical state
HCG 92	5	1	Old

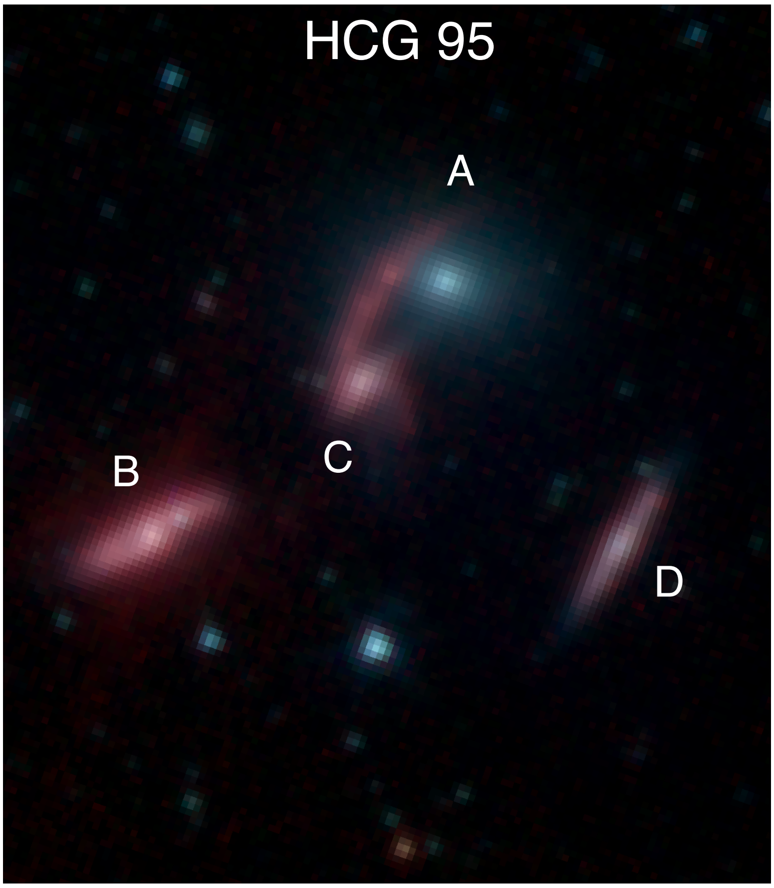

Figure B.35: IRAC true color image. Blue, green and red colors correspond to 3.6, 4.5 and 8.0μm bands, respectively.

group id	apparent members	outliers	Dynamical state
HCG 95	4	1	Old

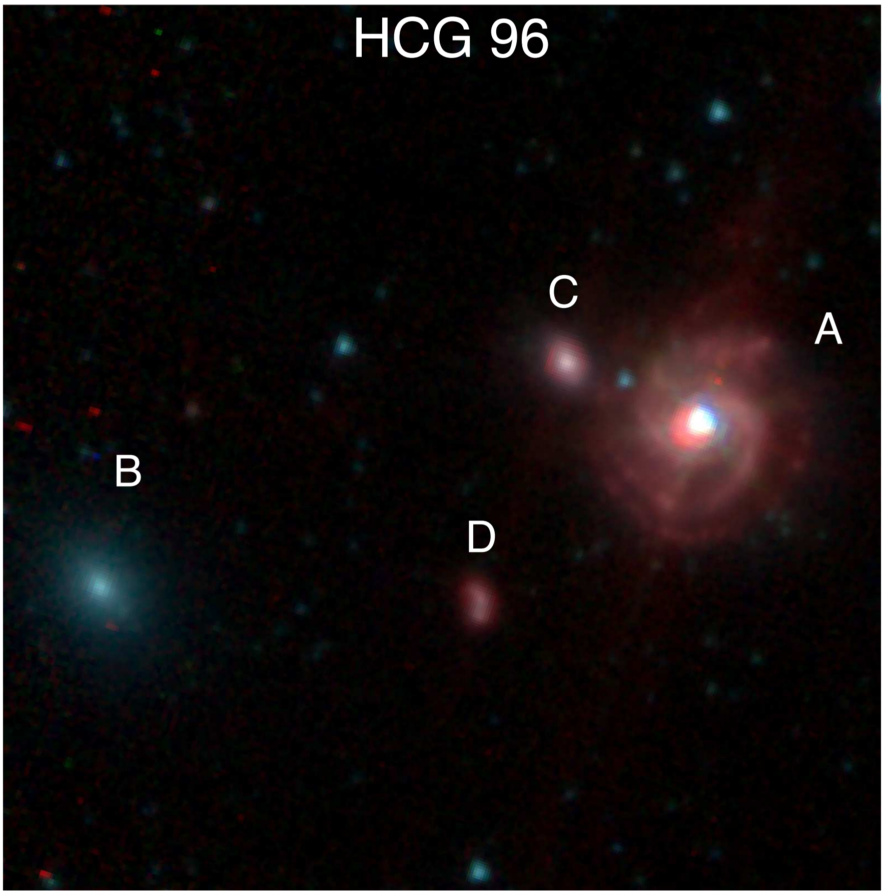

Figure B.36: IRAC true color image. Blue, green and red colors correspond to 3.6, 4.5 and 8.0μm bands, respectively.

group id	apparent members	outliers	Dynamical state
HCG 96	4	-	Young

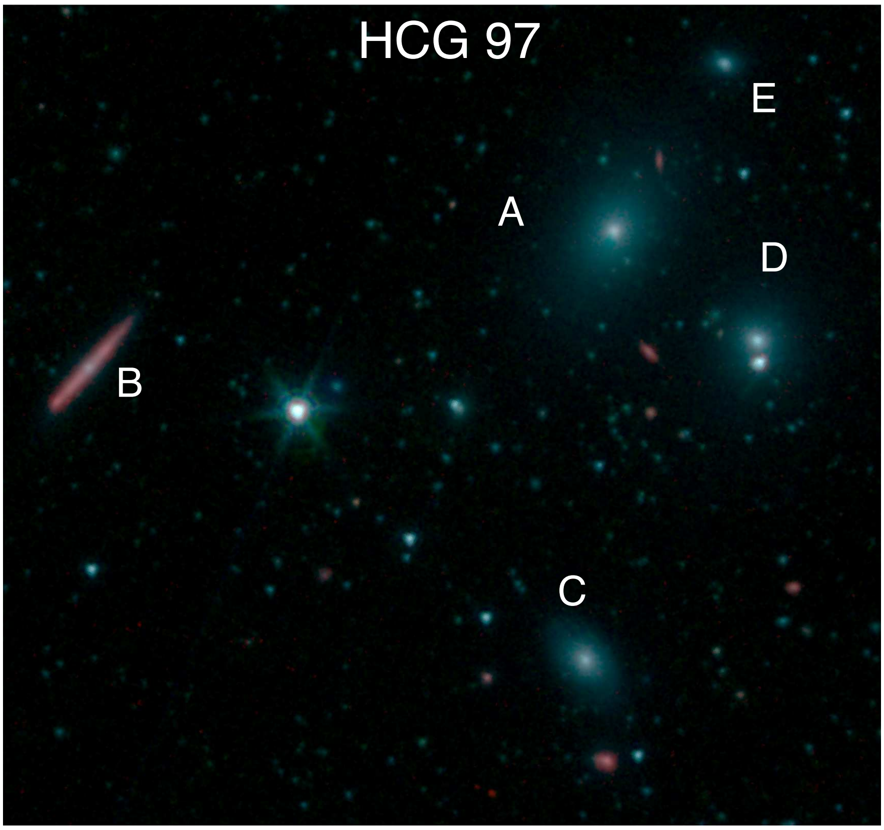

Figure B.37: IRAC true color image. Blue, green and red colors correspond to 3.6, 4.5 and 8.0μm bands, respectively.

group id	apparent members	outliers	Dynamical state
HCG 97	5	-	Old

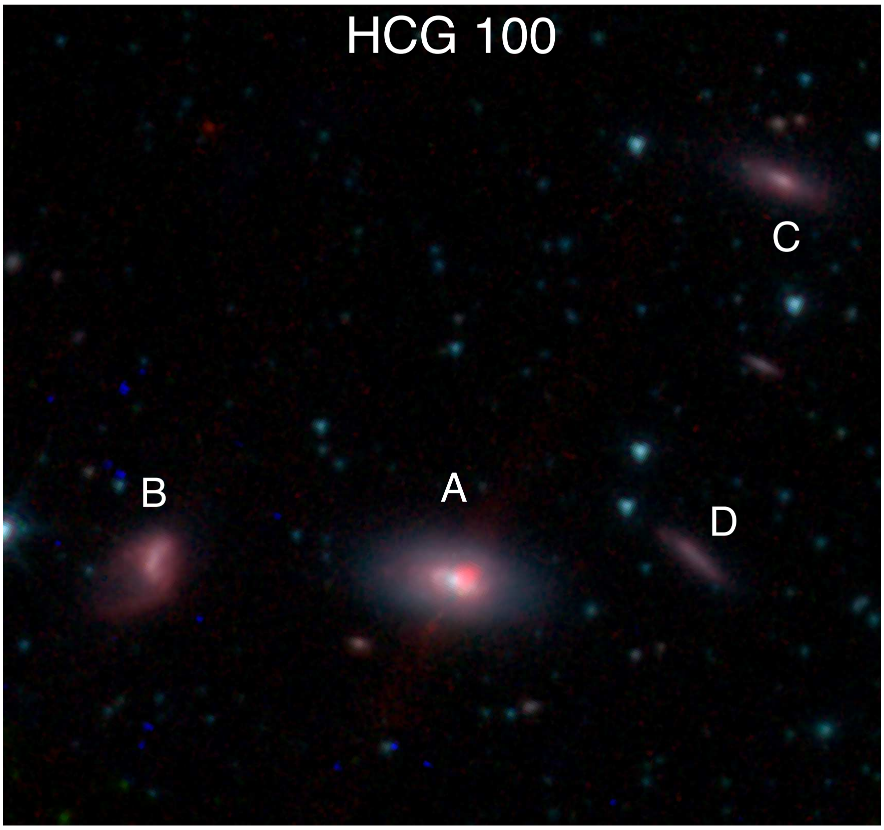

Figure B.38: IRAC true color image. Blue, green and red colors correspond to 3.6, 4.5 and 8.0μm bands, respectively.

group id	apparent members	outliers	Dynamical state
HCG 100	4	-	Young

References

Adelman-McCarthy, J.K. (2008). The sixth data release of the sloan digital sky survey. *ApJS*, **175**. 26

Aguerri, J., Assendorp, R., Longo, G., Braun, M. & Richter, G. (2006). Diffuse light in hickson compact groups: the dynamically young system hcg 44. *A&A*, **457**. 104

Allam, S., Assendorp, R., Longo, G., Braun, M. & Richter, G. (1996). Far infrared properties of hickson compact groups of galaxies. i. high resolution iras maps and fluxes. *A&AS*, **117**. 49, 109

Appleton, P.N., Xu, K.C., Reach, W., Dopita, M.A., Gao, Y., Lu, N., Popescu, C.C., Sulentic, J.W., Tuffs, R.J. & Yun, M.S. (2006). Powerful high-velocity dispersion molecular hydrogen associated with an intergalactic shock wave in stephan's quintet. *ApJ*, **639**. 23, 105

Arnouts, S., Walcher, C.J., Le Fèvre, O., Zamorani, G., Ilbert, O., Le Brun, V., Pozzetti, L., Bardelli, S., Tresse, L., Zucca, E. & coauthors, . (2007). The swire-vvds-cfhtls surveys: stellar mass assembly over the last 10 gyr. evidence for a major build up of the red sequence between z = 2 and z = 1. *A&A*, **476**. 55

Athanassoula, E., Makino, J. & Bosma, A. (1997). Evolution of compact groups of galaxies - i. merging rates. *MNRAS*, **286**. 133

Bahcall, J.N. & Tremaine, S. (1981). Methods for determining the masses of spherical systems. i - test particles around a point mass. *ApJ*, **244**. 102

Balogh, M.L., Baldry, I.K., Nichol, R., Miller, C., Bower, R. & Glazebrook, K. (2004). The bimodal galaxy color distribution: Dependence on luminosity and environment. *ApJ*, **625**. 22

Beichman, G., Neugebauer, G. & Chester, T. (1988). *IRAS Explanatory Supplement*. NASA. 48

Bell, E.F. & de Jong, R.S. (2001). Stellar mass-to-light ratios and the tully-fisher relation. *ApJ*, **550**. 52

Bell, E.F., McIntosh, D.H., Katz, N. & Weinberg, M.D. (2003). The optical and near-infrared properties of galaxies. i. luminosity and stellar mass functions. *ApJS*, **149**. 52, 64, 66, 68, 69, 70, 76, 112

Benson, A.J. (2010). Galaxy formation theory. *PhR*, **495**. 5

REFERENCES

Bertin, E. & Arnouts, S. (1996). Sextractor: Software for source extraction. *A&AS*, **117**. 36, 41

Bicay, M.D. & Giovanelli, R. (1987). Far-infrared properties of cluster galaxies. *ApJ*, **321**. 21

Bigiel, F., Leroy, A., Walter, F., Brinks, E., de Blok, W.J.G., Madore, B. & Thornley, M.D. (2008). The star formation law in nearby galaxies on sub-kpc scales. *AJ*, **136**. 84

Bitsakis, T., Charmandaris, V., Le Floc'h, E., Diaz-Santos, T., Slater, S.K., Xilouris, E. & Haines, M.P. (2010). A mid-ir study of hickson compact groups. i. probing the effects of environment in galaxy interactions. *A&A*, **517**. 25, 33, 57, 64, 82, 86

Bitsakis, T., T., Charmandaris, V., Da Cunha, E., Diaz-Santos, T., Le Floc'h, E. & Magdis, G. (2011). A mid-ir study of hickson compact groups. ii. multiwavelength analysis of the complete galex-spitzer sample. *A&A*, **533**. 25, 26, 49, 58, 70, 74, 81, 82, 88, 94, 96, 100, 102, 104, 109

Blanton, M.R. & Roweis, S. (2007). K-corrections and filter transformations in the ultraviolet, optical, and near-infrared. *AJ*, **133**. 68

Borthakur, S., Yun, M.S. & Verdes-Montenegro, L. (2010). Detection of diffuse neutral intragroup medium in hickson compact groups. *ApJ*, **710**. 22, 74, 104

Brandl, B.R., Bernard-Salas, J., Spoon, H.W.W., Devost, D., Sloan, G.C., Guilles, S., Wu, Y., Houck, J.R., Weedman, D.W., Armus, L. & coauthors, . (2006). The mid-infrared properties of starburst galaxies from spitzer-irs spectroscopy. *ApJ*, **653**. 96

Bressan, A., Panuzzo, P., Buson, L., Clemens, M., Granato, G.L., Rampazzo, R., Silva, L., Valdes, J.R., Vega, O. & Danese, L. (2006). Spitzer irs spectra of virgo early-type galaxies: Detection of stellar silicate emission. *ApJ*, **639**. 86

Brinchmann, J., Charlot, S., White, S.D.M., Tremonti, C., Kauffmann, G., Heckman, T. & Brinkmann, J. (2004). The physical properties of star-forming galaxies in the low-redshift universe. *MNRAS*, **351**. 10, 54, 55, 60, 62, 63, 70, 71

Bruzual, A.G. (1983). Spectral evolution of galaxies. i - early-type systems. *AJ*, **273**. 62

Bruzual, G. & Charlot, S. (2003). Stellar population synthesis at the resolution of 2003. *MNRAS*, **344**. 52, 58

Buat, V., Iglesias-Páramo, J., Seibert, M., Burgarella, D., Charlot, S., Martin, D.C. *et al.* (2005). Dust attenuation in the nearby universe: A comparison between galaxies selected in the ultraviolet and in the far-infrared. *ApJ*, **619**. 54, 67, 68

Calzetti, D., Kennicutt, R.C., Engelbracht, C.W., Leitherer, C. *et al.* (2007). The calibration of mid-infrared star formation rate indicators. *ApJ*, **666**. 53, 64, 65, 76

Carroll, B.W. & Ostlie, D.A. (2006). *An introduction to modern galactic astrophysics and cosmology*. Pearson Education Inc. 9, 12

Cesarsky, C.J. & et al. (1996). Isocam in flight. *A&A*, **315**. 46

Chabrier, G. (2003). Galactic stellar and substellar initial mass function. *PASP*, **115**. 53, 54, 58

Charlot, S. & Fall, S.M. (2000). A simple model for the absorption of starlight by dust in galaxies. *ApJ*, **539**. 58, 59

Charlot, S., Kauffmann, G., Longhetti, M., Tresse, L., White, S.D.M., Maddox, S.J. & Fall, S.M. (2002). Star formation, metallicity and dust properties derived from the stromlo-apm galaxy survey spectra. *MNRAS*, **330**. 55, 62

Charmandaris, V. (2008). Mid-infrared spectroscopic diagnostics of galactic nuclei. *ASPC*, **381**. 96

Chary, R. & Elbaz, D. (2001). Interpreting the cosmic infrared background: Constraints on the evolution of the dust-enshrouded star formation rate. *ApJ*, **556**. 55

Cluver, M.E., Appleton, P.N., Boulanger, F., Guillard, P., Ogle, P., Duc, P.A., Lu, N., Rasmussen, J. *et al.* (2010). Powerful h2 line cooling in stephan's quintet. i. mapping the significant cooling pathways in group-wide shocks. *ApJ*, **710**. 107

Cluver, M.E., Ogle, P., Rasmussen, J., Jarrett, T.H., Lisenfeld, U., Guillard, P., Verdes-Montenegro, L., Antonucci, R., Bitsakis, T., Charmandaris, V., Boulanger, F., Egami, E., Xu, K.C. & Yun, M.S. (2012). Enhanced warm h2 emission in compact groups of galaxies: Evolution in the mid-ir green valley. *ApJ*, **in press**. 105, 106, 107

Combes, F., Boisse, P., Mazure, A. & Blanchard, A. (2002). *Galaxies and cosmology*. Springer. 9, 13, 16

Coulais, A. & Abergel, A. (2000). Transient correction of the lw-isocam data for low contrasted illumination. *A&AS*, **141**. 48

da Cunha, E., Charlot, S. & Elbaz, D. (2008). A simple model to interpret the ultraviolet, optical and infrared emission from galaxies. *MNRAS*, **388**. 54, 55, 57, 58, 59, 60, 65, 66, 67, 68, 73, 76, 78, 82, 84, 96, 109, 131

da Cunha, E., Charmandaris, V., Díaz-Santos, T., Armus, L., Marshall, J.A. & Elbaz, D. (2010a). Exploring the physical properties of local star-forming ulirgs from the ultraviolet to the infrared. *A&A*, **523**. 68

da Cunha, E., Eminian, C., Charlot, S. & Blaizot, J. (2010b). New insight into the relation between star formation activity and dust content in galaxies. *MNRAS*, **403**. 68

Daddi, E., Elbaz, D., Walter, F., Bournaud, F., Salmi, F., Carilli, C., Dannerbauer, H., Dickinson, M., Monaco, P. & Riechers, D. (2010). Different star formation laws for disks versus starbursts at low and high redshifts. *ApJ*, **714**. 23

Dale, D.A., Bendo, G.J., Engelbracht, C.W., Gordon, K.D. & other (2005). Infrared spectral energy distributions of nearby galaxies. *ApJ*, **633**. 32, 44, 86

Dale, D.A., Cohen, S.A., Johnson, L.C., Schuster, M.D., Calzetti, D., Engelbracht, C.W. *et al.* (2009). The spitzer local volume legacy: Survey description and infrared photometry. *ApJ*, **703**. 99

REFERENCES

Dressler, A. (1980). Galaxy morphology in rich clusters - implications for the formation and evolution of galaxies. *ApJ*, **236**. 22

Elitzur, M. (2008). The toroidal obscuration of agn. *NewAR*, **52**. 96

Fazio, G.G., Hora, J.L., Allen, L.E., Ashby, M.L.N., Barmby, P. *et al.* (2004). The infrared array camera (irac) for the spitzer space telescope. *ApJS*, **154**. 44

Goto, T., Szapudi, I. & Granett, B.R. (2012). Cross-correlation of wise galaxies with the cosmic microwave background. *MNRAS*, **422**. 53

Haines, C.P., Gargiulo, A., La Barbera, F., Mercurio, A., Merluzzi, P. & Busarello, G. (2007). The different physical mechanisms that drive the star formation histories of giant and dwarf galaxies. *MNRAS*, **381**. 28

Haines, M.P., . Gargiulo, A. & Merluzzi, P. (2008). The sdss-galex viewpoint of the truncated red sequence in field environments at z 0. *MNRAS*, **385**. 33, 89, 90, 91, 118, 120

Hao, L.e.a. (2005). Active galactic nuclei in the sloan digital sky survey. i. sample selection. *AJ*, **129**. 39

Heller, C.H. (1995). Encounters with protostellar disks. ii. disruption and binary formation. *ApJ*, **455**. 14

Hernquist, L., Katz, N. & Weinberg, D.H. (1995). Physically detached 'compact groups'. *ApJ*, **442**. 20

Hickson, P. (1982). Systematic properties of compact groups of galaxies. *ApJ*, **255**. 20, 21, 25, 26, 86, 127, 130

Hickson, P. (1997). Compact groups of galaxies. *ARA&A*, **35**. 20

Hickson, P., Kindl, E. & Auman, J.R. (1989). A photometric catalog of compact groups of galaxies. *ApJS*, **70**. 21, 38

Hickson, P., Mendes de Oliveira, C., Huchra, J.P. & Palumbo, G.G. (1992). Dynamical properties of compact groups of galaxies. *ApJ*, **399**. 102

Houck, J.R., Roellig, T.L., van Cleve, J., Forrest, W.J., Herter, T., Lawrence, C.R. *et al.* (2004). The infrared spectrograph (irs) on the spitzer space telescope. *ApJS*, **154**. 44

Hwang, H.S., Elbaz, D., Lee, J.C., Jeong, W.S., Park, C., Lee, M.G. & Lee, H.M. (2010). Environmental dependence of local luminous infrared galaxies. *A&A*, **522**. 100

Iglesias-Páramo, J., Buat, V., Takeuchi, T.T., Xu, K., Boissier, S. *et al.* (2006). Star formation in the nearby universe: The ultraviolet and infrared points of view. *ApJS*, **164**. 54, 65

Ilbert, O., Capak, P., Salvato, M., Aussel, H., McCracken, H.J. *et al.* (2009). Cosmos photometric redshifts with 30-bands for 2-deg2. *ApJ*, **690**. 55

Johnson, K.E., Hibbard, J.E., Gallagher, S.C., Charlton, J.C., Hornschemeier, A.E., Jarrett, T.H. & Reines, A.E. (2007). The infrared properties of hickson compact groups. *AJ*, **134**. 22, 46, 98

Kaneda, H., Onaka, T., Sakon, I., Kitayama, T., Okada, Y. & Suzuki, T. (2008). Properties of polycyclic aromatic hydrocarbons in local elliptical galaxies revealed by the infrared spectrograph on spitzer. *ApJ*, **684**. 86

Katgert, P., Mazure, A., Perea, J., den Hartog, R., Moles, M. *et al.* (1996). he eso nearby abell cluster survey. i. description of the dataset and definition of physical systems. *A&A*, **319**. 17

Kauffmann, G., Heckman, T.M., Tremonti, C., Brinchmann, J., Charlot, S., White, S.D.M., Ridgway, S.E., Brinkmann, J. *et al.* (2003a). The host galaxies of active galactic nuclei. *MNRAS*, **346**. 30, 39

Kauffmann, G., Heckman, T.M., White, S.D.M., Charlot, S., Tremonti, C., Brinchmann, J., Bruzual, G., Peng, E.W. *et al.* (2003b). Stellar masses and star formation histories for 105 galaxies from the sloan digital sky survey. *MNRAS*, **341**. 10, 63, 68, 69, 70, 96, 112

Kennicutt, J., R. C., Armus, L., Bendo, G., Calzetti, D. *et al.* (2003). Sings: The sirtf nearby galaxies survey. *PASP*, **115**. 32, 99

Kennicutt, R. (1998). Star formation in galaxies along the hubble sequence. *ARA&A*, **36**. 7, 35

Kewley, L.J., Groves, B., Kauffmann, G. & Heckman, T. (2006). The host galaxies and classification of active galactic nuclei. *MNRAS*, **372**. 10, 30, 39, 96

Kong, X., Charlot, J., S. andBrinchmann & Fall, S.M. (2004). Star formation history and dust content of galaxies drawn from ultraviolet surveys. *MNRAS*, **349**. 54, 68, 70

Lacy, M., Storrie-Lombardi, L.J., Sajina, A., Appleton, P.N., Armus, L., Chapman, S.C., Choi, P.I. *et al.* (2004). Obscured and unobscured active galactic nuclei in the spitzer space telescope first look survey. *ApJS*, **154**. 107

Larson, R.B. & Tinsley, B.M. (1978). Star formation rates in normal and peculiar galaxies. *ApJ*, **219**. 11

Leitherer, C., Schaerer, D., Goldader, J.D., González Delgado, R.M. *et al.* (1999). Starburst99: Synthesis models for galaxies with active star formation. *ApJ*, **123**. 89

Leon, S., Combes, F. & Menon, T.K. (1998). Molecular gas in galaxies of hickson compact groups. *A&A*, **330**. 84

Li, C. & White, S.D.M. (2009). The distribution of stellar mass in the low-redshift universe. *MNRAS*, **398**. 68, 69

Lonsdale, J.C., F., D. & E., H.S. (2006). Ultraluminous infrared galaxies. *arXiv*, **0603031**. 8

Malin, D.F. & Carter, D. (1980). Giant shells around normal elliptical galaxies. *nature*, **285**, 643–645. 13

REFERENCES

Mamon, G.A. (1986). Are compact groups of galaxies physically dense? *ApJ*, **307**. 20

Martínez, M.A., Del Olmo, A., Coziol, R. & Perea, J. (2010). Agn population in hickson compact groups. i. data and nuclear activity classification. *AJ*, **139**. 21, 39

Martinez-Badenes, V., Verdes-Montenegro, L., Lisenfeld, U. & Espada, D. (2010). Molecular gas in hickson compact groups. *ASPC*, **421**. 102

McConnachie, A.W., Ellison, S.L. & Patton, D.R. (2008). Compact groups in theory and practice - i. the spatial properties of compact groups. *MNRAS*, **387**. 20, 28

McConnachie, A.W., Patton, D.R., Ellison, S.L. & Simard, L. (2009). Compact groups in theory and practice - iii. compact groups of galaxies in the sixth data release of the sloan digital sky survey. *MNRAS*, **395**. 24, 26, 28, 29, 39, 111, 130

Mendes de Oliveira, C. & Hickson, P. (1993). Morphology of galaxies in compact groups. *ApJ*, **427**. 21

Mendes de Oliveira, C., Coelho, P., González, J.J. & Barbuy, B. (2005). Ages, metallicities, and -element enhancement for galaxies in hickson compact groups. *AJ*, **130**. 133

Mendes de Oliveira, C.L. & Carrasco, E.R. (2007). Compact group-fossil group connection: Observations of a massive compact group at z=0.22. *ApJ*, **670**. 19

Meurer, G.R., Heckman, T.M. & Calzetti, D. (1999). Dust absorption and the ultraviolet luminosity density at z 3 as calibrated by local starburst galaxies. *ApJ*, **427**. 53, 54, 67, 68, 70, 71

Mihos, J.C. & Hernquist, L. (1996). Gasdynamics and starbursts in major mergers. *ApJ*, **464**. 120, 124

Morrissey, P. & Team, G.S. (2005). A flight performance update for the galaxy evolution explorer (galex). *AAS*, **37**. 35

Mulchaey, J.S., Davis, D.S., Mushotzky, R.F. & Burstein, D. (2003). An x-ray atlas of groups of galaxies. *ApJS*, **145**. 104

Ogle, P., Boulanger, P., F. Guillard, Evans, D.A., Antonucci, R., Appleton, P.N., Nesvadba, N. & Leipski, C. (2010). Jet-powered molecular hydrogen emission from radio galaxies. *ApJ*, **724**. 105

Okada, Y., Murakami, N., Yasuda, A. & et al. (2008). Version 1.3, http://www.ir.isas.jaxa.jp/astro-f/observation/. *AKARI FIS Data Users Manual*. 49

Panuzzo, P., Rampazzo, R., Bressan, A., Vega, O., Annibali, F., Buson, L.M., Clemens, M.S. & Zeilinger, W.W. (2011). Nearby early-type galaxies with ionized gas. vi. the spitzer-irs view. basic data set analysis and empirical spectral classification. *A&A*, **528**. 86

Park, C. & Hwang, H.S. (2009). Interactions of galaxies in the galaxy cluster environment. *ApJ*, **699**. 100

Peebles, P.J.E. (1968). Formation of galaxies in classical cosmology. *Nature*, **220**. 5

Peeters, E., Mattioda, A.L., Hudgins, D.M. & Allamandola, L.J. (2004). Polycyclic aromatic hydrocarbon emission in the 15-21 micron region. *ApJ*, **617**. 9

Plauchu-Frayn, I., Del Olmo, A., Coziol, R. & Torres-Papaqui, J.R. (2012). The star formation histories of hcg galaxies. *A&A*, **546**. 133

Ponman, T.J., Bourner, P.D.J., Ebeling, H. & Böhringer, H. (1996). A rosat survey of hickson's compact galaxy groups. *MNRAS*, **283**. 20, 104, 105, 130

Press, W. & Schechter, P. (1974). Formation of galaxies and clusters of galaxies by self-similar gravitational condensation formation of galaxies and clusters of galaxies by self-similar gravitational condensation formation of galaxies and clusters of galaxies by self-similar gravitational condensation formation of galaxies and clusters of galaxies by self-similar gravitational condensation. *ApJ*, **187**. 5

Proctor, R.N., Forbes, D.A., Hau, G.K.T., Beasley, M.A., De Silva, G.M., Contreras, R. & Terlevich, A.I. (2004). Ages and metallicities of hickson compact group galaxies. *MNRAS*, **349**. 133

Rieke, G.H., Loken, K., Rieke, M.J. & Tamblyn, P. (1993). Starburst modeling of m82 - test case for a biased initial mass function. *ApJ*, **412**. 53

Rieke, G.H., Young, E.T., Engelbracht, C.W., Kelly, D.M., Low, F.J., Haller, E.E. *et al.* (2004). The multiband imaging photometer for spitzer (mips). *ApJS*, **154**. 44

Rieke, G.H., Alonso-Herrero, A., Weiner, B.J., Pérez-González, P.G., Blaylock, M., Donley, J.L. & Marcillac, D. (2009). Determining star formation rates for infrared galaxies. *ApJ*, **692**. 53, 70

Rood, H.J. & Struble, M.F. (1994). coincidence between a number of hickson compact groups and loose groups or clusters. *PASP*, **106**. 20

Rosenberg, J.L., Wu, Y., Le Floc'h, E., Charmandaris, V. *et al.* (2008). Dust properties and star formation rates in star-forming dwarf galaxies. *ApJ*, **674**. 65

Salim, S., Rich, R.M., Charlot, S., Brinchmann, J. *et al.* (2007). Uv star formation rates in the local universe. *ApJS*, **173**. 53, 65, 71

Sanders, D.B. & Morabel, I.F. (1996). Luminous ir galaxies. *A&A review*, **34**. 49

Sanders, D.B., Scoville, N.Z. & Soifer, B.T. (1991). Molecular gas in luminous ir galaxies. *ApJ*, **370**. 108

Schneider, P. (2006). *Extragalactic astronomy and cosmology*. Springer. 15, 17

Schweizer, F. & Seitzer, P. (1988). Ripples in disk galaxies. *ApJ*, **328**. 13

Shimada, M., Ohyama, Y., Nishiura, S., Murayama, T. & Taniguchi, Y. (2000). The nuclear activity of galaxies in the hickson compact groups. *AJ*, **119**. 21, 39

REFERENCES

Shlosman, I., Frank, J. & Begelman, M.C. (1989). Bars within bars - a mechanism for fuelling active galactic nuclei. *Nature*, **338**. 14

Simard, L., Mendel, J.T., Patton, D.R., Ellison, S.L. & McConnachie, A.W. (2011). A catalog of bulge+disk decompositions and updated photometry for 1.12 million galaxies in the sloan digital sky survey. *ApJS*, **196**. 31, 122

Skrutskie, M.F. (2006). The two micron all sky survey (2mass). *AJ*, **131**. 42

Slater, S.K. (2004). Deep near-ir imaging of hickson compact groups: Galaxy evolution during acute interactions. *AAS*, **204**. 41

Smith, B.J., Struck, C., Hancock, M., Appleton, P.N., Charmandaris, V. & Reach, W.T. (AJ). The spitzer spirals, bridges, and tails interacting galaxy survey: Interaction-induced star formation in the mid-infrared. *2007*, **133**. 33, 57, 83

Smith, J.D.T., Draine, B.T., Dale, D.A., Moustakas, J., Kennicutt, J., R. C. *et al.* (2007). The mid-infrared spectrum of star-forming galaxies: Global properties of polycyclic aromatic hydrocarbon emission. *ApJ*, **656**. 86, 87, 96

Sparke, L. & Gallagher, J.S. (2000). *Galaxies in the Universe*. Cambridge University Press. 8, 19

Starck, J.L., Abergel, A., Aussel, H., Sauvage, M., Gastaud, R., Claret, A., Desert, X., Delattre, C. & Pantin, E. (1999). Isocam data processing. *A&AS*, **134**. 46

Stern, D., Eisenhardt, P., Gorjian, V., Kochanek, C.S., Caldwell, N. *et al.* (2005). Mid-ir selection of active galaxies. *ApJ*, **631**. 96, 97

Strateva, I., Ivezić, G.R., Z. Knapp, Narayanan, V.K., Strauss, M.A. *et al.* (2001). Color separation of galaxy types in the sloan digital sky survey imaging data. *AJ*, **122**. 89

Struck, C. (1999). Galaxy collisions. *Physical Reports*, **321**, 1–137. 10, 23, 77, 82

Temi, P., Brighenti, F., Mathews, W.G. & Bregman, J.D. (2004). Cold dust in early-type galaxies. i. observations. *ApJS*, **151**. 32

Toomre, A. (1977). Mergers and some consequences. *egsp.conf*, **401**. 12, 13

Toomre, A. & Toomre, J. (1972). Galactic bridges and tails. *ApJ*, **178**, 623–666. 11

Tremonti, C.A., Heckman, T.M., Kauffmann, G., Brinchmann, J. *et al.* (2004). The origin of the mass-metallicity relation: Insights from 53,000 star-forming galaxies in the sloan digital sky survey. *ApJ*, **613**. 133

Tzanavaris, P., Hornschemeier, A.E., Gallagher, S.C., Johnson, K.E., Gronwall, C., Immler, S., Reines, A.E., Hoversten, E. & Charlton, J.C. (2010). Ultraviolet+infrared star formation rates: Hickson compact groups with swift and spitzer. *ApJ*, **716**. 22, 98

Verdes-Montenegro, L., Yun, M.S., Williams, B.A., Huchtmeier, W.K., Del Olmo, A. & Perea, J. (2001). Where is the neutral atomic gas in hickson groups? *A&A*, **377**. 21, 22, 74, 75, 77, 102, 103, 104, 105, 127

Véron-Cetty, M.P. & Véron, P. (2006). A catalogue of quasars and active nuclei: 12th edition. *A&A*, **455**. 39

Walker, L.M., Johnson, K.E., Gallagher, S.C., Hibbard, J.E., Hornschemeier, A.E., Charlton, J.C. & Jarrett, T.H. (2010). Mid-infrared evidence for accelerated evolution in compact group galaxies. *ASPC*, **423**. 22, 99, 107

Weedman, D.W., Hao, L., Higdon, S.J.U., Devost, D., Wu, Y., Charmandaris, V., Brandl, B., Bass, E. & Houck, J.R. (2005). Mid-infrared spectra of classical agns observed with the spitzer space telescope. *ApJ*, **633**. 96

Williams, B.A., McMahon, P.M. & van Gorkom, J.H. (1991). Vla neutral hydrogen imaging of compact groups of galaxies. ii - hcg 31, 44, and 79. *AJ*, **101**. 104

Wright, E.L., Eisenhardt, P.R.M., Mainzer, A.K., Ressler, M.E., Cutri, R.M., Jarrett, T. *et al.* (2010). The wide-field infrared survey explorer (wise): Mission description and initial on-orbit performance. *AJ*, **140**. 48

Wyder, T.K., Martin, D.C., Schiminovich, D., Seibert, M., Budavári, T., Treyer, M.A. *et al.* (2007). The uv-optical galaxy color-magnitude diagram. i. basic properties. *ApJS*, **173**. 89, 118, 120

Zibetti, S., Charlot, S. & Rix, H.W. (2009). Resolved stellar mass maps of galaxies - i. method and implications for global mass estimates. *MNRAS*, **400**. 52, 65

Zibetti, S., Gallazzi, A., Charlot, S., Pasquali, A. & Pierini, D. (2012). Direct constraints on the impact of tp-agb stars on the sed of galaxies from near-infrared spectroscopy. *IAUS*, **284**. 52